Theoretical Approaches in Non-Linear Dynamical Systems

Editors

JAN AWREJCEWICZ, MAREK KAŹMIERCZAK, JERZY MROZOWSKI

PREFACE

The 15th International Conference "Dynamical Systems - Theory and Applications" (DSTA 2019, 2-5 December, 2019, Lodz, Poland) gathered a numerous group of outstanding scientists and engineers who deal with widely understood problems of theoretical and applied dynamics.

Organization of the conference would not have been possible without great effort of the staff of the Department of Automation, Biomechanics and Mechatronics of the Lodz University of Technology. The patronage over the conference has been taken by the Committee of Mechanics of the Polish Academy of Sciences and Ministry of Science and Higher Education of Poland.

It is a great pleasure that our event was attended by over **180** researchers from **35** countries all over the world, who decided to share the results of their research and experience in different fields related to dynamical systems.

This year, the DSTA Conference Proceedings were split into two volumes entitled *"Theoretical Approaches in Non-Linear Dynamical Systems"* and *"Applicable Solutions in Non-Linear Dynamical Systems"*. In addition, DSTA 2019 resulted in three volumes of Springer Proceedings in Mathematics and Statistics entitled *"Control and Stability of Dynamical Systems", "Mathematical and Numerical Approaches in Dynamical Systems"* and *"Dynamical Systems in Mechatronics and Life Sciences"*. Also, many outstanding papers will be recommended to special issues of renowned scientific journals.

The DSTA Conference Proceedings include papers covering the following topics:
- asymptotic methods in non-linear dynamics,
- bifurcation and chaos in dynamical systems,
- control in dynamical systems,
- dynamics in life sciences and bioengineering,
- engineering systems and differential equations,
- non-smooth systems
- mathematical approaches to dynamical systems
- original numerical methods of vibration analysis,
- stability of dynamical systems,
- vibrations of lumped and continuous systems,
- other problems.

Proceedings of the 15th Conference „Dynamical Systems - Theory and Applications" summarize **106** papers of university teachers and students, researchers and engineers from all over the world. The papers were selected by the Scientific Committee of DSTA 2019 from **360** papers submitted to the conference. Therefore, the reader is provided with an overview of recent developments in dynamical systems and can study the most progressive tendencies in this field of science.

Our experience shows that a broad thematic scope comprising dynamical systems encourages researchers to exchange their opinions on different branches of dynamics. We think that the vivid discussion will influence positively creativity and will result in effective solutions of many problems of dynamical systems in mechanics and physics, both in terms of theory and applications.

We do hope that DSTA 2019 will contribute to establishing new and tightening the already existing relations and scientific and technological cooperation between Polish and foreign institutions.

On behalf of both
Scientific and Organizing Committees

Chairman
Professor Jan Awrejcewicz

CONTENTS

The use of the dynamic vibration absorber for energy harvesting

Leo Acho Zuppa, Jan Awrejcewicz, Nataliya Losyeva, Volodymyr Puzyrov,
Nina Savchenko

Abstract: Vibration energy is abundantly present in many natural and artificial systems and can be assembled by various mechanisms, mainly using piezoelectric and electromagnetic means. In the present article, the electromechanical system with two degrees of freedom is considered. To the main mass, whose vibrations are to be reduced, an additional element (dynamical vibration absorber or DVA) is attached. The DVA consists of a spring, damping and piezoelectric elements for energy harvesting. The goal is to reduce the vibration of the main structure and at the same time collect energy from the vibration of the connected vibration absorber. It is shown that the piezoelectric element allows the effective energy harvesting and at the same has very limit influence on reducing the amplitude of oscillations of main mass.

1. Introduction

In the past few years, interest in energy harvesting has been significantly increasing, and the number of research reports over the past decade has been steadily growing up [1, 3, 4, 5, 6, 7, 9, 10, 11, 12, 13]. A harvesting system can collect electrical energy by converting environmental energy sources such as thermal energy, wind, or mechanical motion. This work is devoted to the possibility of converting the energy of mechanical vibrations into electrical energy, and also explores the effect of energy collection on the overall dynamics.

There are three common conversion mechanisms for energy harvesting, such as piezoelectric, electromagnetic and electrostatic. Among other things, piezoelectricity is one of the most attractive transfer mechanisms during mechanical energy conversion. The advantages of using piezoelectric materials in mechanical vibration systems include their higher specific power and ease of implementation. Piezoelectric materials have the ability to generate electrical stress during deformation due to vibrations (direct impact), and, on the other hand, they are deformed when exposed to external stress (reverse impact). For the energy collection mechanism, this is a direct piezoelectric effect that allows the material to absorb the mechanical energy of vibration from its main structure or environment and converts it into electrical energy, and thus forms the basis of the vibration-based piezoelectric energy collection area.

In the present report we consider the 2–DoF mechanical system with piezoelectric element attached under the external harmonic excitation in the vicinity of resonance. The paper is organized as following. In Section 2 the problem formulation and some auxiliary manipulations are given. In Section 3 the tuning methodology for reducing the maximal responses of the host structure is described. Section 4 deals with optimization of piezoelectric characteristics in order to maximize the harvested power.

2. Formulation of the problem

The primary structure is assumed to be a single degree of freedom system as shown in Fig. 1. The mass, stiffness, and the damping of the primary structure are represented by m_0, k_0, and c_0, respectively, whereas the energy harvesting DVA has an equivalent mass, equivalent stiffness, and damping as m_a, k_a, and c_a, respectively. The electrical capacitance and resistance are denoted by C_p and R_l, respectively. The parameter θ characterizing the coupling between the electrical and mechanical parts of the harvester. The dynamics of the primary mass (m_0), the absorber mass (m_a), and voltage flow can be expressed by three coupled ordinary differential equations [2, 9] as

$$m_0\ddot{x}_0 + c_0\dot{x}_0 + k_0x_0 - k_h(x_a - x_0) - c_a(\dot{x}_a - \dot{x}_0) = F_0\exp^{i\omega t}, \tag{1}$$

$$m_a\ddot{x}_a + c_a(\dot{x}_a - \dot{x}_0) + k_a(x_a - x_0) - \theta v = 0, \tag{2}$$

$$C_p\dot{v} + \frac{v}{R_l} + \dot{x}_a = 0, \tag{3}$$

where x_0 and x_a are the displacement of the primary mass and absorber mass, respectively. The voltage across the load resistor is denoted by v. The electromechanical coupling and the mechanical force are modeled as proportional to the voltage across the piezoceramic in Eq. (2). Equation (3) is obtained from the electrical circuit, where the voltage across the load resistance arises from the mechanical strain through the electromechanical coupling, and the capacitance of the piezoceramic C_p. The primary structure is assumed to be driven by a harmonic excitation with amplitude F_0.

In terms of dimensionless parameters the amplitudes of steady state harmonic responses are

$$
\begin{aligned}
X_0 &= F_0\frac{-(2\zeta a + b)\mu g^2 + bk\mu + [-a\mu g^3 + ([2\zeta b + ak]\mu + p^2)g]i}{\Delta_{Re} + i\Delta_{Im}}, \\
X_a &= -F_0\frac{b\mu g^2 + (a\mu g^3 - p^2 g)i}{\Delta_{Re} + i\Delta_{Im}}, \\
V &= F_0\frac{(-2\zeta\mu pg^2 + k\mu pgi)}{\Delta_{Re} + i\Delta_{Im}},
\end{aligned} \tag{4}
$$
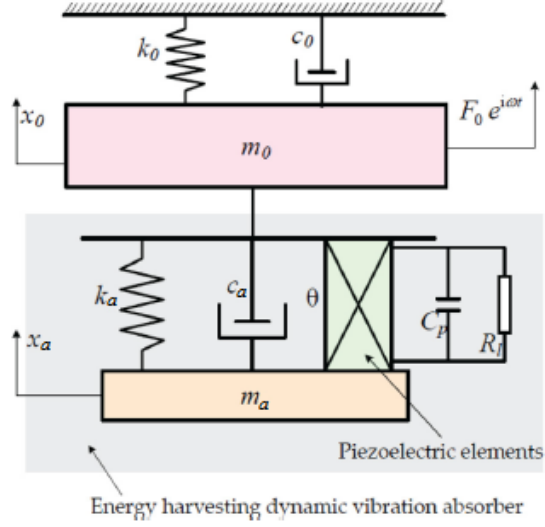
Figure 1. Energy harvesting DVA attached to a primary system.

where $\Delta_{Re} = -[2\zeta a\mu^2 + (2\zeta a + b)\mu]g^4 + (bk\mu^2 + [2\zeta(p^2 + a) + b(k + 1)]\mu)g^2 - bk\mu$,

$\Delta_{Im} = -a\mu g^5 + [(2\zeta b + ak)\mu^2 + [a(k + 1) + 2\zeta b]\mu + p^2]g^3 - [(k(p^2 + a) + 2\zeta b)\mu + p^2]$

and $\mu = m_a/m_0$ is the mass ratio; $\omega_a = \sqrt{k_a/m_a}$ - undamped natural frequency of the DVA considered separately; $\omega_0 = \sqrt{k_0/m_0}$ - undamped natural frequency of the primary system considered separately; $k = \omega_h^2/\omega_0^2$ - tuning factor; $g = \omega/\omega_0$ - forcing frequency ratio; $\zeta = c_a/(2m_a\omega_0)$ - damping ratio; $p = \theta/(\omega_0^2 m_0)$, $a = C_p/(\omega_0^2 m_0)$, $b = 1/(\omega_0^2 m_0 R_l)$.

$$\frac{|X_0|}{(X_0)_{st}} = \sqrt{\frac{(-[2\zeta a + b]\mu g^2 + bk\mu)^2 + (-a\mu g^3 + ([2\zeta b + ak]\mu + p^2)g)^2}{\Delta_{Re}^2 + \Delta_{Im}^2}},$$

$$\frac{|V|}{(X_0)_{st}} = \sqrt{\frac{(-2\zeta\mu pg^2)^2 + (k\mu pg)^2}{\Delta_{Re}^2 + \Delta_{Im}^2}},$$

(5)

where $(X_0)_{st} = F_0/k_0$ – static displacement of the primary mass.

3. Minimizing the responses of the primary mass

3.1. Analytical study

At the beginning, note that the $\lambda-$matrix of the linear ODE system (1) can be written in the following form

$$
\begin{pmatrix}
(1+\mu)g^2\lambda^2 & \mu g^2\lambda^2 & -p \\
\mu g^2\lambda^2 & \mu g^2\lambda^2 + \mu gh\lambda + \kappa & -p \\
pg\lambda & pg\lambda & ag\lambda + b
\end{pmatrix}. \tag{6}
$$

Taking into account that replacing the parameter p with $\widetilde{p}\sqrt{b}$ and the variable v with $\widetilde{v}/\sqrt{b}$, we can formally put the value of parameter b equal to 1. For the sake of simplicity, the symbol "~" is omitted below.

Our first goal is to minimize the peaks of the amplitude-frequency curve, that is, the choice of such parameters of the absorber and piezoelectric element, in which the responses of the host system do not exceed a certain value (in conditions of proximity of frequencies ω and ω_0.

Let us consider a function

$$
f(\mu, k, h, \gamma, a, p) = \frac{\alpha_3\gamma^3 + \alpha_2\gamma^2 + \alpha_1\gamma + \alpha_0}{\beta_5\gamma^5 + \beta_4\gamma^4 + \beta_3\gamma^3 + \beta_2\gamma^2 + \beta_1\gamma + \beta_0},
$$

$$
\alpha_3 = a^2\mu^2, \ \alpha_2 = (a^2h^2 - 2a^2k + 1)\mu^2 - 2ap^2\mu, \ \alpha_1 = (a^2k^2 + h^2 - 2k)\mu^2 +
$$

$$
+2(ak+h)\mu p^2 + p^4, \ \alpha_0 = k^2\mu^2, \ \beta_5 = a^2\mu^2, \ \beta_4 = a^2h^2\mu^4 + 2a^2(h^2 - k)\mu^3 +
$$

$$
+[(h^2 - 2k - 2)a^2 + 1]\mu^2 - 2ap^2\mu, \ \beta_3 = (a^2k^2 + h^2)\mu^4 - 2[(ap^2 + a^2 - 1)h^2 -
$$

$$
-a^2k(k+1) + k]\mu^3 + [(1 - 2ap^2 - 2a^2)h^2 + (k^2 + 4k + 1)a^2 + 4akp^2 - 2k - 2]\mu^2 + \quad (7)
$$

$$
+2p^2(ak + 2a + h)\mu + p^4, \ \beta_2 = k^2\mu^4 + 2[(-ap^2 - a^2 + 1)k^2 + k - h^2]\mu^3 + [(p^4 +
$$

$$
+2ap^2 + a^2 - 2)h^2 + (1 - 2ap^2 - 2a^2)k^2 - 2k(a^2 + ap^2 - 2) + 1]\mu^2 - 2[kp^4 +
$$

$$
+(ak - a - 2h)p^2]\mu - 2p^4, \ \beta_1 = -2k^2\mu^3 + [(p^4 + 2ap^2 + a^2 - 2)k^2 +
$$

$$
+h^2 - 2k]\mu^2 + 2(kp^2 + ak + h)\mu p^2 + p^4, \ \beta_0 = k^2\mu^2,
$$

where $h = 4\zeta^2$, $\gamma = g^2$, $f = (|X_0|/(X_0)_{st})^2$.

We will use the approach proposed in the article [8]. Its idea is as follows. Suppose that the parameters μ, κ, h, a, p are set, while we are interested in a configuration in which the function $f(\gamma)$ takes the same values at the points of maximum γ_1, γ_2. Geometrically, this means that the curve $y = f(\gamma)$ has a common tangent at the points γ_1, γ_2.

Let $f_0 = 1/\kappa$ be some fixed number. Then the equation $f = f_0$ is equivalent to the

following polynomial equation

$$P(\gamma) = a^2\mu^2\gamma^5 + (4\zeta^2 a^2\mu^4 - 2(k - 4\zeta^2)a^2\mu^3 - [2(k - 2\zeta^2 + 1)a^2 - 1]\mu^2 -$$
$$-2ap^2\mu)\gamma^4 + [(a^2k^2 + 4\zeta^2)\mu^4 - 2(4\zeta^2 ap^2 + (4\zeta^2 - k^2 - k)a^2 -$$
$$-4\zeta^2 + k)\mu^3 - [4\zeta^2(ap^2 + 2a^2 - 1) + 4akp^2 + (k^2 + 4k - \varkappa + 1)a^2 - 2k - 2]\mu^2 +$$
$$+2(ak + 2\zeta + 2a)\mu p^2 + p^4]\gamma^3 + (k^2\mu^4 - 2[(ap^2 + a^2 - 1)k^2 + 4\zeta^2 - k]\mu^3 - [4(-p^4 +$$
$$+a^2\varkappa - 2ap^2 - a^2 + 2)\zeta^2 + (2ap^2 + 2a^2 - 1)k^2 - 2(a^2\varkappa - 2ap^2 - a^2 + 2)k +$$
$$+\varkappa - 1]\mu^2 - 2[kp^2 + (2k - \varkappa + 1)a + 4\zeta]\mu p^2 - 2p^4)\gamma^2 - (2k^2\mu^3 -$$
$$-[(p^4 - a^2\varkappa + 2ap^2 + a^2 - 2)k^2 - 4\zeta(\varkappa - 1)^2 + 2(\varkappa - 1)k]\mu^2 +$$
$$+2[(a\varkappa - p^2 - a)k + 2\zeta(\varkappa - 1)]\mu p^2 + p^4(\varkappa - 1))\gamma - (1 + \varkappa)b^2k^2\mu^2. \tag{8}$$

A consequence of the requirement of the equal peaks is the presence of two pairs of multiple (real) roots in the polynomial $P(\gamma)$, that is, it can be represented in the form

$$P(\gamma) = \mu^2(\gamma^2 + M\gamma + N)^2(a^2\gamma + L) > 0, \ M^2 - 4N > 0, \tag{9}$$

where L, M, N are some unknown parameters. Then, we conclude from (8) that

$$[a^2h^2\mu^4 + 2(h^2 - k)a^2\mu^3 + [(h^2 - 2M - 2k - 2)a^2 - L + 1]\mu^2 - 2a\mu p^2]\gamma^4 +$$
$$[(a^2k^2 + h^2)\mu^4 + 2[a^2(-h^2 + k^2 + k) - (ap^2 - 1)h^2 - 2k]\mu^3 + [2a(k - h^2)p^2 +$$
$$+(k^2 - M^2 - 2h^2 - 2N + 4k - \varkappa + 1)a^2 - 2LM + h^2 - 2(k + 1)]\mu^2 +$$
$$+2(ak + 2a + h)\mu p^2 + p^4]\gamma^3 + [k^2\mu^4 + 2[(-ap^2 - a^2 + 1)k^2 - h^2 + k]\mu^3 + [(p^4 -$$
$$-a^2\varkappa + 2ap^2 + a^2 - 2)h^2 + (1 - 2ap^2 - 2a^2)k^2 - 2(MN - k\varkappa + k)a^2 - \tag{10}$$
$$-L(M^2 + 2N) + 4k(1 - ap^2) - \varkappa + 1]\mu^2 - 2[kp^2 + 2ak - a\varkappa + a + 2h]\mu p^2 -$$
$$-2p^4]\gamma^2 + [-2k^2\mu^3 + [(p^4 - a^2\varkappa + 2ap^2 + a^2 - 2)k^2 - N^2a^2 - 2LMN +$$
$$+(h^2 - 2k)(1 - \varkappa)]\mu^2 + 2[(p^2 + a[1 - \varkappa])k + 2h(1 - \varkappa)]\mu p^2 + (1 - \varkappa)p^4]\gamma +$$
$$+(k^2 - LN^2 - k^2\varkappa)\mu^2 \equiv 0.$$

From the coefficient on γ^4 we express

$$L = \mu^2h^2a^2 - 2(ap_1 - h^2 + k)a^2\mu + (h^2 - 2M - 2k - 2)a^2 + 1, \tag{11}$$

where $p_1 = p^2/(a^2\mu^2)$, and from the constant term we get the target function

$$\varkappa = 1 - \frac{1}{k^2}N^2[\mu^2h^2a^2 - 2(ap_1 - h^2 + k)a^2\mu + (h^2 - 2M - 2k - 2)a^2 + 1]. \tag{12}$$

Now we have an "ordinary" problem of conditional extremum of function $\varkappa(k, h, M, N)$ with three conditions

$$\phi_j(k, h, M, N) = 0 \ (j = \overline{1,3}) \tag{13}$$

(the corresponding expressions derive from (10)).[1]

Complementing the equations with the extremum condition,

$$\begin{vmatrix} \frac{\partial \varkappa}{\partial k} & \frac{\partial \varkappa}{\partial h} & \frac{\partial \varkappa}{\partial M} & \frac{\partial \varkappa}{\partial N} \\ \frac{\partial \phi_1}{\partial k} & \frac{\partial \phi_1}{\partial h} & \frac{\partial \phi_1}{\partial M} & \frac{\partial \phi_1}{\partial N} \\ \frac{\partial \phi_2}{\partial k} & \frac{\partial \phi_2}{\partial h} & \frac{\partial \phi_2}{\partial M} & \frac{\partial \phi_2}{\partial N} \\ \frac{\partial \phi_3}{\partial k} & \frac{\partial \phi_3}{\partial h} & \frac{\partial \phi_3}{\partial M} & \frac{\partial \phi_3}{\partial N} \end{vmatrix} = 0. \tag{14}$$

we obtain a system of four equations with four unknowns. This system is highly non-linear and its solutions cannot be expressed in closed form.

However, for purposes of analytical treatment the asymptotic representation may be employed. In engineering applications the mass ratio μ usually has small value. Then we can find the asymptotic solution

$$M = M_0 + M_1\mu_1 + M_2\mu_1^2 + \cdots, \ N = N_0 + N_1\mu_1 + N_2\mu_1^2 + \cdots, \ h = \mu_1(h_0 +$$
$$+h_1\mu_1 + \cdots), k = k_0 + k_1\mu_1 + k_2\mu_1^2 + \cdots, \ p_1 = \mu_1^2(p_{10} + \mu_1 p_{11} + \cdots), \ \mu_1 = \sqrt{\mu}. \tag{15}$$

The parameter μ_1 is taken here, because h and γ have no Taylor expansions on μ. Step by step we find

$$M_0 = -2, N_0 = 1, k_0 = 1, h_0 = \sqrt{\frac{3}{2}}, \ p_{10} = -\frac{k_1(a^4 + 2a^2 + 2)}{a^3(a^2 + 1)},$$

$$M_1 = -k_1, \ N_1 = k_1, \ M_2 = -k_2, \ N_2 = -\frac{\sqrt{2}h_1[(a^2 + 1)^2 - k_1 k_2]}{k_1},$$

$$p_{11} = \frac{1}{2(a^2 + 1)^2 a^4 k_1^2}[2a(a^4 + 5a^2 + 5)k_1^4 + \sqrt{2}[4a^3(a^4 + 3a^2 + 2)h_1 - \tag{16}$$

$$-2(a^4 + 2a^2 + 2)]k_1^3 + a(a^2 + 1)[(a^2 + 1)^2 h_1^2 - 2(a^4 + 2a^2 + 2)k_2 +$$

$$+4a(a^2 + 2)^2]k_1^2 - 2\sqrt{2}a(a^2 + 1)^3 h_1(k_2 + 2)k_1 - 4a(a^2 + 1)^5 h_1^2].$$

3.2. Numerical analysis

We note that numerical experiments show a very insignificant effect of the characteristics of the piezoelectric element on the decrease in the amplitude of oscillations of the main mass. At the same time, if the parameter p has an order of magnitude greater than 10^{-2},

―――――――――――――――――

[1]Here we assume for simplicity that values of a and p_1 are known.

then the amplitude of the oscillations increases significantly (Fig. 2). Moreover, due to the continuous dependence of the function κ on the parameter p, the optimal absorber values for system (1) will differ very slightly from the degenerate case $p = 0$, that is, the values of $k^\star, \zeta^\star$ determined according to formulas (3.17) of article [8].
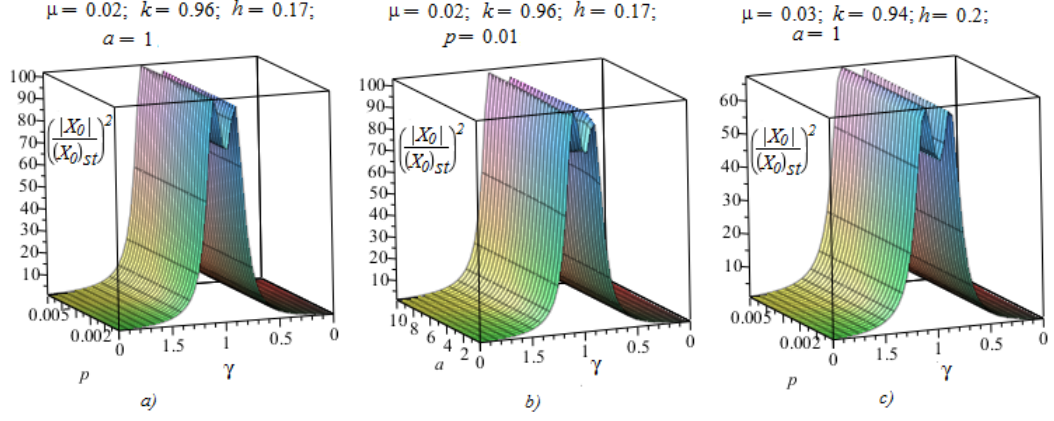
Figure 2. The amplitude of the oscillations.

Thus, we can give the following recommendations for choosing system parameters:

– the parameters of the absorber, when known the mass ratio μ, are taken as $k^\star, \zeta^\star$;

– the parameter p should be taken sufficiently small (for example 0.01 with $\mu = 0.02$);

– the parameter a practically does not affect the value of κ(one can take an arbitrary value in the interval $[0.01, 10]$).

4. Optimization the harvesting power

Our second task is to determine the parameters of the piezoelectric element in order to maximize energy collection. We assume that parameters of the DVA are taken according to section 3. Depending on the specified quality criterion, the procedure for determining these parameters may vary. We will consider the following options.

A) Provided that the frequency of the external action is unknown exactly, but close to the resonant one ($\gamma \in [\gamma^{(1)}, \gamma^{(2)}]$), select the parameters a and p so that the minimum value of the objective function

$$\Phi(a, p, \gamma) = \frac{V^2}{R_l} = \frac{\mu^2 p^2 (h^2 \gamma + k^2)}{\beta_5 \gamma^5 + \beta_4 \gamma^4 + \beta_3 \gamma^3 + \beta_2 \gamma^2 + \beta_1 \gamma + \beta_0} \tag{17}$$

with respect to argument γ turned out to be the greatest possible (with respect to a, p).

Mathematically, this task is easy enough. We have a system

$$\frac{\partial \Phi}{\partial \gamma} = 0, \quad \frac{\partial \Phi}{\partial a} = 0, \quad \frac{\partial \Phi}{\partial p} = 0. \tag{18}$$

The derivative $\partial \Phi / \partial a$ is linear on a, and two others are quadratic on p^2. Their resultant is high order polynomial on γ, however it has no real roots in vicinity of $\gamma_0 = 1$. Hence, the lowest values on γ are taken on the sides of the interval. The relevant values of a, p are calculated accordingly to numeric values of $\mu, \gamma^{(1)}, \gamma^{(2)}$. The typical view of the surface (17) is presented in Fig.3.
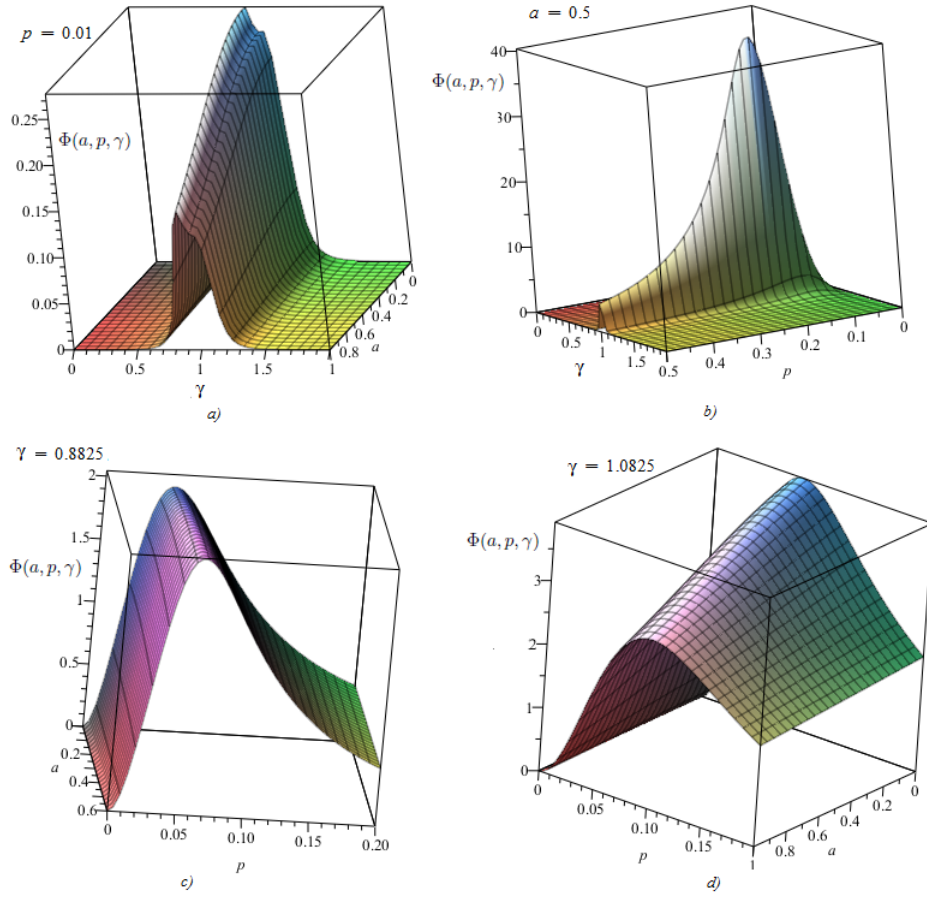
Figure 3. The typical view of the surface (17): $\mu = 0.02, k = 0.96, h = 0.17$.

B) As another criterion, we can take the "neutral" requirement of maximizing the averaged (with respect to γ) value of the function Φ over the interval $[\gamma^{(1)}, \gamma^{(2)}]$. Taking into

account that the expression considered is representable as the sum of tabular integrals, from a technical point of view, solving this problem does not seem complicated. The corresponding calculations can be performed analytically (a computational procedure is similar to that used in the previous case) or numerically. Results are presented in Fig.4.
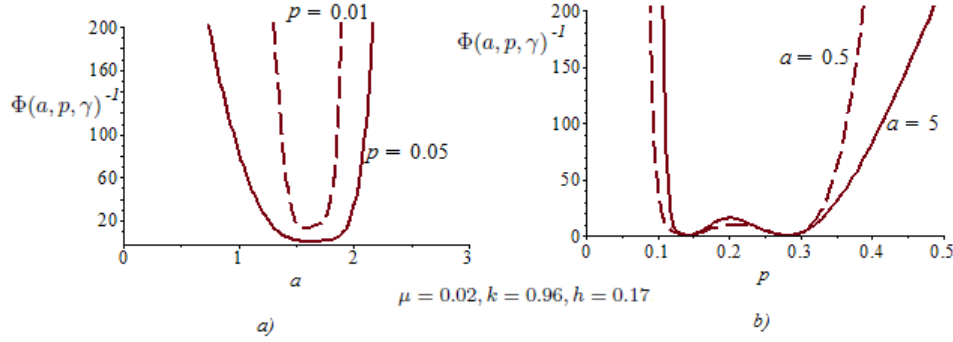
Figure 4. The result of maximizing the averaged value of the function Φ.

5. Conclusions

In this paper, we consider an electro-mechanical system consisting of a primary element and a dynamic absorber and a piezoelectric element connected to it. The goal is to reduce the vibration of the primary structure and at the same time collect the energy through the interaction of the host system and the vibration absorber. An analytical and numerical study of the dynamics of the system is carried out. It is shown that the piezoelectric element practically does not improve the effect of the absorber in terms of reducing the oscillations of the main mass. At the same time, piezoelectric element with improper selected parameters can significantly increase the amplitude of these oscillations. The problem of collecting vibrational energy is also considered. Relations are found between the parameters of the piezoelectric element at which the energy collected has a maximum value.

References

[1] ADHIKARI, S., FRISWELL, M., AND INMAN, D. Piezoelectric energy harvesting from broadband random vibrations. *Smart Mater. Struct. 11*, 18 (2009), 115005.

[2] ALI, S., AND ADHIKARI, S. Energy harvesting dynamic vibration absorbers. *Journal of Applied Mechanics 80*, 1 (2013), 041004–1 – 041004–9.

[3] BEEBY, S., TUDOR, M., AND WHITE, N. Energy harvesting vibration sources for

microsystems applications. *Meas. Sci. Technol. 12*, 17 (2006), 175–195.

[4] BROWN, B., AND SINGH, T. Minimax design of vibration absorbers for linear damper systems. *J. Sound Vib.*, 330 (2011), 2437–2448.

[5] CORNWELL, P., GOETHALS, J., KOWTKO, J., AND DAMIANAKIS, M. Enhancing power harvesting using a tuned auxiliary structure. *J. Intel. Mater. Syst. Struct.*, 16 (2005), 825–834.

[6] GALHARDI, M., GUILHERME, T., AND JUNIOR, V. A review of power harvesting from vibration using piezoelectric materials and applications. *Proceedings of the 7th Brazilian Conference on Dynamics, Control and Applications* (2008).

[7] KAZMIERSKI, T., AND BEEBY, S. *Energy Harvesting Systems Principles, Modeling and Applications.* Editors Springer, 2011.

[8] PUZYROV, V., AND AWREJCEWICZ, J. On the optimum absorber parameters: revising the classical results. *Journal of Theoretical and Applied Mechanics 55*, 3 (2017), 1081–1089.

[9] SHEVTSOV, S., SOLOVIEV, A., PARINOV, I., CHERPAKOV, A., AND CHEBANENKO, V. *Piezoelectric Actuators and Generators for Energy Harvesting.* Springer, 2018.

[10] SODANO, H., INMAN, D., AND PARK, G. A review of power harvesting from vibration using piezoelectric materials. *Shoock Vibr. Dig.Shoock Vibr. Dig. 3*, 36 (2004), 197–205.

[11] STEPHEN, N. On energy harvesting from ambient vibration. *J. Sound Vibr.*, 293 (2006), 409–425.

[12] TANG, X., AND ZUO, L. Enhanced vibration energy harvesting using dual-mass systems. *Journal of Sound and Vibration*, 330 (2011), 5199 – 5209.

[13] ZHU, D., TUDOR, M., AND BEEBY, S. Strategies for increasing the operating frequency range of vibration energy harvesters. *A review. Meas. Sci. Tech. 2*, 21 (2010), 022001.

Leo Acho Zuppa, Professor: Universitat Politecnica de Catalunya, EDIFICI TR5 DESPATX 357 C. COLOM, 11 08222 TERRASSA SPAIN, Spain (ES) (*leonardo.acho@upc.edu*).

Jan Awrejcewicz, Professor: Lodz University of Technology, 1/15 Stefanowski Str., 90-924 Lodz, Poland, Poland (PL) (*jan.awrejcewicz@p.lodz.pl*).

Nataliya Losyeva, Professor: Vasyl Stus Donetsk National University, 600-richia 21, Vinnitsia, Ukraine, Ukraine (UA) (*natalie.loseva@gmail.com*).

Volodymyr Puzyrov, Professor: Vasyl Stus Donetsk National University, 600-richia 21, Vinnitsia, Ukraine, Ukraine (UA) (*v.puzyryov@donnu.edu.ua*). The author gave a presentation of this paper during the conference in the special session "Innovative strategies for vibration control and mitigation" organized by G. Failla and R. Santoro.

Nina Savchenko, Ph.D.: Zhukovsky National Aerospace University "KhAI", 17, Chkalova str., Kharkiv, Ukraine, Ukraine (UA) (*nina_savchenko@hotmail.com*).

Critical tolerance evolution: Classification of the chain-recurrent set

Carlos Argáez, Peter Giesl, Sigurdur Freyr Hafstein

Abstract: Complete Lyapunov functions for non-linear dynamical systems can be obtained by approximately solving a partial differential equation that describes a condition for its orbital derivative. Efficient algorithms to compute them have been implemented. The fact that the partial differential equation is not satisfied at points of the chain-recurrent set is used to determine it; more precisely, all points where the value of the orbital derivative is larger than a fixed, critical tolerance parameter, are an estimate of the chain-recurrent set. The mathematical conditions of smoothness of the orbital derivative are obtained by locally averaging the values of the orbital derivative. Furthermore, convergence to zero is avoided by normalizing the sum of the orbital derivative condition. However, the tolerance parameter to describe the chain-recurrent set has not been considered. This results in an overestimation of the chain-recurrent set. Several algorithms have been proposed to reduce the overestimation of the chain-recurrent set, but no systematic analysis on the dependence on the critical parameter has been made so far. In this paper, we focus on studying this parameter. To proceed, the chain-recurrent set is divided into different subsets of connected components; their evolution per iteration and their different behaviour are studied. The outcome of this research will create an efficient analysis method for locating the chain-recurrent set and aims to reduce its overestimation by obtaining the tightest possible tolerance parameter necessary to classify it.

1. Introduction

Dynamical Systems describe time-depending phenomena in terms of differential equations.

Dynamical systems have vast and diverse applications in economy, biology, physics, mathematics, etc. For an unfamiliar reader, we can point out classical dynamical systems examples such as the pendulum, the population of hunter-prey animal species, the Lorenz attractor, etc.

In general, at any given time, a dynamical system has a state in its own phase-space represented as an ordered n-tuple of numbers in the shape of vectors. In this case, n represents the problem's dimension.

The dynamics can be seen as the instructions' manual to describe the time-evolution of the system on this manifold [26, 24]. The evolution rule of the dynamical system describes all future states from a given initial one. The rule can be either deterministic, i.e. the future states depends only on the current one, or stochastic, where the rule is additionally influenced by random events.

They model real-world systems to describe their often complicated behaviour. Interesting examples can be found in, e.g. the double [13] and triple pendulum with periodic forcing [11] and dry friction [12], which leads to time-periodic and non-smooth systems, or the dynamics of the wobblestone [10].

Let us assume that we have dynamics described as a time-autonomous system of differential equations (ODE), of the form:

$$\dot{\mathbf{x}} = \mathbf{f}(\mathbf{x}), \tag{1}$$

where $\mathbf{x} \in \mathbb{R}^n$, $n \in \mathbb{N}$.

Equation (1) represents a general, continuous-time, deterministic, autonomous dynamical system. In order to understand its dynamics, one can apply several different methods. For example, the direct solutions' calculation with many different initial conditions. However, this approach is computationally costly and can only give limited information about the general behaviour of the system.

Aleksandr Mikhailovich Lyapunov published in 1892 two methods for demonstrating stability of dynamical systems. The first one consisted in constructing a solution to the dynamical system with convergent series. The second method constructs a function $V(x)$ around a system's attractor. The *Lyapunov function* $V(x)$ has the advantage of corresponding to the potential function in classical dynamics. Classically, a (strict) Lyapunov function [25] is decreasing along all solution trajectories in a neighbourhood of an attractor such as an equilibrium or a periodic orbit. The function has the property of:

(I) attaining its minimum at the attractor and

(II) of being strictly decreasing along solutions of the ODE and therefore solutions that start close to the attractor are attracted to it.

We can illustrate this idea with a pedagogical example by considering a heavy solid ball on the top of a smooth hill. If we place the ball on top of the hill, then the ball will always remain there. However, if it is subject to an infinitesimal disturbance, then it will roll down the hill to the bottom due to the gravitational force. At the deepest point of the valley the ball will remain for all times and it would require an external force to push it up the hill. Additionally, if the ball is placed at a starting point near the equilibrium in the valley, the ball will stay near the equilibrium and, moreover, will approach the equilibrium as time tends to infinity.

In this example, the hill's top is an unstable equilibrium and its bottom is (Lyapunov) stable and an attracting equilibrium. The basin of attraction consists of all starting points, such that the ball approaches the stable equilibrium.

For this system, we could propose a Lyapunov function $V(x)$ to be the height. According to the classical definition, the first property is fulfilled since x_0 is the deepest point of the corresponding valley and the second by gravity, which forces the ball to move downhill.

Generally, when modelling (non idealized) dissipative physical systems, the free energy is an obvious candidate for a Lyapunov function. It decreases along solutions due to the system's dissipativity, hence, solutions tend to a local minimum of the energy (I).

The classical definition of a Lyapunov function can be extended to a complete Lyapunov function [17, 18, 21, 22], which characterizes the complete behaviour of the dynamical system as a consequence of its definition on the whole phase space, and not just in a neighbourhood of one particular attractor. By means of its broader information, the state-space can be divided into two disjoint areas, on which the system behaves in fundamentally different ways. The part where the flow is gradient-like, i.e. the systems flows through, and where the flow is chain-recurrent, i.e. infinitesimal perturbations can make the system recurrent.

Definition 1.1 (Complete Lyapunov function). *A complete Lyapunov function (CLF) for the system* (1) *is a continuous scalar function, $V : \mathbb{R}^n \to \mathbb{R}$ that*

- *is constant in each chain-transitive connected component of the chain-recurrent set and*

- *decreases strictly along solution trajectories in other places.*

The property of being decreasing along solutions of the ODE is expressed in the next definition.

Definition 1.2 (Orbital Derivative). *The orbital derivative of a differential function $V : \mathbb{R}^n \to \mathbb{R}$ along the solution to the system* (1) *is defined through:*

$$V'(\mathbf{x}) := \frac{d}{dt} V(\mathbf{x}) = \langle \nabla V(\mathbf{x}), \dot{\mathbf{x}} \rangle = \langle \nabla V(\mathbf{x}), \mathbf{f}(\mathbf{x}) \rangle.$$

Several methods have been proposed to compute CLFs, but they are either computationally very demanding [14, 20, 23], see also [15], or assume that the positions of the attractors are known beforehand [16].

2. Construction of Complete Lyapunov functions

The method to compute CLFs discussed in this paper is inspired by the construction of classical Lyapunov functions using radial basis functions (RBFs) [19]. As the authors have described the method in detail in previous publications [2, 4, 6, 5, 3, 8, 7, 9], we let a short description of the essential ideas and steps suffice.

The main idea is to use collocation using RBFs to obtain a solution to the PDE

$$V'(\mathbf{x}) = -r(\mathbf{x}), \ \ r(\mathbf{x}) \geq 0. \tag{2}$$

The PDE (2) is ill-posed, unless $r(\mathbf{x})$ is identically zero or if the chain-recurrent set of (1) is empty, both of which are not interesting. However, computing a norm-minimal function fulfilling (2) at every point $\mathbf{x}_i \in X$, where X is a set of collocation points, is a well-posed problem. By evaluating, where a solution to the collocation problem fails to fulfill the PDE (2), we locate the chain-recurrent set.

Several parameters have to be fixed when setting up our collocation problem, i.e. the smoothness parameters k, l of the compactly supported Wendland functions used as RBFs, the radius of their support c^{-1}, the density of the hexagonal grid used as collocation points, inversely proportional to the parameter $\alpha_{\text{Hexa-basis}}$, the number $2m = |Y_{\mathbf{x}_i}|$ of evaluation points

$$Y_{\mathbf{x}_i} \quad = \quad \left\{ \mathbf{x}_i \pm \frac{r \cdot k \cdot \alpha_{\text{Hexa-basis}} \cdot \mathbf{f}(\mathbf{x}_i)}{m \cdot \|\mathbf{f}(\mathbf{x}_i)\|} : k \in \{1, \ldots, m\} \right\}$$

per collocation point $\mathbf{x}_i$, aligned along the flow $\mathbf{f}(\mathbf{x}_i)$ through the collocation point $\mathbf{x}_i$, and the parameter $r \in (0, 1)$.

Further, it has turned out to be advantageous to replace system (1) with (almost normalized)

$$\dot{\mathbf{x}} = \hat{\mathbf{f}}(\mathbf{x}), \quad \hat{\mathbf{f}}(\mathbf{x}) := \frac{\mathbf{f}(\mathbf{x})}{\sqrt{\delta^2 + \|\mathbf{f}(\mathbf{x})\|^2}}, \quad \delta^2 \text{ small (e.g. } = 10^{-8}),$$

which has the same solution trajectories and thus the same chain-recurrent set as (1), cf. [4].

Our algorithm to compute CLFs and classify the chain-recurrent set can be summarized as follows:

Algorithm I:

1. Create the set of collocation points X and compute the approximate solution v_0 to $V'(\mathbf{x}) = -1$ using collocation with Wendland functions, as discussed above; set $i = 0$.

2. For each collocation point $\mathbf{x}_j$, compute $v_i'(\mathbf{y})$ for all $\mathbf{y} \in Y_{\mathbf{x}_j}$: if $v_i'(\mathbf{y}) > \gamma$ for a point $\mathbf{y} \in Y_{\mathbf{x}_j}$, then $\mathbf{x}_j \in X_i^0$ (chain-recurrent set), otherwise $\mathbf{x}_j \in X_i^-$ (gradient-like flow), where $\gamma \leq 0$ is a chosen critical value. Subindex i indicates that the approximation of the chain-recurrent set and the gradient-like flow has been obtained in the current step i.

3. Define $\tilde{r}_j = \left(\frac{1}{2m} \sum_{\mathbf{y} \in Y_{\mathbf{x}_j}} v_i'(\mathbf{y}) \right)_-$, where $x_- := \max(x, 0)$, and $r_j = \frac{N}{\sum_{l=1}^{N} |\tilde{r}_l|} \tilde{r}_j$.

4. Compute the approximate solution v_{i+1} of $V'(\mathbf{x}_j) = r_j$ for $j = 1, 2, \ldots, N$.

5. Set $i \to i + 1$ and repeat steps 2 to 4.

Note that the sets X_i^0 and X_i^- change in each step of the algorithm.

In the next section we perform a detailed study of the influence of the critical value $\gamma \leq 0$ in Step 2 of the algorithm for one particular example.

3. Dependence of the critical value γ

To analyse the influence of the numerical values of γ we followed the evolution of the average orbital derivative over all points in X_i^0 as a function of different critical values along 100 iterations.

Once we have obtained the orbital derivative for 100 iterations then, per iteration, we study the chain-recurrent set for 9001 different critical values. That is, for $\gamma \in [-0.9, 0]$ with increments in steps

of 10^{-4}. We then count, as a function of γ and the iteration, how many elements there are per periodic orbit in the approximation of the chain-recurrent as well as the average orbital derivative. For each fixed iteration, we then linearly fit using the method of least squares, the average orbital derivative as a function of γ. In a final analysis the slopes as a function of iteration are compared.

All our computations were done using the software *LyapXool*[1].

3.1. Results

3.2. Two circular periodic orbits

We consider system (1) with right-hand side

$$\mathbf{f}(x,y) = \begin{pmatrix} -x(x^2+y^2-1/4)(x^2+y^2-1)-y \\ -y(x^2+y^2-1/4)(x^2+y^2-1)+x \end{pmatrix}. \tag{3}$$

This system has two periodic circular orbits: an asymptotically stable periodic orbit at $\Omega_1 = \{(x,y) \in \mathbb{R}^2 \mid x^2+y^2 = 1\}$ and a repelling periodic orbit at $\Omega_2 = \{(x,y) \in \mathbb{R}^2 \mid x^2+y^2 = 1/4\}$. Moreover, it has an asymptotically stable equilibrium at the origin.

To compute the CLF with our method we used the Wendland function $\psi_{5,3}$ with $c = 1$. The collocation points were set in a region $[-1.5, 1.5] \times [-1.5, 1.5] \subset \mathbb{R}^2$ and we used a hexagonal grid [19, 2, 4, 6, 5] with $\alpha_{Hexa-basis} = 0.0129$. The evaluation grid was computed using the directional grid with $m = 10$.

We computed this example with the almost-normalized method $\dot{\mathbf{x}} = \hat{\mathbf{f}}(\mathbf{x})$ with $\delta^2 = 10^{-8}$. Finally, the limiting radios for the directional grid was set to be $r = 0.5$.

The CLF and its chain-recurrent set are shown in Fig. 1.
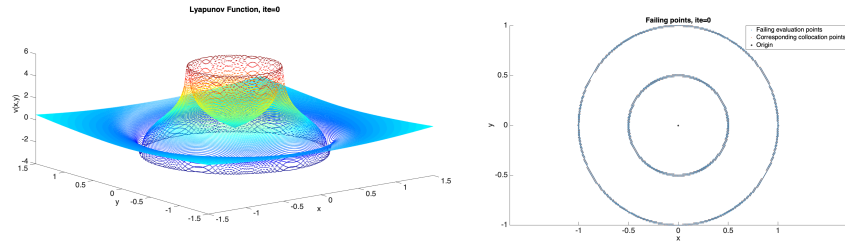
Figure 1. Left figure: Complete Lyapunov function at the initial iteration for system (3). Right figure: Chain-recurrent set for $\gamma = -0.7924$.

Let us start by showing that when approximating the chain-recurrent set, there is a strong dependence on both the number of iterations and the value of γ, Fig. 2.
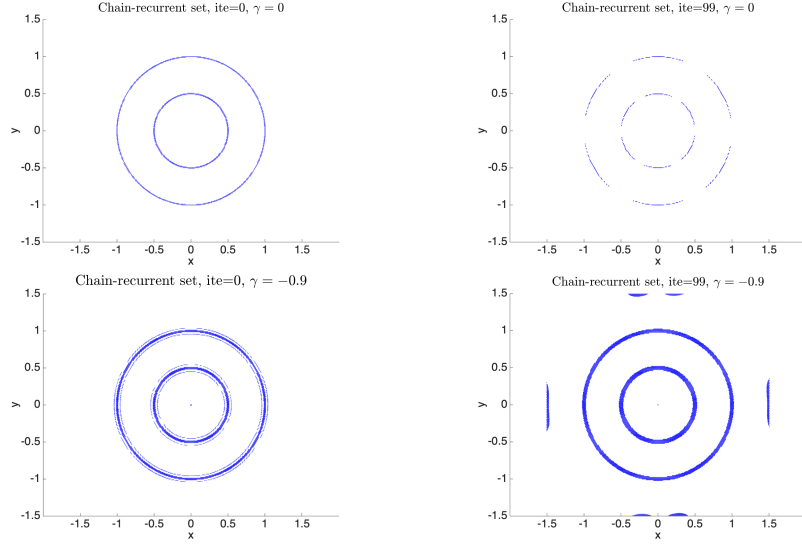
Figure 2. Upper left: Chain-recurrent set obtained for $\gamma = 0$, iteration 0. Upper right: Chain-recurrent set for $\gamma = 0$, iteration 99. Lower left: Chain-recurrent set obtained for $\gamma = -0.9$, iteration 0. Lower right: Chain-recurrent set obtained for $\gamma = -0.9$, iteration 99

Fig. 2 exemplifies how the description and classification of the chain-recurrent set depends not only on the value of γ but also in the amount of iterations. That could be seen in two different ways:

- For a fixed γ, different iterations give different approximations to the chain-recurrent set

- For a fixed iteration, different γ's give different approximations to the chain-recurrent set

For $\gamma = 0$, iteration 0, we see that we do not find a critical point at the origin while we do manage to find the two closed orbits. For iteration 99, the orbits are not connected anymore. For $\gamma = -0.9$, we see that in both cases, iteration 0 and 99, provide overestimated chain-recurrent sets. We see, however, that the overestimation is higher for iteration 99 and there is some noise added at the boundary of the area.

In Fig. 3, we plot the average orbital derivative as well as the amount of elements in each connected component of the chain-recurrent set (i.e. the two orbits and the equilibrium) versus the critical values $\gamma \in [-0.9, 0]$ for iterations 0 and 99.
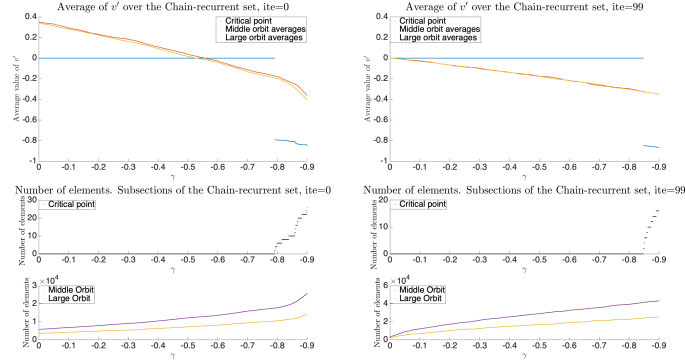
Figure 3. Upper figures: average value of the orbital derivative for the connected components of the chain-recurrent set for all $\gamma \in [-0.9, 0]$. Left: iteration 0, right: iteration 99. Lower: amount of elements in the connected components of the chain-recurrent set for all $\gamma \in [-0.9, 0]$. Left: iteration 0, right: iteration 99.

First, we see in Fig. 3 that for a fixed iteration and on the orbits, the dependence of the average value of the orbital derivative is a linear function function of the critical value is linear. It does not behave the same way for the critical point. The reason is that there are no elements found around the critical point for critical values higher than ca. -0.8.

We notice that as iterations grow in number, the amount of elements in the connected components increases.

Now we use the method of least squares to fit a straight line to each of the curves as in Fig. 3, for each iteration 0 to 99. We compute the slope of each of these curves and show in Fig. 4 how it changes as a functions of the iteration. Note that the slopes are constant for the two orbits after the first 10 iterations. For the equilibrium, however, the slope changes considerably more.
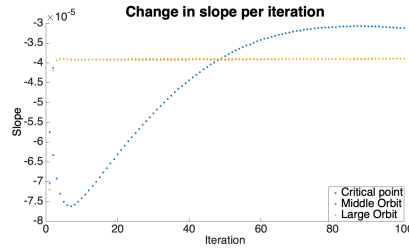
Figure 4. The slope of the fitted straight line, representing the function of average orbital derivative versus γ, as a function of iteration and for the different connected components.

The approximated chain-recurrent set X^0 determined by the algorithm has too many connected components for some values. On the other hand, for other values, the periodic orbits in our example

can also break up in several parts. We now analyse for which critical values the orbits break into several parts.

The construction of the CLF in our approach, as explained in Sec. 2, is done using a collocation grid and we evaluate the orbital derivative on an evaluation grid. Since both grids are scattered, all values obtained for the CLF will be scattered too. That means that the orbits will have blank spaces between their forming points. This is shown in the lefthand side of Fig. 5. Therefore, to find the breaking points we review the approximated chain-recurrent sets looking for anomalous holes beyond the geometrical constructions properties. That is shown in the righthand side of Fig. 5.
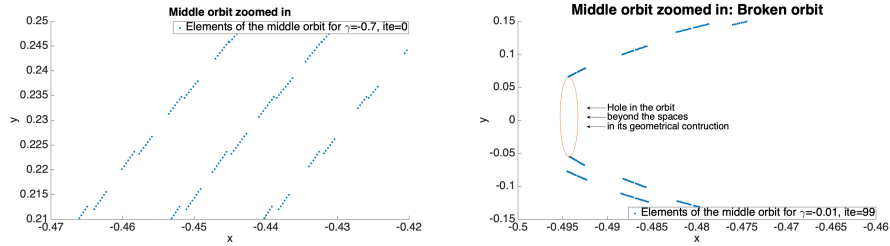
Figure 5. Left figure: Orbit for $\gamma = -0.9$. Right: Zoom in on an orbit for $\gamma = -0.9$.

Looking for the critical value γ_c for an anomalous hole to appear and break the orbit, requires considering all approximations made to the chain-recurrent set for all critical values and for all iterations.

Fig. 6 left shows γ_c as a function of iterations, where the value γ_c is such that for all $\gamma < \gamma_c$ the orbits are connected, and for all $\gamma \geq \gamma_c$ they are not connected. Fig. 6 right shows γ_c as a function of iteration, where the value γ_c is such that for all $\gamma < \gamma_c$ there are no points in X_i^0 near the equilibrium.
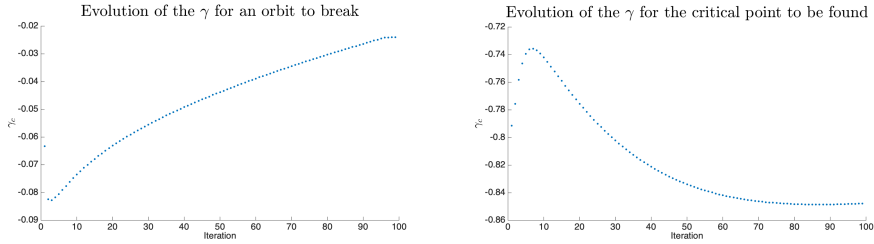
Figure 6. Left: Change the critical values for which the middle orbit is broken. Right: Critical value for which no equilibrium point was found. The results are shown per iteration.

3.3. Discussion and Conclusions

There are some remarkable observations from our study of the different numerical values for the critical parameter γ. First, for large negative values of γ the approximation X_i^0 of the chain-recurrent set grows

Table 1. For iteration 0, amount of elements in the orbits and the critical point for γ = 0.

Ite	Critical Point	Middle Orbit	Large Orbit
0	0	3634	5832
99	0	1612	2524

Table 2. For iteration 99, amount of elements in the orbits and the critical point for γ = −0.9.

Ite	Critical Point	Middle Orbit	Large Orbit
0	26	14351	25822
99	16	25428	43409

as a function of iterations, for lower negative values it is the other way around. This is exemplified in tables 1 and 2. Note, however, that for γ ≈ 0 our algorithm does not identify the equilibrium at the origin as a part of the chain-recurrent set, and for γ = −0.9 a set covering it is identified as a part of the chain-recurrent set and this set decreases in size with more iterations. It remains an open question, whether our algorithm should be used to identify the equilibrium points, that can easily be found by other and simpler means anyways, or if we should first identify them and treat their neighbourhood differently. Our results seem to indicate that our algorithm is more suited for connected components of the chain-recurrent set that are not just one point, which is not surprising because we are using a scattered grid of collocation points. Fig. 7 shows the value of the orbital derivative around the point $(0,0)$. The open red stars represent the values of the 99th iteration while iteration 0 is represented by the dark blue rhomboids.
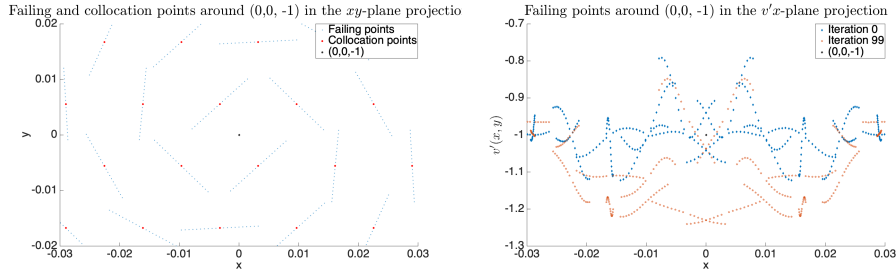
Figure 7. Left: Distribution of the collocation and evaluation points around the origin, as seen in the xy-plane projection. Left: Values of $(x, y, v'(x, y))$ (graph of the orbital derivative) around the point $(0, 0, −1)$ for iterations 0 and 99, as seen in the xz-plane projection. The $v'(x, y)$ axis the value of the orbital derivative.

Second, the evolution of the value $γ_c$ of the critical value γ as a function of iteration is very interest-

ing. Recall that for values $\gamma < \gamma_c$ there are gaps in the approximation X_i^0 of the connected components of the chain-recurrent set. Our study shows that it is necessary to treat the approximations X_i^0 as a function of i when the critical parameter γ is fixed. In future work we will study if it is possible to define the critical parameter $\gamma = \gamma_i$ sensibly as a function of the iteration i such that X_i^0 converges to the true chain-recurrent set. In this regard, note the effect of the normalization in Step 3 of Algorithm I. Since some collocation points are close to the chain-recurrent set, the value of the orbital-derivative at them must be close to zero. Because the sum of the absolute values of the orbital derivative at all collocation points remains fixed, it has to become more negative at other collocation points. This behaviour is not accounted for properly by having a fixed γ.

Acknowledgments

References

[1] ARGÁEZ, C., BERTHET, J.-C., BJÖRNSSON, H., GIESL, P., AND HAFSTEIN, S. F. Lyapxool - a program to compute complete Lyapunov functions. *SoftwareX 10* (2019), 100325.

[2] ARGÁEZ, C., GIESL, P., AND HAFSTEIN, S. *Analysing dynamical systems towards computing complete Lyapunov functions. In* Proceedings of the 7th International Conference on Simulation and Modeling Methodologies, Technologies and Applications (SIMULTECH) *(2017), pp. 134–144. Madrid, Spain.*

[3] ARGÁEZ, C., GIESL, P., AND HAFSTEIN, S. *Computation of complete Lyapunov functions for three-dimensional systems. In* Proceedings IEEE Conference on Decision and Control (CDC), 2018 *(2018), pp. 4059–4064. Miami Beach, FL, USA.*

[4] ARGÁEZ, C., GIESL, P., AND HAFSTEIN, S. *Computational approach for complete Lyapunov functions. In* Dynamical Systems in Theoretical Perspective. Springer Proceedings in Mathematics & Statistics. ed. Awrejcewicz J. (eds). *(2018), vol. 248, pp. 1–11.*

[5] ARGÁEZ, C., GIESL, P., AND HAFSTEIN, S. *Construction of a complete Lyapunov function using quadratic programming. In* Proceedings of the 15th International Conference on Informatics in Control, Automation and Robotics (ICINCO) *(2018). Porto, Portugal.*

[6] ARGÁEZ, C., GIESL, P., AND HAFSTEIN, S. *Iterative construction of complete Lyapunov functions. In* Proceedings of the 8th International Conference on Simulation and Modeling Methodologies, Technologies and Applications (SIMULTECH) *(2018), pp. 211–222. Porto, Portugal.*

[7] ARGÁEZ, C., GIESL, P., AND HAFSTEIN, S. *Clustering algorithm for generalized recurrences using complete Lyapunov functions. In* Proceedings of the 16th International Conference on Informatics in Control, Automation and Robotics (ICINCO) *(2019), pp. 138–146. Prague 2019, Czech Republic.*

[8] ARGÁEZ, C., GIESL, P., AND HAFSTEIN, S. *Improved estimation of the chain-recurrent set. In* Proceedings of the 18th European Control Conference (ECC) *(2019), pp. 1622–1627. Naples, Italy.*

[9] ARGÁEZ, C., GIESL, P., AND HAFSTEIN, S. *Iterative construction of complete lyapunov functions: Analysis of algorithm efficiency. To be published.*

[10] AWREJCEWICZA, J., AND KUDRA, G. *Mathematical modelling and simulation of the bifurcational wobblestone dynamics.* Discontinuity, Nonlinearity, and Complexity 3 *(2014), 123–132.*

[11] AWREJCEWICZA, J., KUDRA, G., AND WASILEWSKI, G. *Experimental and numerical investigation of chaotic regions in the triple physical pendulum.* Nonlinear Dyn 50 *(2007), 755–766.*

[12] AWREJCEWICZA, J., KUDRA, G., AND WASILEWSKI, G. *Chaotic zones in triple pendulum dynamics observed experimentally and numerically.* App. Mech. and Mat. 9 *(2008), 1–17.*

[13] AWREJCEWICZA, J., WASILEWSKIA, G., KUDRA, G., AND RESHMINB, S. *An experiment with swinging up a double pendulum using feedback control.* JCSS 51 *(2014), 176–182.*

[14] BAN, H., AND KALIES, W. *A computational approach to conley's decomposition theorem.* J Comput Nonlin Dyn 1 *(2006), 312–319.*

[15] BJÖRNSSON, J., GIESL, P., AND HAFSTEIN, S. *Algorithmic verification of approximations to complete Lyapunov functions.* Proceedings of the 21st International Symposium on Mathematical Theory of Networks and Systems 180 *(2014), 1181–1188. (MTNS), Groningen, The Netherlands.*

[16] BJÖRNSSON, J., GIESL, P., HAFSTEIN, S., KELLETT, C., AND LI, H. *Computation of lyapunov functions for systems with multiple attractors.* Discrete Contin. Dyn. Syst. 9 *(2015), 4019–4039.*

[17] CONLEY, C. *Isolated Invariant Sets and the Morse Index. CBMS Regional Conference Series no. 38. American Mathematical Society, 1978.*

[18] CONLEY, C. *The gradient structure of a flow I.* Ergodic Theory Dynam. Systems 8 *(1988), 11–26.*

[19] GIESL, P. *Construction of Global Lyapunov Functions Using Radial Basis Functions. Lecture Notes in Math. 1904, Springer, 2007.*

[20] GOULLET, A., HARKER, S., MISCHAIKOW, K., KALIES, W., AND KASTI, D. *Efficient computation of Lyapunov functions for Morse decompositions.* Discrete Contin. Dyn. Syst. Ser. B 20 *(2015), 2419–2451.*

[21] HURLEY, M. *Chain recurrence, semiflows, and gradients.* J Dyn Diff Equat 7*, 3 (1995), 437–456.*

[22] HURLEY, M. *Lyapunov functions and attractors in arbitrary metric spaces.* Proc. Amer. Math. Soc. 126 *(1998), 245–256.*

[23] KALIES, W., MISCHAIKOW, K., AND VANDERVORST, R. *An algorithmic approach to chain recurrence.* Foundations of Computational Mathematics 5 *(2005), 409–449.*

[24] KATOK, A.; HASSELBLATT, B. *Introduction to the Modern Theory of Dynamical Systems. Cambridge: Cambridge University Press, 1995.*

[25] LYAPUNOV, A. M. *The general problem of the stability of motion.* Internat. J. Control 55*, 3 (1992), 521–790. Translated by A. T. Fuller from Édouard Davaux's French translation (1907) of the 1892 Russian original.*

[26] STROGATZ, S. H. *Nonlinear Dynamics and Chaos: with Applications to Physics, Biology and Chemistry. Perseus, 2001.*

Carlos Argáez, Ph.D.: Science Institute, University of Iceland, Dunhagi 5, 107 Reykjavík, Iceland (*carlos@hi.is*).

Peter Giesl, Ph.D.: Department of Mathematics, University of Sussex, Falmer, BN1 9QH, UK (*P.A.Giesl@sussex.ac.uk*).

Sigurdur Hafstein, Ph.D.: Science Institute, University of Iceland, Dunhagi 5, 107 Reykjavík, Iceland (*shafstein@hi.is*).

Oscillations of flexible orthotropic meshed micropolar Timoshenko's plate

J Awrejcewicz, E.Yu. Krylova, I.V. Papkova, V.A. Krysko

*Abstract:*The oscillation's theory of a geometrically nonlinear micropolar orthotropic meshed plate under the action of a normal distributed load is constructed in this paper. The plate's material as a Cosserat continuum with constrained particle rotation (pseudocontinuum). As a result, an additional independent parameter of length l associated with the symmetric bending-torsion tensor will appear in the model. The panel consists of n sets of identical edges, what allows to apply the continuous G. I. Pshenichnov's model. The equilibrium equations for the plate element and the boundary conditions are obtained from the Ostrogradskyi-Gamilton variation principle on the basis of S.P.Timoshenko's kinematic hypotheses. Geometric nonlinearity is taken into account according to the Theodore von Karman model. The system of differential equations in partial derivatives is reduced to theODE system using the Bubnov-Galerkin method. Using the establishment method,theinfluence of the normal load, an additional length's parameter l, and mesh's geometry on the orthotropic plate's behavior consisting of two families of mutually orthogonal edges has been studied.

1. Formulation of the problem

In this paper the mathematical model of the geometrically nonlinear microdimensional anisotropic cylindrical mesh panel oscillations based on the Tymoshenko's hypotheses is constructed. The panel consists n families of densely spaced edges of the same material, which makes it possible to use the G. I. Pshenichnov continuum model [1]. Thus, the original mesh panel is replaced by a continuous layer. In the general formulation, it is necessary to consider the anisotropic material of the panel. Consider a panel assigned to the orthogonal coordinate system, consisting of two families of rods located at angles $\varphi_1 = -\varphi_2$ to the Ox axis.This mesh geometry allows us to consider the panel material as orthotropic, in which the directions of orthotropy coincide with the directions ofcoordinate lines.For a structurally orthotropic panel, we can write the relationship between Young's modulus (E_1 , E_2)and Poisson's ratio (v_{21} , v_{12})through the reduced Young's modulus and Poisson's ratio for the isotropic case (E , v)[2]:

$$E_1 = \frac{E}{m_1} \, , \; E_2 = m_2 E \, , \; v_{21} = v \, , \; v_{12} = \frac{v}{m_1 m_2}, \; G_{13} = n_1 G_{12} \, , \; G_{23} = n_2 G_{12},$$

where m_1, m_2, n_1, n_2 are constants depending on the panel material. Due to mathematical and computational difficulties, many authors [3,4] apply an additional restriction on the shell material when they study orthotropic shells. The shear modulus is not an independent parameter, but is expressed through Young's module and Poisson's ratio, as in the case of isotropy: $G_{12} = \dfrac{E}{2(1+\nu)}$.

Micro size plates and shells are actively used as elements of NEMS and MEMS. Thus, the development of reliable mathematical models is necessary to study the modes of their operation in statics and dynamics. The application of classical mechanics methods in this case will lead to a high error of the result since they do not take into account scale effects. To take into account scale effects at the micro and nano level, many papers use micropolar (moment, asymmetric theory) [5-12]. For continuous shells, a theory was constructed in [13] that takes into account the orthotropy of the material. In this paper, we also use a modified moment theory. That is, along with the usual stress field, moment stresses are also considered. It is assumed that the fields of displacements and rotations are not independent. Given [14] and assuming $n_1 = m_1$ and $n_2 = m_2$ we write the defining relations:

$$\sigma_{xx} = \frac{m_2 E}{m_1 m_2 - \nu^2}\left[e_{xx} + \nu e_{yy}\right], \ \sigma_{yy} = \frac{m_2 E}{m_1 m_2 - \nu^2}\left[m_1 m_2 e_{yy} + \nu e_{yy}\right],$$

$$\sigma_{xy} = \frac{E}{2(1+\nu)}e_{xy}, \ \sigma_{xz} = \frac{m_1 E}{2(1+\nu)}e_{zx},$$

$$\sigma_{yz} = \frac{m_2 E}{2(1+\nu)}e_{yz}, \ m_{mk} = \frac{E l^2}{1+\nu}\chi_{mk}.$$

The non-zero components of the strain tensor can be written in the form:

$$e_{xx} = \frac{\partial u}{\partial x} + \frac{1}{2}\left(\frac{\partial w}{\partial x}\right)^2 + z\frac{\partial \gamma_x}{\partial x},$$

$$e_{yy} = \frac{\partial v}{\partial y} + \frac{1}{2}\left(\frac{\partial w}{\partial y}\right)^2 - k_y w + z\frac{\partial \gamma_y}{\partial y},$$

$$e_{xy} = \frac{1}{2}\left(\frac{\partial u}{\partial y} + \frac{\partial v}{\partial x}\right) + \frac{\partial w}{\partial x}\frac{\partial w}{\partial y} + z\frac{1}{2}\left(\frac{\partial \gamma_x}{\partial y} + \frac{\partial \gamma_y}{\partial x}\right),$$

$$e_{yz} = \frac{1}{2}\left(\gamma_y + \frac{\partial w}{\partial y}\right), \ e_{xz} = \frac{1}{2}\left(\gamma_x + \frac{\partial w}{\partial x}\right), \ e_{zz} = 0.$$

The components of the symmetric bending-torsion tensor will take the form:

$$\chi_{xx} = \frac{1}{2}\left(-\frac{\partial \gamma_y}{\partial x} + \frac{\partial^2 w}{\partial x \partial y}\right), \ \chi_{yy} = \frac{1}{2}\left(\frac{\partial \gamma_x}{\partial y} - \frac{\partial^2 w}{\partial x \partial y}\right),$$

$$\chi_{zz} = \frac{1}{2}\left(-\frac{\partial\gamma_y}{\partial x} + \frac{\partial\gamma_x}{\partial y}\right), \quad \chi_{xy} = \frac{1}{4}\left(-\frac{\partial\gamma_y}{\partial y} + \frac{\partial\gamma_x}{\partial x} + \frac{\partial^2 w}{\partial y^2} - \frac{\partial^2 w}{\partial x^2}\right),$$

$$\chi_{xz} = \frac{1}{4}\left(\frac{\partial^2 v}{\partial x^2} - \frac{\partial^2 u}{\partial x\partial y}\right) + \frac{z}{4}\left(\frac{\partial^2\gamma_y}{\partial x^2} - \frac{\partial^2\gamma_x}{\partial x\partial y}\right),$$

$$\chi_{yz} = \frac{1}{4}\left(\frac{\partial^2 v}{\partial x\partial y} - \frac{\partial^2 u}{\partial y^2}\right) + \frac{z}{4}\left(\frac{\partial^2\gamma_y}{\partial x\partial y} - \frac{\partial^2\gamma_x}{\partial y^2}\right).$$

Here u, v, w - are the axial displacements of the plate middle surface in the directions x, y, z, respectively. γ_x and γ_y are the panel cross-section angles, k_y - is geometric parameter of panel's curvature, σ_{ij} - are components of the stress tensor, m_{ij} -are components of the tensor of higher order, l is additional independent material length parameter associated with the symmetric bending-torsion tensor. The equations of motion, boundary and initial conditions for an equivalent smooth panel were obtained from the variational principle of Ostrogradskiy-Hamilton. Then the forces and moments acting in the smooth panel were expressed in terms of the forces and moments acting in the original mesh panel [15].

As a result, the equations of motion of the micropolar mesh cylindrical panel elementtook the form:

$$A_{40}\frac{\partial}{\partial x}\left(N_{xx}\frac{\partial w}{\partial x}\right) + A_{22}\frac{\partial}{\partial x}\left(N_{yy}\frac{\partial w}{\partial x}\right) + A_{31}\frac{\partial}{\partial x}\left(T\frac{\partial w}{\partial x}\right) + 2A_{31}\frac{\partial}{\partial x}\left(N_{xx}\frac{\partial w}{\partial y}\right) + 2A_{13}\frac{\partial}{\partial x}\left(N_{yy}\frac{\partial w}{\partial y}\right) +$$

$$+2A_{22}\frac{\partial}{\partial x}\left(T\frac{\partial w}{\partial y}\right) + 2A_{31}\frac{\partial}{\partial y}\left(N_{xx}\frac{\partial w}{\partial x}\right) + 2A_{13}\frac{\partial}{\partial y}\left(N_{yy}\frac{\partial w}{\partial x}\right) + 2A_{22}\frac{\partial}{\partial y}\left(T\frac{\partial w}{\partial x}\right) + A_{22}\frac{\partial}{\partial y}\left(N_{xx}\frac{\partial w}{\partial y}\right) +$$

$$+A_{04}\frac{\partial}{\partial y}\left(N_{yy}\frac{\partial w}{\partial y}\right) + A_{13}\frac{\partial}{\partial y}\left(T\frac{\partial w}{\partial y}\right) + A_{20}\frac{\partial Q_{zx}}{\partial x} + A_{11}\frac{\partial Q_{zy}}{\partial x} + A_{11}\frac{\partial Q_{zx}}{\partial y} + A_{02}\frac{\partial Q_{zy}}{\partial y} -$$

$$-k_y\left(A_{22}N_{xx} + A_{04}N_{yy} + A_{13}T\right) - \frac{1}{2}\left[\left(A_{40} - A_{22}\right)\frac{\partial^2 Y_{xx}}{\partial x\partial y} + \left(A_{22} - A_{04}\right)\frac{\partial^2 Y_{yy}}{\partial x\partial y} + \left(A_{31} - A_{13}\right)\frac{\partial^2 Y_{xy}}{\partial x\partial y}\right] -$$

$$-\frac{1}{2}\left[A_{31}\frac{\partial^2 Y_{xx}}{\partial y^2} + A_{13}\frac{\partial^2 Y_{yy}}{\partial y^2} + A_{22}\frac{\partial^2 Y_{xy}}{\partial y^2} + -A_{31}\frac{\partial^2 Y_{xx}}{\partial x^2} - A_{13}\frac{\partial^2 Y_{yy}}{\partial x^2} - A_{22}\frac{\partial^2 Y_{xy}}{\partial x^2}\right] = \rho h\frac{\partial^2 w}{\partial t^2} - \varepsilon\rho h\frac{\partial w}{\partial t}.$$

$$A_{40}\frac{\partial N_{xx}}{\partial x} + A_{22}\frac{\partial N_{yy}}{\partial x} + A_{31}\frac{\partial T}{\partial x} + A_{31}\frac{\partial N_{xx}}{\partial y} + A_{13}\frac{\partial N_{yy}}{\partial y} + A_{22}\frac{\partial T}{\partial y}$$

$$+\frac{1}{2}\left(A_{11}\frac{\partial^2 Y_{xz}}{\partial y^2} + A_{02}\frac{\partial^2 Y_{yz}}{\partial y^2} + A_{01}\frac{\partial^2 Y_{zz}}{\partial y^2} + A_{20}\frac{\partial^2 Y_{\alpha z}}{\partial x\partial y} + A_{11}\frac{\partial^2 Y_{\beta z}}{\partial x\partial y} + A_{10}\frac{\partial^2 Y_{zz}}{\partial x\partial y}\right) = \rho h\frac{\partial^2 u}{\partial t^2} - \varepsilon\rho h\frac{\partial u}{\partial t},$$

$$A_{22}\frac{\partial N_{xx}}{\partial y} + A_{04}\frac{\partial N_{yy}}{\partial y} + A_{13}\frac{\partial T}{\partial y} + A_{31}\frac{\partial N_{xx}}{\partial x} + A_{13}\frac{\partial N_{yy}}{\partial x} + A_{22}\frac{\partial T}{\partial x}$$

$$-\frac{1}{2}\left(A_{20}\frac{\partial^2 Y_{xz}}{\partial x^2} + A_{11}\frac{\partial^2 Y_{yz}}{\partial x^2} + A_{10}\frac{\partial^2 Y_{zz}}{\partial x^2} + A_{11}\frac{\partial^2 Y_{xz}}{\partial x\partial y} + A_{02}\frac{\partial^2 Y_{yz}}{\partial x\partial y} + A_{01}\frac{\partial^2 Y_{zz}}{\partial x\partial y}\right) = \rho h\frac{\partial^2 v}{\partial t^2} - \varepsilon\rho h\frac{\partial v}{\partial t},$$

$$A_{40}\frac{\partial M_{xx}}{\partial x} + A_{22}\frac{\partial M_{yy}}{\partial x} + A_{31}\frac{\partial H}{\partial x} + A_{31}\frac{\partial M_{xx}}{\partial y} + A_{13}\frac{\partial M_{yy}}{\partial y} + A_{22}\frac{\partial H}{\partial y} - A_{20}Q_{zx} - A_{11}Q_{zy}$$

$$+\frac{1}{2}\left(A_{22}\frac{\partial Y_{xx}}{\partial y} + A_{04}\frac{\partial Y_{yy}}{\partial y} + A_{13}\frac{\partial Y_{xy}}{\partial y} - A_{10}\frac{\partial Y_{xz}}{\partial y} - A_{01}\frac{\partial Y_{yz}}{\partial y} - A_{00}\frac{\partial Y_{zz}}{\partial y} + A_{31}\frac{\partial Y_{xx}}{\partial x} + A_{13}\frac{\partial Y_{yy}}{\partial x} + A_{22}\frac{\partial Y_{xy}}{\partial x}\right)$$

$$+\frac{1}{2}\left(A_{20}\frac{\partial^2 J_{xz}}{\partial x\partial y} + A_{11}\frac{\partial^2 J_{yz}}{\partial x\partial y} + A_{10}\frac{\partial^2 J_{zz}}{\partial x\partial y} + A_{11}\frac{\partial^2 J_{xz}}{\partial y^2} + A_{02}\frac{\partial^2 J_{yz}}{\partial y^2} + A_{01}\frac{\partial^2 J_{zz}}{\partial y^2}\right) = \rho h\frac{\partial^2 \gamma_x}{\partial t^2} - \varepsilon\rho h\frac{\partial \gamma_x}{\partial t},$$

$$A_{22}\frac{\partial M_{xx}}{\partial y} + A_{04}\frac{\partial M_{yy}}{\partial y} + A_{13}\frac{\partial H}{\partial y} + A_{31}\frac{\partial M_{xx}}{\partial x} + A_{13}\frac{\partial M_{yy}}{\partial x} + A_{22}\frac{\partial H}{\partial x} - A_{11}Q_{zx} - A_{02}Q_{zy} -$$

$$-\frac{1}{2}\left(A_{40}\frac{\partial Y_{xx}}{\partial x} + A_{22}\frac{\partial Y_{yy}}{\partial x} + A_{31}\frac{\partial Y_{xy}}{\partial x} - A_{10}\frac{\partial Y_{xz}}{\partial x} - A_{01}\frac{\partial Y_{yz}}{\partial x} - A_{00}\frac{\partial Y_{zz}}{\partial x}{}_{zz} + A_{31}\frac{\partial Y_{xx}}{\partial y} + A_{13}\frac{\partial Y_{yy}}{\partial y} + A_{22}\frac{\partial Y_{xy}}{\partial y}\right) -$$

$$-\frac{1}{2}\left(A_{20}\frac{\partial^2 J_{xz}}{\partial x^2} + A_{11}\frac{\partial^2 J_{yz}}{\partial x^2} + A_{10}\frac{\partial^2 J_{zz}}{\partial x^2} + A_{11}\frac{\partial^2 J_{xz}}{\partial x\partial y} + A_{02}\frac{\partial^2 J_{yz}}{\partial x\partial y} + A_{01}\frac{\partial^2 J_{zz}}{\partial x\partial y}\right) = \rho h\frac{\partial^2 \gamma_y}{\partial t^2} - \varepsilon\rho h\frac{\partial \gamma_y}{\partial t},$$

Where
$$A_{sk} = \sum_{j=1}^{n}\frac{\delta_j \cos^s\varphi_j \sin^k\varphi_j}{a_j}; \ s,k = \overline{0,4}, \qquad \left(N_{xx}, N_{yy}, T\right) = \int_{-\frac{h}{2}}^{\frac{h}{2}}\left(\sigma_{xx}, \sigma_{yy}, \sigma_{xy}\right)dz,$$

$$\left(M_{xx}, M_{yy}, H\right) = \int_{-\frac{h}{2}}^{\frac{h}{2}}\left(\sigma_{xx}, \sigma_{yy}, \sigma_{xy}\right)zdz, \quad \left(Q_{xz}, Q_{yz}\right) = \int_{-\frac{h}{2}}^{\frac{h}{2}}\left(\sigma_{xz}, \sigma_{yz}\right)k_s dz, \quad Y_{xx} = \int_{-\frac{h}{2}}^{\frac{h}{2}}m_{xx}dz, \quad Y_{xy} = \int_{-\frac{h}{2}}^{\frac{h}{2}}m_{xy}dz,$$

$$Y_{\alpha z} = \int_{-\frac{h}{2}}^{\frac{h}{2}}m_{xz}dz, \quad x \rightleftarrows y, \quad Y_{zz} = \int_{-\frac{h}{2}}^{\frac{h}{2}}m_{zz}dz, \quad J_{xz} = \int_{-\frac{h}{2}}^{\frac{h}{2}}m_{xz}zdz, \quad x \rightleftarrows y, \ a_j$$ - is the distance between edges

of j-th set, δ_j – is the edge thickness of the j-th set, φ_j – is the angle between the x-axis and the edge axis of the j-th set, stresses with index j refer to rods, ρ - is the density of plate material, h - is the thickness of the panel, k_s - is the function that characterizes the lawdistributionof shear stresses across the panel thickness.

In this model, the bending stiffness of the rods in the plane tangent to the median surface of the panel is not taken into account, therefore, the orders of the differential equations systemsdescribing the behavior of mesh and solid panels coincide. The formulations of the boundary conditions of the corresponding boundary value problemsare coincide[1].

2. Numerical results

The purpose of this work is to study the effect of the materialmicro polarity and mesh geometry on the behavior of arectangular in plan cylindrical panel. The boundary conditions are therigidly clamped along the ends. The cylindrical panel is under the action of a normal distributed load $q(x,y) = const$.

The equations of motion, boundary and initial conditions are reduced to dimensionless form using the following parameters: $x = 2c\bar{x}$, $y = 2b\bar{y}$, $w = h\bar{w}$, $\gamma_x = \dfrac{h}{2c}\bar{\gamma}_x$, $\gamma_y = \dfrac{h}{2b}\bar{\gamma}_y$, $u = \dfrac{h^2}{2c}\bar{u}$,

$v = \dfrac{h^2}{2b}\bar{v}$, $\delta = h\bar{\delta}$, $a = h\bar{a}$, $l = h\bar{l}$, $k_y = \dfrac{1}{2b}\bar{k}_y$, $t = \dfrac{2c2b}{h}\sqrt{\dfrac{\rho}{E}}\bar{t}$, $\varepsilon = \dfrac{h}{(2c)(2b)}\sqrt{\dfrac{E}{\rho}}\bar{\varepsilon}$, $q = \dfrac{Eh^4}{(2c)^2(2b)^2}\bar{q}$,

where c, b - are plate's linear dimensions in x and y direction, ρ - is the panels material density, ε - dissipation coefficient.

Boundary conditions:

$$w = 0, \quad \frac{\partial w}{\partial x} = 0, \quad \frac{\partial w}{\partial y} = 0, \quad at \quad x = -1, \quad x = 1, \quad y = -1, \quad y = 1,$$

$$u = 0, \quad \frac{\partial u}{\partial x} = 0, \quad \frac{\partial u}{\partial y} = 0, \quad at \quad x = -1, \quad x = 1, \quad y = -1, \quad y = 1,$$

$$v = 0, \quad \frac{\partial v}{\partial x} = 0, \quad \frac{\partial v}{\partial y} = 0 \quad at \quad x = -1, \quad x = 1, \quad y = -1, \quad y = 1,$$

$$\gamma_x = 0, \quad \frac{\partial \gamma_x}{\partial x} = 0, \quad \frac{\partial \gamma_x}{\partial y} = 0 \quad at \quad x = -1, \quad x = 1, \quad y = -1, \quad y = 1,$$

$$\gamma_y = 0, \quad \frac{\partial \gamma_y}{\partial x} = 0, \quad \frac{\partial \gamma_y}{\partial y} = 0 \quad at \quad x = -1, \quad x = 1, \quad y = -1, \quad y = 1.$$

Initial conditions are equal zero.

We will consider a panel formed by two systems of identical mutually perpendicular edges $\varphi_1 = 45°$ and $\varphi_2 = 135°$, $a_1 = a_2 = a$, $\delta_1 = \delta_2 = \delta$.(Figure1)

The behavior of the system will be investigated using the establishment method. The dissipation coefficient is $\varepsilon_{cr} = 1$. The system of differential equations in partial derivatives is reduced to the ODE system using the Bubnov-Galerkin method. To satisfy the boundary conditions, we choose the functions u, v, w, γ_x, γ_y in the following form:

$$u(x, y, t) = \sum_{ij} U(t)\mathrm{Sin}^2\left(\frac{2i\pi x}{c}\right)\mathrm{Sin}^2\left(\frac{j\pi y}{b}\right),$$

$$v(x, y, t) = \sum_{ij} V(t)\mathrm{Cos}^2\left(\frac{(2i-1)\pi x}{2c}\right)\mathrm{Cos}^2\left(\frac{(2j-1)\pi y}{2b}\right),$$

$$w(x, y, t) = \sum_{ij} W(t)\mathrm{Sin}^2\left(\frac{i\pi x}{c}\right)\mathrm{Sin}^2\left(\frac{j\pi y}{b}\right),$$

$$\gamma_x(x, y, t) = \sum_{ij} \Gamma_x(t)\mathrm{Sin}^2\left(\frac{i\pi x}{c}\right)\mathrm{Sin}^2\left(\frac{2j\pi y}{b}\right),$$

$$\gamma_y(x, y, t) = \sum_{ij} \Gamma_y(t)\mathrm{Sin}^2\left(\frac{2i\pi x}{c}\right)\mathrm{Sin}^2\left(\frac{2j\pi y}{b}\right).$$
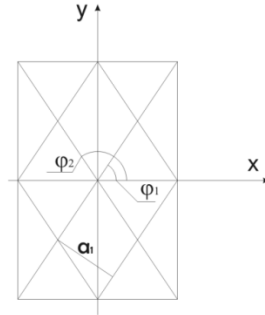
Figure 1. Plate grid geometry.

The Cauchy problem is solved by the Runge – Kutta method of the 4th order of accuracy.Experiment Parameters: $\nu = 0.3$, $\delta = h = 0.002$.

Table 1 shows the "deflection - load" dependences obtained by the Galerkin method and the finite difference method for a Timoshenko cylindrical micropolar mesh panel in the case of an isotropic material$\left(E = 1\,\text{TPa} \right)$. The results obtained by various methods are in good agreement.From the data of the table it is seen that the consideration of moment stresses leads to an increase in the bending stiffness of the panel.

Table 1

"Deflection - load" dependences obtained by the Galerkin method and the finite difference method

	$l = 0$		$l = 0.5$	
q	FDM	Galerkin	FDM	Galerkin
50	1.00688	0.93281	0.85688	0.90181
100	1.23579	1.20664	1.09991	1.18192
150	1.34555	1.39576	1.27119	1.37414
200	1.46420	1.54522	1.41382	1.52557
250	1.56740	1.67087	1.51180	1.65262
300	1.63434	1.78036	1.63388	1.76319
350	1.78429	1.87805	1.77992	1.86174
400	1.99430	1.96668	1.93685	1.95107
450	2.02916	2.04808	2.01818	2.03307
500	2.19714	2.12357	2.14709	2.10907
550	2.26987	2.19411	2.26537	2.18007

In the Figure 2 shows the dependences of the "deflection-load" for otrotropic and isotropic cases ($E_1 = 839.4\,\text{GPa}$ $E_2 = 964\,\text{GPa}$. $E = 1000\,\text{GPa}$. $\nu = 0.3$)
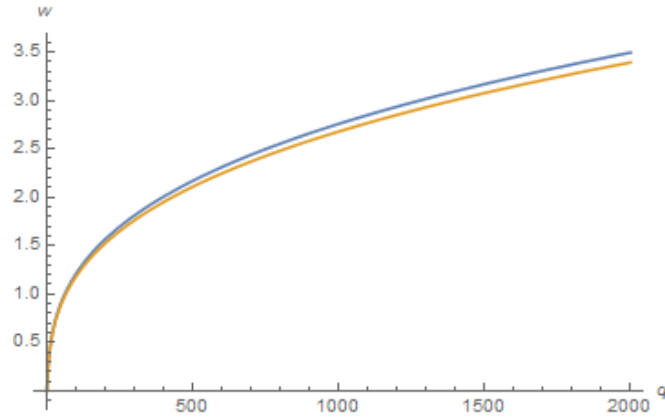
Figure 2. The dependences of the "deflection load" for otrotropic and isotropic cases. Blue line – otrotropic, yellow line -isotropic, green line- $\delta = a$, redline- $a = 0.8\delta$
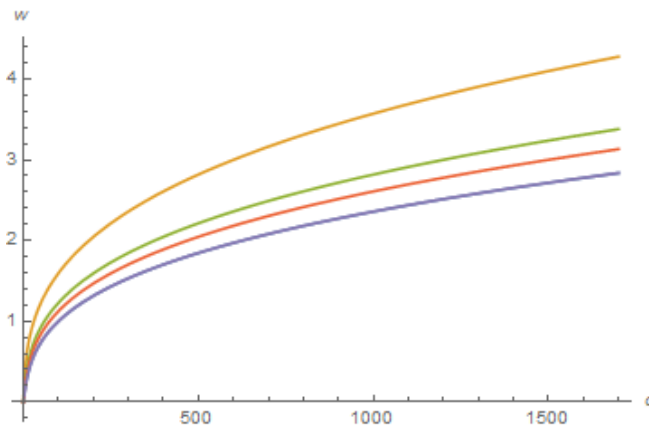
Figure 3. Figure 2. Comparison of a solid panel with a grid, depending on the distance between the edges of the lattice. Blue line –solid panel, yellow line - $a = 2\delta$, green line- $\delta = a$, red line - $a = 0.8\delta$

Taking into account the orthotropic properties of the material leads to an increase in deflections, that is, to a decrease in the bending stiffness of the panel. The greater the difference between the values of the simplicitymodulus, than more noticeable will be the described effect.When obtaining numerical results, an important issue is their reliability. Mathematical models of vibrations of smooth shells were repeatedly compared with the results of other authors and numerical experimenters. It is shown that, as the distance between the edges of the family of the rod core decreases, the deflections of the grid approach the deflections of the continuous (Figure 2). Under these experimental conditions, their

full agreement was achieved with the following values of the geometric parameters of the grid $h = \delta = 0.6a$.

In Figure 3 shows the load-deflection graphs for various values of the curvature parameter ($k_y = \{0;16;24\}$) of the mesh ($a = 0.002$) micropolar ($l = 0.3$) panel. In the case of plate ($k_y = 0$), the graphs are in qualitative agreement with those for smooth plates.In the case of continuous shellswhen $k_y > 12$, an increase in load leads to the phenomenon of "cotton". In the case of a mesh micropolar panel, the phenomenon of "cotton" was not detected.
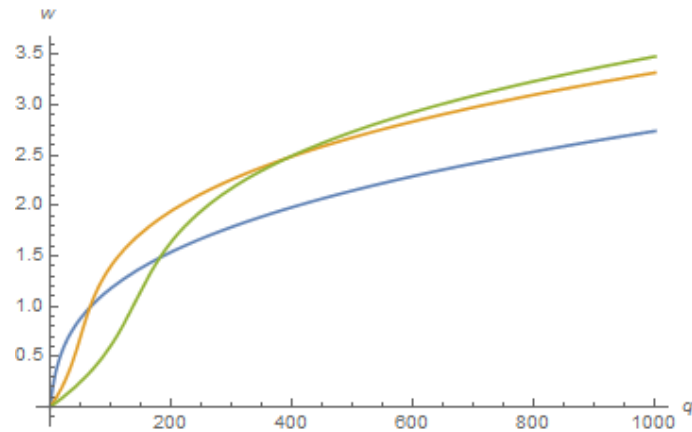
Figure 4. Dependence of the "deflection-load"graphs on the panel curvature parameter.Blue line - $k_y = 0$, yellow line - $k_y = 16$, green line- $k_y = 24$.
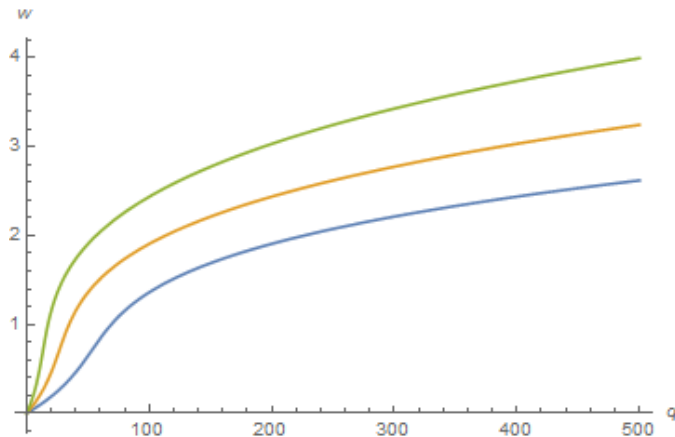
Figure 5. Dependence of the "deflection load" graphs on the distance between ribs. Blue line - $a = \delta = 0.002$, yellow line - $a = 0.004$, green line- $a = 0.008$.

In Figure 4 shows dependence of the graphs $w(q)$ for the micropolar panel with the curvature parameter $k_y = 16$ and the additional length parameter value $l = 0.3$ on the distance between ribs $a = \{0.002; 0.004; 0.008\}$. The figure shows that an increase in the distance between the ribs leads to a decrease in the bending stiffness of the panel.

3. Conclusions

On the basis of Pshenichny's continuum model and Timoshenko's hypotheses, the mathematical model of vibrations of flexible orthotropic micropolar cylindrical mesh panels is constructed.The influence of the additional length's parameter l, and mesh's geometry on the plate's behavior has been studied. The panel consists oftwo families of mutually orthogonal edges. It was revealed that, in contrast to smooth cylindrical panels of large curvature, the phenomenon of "cotton" is absent in mesh micropolar panels. Taking into account the theory of the microfield leads to an increase in the rigidity of the panel. Increasing the distance between the edges of the lattice leads to a decrease in the bending stiffness of the panel.

References

[1] Pshenichnov G. I. Teoriya tonkikh uprugikh setchatykh obolochek i plastinok [Theory of thin elastic mesh shells and plates]. Moscow, Nauka, 1982. 352 p

[2] Burmistrov E.F. Simmetrichnaya deformaciya konstruktivno ortotropnyh obolochek. Izd-voSarat. Un-ta, 1962, 108s.

[3] V.P.Shevchenko Koncentraciya napryazhenij / Pod red. A. N. Guzya, A. S. Kosmodamianskogo, – K.: A.S.K., 1998. – 387 s. (Mekhanika kompozitov: V 12 t. T. 7.)

[4] Krys'ko V.A. Nelinejnaya statika i dinamika neodnorodnyh obolochek. Izd-voSarat. Un-ta, 1976, s. 216

[5]Neff P. A geometrically exact planar Cosserat shell-model with microstructure:existence of minimizers for zero Cosserat couple modulus.*Math. Models Methods Appl. Sci.*, 2007, Vol. 17, Is. 3, P. 363–392.

[6]Birsan M. On Saint-Venant's principle in the theory of Cosseratelastic shells. *Int. J. Eng. Sci.,* 2007, Vol. 45, Is. 2–8, P. 187–198.

[7] Sarkisjan S.O. Micropolar theory of thin rods, plates and shells.*Proceed*-ings National Academy of Sciences of Armenia. Mechanics – Izvestiya N N*rmenii. Mekhanika*, 2005, Vol. 58, No. 2, P. 84–95.

[8] Krylova E Yu, Papkova I V, Sinichkina A O, Yakovleva T B, Krysko-yang V A Mathematical model of flexible dimension-dependent mesh plates IOP Conf. Series: Journal of Physics: Conf. Series 1210 (2019) 012073 doi:10.1088/1742-6596/1210/1/012073

[9] Safarpour H., Mohammadi K. and Ghadiri M. Temperature-dependent vibration analysis of a FG viscoelastic cylindrical microshell under various thermal distribution via modified length scale parameter: a numerical solution Journal of the Mechanical Behavior of Materials 2017, Volume 26, Issue 1-2, Pages 9–24

[10] Sahmani S., Ansari R., Gholami, R., Darvizeh A. Dynamic stability analysis of functionally graded higher-order shear deformable microshells based on the modified couple stress elasticity theory Composites Part B Engineering 51 (2013) 44–53

[11] Varygina M. Numerical modeling of micropolar cylindrical shells on supercomputers with GPUs AIP Conference Proceedings 1895, 080005 (2017)

[12] Xinping Zhou Lin Wang Vibration and stability of micro-scale cylindrical shells conveying fluid based on modified couple stress theory Micro & Nano Letters 2012 Volume: 7 , Issue: 7 , p 679 – 684

[13] Sarkisjan S.O., Farmanyan A.Z. Mathenatical model of micropolar anisotropic (orthotropic) elastic thin shells PNRPU Mechanics Bulletin 2011. № 3. P. 128-145.

[14] F. Yang, A. C. M. Chong, D. C. C. Lam, and P. Tong, "Couple stress based strain gradient theory for elasticity", Int. J. Solids Struct. 39 (2002), 2731–2743.

[15] Krylova E. Yu., Papkova I. V., Yakovleva T. V., Krysko V. A. Theory of Vibrations of Carbon Nanotubes Like Flexible Micropolar Mesh Cylindrical Shells Taking into Account Shift. Izv. Saratov Univ. (N. S.), Ser. Math. Mech. Inform., 2019, vol. 19, iss. 3, pp. 305–316 (in Russian). DOI: https://doi.org/10.18500/1816-9791-2019-19-3-305-316

Jan Awrejcewicz, Professor: Lodz University of Technology, Faculty of Mechanical Engineering, Department of Automation, Biomechanics and Mechatronics, 1/15 Stefanowskego Str., 90-924 Lodz, Poland (jan.awrejcewicz@p.lodz.pl);

Ekaterina Yu. Krylova Associate Professor: Department of Mathematics and Modeling, Saratov State Technical University, Politehnicheskaya 77, 410054 Saratov, Russian Federation (kat.krylova@bk.ru);

Irina V. Papkova Associate Professor: Department of Mathematics and Modeling, Saratov State Technical University, Politehnicheskaya 77, 410054 Saratov, Russian Federation (ikravzova@mail.ru);

Vadim A. Krysko, Professor: Department of Mathematics and Modeling, Saratov State Technical University, Politehnicheskaya 77, 410054 Saratov, Russian Federation (tak@san.ru).

Bending vibration systems as tactile sensors for contact point detection using natural frequencies

Carsten Behn, Daniel Baldeweg, Christoph Will

Abstract: In recent years, bending beam vibrations are analyzed in context to develop biologically inspired sensor systems. Here, this paper contributes to this field and we extend results from conservative systems to dissipative ones herein. We use mechanical models -inspired by the vibrissae of rats and mice- to determine the distance to an object (contact detection) and to get hints for a technical implementation. In contrast to literature, we extend our models to more realistic ones in incorporating fundamental features of a vibrissae: the viscoelasticity of the Follicle-Sinus complex (FSC, support of the vibrissa) and of the skin. Moreover, the conical shape is taken into account, as well, to study the impact of these features on the dynamics. Due to the complexity of previous models, we model the FSC as a viscoelastic-foundation, the skin as a discrete spring-damper-combination, and the conical shape using a three segmented rod with different diameters. The contact point is firstly modeled as a (fixed) bearing. To determine the distance out of the eigenvalues / natural frequencies (later measured in experiments), we develop an algorithm that is tested to be valid for our models.

1. Introduction

In recent decades, the analysis and investigation of biological tactile sensors were done by researchers of the life sciences [7, 9, 3, 20], and the modeling and development of technical tactile sensors inspired by the so-called "vibrissae" of mammals by engineers was started. These tactile sensors gain great interest, e.g., in application to mobile robotics, see [16, 14, 10, 18], because the animals use these vibrissae for several tasks (depending on their the location on the body): object recognition [4], object contour discrimination [5], perception of (air and/or water) flow [6, 23], and just for some social behavior [11].

Although there are several facts from anatomy and functionality of these vibrissae (they are thicker, longer and stiffer than normal body hairs [20] / each vibrissa is supported by its own follicle-sinus complex (FSC) combined with a outstanding arrangement of blood vessels, mechanoreceptors, neural connections and several muscle groups [7] / the vibrissa hair shaft is made of dead material and, therefore, has no receptors along the shaft and is used as a transmission element [8] / the hair shaft exhibits an inherent curvature and a conical shape [17]), there exist a lot of different (mechanical) models, which can be generally divided into

multi-body systems (MBS) and continuous systems (CS). For a first overview on mechanical models the reader's attention is invited to [2, 12].

Of course there are several approaches, the used models differ in dependence on the goal of examination. Both types of models are used in [15] for flow detection. For CS, the vibrissa is usually modeled as a beam. For the vibrissa (major length to minor diameter) the classical Euler-Bernoulli bending beam theory is almost exclusively used in literature. In the case of a static analysis, [16, 21] focus object contour recognition, and of a dynamic analysis, [2] focusses on basic investigations in modeling vibrissae as continuous models, [13] tries to set up mechanical models to verify measured vibration frequencies of natural vibrissae, and [22] investigates the spectrum of natural frequencies during several whisking modes of a vibrissa to state, that the resonance of vibrissae could play a role in the texture recognition.

The most related works to the present one are [19] and [1]. The work [19] forms the basis of this present work. The authors therein try to identify the contact point of a technical vibrissa (or called antenna from insects) with an object in observing the shift of the natural frequencies due to the changing boundary conditions of the tactile sensor (bending beam). A simple mechanical model in form of an one-sided clamped Euler-Bernoulli bending beam,
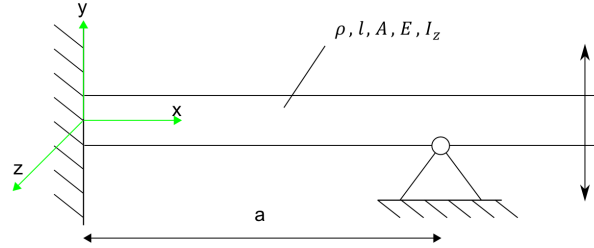
Figure 1. Basic model, adapted from [19].

see Fig. 1, is considered, where the contact with an object is modeled as a "sudden" bearing. Because of the structure of the system is known (there also exist a look-up table of the natural frequencies), it is possible to determine the distance of the contact point to the clamping position in "measuring" the natural frequencies. But, it is not possible to determine the object distance purely in observing the one single natural frequency (see Fig. 2(left) because no curve is bijective). Further on, it is quite impossible to determine the contact point in observing the first two natural frequencies, see Fig. 2(right), because of a nearly intersection of the curve, which can be possible due to measurement noise.

This drawback was the starting point of [1]. The authors improved the model in adding a spring foundation (due to the FSC of the vibrissa) and a single spring coupling (due to the skin support of the vibrissa). Then, it was possible to widen the curve $\omega_2(\omega_1)$ to get a
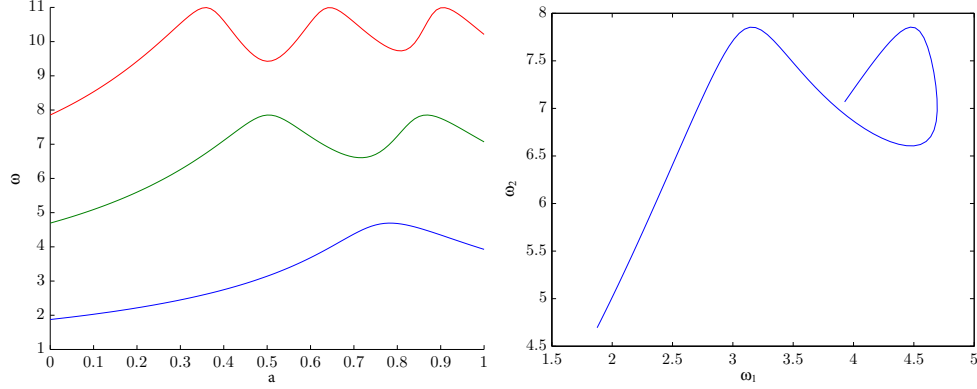
Figure 2. Behavior of the first three natural frequencies in dependence on object distance a (left); curve of the first two natural frequencies $\omega_2 = \omega_2(\omega_1)$ in dependence on a (right); adapted from [19].

unique dependence on the contact point position. The problem was hear also, that there is nearly an intersection of the curve, moreover, a spring foundation is only shifting the curve in the plane, the single spring coupling can widen the curve a bit.

The biological paradigm exhibit some viscosity, hence the investigation of the viscosity on the $\omega_2(\omega_1)-$curve is addressed to the present work.

2. Mechanical and mathematical modeling

As mentioned above, we extend the results found in [1]. Therein, only conservative systems were analyzed. Depending on measured natural frequencies of a transversal vibration beam, three algorithms are developed –based on the measured natural frequencies– determining the distance to an object. Several models were investigated, see Section 1, and we complement these models in adding some damping elements: a single spring-damper-combination to model the viscoelasticity of the skin and a continuously distributed spring-damper arrangement to model the FSC, see Fig. 3. Due to this stage of modeling, we set up two different models exhibiting the mentioned improvements step by step, see Figs. 4 and 5. The first model offers a clamping and an elastic foundation as a support (FSC) with a single spring-damper combination to model the viscoelasticity of the skin, see Fig. 4. The second model focusses a clamping and a viscoelastic foundation as a support (FSC) of the technical vibrissa. Here, we firstly neglect the possible viscosity of the skin, see Fig. 5.

Remark 1. *In the following, we present the examination of Model 1, whereas the analysis of the other model has to be done in an analogous way.*
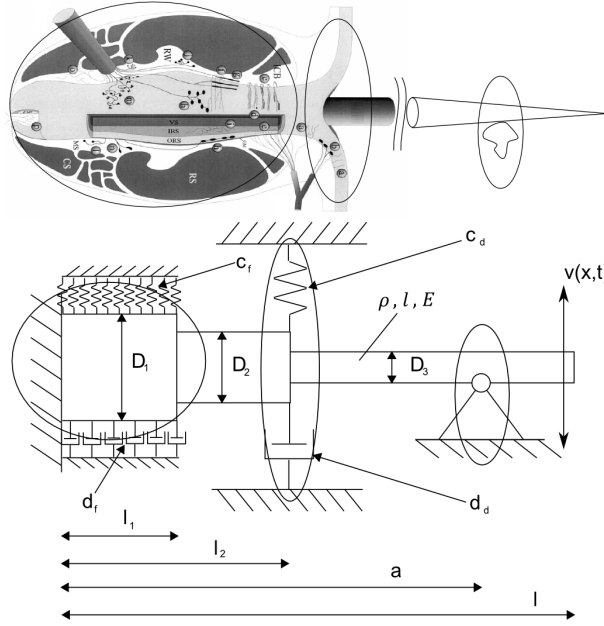
Figure 3. Modeling of a vibrissa: above - vibrissa with contact [9]; below - model of a vibrissa with contact.
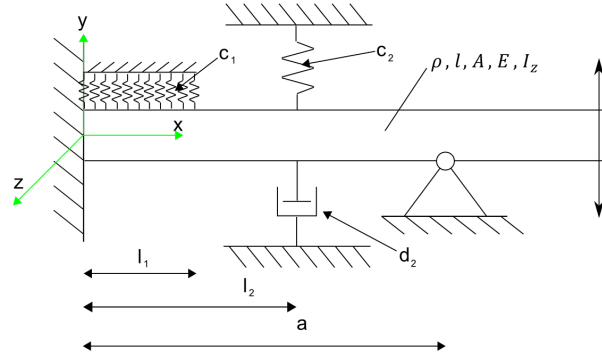
Figure 4. Model 1 with a single spring-damper coupling.

Let us consider the beam with parameters length l, area of cross section A (constant, described by diameter D – cylindrical beam), second moment of area w.r.t. the z-axis I_z (constant), Young's modulus E (constant) and density ϱ. The stiffness of the springs are given by the ratios c_1 and c_2 of the continuously distributed and discrete ones, respectively. The damping ratio is given by d_2. The contact between the beam and an object is modeled
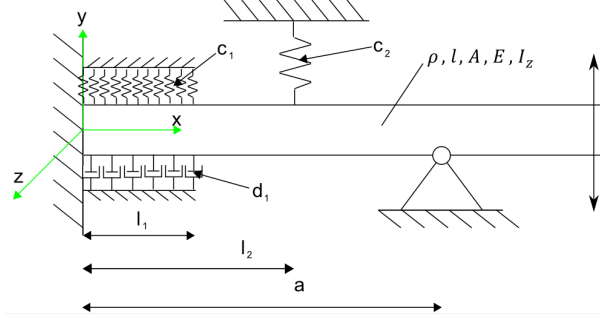
Figure 5. Model 2 with a continuously distributed spring-damper foundation.

as a bearing (simplification) in a distance of a to the clamping.

Then, it is well-known, that the bending beam vibrations of small amplitude are described by the partial differential equations (PDEs)

$$\varrho\, A\, v_{,tt}\,(x,t) + E\, I_z\, v_{,xxxx}\,(x,t) + c_1\, v(x,t) = 0\,, \quad \forall\, (x,t) \in (0,l_1) \times \mathbb{R}_+ \tag{1}$$

and

$$\varrho\, A\, v_{,tt}\,(x,t) + E\, I_z\, v_{,xxxx}\,(x,t) = 0\,, \quad \forall\, (x,t) \in (l_1,l_2) \cup (l_2,a) \cup (a,l) \times \mathbb{R}_+\,, \tag{2}$$

Solutions of the arising boundary-value problem (BVP) are investigated using separation of variables, that yields the following solution on several sections:

$$\begin{aligned} v_i\,(x,t) &= T_i\,(t) \cdot X_i\,(x) \\ &= \Big(C_{1i}\, \cos(\omega_i t) + C_{2i}\, \sin(\omega_i t) \Big) \cdot \Big(C_{3i}\, \cos(\lambda_i x) + C_{4i}\, \sin(\lambda_i x) \\ &\quad + C_{5i}\, \cosh(\lambda_i x) + C_{6i}\, \sinh(\lambda_i x) \Big), \end{aligned} \tag{3}$$

whereby, for all $t \in \mathbb{R}_{>0}$, we have $v_1(x,t)$ with $x \in (0,l_1)$, $v_2(x,t)$ with $x \in (l_1,l_2)$, $v_3(x,t)$ with $x \in (l_2,a)$, and $v_4(x,t)$ with $x \in (a,l)$.

At this stage, the connection between the eigenvalues has to be clarified. At first, we have for the PDE coefficient

$$k_1^4 = k_2^4 = k_3^4 = k_4^4 := k^4.$$

because all parameters of the beam are the same in each section. Then, because of $\omega_1 = \omega_2 = \omega_3 = \omega_4 =: \omega$ we conclude

$$\left. \begin{aligned} \omega_1^2 = \omega_2^2 &\quad\Rightarrow\quad \lambda_1^4\, k^4 + \tfrac{c_1}{\rho\, A} = \lambda_2^4\, k^4 \quad\Rightarrow\quad \lambda_2 = \sqrt[4]{\lambda_1^4 + \tfrac{c_1}{E\, I_z}}\,, \\ \omega_1^2 = \omega_3^2 &\quad\Rightarrow\quad \lambda_3 = \sqrt[4]{\lambda_1^4 + \tfrac{c_1}{E\, I_z}}\,, \\ \omega_1^2 = \omega_4^2 &\quad\Rightarrow\quad \lambda_4 = \sqrt[4]{\lambda_1^4 + \tfrac{c_1}{E\, I_z}}\,. \end{aligned} \right\} \tag{4}$$

As to be seen in the Figs. 4 to 5, all mechanical beam models offer 4 sections, therefore, with respect to the general solution (3) of the PDE (1), we have to formulate 16 BCs for the systems:

$$
\left.
\begin{array}{ll}
01.\ v_1(0,t) = 0\,, & 02.\ v_1'(0,t) = 0 \\
03.\ v_1(l_1,t) = v_2(l_1,t)\,, & 04.\ v_1'(l_1,t) = v_2'(l_1,t) \\
05.\ v_1''(l_1,t) = v_2''(l_1,t)\,, & 06.\ v_1'''(l_1,t) = v_2'''(l_1,t) \\
07.\ v_2(l_2,t) = v_3(l_2,t)\,, & 08.\ v_2'(l_2,t) = v_3'(l_2,t) \\
09.\ v_2''(l_2,t) = v_3''(l_2,t)\,, & \\
10.\ v_2'''(l_2,t) = v_3'''(l_2,t) + \frac{c_2}{E\,I_z}\,v_2(l_2,t) & +i\,\lambda^2\,\frac{d_2}{E\,I_z}\,\sqrt{\frac{E\,I_z}{\varrho\,A}}\,v_2(l_2,t) \\
11.\ v_3(a,t) = v_4(a,t)\,, & 12.\ v_3'(a,t) = v_4'(a,t) \\
13.\ v_3(a,t) = 0\,, & 14.\ v_3''(a,t) = v_4''(a,t) \\
15.\ v_4''(l,t) = 0\,, & 16.\ v_4'''(l,t) = 0
\end{array}
\right\}
\tag{5}
$$

Writing $\lambda := \lambda_1$ in (4) and substituting in (3) we can evaluate the BCs (5) by means of the four solutions (3) to determine the eigenvalue equation, to govern the eigenvalues and natural frequencies in the following.

3. Simulations

For the models, different values of the system parameters are needed to calculate the natural frequencies and eigenvalues for the dynamic analysis. Therefore, a parameter set is created. Since the goal is not the replica of the biological paragon 'vibrissa', but the understanding of influences of system parameters, a technical set is used, see Table 3. Of course, this data are unrealistic for a natural vibrissae of rats, but they represent the relationships better and can be considered as parameters for a tactile sensor.

Table 1. Technical set of the steel beam.

ρ	7850 $\frac{\text{kg}}{\text{m}^3}$
E	210 GPa
D	10 mm
l_1	250 mm
l_2	500 mm
l	1000 mm

Remark 2. *We prefer dimensionless notation throughout by using the following units of measurement matching data of the real background system (L, ρ, A, E, I_z beam parameters;*

48

dimensionless variables only here with a tilde which is dropped afterwards):

$$x = \tilde{x} \cdot L, \quad t = \tilde{t} \cdot L^2 \sqrt{\frac{\rho A}{E I_z}}, \quad \omega = \tilde{\omega} \cdot \frac{1}{L^2} \sqrt{\frac{E I_z}{\rho A}},$$

$$c_1 = \tilde{c}_1 \cdot \frac{E I_z}{L^4}, \quad c_2 = \tilde{c}_2 \cdot \frac{E I_z}{L^3}, \quad d_2 = \tilde{d}_2 \cdot \frac{1}{L} \sqrt{\rho A E I_z}.$$

The following spring rates are chosen, according to Remark 2, $\tilde{c}_1 = 10$ und $\tilde{c}_2 = 10$.

The first simulation is devoted to model 1 with a single damping element. Figure 6(left) shows that the natural frequencies decrease with an increasing d_2. As expected from the classical vibration theory, the effect of changing parameters has the largest effect on the first natural frequency. Focusing Fig. 6(right), the $\omega_2(\omega_1)-$curve will become an intersection if the damping ratio is too large. Then, no determination of the contact point is possible.
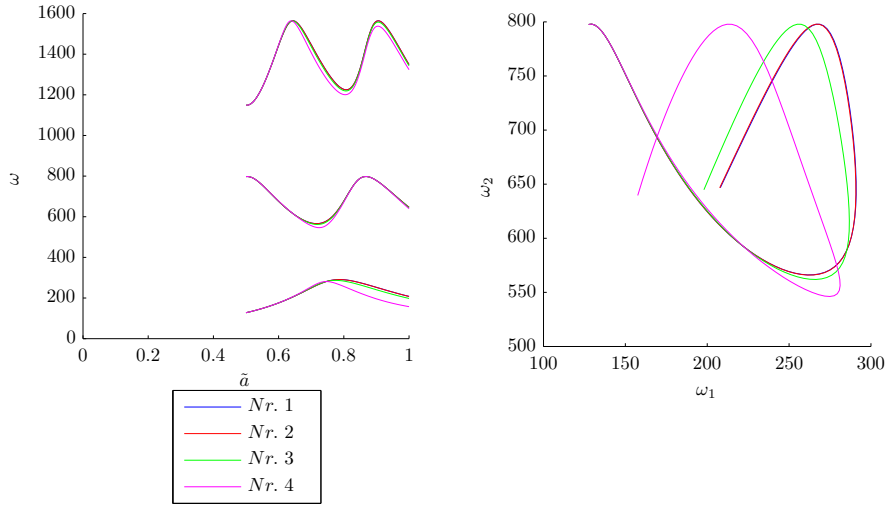
Figure 6. First three natural frequencies vs. length (left); curve ω_2 vs. ω_1 (right); both in dependence on various values of d_2 (Nr. $1 - d_2 = 0$, Nr. $2 - d_2 = 1$, Nr. $3 - d_2 = 5$, Nr. $4 - d_2 = 10$.

Having a glance to the simulation of model 2, one can clearly the an increase of all natural frequencies due to an increasing ratio d_1, see Fig. 7(left). It is obvious, that a visco-elastic foundation has nearly no influence on the behavior of the natural frequencies, see Fig. 7. But, there is no intersection of the $\omega_2(\omega_1)-$curve, and hence, there is a unique identification of the contact point a in observing the first two natural frequencies.

Summarizing, the single damping element has more impact on the behavior of the natural frequencies, but with a damping ratio that is too big, then no identification of the contact
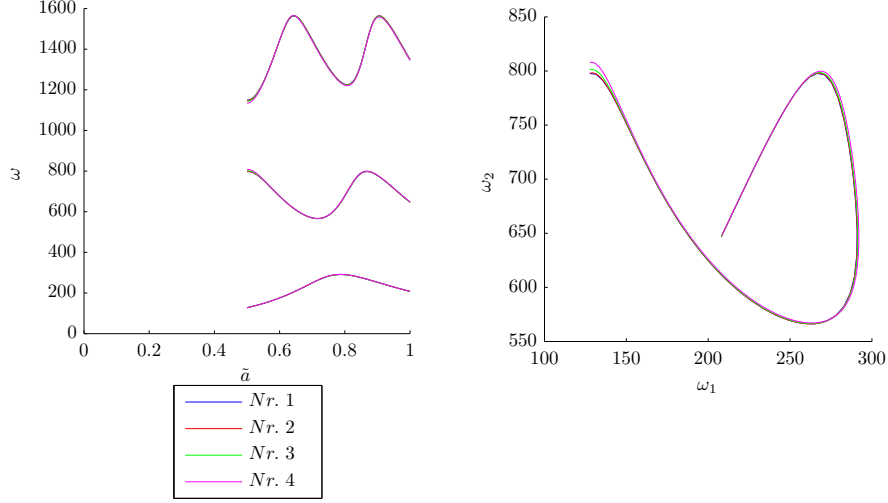
Figure 7. First three natural frequencies vs. length (left); curve ω_2 vs. ω_1 (right); both in dependence on various values of $\tilde{d}_1$ (Nr. 1 – $\tilde{d}_1 = 0$, Nr. 2 – $\tilde{d}_1 = 10$, Nr. 3 – $\tilde{d}_1 = 30$, Nr. 4 – $\tilde{d}_1 = 50$.

point is possible.

4. Conclusions

This paper was devoted to the dynamic analysis of vibrating technical sensors –inspired by natural vibrissae– to determine the contact point due to an object. This is done in purely observing the shift of the spectrum of natural frequencies. Because previous works showed, that this general procedure is possible, but only considered conservative systems, this work was addressed to investigate the influence of damping elements to the behavior of the natural frequencies to determine the contact point. It was shown, that a single damper coupling has more impact on the natural frequencies than a damping foundation (maybe due to the follicle-sinus complex of the biological paragon). Generally, the single damping elements contributes to the identification of the contact point if the ratio is not too large.

Future work shall not be addressed to set up more realistic models, i.e., not neglecting the elasticity of the support (as done here in using a clamping), or to incorporate the conicity or the inherent curvature to the model. It would be questionable, if there are more insights. Rather, experiments should be carried out to verify the investigations.

References

[1] BALDEWEG, D., WILL, C., AND BEHN, C. Transversal vibrations of beams in context of vibrassae consisting of foundations, discrete supports and various sections. In *Proceedings of Ilmenau Scientific Colloquium – Shaping the Future by Engineering Vol. 58* (Technische Universität Ilmenau, Germany, September 2014), ilmedia.

[2] BEHN, C. Mathematical modeling and control of biologically inspired uncertain motion systems with adaptive features. Habilitation, Technische Universität Ilmenau, Germany, 2013, Supervisors: K. Zimmermann (TU Ilmenau), H. Witte (TU Ilmenau), J. Awrejcewicz (Lodz University of Technology).

[3] BERG, R., AND KLEINFELD, D. Rhythmic whisking by rat: retraction as well as protraction of the vibrissae is under active muscular control. *Journal of Neurophysiology 89*, 1 (2002), 104–117.

[4] BRECHT, M., PREILOWSKI, B., AND MERZENICH, M. M. Functional architecture of the mystacial vibrissae. *Behavioural Brain Research 84* (1997), 81–97.

[5] CARVELL, G. E., AND SIMONS, D. J. Biometric analyses of vibrissal tactile discrimination in the rat. *The Journal of Neuroscience 10*, 8 (1990), 2638–2648.

[6] DEHNHARDT, G., MAUCK, B., AND BLECKMAN, H. Seal whiskers detect water movements. *Nature 394* (1998), 235–236.

[7] DÖRFL, J. The musculature of the mystacial vibrissae of the white mouse. *Journal of Anatomy 135* (1982), 147–154.

[8] EBARA, S., KUMAMOTO, K., MATSUURA, T., MAZURKIEWICZ, J. E., AND RICE, F. L. Similarities and differences in the innervation of mystacial vibrissal follicle-sinus complexes in the rat and cat: A confocal microscopic study. *The Journal of Comparative Neurology 449*, 2 (2002), 103–119.

[9] FUNDIN, B. T., ARVIDSSON, J., AND RICE, F. L. Innervation of nonmystacial vibrissae in the adult rat. *The Journal of Comparative Neurology 357*, 4 (1995), 501–512.

[10] KIM, D., AND MÖLLER, R. Biomimetic whiskers for shape recognition. *Robotics and Autonomous Systems 55*, 3 (2007), 229–243.

[11] LONG, S. Y. Hair-nibbling and whisker-trimming as indicators of social hierarchy in mice. *Animal Behaviour 20*, 1 (1972), 10–12.

[12] LUCIANNA, F. A., ALBARRACÍN, A. L., VRECH, S. M., FARFÁN, F. D., AND FELICE, C. J. The mathematical whisker: A review of numerical models of the rat's vibrissa biomechanics. *Journal of Biomechanics 49*, 10 (2016), 2007–2014.

[13] NEIMARK, M. A., ANDERMANN, M. L., HOPFIELD, J. J., AND MOORE, C. I. Vibrissa resonance as a transduction mechanism for tactile encoding. *The Journal of Neuroscience 23*, 16 (2003), 6499–6509.

[14] PEARSON, M. J., GILHESPY, I., MELHUISH, C., MITCHINSON, B., NIBOUCHE, M., PIPE, A. G., AND PRESCOTT, T. J. A biologically inspired haptic sensor array for use in mobile robotic vehicles. In *Towards Autonomous Robotic Systems (TAROS)* (2005), pp. 189–196.

[15] SCHARFF, M., SCHORR, P., BECKER, T., RESAGK, C., ALENCASTRE MIRANDA, J. H., AND BEHN, C. An artificial vibrissa-like sensor for detection of flows. *Sensors 19*, 18 (2019), e3892.

[16] SCHOLZ, G. R., AND RAHN, C. D. Profile sensing with an actuated whisker. *IEEE Transactions on Robotics and Automation 20*, 1 (2004), 124–127.

[17] TOWAL, R. B., QUIST, B. W., GOPAL, V., SOLOMON, J. H., AND HARTMANN, M. J. Z. The morphology of the rat vibrissal array: A model for quantifying spatiotemporal patterns of whisker-object contact. *PLoS Computational Biology 7*, 4 (2011), 1–17.

[18] TUNA, C., SOLOMON, J. H., JONES, D. L., AND HARTMANN, M. J. Z. Object shape recognition with artificial whiskers using tomographic reconstruction. In *IEEE International Conference on Acoustics, Speech and Signal Processing (ICASSP)* (2012), pp. 2537–2540.

[19] UENO, N., SVININ, M. M., AND KANEKO, M. Dynamic contact sensing by flexible beam. *IEEE/ASME Transactions on Mechatronics 3*, 4 (1998), 254–264.

[20] VOGES, D., CARL, K., KLAUER, G. J., UHLIG, R., SCHILLING, C., BEHN, C., AND WITTE, H. Structural characterization of the whisker system of the rat. *IEEE Sensors 12*, 2 (2012), 332–339.

[21] WILL, C. *Continuum models for biologically inspired tactile sensors – Theory, numerics and experiments.* PhD thesis, Technische Universität Ilmenau, Germany, 2018. Supervisors: C. Behn (TU Ilmenau), H. Witte (TU Ilmenau), A. Müller (Johannes Kepler University Linz).

[22] YAN, W., KAN, Q., KERGRENE, K., KANG, G., FENG, X.-Q., AND RAJAN, R. A truncated conical beam model for analysis of the vibration of rat whiskers. *Journal of Biomechanics 46*, 12 (2013), 1987–1995.

[23] YU, Y. S. W., GRAFF, M. M., BRESEE, C. S., MAN, Y. B., AND HARTMANN, M. J. Z. Whiskers aid anemotaxis in rats. *Science Advances 2*, 8 (2016), e1600716.

Carsten Behn, Professor: Schmalkalden University of Applied Sciences, Dept. of Mechanical Engineering, Blechhammer 4-9, 98574 Schmalkalden, Germany (*c.behn@hs-sm.de*). The author gave a presentation of this paper during one of the conference sessions.

Daniel Baldeweg, M.Sc.: Schaeffler Technologies AG&Co. KG, Industriestraße 1-3, 91074 Herzogenaurach, Germany (*daniel.baldeweg@schaeffler.com*).

Christoph Will, Ph.D.: Technische Universität Ilmenau, Dept. of Mechanical Engineering, Max-Planck-Ring 12, 98693 Ilmenau, Germany (*christophwill@gmx.net*).

Bending vibrations with boundary damping
— unlike behavior of tactile sensors

Carsten Behn, Christoph Will, Joachim Steigenberger

Abstract: The paper is devoted to an unlike behavior of natural frequencies in beam vibrations. Guided by the biological paragon vibrissa we investigate small vibrations of an Euler-Bernoulli beam and focus in particular on the question how the natural frequencies depend on the main features of this tactile system. Precisely, a clamped and boundary visco-elastically supported beam serves as a first model to determine the spectrum of natural frequencies (later using these frequencies to detect an obstacle contact). The damping element significantly increases the complexity of the two-point boundary-value problem and leads to a surprising phenomenon: there exist some natural frequencies which break down to zero for a certain range of parameters. This fact is well-known in 1-DoF systems (i.e., strong damping, creeping behavior). The study demonstrates that the oscillation behavior of an elastic beam differs remarkably from the behavior of such a classical system: a) The natural frequencies may increase with growing boundary damping; b) for specific damping parameter values, the natural frequencies grow for decreasing boundary stiffness.

1. Introduction

In recent years, bio-inspired sensor systems come into more focus because they can complement "classical" senses like vision for mobile robotics. The paradigm from biology is the animal vibrissa with its transmission element "hair" (hair shaft). Its is used for the transmission of signals to the vibrissa base (follicle sinus complex) where the information is processed to the CNS, see [7]. Hence, we have to analyze bending beam vibrations caused by contacts with objects, further on, these vibrations can also be induced by the animal on its own in using the surrounding muscles, [1]. The literature offers some works, see [10] for a detailed overview.

Here, we firstly consider bending beam vibrations of a system with a discrete visco-elasticity (a discrete spring-damper-pair at the boundary), see Fig. 1, which is inspired by the skin of the animal. Since we do not want to deal with several sections, we restrict the model to only one section.

Remark 1. *The model given in Fig. 1 looks simple, but it will offer some unlike dynamical behavior in the following. Similar models are not analyzed in literature, but given as exercises (?) without any solution, see [9]. Often, only conservative systems are analyzed and*
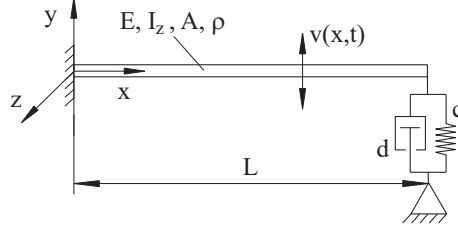
Figure 1. Considered mechanical model.

well studied with discrete or continuously distributed springs. Systems focussing on discrete damped elements in context of bending beam vibrations (non-conservative ones) are rarely analyzed, see [3, 4, 5, 8]. We will analyze our "simple" system and extend some results given in [2] in an analytical way.

2. Vibrations of a bending beam with boundary support clamped / viscoelastic

Bending beam vibrations of small amplitude are described by the partial differential equation (PDE)

$$v_{,xxxx} + v_{,tt} = 0\,, \quad \forall\ (x,t) \in (0,1) \times \mathbb{R}_+ \tag{1}$$

under particular boundary conditions (BCs). Solutions of this boundary-value problem (BVP) are investigated using separation of variables.

Remark 2. *It is well-known, that we claim a constant cross section A of the beam, as well as a constant second moment of area I_z, to arrive at the PDE (1).*

Remark 3. *We prefer dimensionless notation throughout by using the following units of measurement matching data of the real background system (L, ρ, A, E, I_z beam parameters; dimensionless variables only here with a tilde which is dropped afterwards):*

$$
\begin{aligned}
x &= \tilde{x} \cdot L\,, \quad t = \tilde{t} \cdot L^2 \sqrt{\frac{\rho\,A}{E\,I_z}}\,, \quad \omega = \tilde{\omega} \cdot \frac{1}{L^2} \sqrt{\frac{E\,I_z}{\rho\,A}}\,, \\
c &= \tilde{c} \cdot \frac{E\,I_z}{L^3}\,, \quad d = \tilde{d} \cdot \frac{1}{L} \sqrt{\rho\,A\,E\,I_z}\,.
\end{aligned}
$$

The boundary conditions (BCs) of the considered system in Fig. 1 are:

$$
\begin{aligned}
v(0,t) &= 0\,, \\
v_{,x}(0,t) &= 0\,, \\
v_{,xx}(1,t) &= 0\,, \\
v_{,xxx}(1,t) &= c\,v(1,t) + d\,v_{,t}(1,t)\,.
\end{aligned} \tag{2}
$$

Separation of variables,

$$v(x,t) = X(x)T(t) \;\Rightarrow\; \frac{X^{(4)}}{X}(x) = -\frac{\ddot{T}}{T}(t) =: \lambda^4, \quad \lambda \in \mathbb{C}, \tag{3}$$

yields the solutions

$$X(x) = A \cosh(\lambda\,x) + B \cos(\lambda\,x) + C \sinh(\lambda\,x) + D \sin(\lambda\,x),$$
$$T(t) = C_1 \exp(i\,\lambda^2\,t) + C_2 \exp(-i\,\lambda^2\,t). \tag{4}$$

The constants $A, \ldots, D, C_1, C_2$ are (complex) integration constants.

Supposing $\lambda \neq 0$ (else only the zero solution results) the first two BCs yield $B = -A$, $D = -C$, and the third one then entails

$$0 = A \{\cosh(\lambda) + \cos(\lambda)\} + C \{\sinh(\lambda) + \sin(\lambda)\} \tag{5}$$

The fourth BC writes

$$X'''(1)\,T(t) = c\,X(1)\,T(t) + d\,X(1)\,\dot{T}(t), \tag{6}$$

and after differentiation and using (3) there follows

$$\left[X'''(1) - c\,X(1)\right]\dot{T}(t) = -d\,X(1)\,\lambda^4\,T(t).$$

In order to eliminate $\dot{T}(t)$ we multiply by $d\,X(1)$ and, using (6), we obtain

$$\left[X'''(1) - c\,X(1)\right]^2 T(t) = -(d\,X(1))^2\,\lambda^4\,T(t). \tag{7}$$

Remark 4. *The term $d\,X(1) = 0$ would do no trouble: $d = 0$ is trivial and of no interest here, $X(1) = 0$ implies $X'''(1) = 0$, which together with $X''(1) = 0$ yields $\lambda = 0$ and the trivial solution.*

Dropping $T(t)$, there results

$$X'''(1) = (c \pm i\,d\,\lambda^2)\,X(1). \tag{8}$$

With (5) this generates the homogeneous linear equations for A and C

$$0 = A \{\cosh(\lambda) + \cos(\lambda)\} + C \{\sinh(\lambda) + \sin(\lambda)\},$$
$$0 = A \{\lambda^3 [\sinh(\lambda) - \sin(\lambda)] + (c \pm i\,d\,\lambda^2) [\cosh(\lambda) - \cos(\lambda)]\}$$
$$+C \{\lambda^3 [\cosh(\lambda) + \cos(\lambda)] + (c \pm i\,d\,\lambda^2) [\sinh(\lambda) - \sin(\lambda)]\}, \tag{9}$$

the zero determinant of which gives the characteristic equation for λ:

$$\lambda^3 [1 + \cosh(\lambda)\,\cos(\lambda)] + (c \pm i\,d\,\lambda^2) [\cosh(\lambda)\,\sin(\lambda) - \sinh(\lambda)\,\cos(\lambda)] = 0. \tag{10}$$

These are, because of the $\pm$-sign, in fact *two* equations. Let their left-hand sides (lhs, and rhs, respectively) be symbolized as $eq(\lambda; c, d; +)$ and $eq(\lambda; c, d; -)$, respectively. It is easy matter to verify the following Proposition 1.

Proposition 1. *If $eq(\lambda; c, d; +) = 0$ then $eq(\overline{\lambda}; c, d; -) = 0$, where $\overline{\lambda}$ is the complex conjugate of λ. This means that the eigenvalues of the BVP appear as a sequence of conjugate pairs. Moreover, $eq(i\lambda; c, d; +) = -i \cdot eq(\lambda; c, d; -)$ and $eq(-\lambda; c, d; \pm) = -eq(\lambda; c, d; \pm)$ implies that each eigenvalue λ entails the $8 - tuple$ $(\pm\lambda, \pm\overline{\lambda}, \pm i\lambda, \pm i\overline{\lambda})$ of eigenvalues.*

Proposition 2. *Let λ be any eigenvalue. Then we have*

$$\cosh(\lambda) + \cos(\lambda) \neq 0,$$

i.e., the first equation of (9) can be solved for A, so that C is left as sole coefficient in the respective eigenfunction.

Let λ be an eigenvalue. Then we obtain from (4) and (5) the corresponding complex-valued eigenfunction

$$X(x) = [\cosh(\lambda) + \cos(\lambda)]\{\sinh(\lambda x) - \sin(\lambda x)\}$$
$$- [\sinh(\lambda) + \sin(\lambda)]\{\cosh(\lambda x) - \cos(\lambda x)\}, \quad (11)$$

which could be normed by a factor $1/X(1)$ or $1/\sqrt{\int_0^1 \mid X^2(x) \mid dx}$. The eigenfunction corresponding to $\overline{\lambda}$ then is $\overline{X(x)}$, the ones corresponding to $i\lambda$ and $-\lambda$ are, respectively, $iX(x)$ and $-X(x)$.

In general, we may see the eigenvalues as a sequence of *complex* numbers (in particular if $d > 0$), which are ordered in complex conjugate pairs $(\lambda_\nu, \overline{\lambda_\nu} \mid \nu \in \mathbb{N})$ — the remaining ones of the above mentioned 8-tuple are irrelevant with regard to the eigenfunctions.

The (x, t)-dependent solutions of the BVP which belong to this conjugate pair are

$$\begin{aligned}\lambda: \quad & X(x)\{C_1 \exp(i\lambda^2 t) + C_2 \exp(-i\lambda^2 t)\}, \\ \overline{\lambda}: \quad & \overline{X}(x)\{C_3 \exp(i\overline{\lambda}^2 t) + C_4 \exp(-i\overline{\lambda}^2 t)\},\end{aligned} \quad (12)$$

where $C_1, \ldots, C_4$ are complex integration constants. If we let $\lambda = \alpha + i\beta$ and $\lambda^2 = \omega + i\delta$ ($\overline{\lambda}^2 = \omega - i\delta$), then we have $\omega = \alpha^2 - \beta^2$, and $\delta = 2\alpha\beta$. In Section 4 we shall see that $\alpha > 0$, $\beta \geq 0$, hence $\delta \geq 0$. Each of the above functions contains a term with factor $\exp(\delta t)$ that implies an increase in time if $\delta \neq 0$. In case of damping ($d > 0$) this cannot occur, therefore, the respective terms must be killed by putting $C_2 = C_3 = 0$. Let $X = U + iV$ and $C_1 = a_1 + i a_2$, $C_4 = b_1 + i b_2$. Then there remains
for λ:

$$\begin{aligned}&\{[U(x)(a_1 \cos(\omega t) - a_2 \sin(\omega t)) - V(x)(a_1 \sin(\omega t) + a_2 \cos(\omega t))]+ \\ &+ i[V(x)(a_1 \cos(\omega t) - a_2 \sin(\omega t))] + U(x)(a_1 \sin(\omega t) + a_2 \cos(\omega t))]\}e^{-\delta t},\end{aligned} \quad (13)$$

for $\overline{\lambda}$:

$$\{[U(x)(b_1\cos(\omega t) + b_2\sin(\omega t)) + V(x)(b_2\cos(\omega t) - b_1\sin(\omega t))]+$$
$$+i[-V(x)(b_1\cos(\omega t) + b_2\sin(\omega t))] + U(x)(b_2\cos(\omega t) - b_1\sin(\omega t))]\}e^{-\delta t}\,, \tag{14}$$

where a_1, a_2, b_1, b_2 are real integration constants.

Now, to each $\nu \in \mathbb{N}$, there belong the eigenvalues $\lambda_\nu, \overline{\lambda}_\nu$ and the *complex eigenspace* spanned by the corresponding eigenfunctions $X_\nu =: U_\nu + i\,V_\nu$ and $\overline{X_\nu} =: U_\nu - i\,V_\nu$. The linear combinations $\frac{1}{2}(X_\nu + \overline{X_\nu})$ and $\frac{1}{2i}(X_\nu - \overline{X_\nu})$ exhibit the pair (U_ν, V_ν) as a *real* basis of that complex eigenspace (which shrinks to a one-dimensional space in the real case for $d = 0$).

Open question: *Can the space span*$\{X_\nu, \overline{X_\nu} \mid \nu \in \mathbb{N}\}$ *be made a Hilbert space by means of a suitable scalar product? And is then an orthonormal basis a complete one? Same question in the real case that happens for zero damping $d = 0$. What is the meaning of the drop of dimension in going from $d > 0$ to $d = 0$?*

3. Eigenvalues and natural frequencies

Since the eigenvalues of the problem are in general complex numbers, we formally replace λ by z, and we let

$$F_0(z) := \cosh(z)\cos(z) + 1\,,$$
$$F_1(z) := \cosh(z)\sin(z) - \sinh(z)\cos(z)\,, \text{ and finally} \tag{15}$$
$$F(z; c, k) := z^3\,F_0(z) + (c + i\,d\,z^2)\,F_1(z)\,.$$

Obviously, $F(z, 0, 0) = F_0(z)$, and $F_0(z) = 0$ is the characteristic equation of the bending problem "clamped-free", see Fig. 2 (left). Its first three (real[1]) solutions $z^{(0)}$ and the respective natural frequencies $\omega^{(0)} = (z^{(0)})^2$ are

$$z_\nu^{(0)} = 1.875104,\ 4.694091,\ 7.854757,\ \ldots$$
$$\omega_\nu^{(0)} = 3.516015,\ 22.034492,\ 61.697214,\ \ldots$$

Equally, $F(z, \infty, d) = F(z, c, \infty) = F_1(z)$, and $F_1(z) = 0$ is the characteristic equation of the bending problem "clamped-pivoted", see Fig. 2 (right). Its first three non-zero (real) solutions $z^{(1)}$ and the respective natural frequencies $\omega^{(1)} = (z^{(1)})^2$ are

$$z_\nu^{(1)} = 3.926602,\ 7.068583,\ 10.210176,\ \ldots$$
$$\omega_\nu^{(1)} = 15.418206,\ 49.964862,\ 104.247696,\ \ldots$$

---

[1]From (12) and (14) we see that the solutions are periodic in time iff $\delta = 0$, i.e., iff λ is a real number. Else, a non-real λ demands the existence of a viscous part of the system, i.e., $d \neq 0$. So if $d = 0$, then there are only real eigenvalues.
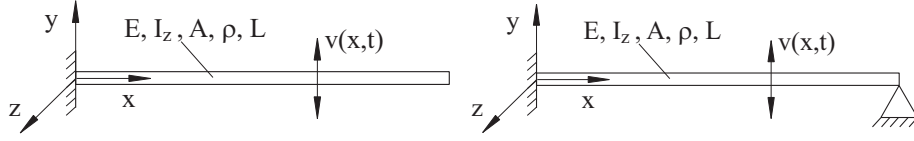
Figure 2. Mechanical models: "clamped-free" (left), and "clamped-pivoted" (right).

If $z(c, d)$ denotes a solution of $F(z, c, d) = 0$, then, supposing continuity w.r.t. (c, d), the limit values $z(+\infty, d)$ and $z(c, +\infty)$ are zeros of F_1 (maybe non-zero, i.e., eigenvalue, or not!). This is visually plausible as big c or d harden the support towards a pivot.

The following figures are to give a first impression of how the parameters c and d influence important state variables. Figure 3 sketches the dependence on c of the eigenvalues and, for moderate values of c, of the natural frequencies ω.
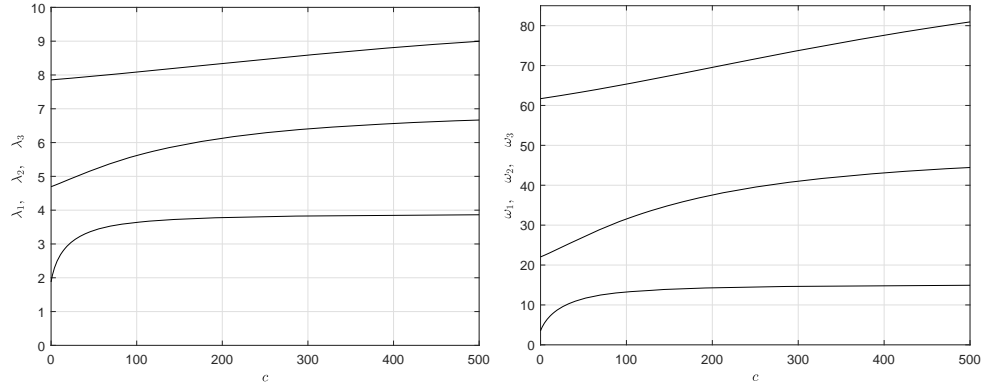
Figure 3. First three eigenvalues $z(c, 0)$ (left) and natural frequencies $\omega(c, 0)$ (right) vs. c.

The following Fig. 4 shows the connection of the real eigenvalues by curves in the complex plane for $d = 0$ and c running from 0 to $+\infty$, and for $c = 0$ and d running from 0 to $+\infty$, this is a bit similar to [6] (neglecting the stiffness c).

Of immediate practical interest is the dependence of the natural frequencies $\omega(c, d) = \mathrm{Re}(z(c, d)^2)$ on c and d, and of the decrease rates $\delta(c, d) = \mathrm{Im}(z(c, d)^2)$ as well. The next figure (Fig.5) shows a preliminary sketch of the behavior of ω.

Although the figure is still rather roughly created (what about the empty region on the right?), one peculiarity is obvious: for not too big c the natural frequency tends to zero and vanishes at some finite value of d. This is a (c-dependent) critical value of the damping coefficient, that causes the system to turn from a damped oscillation to creeping. This
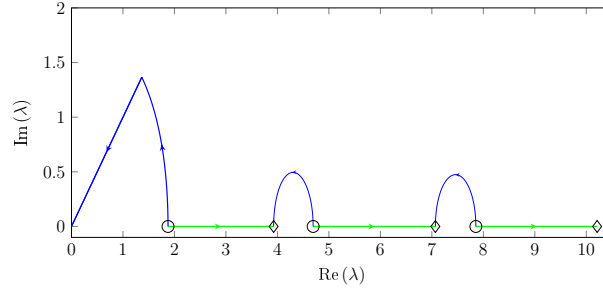
Figure 4. Connection of eigenvalues in complex plane: circles – zeros of F_0 (starting points); diamonds – zeros of F_1; blue $-c = 0$, $d = 0, \ldots, +\infty$; green $-d = 0$, $c = 0, \ldots, +\infty$.
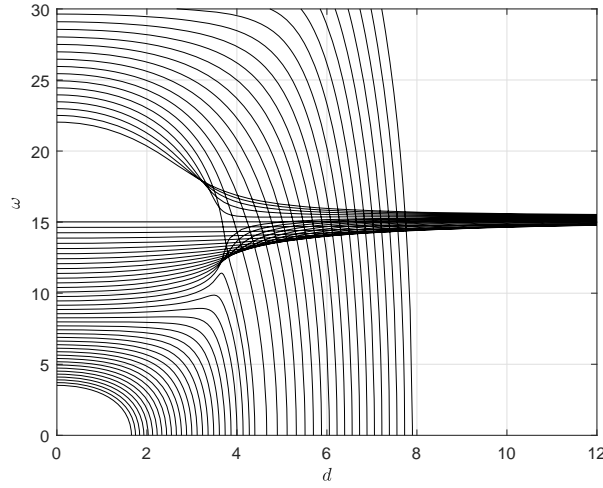
Figure 5. Natural frequencies $\omega(c, d)$ vs. d, c is family parameter.

reminds one to the behavior of the one-dimensional oscillator

$$\ddot{x} + d\,\dot{x} + c\,x = 0\,,$$

whose critical damping coefficient is $d = 2\sqrt{c}$. But in our context, such critical damping does seemingly not exist for every value of c. Physically, this means that with big values of c the system is nearer to the clamped-pivoted system with no damping than to the clamped-viscoelastic one. Details can possibly be discovered by a closer inspection of the (c, d)-dependent complex eigenvalues. This shall be attacked in the next section.

4. The complex eigenvalues

Let $z = x + iy$ be an eigenvalue. Following (12), the corresponding natural frequency is $\omega = \mathrm{Re}(z^2) = x^2 - y^2$. Hence, zero frequency originates in an eigenvalue of the form $z = a(1 \pm i)$, $a \in \mathbb{R}$. It is simple matter to find by means of addition theorems

$$
\begin{aligned}
F(a(1 \pm i), c, d) = (1 \pm i)\{ & a[\cosh^2(a) + \cos^2(a)] \\
& + \left(\frac{c}{2a^2} \mp d \right)[\sinh(a)\cosh(a) - \sin(a)\cos(a)]\}. \quad (16)
\end{aligned}
$$

Proposition 3. *Any zero natural frequency $\omega = 0$ originates in an eigenvalue $z = a\,(1 \pm i)$, $a \in \mathbb{R}$, that is located on a diagonal in the complex plane. Further, $z = a\,(1 \pm i)$, $a \in \mathbb{R}$, is an eigenvalue iff*

$$
G(a, c) = \pm d\,, \qquad (17)
$$

where

$$
G(a, c) := a\frac{\cosh(2\,a) + \cos(2\,a) + 2}{\sinh(2a) - \sin(2a)} + \frac{c}{2a^2}\,. \qquad (18)
$$

Since, with non-negative c, $G(\cdot, c)$ is an even, positive valued function, the minus-sign in (17) drops.

The analysis of (17) is simple in an a, d-plane by means of the graphs of $G(\cdot, c)$ with $c \in \mathbb{R}_{\geq 0}$.

Proposition 4. *For every $c \geq 0$ there is a critical d_c such that for $d = d_c$ there exists exactly one and for every $d > d_c$ there exist two real a, one tending to zero and the other tending to infinity for $d \to +\infty$.*

Remark 5. *Have a look to Fig. 5. Let, e.g., $c = 0$; with increasing d, the respective $\omega(0, d)$ is zero first at the critical $d = d_0$, and then it stays zero for all $d > d_0$.*
There are still some unclear things:

   (i) *If, at fixed c, the increasing parameter d passes the value d_c, which branch then runs a, towards zero or towards infinity? In particular this is of relevance for the decrease rate $\delta = Im(z^2) = 2a^2$.*

   (ii) *Evaluating $z(c, d)$ with fixed c and increasing d one eventually observes uncertainties in choosing the left or right branch for a by the computer.*

   (iii) *Again in Fig. 5: What about those $\omega(c, \cdot)$ which do not tend to zero for big d? Although there is a critical d_c for every c!*

The non-constant distances of the points give a hint for choosing the step-size of d in computing $z(c, d)$ with d starting at zero. This has been utilized in creating the following plots of $\omega(c, d)$ and $\delta(c, d)$ (via the originating eigenvalues $z(c, d)$). Again, each curve is labeled by c and parameterized by d running from 0 to some arbitrarily chosen (big) value (no d_c known in advance!).

The following Fig. 6 shows $\omega_1(c, d)$ (via the originating eigenvalues $z(c, d)$). Again, each curve is labeled by c and parameterized by d running from 0 to some arbitrarily chosen (big) value (no d_c known in advance!).
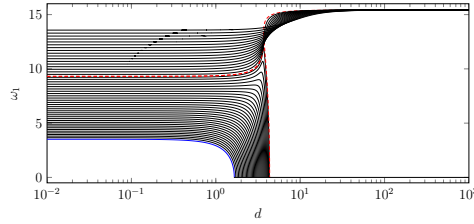
Figure 6. Natural frequency $\omega_1(c, d)$ vs. d; c is family parameter.

Again, we find ω-curves leading to zero and others tending to $\omega_1^{(1)} \approx 15.4$. These two types of $\omega(c, .)$ are separated at $c_1^* \approx 23.6495$. The c^*-value was approximated by computing. The feet of the first type curves continue with $\omega = 0$ for increasing d.

Same issues can be found for higher natural frequencies: For Fig. 7 (left) we can compute $c_2^* \approx 153.9398$ with $\omega_2^{(1)} \approx 50$, for Fig. 7 (right) we have $c_3^* \approx 473.65$ and $\omega_3^{(1)} \approx 104.25$.
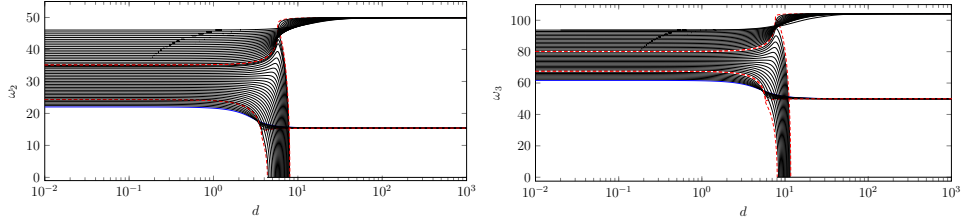
Figure 7. Natural frequencies $\omega_2(c, d)$ (left) and $\omega_3(c, d)$ (right) vs. d; c is family parameter.

The next Figs. 8 and 9 present a more extended family of curves $z(c, .)$. It allows one to clearly distinguish between those eigenvalues which entail natural frequencies leading to zero and those without this property – compare Fig. 6 with 8 and 7 with 9. The corresponding separatrices are emphasized. The real eigenvalues $z_\nu^{(1)}, \nu = 1, 2, ..,$ exhibit themselves to be sinks. The empty domain between $z_1^{(1)}$ and $z_2^{(0)}$ does not contain any curves for $c \geq 0$.

Expectation: the depicted structure continues to the right repeating all its features.
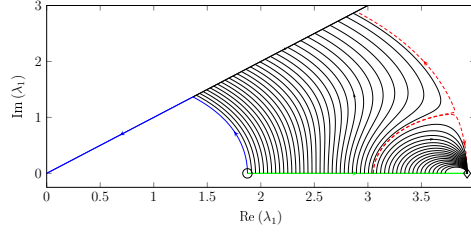
Figure 8. First eigenvalue $z_1(c,d)$ in the first octant.
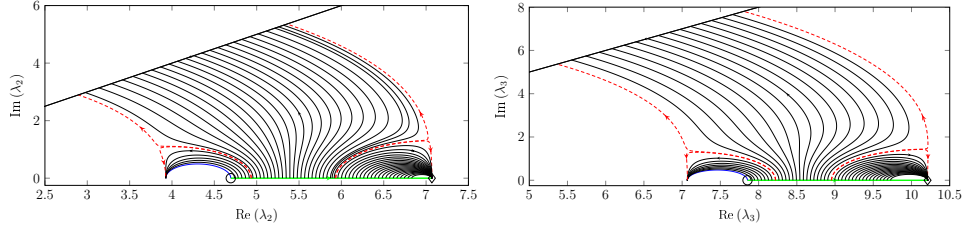
Figure 9. Second (left) and third (right) eigenvalue in the first octant.

Finally, the Fig. 10 is summing up all results and concerns all other eigenvalues $z(c,d)$ and natural frequencies $\omega(c,d)$. One can clearly see the separatrices in the complex plane arising for c_i^*. For example, the separatrix 1 runs into the diagonal at $(1+i)a_{c^*}$, $c^* \approx 23.65$. Since $c \mapsto a_c$ is bijective , it follows that the separatrix 2 starts at $z(c^*,0) \in (z_2^{(0)}, z_2^{(1)})$. Therefore, a continuous re-encounter of c^* in correspondence with the 'higher' separatrices is expected.
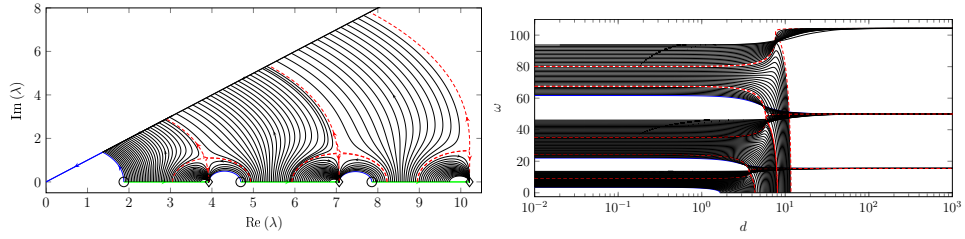
Figure 10. First three natural frequencies vs. d (c is family parameter) (left) and first three eigenvalues (right) in the first octant.

Remark 6. *Let us note, that each c_i^* forms a saddle point in the complex plane.*

At the end, let us point out, that we plotted only the first octant to present the eigenvalues due to Proposition 1. The following Fig. 11 presents the eigenvalues determining the

first natural eigenfrequency in the complex plane without any octant-restriction..
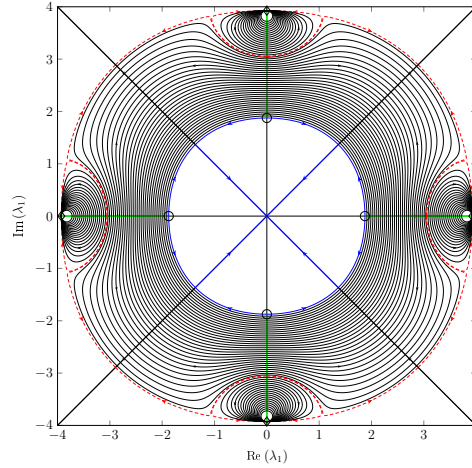
Figure 11. First eigenvalue $z_1(c, d)$ in the complex plane.

5. Conclusions

We introduced a certain model which arises in investigating some vibration problems of bio-inspired, vibrissa-like sensor systems. Due to the functionality and complexity of the considered paragon, we had to deal with bending problems of continuous beam systems. We presented a mechanical model with a discrete viscoelastic coupling to model biological tissue. The system under investigation looks very simple, but offered a very complex behavior in observing its eigenvalues and the resulting natural frequencies: due to some computed critical parameters, a) the natural frequencies increased with growing boundary damping, or b) for a specific damping parameter, the natural frequencies grow with decreasing boundary stiffness, or c) break down to zero. These behavior is divided by separatrices for the eigenvalues in the complex plane (existing saddle points).

The zero-break-down for specific system parameeters (c, d) may be useful to fade out eigenmodes of the system in applications.

Further work shall be addressed to analyze more realistic vibrissa-like sensor systems (incorporating continuously distributed couplings, conicity of the hair shaft, pre-curvature of the beam).

References

[1] BEHN, C. Mathematical modeling and control of biologically inspired uncertain motion systems with adaptive features. Habilitation, Technische Universität Ilmenau, Germany, 2013, Supervisors: K. Zimmermann (TU Ilmenau), H. Witte (TU Ilmenau), J. Awrejcewicz (Lodz University of Technology).

[2] BEHN, C., WILL, C., AND STEIGENBERGER, J. Unlike behavior of natural frequencies

in bending beam vibrations with boundary damping in context of bio-inspired sensors. In *ICIS 2014* (2014).

[3] GÜRGÖZE, M. Determination of the frequency response function of a cantilevered beam simply supported in-span. *Journal of Sound and Vibration 208*, 1 (1997), 153–158.

[4] GÜRGÖZE, M., AND EROL, H. Determination of the frequency response function of a cantilevered beam simply supported in-span. *Journal oF Sound and Vibration 247*, 2 (2001), 372–378.

[5] KRYS'KO, V., AND AWREJCEWICZ, J. On the vibration of the euler-bernoulli beam with clamped ends deflection constraints. *International Journal of Bifurcation and Chaos 15*, 6 (2005), 1867–1878.

[6] PIERSON, H., BREVICK, J., AND HUBBARD, K. The effect of discrete viscous damping on transverse vibration of beams. *Journal oF Sound and Vibration 332*, 1 (2013), 4045–4053.

[7] VOGES, D., CARL, K., KLAUER, G., UHLIG, R., SCHILLING, C., BEHN, C., AND WITTE, H. Structural characterization of the whisker system of the rat. *IEEE Sensors 12*, 2 (2012), 332–339.

[8] WANG, Y.-R., AND CHANG, C.-M. Elastic beam with nonlinear suspension and a dynamic vibration absorber at the free end. *Transactions of the Canadian Society for Mechanical Engineering 38*, 1 (2014), 107–137.

[9] WAUER, J. *Kontinuumsschwingungen*, 2 ed. Springer, 2014.

[10] WILL, C. *Continuum models for biologically inspired tactile sensors – Theory, numerics and experiments*. PhD thesis, Technische Universität Ilmenau, Germany, 2018. Supervisors: C. Behn (TU Ilmenau), H. Witte (TU Ilmenau), A. Müller (Johannes Kepler University Linz).

Carsten Behn, Professor: Schmalkalden University of Applied Sciences, Dept. of Mechanical Engineering, Blechhammer 4-9, 98574 Schmalkalden, Germany (*c.behn@hs-sm.de*). The author gave a presentation of this paper during one of the conference sessions.

Christoph Will, Ph.D.: Technische Universität Ilmenau, Dept. of Mechanical Engineering, Max-Planck-Ring 12, 98693 Ilmenau, Germany (*christophwill@gmx.net*).

Joachim Steigenberger, Professor, ret.: Technische Universität Ilmenau, Institute of Mathematics, Weimarer Straße 25, 98693 Ilmenau (*joachim.steigenberger@tu-ilmenau.de*).

The mechanical background of devices for balancing skill development

László Bencsik, Dalma J. Nagy, Ambrus Zelei, Tamás Insperger

Abstract: In the studies dealing with the analyses of balancing, the falling in elderly age is mentioned as the main motivation. It can be considered as a generation problem in our aging society. Besides, the motion therapy is another important field, where the understanding of the mechanism of balancing can help. In our society the number of premature babies is increasing, many of them requires intensive motion therapy. The natural learning of different motions and upright standing is a really long process during infancy and childhood. In case of children with dyspraxia or other disabilities the learning process has to be assisted and accelerated.

Most of the balancing improvement trainings are based on simple devices like the balance board, the Bosu ball or the Huple which is a Hungarian development especially for children. By means of the destabilization effect, these devices make the upright standing harder, which is not simple anyway. One can feel that standing on one of these devices is much more unstable and requires high concentration.

The aim of this is work is to analyse the mechanical background of this problem and verify the usability of these devices with motion capturing. By using engineering approaches, quantitative performance measures are introduced, which assist the mainly visual observation based existing scoring systems. The proposed process utilizes the mechanical model of the human and the balancing device.

1. Introduction

Due to the expected increase in median age of the human population, significance of human balancing has been increeased considerably. Accidental injuries and esepcially fall overs are a major cause of fatal injury leading to the death. Death caused by fall over has a similar number as heart cerebrovascular disease, cancer and respiratory system disease among all the causes and it is the first among the non-disease causes [3].

The occurrence of fall overs is related to physiological condition, disease, environment, psychological status, and so on. Among the physiological factors, the increasing reaction delay and the reducing muscle capacity of the elderly are important causes of falls. More falls occur during standing and weight transferring than during walking.

The balancing skill development of premature birth children is also a key motivation in the human balancing research, besides the fall overs in elderly age [7].

In the prevention of fall overs, and in the balancing skill development of children, a key step is the understanding of the human balancing process and to discover the effect of the above mentioned physiological factors. Although, there has been considerable amount of research related to feedback process which is implemented by central nervous system, there are still open questions related to the working principle of the process. Our main research focus is on the modelling of the neural process during postural balancing with a special focus on the developement of the balancing skills.

The Huple [1] is a well-tried skill development tool for children in early age. The structure is basically a hemisphere in which the children can stand or sit, meanwhile they solve some interesting task.

In the present proof of concept study, the goal is to demonstrate the applicability of quantitative parameters for the analysis of the balancing abilities.

2. Undearctuation as the stimulation of the human balancing system

From the mechanical point of view, postural balancing (e.g. standing still on the ground or balancing in the Huple) is the stabilisation of an unstable equilibrium point. The sensory organs collect the relevant information from the environment, subsequently all these information is processed in the brain and finally the muscles receive the activation signals. In this whole process the strategy of decision on the muscle activation is unknown, and there are several cancidate models for it [4].

The rolling balance tools such as the Huple increase the degrees of freedom of the system, while the variety of control inputs does not change. Fig 1 demonstrates, how the Hupple involves the issue of underactuation [6]. When standing on the ground, both the hip and the ankle joint are acuated, consequently the system is fully-actuated. In constrans, when standing on a rolling object, the joint that is formed by the rolling contact with the ground is passive. Therefore the system is underactuated.

The underactuation makes the balancing task harder, so the subject of the training are forced to the border of their balancing abilities. Such that, we hypothesize that the balancing skills develop.

3. Methods

3.1. Experimental protocol

In this study, the measurements were accomplished for the proof of concept. We tested different benchmark balancing tasks: 1) standing in the Huple with aiming for minimum
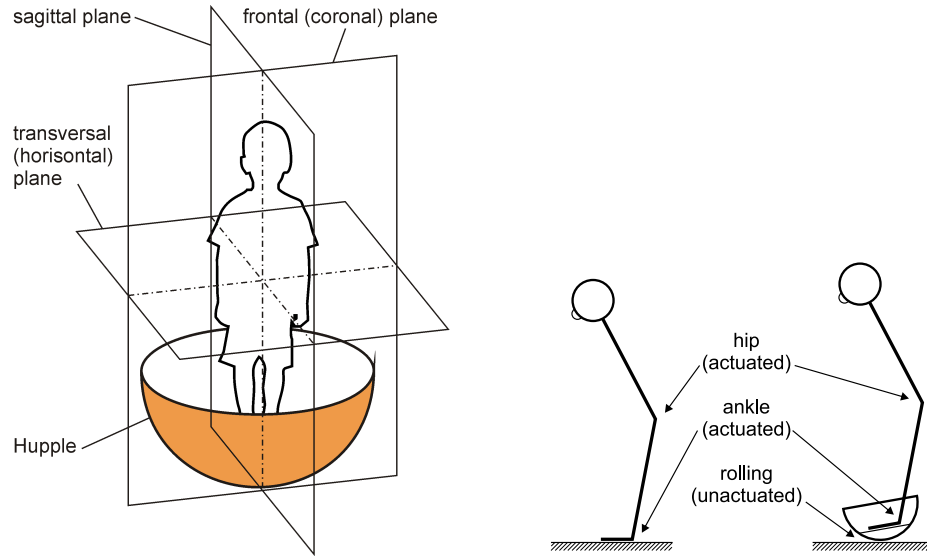
Figure 1. Left panel: Hupple skill development tool together with the anatomical planes. Right Panel: illustrative figure for the demonstraion of the underactuation during balancing on the balance board or in the Hupple.

sway motion (see Fig. 1 left); 2) sitting in the Huple with aiming for minimum sway motion; 3) sitting in the Huple and recover the vertical still position from a intentionally tilted Huple position. Each measurement was 30 seconds long.

The motion of the children was recorded by OptiTrack® [2] motion tracking system. The reflective markers were placed on the head, the shoulders, on the hip and on the Huple device. The spatial position of the markers were recorded with 120 Hz sampling frequency. The maximum position error was 0.2 mm (reported by the Motive software [2] after our on-site calibration).

Ten children were involved in the measurements; however only six was technically successful. Four children couldn't really follow the instructions, therefore a couple of markers couldn't be tracked during the whole task. The data processing and the results of the six successful measurements are explained in the followings.

3.2. Experimental data processing

In this proof of concept study, the motion is decomposed into frontal and sagittal plane as it is depicted in Fig. 2. Based on the symmetrically placed markers (e.g. shoulders, hip), the frontal plane and then the sagittal plane were identified. The angle of the subject

Figure 2. Experimetal setup: the Huple and the motion tracking system.

was considered according to the single inverted pendulum model [5]. The head and marker positions were averaged, and the contant point of the Huple with the ground was also located. The body angle was determined from these two point.

Besides of the body angle, the angle of the Huple device was also processed. Here the frontal plane and the sagittal plane was distinguished too, respectively to the planes of the human body.

4. Results

Among the above presented tasks, the results of the first task (standing in the Huple with aiming for minimum sway motion) are the best for characterization of the balancing ability. Figures 3-7 summarize the results of the measurements. The subjects are listed in the horizontal axis, with the age and the gender shown.

In Fig. 3, the angular oscillation in the frontal plane of the body is depicted. The upper panel shows the maximal oscillation while the lower panel show the Root-mean-square (RMS) value of the oscillation angle. Except the third subject, the maximum angle and the RMS are in correlation: higher RMS goes with higher maximum amplitude. Fig. 4 shows the angular oscillation in the sagittal plane of the body is depicted in the same structure. It is

not possible to show statistically significant correlation between the sagittal and the frontal plane oscillation amplitudes and RMS values.
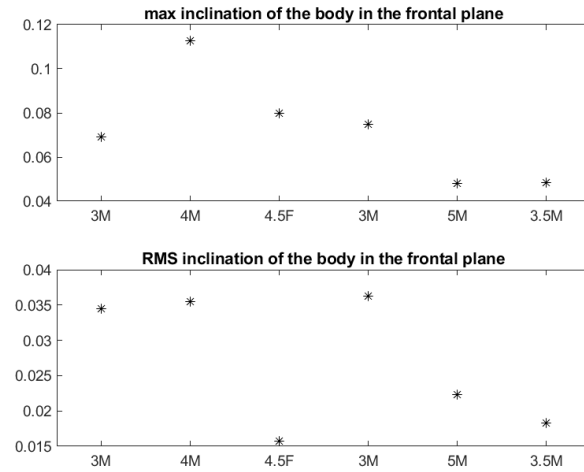
Figure 3. Angular oscillations in the frontal plane (maximal value on the upper panel, RMS value on the lower panel).
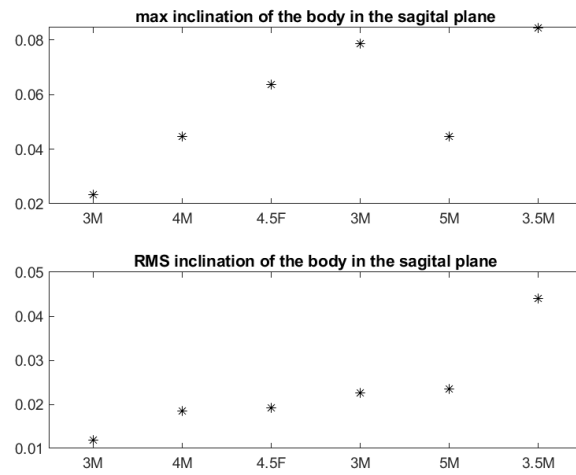
Figure 4. Angular oscillations in the sagital plane (maximal value on the upper panel, RMS value on the lower panel).

Figures 5, 6 show the angular values of the Huple. The results are in good correspondence with body the angles.
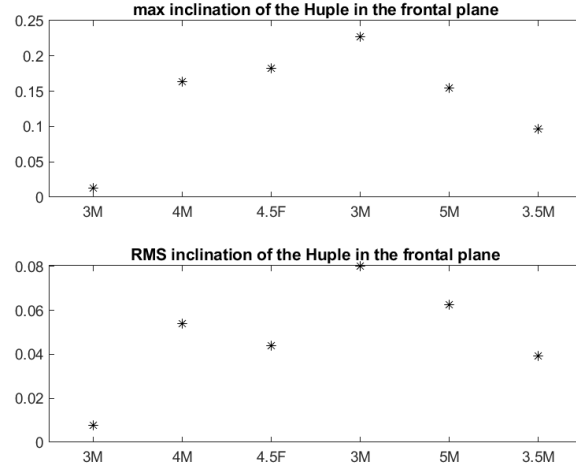
Figure 5. Tilt angle of the Hupple in the frontal plane (maximal value on the upper panel, RMS value on the lower panel).
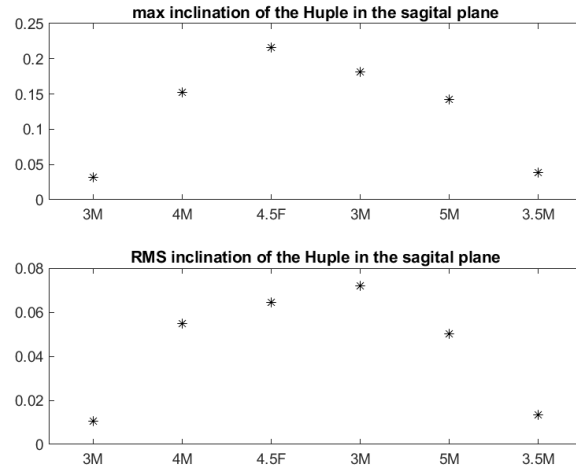
Figure 6. Tilt angle of the Hupple in the sagital plane (maximal value on the upper panel, RMS value on the lower panel).

Figure 7 shows the correlation of frequency spectrum of the Huple and the body angles in the sagittal plane. By the comparison of the angular sway and correlation, it can be concluded that in case of higher correlation the angular sway is smaller for both the body and the Huple. Physically it means that the subjects, who "feel" the dynamics of the Huple are better in balancing during standing.
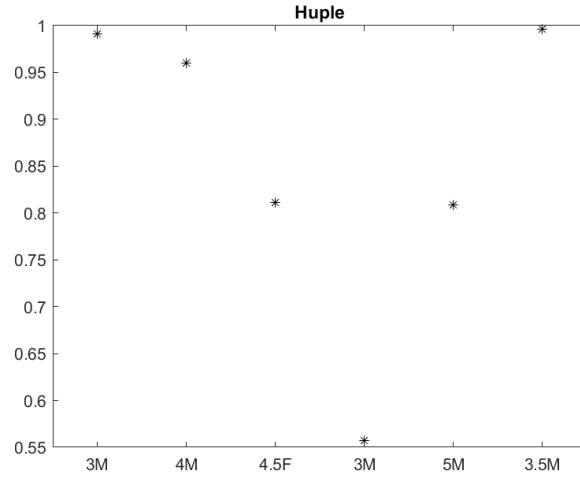
Figure 7.   Correlation of the frequency spectrum of the Huple and the body angles.

5. Conclusions

Regarding the issue of quantitative analysis of the balancing capabilities, we showed that using an optical motion tracking system, it is possible to create quantitative paraeters for the balancing skills: the maximum tilt angle amplitude, the RMS value of the tilt angle and the correltaion of the frequency spectrum of the body angle and the angle of the Huple. It is presented that the correlation in the frequency spectrum of the Huple and the body angle in the sagittal plane is a good measure of the balancing ability.

We emphasized that introducing underactuation in the balancing scenario makes harder to perform the balancing task and therefore underactutaion stimulate the development of balancing skills.

As a future plan, the newly introduced quantitative parameters will be applied for the analysis of the development of the balancing abilities.

Acknowledgments

References

[1] Huple. http://www.huple.hu/main.php. Accessed: 2019-10-10.

[2] Optitrack. https://optitrack.com. Accessed: 2019-10-10.

[3] The top 10 causes of death. https://www.who.int/news-room/fact-sheets/detail/falls. Accessed: 2019-10-10.

[4] HIDENORI, K., AND JIANG, Y. A pid model of human balance keeping. *IEEE Control Systems Magazine 26*, 6 (2006), 18–23.

[5] MILTON, J., INSPERGER, T., AND STEPAN, G. *Human Balance Control: Dead Zones, Intermittency, and Micro-chaos.* 02 2015, pp. 1–28.

[6] SPONG, M. W. Underactuated mechanical systems. In *Control Problems in Robotics and Automation* (Berlin, Heidelberg, 1998), B. Siciliano and K. P. Valavanis, Eds., Springer Berlin Heidelberg, pp. 135–150.

[7] SUKAL-MOULTON, T., KROSSCHELL, K. J., GAEBLER-SPIRA, D. J., AND DEWALD, J. P. A. Motor impairment factors related to brain injury timing in early hemiparesis, part i: Expression of upper-extremity weakness. *Neurorehabilitation and Neural Repair 28*, 1 (2014), 13–23.

László Bencsik, Ph.D.: MTA-BME Research Group on Dynamics of Machines and Vehicles, Muegyetem rkp. 3. Budapest, H-1111, Hungary (*bencsik@mm.bme.hu*).

Dalma J. Nagy, MSc: Budapest University of Technology and Economics, Muegyetem rkp. 3. Budapest, H-1111, Hungary (*dalma.nagy@mm.bme.hu*).

Ambrus Zelei, Ph.D.: MTA-BME Research Group on Dynamics of Machines and Vehicles, Muegyetem rkp. 3. Budapest, H-1111, Hungary (*zelei@mm.bme.hu*). The author gave a presentation of this paper during one of the conference sessions.

Tams Isnperger, Professor: MTA-BME Lendület Human Balancing Research Group, Muegyetem rkp. 3. Budapest, H-1111, Hungary (*insperger@mm.bme.hu*).

Dynamic identification method for determining the plastic properties of the material used as a front layer of impact shields

Miroslaw Bocian, Krzysztof Jamroziak, Maciej Kulisiewicz

Abstract: Impact shields are now being built from several layers of materials with various mechanical properties. Substantially the first protective layer (front one) is made of lightweight materials with plastic or plastic-elastic properties, while the next layer is remarkably elastic (e.g., armored steel). The above makes it necessary to analyze the phenomenon of piercing using a model in the form of a dynamic Maxwell-type system, and to determine its parameters. This paper presents the original method of determining the parameters characterizing the plastic properties of the front layer. In the Maxwell model it was assumed that these properties describe two rheological elements. These are a linear damper in a parallel connection with a Coulomb friction element. The components occur next to a linear spring element. However, the next layer appearing in the model has elastic properties. In the development of the identification method, the method of energy balance for harmonic excitation was used.

1. Introduction

The use of modern materials for anti-impact systems (the butts) becomes a challenge for designers. The task of such a construction is primarily to ensure safe operation of the shooting range object. A projectile fired from a weapon poses two basic threats. The first of them is the possibility of penetrating the shield behind the target or the tested sample, which, in consequence, enables the further flight of the projectile and poses a real threat to life. Ricocheting is another threat that occurs when inadequate shielding is used. It consists in the fact that a projectile falling at an appropriate angle to the shield bounces off it.

To sum up, the goal of the main butts is to block the further flight of the projectile without changing direction (preventing the penetration of the shield) and to protect against movement of bullets bounced off the butts.

The current traditional construction solutions of butts, for which natural raw materials such as sand [1], concrete [2], wood and steel [3, 4] were used, are being replaced by modern materials. These include rubber and plastic granules of appropriate granulation or segments in the form of blocks produced from natural raw and recycled materials cross-linked with polymer matrix [5-7] as well as various types of materials including liquid-based ones [8-10].

The front protective layer of the anti-impact shields (the so-called front layer) is designed to reduce to the maximum extent the speed of the projectile impact on the proper shielding. The latter is formed

traditionally, e.g., from the armor plate. Therefore, the issue of the penetration of the projectile in the target material needs to be understood. In this respect, the researchers divide the projectile penetration into a pierced medium into several stages. There were three phases adopted in work [11], while four ones in the paper [12]. The authors of the study divided this phenomenon into two steps [13, 14]. A characteristic feature of each one is that the initial impact on the medium and penetration are observed in the first stage. The interaction of the projectile with a target when a crater is formed is the dynamics of this phase. The second phase is often considered a quasi-stationary state, where the force acting on the penetrator changes relatively slowly over time until the projectile stops [15-18]. However, modeling of this process is done exclusively on the basis of determination of substitute rigidity values originating from the general elasticity theory for isotropic bodies. [19-21]. Also neoclassical methods for modeling synthesis, analyzing and testing sensitivity of models can be found in papers [22-27].

The paper assumes that the task of the anti-impact system (butts) protecting the environment from the effects of striking the essential protection of the structure, is to stop the projectile after the hit and limit possible damage to the shield. It is necessary to develop and analyze an appropriate theoretical model (mechanical one) to design such a system most optimally. In order for the conclusions of this analysis to be practically useful, the model must be simple and include the most relevant aspects of the impact process.

Therefore, the paper aims to present the experimental identification method for the determination of certain constants describing the mechanical properties of the frontal layer at high velocities that are dealt with when a projectile fired from small arms penetrates an object.

2. Assumptions for the penetration model

The front protective layer of the anti-impact shields (the so-called front layer) is designed to reduce to the maximum extent the speed of the projectile impact on the proper shielding. The latter is formed traditionally, e.g., from the armor plate. Its main task is to disperse the kinetic energy of the projectile maximally before it hits the central shield. Such an approach has long been used in defense (e.g., bags with sand on ramparts). In the case when the front layer is made of chambers filled with loose material, such material is not destroyed. A similar situation occurs when the projectile passes through a muddy layer. The resistance of the medium and dissipation of energy may be different depending on the moisture level in such a layer. The mechanical properties of modern energy-dissipating materials used today (e.g., aramid fibers, polyethylene fibers, sand, ballistic gels or various types of steel alloys with nano additives) have mainly the characteristics of viscous plastic materials. Their dynamic behavior is the same to some extent: dry friction occurs in combination with force depending on the speed at which the projectile moves in the material. Given the above, the general model of the analyzed penetration process in the form presented in Figure 1 was taken as a starting point in this paper.
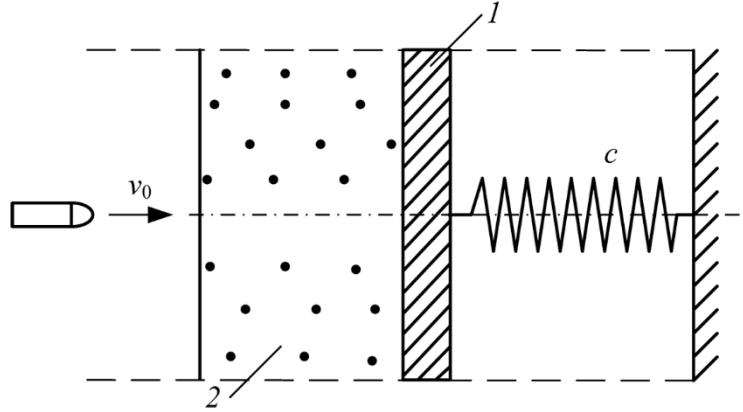
Figure 1. General model of the analyzed piercing process.

This model assumed that the ballistic shield *1* is preceded by a front layer *2* created from a material capable of absorbing the kinetic energy of the projectile as much as possible. In order to be indestructible, this layer was made of a material with visco-plastic properties (e.g., dense liquids, gels, sands, muddy soils, etc.). From the point of view of mechanical properties, materials of this type give resistance to a projectile moving in it in the form of force depending on the projectile velocity. In this paper, it was assumed that the model of such force is the function $R(v)$ in the form:

$$R(v) = h\,sgn(v) + \beta v \tag{1}$$

where h – a constant determining the so-called dry friction and β – a constant specifying the viscous friction proportional to the velocity. These values can be relatively easily set in quasi-static conditions, i.e., at low deformation speeds (e.g., when using testing machines up to 0.03 m/s and up to 20 m/s when using drop hammers).

3. Dynamic model and its analysis

Under conditions of any selected range of velocity variations, the identification of the constant values h and β is possible when the test material is part of a dynamic system with the scheme shown in Figure 2.

That is a discrete dynamic system with two degrees of freedom and two concentrated masses m, m_0, which can move only in the vertical direction. If the generalized coordinate x defines the mass m displacement and the generalized coordinate η the mass m_0 displacement, then the differential equations of the system motion are:

$$m\ddot{x} = p - c_0(x - \eta) - \beta(\dot{x} - \dot{\eta}) - h\,sgn(\dot{x} - \dot{\eta}) - k\dot{x} \tag{2}$$

$$m_0\ddot{\eta} = c_0(x - \eta) + \beta(\dot{x} - \dot{\eta}) + h\,sgn(\dot{x} - \dot{\eta}) - c\eta \tag{3}$$
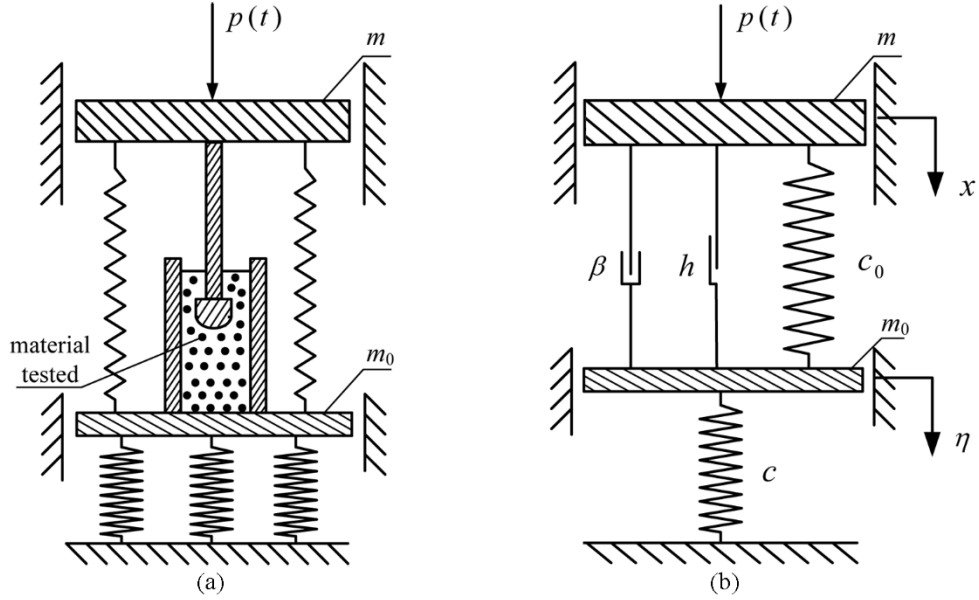
Figure 2. Diagram of the adopted dynamical system: (a) physical layout diagram, (b) model diagram.

where c_0 and c are constants of elasticity of appropriate elastic elements, while p means any excitation force applied to mass m. The model also includes the possible occurrence of resistance force of mass m movement of the size $W = k\dot{x}$ resulting from, e.g., air resistance.

When using the equation (2), the equation (3) can be written as follows:

$$m_0\ddot{\eta} + c\eta = p - m\ddot{x} - k\dot{x} \tag{4}$$

which further gives:

$$\frac{m_0}{m}\ddot{\eta} + \frac{c}{m}\eta = \frac{p}{m} - \ddot{x} - \frac{k}{m}\dot{x} \tag{5}$$

The dynamic system can be constructed in such a way that the mass m is very high compared to the mass m_0. Then, for

$$m \gg m_0 \tag{6}$$

from the equation (5) we have:

$$\eta = \frac{p}{c} - \frac{m}{c}\ddot{x} - \frac{k}{c}\dot{x} \tag{7}$$

Considering the relationship (7), the equation (2) takes the form:

$$m\ddot{x} = p - c_0\left(x - \frac{p}{c} + \frac{m}{c}\ddot{x} + \frac{k}{c}\dot{x}\right) - \beta\left(\dot{x} - \frac{\dot{p}}{c} + \frac{m}{c}\dddot{x} + \frac{k}{c}\ddot{x}\right) +$$
$$-h\,sgn\left(\dot{x} - \frac{\dot{p}}{c} + \frac{m}{c}\dddot{x} + \frac{k}{c}\ddot{x}\right) - k\dot{x} \tag{8}$$

Formula (8) is a non-linear third-order non-linear differential equation. The analytical form of the solution to this equation for any driving force $p(t)$ is not possible to derive.

Further, a fixed response $x(t)$ to the periodic force was assumed in the analyzed system there was:

$$x(t) = x(t + T) \quad \text{jeśli} \quad p(t) = p(t + T) \tag{9}$$

which should be fulfilled for the positive parameters m, c_0, c, h, β and k.

By entering the variable $z(t)$ of the form:

$$z(t) = x - \frac{p}{c} + \frac{m}{c}\ddot{x} + \frac{k}{c}\dot{x} \tag{10}$$

the equation (8) takes the form:

$$(c + c_0)\, z + \beta\dot{z} + h\, sgn(\dot{z}) = c\, x \tag{11}$$

and, if the conditions (9) are met, the following applies as well:

$$z(t) = z(t + T) \tag{12}$$

The equation (11) allows deriving easy-to-use identification compounds to determine the searched material constant values h and β.

4. Identification method

Favorable compounds for identification can be derived using the energy balance equation method [28-30]. In this case, for the differential equation of the form (11). Multiplying this equation by the differential dz and then integrating it within the period T, one obtains successively:

$$\int_{z(t)}^{z(t+T)} (c + c_0)\, z\, dz = \frac{1}{2}(c + c_0)\,[z^2(t + T) - z^2(t)] = 0 \tag{13}$$

$$\int_{z(t)}^{z(t+T)} \beta\, \dot{z}\, dz = \beta \int_{t}^{t+T} \dot{z}^2\, dt = \beta\, \alpha_z^{\dot{z}} \tag{14}$$

$$\int_{z(t)}^{z(t+T)} h\, sgn(\dot{z}) dz = h\, \alpha_z^{sgn(\dot{z})} \tag{15}$$

$$\int_{z(t)}^{z(t+T)} c\, x\, dz = c\, \alpha_z^x \tag{16}$$

where the variables α occurring in the equations (14), (15), (16) are equal to the fields contained within the dependency loop: $\dot{z}(z)$ for the equation (14), $sgn(\dot{z})(z)$ for the equation (15), and $x(z)$ for the equation (16). These loops are closed if the conditions of periodicity (see Eq. 9), (see Eq. 12) are fulfilled. Considering the results (13), ... (16), the differential equation (11) boils down to the algebraic equation of the form:

$$\beta\, \alpha_z^{\dot{z}} + h\, \alpha_z^{sgn(\dot{z})} = c\, \alpha_z^x \tag{17}$$

It is easy to notice that the differential dz has the dimension of displacement, while the results of integration (14), (15), (16) as a product of specific forces by displacement have the dimension of work. Therefore, (17) presents the equation of energy balance. The only condition is that the stiffness c of the suspension of mass m_0 is initially known to make it possible to estimate the value of the parameters β, and h from that equation. Introductory knowledge of the value of viscous friction acting independently

on mass m, i.e. knowing the coefficient k, is indispensable. Therefore, the experiment requires the measurement of the value $\alpha_z^{\dot{z}}, \alpha_z^{sgn(\dot{z})}, \alpha_z^x$ for several (at least two) different periodic dynamic forces for which the responses are cyclical. A further procedure may involve the use of, for instance, statistical regression analysis.

5. Experimental verification

Simulation tests were carried out in the Simulink program according to the diagram (see Figure 3).
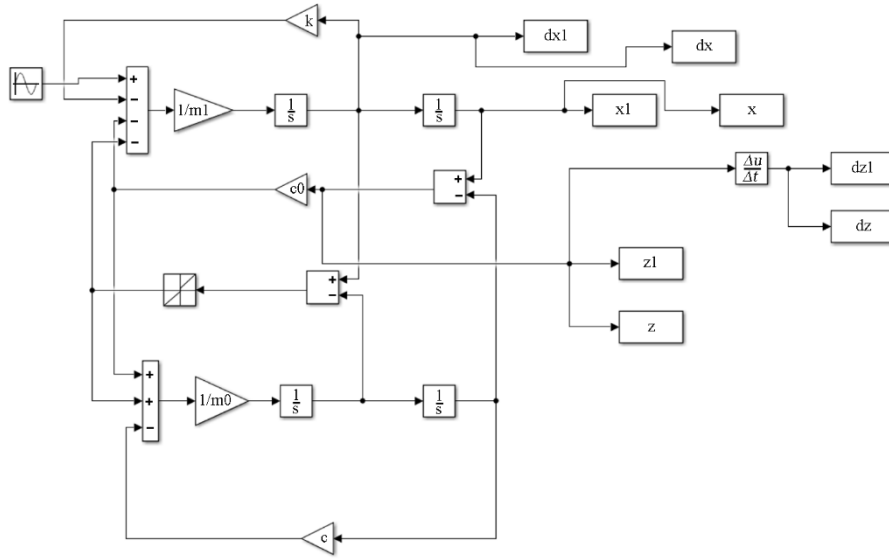
Figure 3. Diagram of the simulation system.

Force $p(t)$ were set in purely harmonic from with varying amplitude and frequency. The amplitude was varied in the range from 1000 N to 1900 N, while the frequency in the range from 3 Hz to 3.9 Hz. In the simulated model, the following values of parameters were assumed:

$$m = m_1 = 100 \text{ [kg]}; \quad c_0 = 2.0 \cdot 10^3 \left[\frac{N}{m}\right]; \quad c = 4.0 \cdot 10^3 \left[\frac{N}{m}\right]; \quad k = 60 \left[\frac{kg}{ms}\right];$$

$$m_0 = 0.01 \text{ [kg]}; \quad h = 10 \text{ [N]}; \quad p = 1000 \text{ [N]}; \quad f_1 = 1 \text{ [Hz]}; \quad \beta = 120 \left[\frac{kg}{ms}\right] \tag{18}$$

Figures 4 and 5 show the answers in the form of x and z displacement, and velocity $\dot{x}$ and $\dot{z}$ of the system for purely harmonic excitations. The developed identification method is based on closed loops (see Figures 6-8), therefore the measurement of the loop can only be made after the system has been established. Analyzing the system, we force it successively with many different excitations and determine for these subsequent excitations the values of the fields of the respective loops in steady state vibrations. For this reason, the total analysis time depends on the time it took to a single determine test.

It turns out that the time to be determined depends mainly on the damping value k, which is dependent on the air resistance. It should be noted that at low values of this coefficient, it will take a very long time for the response to reach the periodic vibration system, which in turn may prevent analysis.
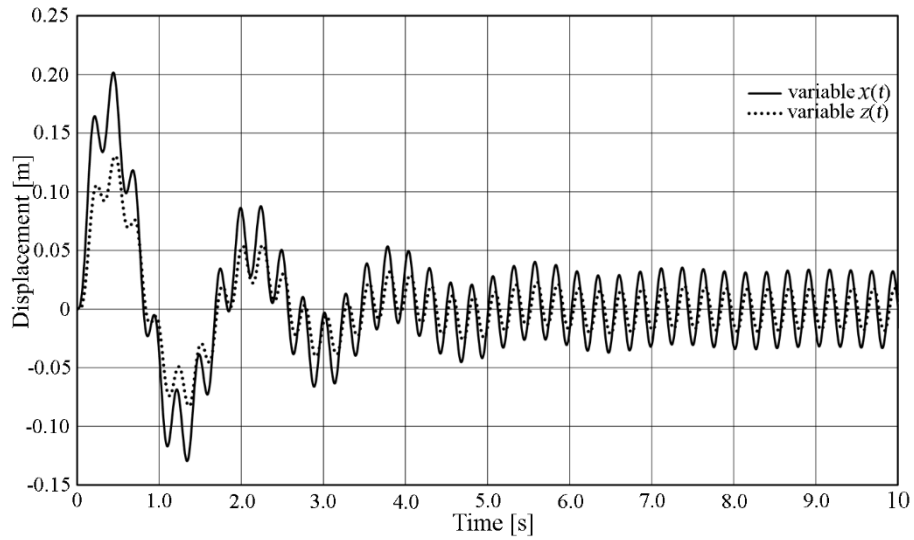
Figure 4. Displacement as a result of excitation of system by force p of the mass m after periodic vibrations was determined.
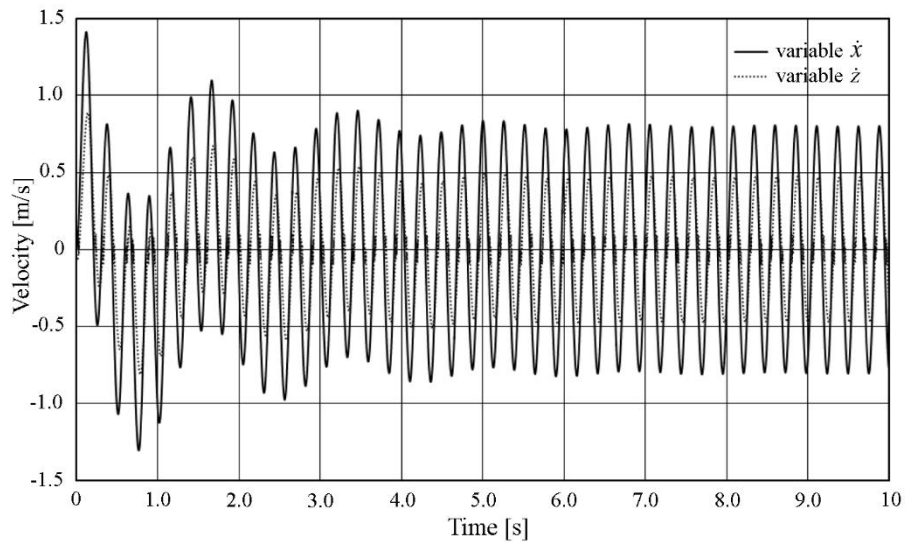
Figure 5. Velocity as a result of excitation of system by force p of the mass m after periodic vibrations was determined.

The following Figures (see Figures 6-8) shows the appropriate loops, the fields of which were used to determine the parameters of the model. Taken measurements of fields (after established responses) for appropriate loops α result in obtaining values shown in Table 1.

Table 1. Field loops values α obtained from computer simulation.

No.	Amp. [N]	Freq. [Hz]	$\alpha_z^{\dot{z}}$	$\alpha_z^{sgn(\dot{z})}$	α_z^{x}
1.	1000	3.0	0.0824	0.3207	12.9920
2.	1100	3.1	0.1004	0.3542	15.5141
…	…	…	…	…	…
…	…	…	…	…	…
89.	1800	3.9	0.1199	0.3445	17.8059
90.	1900	3.9	0.1343	0.3648	19.7498

(a)   (b)
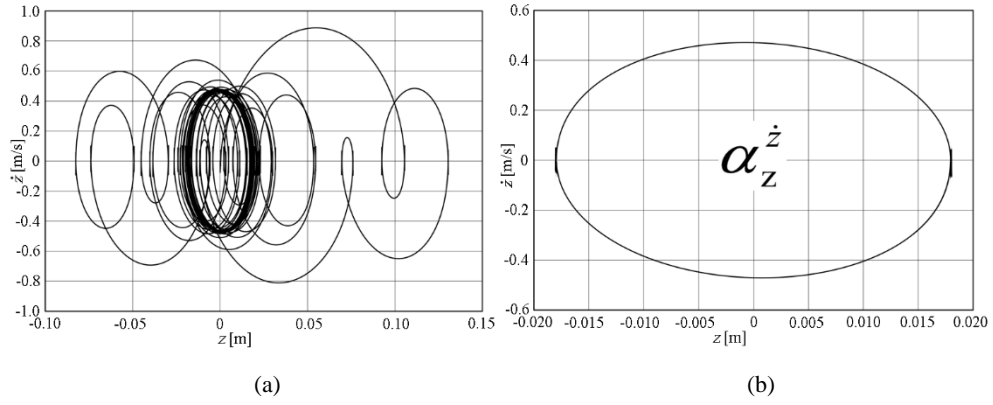
Figure 6. Example loops for tested system based according Eq. (14): (a) simulation for 90 loops, (b) loop for the last period of the simulation range.

(a)   (b)
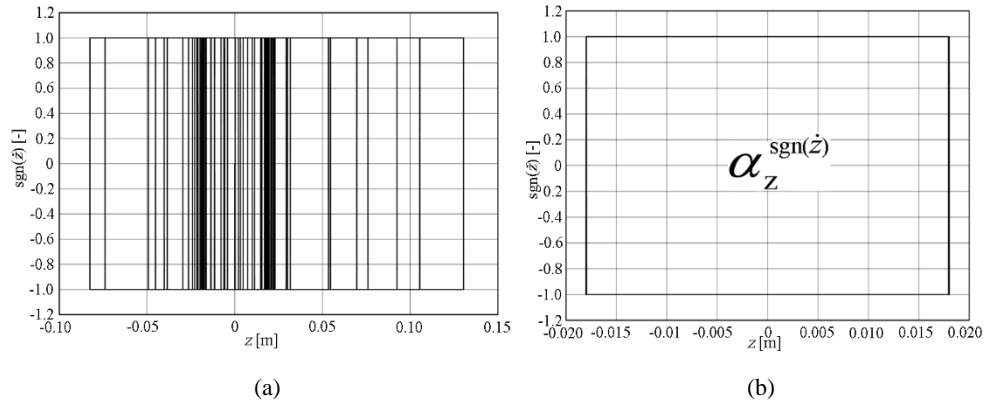
Figure 7. Example loops for tested system based according Eq. (15): (a) simulation for 90 loops, (b) loop for the last period of the simulation range.

(a)   (b)
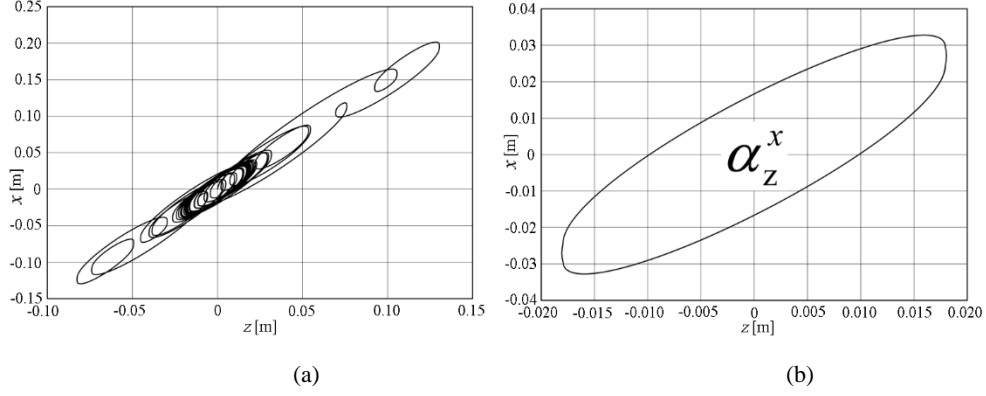
Figure 8. Example loops for tested system based according Eq. (16): (a) simulation for 90 loops, (b) loop for the last period of the simulation range.

The obtained loop fields in many simulations with a changed excitations frequency of repetitions allowed to estimate the model parameters using linear regression method (see Table 2).

Table 2. Assumed parameters obtained from linear regression method.

Assumed parameters		Obtained parameters
h [N]	10.0	[9.0880÷9.1814]
$\beta \left[\dfrac{\text{kg}}{\text{ms}}\right]$	120.0	[122.0525÷122.3054]

Based on the tests, a regression analysis was performed (see Eq. 18), determining the coefficients of our system h and β. The obtained values slightly differ from assumed values (error about 10%) which is an acceptable result considering the strong non-linearity associated with dry friction h. During the analysis, it could be clearly seen that the higher the dry friction value, it was the greater the error in estimating h and β values.

6.   Conclusions

The issue of impulse loading of small arms projectiles was considered in the paper. This phenomenon was presented in the form of the adopted Maxwell dynamic system, in which its relevant parameters were adopted. Identification was carried out using the energy balance method for harmonic excitation by deriving it into the form of an algebraic equation (see Eq.17). The result of this analysis was:

1) Derivation of balance equations (see Eq. 14, 15 and 16).

2) Determining the value of loop fields $\alpha_z^{\dot{z}}, \alpha_z^{sign(\dot{z})}, \alpha_z^x$ (see Table 1) for given model parameters (see Eq. 18).

3) Estimate the assumed parameters h and β, which are largely responsible for the dissipation of impact energy (see Table 2).

4) Using statistical regression analysis method , the behavior of model parameters was verified at different amplitudes and frequencies of excitations for his responses (see Table 1).

Based on a simple modification of the regression equation, the sensitivity of the model to its parameters can be investigation. It is clearly seen (see Figure 9) that too much dry friction causes loss of collinearity of points what can be observed for $h = 30$ N. This collinearity correlates well at $h = 10$ N.
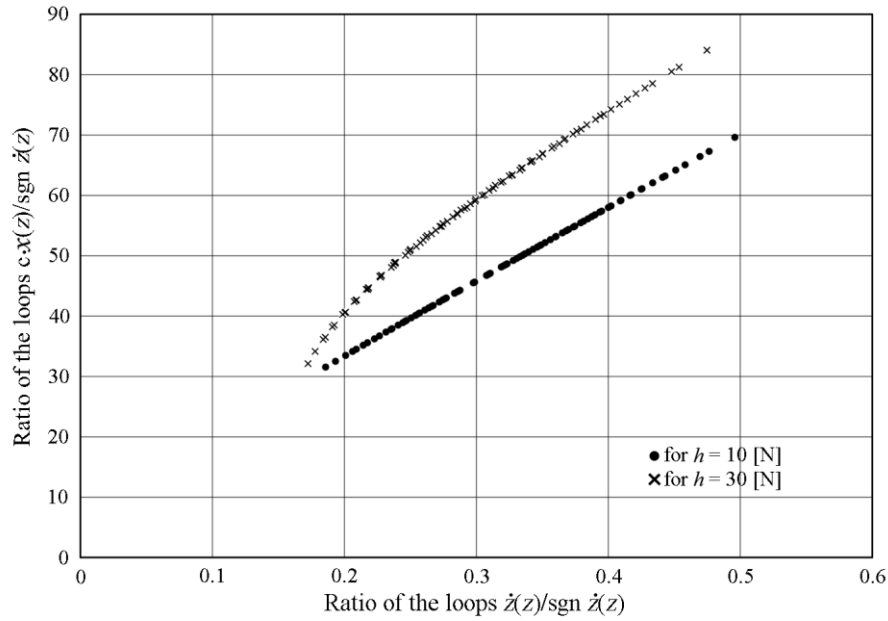
Figure 9. Graph showing linear regression based on force balance equation for declared dry friction values.

The presented method to assess the efficiency of butt can be used to identify the process of stopping a striking projectile and forecast its durability for damage. This method is currently being verified on the ballistic track, and the results of the research will be published in subsequent papers.

References

[1]   Braslau, D. Partitioning of energy in hypervelocity impact against loose sand targets. *J. Geophys. Res.,* 75, 20 (1970), 3987-3999

[2]   Choi, M.K., Han, J., Park, S., and An, W.J. Eefficient method to evaluate critical ricochet angle of projectile penetrating into a concrete target. *Math. Probl. Eng.,* (2018), art. ID: 3696473, 1-12. https://doi.org/10.1155/2018/3696473

[3]   Koene, L., Hermsen, R., and Brouwer, S.D. Projectile ricochet from wooden targets. *Proceedings 27th International Symposium on Ballistics*. Germany, April 22-26, (2013), 1195-1205.

[4]   Omidvar, M., Iskander, M., and Bless, S. Response of granular media to rapid penetration. *Int. J. Impact Eng.,* 66 (2014), 60-82.

[5]   Maamir, S., and Haghi, A.K. *Mechanical and physico-chemical characteristics of modified materials. Performance evaluation and selection.* CRC Press Taylor & Francis Group, Boca Raton, 2016.

[6]   Rosenberg Z., and Dekel, E. *Terminal ballistics.* Springer-Verlag, Berlin, 2012.

[7]   Baranowski, P., Platek, P., Antolak-Dudka, A., Sarzynski, M., Kucewicz, M., Durejko, T., Malachowski, J., Janiszewski, J., and Czujko, T. Deformation of honeycomb cellular structures manufactured with Laser Engineered Net Shaping (LENS) technology under quasi-static loading: Experimental testing and simulation. *Additive Manufacturing,* 25, (2019), 307-316.

[8]   Wallace, J. S. *Chemical analysis of firearms, ammunition and gunshot residue.* Second edition. CRC Press Taylor & Francis Group, Boca Raton, 2018.

[9]   Baillargeon, P., and Bergeron, G. Prediction of projectile ricochet behavior after water impact. *J. Forensic Sci.,* 57, 6 (2012), 1556-1561.

[10] Werner, D., Rhumorbarbe, D., Kronseder, P., and Gallusser, A. Technical Note: Comparison of three bullet recovery systems. *Forensic Sci. Int.*, 290 (2018), 251-257.

[11] Phase three penetration. *Int. J. Impact Eng.,* 20 (1997), 601-616.

[12]   Christman, D.R., and Gehring, J.W. Analysis of high-velocity projectile penetration mechanics. *J. Appl. Phys.,* 37, 4 (1966), 63-68.

[13] Kulisiewicz, M., , Bocian, M. and Jamroziak, K. Criteria of material selection for ballistic shields in the context of chosen degenerated models. *J. Achiev. Mater. Manuf. Eng.,* 31, 2 (2008), 505-509.

[14] Bocian, M., Jamroziak, K., and Kulisiewicz, M. An identification of nonlinear dissipative properties of constructional materials at dynamical impact loads. *Meccanica,* 49 (2014), 1955-1965.

[15] Goldman, D.I., and Umbanhowar, P. Scaling and dynamics of sphere and disk impact into granular media. *Phys. Rev. E.,* 77 (2008), 021308(1-14).

[16] Kondic, L., Fang, X., Losert, W., O'Hern, C.S., and Behringer, R.P. Microstructure evolution during impact on granular matter. *Phys. Rev. E.,* 85 (2012), 011305(1-17).

[17] Bocian, B., Jamroziak, K., and Kulisiewicz, M. Identification of the mechanical properties of the systems subjected to the shock loads using the non-linear dynamic models. *Proceedings 8th European Nonlinear Dynamics Conference*. Austria, July 6-11, (2014), Paper ID 172.

[18] Zukas, J.A. and Scheffler, D.R. Impact effects in multilayered plates. *Int. J. Impact Eng.,* 38, 19, (2001), 3321-3328.

[19] Kosza, P., and Sayir, M.B. Failure patterns in the core of sandwich structures under impact loading. *Int. J. Impact Eng.,* 15, 4, (1994), 501-517.

[20] Liang, C.C., Jen, C.Y., Yang, M.F., and Wu, P.W. Resistant performance of perforation in protective structures using a semi-empircal method with marine applications. *Ocean Eng.,* 30, 9, (2003), 1137-1162.

[21] Carlucci, D.E., and Jacobson, S.S. *Ballistic: Theory and desing of guns and ammunition*. 3rd Edition. CRC Press, Boca Raton, 2018.

[22] Bialas, K., Buchacz, A., and Galeziowski, D. Application of electric subsystem as implementation of reduction of mechanical vibrations. *Solid State Phenomena,* 220-221, (2015), 9-14.

[23] Buchacz, A., and Galeziowski, D. Synthesis as a designing of mechatronic vibrating mixed systems. *J. Vibroeng.,* 14, (2012), 553-559.

[24] Krason, W., and Malachowski, J. Multibody rigid models and 3D FE models in numerical analysis of transport aircraft main landing gear. *Pull. Pol. Acad. Sci.-Te.,* 63 , 3, (2015), 745-757.

[25] Rusinski, E., Czmochowski, J., and Pietrusiak, D. Problems of steel construction modal models identification. *Eksploat. Niezawodn.,* 14, (2012), 54-61.

[26] Wrobel, A. Kelvin Voigt's model of single piezoelectric plate. *J. Vibroeng.,* 14, 2, (2012), 534-537.

[27] Zolkiweski, S. Dynamic flexibility of the supported-clamped beam in transportation. *J. Vibroeng.,* 13, 4, (2011), 810-816.

[28] Kulisiewicz, M. *Modeling and identification of nonlinear mechanical systems under dynamic complex loads*. University of Technology, Wroclaw, 2005.

[29] Jamroziak, K., Bocian, M., and Kulisiewicz, M. Energy consumption in mechanical systems using a certain nonlinear degenerate model. *J. Theor. App. Mech-Pol.,* 51, 4 (2013), 827- 835.

[30] Bocian, M., Jamroziak, K., Kosobudzki, M., and Kulisiewicz, M. Analysis of purely harmonic vibrations in non-linear dynamic systems on the example of the non-linear degenerate system. *Procedia Engineer.,* 199 (2017), 522-527.

Miroslaw Bocian, DSc. Eng.: Wroclaw University of Science and Technology, Department of Mechanics, Materials Science and Engineering, Smoluchowskiego 25, 50370 Wroclaw, Poland (miroslaw.bocian@pwr.edu.pl).

Krzysztof Jamroziak, Assoc.. Prof.: Wroclaw University of Science and Technology, Department of Mechanics, Materials Science and Engineering, Smoluchowskiego 25, 50370 Wroclaw, Poland (krzysztof.jamroziak@pwr.edu.pl).

Maciej Kulisiewicz, Professor: Faculty of Technology and Engineering, Wroclaw University of Science and Technology, Armii Karjowej 78, 58302 Walbrzych, Poland (maciej.kulisiewicz@pwr.edu.pl). The author gave a presentation of this paper during one of the conference sessions.

Thrust programming for the range maximization and modified brachistochrone problem

Cherkasov Oleg , Nina Smirnova, Sheng Huang

Abstract. The brachistochrone problem with penalty for fuel expenditures of mass-point moving in the vertical plane driven by gravity, nonlinear viscous drag, and thrust is considered. The lifting force or normal component of the reaction force of the curve and the thrust are considered as a control variables. Principle maximum procedure allows to reduce the optimal control problem to the boundary value problem for a set of systems of two nonlinear differential equations. The qualitative analysis of the resulting system allows to study the key features of the extremal trajectories, including asymptotic behavior. Thrust control depending on the velocity and slope angle is designed. The structure of the extremal thrust control program is determined and consequence of the subarcs is established analytically.

1   Introduction

The motion of a material point by a mass in the vertical plane in a homogeneous field of gravity and in a homogeneous, resisting medium is considered. Drag force is assumed to be proportional to the velocity in to the power . The normal component of the reaction force of the curve and the thrust are considered as a control variables. The goal function consists of two terms: the horizontal range (terminal term) and energy costs (integral term) at a given time of the process. Along with the problem of maximizing the range, we consider the modified brachistochrone problem, formulated as follows: to find a curve joining two points in a vertical plane along which a particle under the influence of uniform gravity and a non-conservative force travels from the initial to the final point in the shortest time and the total control efforts must be penalized. It is assumed that the dependence of the maximum range on time is monotonic. Then the problem of brachistochrone and the problem of maximizing the range in a given time are interrelated in the following sense. Let us take the maximum distance value obtained as a result of solving the problem with fixed time as a given final condition for the brachistochrone problem. Then the minimum time, obtained as a result of the solution of the latter, coincides with the time that was fixed when solving the problem of maximizing the range. Trajectories also coincide.

The classical theory of the calculus of variations and, later, optimal control theory were applied to the problem of maximizing the altitude of a rocket in vertical flight, for a given amount of propellant.

It was pioneering works studying optimal thrust programming along given one-dimensional trajectory. Two particular cases, namely, one with linear drag dependence on velocity and the other with quadratic drag dependence on velocity were examined in the paper [1]. In [2] the optimal flight in the vertical plane with an intermediate vehicle model was studied. Flight-path angle was taken on the role of a control variable, free final value of the fuel was assumed. This model is suitable for investigating the optimal motion of special types of aircraft classes for which it is possible to change the lift force without changing the resistance or as an intermediate model as a first approximation. The intermediate model can also be used to describe the motion of rotating bodies, in which the Magnus force plays the role of a lifting force. For various modifications of the Brachistochrone problem with viscous friction the normal component of the reaction force of the curve also allows to change the slope angle without changing the drag force [3]. Note, that for the case of Coulomb friction, acting on the point moving along the wire, the elevation of slope angle to control status is not possible [4, 5, 6]. Generalizations of the classical problem of brachistochrone with the accelerating force were considered, for example, in the paper [3], where the results of numerical simulation for the case of an accelerating force proportional to the velocity were presented. In [7] the solution of the same problem was obtained using a genetic algorithm to demonstrate the performance of it. In [8] the problem of a brachistochrone with a constant accelerating force was studied. The brachistochrone problem in the presence of a constant accelerating force and the force of linear viscous friction was studied in [9]. In the paper [10] the case of a quasi-constant acceleration force is considered for the special class of optimal trajectories. The properties of trajectories with a quasi-constant acceleration force without friction was studied analytically in [11]. The range maximization and brachistochrone problems with a constant accelerating force were considered in [12], where the qualitative methods for dynamic systems were applied to determine characteristic features of the extremal trajectories.

In this paper two control variables are considered: the thrust and the normal component of the reaction force of the curve. The paper continues the studies [13, 14] for the model of non-linear viscous friction and expands the results for the case of fixed final altitude.

.

2   Problem formulation

Equations of motion of the particle with constant mass in dimensionless variables are as follows:

$$
\begin{cases}
\dot{x} = v\cos\theta, \\
\dot{y} = v\sin\theta, \\
\dot{v} = p - v^n - \sin\theta, \\
\dot{\theta} = u - \cos\theta / v,
\end{cases}
\tag{1}
$$

Here x, y are the horizontal distance and vertical altitude respectively; v is the module of the velocity; $u = N/(mv)$ is a control, linked with a normal component of the reaction force of the curve N, m is the mass of the particle. The control u is supposed to has no constraints. Further, p is the thrust, another control variable subjected to the inequality $-\bar{p} \leq p(t) \leq \bar{p}$, where $\bar{p}$ is positive constant; both controls are piecewise continuous function, n positive constant. Particular cases $n \in \{1; 2\}$ correspond to linear and quadratic resistance law, respectively. The dot over symbols indicates the differentiation with respect to a dimensionless time.

Boundary conditions for the system (1) are as follows:

$$x(0) = x_0, \ y(0) = y_0, \ v(0) = v_0, \ y(T) = y_T. \tag{2}$$

The goal of the control is the minimization of the functional

$$J = -x(T) + \int_0^T p^2 dt \to \min_{u,p} \tag{3}$$

In other words, the problem is to maximize the horizontal distance with penalty for thrust expenditure, when the duration T of the process is fixed.

The problem (1)–(3) is a singular optimal control problem [15], for which necessary optimal conditions in the form of the Maximum Principle satisfied trivially. One of the common approaches of research of such problems is replacement of the degenerate irregular problems to a regular problem that includes all the elements for the subsequent construction of the desired solution [15]. Note that only the last equation of system (1) has an explicit form of u, and the control u is supposed to has no constraints, boundary conditions for variable θ are free. This permits the deletion of this equation and the elevation of slope angle θ to control status. Let introduce new variable ξ by formula $\xi(t) = \int_0^t p^2(\tau) d\tau$, and reduce the problem (1-3) to the following Mayer's optimal control problem for the system:

$$\begin{cases} \dot{x} = v \cos\theta, \\ \dot{y} = v \sin\theta, \\ \dot{v} = p - v^n - \sin\theta, \\ \dot{\xi} = p^2, \end{cases} \tag{4}$$

with initial conditions

$$x(0) = x_0, \ y(0) = y_0, \ v(0) = v_0, \ \xi(0) = 0, \ y(T) = y_T. \tag{5}$$

The goal function (3) could be rewritten as follows

$$J = -x(T) + \xi(T) \to \min_{\theta, p}, \tag{6}$$

where θ is new control variable.

3 Problem analysis

The Hamiltonian of the problem (4)-(6) has a form [16]:

$$H = \psi_x v \cos \theta + \psi_y v \sin \theta + \psi_v (p - v^n - \sin \theta) + \psi_\xi p^2 = C, \tag{7}$$

where C is unknown constant. Equations for co-state variables are written as follows:

$$\dot{\psi}_x = 0, \dot{\psi}_y = a, \dot{\psi}_\xi = 0, \dot{\psi}_v = -\cos \theta + n v^{n-1} \psi_v, \tag{8}$$

where a is unknown constant. From the transversality conditions it follows that

$$\psi_x(t) = 1, \ \psi_y(t) = a, \ \psi_\xi(t) = -1, \ t \in [0, T], \ \psi_v(T) = 0.$$

The necessary condition for the maximum of the function H with respect to control θ is written in the form

$$\partial H / \partial \theta = -v \sin \theta + a v \cos \theta - \psi_v \cos \theta = 0. \tag{9}$$

From the transversality conditions and the relations (9) it follows:

$$\psi_v = v(a - \tan \theta), \ \tan \theta(T) = a \ .$$

The necessary condition for the maximum of the function H with respect to control p is written in the form

$$\partial H / \partial p = \psi_v - 2p.$$

The inequality $H''_{\theta\theta} \cdot H''_{pp} - (H''_{p\theta})^2 = 2v / \cos \theta > 0$ means that the extremum exists. From the relations $\partial^2 H / \partial p^2 = -2 < 0$; $\partial^2 H / \partial \theta^2 = -v / \cos \theta < 0$ it follows that function H reaches its maximum if $\cos \theta > 0$. The extremal thrust control is as follows

$$p_0 = \psi_v / 2 = v(a - tg\theta) / 2.$$

So we get the following control logic:

$$p(t) = \begin{cases} \bar{p}, & \text{if } p_0 \geq \bar{p}, \\ p_0, & \text{if } -\bar{p} \leq p_0 \leq \bar{p}, \\ -\bar{p}, & \text{if } p_0 \leq -\bar{p}. \end{cases} \tag{10}$$

By differentiating the relation (9) with respect to time according the systems (4), (8) the equation for the value of $\dot{\theta}$ could be found. Thus, the optimal control problem (4)-(6) is reduced to the following boundary-value problem:

$$\begin{cases} \dot{v} = p(t) - v^n - \sin\theta, & v(0) = v_0, \\ \dot{\theta} = \dfrac{\cos\theta}{v}\Big(1 + \big((n+1)v^n - p(t)\big)(\sin\theta - a\cos\theta)\Big), & \tan\theta(T) = a, \end{cases} \quad (11)$$

The singular control related with the support reaction of the curve taking into account the fourth equation of the system (1) has a form

$$u = \frac{\cos\theta}{v}\Big(2 + \big((n+1)v^n - p(t)\big)(\sin\theta - a\cos\theta)\Big).$$

Therefore, singular control is obtained as a function of the initial variables of the system (1). Note that if the value of the reaction force is bounded, the optimal synthesis problem is more complicated (see, for example, [17, 18].

a)   b)
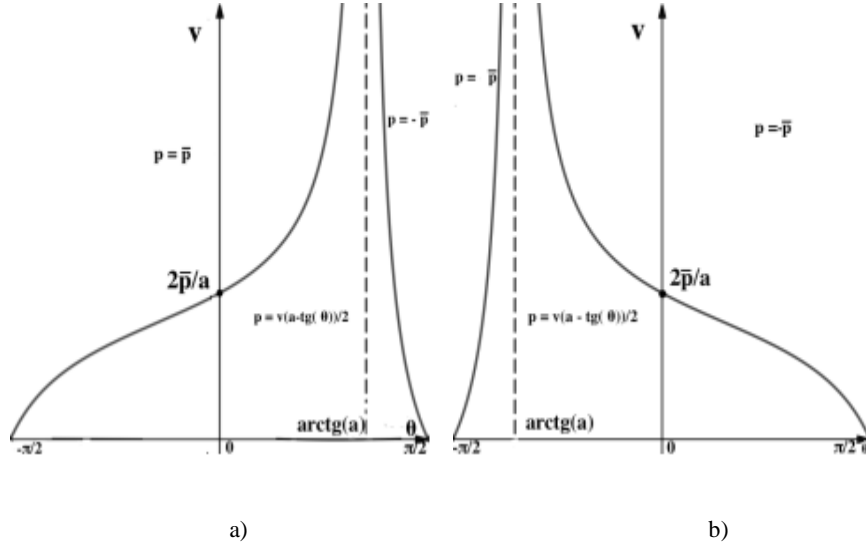
Fig. 1. The domains of the intermediate and boundary thrust for a) $a = 2$, b) $a = -2$.

Following to the presented logic, one can divide the plane (v, θ) into domains where the thrust takes boundary values, and where the value of the thrust belongs to internal range of the set of admissible values depending on $a = \psi_y(t)$ (see Fig.1).

We restrict the further study to the special case of a linear viscous drag. Boundary value problem (11) has a form

$$\begin{cases} \dot{v} = p(t) - v - \sin\theta, & v(0) = v_0, \\ \dot{\theta} = \dfrac{\cos\theta}{v}\Big(1 + \big(2v - p(t)\big)(\sin\theta - a\cos\theta)\Big), & \tan\theta(T) = a, \end{cases} \quad (12)$$

where the choice of $p(t)$ is subjected to the rule (10).

With the purpose to get qualitative features of the solution of the system (11) let us consider phase portrait of the system (12).

Consider the case of boundary values of the thrust $p(t) = \bar{p}$. From the equations $\bar{p} - v - \sin\theta = 0$, $\cos\theta / v = 0$ it is easy to find two states of equilibrium of the system (12). The stationary solution $v_1 = \bar{p} + 1, \theta_1 = -\pi/2$ corresponds to the motion vertically downwards in the plane $(x; y)$. The second stationary solution $v_2 = \bar{p} - 1, \theta_2 = \pi/2$ appears if $\bar{p} > 1$. In the plane $(x; y)$ this point corresponds to the motion vertically upwards. The analysis of the eigenvalues of the system (12) linearized in the vicinity of the stationary solutions (v_1, θ_2) and (v_2, θ_2) shows, that these points are stable proper nodes. The case

$$\begin{cases} \bar{p}(t) - v - \sin\theta = 0, \\ \left(1 + \left(2v - p(t)\right)\right)(\sin\theta - a\cos\theta)) = 0 \end{cases} \tag{13}$$

is more difficult for analysis. The system (12) reduces to the equation

$$f(\theta) = 1 + (\bar{p} - 2\sin\theta)(\sin\theta - a\cos\theta) = 0. \tag{14}$$

Note that $f(-\pi/2) = -\bar{p} - 1$, $f(\pi/2) = \bar{p} - 1$, therefore, for the values $\bar{p} > 1$, the equation (14) has a solution, corresponding to the inclined motion in the plane $(x; y)$ Phase portraits of the system (12) is presented in Fig 2 a),b). It allows to conclude, that this stationary solution is saddle point. An analytical study of this solution in the case of free final altitude was held in paper [13].

a)   b)
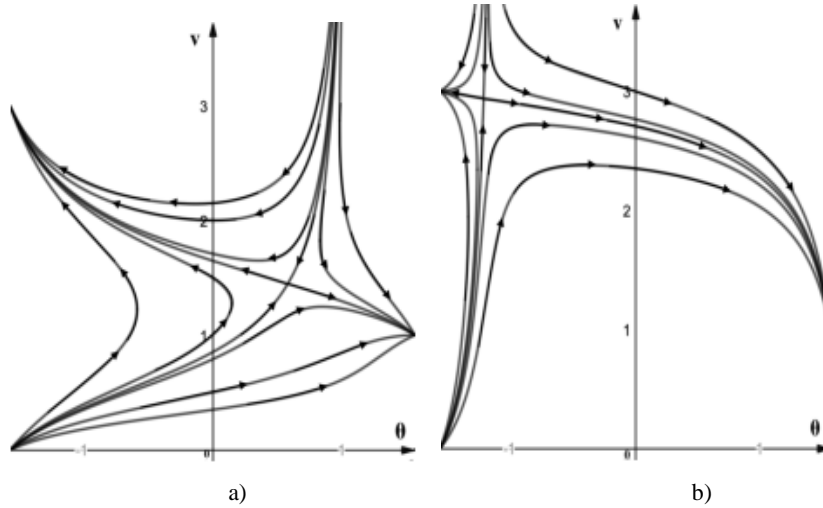
Fig. 2. Phase portrait of the system (11) a) for $\bar{p} = 2, a = 2$, b) for $\bar{p} = 2, a = -2$.

Consider the case of the intermediate thrust $p_0 = v(a - tg\theta)/2$. Phase portraits of the system (12) for various values of a, corresponding to the motion under intermediate thrust are presented in Fig 3 a),b), Fig 4 a),b). There is the single stationary solution in the domain $v > 0, \theta \in (-\pi/2; \pi/2)$, that corresponds to the saddle point evidently. The proof of the type of the stationary solution could be done analytically for the values of $a = 0$ and $a = 2$. Phase portraits in Figs 3-4 were designed as a function (7) level lines, in other words, as a level lines of the first integral of the system (12). Qualitative analysis of the system (12) allows to choose the starting value of $\theta(0)$ for solving BVL problem (12). It should be selected between the separatrix entering the saddle point and the finite set $\tan\theta(T) = a$.

In order to determine the possible number of thrust switching along the trajectory, we consider a system of equations consisting of the first integral of system (12) and the equation of the switching line:

$$\begin{cases} v\cos\theta + av\sin\theta + (av - vtg\theta)(p - v - \sin\theta) - p^2 = C, \\ p = (-vtg\theta + av)/2. \end{cases}$$

Expressing the velocity from the second equation of the system and substituting in the first equation, we obtain

$$(C - p^2)(a\cos\theta - \sin\theta) + 4p^2\cos\theta - 2\bar{p} = 0, \tag{15}$$

a)   b)
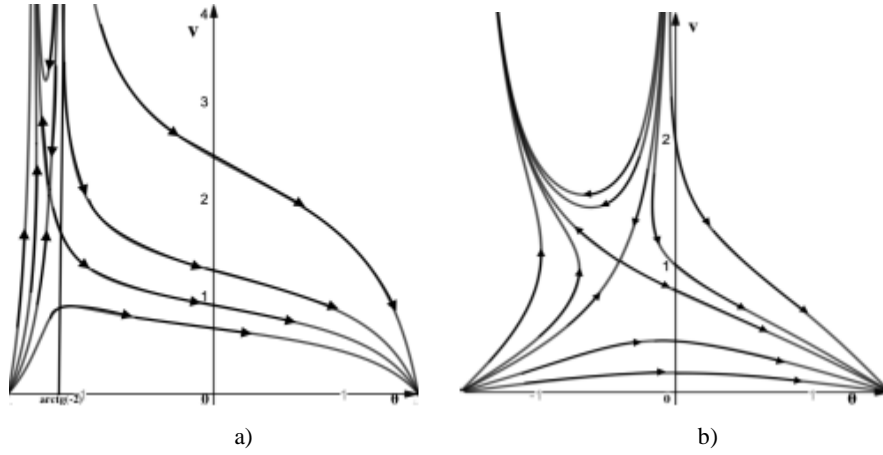
Fig. 3. Phase portrait of the system (11) a) for $a = -2$, b) for $a = 0$.

a)   b)
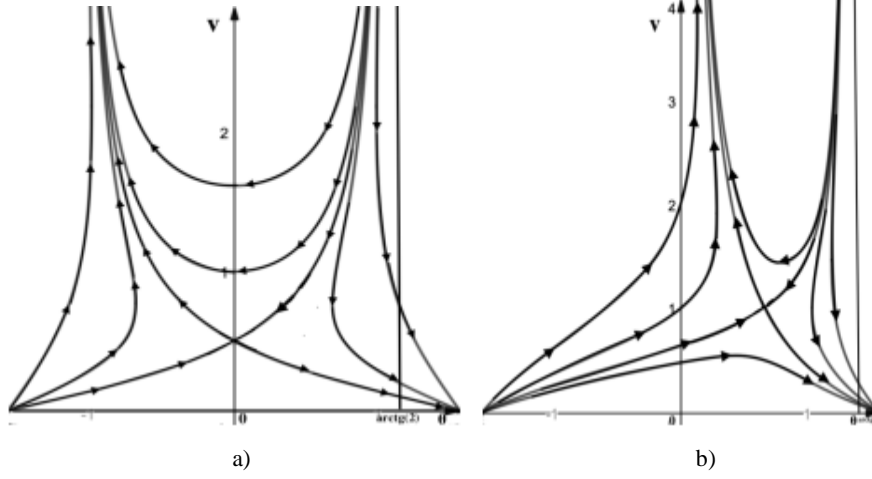
Fig. 4. Phase portrait of the system (11) a) for $a = 2$, b) for $a = 4$.

By expressing the trigonometric functions of equation (15) through the half-angle tangent, we get the following problem: determine the number of the solutions of the equation

$$f(t) = ((4-a)p^2 + 2p + aC)t^2 + 2(C - p^2)t + 2p - aC + (a-4)p^2 = 0, t = \tan(\theta/2).$$

This equation has no more than two solutions belonging to the interval $t \in (-1; 1)$ depending on the parameters a, C and $\bar{p}$. Therefore, the extremal trajectory of the problem (4)-(6) consists either of single arc (intermediate thrust), or two arcs, $p = \bar{p}$ and intermediate thrust, or three arcs: "intermediate-maximum-intermediate". The same consequency of the thrust arcs was determined in the paper [13] for the case of free altitude final value.

4   Numerical simulation

This section presents the results of the numerical solution of the BVL problem (11). For solving the problem (12) the value of a was assumed to be fixed; shooting method was applied. In Fig.5a) the extremal thrust corresponding to the set of parameters $\bar{p} = 1, T = 1, v(0) = 1, y(T) = 0.17$ is shown. For this set of parameters extremal thrust program consists of single arc (intermediate value of the thrust). In Fig.5b) the extremal thrust corresponding to the set of parameters $\bar{p} = 0.3, T = 1, v(0) = 1, y(T) = -0.8$ is demonstrated. For this set of parameters extremal thrust program consists of two arcs, starting from the arc with maximum thrust and ending with intermediate thrust. In Fig.5c) the extremal control and trajectory are presented for the set of parameters $\bar{p} = 0.33, T = 3, v(0) = 0.3, y(T) = -1.3$, for which the thrust program consist of three arcs, "intermediate-maximum-intermediate". The trajectories in the

plane (x, y) for various values of parameter $a = \psi_y(T)$ and $\bar{p} = 1, T = 1, v(0) = 1$ are shown in Fig.6a) for the set $\bar{p} = 1, T = 1, v(0) = 1$ and in Fig 6b) for the set $\bar{p} = 1, T = 3, v(0) = 3$. It is easy to observe monotone dependence of the final altitude depending on parameter $c = a$.
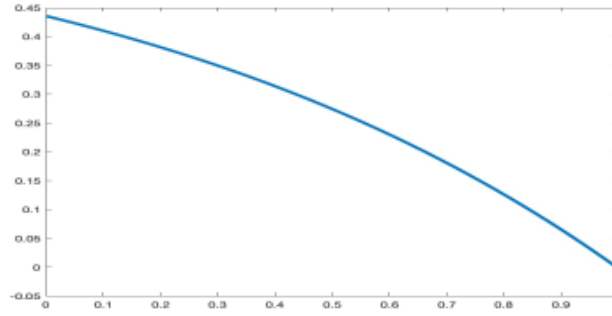
a)
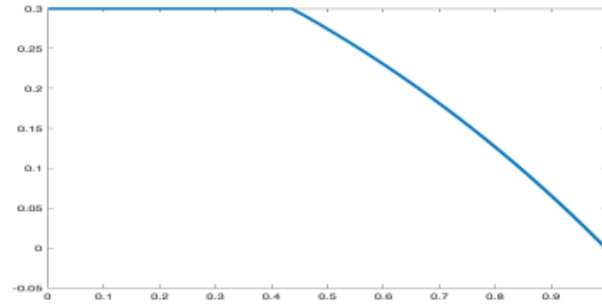
b)
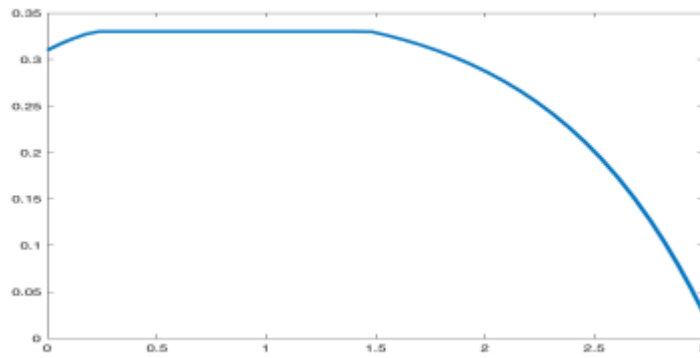
c)

Fig. 5. The extremal thrust as a function of time.
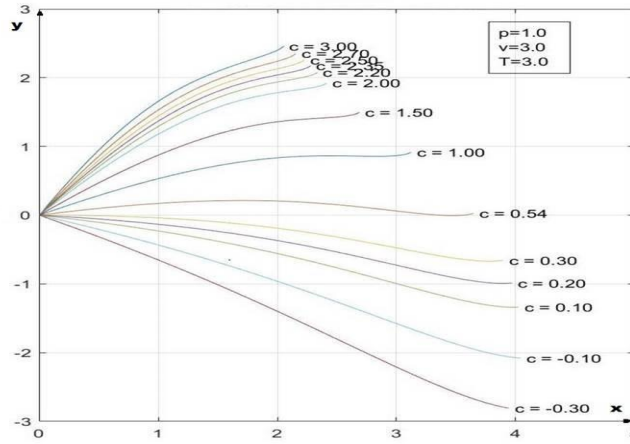
Fig. 6. Extremal trajectories in the plane (x, y).

5   Conclusions

For the brachistochrone problem with penalty for fuel expenditures of mass-point moving in the vertical plane driven by gravity, nonlinear viscous drag, and thrust the extremal synthesis for the controls is determined. It is established that the extreme thrust control program consists either of single arc with intermediate thrust control, or two arcs, starting with maximum thrust and ending with the intermediate thrust or three arcs: "intermediate-maximum-intermediate. The resulting optimal thrust structure coincides with that determined for the case of a free value of final altitude [13].

References

1. Tsien, H. S., Evans, R. C. Optimum Thrust Programming for a Sounding Rocket. Journal of American Rocket Society 21(5), 99-107 (1951).

2. Menon, P.K.A., Kelley, H.J., and Cliff, E.M. Optimal Symmetric Flight with an Intermediate Vehicle Model. J. Guidance 8(3), 312-319 (1985).

3. Vratanar, B., Saje, M. On the Analytical Solution of the Brachistochrone Problem in a Non-conservative Field. Int. J. Non-Linear Mechanics 33(3), 489-505 (1998).

4. J. C. Hayen, "Brachistochrone with Coulomb friction". International Journal of Non-Linear Mechanics 40, 1057-1975 (2005).

5. S. Salinic, Contribution to the brachistochrone problem with Coulomb friction. Acta Mech. 208, 97-115 (2009).

6. A.S. Sumbatov. Brachistochrone with Coulomb friction as the solution of an isoperimetrical variational problem International Journal of Non–Linear Mechanics 88, 135-141 (2017).

7. Chen, D., Liao, G.,Wang, J. The Solution of Brachistochrone Problem Based on the Genetic Algorithm. International Journal of Mechanics Research 4, 76-88 (2015).

8. Thomas V. (1963). The use of variational techniques in the optimization of flight trajectories. Ph.D. thesis, University of Arizona, Parks, E.K.(1963).

9. Drummond, J.E., Downes, G.L. The Brachistochrone with Acceleration: A Running Track. Journal of Optimization Theory and Applications 7(6), 444-449 (1971).

10. Vondrukhov, A.S., Golubev, Yu.F. Brachistochrone with an Accelerating Force. Journal of Computer and Systems Sciences International 53(6), 824-838 (2014).

11. Vondrukhov A.S., Golubev Yu.F. Brachistochrone with an Accelerating Force. Journal of Computer and Systems Sciences International 54(4), 514-524 (2015).

12. Zarodnyuk, A.V., Cherkasov, O.Yu. (2017). On the Maximization of the Horizontal Range and the Brachistochrone with an Accelerating Force and Viscous Friction. Journal of Computer and Systems Sciences International, 56(4), 553-560 (2017).

13. Cherkasov O.Yu, Zarodnyuk A.V. Optimal Controlled Descent in the Atmosphere and the Modified Brachistochrone Problem. In Conference Proceedings IFAC CAO 2018, Yekaterinburg, Russia, October 15-19, 630-635, (2018).

14. Oleg Cherkasov, Alena Zarodnyuk, Nina Smirnova. Optimal Thrust Programming Along the Brachistochronic Trajectory with Non-linear Drag. International Journal of Nonlinear Sciences and Numerical Simulation, Freund Publishing House Ltd.(Israel), 20(1), 1-6 (2019).

15. Kelley, H.J., 'A Transformation Approach to Singular Subarcs in Optimal Trajectory and Control Problems', SIAM Journal of Control 2, 234-240 (1965).

16. L.S. Pontryagin, et al., The Mathematical Theory of Optimal Processes.Wiley-Interscience, New York, New York, (1962).

17. Radoslav Radulović, Bojan Jeremić, Slaviša Šalinić, Aleksandar Obradović, Milan Dražić. A new approach for the determination of the global minimum time for the brachistochrone with preselected interval for the normal reaction force value. International Journal of Non-Linear Mechanics 101, 26-35, (2018).

18. Slaviša Šalinic, Aleksandar Obradovi´c, Zoran Mitrovi´c, Srdjan Rusov Brachistochrone with limited reaction of constraint in an arbitrary force field. Nonlinear Dyn 69, 211-222, (2012).

Cherkasov Oleg, Lomonosov Moscow State, Moscow, 119991, Russia

Nina Smirnova, Lomonosov Moscow State, Moscow, 119991, Russia

Sheng Huang, National Taiwan University10617 No.1, Sec. 4, Roosevelt Road, Taipei, Taiwan
(oyuche@yandex.ru)

An experimental investigation on noisy intermittency

Ezequiel Del Rio, Sergio Elaskar

Abstract: Intermittency is a route to chaos when transitions between laminar and chaotic dynamics occur. The main attribute of intermittency is the reinjection mechanism, described by the reinjection probability density (RPD), that maps trajectories of the system from the chaotic region into the laminar one. Results on chaotic intermittency depend on the RPD, that was taken as a constant. Recently, a generalized no uniform RPD has been observed in a wide class of 1D maps, hence the intermittency theory has been generalized, including the classical one as a particular case. Noise has an impact on the intermittency phenomena and the generalized RPD introduces a novel scenario because it is affected by the noise. An analytical approach was introduced to estimate the noisy RPD. In this work, by using the Poincaré map, we apply our noisy theory of 1D maps to an experimental continuous system. We found that noisy data provides a description of both, noisy and an ideal noiseless system. We found that the response to the noise of the experimental Poincaré map is different than the obtained by numerical simulations.

1. Introduction

Intermittency is one of the main route to deterministic chaos. It is characterized by irregular changes between regular phase (called laminar) and chaotic burst. According to Pomeau and Manneville, intermittency can be classified into three types depending on the local geometry of their Poincaré map: type-I for quadratic maps and type-II and type-III for cubic ones [1]. However, other non linear types have been reported [2, 3, 4] In every the types, the fixed point of the system becomes unstable for positive values of small values of a parameter ε.

Another condition for a one-dimensional map to possess intermittency is to have a reinjection mechanism mapping back the trajectories from the chaotic zone into the laminar one. This mechanism is described by the so-called reinjection probability density (RPD), which is determined by the chaotic dynamics of the system itself. Both, the function RPD and the local map determine all the dynamical properties of the system. In general it is difficult to get an analytical expression for the RPD, hence different approximations have been used. The most common approximation in classical intermittency theory has been to consider the RPD uniform [1, 5, 6, 7, 8, 9, 10, 11]. However, it has been introduced a more general RPD that includes the uniform reinjection as a particular case, hence the classical results on chaotic intermittency have been generalized. The new RPD has been found in

many 1D maps and the analytical predictions of the new theory have been numerically confirmed. For a review of the generalized theory see [12]. Note that, continuous systems that contract volume in phase spaces can be described by the 1D maps [13]. In this way, the mentioned generalization of the intermittency theory has been confirmed in an experimental analog circuit [14].

An important quantity related to the intermittency phenomenon is the probability density of the laminar lengths $\psi(l)$, being $\psi(l)\,dl$ the probability of finding a laminar phase of a given length lying between l and $l + dl$, where l indicates the number of iterations in the laminar region. Note that the function $\psi(l)$ is determined by the RPD and the non linearity of the laminar region [1, 12].

2. Theoretical framework

First of all, let us briefly describe the theoretical framework that accounts for a wide class of dynamical systems exhibiting intermittency. We consider a general 1D map

$$x_{n+1} = F(x_n), \qquad F : \mathbb{R} \to \mathbb{R} \tag{1}$$

Having a point with infinity tangent or an extreme point, that is mapped into the laminar region, then under a wide general conditions, the generalized RPD for the map (1) is given by the following power law [3, 4, 15].

$$\phi(x) = b(x - \hat{x})^{\alpha} \tag{2}$$

which drives the reinjection mechanism for intermittencies of type I, II and III. Later was fond the RPD describes by Eq. (2) in type V intermittency [16, 17]. The RPD (2) has two free parameters, $\hat{x}$ and α, determined by the dynamics in the chaotic region. The parameter $\hat{x}$ corresponds with the so-called lower bound of reinjection (LBR), that is $\hat{x} \leq x$. The symmetry case where, $x \leq \hat{x}$, can be taken into account by substituting in the RPD (2) $(x - \hat{x})$ by $(\hat{x} - x)$ and for sake of clarity we consider only the RPD given by Eq. (2).

The exponent α is determined by the geometry of the map in a vicinity of a point with infinite or zero tangent, and b is determined by the usual normalization condition. Note that the RPD of (2) includes the constant reinjection approach as the particular case $\alpha = 0$.

The main task to determine the properties of a specific intermittency is to find the two free parameters of the RPD Eq. (2). In this way, an analytical procedure to obtain the value of α has been proposed in [18], where it was demonstrated that in the case of direct reinjection from an extreme point x_m into laminar zone, for $x \to x_m$ we have $F^{(i)}(x) \to 0$ for $i \leq q$, where $F^{(i)}(x)$ denotes the i-derivative of the function $F(x)$, and if the derivative

$F^{(q+1)} \neq 0$ exits, we have

$$\alpha = -\frac{q}{q+1}. \tag{3}$$

For indirect reinjection, that is the case considered in the following sections, the previous result also works [18]. We will apply this method in the following sections.

On the other hand, a simple methodology to evaluate the free parameters $\hat{x}$ and α from numerical or experimental data (when the map (1) is analytically unknown) has been proposed by using the function $M(x)$ defined as

$$M(x) = \begin{cases} \frac{\int_{x_s}^x \tau\ \phi(\tau)\ d\tau}{\int_{x_s}^x \phi(\tau)\ d\tau} & \text{if } \int_{x_s}^x \phi(\tau)d\tau \neq 0 \\ 0 & \text{if } \int_{x_s}^x \phi(\tau)d\tau = 0, \end{cases} \tag{4}$$

where x_s is a suitable starting point having $x_s < x$ for all reinjected points x. The domain of definition of $M(x)$ is the laminar region. As $M(x)$ is defined by means of integrals, it is easier to compute than $\phi(x)$, and also the effects coming from the statistical fluctuations are reduced, even for a relatively low number of data [19]. Moreover, note that for a given value of x, $M(x)$ is the average of reinjection points in the interval (x_s, x), hence, if we sort the reinjections according to the relation $x_j < x_{j+1}$, a simple estimation of the function $M(x)$ is obtained by means of

$$M(x_l) \approx \frac{\sum_{j=1}^l x_j}{l}, \tag{5}$$

which is useful to evaluate the function $M(x)$ instead of using the definition Eq. (4).

An important property of the function $M(x)$ is that for the RPD given by Eq. (2), it becomes linear as follow

$$M(x) = \begin{cases} 0 & x \leq \hat{x} \\ m(x - \hat{x}) + \hat{x} & x > \hat{x} \end{cases} \tag{6}$$

where the exponent α is determined by the slope m as,

$$\alpha = -\frac{1 - 2m}{1 - m}, \tag{7}$$

Assuming $\alpha > -1$, that is $0 < m < 1$, Eq. (2) and Eq. (6) provide equivalent descriptions of the RPD [12]. According to Eq.(7), the particular value $m = 1/2$ correspond to the classical approach $\phi(x) = cte$ considered in the literature.

2.1. The noise effect

Because the noise is always present in experiments, it is of a fundamental importance to know the effect of noise on the intermittency phenomenon, in particular on the RPD.

For noisy 1D maps it is common to introduce an additive external noise to the map (1) as following

$$x_{n+1} = F(x_n) + \sigma\xi_n \tag{8}$$

where ξ_n is a uniform distributed noise with $< \xi_m, \xi_n > = \delta(m-n)$ and $< \xi_n > = 0$, σ is the noise strength.

There are many papers devoted to study noise effect on chaotic intermittency, by means of the normalization group analysis [2], or by using the Fokker-Plank equation [20, 21, 11, 22] among the others. Note that, in spite of the fact that the noise affects the whole region where the system dynamics takes place, in all of the cases, the researches are devoted to the noise effect on local Poincaré map and there was no study in classical theory of intermittency focused on the effect of noise on the RPD, as far as the authors know.

Actually, Eq. (2) introduces a novel scenario because, whereas the classical uniform reinjection should remain almost constant under a wide class of noise distributions, the RPD of Eq. (2) can be affected by the noise. For 1D map, an analytical approach to the noise reinjection probability density (NRPD) has been present in a publication with Prof. Sanjuán [23]. Other application of this noisy theory for 1D maps has been developed [24, 25, 26] and even for the case on continuous experimental system [14]. In last case, there have been observed some differences with respect to the numerical experiments. This will be investigated in the subsection 3.2. Before this, let us briefly summarize the noisy theory applied to the RPD. In summary, the NRPD (denoted here by capital case $\Phi(x)$, whereas the lower case $\phi(x)$ denotes the noiseless RPD) is given by

$$\Phi(x) = \int \phi(y)G(x-y,\sigma)\mathrm{d}y \tag{9}$$

where $G(x-y,\sigma)$ is the probability density of the internal noise depending on the noise strength parameter σ. It is important to note that Eq. (9) describes how the noise in the 1D map or in the experimental Poincaré map transforms the noiseless RPD, $\phi(x)$, into the NRPD $\Phi(x)$. Note that to evaluate the convolution (9), it is necessary to know $\phi(x)$. It is possible to get $\phi(x)$ even in the case of noisy system by applying the noiseless mathematical framework described in section 2 [23].

In fact, for uniform distributed noise, the integral (9) increments the deterministic value α in one unit, $\alpha_n = \alpha + 1$, in the region $x \in (\hat{x} - \sigma, \hat{x} + \sigma)$. According with Eq. (7) this also

changes the value of the deterministic m into a new one, m_n, driven by substituting α_n in Eq. (7). The value of $\hat{x}$ is also shifted by the noise to a new one: $\hat{x}_n = \hat{x} - \sigma$. Concerning with points far from $\hat{x}$, the value of α in the deterministic case does not change. Note that in this region the value of m also remains constant [23, 24, 25, 26]. Finally, the noisy function $M(x)$, just after the first iteration of the map can be expressed by a piecewise linear function as following

$$
M(x) = \begin{cases} 0 & x \leq \hat{x}_n \\ m_n(x - \hat{x}_n) + \hat{x}_n & \hat{x} - \sigma < x < p \\ m(x - \hat{x}') + \hat{x}' & x > p \end{cases}
\tag{10}
$$

where the parameter $\hat{x}'$ must be determined by fitting the data and the point p is determined by the intersection between the two straight lines in equation of $M(x)$ (10). Note that p is not a free parameter because is determined by $\hat{x}'$.

3. Noisy RPD

In this section we compare the previous framework on the reinjection probability density to two cases; an experimental system and a numerical Poincaré map fitting such experiment.

3.1. Experimental NRPD

To illustrate how Eq (9) is used, let us consider an experimental circuit that can work with large noise-signal ratio [14]. The corresponding experimental Poincaré map is shown in Fig. 1.a for a noisy case. It is also shown in this figure (black line) a polynomial approximation of the experimental map that will be used in following sections.

The NRPD of the Poincaré map of Fig. 1.a is given by Eq. (9), where $G(x - y, \sigma)$ is the probability density of the internal noise perturbing the experimental Poincaré map. This function is in general unknown, however, we can approach it by a uniform distributed noise as follows

$$
G(x, \sigma) = \frac{\Theta(x + \sigma) - \Theta(x - \sigma)}{2\sigma},
\tag{11}
$$

where $\Theta(x)$ is the Heaviside step function which is zero for negative argument and one for positive argument. Now, after evaluating the integral (9), the NRPD reaches

$$
\Phi(x) = \begin{cases} 0 & x < \hat{x} - \sigma \\ \frac{b}{2\sigma(\alpha+1)}(x - \hat{x} + \sigma)^{\alpha+1} & \hat{x} - \sigma \leq x \leq \hat{x} + \sigma \\ \frac{b\left[(x-\hat{x}+\sigma)^{\alpha+1} - (x-\hat{x}-\sigma)^{\alpha+1}\right]}{2\sigma(\alpha+1)} & \hat{x} + \sigma < x \end{cases}
\tag{12}
$$
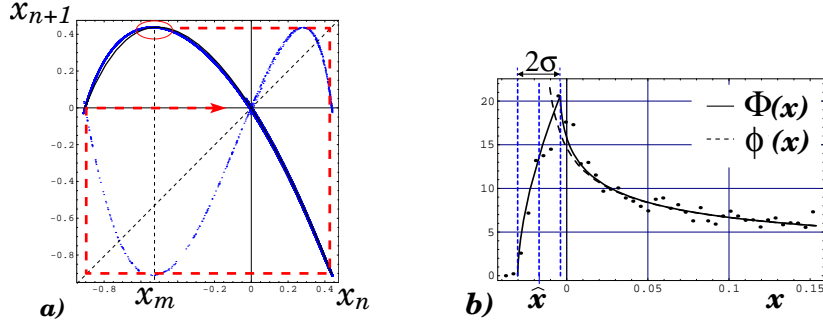
Figure 1. a) Experimental Poincaré map in Blue dots and its analytical approximation in black line (see main text). Dashes red line shows the three iterations from the maximum to the laminar region around $x = 0$. b) Noisy RPD. Dots show the experimental data whereas continuous line shows the analytical estimation according with Eq.(12). See [14].

.

It was determined in the experiment that $\sigma = 0.013$ [14]. With this value, Eq. (12) reproduces well the experimental data as Fig. 1.b shows. Note that whereas the points near the maximum x_m need three iterations to reach the laminar region around $\hat{x} = 0$, we have made the convolution (9) just once. This is the main difference with respect to the noisy framework applied to numerical experiments, as we explain in the following section.

3.2. Numerical simulations of the experimental Poincaré map

In this section we compare the previous experimental results on the noisy Poincaré map with an analytical polynomial function fitting the experimental map as it is shown in black continuous line in Fig. 1.a. We have choose such map as the lower degree polynomial, having the same properties than the experimental map as following,

$$x_{n+1} = P(x_n) = a_5 \, x_n{}^5 + a_4 \, x_n{}^4 + a_3 \, x_n{}^3 + a_2 \, x_n{}^2 + a_1 \, x_n + a_0 \tag{13}$$

In this way, we identified some relevant points in the experimental Poincaré map, $B_i = (b_i, b_{i+1})$ with $i = 1, 2, 3, 4, 5$ as it is shown in Fig. 2, where it is plotted the map (13) in yellow continuous line.

Note that we have $b_1 = x_m$, and $B_4 = (0, 0)$ is the reinjection point of x_m. The five equations

$$P(b_i) = b_{i+1} \quad i = 1, 2, 3, 4, 5 \tag{14}$$

together with

$$5a_5 \, b_1{}^4 + 4a_4 \, b_1{}^3 + 3a_3 \, b_1{}^2 + 2a_2 \, b_1 + a_1 = 0 \tag{15}$$

determine the six parameters a_i in $P(x_n)$. Note that the last equation is necessary to get the maximum at B_1, because we have chosen $b_1 = x_m$. The map (13) is shown in black color in Fig. 1.a together with the experimental Poincaré map. According with the section
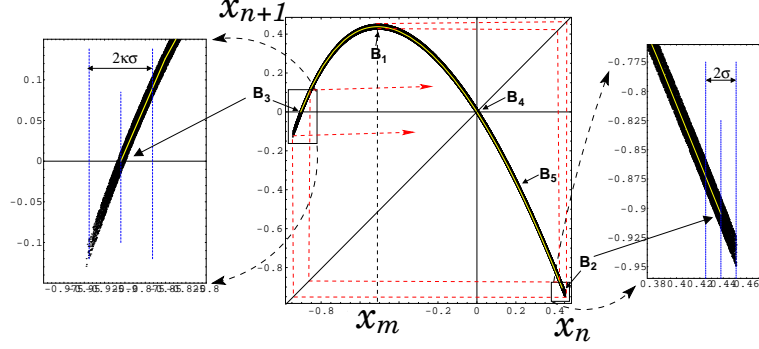
Figure 2. The yellow line shows the map given by Eq.(13). Black dots are coming from numerical interactions of the map (17) with $\sigma = 0.013$ (see main text). To observe better the noise effect, the lateral figures show enlargements of the indicated box in main figure.

2, we can determine analytically the RPD for the map (13). Note that $P'(x_m) = 0$ whereas $P''(x_m) \neq 0$, hence we have $q = 1$ in Eq.(3) so we get $\alpha = -1/2$ and $m = 1/3$. By construction of the map (13) we have $\hat{x} = 0$, so the function $M(x)$ (see Eq. 6) and the RPD of Eq.(2) is given by

$$M(x) = \frac{x}{3} \quad \text{and} \quad \phi(x) = b\,x^{-\frac{1}{2}} \tag{16}$$

Note that the value of m and α in Eq.(16) provides the analytical description of the reinjection process referred to the first iteration after the maximum x_m (from B_1 to B_2 in Fig. 2). However, this result are robust after iteration of the map if the trajectory does not include point with zero or infinity slope. Figure 3 displays the analytic functions $M(x)$ and $\phi(x)$ (see Eq. (16)) together with numerical simulations of the map (13) showing that the results of Eq. (16) are robust after three iterations of the map.

Regarding with the noisy case, we introduce an additive external noise to the map (13) as following

$$x_{n+1} = P(x_n) + \sigma\xi_n \tag{17}$$

where ξ_n is a uniform distributed noise with $< \xi_m, \xi_n > = \delta(m - n)$ and $< \xi_n > = 0$ and σ is the noise strength. We have used $\sigma = 0.013$ in order to compare it with the experimental case, but this specific value is no relevant for our propose. Figure 2 shows the map (17)
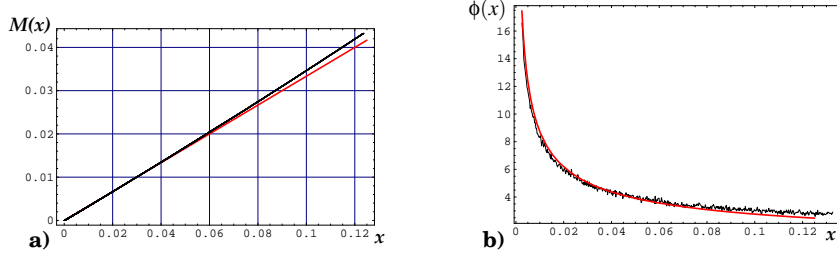
Figure 3. Numerical iteration of 10^8 points of the map (13) superimposed to the analytical predictions (red lines) of Eq. (16) without any data fitting. a) Function $M(x)$, b) RPD $\phi(x)$.

.

(black dots) superimposed with the map (13) in continuous yellow line. The enlargement on the right (left) of the main figure shows the noise effect on the first (second) iteration from points mapped from a neighborhood of x_m. On the right (left) enlargement, the middle blue dashes line indicate the limit of the deterministic map (13) at the point B_2 (B_3), whereas the lateral blue lines delimit the main region affected by the noise with a 2σ (2σ) width.

As in the experimental map, the reinjection is not directly from the maximum x_m, however, contrary to the experimental case, to get the NRPD, we must apply the convolution (9) step by step, not just once as it was applied in the experimental case.

Hence, for a neighborhood of the point B_2 in Fig. 2, the NRPD is given by the convolution (9). After integration, we get the following expression

$$\Phi(x) = \begin{cases} 0 & x > \hat{x}_2 + \sigma \\ \frac{b}{2\sigma(\alpha+1)}(\hat{x}_2 - x + \sigma)^{\alpha+1} & \hat{x}_2 - \sigma \le x \le \hat{x}_2 + \sigma \\ \frac{b\left[(\hat{x}_2-x+\sigma)^{\alpha+1}-(\hat{x}_2-x-\sigma)^{\alpha+1}\right]}{2\sigma(\alpha+1)} & x < \hat{x}_2 - \sigma \end{cases} \tag{18}$$

where $\hat{x}_2 = b_2$ because the Eq.(18) is referred to the point B_2. Note that some signs have changed with respect to Eq.(12). This is because the reinjection around B_2 is produced in reverse order with respect to the reinjection on $\hat{x} = 0$ (see [12] for details). Figure 4 shows numerical estimation of noisy $M(x)$ and NRPD for the map (17) together with its corresponding analytical estimations given by Eq. (10) and Eq. (18) respectively. Note that the NRPD shows the typical vertex point at $x = \hat{x} - \sigma$ [24, 25]. It is important to emphasize that the vertex point appears at the first iteration given by Eq. (18) because it was obtained by the integral (9), that involves a no continuous function, hence the result is just continuous but not differentiable. The vertical middle blue line in Fig. 4.b indicates the asymptotic limit for the deterministic RPD, whereas the lateral blues lines show the region of 2σ width where the influence of the noise to the deterministic RPD is stronger. The blue lines are the sames
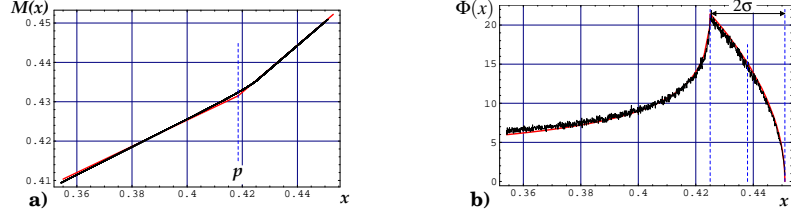
Figure 4. Numerical estimations of $M(x)$ and $\Phi(x)$ determined by the map (17) with $\sigma = 0.013$ near to the point B_2 (black color). In red line it is shown the analytical predictions for **a)** Function $M(x)$ according with Eq. (10). The blue dashes line indicates the value of p such equation. **b)** Noisy RPD according with Eq. (18). The vertical lateral blue dashes show the limit of the interval $x \in (\hat{x}_2 - \sigma, \hat{x}_2 + \sigma)$ in Eq. (18).

that displayed in left enlargement of Fig. 2. Note that NRPD given by Eq. (18) tends to the $b(\hat{x}_2 - x)^\alpha$ as $\sigma/(\hat{x}_2 - x) \to 0$. That is for $x << \hat{x}$ the function $M(x)$ has the same slope m than in the noiseless case. Following the previous argument, the new NRPD referred to the point B_3 of Fig 2 is given by the integral Eq. (9) applied to Eq. (18), hence it will produce a differentiable function. To evaluate the integral we approach the map (13) around point B_2 as a linear function with slope κ. After evaluating the integral, the NRPD around the point B_3 reaches,

$$\Phi(x) =$$

$$= \begin{cases} 0 & x < \hat{x}_3 - 2\kappa\sigma \\ b' \left[(x - \hat{x}_3 + 2\kappa\sigma)^{\alpha+2} \right] & \hat{x}_3 - 2\kappa\sigma \leq x < \hat{x}_3 \\ b' \left[(x - \hat{x}_3 + 2\kappa\sigma)^{\alpha+2} - 2(x - \hat{x}_3)^{\alpha+2} \right] & \hat{x}_3 \leq x < \hat{x}_3 + 2\kappa\sigma \\ b' \left[(x - \hat{x}_3 + 2\kappa\sigma)^{\alpha+2} + (x - \hat{x}_3 - 2\kappa\sigma)^{\alpha+2} - 2(x - \hat{x}_3)^{\alpha+2} \right] & \hat{x}_3 + 2\kappa\sigma \leq x \end{cases}$$

$$(19)$$

where we define $b' = b/[(2\kappa\sigma)^2(\alpha + 1)(\alpha + 2)]$. Note that the function (19) is differentiable just once and tends to the $b(x - \hat{x}_3)^\alpha$ as $\sigma/(x - \hat{x}_3) \to 0$. That is for $x >> \hat{x}$ we recover for the function $M(x)$ the same slope m than in the noiseless case. This means that the value of m and α can be found even after noisy indirect reinjection.

In figure 5.a is represented the NRPD given by Eq. (19) together with the corresponding numerical evaluation. We can observe some differences between numerical and analytical evaluations that are coming from the linear approximation of the map (17) near the point B_2.

Finally, by applying the convolution (9) to the NRPD referred to point B_3 given by Eq. (19), we have the NRPD at the unstable point $\hat{x} = 0$, which is a twice differentiated reinjection function (see Fig. 5.b). The analytical expression of this function is very long so in order to salve space we prefer to omit. Remember that for the experimental case we found a non differentiable NRPD in the unstable point with a vertex point, similar for the numerical NRPD referred at B_2.
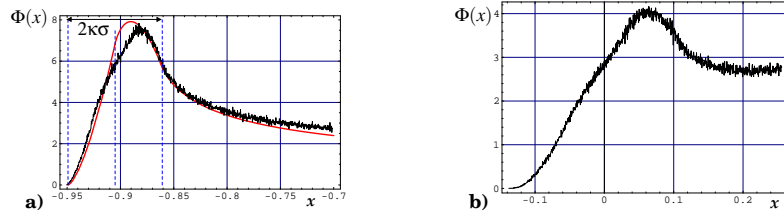
Figure 5. Numerical estimation of the NRPD referred to the map (17) with $\sigma = 0.013$. a) NRPD near the point B_3 of Fig. 2. The red line shows the function (19) with $\kappa = 1.7$. The vertical lateral blue dashes show the limit of the interval $x \in (\hat{x}_3 - 2\kappa\sigma, \hat{x}_3 + 2\kappa\sigma)$. b) NRPD near $\hat{x} = 0$.

.

4. Conclusions

Based in the framework presented in section 2 we have evaluated the noisy reinjection probability density (NRPD) in two cases: an experimental system and its Poincaré approximation by a 1D polynomial map. We found quite different results between both cases as it is shown in Fig. 1.b and Fig. 5.b. These differences can be explained because for the experimental Poincaré map we applied the convolution (9) just once, whereas in the numerical case we have needed three consecutive evaluations of (9) to get the NRPD. We can conclude that, in the noiseless case, the analytical map, Eq. (13), fitting the experimental one shows a similar RPD function, whereas in the noisy case, both maps show different noisy RPD. It remains as an open question to investigate in which case the experimental system and its numerical map show a similar RPD even in the noisy case.

Acknowledgments

References

[1] SCHUSTER, H., AND JUST, W. *Deterministic Chaos. An Introduction.* (WILEY-VCH Verlag GmbH and Co. KGaA, Weinheim, Germany), 2005.

[2] HIRSCH, J. E., NAUENBERG, M., AND SCALAPINO, D. J. Intermittency in the Presence of Noise: A Renormalization Group Formulation. *Phys. Lett. A*, 87 (1982), 391–393.

[3] DEL RIO, E., AND ELASKAR, S. (2010) New Characteristic Relations in type-II Intermittency. *Int. J. of Bifurcation and Chaos*, 20 (2010), 1185–1191

[4] DEL RIO, E., ELASKAR, S., AND DONOSO, J. M. Laminar length and characteristic relation in type-I intermittency. *Commun. Nonlinear Sci. Numer. Simulat.* 19 (2014) 967–976.

[5] MANNEVILLE, P. Intermittency, self-similarity and 1/f spectrum in dissipative dynamical systems. *Le Journal de Physique* 41 (1980) 1235–1243.

[6] DUBOIS, M., RUBIO, M., AND BERGE, P. Experimental Evidence of Intermittencies Associated with a Subharmonic Bifurcation. *Phys. Rev. Lett.* 51 (1983) 1446–1449.

[7] PIKOVSKY, A., OSIPOV, G., ROSENBLUM, M., ZAKS, M., AND J. KURTHS Attractor-repeller collision and eyelet intermittency at the transition to phase synchronization *Phys. Rev. Lett.* 79 (1997) 47–50.

[8] KIM,C.M., KWON, O.J., EOK-KYUN LEE, AND HOYUN LEE New Characteristic Relations in type-I Intermittency. *Phys. Rev. Lett.* 73 (1994) 525–528.

[9] KIM, C.M., YIM, G.S., RYU, J.W. AND PARK, Y.J. CHARACTERISTIC RELATIONS OF TYPE-III INTERMITTENCY IN AN ELECTRONIC CIRCUIT *Phys. Rev. Lett.* 80 (1998) 5317–5320.

[10] CHO,J.H., KO, M.S., PARK, Y.J. AND KIM, C.M. Experimental observation of the characteristic relations of type-I intermittency in the presence of noise. *Phys. Rev. E* 65 (2002) 036222.

[11] KYE, W.H., RIM,S., KIM,C.M., LEE, J.H., RYU,J., W., YEOM,B.S. AND PARK, Y.J. Experimental observation of characteristic relations of type-III intermittency in the presence of noise in a simple electronic circuit *Phys. Rev. E* 68 (2003) 362031–362035

[12] ELASKAR, S., AND DEL RIO, E *New Advances on Chaotic Intermittency and its Applications.* Springer, 2017

[13] OTT, E. (2008) *Caos in Dynamical Systems*, (Cambridge University Press, Cambridge).

[14] DEL RIO, E., AND ELASKAR, S. Experimental evidence of power law reinjection in chaotic intermittency. *Commun Nonlinear Sci Numer Simulat* 64 (2018) 122–134

[15] ELASKAR,S., DEL RIO, E., AND J. M. DONOSO Reinjection Probability Density in type-III Intermittency. *Physica A* 390 (2011) 2759-2768.

[16] ELASKAR, S., AND DEL RIO, E. Discontinuous reinjection probability density function in type V intermittency. *J. Comp. Nonlinear Dynam.* 13 (2018) 121001-10.

[17] ELASKAR, S., DEL RIO, E., AND GUTIERREZ MARCANTONI, L. Non-uniform reinjection probability density function in type V intermittency. *Nonlinear Dynam.* 92 (2018) 683–697.

[18] DEL RIO, E., AND ELASKAR, S. On the theory of intermittency in 1D map. *International Journal of Bifurcation and Chaos* 26 (2016) 1650228.

[19] del Rio, E., Elaskar, S., and Makarov, A. (2013) THEORY OF INTERMITTENCY APPLIED TO CLASSICAL PATHOLOGICAL CASES *Chaos* **23**, 033112.

[20] PIKOVSKY,A.S. J. heim (2005) A new type of intermittent transition to chaos. *Phys A* 16 (1983) L109–L112.

[21] HIRSCH,J. E., HUBERMAN,B. A., AND SCALAPINO,D.J., Theory of intermittency. *Phys. Rev. A* 25 (1982) 519–532.

[22] KORONOVSKII, A.A., AND HRAMOV, A.E. type-II intermittency characteristics in the presence of noise *Eur. Phys. J. B* 62 (2008) 447–452.

[23] DEL RIO, E., SANJUÁN, M.,A.,F., AND ELASKAR, S., Effect of noise on the reinjection probability density in intermittency, *Commun. Nonlinear Sci. Numer. Simulat.* 17 (2012) 3587–3596.

[24] KRAUSE, G., ELASKAR, S., AND DEL RIO, E. Noise effect on statistical properties of type-I intermittency *Physica A* 402 (2014) 318–329.

[25] ELASKAR,S., DEL RIO, E., KRAUSE, G., AND COSTA, A., Effect of the lower boundary of reinjection and noise in Type-II intermittency *Nonlinear Dynamics.* 79 (2015) 1411–1424

[26] ELASKAR S., DEL RIO., AND E, COSTA A., Reinjection Probability Density for Type-III Intermittency With Noise and Lower Boundary of Reinjection *Journal of computational and nonlinear dynamics* 12 (2017) 031020–031020

Ezequiel Del Rio, Associate Professor: Universidad Politécnica de Madrid, ETSI Aeronáutica y del Espacio , Dpto. Físia Aplicada, Plaza Cardenal Cisneros, 28040 Madrid, Spain (ES) (*ezequiel.delrio@upm.es*). The author presented this contribution at the conference in the special session "A special session dedicated to Prof. Miguel A.F. Sanjuán on the occasion of the celebration of his 60th anniversary" organized by J. Awcewicz.

Sergio Elaskar, Professor: Universidad Nacional de Córdoba, Instituto de Estudios Avanzados en Ingeniera y Tecnologa CONICET, Avd. Velez Sarsfield 1611. Cordoba,, Argentina (AR) (*sergio.elaskar@gmail.com*).

Numerical and analytical investigation of chatter suppression by parametric excitation

Fadi Dohnal, Wolfgang Hörtnagel, Mariusz Zamojski

Abstract: A concept for increasing process stability during milling is presented utilizing the time-periodic modulation of the tool support. A simple time-delayed system describing the effect of regenerative chatter is enhanced by a time-periodic variation of the support. Such a system leads to entirely new dynamics. Numerical results of stability charts are discussed in terms of spindle speed and cut depth and show classic chatter lobes that are modified by the parametric excitation. This kind of parametric excitation is more general than the one occurring for varying spindle speed because its frequency is independent of the cutting frequency of the tool and therefore independent of the spindle speed and number of teeth. First analytical approximations on the stability of the modified lobes are benchmarked against numerical predictions. This study is a preparation for experimental tests.

1. Introduction

Machine tool vibrations affect the wear, tool life and surface quality [9] leading to an increase of production cost and time. A simple model for chatter is the regenerative effect that is summarised in [7, 6]. Chatter occurs typically within instability lobes in the spindle speed diagram. Tools and methods for influencing (shift and distortion) these lobes are discussed in detail in the pioneering work [2]. Several countermeasures can be derived like tuning the support and tool stiffness, the cutting feed, the spindle speed, the geometry of the cutter profile and the number of teeth. The so-called process damping helps also and is always present in real machines. Another possibility is attaching a passive linear or nonlinear vibration absorber to the cutting tool as introduced recently in [5]. A semi-active mean was proposed in [1] in which the bearing stiffness of the spindle was modulated time-periodically showing an increase in damping. Active means in this context employ piezoelectric actuators mounted on the workpiece directly, see for example [3].

All these measures have benefits and drawbacks and a successful implementation depends strongly on parameters like machine throughput and complexity of the cut which directly translates into cost and time. The present contribution addresses the regenerative effect in metal cutting as defined in [7] but extends the system with a time-harmonic modulation of the support stiffness of the cutting tool. The reason for this is motivated by the observation of parametric anti-resonances in [4].

2. Regenerative effect

The simplest mechanical model for regenerative chatter is shown in Fig. 1. The equations of motion of this single degree-of-freedom model of a cutting tool in turning machinery is given by

$$m\ddot{x} + c\dot{x} + kx = F_x \tag{1}$$

where m is the mass, c the damping coefficient and k the stiffness coefficient of the cutting tool. The workpiece is assumed to be rigid. F_x is the component of the cutting force in the cutting direction. It can be expressed by the empirical power law [2]

$$F_x(t) = K_x\, w\, h^r(t) \tag{2}$$

where w is the chip depth, K_x is the cutting force coefficient, r the cutting force exponent and $h(t)$ the time-dependent chip thickness

$$h(t) = v_f \tau + x(t - \tau) - x(t) \tag{3}$$

Choosing $r = 3/4$ and expanding the cutting force F_x and the tool displacement x into its Taylor series around $h_0 = v_f \tau$ yields the linearized, delayed equations of motion in $\tilde{x}$ with constant coefficients (see [7, 5] for more details)

$$m\ddot{x} + c\dot{x} + kx = k_1\left(x(t - \tau) - x(t)\right) \tag{4}$$
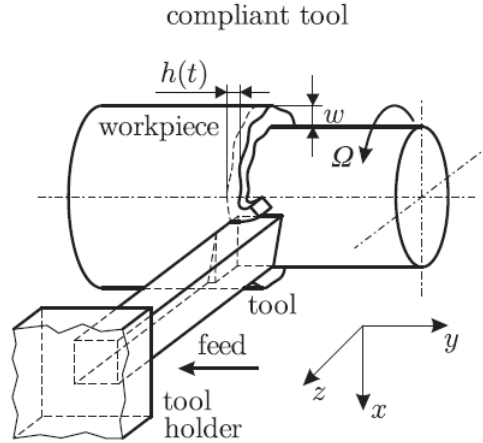
Figure 1. Mechanical system according to [6].
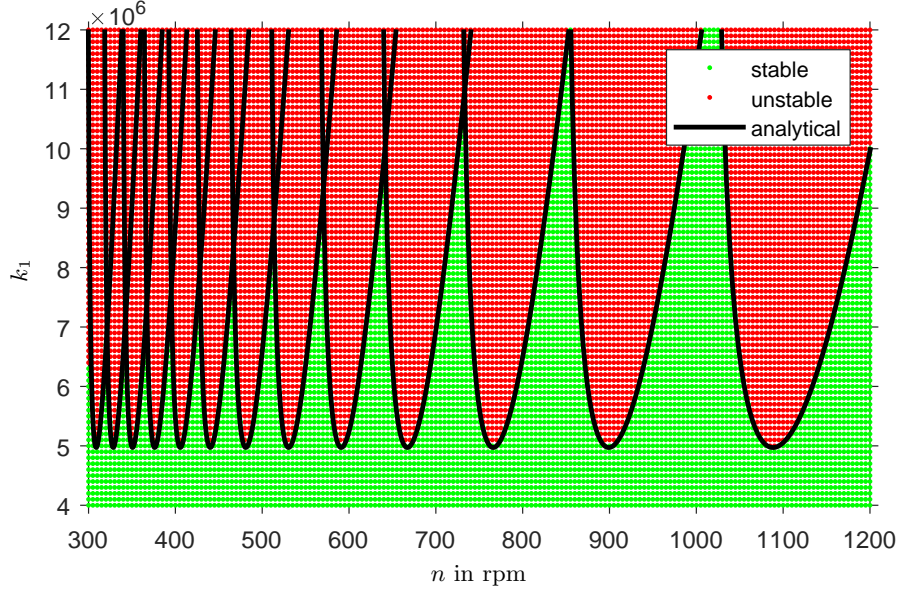
Figure 2. Stability chart for chatter tool with constant support characteristic: direct numerical simulation in comparison with analytical prediction in eq. (7).

or

$$\ddot{x} + 2\zeta\omega_n\dot{x} + \omega_n^2 x = \frac{k_1}{m}\left(x(t-\tau) - x(t)\right) \tag{5}$$

where $\zeta = c/(2\sqrt{km})$ and $k_1 = 3/4\,K_x\,w\,h_0^{-1/4}$ and tilde is omitted. Analytical stability conditions can be derived for predicting the onset of unstable vibrations (instability lobes) as described in more detail in [7]. Inserting the ansatz $x = A\exp(\lambda t)$ yields a complex-valued characteristic equation. Evaluated at $\lambda = i\omega$ gives the stability limit curves

$$-\omega^2 + \omega_n^2 + \frac{k_1}{m}\big(1 - \cos(\omega\tau)\big) = 0, \qquad 2\zeta\omega_n\omega + \frac{k_1}{m}\sin(\omega\tau) = 0 \tag{6}$$

These equations can be transformed to ([7, 5])

$$k_{1,cr} = \frac{m}{2}\frac{(\omega - \omega_n)^2 + (2\zeta\omega_n\omega)^2}{\omega^2 - \omega_n^2}, \qquad n_{cr} = \frac{30\omega}{j\pi - \arctan\!\left(\dfrac{\omega^2 - \omega_n^2}{2\zeta\omega_n\omega}\right)} \quad j = 1, 2, \ldots \tag{7}$$

System parameters for an example system are chosen from [7] and are listed in Table 1. The direct numerical integration of the equations of motion in eq. (4) in the parameter space n-k_1 is shown in Fig. 2. Green dots indicate a stable and red dots an unstable system response. The analytically predicted stability limits in eq. (7) fit perfectly.

symbol	value
m	347 kg
k	$97 \cdot 10^6$ N/m
c	9173 Ns/m

3. Regenerative effect at time-harmonic modulation of the tool stiffness

We add in the system in eq. (4) a time-periodic modulation of the tool support stiffness

$$m\ddot{x}(t) + c\dot{x}(t) + k\big(1 + \varepsilon \sin(\Omega_{PE} t)\big)\, x(t) = k_1\big(x(t-\tau) - x(t)\big) \tag{8}$$

This is a generalisation of the commonly studied delayed differential equation with parametric excitation because we assume that $\Omega_{PE} \neq 60/\tau$, i.e. the frequency of the parametric excitation is *not* a multiple of the spindle speed. A parametric excitation introduces in general a modulation of the system response that leads to side-bands in the frequency spectra, see e.g. [4]. The focus of our investigation lies on the stability boundary in the parameter space, more specifically the distortion of the stability boundary in Fig. 2 by the newly introduced parameters ε and Ω_{PE} in eq. (8). The stability boundaries at $\varepsilon = 5\%$ and $\varepsilon = 10\%$ at an arbitrarily chosen parametric excitation frequency $\Omega_{PE} = 40$ rad/s are shown in Fig. 4. The stability boundaries show a shift towards higher values of k_1 (larger cutting depth) in the vicinity of 570 rpm. The chosen value of Ω_{PE} is indicated by the vertical solid line n_{PE} while the beneficial region lies at n_{opt}.
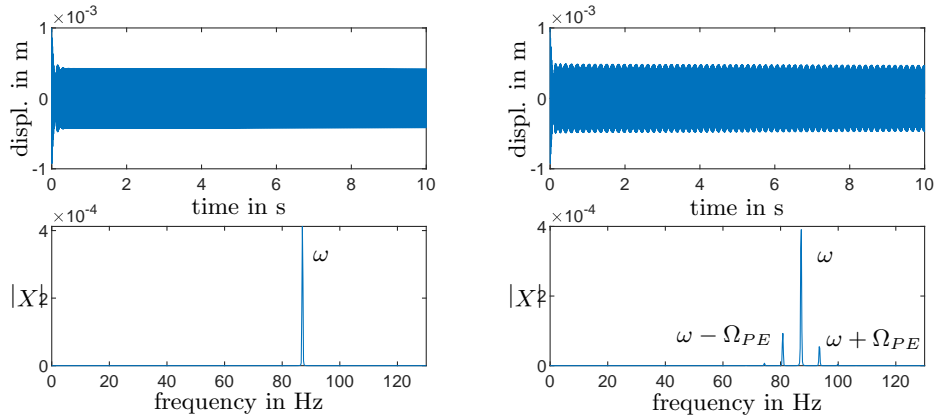
Figure 3. Time histories of chatter tool at 600 rpm at stability boundary: (left) constant tool stiffness ($\varepsilon = 0\%$) at $k_1 = 5.24 \cdot 10^6$ N/m, (right) time-periodic tool support ($\varepsilon = 5\%$) at $k_1 = 5.75 \cdot 10^6$ N/m and $\Omega_{PE} = 40$ rad/s.
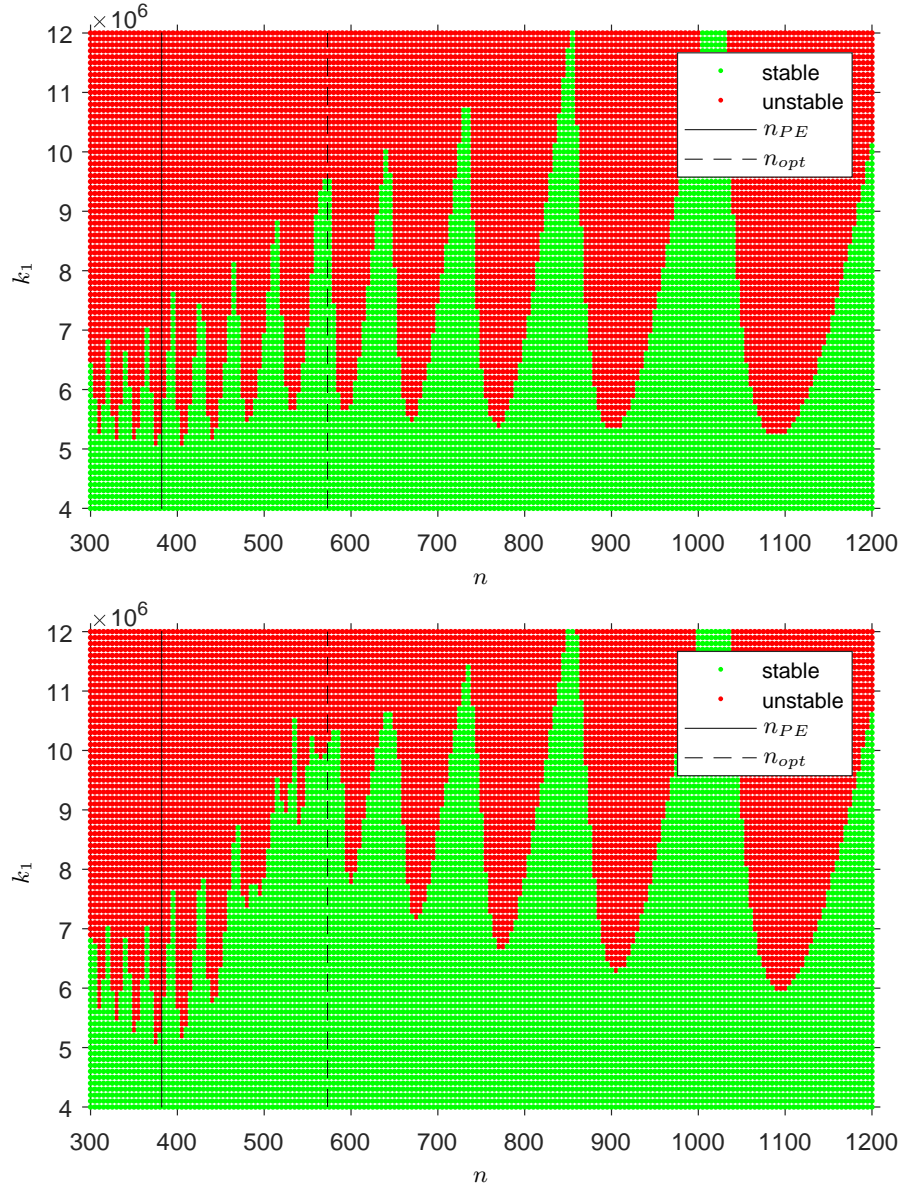
Figure 4. Stability chart for chatter tool with support stiffness modulated at 40 rad/s: (top) $\varepsilon = 5\%$, (bottom) $\varepsilon = 10\%$.

Two exemplary time histories are shown together with their frequency content in the steady-state region in Fig. 3. This comparison confirms the frequency modulation induced by parametric excitation at $\omega \mp \Omega_{PE}$. Increasing the strength of the time-periodicity by increasing ε also leads to sidebands at $\omega \mp j\Omega_{PE}$ for $j = 1, 2, \ldots$. The analytical stability boundary is approximated by applying the method of harmonic balance [8]. The observation above allows for the following ansatz

$$x(t) = c_0 e^{i\omega t} + c_{1p} e^{i(\omega + \Omega_{PE})t} + c_{1m} e^{i(\omega - \Omega_{PE})t} + \text{complex conjugate} + \mathcal{O}(\varepsilon^2) \tag{9}$$

For achieving convergence we assume that c_0 is of order 1 and $c_{1p,1m}$ of order ε. Inserting eq. (9) into eq. (4) and collecting coefficients of the exponential functions $\mp i\omega t$, $\mp i(\omega \mp \Omega_{PE})t$ yields

$$\begin{bmatrix} g(\omega) & \varepsilon k/2 & \varepsilon k/2 \\ \varepsilon k/2 & g(\omega + \Omega_{PE}) & 0 \\ \varepsilon k/2 & 0 & g(\omega - \Omega_{PE}) \end{bmatrix} \begin{bmatrix} c_0 \\ c_{1p} \\ c_{1m} \end{bmatrix} = \mathbf{0} \tag{10}$$

with the abbreviation

$$g(\omega) = k - m\omega^2 + i\omega c + k_1\left(1 - e^{i\omega\tau}\right) \tag{11}$$

An equivalent set of equations is obtained for the complex conjugate coefficients $\overline{c}_i$ which is omitted here. The corresponding characteristic equation for a non-trivial solution in eq. (10) reads

$$4g(\omega)\,g(\omega + \Omega_{PE})\,g(\omega - \Omega_{PE}) - \varepsilon^2 k^2\Big(g(\omega + \Omega_{PE}) + g(\omega - \Omega_{PE})\Big) = 0 \tag{12}$$

The numerical evaluation of this stability boundary matches well with the point-wise numerical time integration of the system in Fig. 4. However, the expressions are cumbersome and further simplifications are needed.

For the numerical values in Table 1 and Fig. 4, the parametric excitation frequency is close to the natural frequency of the system which justifies a Taylor expansion of the form

$$\bar{g}\left(1 \pm \frac{\Omega_{PE}}{\omega}\right) = \bar{g}(1) \pm \left(-2m\omega + i\big(c - k_1 e^{i\omega\tau}\big)\right)\Omega_{PE} + \mathcal{O}\left(\frac{\Omega_{PE}}{\omega}\right) \tag{13}$$

which approximates eq. (12) to

$$g(\omega)^2 - \left(-2m\omega + i\big(c - k_1 e^{i\omega\tau}\big)\right)^2\Omega_{PE}^2 - \varepsilon^2 k^2/2 \approx 0 \tag{14}$$

This equation can be rearranged to a quadratic polynomial in k_1

$$a_2(\omega\tau, \Omega_{PE}^2)\,k_1^2 + a_1(m, c, k, \omega, \tau, \Omega_{PE}^2)\,k_1 + a_0(m, c, k, \omega, \Omega_{PE}^2) - \varepsilon^2 k^2/2 \approx 0 \tag{15}$$

with coefficient functions $a_i(\cdot)$. Evaluation of eq. 15 for the system parameters chosen in Table 1 and $\Omega_{PE} = 40$ rad/s and 570 rpm gives a lower limit of $k_{1,cr} \approx 9 \cdot 10^6$ N/m for both values of ε. This fits well to the stability boundary curves shown in Fig. 4 close to the speed n_{opt}. Finally, the approximate relation in eq. (14) can be evaluated for finding the necessary parametric excitation frequency Ω_{PE} at given system and operation parameters.

4. Conclusions

The mitigation of regenerative chatter using a time-periodic support of the tool was investigated. The model equations and analytical stability limit curves of the classical regenerative chatter model are revisited and extended to a delayed and parametrically excited equation of motion. The frequency of parametric excitation in chatter vibrations is usually assumed to occur at a multiple of the spindle speed, depending on the number of tool teeth. In the present work we deliberately introduce a parametric excitation frequency ω_{PE} which is independent of the tool speed. This first study shows that such a time-modulation is capable of distorting the stability limit curves and creating large regions of larger cutting depths for certain speed intervals. Further investigations are needed for improving the quality of the analytical prediction and for experimental validation of the benefit of the proposed concept.

References

[1] ABELE, E., DOHNAL, F., FEULNER, M., SIELAFF, T., AND DAUME, C. Numerical investigation of chatter suppression via parametric anti-resonance in a motorized spindle unit during milling. *Production Engineering 12* (2018), 309–317.

[2] ALTINTAS, Y. *Manufacturing automation: metal cutting mechancis, machine tool vibrations, and CNC design.* Cambridge university press, 2012.

[3] CAO, H., ZHANG, X., AND CHEN, X. The concept and progress of intelligent spindles: a review. *International Journal of Machine Tools and Manufacture 112* (2017), 21–52.

[4] DOHNAL, F. *A contribution to the mitigation of transient vibrations, Parametric anti-resonance: theory, experiment and interpretation.* Habilitation thesis, Technical University Darmstadt, 2012.

[5] HABIB, G., KERSCHEN, G., AND STEPAN, G. Chatter mitigation using the nonlnear tuned vibration absorber. In *Proceedings of ISMA 2016 - International Conference on Noise and Vibration Engineering and USD2016 - International Conference on Uncertainty in Structural Dynamics* (Leuven, September 2016), D. W. KU Leuven, Ed., pp. 3671–3685.

[6] INSPERGER, T., LEHOTZKY, D., AND STEPAN, G. Regenerative delay, parametric forcing and machine tool chatter: A review. In *Proceedings of 12th IFAC Workshop on Time Delay Systems* (Ann Arbor, MI, USA, June 2015), pp. 322–327.

[7] Stepan, G. Modelling nonlinear regenerative effects in metal cutting. *Philosophical Transactions of the Royal Society of London A: Mathematical, Physical and Engineering Sciences 359* (2001), 739–757.

[8] Thomsen, J. J. *Vibration and Stability: Advanced Theory, Analysis and Toolss*, 2nd ed. Springer-Verlag, 2003.

[9] Tlusty, J., and Spacek, L. *Self-excited vibrations on machine tools (in Czech).* Nakl CSAV, Prague, 1954.

Fadi Dohnal, Professor: UMIT, Division for Mechatronics Lienz, Linker Iselweg 21, 9900 Lienz, Austria (*fadi.dohnal@umit.at*). The author gave a presentation of this paper during one of the conference sessions.

Wolfgang Hörtnagel, M.Sc. (Ph.D. student): UMIT, Division for Mechatronics Lienz, Linker Iselweg 21, 9900 Lienz, Austria (*wolfgang.hoertnagel@umit.at*).

Mariusz Zamojski, M.Sc. (Ph.D. student): UMIT, Division for Mechatronics Lienz, Linker Iselweg 21, 9900 Lienz, Austria (*mariusz.zamojski@umit.at*).

On features of the contact model of an elastic brake shoe with a wheel

Marat Z. Dosaev

Abstract: A mechanical system consisting of a wheel rotating around a fixed point and a brake shoe fixed by a cylindrical joint is considered. The flexibility of the shoe is modeled using a "small" body-platform, attached to the shoe by means of an elastic spring. The shoe is pressed against the wheel using a pusher device located at a point opposite to the cylindrical hinge. A constant torque is applied to the wheel. The contact between the shoe and the wheel occurs with Coulomb friction. Nonlinear equations of motion of the mechanical system are obtained. The linearized dynamic system is a system of variable structure of the 3rd order. The variability of the structure gives the system properties that are characteristic for nonlinear systems. A second-order system describing the rotation of the shoe is separated. In this system, depending on the mode of the motion, there are several special points. A numerical simulation of the dynamic system in the in the neighborhood of singular points has been carried out in order to identify the features of the behavior of a mechanical system. Two characteristic types of motion were found: damping of the oscillations of the shoe after the wheel stopped, and oscillations of the shoe with increasing amplitude and simultaneous "rattling" of the wheel with constant amplitude and frequency. In particular, it is shown that due to dry friction in the presence of torque, the shoe begins oscillating even from the position of static equilibrium.

1. Introduction

The problems of the motion of mechanical systems with dry friction attract the attention of scientists in both fundamental and applied aspects. One of these problems is the contact of a brake pad (shoe) with a wheel. A.I. Neymark and N.V. Fufaev [1] suggested adding an additional viscoelastic element that would model compliance in the vicinity of the contact. In the work [2] V.A. Samsonov considered the model problem of the interaction of a wheel with a brake shoe, in which he discussed possible problems associated with the phenomenon of "shock of friction", and drew attention to such parameter values at which the problem of searching for constrain reactions has an infinite number of solutions. The main conclusions for the paradoxical range of parameters value were confirmed experimentally in [3]. In [4], a nonlinear statement of the problem of the contact of a brake shoe with a wheel at two different points was proposed. For the case of different stiffnesses of modeling springs, conditions are found under which self-oscillations with increasing amplitude are possible.

In this work, in addition to a visco-elastic element simulating material compliance in an area of a contact of a wheel with a brake shoe, an elastic force acts on the shoe from the side of a pusher pressing the shoe against the wheel. It is shown that in the case of a small coefficient of friction, and in the case of a large one, the braking process of the wheel can be nonmonotonic for wide range of other parameters.

2.   Problem statement

Let us consider a mechanical system (Fig. 1) of the wheel B of radius R rotating around the fixed point O_1 and the rectangular brake shoe A of mass m fixed with the cylindrical hinge at point O_2. The brake shoe length is equal $2b$ and width is equal a.
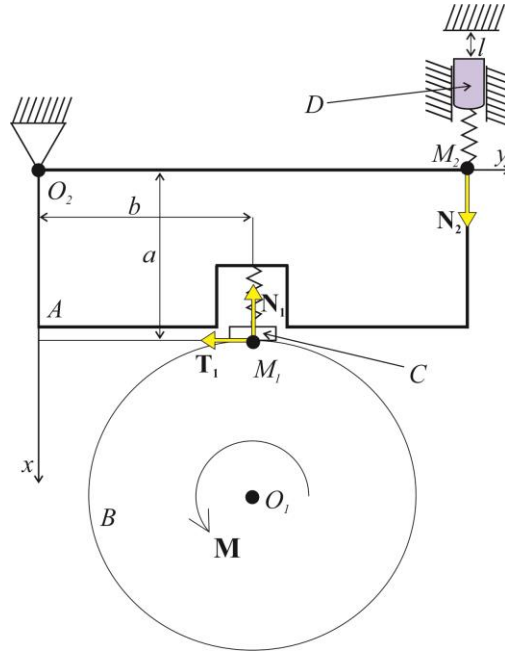
Figure 1. Mechanical system: brake shoe A, wheel B, body-pad C.

We model the flexibility of the brake shoe in the direction normal to its surface. For this purpose, following [1], we place a viscoelastic spring (spring 1), with a sufficiently large stiffness coefficient k_1 and viscosity coefficient h_1, between the brake shoe and the wheel. We attach one end of the spring to the shoe, and to the other end we attach the "small" body-pad C, which can move relative to the shoe along the normal to the contact surface. Body C simulates the inertial properties of the deformed part of the brake shoe. We assume that the brake shoe is pressed against the wheel using a device located at a point opposite to point O_2. To simulate the compliance of the brake shoe in this area, to

the brake shoe in point M_2 we attach another small spring (spring 2) with sufficiently large stiffness coefficient k_2 and viscosity coefficient h_2. The other end of the spring 2 is mounted to the pusher D. The mass and dimensions of the body C, as well as the lengths of the unstrained springs, are negligible. In the process of interaction, brake shoe B turns slightly, but for simplicity we assume that the platform C keeps its orientation. Let us assume that at the moment of contact with the wheel, the spring 1 is in an undeformed state, and the spring 2 is compressed by the distance l. This means that from the side of the spring 2 a certain force constantly acts on the brake shoe. On the contrary, from the side of spring 1, the compression force of the spring acts on the brake shoe only during the contact of body C with the wheel. Thus, a unilateral constraint is superimposed on body C at point M_1. We introduce a fixed coordinate system O_2xyz. The O_2x and O_2y axes are directed along the sides of shoe at the moment of contact, the O_2z axis complements the coordinate system to the right-handed one. The position of the brake shoe is set using the angle φ of rotation of the brake shoe around the hinge O_2. The angle is counted counterclockwise. At the moment when the body C touches the wheel $\varphi = 0$, and this contact is possible only with negative values of the angle φ. The orientation of the wheel is set by the angle ψ of wheel rotation around the hinge O_1. The angle ψ is the cyclic coordinate.

We assume that the torque $\mathbf{M}$ acting upon the wheel B is constant. Let us describe the forces acting on the brake shoe. From the side of the spring 2, the force $\mathbf{N_2}$ acts on the brake shoe. From the side of body C, a force of compressed spring and the lateral reaction $\mathbf{L}$ act on the brake shoe. The interaction between body C and the wheel B is described by the forces of normal pressure $\mathbf{N_1}$ and tangential dry friction $\mathbf{T_1}$, determined according to the Coulomb law with a friction coefficient f. Due to the small mass of the body C (it is in equilibrium), we assume that $\mathbf{L} = \mathbf{T_1}$.

So, three following forces act to the shoe contacting with the wheel:

$$\mathbf{N_1} = -(k_1\Delta l_1 + h_1\dot{\Delta l_1})\mathbf{e_x} = -N_1\mathbf{e_1},$$

$$\mathbf{N_2} = (k_2\Delta l_2 + h_2\dot{\Delta l_2})\mathbf{e_x} = N_2\mathbf{e_1}, \tag{1}$$

$$\mathbf{T_1} = T_1\mathbf{e_y} = \begin{cases} fN_1\mathbf{e_2} & \omega > 0 \\ M/R & \omega = 0 \end{cases},$$

where $\Delta l_1, \Delta l_2$ are the springs deformations, $\dot{\Delta l_1}, \dot{\Delta l_2}$ are the deformation rates of these springs, M is the z-component of the torque $\mathbf{M}$ acting to the wheel, $\omega = \dot{\psi}$ is the angular velocity of the wheel, $\mathbf{e_i}$ $(i = 1,2,3)$ are unit vectors of coordinate system O_2xyz.

3. Dynamic system

We write down the equations of motion using the angular momentum theorem in case of rotation about a fixed axis.

$$J_1\ddot{\varphi} = M_{O_2}(N_1) + M_{O_2}(N_2) + M_{O_2}(T_1),$$
$$J_2\dot{\omega} = M + M_{O_1}(-T_1),$$

(2)

where J_1, J_2 moments of inertia of the shoe and the wheel around axes of their rotation correspondingly, $M_{O_2}(N_1), M_{O_2}(N_2), M_{O_2}(T_1)$ are z-components of the moments $\mathbf{M_{O_2}(N_1)} = \mathbf{O_2M_1} \times \mathbf{N_1}$, $\mathbf{M_{O_2}(N_2)} = \mathbf{O_2M_2} \times \mathbf{N_2}$, $\mathbf{M_{O_2}(T_1)} = \mathbf{O_2M_1} \times \mathbf{T_1}$ of the forces (1) correspondingly, and $M_{O_1}(T_1)$ is the z-component of the torque $\mathbf{M_{O_1}(T_1)} = \mathbf{O_1M_1} \times \mathbf{T_1}$.

We calculate the corresponding values of the moments of forces:

$$\mathbf{M_{O_2}(N_1)} = \begin{pmatrix} \mathbf{e_1} & \mathbf{e_2} & \mathbf{e_3} \\ x_1 & y_1 & 0 \\ -N_1 & 0 & 0 \end{pmatrix} = N_1 y_1 = N_1(a\sin\varphi + b\cos\varphi)\mathbf{e_3},$$

$$\mathbf{M_{O_2}(N_2)} = \begin{pmatrix} \mathbf{e_1} & \mathbf{e_2} & \mathbf{e_3} \\ x_2 & y_2 & 0 \\ N_2 & 0 & 0 \end{pmatrix} = -N_2 y_2 = -2N_2 b\cos\varphi\mathbf{e_3},$$

$$\mathbf{M_{O_2}(T_1)} = \begin{pmatrix} \mathbf{e_1} & \mathbf{e_2} & \mathbf{e_3} \\ x_1 & y_1 & 0 \\ 0 & -T_1 & 0 \end{pmatrix} = -T_1 x_1 \mathbf{e_3} = T_1(-a\cos\varphi + b\sin\varphi)\mathbf{e_3},$$

$$\mathbf{M_{O_1}(-T_1)} = \begin{pmatrix} \mathbf{e_1} & \mathbf{e_2} & \mathbf{e_3} \\ x_1 - a - R & y_1 - b & 0 \\ 0 & T_1 & 0 \end{pmatrix} = T_1(x_1 - a - R)\mathbf{e_3} = T_1(a\cos\varphi - b\sin\varphi - a - R)\mathbf{e_3}$$

where x_1, y_1 are coordinates of vector $\mathbf{O_2M_1}$ and x_2, y_2 are coordinates of vector $\mathbf{O_2M_2}$ in the coordinate system O_2xyz correspondingly.

After linearization of the system (2), assuming that the angle φ and angular velocity $\dot{\varphi}$ are small, for case of rotating wheel we obtain the following dynamic system of variable structure:

$$J_1\ddot{\varphi} = \begin{cases} -b^2(k_1\varphi + h_1\dot{\varphi}) - 2b[k_2(l + 2b\varphi) + 2bh_2\dot{\varphi}] + abf(k_1\varphi + h_1\dot{\varphi}), & \text{if } \varphi < 0 \\ -2b[k_2(l + 2b\varphi) + 2bh_2\dot{\varphi}], & \text{if } \varphi \geq 0 \end{cases}$$
$$J_2\ddot{\psi} = \begin{cases} M + fb(k_1\varphi + h_1\dot{\varphi})R, & \text{if } \varphi < 0 \\ M, & \text{if } \varphi \geq 0 \end{cases}$$

(3)

Note that system (3) does not have an equilibrium position. However, the separable first equation of (3), which describes the motion of the brake shoe, has fixed point. We represent this equation in the

standard form: $\ddot{\varphi} + a_2\dot{\varphi} + a_1\varphi + a_0 = 0$, where summand $a_2\dot{\varphi}$ constitutes the dissipative force, $a_1\varphi$ is the potential force, a_0 is the constant force. If φ does not change its sign, then the solution to this equation can be written as follows:

$$\varphi(t) = C_1 e^{\lambda_1 t} + C_2 e^{\lambda_2 t} - a_0 / a_1; \quad a_1 \neq 0, \lambda_{1,2} \neq 0, \tag{4}$$

Where C_1, C_2 are unknown constants, $\lambda_{1,2}$ are eigenvalues of the homogeneous equation.

4. Contact with rotating wheel

Consider the range of values $\varphi < 0$, body C touches the rotating wheel. In this case:

$$\varphi(t) \equiv \varphi^* = -a_0 / a_1, \tag{5}$$

is a fixed point of the first equation of (3). If the friction is low $af \leq b$ then $a_1 > 0$, $a_2 > 0$. The elastic potential force limits the motion of the brake shoe, the presence of dissipation leads to the damping of the resulting oscillations. For the great enough friction: $f > b(k_1 + 4k_2)/(ak_1)$, the coefficient a_1 becomes negative, and the elastic force becomes repulsive. For $f > b(h_1 + 4h_2)/(ah_1)$ the coefficient a_2 is negative, that leading to antidissipation. For the sake of simplicity we consider the case of elastic springs without viscosity $h_1 = h_2 = 0$. Then $a_2 = 0$.

System (3) takes the form:

$$J_1\ddot{\varphi} = -b^2 k_1\varphi - 2bk_2(l + 2b\varphi) + abfk_1\varphi$$
$$J_2\ddot{\psi} = M + fbk_1\varphi R \tag{6}$$

The eigenvalues of the first of equations (6) are

$$\lambda_{1,2} = \pm\sqrt{-a_1} = \pm\sqrt{-b(k_1(b - af) + 4bk_2)/J}. \tag{7}$$

For small friction, when $af \leq b$, the radical expression in (7) is negative, and the eigenvalues are conjugate purely imaginary values. Solution (4) is oscillations around a fixed point (5) with the period $T = 2\pi / \sqrt{b(k_1(b - af) + 4bk_2)/J_1}$. Consider the simplest case of equal spring stiffnesses: $k_1 = k_2 = k$. Then equations (6) take the following form:

$$J_1\ddot{\varphi} = bk(-2l + (af - 5b)\varphi)$$
$$J_2\dot{\omega} = M + fbkR\varphi \tag{8}$$

As mentioned above, the first equation (8) has the fixed point; expression (5) for this point can be simplified:

$$\varphi(t) \equiv \varphi^* = 2l / (af - 5b). \tag{9}$$

The purely imaginary eigenvalues (7) are also simplified: $\lambda_{1,2} = \pm\sqrt{-bk(5b - af) / J_1} = \pm\omega_1 i.$ The solution of the first equation (8) looks like following:

$$\varphi(t) = C_1 \sin(\omega_1 t) + C_2 \cos(\omega_1 t) - 2l / (5b - af), \tag{10}$$

$C_1 = \dot{\varphi}_0 / \omega_1, C_2 = \varphi_0 + 2l / (5b - af) = \varphi_0 - \varphi^*.$

We substitute the solution (10) into the second equation of (8) and obtain a linear inhomogeneous equation. Let the shoe be stationary at the initial moment of time and $\omega(0) = \omega_0$. The solution of the second equation of (8) is following:

$$\omega(t) = \frac{fbkR}{J_2\omega_1} C_2 \sin(\omega_1 t) + \frac{t}{J_2}(M - \frac{2lfbkR}{5b - af}) + \omega_0 \tag{11}$$

If the brake shoe is close to its equilibrium position, then the first term of the right-hand side of (11) is small, and the sign of the right-hand side of (11) depends on its second term.

5. Nonmonotonic process of braking of the wheel

For simplicity, we assume that the brake shoe is in equilibrium $\varphi = \varphi^*$. The angular speed of the wheel will decrease only if the condition is met: $M < \dfrac{2lfbkR}{5b - af}$. Let this condition be met and see how the shoe will move henceforth. Some time later, the wheel will stop. At this moment, the friction will instantly change, and became to be equal M/aR. The equilibrium position of the shoe will also change: $\varphi(t) \equiv \varphi^{**} = (-Ma / R - 2bkl)\big/(5b^2 k)$. It can be shown that $\varphi^{**} - \varphi^* > 0$. The shoe will move to its new equilibrium position, that is, it will begin to move away from body C. The shoe speed will grow and shoe will slip the new equilibrium position $\varphi = \varphi^{**}$. The contact of body C with the wheel is unlikely to be lost. When angle φ reach value $\varphi = \varphi_1 = -M / (fbkR)$, the friction will no longer hold the wheel, and under the influence of the torque **M**, the angular velocity of the wheel will begin to increase. A sliding motion will start. So, the balance position of the shoe will again change. The brake shoe will begin to press against the body C and the wheel. After some time, the wheel braking process will begin again. Since the gained angular velocity of the wheel may not be large enough, the shoe may not reach its equilibrium position, when the wheel stops again and the balance position of

the shoe changes again. Thus, even with low friction, the braking of the wheel can be nonmonotonic. The example of numerical calculation of dynamic system presenting such nonmonotonic behavior is shown in Fig.2. The left hand side of Fig. 2 presents the phase plane for angle φ. The right hand side of Fig. 2 shows time-dependence of the angular speed of the wheel. Initial conditions for calculations are following: $\varphi(0) = 0, \dot{\varphi}(0) = 0, \omega(0) = 1$.
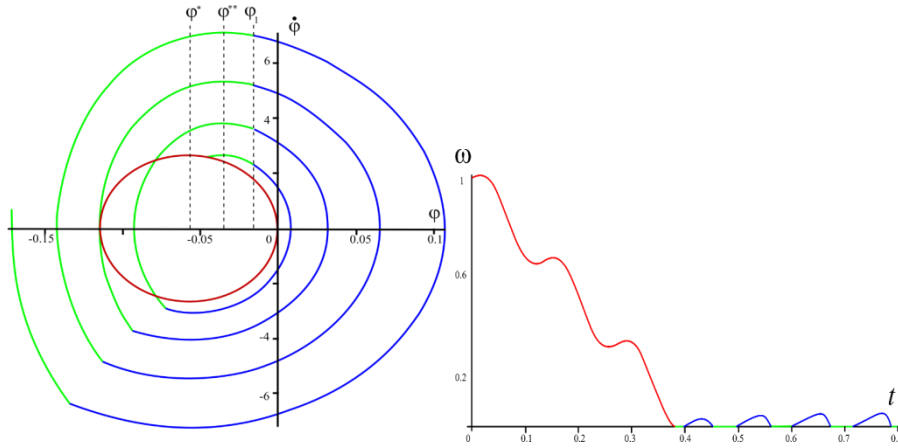
Figure 2. Calculation of trajectory of dynamic system.

In the first stage of motion, the shoe start oscillations around the balance position $\varphi = \varphi^*$, the wheel angular speed decreased (the red curves). When the wheel stops (green curves), the shoe starts to move around the balance position $\varphi = \varphi^{**}$. After some time, when the angle φ reach the value $\varphi = \varphi_1$, the wheel starts rotation (blue curves), but due to increasing friction stops again. The amplitude of such "wrenching" motion of the wheel increases.

6. Conclusions

We have shown that even with low friction, the braking of the wheel can be nonmonotonic. In describing this process, we assumed that at its beginning the brake shoe was in its equilibrium position for the case of the moving wheel. If we took into account the natural vibrations of the brake shoe, the braking process would be even more nonmonotonic. With a certain selection of parameters, the existence of cyclic trajectories of the system is possible.

Note that similar cyclic processes are possible with high friction. As pointed out by S.S. Grigoryan in [5], when the pressure between the brake shoe and the wheel reaches a certain sufficiently large critical value, the friction coefficient can decrease sharply. In this case, the shoe "bounces" from the wheel. During the time until the shoe comes into contact with the wheel, on the

one hand, the wheel will acquire some speed and will accelerate until the next contact, on the other hand, the contact of the wheel and the brake shoe will begin with low pressure, and the friction coefficient will be restored.

Acknowledgments

References

[1] Neimark, Y.I., Fufaev, N.A.: The Painlevé paradoxes and the dynamics of a brake shoe. *J. Appl. Math. Mech.* 59, 3 (1995), 343-352.

[2] Samsonov, V. A. The dynamics of a brake shoe and "impact generated by friction". *J. of Appl. Math. Mech.* 69, 6 (2005), 816–824.

[3] Ivanova, T.B., Erdakova, N.N., Karavaev, Y.L. Experimental investigation of the dynamics of a brake shoe. *Dokl. Phys*. 61, 12 (2016), 611-614. https://doi.org/10.1134/S1028335816120028

[4] Dosaev, M.Z. On Instability of a Brake Shoe *Proceedings of the 14th IFToMM World Congress*. (2015). 93-96. DOI：http://dx.doi.org/10.6567/IFToMM.14TH.WC.OS4.015

[5] Grigoryan, S.S. The solution to the Painleve paradox for dry friction. *Dokl. Phys.* 46, 7 (2001), 499-503. https://doi.org/10.1134/1.1390406

Marat Z. Dosaev, Leading Researcher: Lomonosov Moscow State University, Institute of Mechanics, 1, Michurinskiy Pr-t, Moscow, 119192, Russian Federation (*dosayev@imec.msu.ru*).

Friction coefficient estimating in problem of planar motion of a friction-powered robot

Marat Z. Dosaev, Vitaly A. Samsonov, Shyh-Shin Hwang

Abstract: The design of the robot, driven by friction against the surface of the support and displacement of internal masses, is considered. The robot has one unbalanced rotor and one flywheel. A mathematical model of its plane-parallel motion is constructed. Friction is modeled using Coulomb's law. Angular accelerations of rotating structural elements are selected as control functions. To implement the forward translational motion of the robot, it is necessary to know the coefficient of friction of the body against the surface of the support. An algorithm for estimating this coefficient is proposed.

1.   Introduction

In recent years, there has been growing interest in the development of new types of robotic devices that are driven by internal masses and internal forces. The applications of such a system are quite widespread, such as the use of the robot in hard-to-reach places, in aggressive environments, in various types of pipes; the use of microrobots in medicine for accurate diagnosis or drug delivery directly to the treatment site inside the body, etc.

Chernousko ([1-3]) made a significant contribution to the study of vibration robots. In particular, together with Shmatkov [4] he recently considered the two-dimensional problem on the fastest turn of a rigid body by moving an internal mass. To determine unknown variables, they proposed numerical calculation of two nonlinear scalar equations based on boundary conditions.

The dynamics of a two-link robot with unbalanced vibration exciters was considered in [5]. For the case of small friction the averaging method was used. The three-linked robot was analyzed in [6]. It was noticed that the phase shifts among the internal excitations play a significant role in the appearance of stick–slip motions.

Another interesting object that uses friction to move is a ball-robot. Many different versions of ball-robot designs are proposed (for example, [7-9]). A spherical robot with an axisymmetric pendulum actuator on an inclined plane is considered in [9]. It is shown that the steady solutions exist only at an inclination angle less than some critical value and only for constant control action.

Rotation of the body with internal masses on a rough plane was considered in [10]. Cases of a hard horizontal disk and two material points as internal movable masses are analyzed.

A vibration-driven system, which consists of a rigid body with an internal mass that uniformly circular moving inside the body, was considered in [11]. It was shown that there always exists a periodic mode of motion.

In [12], a robot design with one unbalanced rotor was considered for accelerated angular motion of the rotor. A method for constructing a control algorithm was proposed, which ensures the straight-line motion of the robot on a rough surface.

A vibration robot with two unbalanced rotors was considered in [13]. Trajectories of the center of mass of the robot obtained numerically using various ratios of angular velocities.

In [14], a design of an inertial robot with one unbalanced rotor and one flywheel was proposed. The plane mathematical model of the mechanical system was constructed. A control algorithm was developed, at which the body moves in a given direction.

This work continues the paper [14]. We assume that dry friction acts between rectangular body and rough horizontal plane. We model friction using Coulomb's law. To organize a motion of the body to needed direction it is necessary to know a coefficient of friction. An algorithm for estimating the friction coefficient is proposed.

2. Problem statement

We consider the mechanical system consisting of three links: the rectangular robot body 1 itself, the uniform round cylinder 2 (flywheel), and the crank 3 (Fig. 1).
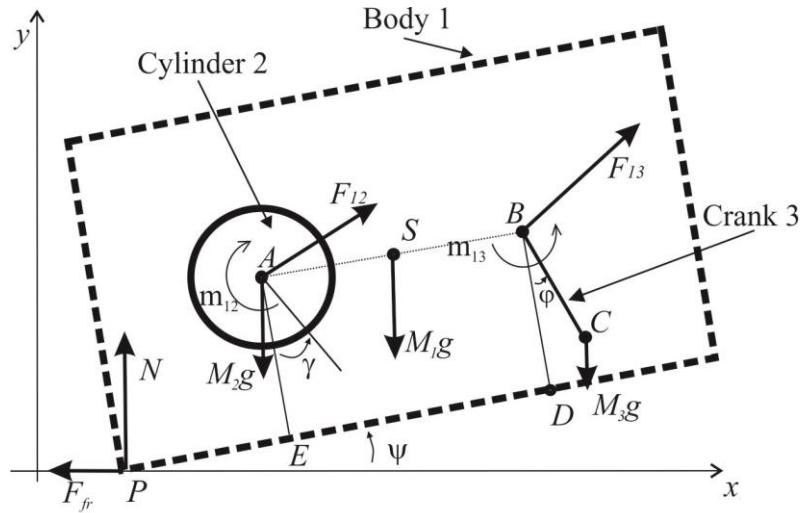
Figure 1. Mechanical system. External and internal forces.

The boundaries of body 1 in Fig. 1 are shown by a dashed line. The cylinder is driven by the motor around point *A*. The rod (crank) *BC* of length *r* rotates by another motor around point *B*. Consider that the body can perform a plane-parallel motion along a rough supporting surface.

The body slides on a horizontal plane, touching it with its rear edge (point *P*). The point *S* is the center of mass of the body 1. For simplicity, we assume that the mass of the rod is concentrated at point *C*. Other geometrical parameters are as follows: $PE = a$, $AE = BD = b$, $AS = SB = c$.

We consider the following external forces acting on the system: the gravity forces of each element of the system: $M_1\vec{g}$, $M_2\vec{g}$, $M_3\vec{g}$, as well as the normal reaction force $\vec{N}$ of the support and the friction force $\vec{F}_{fr}$. Here $M_i, (i = 1,2,3)$ are masses of the body 1, flywheel 2 and crank 3 correspondingly, $\vec{g}$ is the gravity acceleration. The reaction force $\vec{N}$ and the friction force $\vec{F}_{fr}$ are applied to the body at point P, with the exception of the case when the lower edge of the body is in full contact with the reference plane. In this case, the point of application of the reactions is unknown.

Let us describe the internal forces acting between the elements of the system:

1. The motor torque $\vec{m}_{12}$ acts from the body on the flywheel 2. Accordingly, the torque $\vec{m}_{21} = -\vec{m}_{12}$ acts from the flywheel on the body.

2. The motor torque $\vec{m}_{13}$ acts from the body on the rod *BC*. Accordingly, the torque $\vec{m}_{31} = -\vec{m}_{13}$ acts from the rod upon the body.

3. Reaction force $\vec{F}_{12} = -\vec{F}_{21}$ acts from the body to the flywheel. Hereinafter it is indicated $\vec{F}_{ij}$ is the force with which the *i*-th body acts on the *j*-th body.

4. The reaction force $\vec{F}_{13} = -\vec{F}_{31}$ acts from the body 1 to the rod 3.

The mechanical system has 4 degrees of freedom. The system position is set by the following four coordinates: the cyclic coordinate *x* sets the position of the contact point *P* between the body and the supporting surface; ψ is the angle between the horizontal and the lower edge of the body; γ is the cyclic angle of the rotation of the flywheel around point *A*; φ is the angle between the straight line *BD* fixed in the body and the rod *BC*. The velocity $\vec{V}_P$ of the contact point *P* is horizontal. $V_P = \dot{x}$

3. Dynamic system

The system of equations describing the behavior of the mechanical system in consideration can be obtained from the theorem of the center of mass motion and the angular momentum theorem. In the dimensionless form, for the case $\dot{\psi} = \ddot{\psi} = 0$ the dynamic system looks as follows:

$$(1+m_{20}+m_{30})x_0'' = -F_{fr0} - m_{30}r_0(\varphi''\cos\varphi - \varphi'^2\sin\varphi)$$

$$1+m_{20}+m_{30} = N_0 - m_{30}r_0(\varphi''\sin\varphi + \varphi'^2\cos\varphi)$$

$$m_{30}r_0\cos\varphi x_0'' = m_{30}r_0\varphi''(-r_0 - c_0\sin\varphi) - m_{30}r_0\sin\varphi - $$

$$-J_{20}\gamma'' + c_0(m_{20} - m_{30} - m_{30}r_0\cos\varphi) - N_0 x_{NR0} - \mu b_0 N_0$$

$$\tag{1}$$

Here: $m_{20} = M_2/M_1, m_{30} = M_2/M_1$, $b_0 = b/a, c_0 = c/a, r_0 = r/a$, $J_0 = J_2/(m_1 a^2)$ is the dimensionless moment of inertia of the flywheel, $N_0 = N t^{*2}/(m_1 a)$ and $F_{fr0} = F_{fr}t^{*2}/(m_1 a)$ are the dimensionless normal reaction and the dimensionless friction correspondingly, t^* is the characteristic time, $x_{NR0} = x_{NR}/a$, $x_{NR} \leq a + c$ is the unknown arm of the normal reaction, μ is the friction coefficient between body and supporting plane. The prime means differentiation by dimensionless time $\tau = t/\sqrt{a/g}$.

4. Determination of the coefficient of friction between the plane and the body.

To evaluate the coefficient of friction, we place an accelerometer measuring horizontal acceleration on the robot body. We fix the cylinder $\dot\gamma \equiv \ddot\gamma \equiv 0$. Consider the following motion:

In the initial position, the body is at rest, the crank is at rest in the lower position. To start the motion we set maximum angular acceleration to the crank. Since when the crank moves up, the body will be pressed harder to the surface, then the vertical motion of the body will not occur. On the other hand, if there were no friction, then the body would immediately begin to move horizontally, maintaining the position of the center of mass of the system. We assume that the angular acceleration of the crank is sufficient to overcome the friction, the body begins to move.

The equations of this motion can be obtained from the theorem on the motion of the center of mass of a mechanical system:

$$\begin{cases} M_1\ddot{x}_S + M_2\ddot{x}_A + M_3\ddot{x}_C = (M_1+M_2+M_3)\ddot{x} + M_3 r(\ddot\varphi\cos\varphi - \dot\varphi^2\sin\varphi) = -F_{fr} \\ M_1\ddot{y}_S + M_2\ddot{y}_A + M_3\ddot{y}_C = M_3 r(\ddot\varphi\sin\varphi - \dot\varphi^2\cos\varphi) = N - (M_1+M_2+M_3)g \end{cases}$$

$$\tag{2}$$

From the second equation of (2) we can determine the normal reaction. At the moment when the body begins to move, we use the accelerometer to measure its acceleration. Then the coefficient of friction can be obtained from the following formula:

$$\mu = -\left[(M_1+M_2+M_3)\ddot{x} + M_3 r(\ddot\varphi\cos\varphi - \dot\varphi^2\sin\varphi)\right]/N .$$

$$\tag{3}$$

To clarify this coefficient, we carry out such a process several times. As an estimate, we take the average value of the obtained friction coefficients. Knowing the friction coefficient it is possible to construct a control algorithm that provides a plane-parallel motion of body in the given direction.

5. Realization of the control algorithm

Let us construct the trajectory of the mechanical system along which the body will translationally move along the plane in a given direction. The trajectory can be obtained by numerical simulation. The example of such trajectory is presented by blue curve on the phase plane as dependence of angular speed φ' on the angle φ (Fig. 2). Parameters for the calculation were chosen as follows:

$m_{20} = 0.2;\ m_{30} = 0.2;\ r_0 = 1; c_0 = 1; b_0 = 1; \mu = 1.$

We assume that the angular acceleration γ'' can be set in such a way that the third equation of (1) holds for different values of other variables. To prevent rotation of the body, we also control the following inequality: $x_{NR0} \leq 1 + c_0$. Under these conditions, the first two equations of the system (1) are separated. Below we will consider only these two equations. To satisfy the condition $N = 0$, from the second equation of (1) we obtain the following equation:

$$\varphi'' \sin \varphi + \varphi'^2 \cos \varphi = \frac{-(1 + m_{20} + m_{30})}{m_{30} r_0} . \tag{4}$$
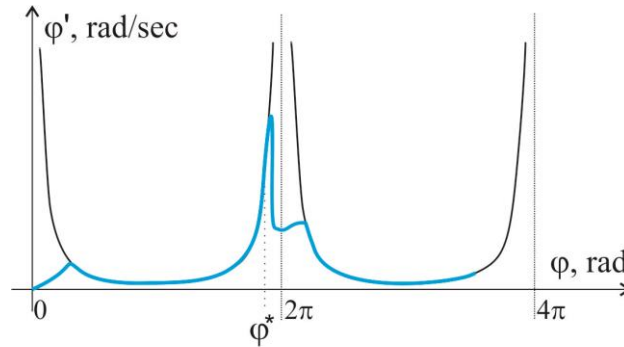
Figure 2. Phase trajectory of the angle φ providing the translational motion of the body.

The solution of the equation (4) looks as following:

$$\varphi = \arccos(-1 + \frac{1 + m_{20} + m_{30}}{2 m_{30} r_0} t^2), \varphi' = \frac{\sqrt{2(1 + m_{20} + m_{30})(1 + \cos \varphi)}}{\sqrt{m_{30} r_0} \left| \sin \varphi \right|} . \tag{5}$$

This dependence is shown by black solid curves in the Fig. 2.

In the initial position, the body is at rest, the crank is at rest in the lower position. To start the motion we set crank angular acceleration such a way that after some time angle φ and angular speed φ' satisfy the second expression of (5). Then the rotation of the crank is such that the relation (5) is satisfied, that is, the condition $N = 0$ is met. During these two stages the body continues to be at rest.

When the angle φ reaches some value $\varphi = \varphi^*, \varphi^* < 2\pi$. At the moment we "switch" the angular acceleration of the rod. In example shown if Fig. 2 we change the sign of the angular acceleration to the opposite and increase its absolute value. The reaction ceases to be equal to zero, and the body starts moving in the desired direction. The angular speed φ' decreases rapidly. When φ' decreases more than two times, we switch off the angular acceleration: $\varphi'' = 0$. The angle φ continue increasing and still approaching value $\varphi = 2\pi$. At the same time the speed of the body decreases, and the body stops.

During next stage the body is motionless again. To ensure this immobility, the friction force must be less than the sliding friction force, that is, the following inequality must be satisfied:

$$|F_{fr0}| < \mu N_0. \tag{5}$$

The friction force value F_{fr0} and the support reaction N can be obtained from the first two equations of (1):

$$F_{fr0} = m_{30} r_0 (\varphi'' \cos\varphi - \varphi'^2 \sin\varphi)$$
$$N_0 = m_{30} r_0 (\varphi'' \sin\varphi + \varphi'^2 \cos\varphi) + (1 + m_{20} + m_{30})$$

We wait for the moment, when $\varphi = 2\pi$, and then "turn on" the angular acceleration of the rod again. In example presented in Fig. 2 we set the angular acceleration φ'' linearly dependent on time. Such mode of acceleration increase is enough to provide needed values of the angle φ and the rod angular velocity φ' satisfying the curve (5). Checking condition (9), we control that during the process the speed of the body is zero. Later the trajectory passes along the curve (8). After some time the angle φ becomes equal to φ^*, and the system comes to the state that is identical to the initial conditions of the previous stage.

6. Conclusions

The design of the inertial robot containing one unbalanced rotor and one flywheel is considered. A mathematical model of its plane-parallel motion is constructed. Angular accelerations of rotating structural links are used as control functions. The procedure is proposed for estimating the friction coefficient between the robot body and the supporting plane. The control algorithm for providing the motion of the robot body in needed direction is proposed using obtained friction coefficient value. The numerical calculation was realized. For chosen set of parameters the forward translational motion of the body is realized.

Acknowledgments

References

[1] Chernous'ko F.L., Optimal motion of a Two-Body System in a Resistive Medium. *J. Optim. Theory Appl.* 147, 2 (2010), 278-297.

[2] Chernous'ko F.L., Bolotnik N.N., Figurina T.Yu. Optimal Control of Vibrationally Excited Locomotion Systems. *Regul. Chaotic Dyn.* 18, 1-2 (2013), 85-99

[3] Chernous'ko F.L., Optimal Control of the Motion of a Two-Mass System. *Doklady Mathematics* 97, 3 (2018), 295-299 .

[4] Chernousko, F. L., Shmatkov, A. M. Optimal Control of Rotation of a Rigid Body by a Movable Internal Mass. *Journal of Computer and Systems Sciences International* 58, 3 (2019), 335-348. · DOI: 10.1134/S1064230719030067

[5] Zimmermann, K., Zeidis, I., Bolotnik, N., Pivovarov, M. Dynamics of a Two-Module Vibration Driven System Moving Along a Rough Horizontal Plane. *Multibody Sys. Dynamics.* 22, 1 (2009), 199-219 .

[6] Fang, H.B., and Xu, J. Dynamics of a Three-Module Vibration-Driven System with Non-Symmetric Coulomb's Dry Friction. *Multibody Syst. Dyn.* 27, 4 (2012), 455-485.

[7] Zheng, M., Zhan, Q., Liu, J., Cai, Y. Control of a spherical robot: Path following based on nonholonomic kinematics and dynamics. *Chinese Journal of Aeronautics.* 24, 3 (2011), 337-345.

[8] Ivanov, A.P. On The Control of a Robot Ball Using Two Omniwheels. *Regular and Chaotic Dynamics.* 20, 4 (2015). 441-448.

[9] Ivanova, T.B., Kilin, A.A., Pivovarova, E.N. Controlled Motion of a Spherical Robot of Pendulum Type on an Inclined Plane *Dokl. Phys.* 63, 7 (2018), 302-307. https://doi.org/10.1134/S1028335818070091.

[10] Lupekhina, I.V., Bezmen, P.A., Yatsun, C.F. Plane-parallel Motion of a Vibration Robot on a Horizontal Rough Surface. *Natural and Tech. Sciences*. 4, 60 (2012), 41-44.

[11] Sakharov, A.V. Rotation of the body with movable internal masses around the center of mass on a rough plane. *Regular and Chaotic Dynamics* 20, 4 (2015), 428-440. DOI: 10.1134/S15603547715040024

[12] Bardin, B. S., Panev, A. S. On the Motion of a Body with a Moving Internal Mass on a Rough Horizontal Plane. *Russian Journal of Nonlinear Dynamics* 14, 4 (2018), 519–542.

[13] Golitsyna, M.V.: Periodic Mode of Motion of the Vibration Robot with a Control Constraint. Appl. Math. and Mech. 1, 627-636 (2018) (in Russian)

[14] Dosaev, M., Samsonov, V., Holub, A. Plane-Parallel Motion of a Friction-Powered Robot Moving Along a Rough Horizontal Plane. *Advances in Mechanism and Machine Science. IFToMM WC 2019. Mechanisms and Machine Science*, 73 Springer, Cham, 2019

Marat Z. Dosaev, Leading Researcher: Lomonosov Moscow State University, Institute of Mechanics, 1, Michurinskiy Pr-t, Moscow, 119192, Russian Federation (*dosayev@imec.msu.ru*).

Vitaly A. Samsonov, Principle Researcher: Lomonosov Moscow State University, Institute of Mechanics, 1, Michurinskiy Pr-t, Moscow, 119192, Russian Federation (*samson@imec.msu.ru*).

Shyh-Shin Hwang, Professor: Chien Hsin University of Science and Technology, Department of Mechanical Engineering, 229 Chien-Hsin Rd., Jhong-Li District, Taoyuan County, 32097, Taiwan (*stanhwang@uch.edu.tw*).

Condition evaluation of components of multi-parametric space determining the evolution of carcinogenesis in biological systems

Larysa Dzyubak, Oleksandr Dzyubak, Jan Awrejcewicz

Abstract: The multi-parametric space 'number of tumor cells – tumor cell volume – glucose level – diffusion saturation level' and its corresponding 3D initial state space components were studied. It was shown that the choice of parameter sets from this space controls the carcinogenesis in biological systems. The model describing interactions of the tumor cells, matrix-metalloproteinases, matrix-degradative enzymes and oxygen was used to simulate the nonlinear multi-scale cancer invasion. The technique based on wandering trajectories analysis was applied to quantify chaotic cancerous attractors in the studied model. Presented are the results of evaluation of conditions in all control parameter planes as well as the modes to inhibit and/or stabilize carcinogenesis.

1. Introduction

This work is a continuation of the study presented in [1] where, based on the performed analysis of the mathematical model describing the tumor development in a biological system, the parameter sets resulting in occurring cancer chaotic attractors have been found in control parameter plane 'number of tumor cells versus diffusion saturation level'. Also it was ascertained a significant influence of the biological system initial state to carcinogenesis and it was illustrated by regions in phase planes of initial conditions. The obtained resluts allowed under definite conditions a controlling and stabilizing unpredictable behavior of metabolic reactions and suppressing carcinogenesis.

It should be noted, that the contradictions found in the recent literature (it is reported, for instance, in [2]) concerning to an influence of glucose level and oxygen concentration on carcinogenesis can be explained *not only* by fact that in those studies the initial state of the biological system was not taking into account, but also that a mutual influence of *all* components of the multy-parametric space of the models studied was not taking into account. In the present work a significant and complex mutual influence of all components of the multy-parametric space 'number of tumor cells – tumor cell volume – glucose level – diffusion saturation level' as well as of the 3D initial state space components on inhibition/amplification of carcinogenesis in biological systems was ascertained. The evolution of conditions conducive to cancer invasion was defined depending on parameters of the multy-parametric space.

2. Mathematical model

Cancer is generally defined as a malignant tissue growth resulting from an uncontrolled division of cells [3]. In the model studied in this work, the tumor development is governed by the inhomogeneous dissipative set of differential equations [4–7, 2]:

$$\dot{n} = 0, \tag{1}$$

$$\dot{f} = \alpha \eta (m - f), \tag{2}$$

$$\dot{m} = \beta \kappa n + f(\gamma - c) - m, \tag{3}$$

$$\dot{c} = \nu f m - \omega n - \delta \phi c, \tag{4}$$

where n denotes the tumor cell density, f is the matrix–metalloproteinases (MM) concentration, m corresponds to the matrix-degradative enzymes (MDE) concentration, and c denotes the oxygen concentration. Parameters α is a tumor cell volume, β – glucose level, γ – number of tumor cells, δ – diffusion saturation level; η and κ are coefficient that characterise the growth and decay of MM and MDE concentration respectively; υ , ω, φ are parameters that govern growth and decay of the oxygen concentration.

The model (Eqs. 1–4) possesses three chemical equilibria

$$m^e_{1,2,3} = f^e_{1,2,3} = A + B, -\frac{A+B}{2} \pm \frac{A-B}{2}\sqrt{-3}, \tag{5}$$

$$c^e_{1,2,3} = \frac{1}{\delta \phi}\left(\nu \left(f^e_{1,2,3}\right)^2 - \omega n\right), \tag{6}$$

$$A = \sqrt[3]{-\frac{q}{2} + \sqrt{\frac{q^2}{4} + \frac{p^3}{27}}}, B = \sqrt[3]{-\frac{q}{2} - \sqrt{\frac{q^2}{4} + \frac{p^3}{27}}}, \tag{7}$$

$$p = \frac{\delta \phi}{\nu}(1 - \gamma - \omega n), q = \frac{\delta \phi}{\nu}\beta \kappa n. \tag{8}$$

As mentioned in [8] pertaining to the self-organizing chemical systems: as soon as the product is also a part of the same chemical reaction, the system can express unstable behaviour which can be controlled by the reaction parameters. Depending on control parameter values and initial conditions, the considered biological cancerous cell system can also approach different states: a) stationary equilibrium state where any changes are damped; b) stable periodic chemical process or so called 'chemical clock' (a limit cycle); c) state of chemical instability with chaotic behaviour of MM, MDE and oxygen concentrations.

3. Numerical results

Cancer chaotic attractors exist within certain parameter ranges of mathematical model (Eqs. 1–4) describing the tumor development in a biological system. In this section multy-parametric space

'number of tumor cells – tumor cell volume – glucose level – diffusion saturation level' is studied. To quantify conditions for carcinogenesis the technique based on the wandering trajectories analysis [9, 10, 1] was applied.

After a discretisation of the multy-parametric space, the governing equations (Eqs. 1–4) are twice solved numerically with two nearby initial conditions. Initial conditions of the nearby trajectories are distinguished by 0.5 percent with ratio to the characteristic vibration amplitudes A_f, A_m, A_c defined as follows

$$A_f = \frac{1}{2}\left| \max_{t_1 \leqslant t \leqslant T} f(t) - \min_{t_1 \leqslant t \leqslant T} f(t) \right| , \tag{5}$$

$$A_m = \frac{1}{2}\left| \max_{t_1 \leqslant t \leqslant T} m(t) - \min_{t_1 \leqslant t \leqslant T} m(t) \right| , \tag{6}$$

$$A_c = \frac{1}{2}\left| \max_{t_1 \leqslant t \leqslant T} c(t) - \min_{t_1 \leqslant t \leqslant T} c(t) \right| , \tag{7}$$

e.g. the starting points of these trajectories are in the three-dimensional parallelepiped

$$\left| f(t_0) - \widetilde{f}(t_0) \right| < 0.005\, A_f \tag{8}$$
$$\left| m(t_0) - \widetilde{m}(t_0) \right| < 0.005\, A_m \tag{9}$$
$$\left| c(t_0) - \widetilde{c}(t_0) \right| < 0.005\, A_c. \tag{10}$$

Characteristic vibration amplitudes A_f, A_m, A_c are calculated for all nodal points of the multy-parametric space simultaneously with integration of the governing equations (Eqs. 1–4). After integration of the governing equations (Eqs. 1–4), the condition

$$\exists t^* \in [t_1, T]: \quad \{(\left| f(t^*) - \widetilde{f}(t^*) \right| > \alpha A_f) \vee (\left| m(t^*) - \widetilde{m}(t^*) \right| > \alpha A_m) \vee (\left| c(t^*) - \widetilde{c}(t^*) \right| > \alpha A_c)\} \tag{11}$$

was verified. Here T is the time period for the simulation; $[t_0, t_1]$ is the time interval, where transient processes are damped. The manifold of the nodal points of the multy-parametric space, for which the inequality (Eq. 11) is satisfied, resulting in setting up the regions of chaos.

An evolution of the chaotic regions in the control parameter plane 'tumor cell volume vs glucose level' ($\beta \kappa n$, $\alpha \eta$), ($0 \leqslant \beta \kappa n \leqslant 300$, $0 \leqslant \alpha \eta \leqslant 10$), depending on magnitude of diffusion saturation level $\delta\varphi = 0.5$, $\delta\varphi = 1.0$ and $\delta\varphi = 2.0$ for the model (Eqs. 1–4) is observed in Fig. 1 (a), (b), (c). Other parameters $n = 50$, $\gamma = 100$, $\eta = 50$, $\kappa = 1$, $\upsilon = 0.5$, $\omega = 0.57$, $\varphi = 0.025$ are fixed and the initial conditions are taken $f(0) = 5.0$; $m(0) = 5.0$; $c(0) = 10.0$.

On the increase of the diffusion saturation level, the regions of conditions conducive to cancer invasion are expanding. For the parameter ranges considered chaotic cancer attractors are generated

(a)   (b)

(c)
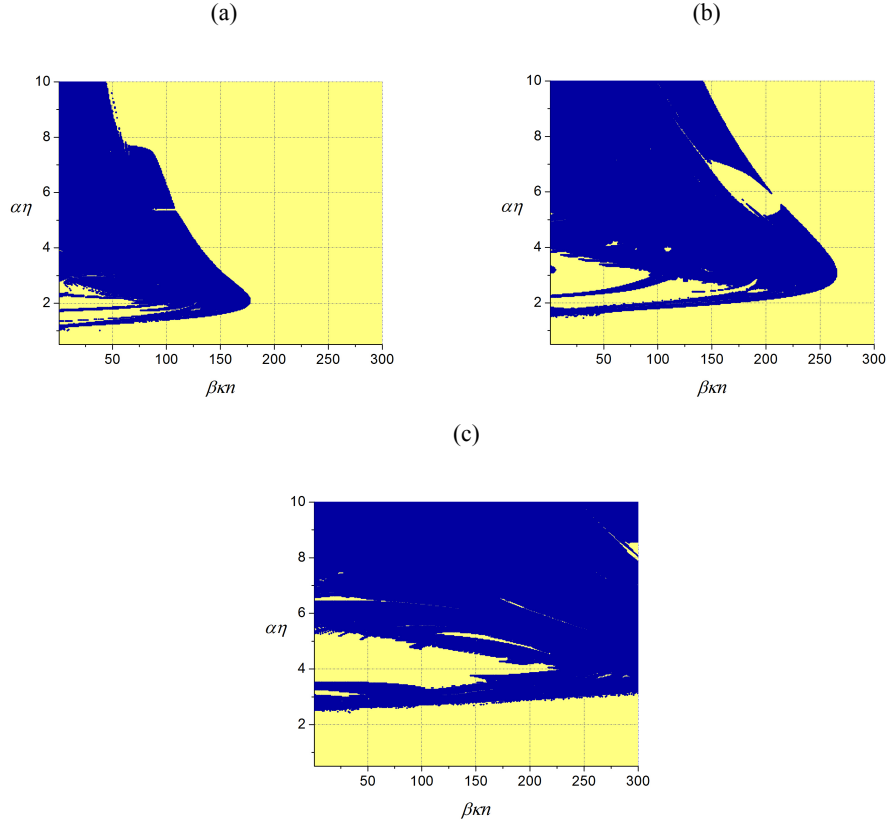
Figure 1. Control parameter plane ($\beta\kappa n$, $\alpha\eta$) – 'tumor cell volume vs glucose level': evolution of conditions conducive to cancer invasion with increasing magnitude of diffusion saturation level (a) $\delta\varphi$=0.5; (b) $\delta\varphi$=1.0; (c) $\delta\varphi$=2.0.

for glucose levels $\beta\kappa n < \beta_{cr}\kappa n$, where $\beta_{cr}\kappa n$=175.0 at diffusion saturation level $\delta\varphi$=0.5 (Fig. 1, (a)), $\beta_{cr}\kappa n$=270.0 at $\delta\varphi$=1.0 (Fig. 1, (b)) and for any glucose level at $\delta\varphi$=2.0 (Fig. 1, (c)). It should be noted, all obtained regions in the parametric space have complex structure and substantially depend on other parameters of the model (Eqs. 1–4) including initial conditions.

An evolution of the chaotic regions in control parameter plane 'number of tumor cells vs tumor cell volume' ($\alpha\eta$, γ), ($0 \leq \alpha\eta \leq 10$, $0 \leq \gamma \leq 200$), depending on glucose level $\beta\kappa n$=2.5, $\beta\kappa n$=250.0, and $\beta\kappa n$=500.0 for the model (Eqs. 1–4) is observed in Fig. 2 (a), (b), (c). Other parameters $\delta\varphi$=1.2, n=50, δ=48.0, η=50, κ=1, υ=0.5, ω=0.57, φ=0.025 are fixed and the initial conditions are taken $f(0)$=5.0; $m(0)$=5.0; $c(0)$=10.0.

Fig. 2 demonstrates, that for the parameter ranges considered, increase in glucose level substantially decreases a risk of cancer invasion in the biological system (see Fig. 2 (c): no chaotic

(a) (b)

(c)
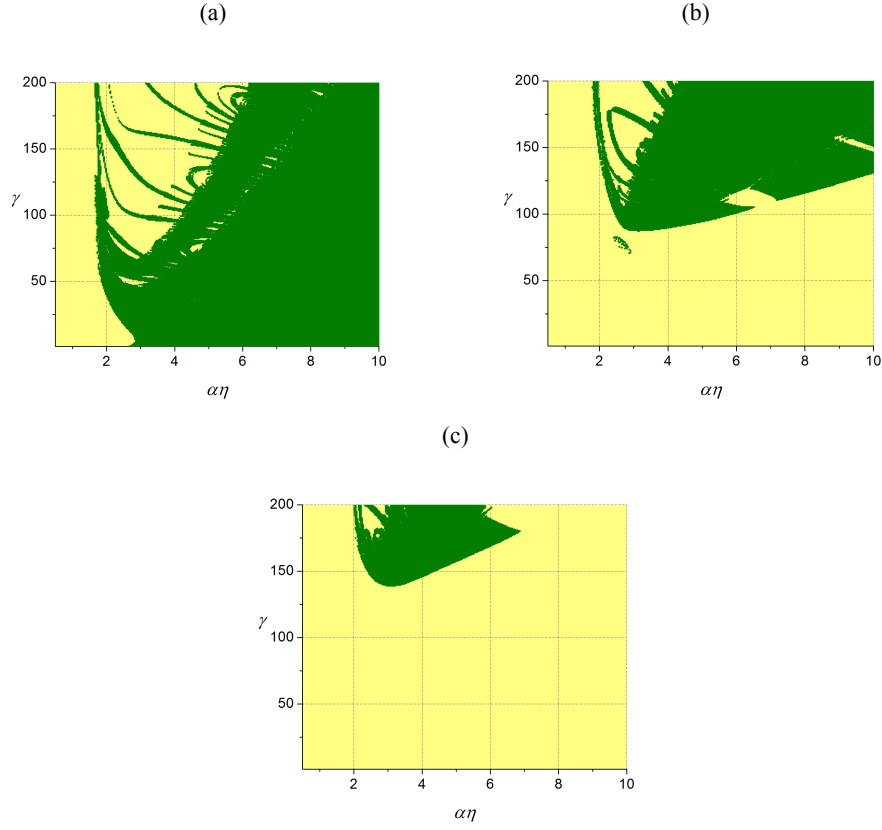
Figure 2. Control parameter plane ($\alpha\eta$, γ) – 'number of tumor cells vs tumor cell volume': evolution of conditions conducive to cancer invasion with increasing glucose level: (a) $\beta\kappa n$=2.5; (b) $\beta\kappa n$=250.0; (c) $\beta\kappa n$=500.0.

cancer attractors when γ<140.0 $\vee$ $\alpha\eta$<2.0 $\vee$ $\alpha\eta$>7.0 at $\beta\kappa n$=500.0). It should be noted, depending on accepted parameters, increase in the diffusion saturation level can lead to both suppression and generation of conditions conducive to cancer invasion (figures and diagrams, confirming this statement, are not presented here due to a brief content of this paper).

We can observe also, in the parametric space 'number of tumor cells vs tumor cell volume' there is some critical threshold α=α_{cr}, that chaotic cancerous attractors exist only for α>α_{cr} (see Fig. 2 (a), (b), (c): α_{cr} = 1.9). It is clear, α_{cr} depends on other parametes of the model (Eqs. 1–4) and α_{cr} increases for bigger magnitudes of diffusion saturation level.

An evolution of the chaotic regions in the control parameter plane 'tumor cell volume vs diffusion saturation level' ($\delta\varphi$, $\alpha\eta$), (0≤$\delta\varphi$≤3.0, 0≤$\alpha\eta$≤10.0), depending on number of tumor cells

(a)   (b)

(c)
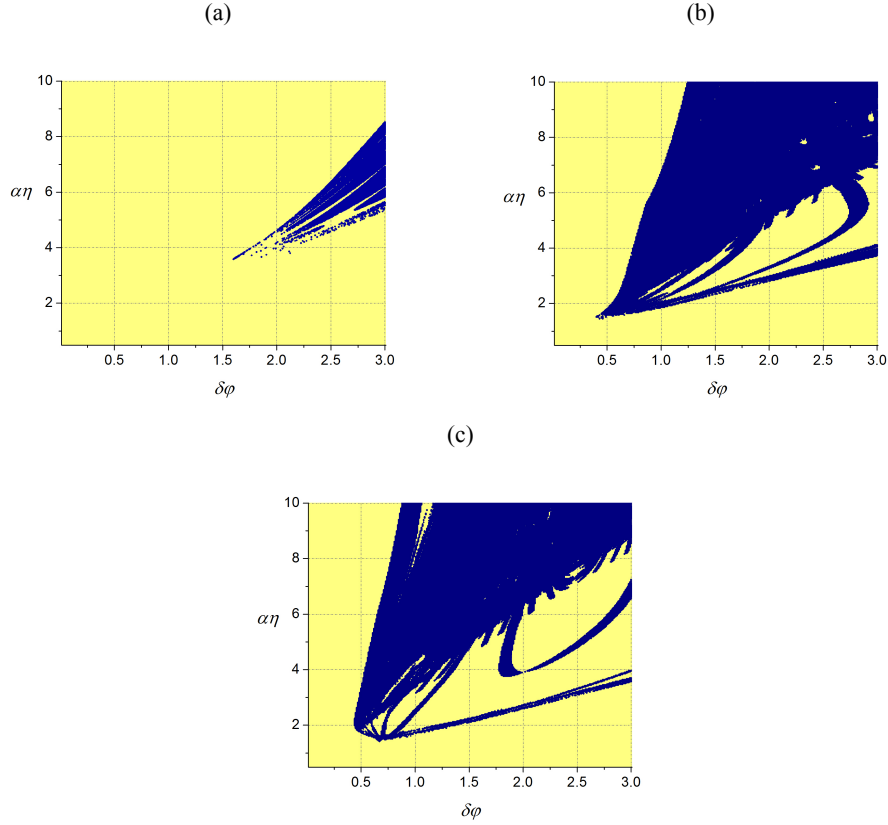
Figure 3. Control parameter plane ($\delta\varphi$, $\alpha\eta$) – 'tumor cell volume vs diffusion saturation level':

evolution of conditions conducive to cancer invasion with increasing number of tumor cells:

(a) γ=70.0; (b) γ=150.0; (c) γ=200.0.

γ=70.0, γ=150.0 and γ=200.0 for the model (Eqs. 1–4) is observed in Figure 3 (a), (b), (c). Other parameters $\beta\kappa n$= 300.0, n=50, β=6.0, η=50, κ=1, υ=0.5, ω=0.57, φ=0.025 are fixed and the initial conditions are taken f(0)=5.0; m(0)=5.0; c(0)=10.0.

The study of the parametric space 'tumor cell volume vs diffusion saturation level' confirms again a substantial mutual influence of all parameters of the model (Eqs. 1–4) to cancer invasion. Indeed, at comparatively low glucose levels (for instance, $\beta\kappa n$=2.5) regions of chaotic cancerous attractors are suppressed with an increase of number of tumor cells (figures and diagrams, confirming this statement, are not presented here due to a brief content of this paper) while for higher glucose levels (for instance, $\beta\kappa n$=300.0) cancer invasion risk strengthens on the increase of number of tumor cells (see Fig. 3 (a), (b), (c)). Generally, at fixed number of tumor cells the increase in glucose level

(a)   (b)

(c)
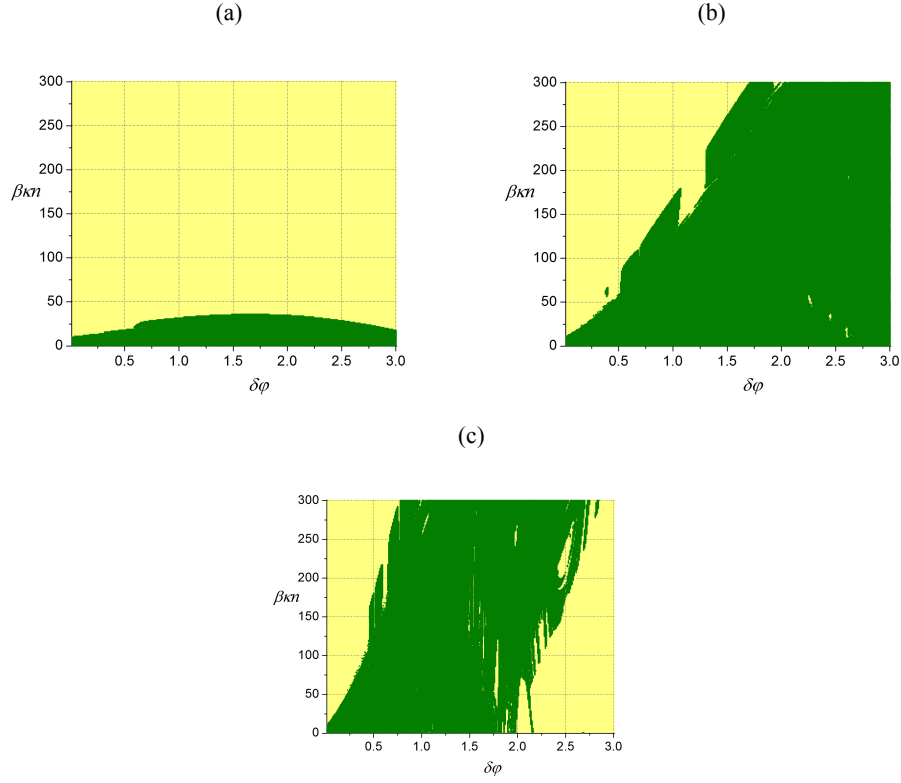
Figure 4. Control parameter plane ($\delta\varphi$, $\beta\kappa n$) – 'glucose level vs diffusion saturation level': evolution of conditions conducive to cancer invasion with increasing number of tumor cells: (a) γ=20.0; (b) γ=100.0; (c) γ=200.0.

has a suppressing effect on carcinogenesis (figures and diagrams, confirming this statement, are not presented here due to a brief content of this paper).

An evolution of the chaotic regions in the control parameter plane 'glucose level vs diffusion saturation level' ($\delta\varphi$, $\beta\kappa n$), ($0\leq\delta\varphi\leq3.0$, $0\leq\beta\kappa n\leq300$), depending on number of tumor cells γ=20.0, γ=100.0 and γ=200.0 for the model (Eqs. 1–4) is observed in Figure 4 (a), (b), (c). Other parameters $\alpha\eta$= 8.0, n=50, α=0.16, η=50, κ=1, υ=0.5, ω=0.57, φ=0.025 are fixed and the initial conditions are taken f(0)=5.0; m(0)=5.0; c(0)=10.0.

For the considered planes 'glucose level vs diffusion saturation level' as sections of the multy-parametric space of the model (Eqs. 1–4) both for comparatively small and for comparatively large tumor cell volumes, a consistent pattern is observed: with an increase in the number of tumor cells, the regions of chaotic cancerous attractors in this plane ($\delta\varphi$, $\beta\kappa n$) first increase (see transition from

(a)   (b)

(c)
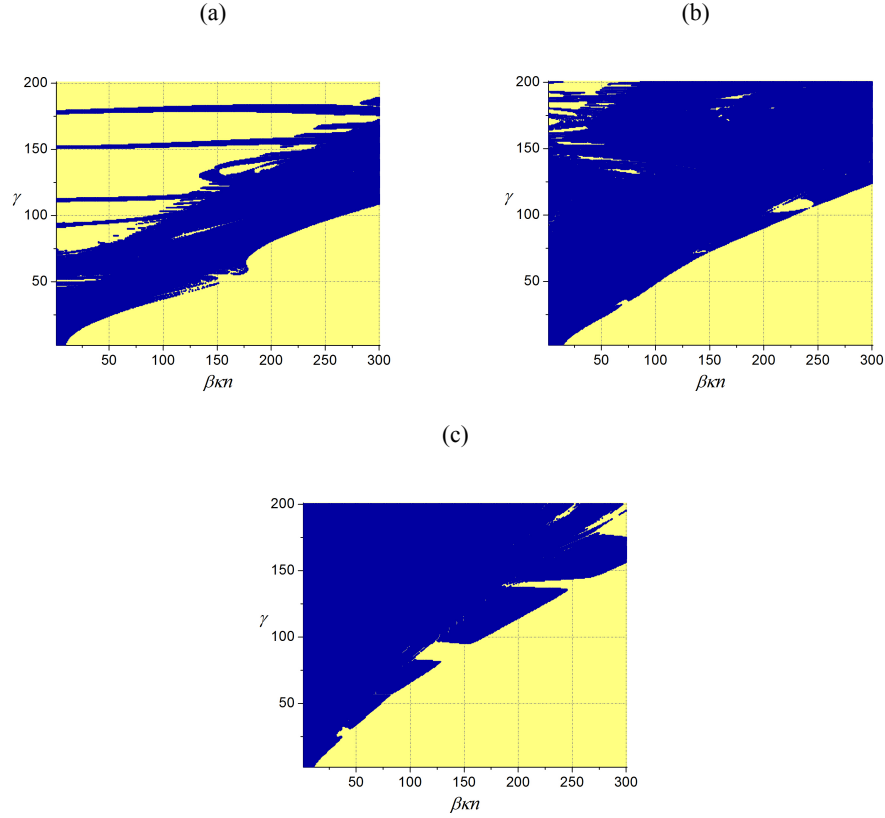
Figure 5. Control parameter plane ($\beta\kappa n$, γ) – 'number of tumor cells vs glucose level': evolution of conditions conducive to cancer invasion with increasing tumor cell volume: (a) $\alpha\eta$=3.0; (b) $\alpha\eta$=5.0; (c) $\alpha\eta$=8.0.

Fig. 4 (a) to Fig. 4 (b)) and then decrease (see transition from Fig. 4 (b) to Fig. 4 (c)). In most of the previous cases, an increase in glucose level led to the suppression of regions of chaotic cancerous attractors. However, in the parametric plane ($\delta\varphi$, $\beta\kappa n$) there are regimes (for instance, at $\alpha\eta$= 3.0, γ= 100.0; $\alpha\eta$= 5.0, γ= 100.0, etc.) corresponding to absence of conditions for carcinogenesis at definite values of glucose level, while a cancer invasion appears when glucose level increases (figures and diagrams, confirming this statement, are not presented here due to a brief content of this paper).

An evolution of the chaotic regions in the control parameter plane 'number of tumor cells vs glucose level' ($\beta\kappa n$, γ), ($0 \leq \beta\kappa n \leq 300$, $0 \leq \gamma \leq 200$), depending on tumor cell volume $\alpha\eta$=3.0, $\alpha\eta$=5.0 and $\alpha\eta$=8.0 for the model (Eqs. 1–4) is observed in Figure 5 (a), (b), (c). Other parameters $\delta\varphi$=1.0, n=50,
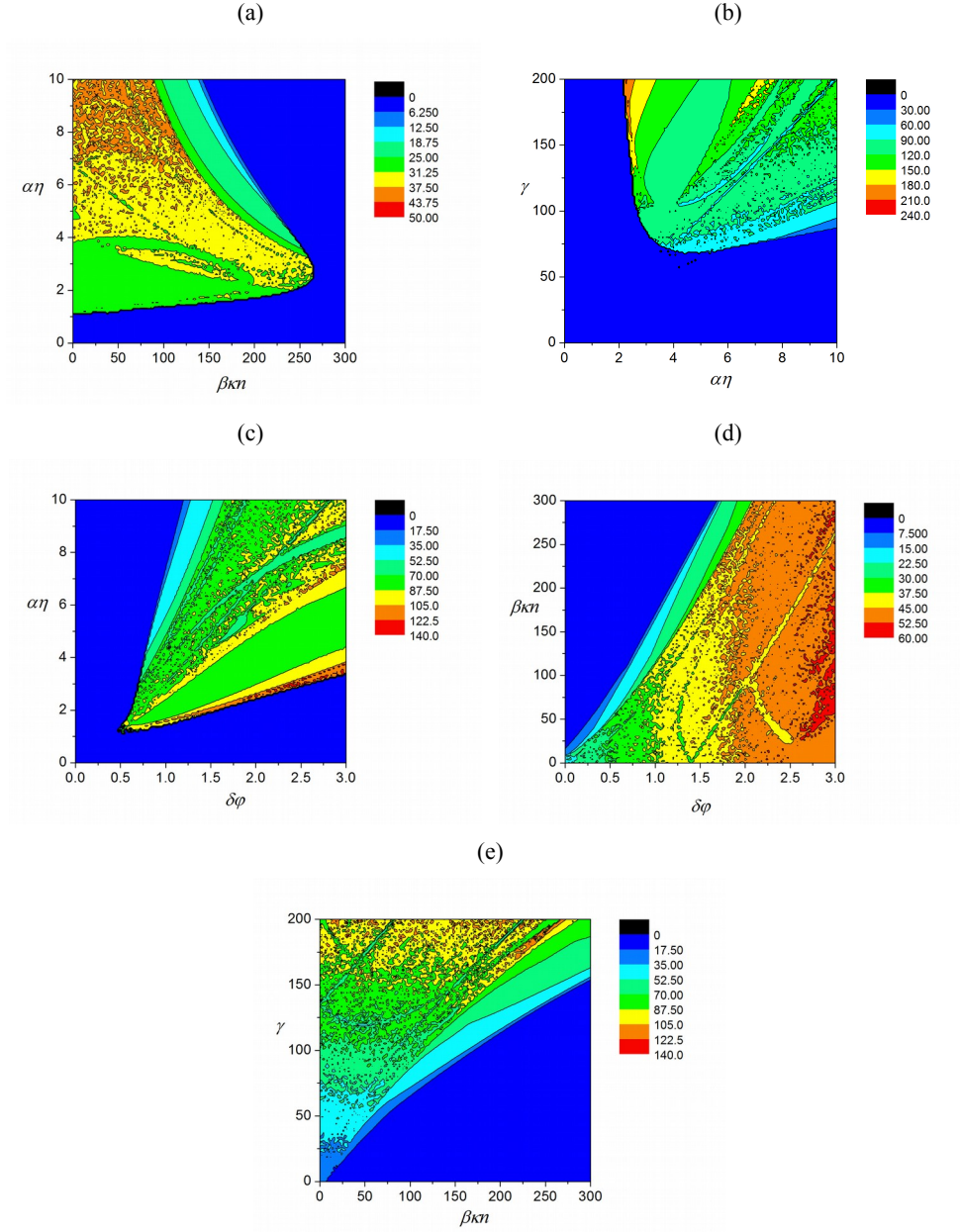
Figure 6. Amplitude level contours of (a) MM concentration in ($\beta\kappa n$, $\alpha\eta$) control parameter plane at γ=100.0, $\delta\varphi$=1.0; (b) MDE concentration in ($\alpha\eta$, γ) plane at $\beta\kappa n$=250.0, $\delta\varphi$=2.0; (c) oxygen concentration in ($\delta\varphi$, $\alpha\eta$) plane at $\beta\kappa n$=300.0, γ=150.0; (d) MM concentration in ($\delta\varphi$, $\beta\kappa n$) plane at $\alpha\eta$=8.0, γ=100.0; (e) MDE concentration in ($\beta\kappa n$, γ) plane at $\alpha\eta$=8.0, $\delta\varphi$=1.0.

δ=40.0, η=50, κ=1, υ=0.5, ω=0.57, φ=0.025 are fixed and the initial conditions are taken $f(0)$=5.0; $m(0)$=5.0; $c(0)$=10.0.

Under conditions considered for comparatively low diffusion saturation levels, for instance $\delta\varphi$= 0.5, chaotic cancerous attractors regions are suppressed with increasing tumor cell volumes and vice versa: for more higher diffusion saturation levels, for instance $\delta\varphi$= 2.0, with increasing tumor cell volumes ($\alpha\eta$= 3.0, $\alpha\eta$= 5.0, $\alpha\eta$= 8.0) the cancer invasion is increased (figures and diagrams for both cases of diffusion saturation levels $\delta\varphi$= 0.5 and $\delta\varphi$= 2.0, confirming this statement, are not presented here due to a brief content of this paper). In Fig. 5 (b), (c) we can observe: there is some glucose level threshold β_{cr}= $\beta_{cr}(\gamma)$ such that no carcinogenesis while β>$\beta_{cr}(\gamma)$. So, passing this threshold in the direction of increase, the definite glucose level completely suppresses carcinogenesis. It should be noted, Fig. 5 (a), where chaotic cancer attractors regions have an inclined stripe form, demonstrates another scenario. Thus, at $\alpha\eta$= 3.0, $\delta\varphi$=1.0 (Fig. 5 (a)) (or in other cases, for instance, ($\alpha\eta$= 3.0, $\delta\varphi$=2.0) or ($\alpha\eta$= 5.0, $\delta\varphi$=2.0) etc.) in the parametric plane ($\beta\kappa n, \gamma$) with increasing of glucose level the state 'no conditions for carcinogenesis' passes to the state 'cancer invasion' and then again passes to the state 'no conditions for carcinogenesis'. That is, depending on other parameters of the model (Eqs. 1–4), increasing in glucose level can both suppress and generate carcinogenesis.

For all studied control parameter planes the corresponding amplitude level contours of matrix-metalloproteinases (MM), matrix–degradative enzymes (MDE) and oxygen concentrations have been obtained and juxtaposed with them. In all cases the carcinogenesis is accompanied by significant increase in chemical oscillation amplitudes of the MM, MDE and oxygen concentrations. Some amplitude level contours of these characteristics are reported in Fig. 6.

Amplitude level contours of matrix-metalloproteinases (MM) concentrations are presented in Fig. 6, cases (a) and (d). Case (a): control parameter plane ($\beta\kappa n, \alpha\eta$) 'tumor cell volume vs glucose level' at γ= 100.0, $\delta\varphi$= 1.0 in accordance with Fig. 1 (b) with the same other fixed parameters as for the case of Fig. (b). Case (d): control parameter plane ($\delta\varphi, \beta\kappa n$) 'glucose level vs diffusion saturation level' at $\alpha\eta$=8.0, γ=100.0 in accordance with Fig. 4 (b) with the same other fixed parameters as for the case of Fig. 4 (b).

Amplitude level contours of matrix–degradative enzymes (MDE) concentrations are presented in Fig. 6, cases (b) and (e). Case (b): control parameter plane ($\alpha\eta, \gamma$) 'number of tumor cells vs tumor cell volume' at $\beta\kappa n$= 250.0, $\delta\varphi$= 2.0 in accordance with Fig. 2 (b) with the same other fixed parameters as for the case of Fig. 2 (b). Case (e): control parameter plane ($\beta\kappa n, \gamma$) 'number of tumor cells vs glucose level' at $\alpha\eta$=8.0, $\delta\varphi$=1.0 in accordance with Fig. 5 (c) with the same other fixed parameters as for the case of Fig. 5 (c).

And finally, amplitude level contours of oxygen concentration is presented in Fig. 6 (c) in control parameter plane ($\delta\varphi$, $\alpha\eta$) 'tumor cell volume vs diffusion saturation level' at $\beta\kappa n=300.0$, $\gamma=150.0$ in accordance with Fig. 3 (b) with the same other fixed parameters as for the case of Fig. 3 (b).

Figure 6 demonstrates, that in all cases the carcinogenesis is accompanied by a significant increase in chemical oscillations amplitudes of MM, MDE and oxygen concentrations.

4. Conclusions

In this study it was demonstrated a significant and complex mutual influence of all components of the multy-parametric space 'number of tumor cells – tumor cell volume – glucose level – diffusion saturation level' as well as of the 3D initial state space components on inhibition/amplification of carcinogenesis in biological systems. A nonlinear multi-scale diffusion cancer invasion model that describes the interactions of the tumor cells, matrix-metalloproteinases, matrix-degradative enzymes and oxygen was used for simulation. To quantify chaotic cancer attractors the technique based on the wandering trajectories analysis was applied. Conditions conducive to cancer invasion were defined depending on parameters of the multy-parametric space. The numerous figures presented describe the evolution of these conditions in the process when some parameters of the multy-parametric space were changed. Amplitude level contours of matrix–metalloproteinases, matrix–degradative enzymes and oxygen concentrations have been obtained and juxtaposed with the corresponding parametric planes. In all cases the carcinogenesis is accompanied by significant increase in chemical oscillation amplitudes of matrix–metalloproteinases, matrix–degradative enzymes and oxygen concentrations. The results obtained allow evaluation of conditions in all control parameter planes as well as the modes to inhibit and/or stabilize carcinogenesis.

References

[1] Dzyubak, L., Dzyubak, O., Awrejcewicz, J. Controlling and stabilizing unpredictable behaviour of metabolic reactions and carcinogenesis in biological systems. *J. Nonlinear Dyn* 97 (2019), 1853–1866 (doi: https://doi.org/10.1007/s11071-018-04737-1).

[2] Harney, M., Yim, W. Chaotic Attractors in Tumor Growth and Decay: A Differential Equation Model. In: Vlamos P., Alexiou A. (eds) *GeNeDis* 2014. *Advances in Experimental Medicine and Biology* 820. Springer, Cham, 2014, 193–206.

[3] Watson, J.D., Baker, T.A., Bell, S.P., Gann, A., Levine, M., Losick, R. *Molecular Biology of the Gene.* Pearson, New York, 2014.

[4] Anderson, A.R.A., Chaplain, M.A.J., Newman E.L., Steele, R.J.C., Thompson, A.M. Mathematical modelling of tumor invasion and metastasis. *Journal of Theoretical Medicine* 2, 2000, 129–154.

[5] Anderson, A.R.A. A hybrid mathematical model of solid tumor invasion. *Mathematical Medicine and Biology* 22 (2005), 163–186.

[6] Ivancevic, T.T., Bottema, M.J., Jain, L.C. A theoretical model of chaotic attractor in tumor growth and metastasis. *arXiv: 0807.4272 in Cornell University Library's arXiv.org* (2008), 1–17.

[7] Harney, M., Seal, J. Design of a compensator network to stabilize chaotic tumor growth. *Adv Exp Med Biol*. 988 (2017), 31–37 (doi: 10.1007/978-3-319-56246-9_2).

[8] Prigogine I., Stengers, I. *Order Out of Chaos*. Heinemann, London, 1984.

[9] Awrejcewicz, J., Dzyubak, L.P. Chaos caused by hysteresis and saturation phenomenon in 2-dof vibrations of the rotor supported by the magneto-hydrodynamic bearing. *International Journal of Bifurcation and Chaos* 15(6) (2011), 2041–2055.

[10] Awrejcewicz, J., Dzyubak, L.P. Modelling, chaotic behavior and control of dissipation properties of hysteretic systems. In: *Models and Applications of Chaos Theory in Modern Sciences*, Z. Elhadj, (Ed.), CRC Press Taylor & Francis Group, 2011, 645-667.

Larysa Dzyubak, Associate Professor: Department of Applied Mathematics, National Technical University, 2 Kyrpychova Str., 61002 Kharkiv, Ukraine (*lpdzyubak@gmail.com*). The author gave a presentation of this paper during one of the conference sessions.

Oleksandr Dzyubak, Ph.D.: Ascension All Saint Cancer Center, 3809 Spring Street, Racine, WI 53405, USA (*Dzyubak.Oleksandr@gmail.com*).

Jan Awrejcewicz, Professor: Department of Automation, Biomechanics and Mechatronics, the Lodz University of Technology, 1/15 Stefanowski Str., 90-924 Lodz, Poland (*jan.awrejcewicz@p.lodz.pl*).

Influence of the sliding bearing parameters on the dynamic behavior of external gear pumps

Wiesław Fiebig, Piotr Kruczek

Abstract: Variable forces resulting from pressure as well as from the interlocking of teeth in the gearing are responsible for the vibration and noise development in gear pumps. These various forces are transmitted to the pump housing and cause it to vibrate, as well as mechanical connected elements like electric motor, valves, tank and piping system. These dynamic loads are transmitted through the sliding bearings to the pump housing and they can reach very high values, especially at higher pressures. In this paper the model to determine dynamic forces in the gear pump, taking into account the influence of sliding bearings has been presented.

1.   Introduction

External gear pumps are a commonly used type of positive displacement pumps, because of their low price and readily available production technology. The downside of gear pumps is their noisiness, which for normal working conditions can reach 80-90 dB and more [8]. The causes of noise in gear pumps can be divided into two categories: hydraulic and mechanical. The hydraulic causes are related to flow of the fluid. Among these, causes such as pressure pulsations, impact pressure changes in trapped volume, cavitation, aeration of the hydraulic fluid and other can be mentioned [1-13].

The noise from the pump propagates to the surrounding via vibration of the casing, this however is stimulated by dynamic forces from the above mentioned mechanical and hydraulic causes. These forces are transmitted from the gears to the shafts, and from shafts through bearings to the casing. Because bearings are a single point of contact between the excited dynamic forces and the vibration-prone casing it is very important to investigate the bearings influence on force transmission.

There are many studies on noise generation in external gear pumps [1-13]. The variable pressure loads and pressure overdue in the trapped volumes as well as mechanical noise are considered to be the main reasons for vibration and noise generation. The shape of the teeth profile as well as the position and shape of the pressure relief grooves have big influence on the pressure courses in the trapped volumes.

In [3] the solution has been proposed to reduce pressure gradients in the trapped volume by gear pumps by attaching a certain additional volume. So far, the most effective solution [2] is a cycloid teeth

profile "Silent Plus" pump", in which trapped volume is not present and due to a sloping mesh, the smooth change of loads and the pressure on the toothed wheels is achieved.

There are known approaches based on multi body dynamics [2, 8, 10, 14] and FE- analysis [16, 17]. Based on such models the dynamical forces inside the pumps, the natural frequencies and dynamic deformations of pump housings are determined.

A discrete model describing dynamic loads in an external gear pump bearings is described in [14]. Calculating pump housing vibrations, e.g. by means of FEM, the sound pressure distribution on a defined surface surrounding the pump can be determined using BEM, which is caused by vibrations on the pump housing surface [12].

The task of this paper is to examine the influence of geometry of the bearings used in external gear pumps on dynamic forces transferred to the casing and collection of data on dynamic forces in bearings to allow further analysis of vibration and noise in external gear pumps.

2.   Mathematical model of sliding bearings

The basis of the theory of hydrodynamic lubrication (HD) is Reynolds equation [4, 5] that describes the flow of a viscous fluid in an arrow gap between the surfaces of a regular curvature.

In sliding bearing the journal 1 slides on the bearing surface 2. (Fig. 1).
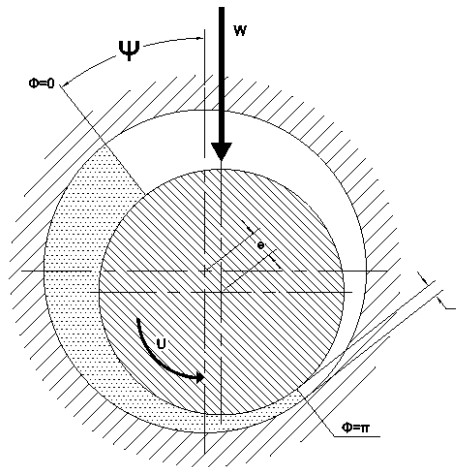
Figure 1. Shaft position in the sliding bearing [4]

Since both of these surfaces are curves, as approaching to each other the distance h(x) decreases, so that a wedge is formed. For such a case, the Reynolds equation for transverse sliding bearings will take the form [4,14,15]:

$$\frac{\partial}{\partial x}\left(\frac{h^3}{\mu}\frac{\partial p}{\partial x}\right) + \frac{\partial}{\partial z}\left(\frac{h^3}{\mu}\frac{\partial p}{\partial z}\right) = 6(v_1 + v_2)\frac{\partial h}{\partial x} +$$
$$12\frac{\partial h}{\partial t} \hspace{6cm} (1)$$

where: p – local pressure in the liquid layer, ρ, μ-density and dynamic viscosity of the oil, h - thickness of the liquid layer, v_1, v_2–velocity of the surface 1 and 2.

From Reynolds equation the pressure distribution on the perimeter can be determined, which in turn allows for bearing-load capacity or minimum lubricant film thickness calculation.

For the range of practical application of the Reynolds equation below assumptions should be made [4]:

- mass and gravitational forces are negligible,
- lubricant liquid is a Newtonian liquid,
- viscosity of the liquid is constant independent of pressure and temperature,
- the lubricant fluid is incompressible,
- in comparison with other dimensions lubricant film thickness is negligibly small,
- there is no slippage on the liquid-solid border,
- the effect of surface tension is negligibly small,
- contacting surfaces are non-deformable.

If one accepts the line connecting centers of the shaft and bearing as a reference when measuring the angle φ, one can write

$$h = c + e cos\phi = c(1 + \varepsilon cos\phi) \hspace{4cm} (2)$$

Therefore:

$$\frac{dh}{d\phi} = -c\varepsilon sin\phi \hspace{5cm} (3)$$

Geometric characteristics dimensions of the bearing are following:

- d [mm] – nominal diameter of the bearing, shall be d=d1
- d_1 [mm] –journal diameter
- d_2 [mm] –bearing diameter
- l [mm] – nominal width of the bearing (bearing's length)
- s [μm] –nominal clearance between journal and bearing; $s = d_2 - d_1$
- c [μm] –radial clearance in bearing; $c = s/2$
- w–journal elative clearance in bearing (resulting from the assumed journal fitting in bearing),

$$w = \frac{s}{d} = (d_2 - d_1)/d_1 \hspace{4cm} (4)$$

Operation characteristics of the bearing are following:

- e [μm] - eccentricity; $e = \frac{s}{2} - h_0 = \varepsilon w \frac{d}{2}$

- ε –relative eccentricity; $\varepsilon = \frac{2e}{s} = 1 - \delta$

- δ - relative minimum lubricating oil layer thickness; $\delta = \frac{2h_0}{s} = \frac{2h_0}{wd}$

Functional characteristics of the bearing are following:

- F [N] – radial load of the bearing

- $\bar{p}$[MPa] - average nominal individual unit bearing load

$$\bar{p} = \frac{F}{ld}$$

- n [min^{-1}] –nominal shaft speed

- ω [s^{-1}] – nominal angular velocity of the shaft

- μ [$Pa \cdot s$] – nominal value of the dynamic viscosity coefficient of lubricating oil

The simulation model and the research will be carried out based on the data of the hydraulic external gear pump with the unit volume of 31 cm3/rev.

The calculations will be carried out in the LMS Virtual Lab Rev. 11-SL1. This is the integrated software for CAE simulation and optimization of structural integrity, noise and vibrations, dynamics and durability of all mechanical systems [16].

The development of the model and the task of excitation forces (excluding the definition of hydrodynamic bearings) will be carried out in the Motion module. Motion module provides advanced solutions in solid modeling, parameterization, geometry, CAD solutions of elements, possibilities of control and motion control, solver, animation and presentation of results.

Using the Motion module, it is possible to create and refine virtual prototype models by using fully integrated CAD engine supporting Software CATIA v5. Solid modeling allows for a full implementation of parameters of the model. There are mechanical components such as spring, friction, contact force and developed a list of connections and bonds. Stable and efficient solver provides accurate and efficient calculations of complex problems with results such as displacement, velocity, acceleration and reaction forces for all bodies in the simulation. For comparison purposes, the model of bearing using the Hydro dynamic bearings (CUIMPD method) has been used.
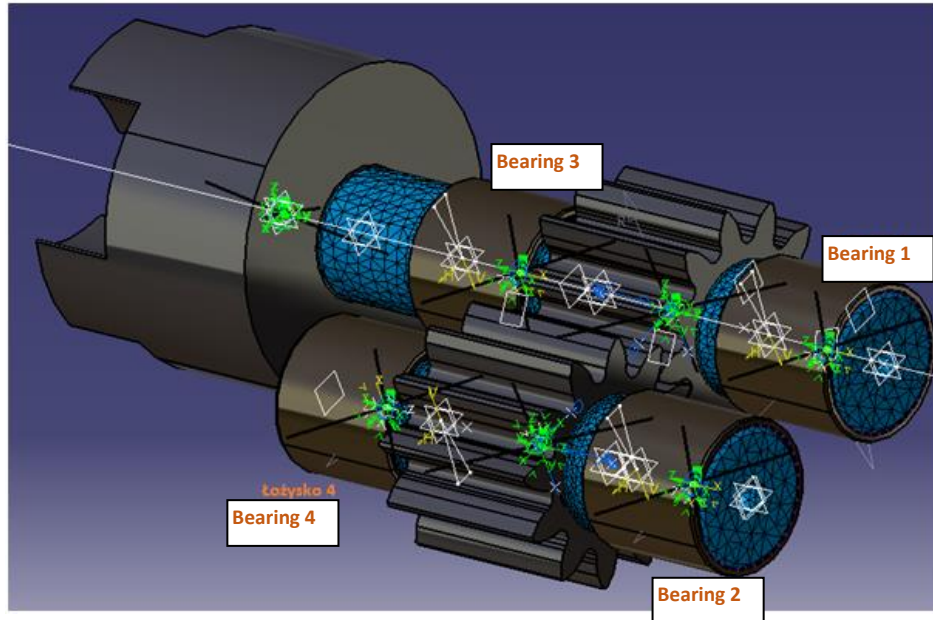
Figure 2. Model of the gear pump with the sliding bearings in VirtualLab

The pressure distribution at the begin of simulation will be shown in Fig. 3.
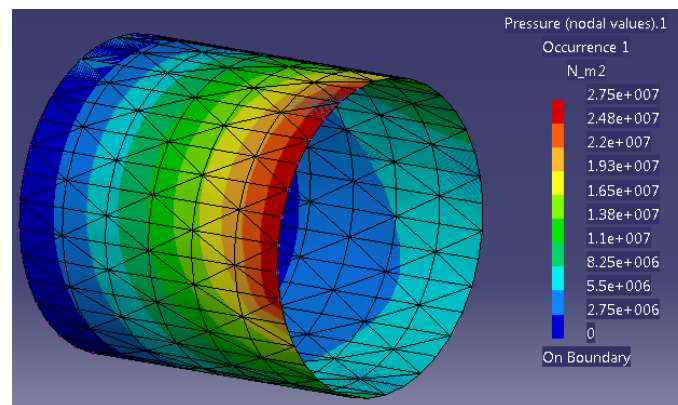
Figure 3. The initial bearing pressure (without load from the pump delivery pressure)

Comparison of the results obtained on the four bearings is aimed to show the relation between the bearings on the drive shaft and the corresponding bearings on the driven shaft.

In Tab. 1 the parameters for simulation has been described.

Table 1. Parameters for the simulation

Description	Symbol	Value	Dimension
Width of the gears	d_g	36.3	mm
Number of teeth	z	12	-
Module	m	3,387	mm
Pressure angle	α	25	stopnie
Gap between teeth	c_k	0,5	mm
Damping coefficient in the gearing	k_{k1}	4873	kg/s
Torsional stiffness of the driving shaft	c_w	29868	N*m/rad
Torsional damping coefficient of the driving shaft	k_f	0,04	kg/(s*rad)
Mass of the driving shaft	m_{s1}	0,686	kg
Moment of inertia of the driving shaft	I_{s1}	$5.591*10^{-5}$	kg*m²
Mass of the driver shaft	m_{s2}	0,456	kg
Moment of inertia of the driver shaft	I_{s2}	$4.235*10^{-5}$	kg*m²
Mass of the gear	m_g	0,21	kg
Moment of inertia of the gear	I_g	$6.421*10^{-5}$	kg*m²
Mass of the coupling	m_s	0,928	kg
Moment of inertia of the coupling	I_s	$5.485*10^{-4}$	kg*m²
Young module - steel	E_s	$2*10^{11}$	N/m²
Density - steel	ρ_s	7860	kg/m³
Young module- bronze	E_b	$1,1*10^{11}$	N/ m²
Density - bronze	ρ_b	8860	kg/m³

Parameters of the fluid were following:

The kinematic viscosity is given by [1]:

$$\nu_{T=20^oC} = 250 \left[cSt = \frac{mm^2}{s}\right]$$

$$\nu_{T=50^oC} = 50 \div 55 \, [cSt]$$

$$\nu_{T=100^oC} = 9,5 \, [cSt]$$

This is the temperature range and the corresponding viscosity at the entrance of the bearing, which is the oil temperature in the tank. The oil in the bearing will have a higher temperature due to friction inside the pump. The above values dynamic viscosity will be used to study the impact of temperature changes on the viscosity and dynamic response. The rest of the calculation is adopted has become a oil dynamic viscosity µ = 0.23 [Pa s] corresponding to the operating temperature of approximately 75 °C.

3. The influence of the gap inside the bearing

Four combinations were analyzed at working pressure (100 and 275 bar) and pump speed (1500 and 3000 rpm). On the basis of the results, the following conclusions has been obtained:

• Change the gap inside the bearing practically does not affect the torque and inter teeth force,

• The increasing of the gap in both bearings cause decrease of the maximum dynamical reaction force in horizontal direction by $\Delta = 300$ N (bearing 1) and by $\Delta = 1600$N (bearing 2).

• The influence of the gap is opposite for vertical dynamic reaction forces. The increase of the force on the bearing 1 amounted to $\Delta = 900$N and on the bearing 2 to $\Delta = 600$N.

• Comparing these values it is to notice that the increasing of the gap inside the bearings has a positive influence on the dynamic reaction forces in the bearings. This is resulting from the higher damping in case of bigger thickness of the oil layer between the shaft and sleeve.

gap value c=0,0235mm, n=3000 rpm, p=27,5 MPa
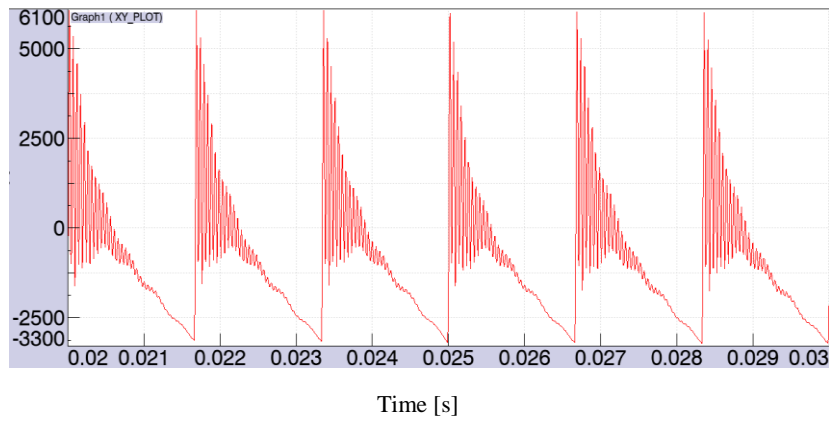
Time [s]

Figure 4. The dynamic reaction force Fxb2 in the bearing- driven gear

gap value c=0,0235mm, n=3000 rpm, p=27,5 MPa

Time [s]

Figure 4. The dynamic reaction force F_{yb2} in the bearing- driven gear

gap value c=0,065 mm, n=3000 rpm, p=27.5 MPa
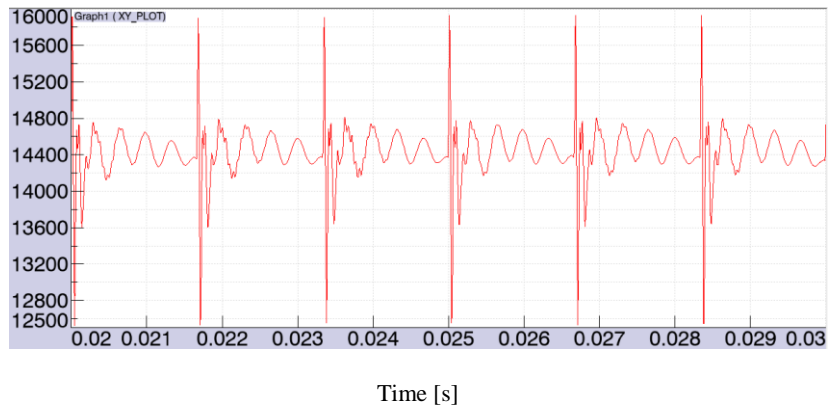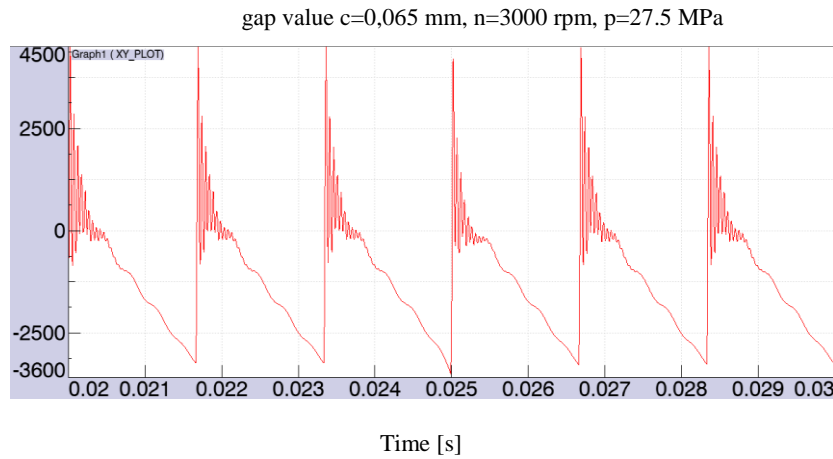
Figure 5. The dynamic reaction force F_{xb2} in the bearing- driven gear

gap value c=0,065 mm, n=3000 rpm, p=27.5 MPa
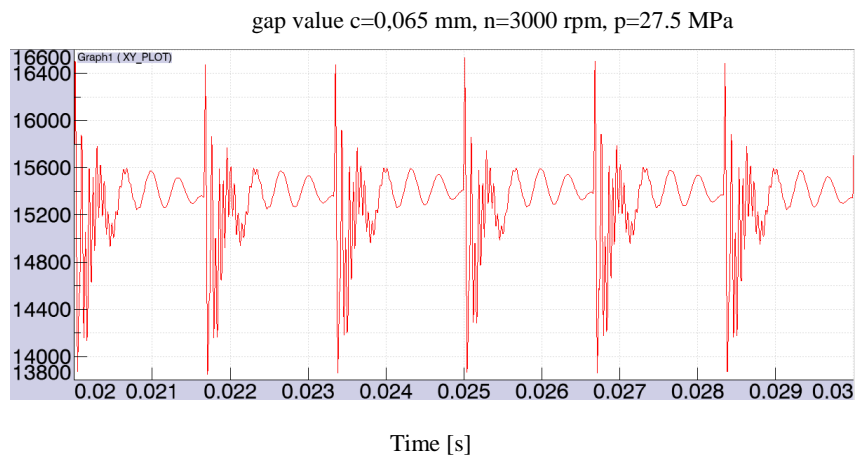
Figure 6. The dynamic reaction force F_{yb2} in the bearing- driver gear

4.   Conclusions

The influence of the gear pump and the sliding bearings parameters on the dynamic reaction forces inside the bearings has been analyzed with the model presented. The model has been developed in Virtual Lab which contains the module for calculation of sliding bearings. The influence of the pressure, rotational speed, the gap in the bearing and temperature on torsional torque on the drive shaft, the inter teeth force, the components of the dynamic reaction forces in the bearings and the position of the shaft inside the bearing can be analyzed.

On the basis of the simulation has been stated that the biggest influence on the dynamic reaction forces have the clearance inside the bearing. The values of the clearances in the sliding bearings are variable and depend on the manufacturing accuracy of the gear wheels and bushes in the bearings.

It was noted that increasing gap has a positive effect on the reaction forces in the bearings. From that one can state that the pump coming out from the same manufacturing process may have different noise radiation and the rate of surface wear.

The final result of the work are dynamic forces passes in the bearings, which can be used for further analysis through their input on the housing of the pump and examination of vibration, and as a result, the noise radiation of the pump.

References

[1]   Bonanno, A.; Pedrielli, F. *A study of the structure borne noise of hydraulic gear pumps*. In Proceedings of the 7th JFPS International Symposium on Fluid Power, Toyama, Japan, 15–18 September 2008; pp. 641–646.

[2]   Casoli, P.,Vacca, A., Franzoni,G. *A numeriacal model for the simulation of external gear pumps*, Proceedings of the 6 th JPFS international symposium on fluid power, Tsukuba, November 2005.

[3]   Fiebig, W. *Influence of the Inter Teeth Volumes on the Noise Generation in External Gear Pumps*, Archives of Acoustics, Vol. 39, Vol. 39, No. 2, 2014, 261–266.

[4]   Mucchi, E.; Dalpiaz, G.; Del Rincon, A.F. *Elastodynamic analysis of a gear pump. Part I: Pressure distribution and gear eccentricity*. Mech. Syst. Signal Proc. 2010, 24, 2160–2179.

[5]   Wang, S.; Sakurai, H.; Kasarekar, A. *The optimal design in external gear pumps and motors*. IEEE/ASME Trans. Mechatron. 2011, 16, 945–952.

[6]   Dhar, S.; Vacca, A. *A fluid structure interaction-EHD model of the lubricating gaps in external gear machines: Formulation and validation*. Tribol. Int. 2013, 62, 78–90.

[7]   LMS Virtual Lab Tutorial rev. 11-SL1

[8]   Mucchi, E.; Tosi, G.; D'Ippolito, R.; Dalpiaz, G. *A robust design optimization methodology for external gear pumps*. In Proceedings of the ASME 2010 10th Biennial Conference on Engineering Systems Design and Analysis ESDA 2010, Istanbul, Turkey, 12–14 July 2010; pp. 1–10.

[9]   Fiebig, W. *Location of noise sources in fluid power machines*. Int. J. Occup. Saf. Ergon. 2007, 13, 441–450.

[10]   Fiebig, W., Korzyb, M. *Vibration and dynamical loads in externel gear pumps*, ACME, Vol. 15, No. 3, 2015, 680-688.

[11]   J.J. Zang, I.I. Esat, Y.H. Shi, *Load analysis with varying mesh stiffness*, Computers and Structures 70/3 (1999) 273–280.

[12]   R. Muthukumar, M.R. Raghavan, *Estimation of gear tooth deflection by the finite element method,* Mechanisms and Machinery Theory 22 (1987) 177–181.

[13]   [30] K. Umezawa, T. Suzuki, T. Sato, *Vibration of power transmission helical gears (approximate equation of tooth stiffness),* Bulletin of JSME 29 (1986).

[14]   [31] Y. Cai, *Simulation on the rotational vibration of helical gears in consideration of the tooth separation phenomenon (a new stiffness function of helical involute tooth pair)*, Journal of Mechanical Design 177 (1995) 460–469.

[15]   Blankenship G.W., Rajendra Singh R., *A new gear mesh interface dynamic model to predict multi-dimensional force coupling and excitation*, Mechanisms and Machinery Theory 30 (1995) 43–57.

[16]   Blankenship G.W., Rajendra Singh R., *Dynamic force transmissibility in helical gear pairs*, Mechanisms and Machinery Theory 30 (1995) 323–339.

[17]   Wang S., Umezawa K, Houjoh H., Matsumura S., *An analytical investigation of the dynamic behaviour of a helical gear system*, in: Proceedings of the Power Transmission and Gearing Conference, vol. 88, Scottsdale, Arizona, 1996.

[18]   Wang S., *Analysis of nonlinear transient motion of a geared torsional*, Journal of Engineering for Industry 96 (1974) 51–59.

[19]   Carletti, E.; Miccoli, G.; Pedrielli, F.; Parise, G. *Vibroacoustic measurements and simulations applied to external gear pumps: An integrated simplified approach*. Arch. Acoust. 2016, 41, 285–296.

[20]   Mucchi E.; Dalpiaz G. *Numerical vibro-acoustic analysis of gear pumps for automotive applications.* In Proceedings of the International Conference on Noise and Vibration Engineering ISMA 2012, Leuven, Belgium, 17–19 September 2012; pp. 3951–3961.

[21]   Boedo S.; Booker, J.F. *"CUIMPX Reference Manual Version 1.0"* Tribology Assosciates, Itaha, New York 1998

[22]   Booker J.F.*"A Table of the Journal Bearing Integral"* ASME Journal of Basic Engineering vol. 87, 1965

[23]   Booker J.F., Huebne K.H., *"Application of Finite Elements to Lubrication: An Engineerimg Approach,"* Journal of Lubrication Technology, Trans. ASME, vol. 24, no. 4, pp. 313-323, 1972.

[24]   Basri S.,Gethin D.T., *"A Comparative Study of the Thermal Behaviour of Profile Bore Bearings,"* Tribology International, vol. 4, no. 12, pp. 265-276, 1990.

[25]   Ma M.T. and Taylor C.M., *"A Theoretical and Experimental Study of Thermal Effects in a Plain Circular Steadily Loaded Journal Bearing,"* Transactions IMechE, vol. 824, no. 9, pp. 31-44, 1992.

[26]   Gethin D.T., *"Thermohydrodynamic Behaviour of High Speed Journal Bearings,"* Tribology International, vol. 29, no. 7, pp. 579-596, 1996. [8] S.M. Chun, "Thermohydrodynamic lubrication analysis of high-speed journal bearing considering variable density and variable specific heat," Tribology International, vol. 37, pp. 405-413, 2004

Wieslaw Fiebig, Professor, Wroclaw University of Science and Technology, Faculty of Mechanical Engineering, Łukasiewicza 7/9, 50-370 Wrocław, Poland (wieslaw.fiebig@pwr.edu.pl). The author gave a presentation of this paper during one of the conference sessions.

Piotr Kruczek, M.Sc., Collins Aerospace, ul. Bierutowska 65-67, 51-317 Wrocław, Poland (piotr.kruczek@collins.com).

Deterministic chaos in a damage dynamics of the engineering structures under varying environmental and operational conditions

Alexander V. Glushkov, Vasily V. Buyadzhi, Alexander Mashkantsev,
Alexey Lavrenko

Abstract: The paper is devoted to problem of development of effective mathematical and computational tools to studying and forecasting evolutionary dynamics of complex engineering systems (structures), based on the combined using the non-linear analysis methods and chaos theory. An advanced chaos-geometric approach to analysis, processing measurement data and their prediction for a damage parameter time series of the engineering structures is presented. The approach includes a combined group of non-linear analysis and chaos theory methods such as a correlation integral approach, average mutual information, surrogate data, false nearest neighbours algorithms, the Lyapunov's exponents and Kolmogorov entropy analysis, nonlinear prediction models etc. As illustration we present the results of the numerical investigation of the chaotic elements in the dynamical parameters time series for experimental cantilever beam (forcing and environmental conditions are imitated by the damaged structure, variable temperature and availability of a pink-noise force). The data on the topological and dynamical invariants are listed. The perspectives of application to different engineering structures analysis are indicated.

1. Introduction

An analysis, identification and further prediction of the presence of damages (cracks), which above a certain level may present a serious threat to their performance of the technical structures, remains challenging problem in their monitoring. the engineering structures. The treatment requires extensive use of measurement and advanced mathematical and computational tools of processing. Usually change of structural dynamic properties due to environmental, operational and other effects (temperature, moisture, pressure etc) allows to detect an existence, location and size of damages. Changing these conditions may cause significant changes in their properties and result in the damage detection algorithms to false decisions [1-9].

From experimental viewpoint, especially valuable are now methods of nondestructive testing, in particular, vibrodiagnostics (c.g., Refs. [1-4]). Each class and even each type of equipment is characterized by its own separate sets of criteria for assessing the vibration state, depending on the conditions of assembly, installation, operation, etc. A certain one-sidedness of the vibrodiagnostic methods, based primarily on the primary Fourier transform of the signal, does not allow for an

integrated approach to solving the problem. The wide spread and more advanced methodologies such as wavelet analysis, subspace-based identification methodologies, regression analysis, singular value decomposition, auto-associative neural network and factor analysis under situation etc have been discussed [1-5]. Especial interest attracts the pointwise summation of similar Wavelet Transform Modulus Maxima decay lines, which was used in [3] to detect the damages under varying environmental and operational conditions. However, a problem of development of new advanced mathematical and computational tools for analysis remains actual.

In this paper we present and apply an advanced computational approach to analysis, modelling and processing the corresponding chaotic time series, which represent the structural dynamic properties of the engineering structures. The computational code applied includes a combined set of non-linear analysis and chaos theory methods such as an autocorrelation function method, correlation integral approach, average mutual information, surrogate data, false nearest neighbours algorithms, the Lyapunov's exponents (LE) and Kolmogorov entropy analysis, spectral methods and nonlinear prediction (predicted trajectories, neural network etc) algorithms (in versions [10-24]). The results of the numerical investigation of the chaotic elements in time series for the experimental cantilever beam [3] (the forcing and environmental conditions are imitated by the damaged structure, the variable temperature and availability of the pink-noise force) are presented. All computing is performed with using "Geomath" and "Quantum Chaos" computational codes [20-36].

2. A nonlinear analysis and processing data of the engineering structure dynamical parameter time series: Chaos-geometric approach

The chaos-geometric computational approach to analysis and processing the measurement data for the complex non-linear systems results in a few steps. In Figure 1 we present the flowchart of the combined vibration-dynamical and chaos-geometric approach to nonlinear analysis and prediction of chaotic dynamics, damage detection and locations of the complex engineering structures (see detailed description of all algorithms in Refs. [5,9,20-25]). Keeping in mind analysis of measurement data on damage detection in the engineering structure, we represent the typical dynamical parameter (say, the displacement quantity) as some scalar series $s(n)=s(t_0+ n\Delta t) = s(n)$, where t_0 is a start time, Δt is time step, and n is number of the values measurements. The main task is to reconstruct phase space using as well as possible information contained in $s(n)$. The method of using time-delay coordinates by Packard et al [11] can be used. The direct using lagged variables $s(n+\tau)$ (here τ is the lag time) results in a coordinate system where a structure of orbits in phase space can be captured. A set of time lags is used to create a vector in d dimensions, $\mathbf{y}(n)= [s(n), s(n + \tau), s(n + 2\tau), .., s(n +(d-1)\tau)]$, the required coordinates are provided. Here d is the embedding dimension, d_E. To determine the proper time lag at the beginning one should use the known method of the linear autocorrelation function $C_L(\delta)$ and look

I. Vibration-dynamical modelling and computing of the damaged complex engineering structures systems
1. Preliminary analysis and processing dynamical variable series for the engineering structure
2. Blind source separation monitoring

⇓

II. Chaos-geometric method. Preliminary study and assessment of the presence of chaos:
1. The Gottwald-Melbourne test: $K \rightarrow 1$ – chaos;
2. Fourier decompositions, irregular nature of change – chaos;
3. Spectral analysis, Energy spectra statistics, the Wigner distribution, the spectrum of power, "Spectral rigidity";

⇓

III. The geometry of the phase space. Fractal Geometry:
1. Computation time delay τ using autocorrelation function or mutual information;
5. Determining embedding dimension d_E by the method of correlation dimension or algorithm of false nearest neighbouring points;
6. Calculation multi-fractal spectra. Wavelet analysis;

⇓

IV. Prediction model:
7. Computing global Lyapynov dimensions LE: λ_α; Kaplan-York dimension d_L, KE, average predictability measure Pr_{max};
8. Determining the number of nearest neighbour points NN for the best prediction results;
9. Methods of nonlinear prediction. Neural network algorithm, the algorithm optimized trajectories, stochastic propagators etc ...;

Figure 1. Flowchart of the advanced chaos-geometric approach to nonlinear analysis and prediction of chaotic dynamics, damage detection and locations of the complex engineering structures

for that time lag where $C_L(\delta)$ first passes through 0. The alternative additional approach is provided by the method of average mutual information (for example, see [5,17-22]).

The further next step is to determine the embedding dimension, d_E, and correspondingly to reconstruct a Euclidean space R^d large enough so that the set of points d_A can be unfolded without ambiguity. The dimension, d_E, must be greater, or at least equal, than a dimension of attractor, d_A, i.e. $d_E > d_A$. To reconstruct the attractor dimension (see details in [5,11-20]) and to study the signatures of chaos in a time series, one could use different methods, however, the most effective ones are represented by the correlation integral algorithm and the false nearest neighbours [5,13,16]. The principal question of studying any complex system with a non-linear chaotic dynamics is to build the

corresponding prediction model and define how predictable is a chaotic system. At preliminary step it means the obligatory determination of such characteristics as the Kolmogorov entropy K_{entr} (and correspondingly the predictability measure as it can be estimated by K_{entr}), the LE, the Kaplan-Yorke dimension. Let us remind that according to the standard definition, the LE are usually defined as asymptotic average rates and they are related to the eigenvalues of the linearized dynamics across the attractor. Naturally, the knowledge of the whole spectrum of the LE allows to determine other important invariants such as the Kolmogorov entropy and the attractor's dimension. The Kolmogorov entropy is determined by the sum of the positive LE. The estimate of the dimension of the attractor is provided by the Kaplan-Yorke conjecture. The details of construction of the possible prediction models for non-linear systems with a chaotic elements can be found in Refs. [5,9-30].

3.   Input data, numerical results and conclusions

As the initial data we use the data of the corresponding cantilever beam (excited by white and pink noise forces) time domain response series [3]. The detailed description of the experimental setup of a cantilever beam is presented in Ref. [3]. Here we only note that it consists of steel having the following dimensions: length 592 mm, width 30 mm, and thickness 1.5 mm, a density of $7.87 \cdot 10^{-6}$ kg/mm^3, Young modulus of $200 \cdot 10^6$ mN/mm^2, and second moment of area of 8.44 mm^4. The electrodynamic shaker was used to excite the cantilever beam and it was connected to the beam via a stringer rod to minimize the interaction between the shaker and the structure.

Figure 1 shows the the typical experimental cantilever beam time domain response series under the definite environmental and forcing conditions (the series is related to the case of the damaged structure, the variable temperature and availability of the pink-noise force) [3]. In table 1 we list data on the time delay (τ), depending on the different values of the autocorrelation function (C_L) and the first minimum of mutual information (I_{min1}) for the studied time domain response series in a case of the damaged structure, the variable temperature and availability of the pink-noise force. The correlation exponents (d_2) and embedding dimensions determined by false nearest neighbours method (d_N) with percentage of false neighbours (in parentheses) are listed in Table 1 too. Analysis of the obtained data shows that the correlation exponent d attains saturation with an increase in the embedding dimension, and the system is generally considered to exhibit chaotic elements.

The Table 2 summarizes the data of computational reconstruction of the attractors (correlation dimension   (d_2), embedding dimension (d_E), the first two LE   (λ_1 and λ_2), the Kaplan-Yorke dimension (d_L), as well as the Kolmogorov entropy (K_{entr}), and average limit of predictability (Pr_{max}). The saturation value of the correlation exponent is defined as the correlation dimension (d_2) of the attractor. The similar data for a reconstruction of the attractor dimension have been obtained by using the alternative false nearest neighbouring points method (version [5]).
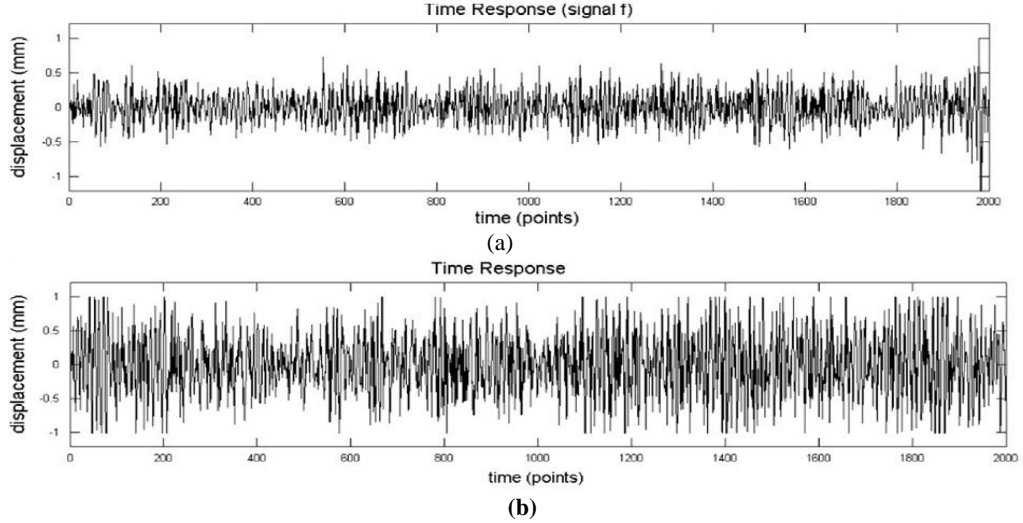
Figure 2. The cantilever beam time domain response series [3] for the case of the damaged structure:
(a) constant T, pink-noise force; (b) variable temperature and pink-noise force (see text).

Table 1. The time delay (lag), depending on the different values of the autocorrelation function (C_L), the first minimum of mutual information (I_{min1}) and the correlation exponents (d_2) and embedding dimensions determined by false nearest neighbours method (d_N) with percentage of false neighbours (in parentheses) calculated for various time lags (τ) for the time series studied (see text)

		d_2	d_N
$C_L = 0$	114		
$C_L = 0.1$	68	7.68	9 (9.1)
$C_L = 0.5$	6	5.45	6 (1.3)
I_{min1}	9	5.48	6 (1.3)

Table 2. Correlation dimension (d_2), embedding dimension (d_E), first two LE (λ_1 and λ_2), Kaplan-Yorke dimension (d_L), the Kolmogorov entropy (K_{entr}), average limit of predictability (Pr_{max})

d_2	d_E	λ_1	λ_2	d_L	K_{entr}	Pr_{max}
5.45	6	0.0197	0.0061	3,98	0.026	39

The dimension of the attractor is defined as the embedding dimension, in which the number of false nearest neighbouring points is less than 3%. The Kaplan-Yorke dimension is less than the embedding dimension that confirms the correct choice of the latter. The presence of the two positive λ_i suggests the conclusion above regarding presence of the chaotic elements. The concrete technical realization of the methodologies supposes a comparison of the real signals and some elementary ones. Their structure, character and dynamical and topological parameters can be different from each other, which made it possible in the future to relate the invariants of real signals to the attractors of "elementary"

signals and determine the nature of the defect. As the result of analysis of reconstructed attractors on the basis of real signals, a qualitative conclusion can be drawn about the presence and development of the defects in a system and to predict how close the state of a system is to the critical one. It is of a great interest to apply the approach to studying the damages, which above a certain level may present a serious threat to the engineering structures such as the hydrotechnical systems, equipment, including turbochargers, atomic reactors etc for different conditions (c.g., [1-9,31-36]).

Acknowledgments

References

[1] Sadhu, A., Hazra B. A novel damage detection algorithm using time-series analysis-based blind source separation. *Shock and Vibration*. 20 (2013), 423–438.

[2] Gubanova, E.R., Glushkov, A.V., Khetselius, O.Yu., Bunyakova, Yu.Ya., Buyadzhi, V.V., Pavlenko, E.P. *New methods in analysis and project management of environmental activity: Electronic and radioactive waste*. FOP, Kharkiv, 2017.

[3] Tjirkallis, A., Kyprianou, A. Damage detection under varying environmental and operational conditions using Wavelet Transform Modulus Maxima decay lines similarity. *Mech. Syst. Signal Process*. 66-67 (2016), 282–297

[4] Limongelli, M.P. Frequency response function interpolation for damage detection under changing environment. *Mech.Syst.SignalProcess*. 24 (2010), 2898–2913.

[5] Glushkov, A.V. *Methods of a chaos theory*. Astroprint, Odessa, 2012.

[6] Glushkov, A.V., Khetselius, O.Yu., Kuzakon,V.M., Prepelitsa, G.P., Solyanikova, E.P., Svinarenko, A.A. Modeling of interaction of the non-linear vibrational systems on the basis of temporal series analyses (application to semiconductor quantum generators). *Dynamical Systems - Theory and Applications,* Lodz Univ. (2011), BIF110.

[7] Glushkov, A.V., Prepelitsa, G.P., Svinarenko, A.A., Zaichko, P.A. Studying interaction dynamics of the non-linear vibrational systems within non-linear prediction method (application to quantum autogenerators). *Dynamical Systems Theory*, eds. J. Awrejcewicz, M. Kazmierczak, P. Olejnik, J, Mrozowski. Lodz Univ., Łódz. T1 (2013), 467-477.

[8] Glushkov, A.V., Kuzakon, V.M., Ternovsky, V.B., and Buyadzhi, V.V. Dynamics of laser systems with absorbing cell and backward-wave tubes with elements of a chaos. *Dynamical Systems Theory*, eds. J. Awrejcewicz, M. Kazmierczak, P. Olejnik, J, Mrozowski. Lodz Univ., Łódz. T1 (2013), 461-466.

[9] Buyadzhi, V., Glushkov, A., Gurskaya, M., Khetselius, O., Ternovsky, E., Mashkantsev, A., Kirianov, S. A novel combined chaos-geometric and vibration blind source monitoring approach to damage analysis and detection of engineering structures (nuclear reactors) under varying environmental, operational conditions and emergency accidents. *Sens. Electr. and Microsyst. Techn*. 14, 4 (2017), 60-72.

[10] Gottwald, G.A., Melbourne, I. Testing for chaos in deterministic systems with noise. *Physica D.* 212 (2005), 100–110.

[11] Packard, N.H., Crutchfield, J.P., Farmer, J.D., Shaw, R.S. Geometry from a time series. *Phys. Rev. Lett.* 45 (1980), 712–716.

[12] Kennel, M.B., Brown, R., Abarbanel, H. Determining embedding dimension for phase-space reconstruction using a geometrical construction. *Phys. Rev.* A 45 (1992) 3403-3411.

[13] Abarbanel, H.D.I., Brown, R., Sidorowich, J.J., Tsimring, L.Sh. The analysis of observed chaotic data in physical systems. *Rev. Mod. Phys.* 65 (1993), 1331–1392.

[14] Schreiber, T. Interdisciplinary application of nonlinear time series methods. *Phys. Rep.* 308 (1999), 1–64.

[15] Fraser, A.M., Swinney, H.L. Independent coordinates for strange attractors from mutual information. *Phys. Rev. A.* 33 (1986), 1134–1140.

[16] Grassberger, P., and Procaccia, I. Measuring the strangeness of strange attractors. *Physica D.*9 (1983), 189–208.

[17] Khetselius, O.Yu. Forecasting evolutionary dynamics of chaotic systems using advanced non-linear prediction method. *Dynamical Systems Applications*, ed. J. Awrejcewicz, M. Kazmierczak, P. Olejnik, J, Mrozowski. Lodz Univ., Łódz. T2 (2013), 145-152.

[18] Glushkov, A.V., Khetselius, O.Y., Bunyakova, Yu.Ya., Prepelitsa, G.P., Solyanikova, E.P., and Serga E.N. Non-linear prediction method in short-range forecast of atmospheric pollutants: low-dimensional chaos. *Dynamical Systems - Theory and Applications,* Lodz. (2011), LIF111.

[19] Glushkov, A.V., Khetselius, O.Y., Brusentseva, S.V., Zaichko, P.A., Ternovsky, V.B. Studying interaction dynamics of chaotic systems within a non-linear prediction method: application to neurophysiology. *Advances in Neural Networks, Fuzzy Systems and Artificial Intelligence, Series: Recent Advances in Computer Engineering*, Ed. J.Balicki. WSEAS Pub., Gdansk. 21 (2014), 69-75.

[20] Glushkov, A.V., Svinarenko, A.A., Buyadzhi, V.V., Zaichko, P.A., Ternovsky, V.B. Chaos-geometric attractor and quantum neural networks approach to simulation chaotic evolutionary dynamics during perception process. *Advances in Neural Networks, Fuzzy Systems and Artificial Intelligence, Series: Recent Advances in Computer Engineering*, Ed. J.Balicki. WSEAS Pub., Gdansk. 21 (2014), 143-150.

[21] Glushkov, A.V., Safranov, T.A., Khetselius, O.Yu., Ignatenko, A.V., Buyadzhi, V.V., Svinarenko A.A. Analysis and forecast of the environmental radioactivity dynamics based on methods of chaos theory: General conceptions. *Environmental Problems*. 1, 2 (2016), 115-120.

[22] Khetselius, O.Yu., Brusentseva, S.V., and Tkach, T.B. Studying interaction dynamics of chaotic systems within non-linear prediction method: Application to neurophysiology. *Dynamical Systems Applications*, ed. J. Awrejcewicz, M. Kazmierczak, P. Olejnik, J, Mrozowski. Lodz Univ., Łódz. T2 (2013), 251-259.

[23] Glushkov, A.V., Buyadzhi, V.V., Kvasikova, A.S., Ignatenko, A.V., Kuznetsova, A.A., Prepelitsa, G.P., and Ternovsky, V.B. Nonlinear chaotic dynamics of Quantum systems: Molecules in an electromagnetic field and laser systems. *Quantum Systems in Physics, Chemistry, and Biology. Series: Progress in Theoretical Chemistry and Physics,* ed. A.Tadjer, R.Pavlov, J.Maruani, E.Brändas, G.Delgado-Barrio. Springer, Cham. 30 (2017), 169-180.

[24] Glushkov, A.V. *Relativistic Quantum theory. Quantum Mechanics of Atomic Systems.* Astroprint, Odessa, 2008.

[25] Glushkov, A.V., Ternovsky, V.B., Buyadzhi, V.V., Prepelitsa, G.P. Geometry of a Relativistic Quantum Chaos: New approach to dynamics of quantum systems in electromagnetic field and uniformity and charm of a chaos. *Proc. Intern. Geom. Center*. 7, 4 (2014), 60-71.

[26] Glushkov, A.V., Gurskaya, M.Yu., Ignatenko, A.V., Smirnov, A.V., Serga, I.N., Svinarenko, A.A., Ternovsky, E.V., Computational code in atomic and nuclear quantum optics: Advanced computing multiphoton resonance parameters for atoms in a strong laser field. *J. Phys: Conf. Ser*. 905, 1 (2017), 012004.

[27] Bunyakova, Yu.Ya., Glushkov, A.V. *Analysis and forecast of the impact of anthropogenic factors on air basein of an industrial city*. Ecology, Odessa, 2010.

[28] Bunyakova, Yu.Ya., Khetselius, O.Yu. Non-linear prediction statistical method in forecast of atmospheric pollutants. *Proc. of 8th International Carbon Dioxide Conference*. T2-098 (2009).

[29] Buyadzhi, V.V., Glushkov, A.V., Mansarliysky, V.F., Ignatenko, A.V., Svinarenko A.A. Spectroscopy of atoms in a strong laser field: New method to sensing AC Stark effect, multiphoton resonances parameters and ionization cross-sections. *Sensor Electr. and Microsyst. Techn*. 12, 4 (2015), 27-36.

[30] Glushkov, A.V., Mansarliysky, V.F., Khetselius, O.Yu., Ignatenko, A.V., Smirnov, A., and Prepelitsa, G.P. Collisional shift of hyperfine line for thallium in an atmosphere of the buffer inert gas. *J. Phys.: Conf. Ser*. 810 (2017), 012034.

[31] Glushkov, A., Khetselius, O., Svinarenko, A., Serbov, N. The sea and ocean 3D acoustic waveguide: rays dynamics and chaos phenomena. *J. Acoust. Soc. America*. 123, 5 (2008), 3625.

[32] Prepelitsa, G.P., Buyadzhi, V.V., Ternovsky, V.B. Non-linear analysis of chaotic self-oscillations in backward-wave tube. *Photoelectronics.* 22, (2013), 103-107.

[33] Glushkov, A.V., Svinarenko, A.A., Loboda, A.V. *Theory of neural networks on basis of photon echo and its program realization*. TEC, Odessa, 2003.

[34] Glushkov, A; Khetselius, O; Svinarenko, A.; Buyadzhi, V. *Spectroscopy of autoionization states of heavy atoms and multiply charged ions*. TEC, Odessa, 2015.

[35] Khetselius, O., Glushkov, A., Dubrovskaya, Yu., Chernyakova, Yu., Ignatenko, A., Serga, I., Vitavetskaya, L., Relativistic quantum chemistry and spectroscopy of exotic atomic systems with accounting for strong interaction effects. *Concepts, Methods and Applications of Quantum Systems in Chemistry and Physics*. Springer, Cham, 31 (2018), 71-91.

[36] Glushkov, A.V., Khetselius, O.Yu., Svinarenko, A.A., Buyadzhi, V.V. *Methods of computational mathematics and mathematical physics*. *P.1*. TES, Odessa, 2015.

Alexander V. Glushkov, Professor: Odessa State Environmental University, Pure and Applied Mathematics Department, L'vovskaya str. 15, 65009 Odessa, Ukraine (*glushkovav@gmail.com*). The author gave a presentation of this paper during one of the conference sessions

Vasily V. Buyadzhi, Assoc.-Professor: Odessa State Environmental University, Pure and Applied Mathematics Department, L'vovskaya str. 15, 65009 Odessa, Ukraine (*buyadzhivv@gmail.com*).

Alexander Mashkantsev, M.Sc. (Ph.D. student): Odessa State Environmental University, Pure and Applied Mathematics Department, L'vovskaya str. 15, 65009 Odessa, Ukraine.

Alexey Lavrenko, M.Sc. (Ph.D. student): Odessa State Environmental University, Pure and Applied Mathematics Department, L'vovskaya str. 15, 65009 Odessa, Ukraine.

Complex Patterned Precipitation Dynamics in Toroidal Reactors with Two Diffusion Sources

Huria Ibrahim, Dalia Ezzeddine, Rabih Sultan

Abstract: A toroidal reactor of 1.00 cm cross-sectional diameter, 6.50 cm inner diameter and 8.5 cm outer diameter is filled with $CoCl_2 \cdot 6H_2O$ (0.050 M) and 1% agar gel solution. Two outer electrolytes, of suitably chosen concentrations, are employed to diffuse into the gelled solution: from one end NH_4OH to precipitate $Co(OH)_2$, and from the other end Na_3PO_4 to precipitate $Co_3(PO_4)_2$. The resulting diffusion-precipitation (Liesegang) pattern exhibits unusual trends wherein gaps, and formation of cobalt phosphate hydrates are observed. The self-organized structure reveals a complex underlying dynamical scenario. Using the well-known generic empirical laws, we attempt the computation of the band locations and represent them graphically within the torus.

1. Introduction

Periodic precipitation [1] is the beautiful display of macroscopic precipitate strata, obtained when two co-precipitate ions interdiffuse in a gel medium. Parallel discs of precipitate are obtained in 1D, and concentric rings are observed in 2D [2]. A paradigm of this beautiful outcome scene for the $Co(OH)_2$ system is portrayed in Fig. 1.
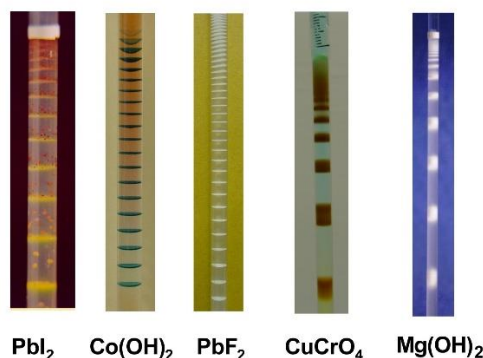
Figure 1. Examples of typical Liesegang patterns for different sparingly soluble salts.

This phenomenon is coined Liesegang banding after R. E. Liesegang for his pioneering discovery in 1896 [3]. A typical analogy with Liesegang patterns in natural landscapes is the alternating bands of geological minerals observed in rocks [4-6]. A further wide spectrum of analogous band formation in a variety of systems is observed in Biology, Physics, Engineering and Medicine. A comprehensive

review of such diversified Liesegang structures is presented in Ref. [7].

Extensive studies on the wealth of features in Liesegang patterns have subsequently followed, and enriched the Physical Chemistry literature. Features include, but are not restricted to, the empirical laws (band location and morphology, spacing, width) [8-10], the intriguing revert spacing [11,12], multiple precipitate systems [13], flow reactors [14] and theoretical modeling [15,16].

Toroidal reactors design has long triggered interest in the chemistry and chemical engineering literature, notably in fluid hydrodynamics. Toroidal reactors with high velocity swirling flow were designed [17] to improve the distribution of mixing energy and jet entrainment ratio in comparison with spherical or hemispherical reactors. The reactor was used to study the $CO+H_2$ combustion and correlate results with predictions based on a coalescence-dispersion model. Using a toroidal reactor operable in both batch and continuous modes, Benkhelifa et al. [18] carried out the flow modeling of a torus reactor for mixing water and glucose solutions. They established that the reactor hydrodynamics is characterized by the presence of two flow regimes: a laminar one and a turbulent one, corresponding to specifically determined ranges of the Reynolds number. Argawal and Nigam [19] used toroidal geometry approximation to model the convective diffusion equation with reaction in helically coiled tubes. They studied the influence of secondary flow for high Dean numbers, under the assumption of neglected axial diffusion. The hydrodynamic behavior of both fine and coarse fused alumina particles moving under the propulsion of gas jets in an annular ring was investigated by Shu et al. [20]. The measured behavior was found to be well predictable by conventional hydrodynamic models. Self-engineered torus fibrils of spectrin were obtained [21] by polymerization of the protein through fractionation and differential precipitation with Ca-ATPase. A variant from these studies in the present work is a longer time scale with diffusion-precipitation reactions carried out in gel.

In the present paper, we investigate the Liesegang phenomenon in a toroidal reactor, wherein the diffusion of two different anions (OH^- from NH_4OH, and PO_4^{3-}) is realized from two opposing ends, into a semi-torus gel medium containing a common cation system (Co^{2+}), thus precipitating $Co(OH)_2$ and $Co_3(PO_4)_2$.

2. Experimental procedure

2.1. 1D tubes

Before starting the reaction in the torus tube, we carry out measurements to establish the spacing and width laws in a 1D tubular reactor, for both $Co(OH)_2$ and $Co_3(PO_4)_2$ patterned precipitations. The detailed procedures were described in Refs. [22] and [23]. A typical appearance of the obtained patterns for the two precipitates is shown in Fig. 2.
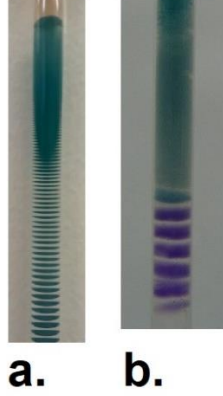
Figure 2. $Co(OH)_2$ pattern (a) and $Co_3(PO_4)_2$ pattern (b) in 1D tubes.

We measure the location of the bands for different values of the outer electrolyte concentration (a_0) and the inner electrolyte concentration (b_0), then determine the spacing coefficient p in the well-known Jablczynski spacing law [4]:

$$\frac{x_{n+1}}{x_n} = 1 + p(a_0, b_0) \tag{1}$$

where x_n is the location of band numbered n. Then the spacing coefficient p is taken to obey the so-called Matalon-Packter law [9,24]:

$$p(a_0, b_0) = F(b_0) + G(b_0)/a_0 \tag{2}$$

where $F(b_0)$ and $G(b_0)$ are taken to be constants for a given b_0. We then determine $F(b_0)$ and $G(b_0)$ by fitting the plot of the spacing coefficient p versus $1/a_0$ into a straight line. We perform the measurements in a regular tube (not the torus), and then we equate the band location x_n to the length of the circular arc within the torus starting from a preset origin. The band location from that origin corresponds to the angle θ_n swept within the torus, corresponding to the arc of length x_n, given by:

$$\theta_n = x_n/r \tag{3}$$

where r is the radius of the torus reactor.

The values from the fittings for $Co(OH)_2$ and $Co_3(PO_4)_2$ are recorded in Table 1.

	F (b_0)	**G (b_0)**
$Co(OH)_2$	0.016	0.0983
$Co_3(PO_4)_2$	0.071	0.010

Table 1. Functions $F(b_0)$ and $G(b_0)$ for the salts $Co(OH)_2$
and $Co_3(PO_4)_2$ obtained by curve fitting.

2.2. Experiments in a torus

0.50 g of agarose (Sigma-Aldrich) were weighed and added to 50.0 ml of a pre-prepared 0.050 M $CoCl_2.6H_2O$ (Fluka) in double distilled water. The resulting mixture was heated to 87°C under constant stirring thus yielding a 1.0% (w/w) agar-agar gel. A Pyrex tubular reactor of toroidal shape is clamped in a vertical, upright position; then using a long ended Pasteur pipette, the Co^{2+}-doped gel solution is transferred to the torus, until the two ends of the torus become evenly leveled (a semi-circle). The mixture is left for 4 hours to settle and gel. Afterwards, two solutions, 0.50 M Na_3PO_4 and 2.0 M NH_4OH, were delivered simultaneously (using Pasteur pipettes) at the two ends of the torus reactor on top of the gel. The two ends of the (open) toroidal reactor are covered with parafilm paper and placed in a thermostated medium at 20°C. The appearance of the obtained pattern after 4 weeks is displayed in Fig. 3.

Figure 3. Complex pattern obtained by precipitation of $Co(OH)_2$ and $Co_3(PO_4)_2$ in a Liesegang-type experiment carried out in a glass toroidal tube.

3. Analysis of the torus pattern

We distinguish between five main zones in this pattern with rich morphological characteristics. We label those zones A, B, C, D and E, as shown in Fig. 4.a.
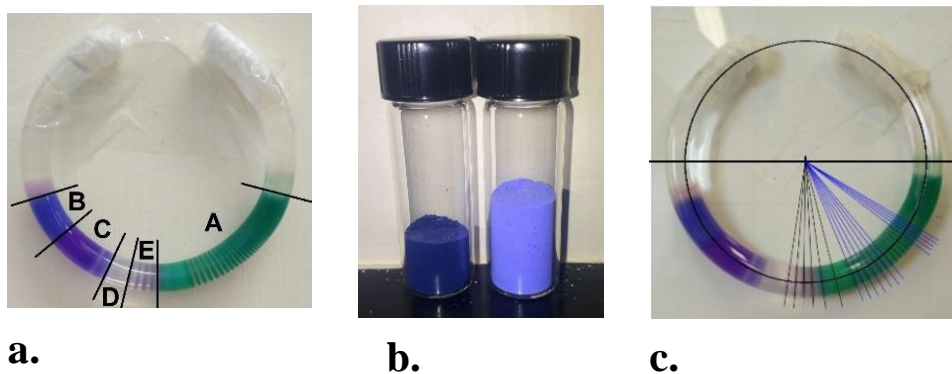
Figure 4. (a) The toroidal pattern shown in Fig. 2, with distinct zones A-E. (b) Dark blue ($Co_3(PO_4)_2 \cdot 4H_2O$) and violet ($Co_3(PO_4)_2$ anhydrous) precipitates after extraction and freeze drying. (c) Angular position of the bands as calculated from their circular arc locations (Eq. 3).

Zone A (right) is α-cobalt hydroxide $Co(OH)_2$, characterized by IR and X-ray diffraction. The color of α-cobalt hydroxide is typically blue (when the crystals or the bands are grown in gelatin). It shifts to green blue in agarose gel, as seen in our experiment. The pattern at the left, wherein the phosphate ion PO_4^{3-} diffuses (from the Na_3PO_4 solution at the left end) notably has a complex structure and morphology. Zone B is characterized as $Co_3(PO_4)_2 \cdot 4H_2O$, of dark blue color shown in the left vial of Fig. 4.b (after freeze drying). Following is zone C, consisting of a mixture of blue $Co_3(PO_4)_2 \cdot 4H_2O$ and anhydrous $Co_3(PO_4)_2$ of typical violet color (see right vial in frame 4.b), hence zone C is an equilibrium between the tetrahydrate and the anhydrous salts. After zone C, we observe a region apparently void of precipitate (zone D). In reality, zone D is predominantly light pink $Co_3(PO_4)_2 \cdot 8H_2O$ [23], which subsequently dehydrates into the violet $Co_3(PO_4)_2$, continuing to form as Liesegang bands.

The pattern on the phosphate side (left of the torus in the photos) thus seems to be controlled by a series of hydration-dehydration steps, as evident from the spectral analysis of the extracted precipitates. The reaction schemes are as follows:

$$3\ CoCl_2 \cdot 6H_2O\ (aq) + 2\ PO_4^{3-}\ (aq) \rightleftharpoons Co_3(PO_4)_2 \cdot 4H_2O\ (s) + 6\ Cl^-\ (aq) + 2\ H_2O\ (l) \tag{4}$$

$$Co_3(PO_4)_2 \cdot 4H_2O\ (s) \rightleftharpoons Co_3(PO_4)_2\ (s)\ + 4\ H_2O\ (l) \tag{5}$$

$$Co_3(PO_4)_2\ (s) + 8\ H_2O\ (l) \rightleftharpoons Co_3(PO_4)_2 \cdot 8H_2O\ (s) \tag{6}$$

$$Co_3(PO_4)_2 \cdot 8H_2O\ (s) \rightleftharpoons Co_3(PO_4)_2\ (s) + 8\ H_2O\ (l) \tag{7}$$
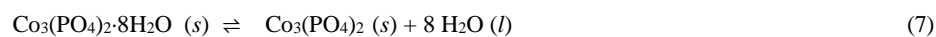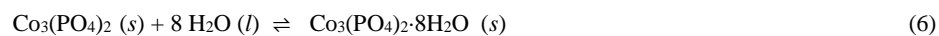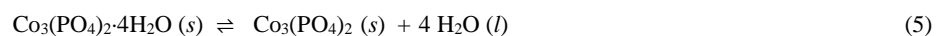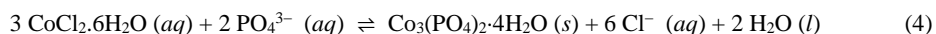
This sequence of reactions, coupled to diffusion in space, leads to the pattern in the torus (Figure 4-left side). The products in reactions (4)-(7) correspond to the dominant precipitates in regions B to E (Figure 4.a) respectively.

4. Simulation

We now turn to the simulation of the pattern using the spacing law and the width law for both the $Co(OH)_2$ and $Co_3(PO_4)_2$ precipitates. The width law [10] is an additional tool to measure the width of a given band as a function of its position, which is an important parameter to include it in the simulation. The relation between the width (w_n) of band n and its position is x_n is:

$$w_n = a \, (x_n)^\alpha \tag{8}$$

With the aid of Fig. 4.c showing the angles from the interfaces at both ends, we incorporate all the parameters of the model into a Mathematica [25] notebook to compute the position and the width of all the bands. We then use graphics to depict the pattern. The result is shown in Fig. 5.

b.

a.
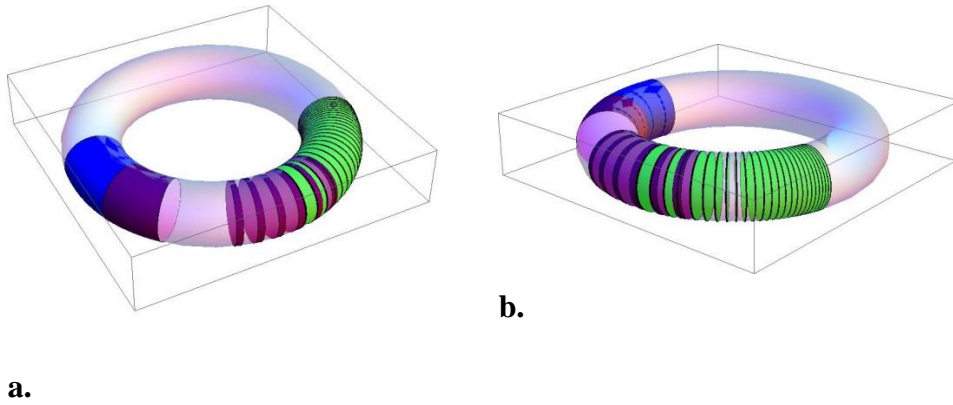
Figure 5: Simulation of the toroidal pattern using Mathematica. (a) focus view on the $Co_3(PO_4)_2$ bands. (b) focus view on the $Co(OH)_2$ bands.

The above simulation code serves as generator of a 'prototype' pattern, which predicts the detailed morphology of the bands obtained upon variation of the parameters of the problem such as the concentrations a_0 and b_0.

5. Conclusions

The main results of the present study may be as summarized as follows:

1. Using a glass toroidal reactor, we carry out Liesegang-type experiments that lead to complex patterns.
2. The phosphate end of the tube yields various patterning zones mediated by various hydration levels of the cobalt phosphate salt, which couple to the existing diffusion-reaction processes.
3. Using the empirical laws, we generate a graphical output of the patterns produced in the torus, which could serve as a model of prediction of the pattern to be formed.

Acknowledgments

References

[1] R. E. Liesegang, R. E., Chemische Fernwirkung. *Lieseg. Photograph. Arch.* 37, 800 (1896) 305-309; continued in 37, 801, 331-336.

[2] Henisch, H. K., *Crystals in Gels and Liesegang Rings*, Cambridge University Press, Cambridge, 1988.

[3] Liesegang, R. E., Über Einige Eigenschaften von Gallerten, *Naturw. Wochenschr.* 11 (1896) 353-362.

[4] Jamtveit B., and Meakin, P., Eds., *Growth, Dissolution and Pattern Formation in Geosystems*, Kluwer, Dordrecht, 1999.

[5] Kruhl, J. H., Ed., *Fractals and Dynamic Systems in Geoscience*, Springer-Verlag, Berlin, 1994.

[6] Ortoleva, P., *Geochemical Self-Organization*, Oxford University Press, New York, 1994.

[7] Sadek, S., and Sultan, R., Liesegang Patterns in Nature: A Diverse Scenery Across the Sciences, in: *Precipitation Patterns in Reaction-Diffusion Systems*, I. Lagzi, Editor, Research Signpost publications, Trivandrum, 2011. Chapter 1, pp. 1-43.

[8] Jablczynski, C. K., Mémoires Présentés à la Société Chimique. Les Anneaux de Liesegang, *Bull. Soc. Chim. France*, 33 (1923) 1592-1602.

[9] Antal, T., Droz, M., Magnin, J., Rácz, Z., and Zrinyi, M., Derivation of the Matalon-Packter Law for Liesegang Patterns, *J. Chem. Phys.*, 109 (1998), 9479-94860

[10] Droz, M., Magnin, J., and Zrinyi, M., Liesegang Patterns: Studies on the Width Law, *J. Chem. Phys.*, 110, 19 (1999), 8618-9622.

[11] Karam, T., El-Rassy, H., and Sultan, R., Mechanism of Revert Spacing in a $PbCrO_4$ Liesegang System, *J. Phys. Chem. A* 115 (2011), 2994-2998.

[12] Kalash, L., Farah, H., Zein Eddin, A., and Sultan, R. Dynamical Profiles of the Reactive Components in Direct and Revert Liesegang Patterns, *Chem. Phys. Lett.* 590 (2013) 69-73.

[13] Sultan, R., Al-Kassem, N., Sultan, A., and Salem, N., Periodic Trends in Precipitate Patterning Schemes Involving Two Salts *Phys. Chem. Chem. Phys. (PCCP)* 2 (2000), 3155-3162.

[14] Das, I., Pushkarna, A. and Bhattacharjee, A., Dynamic Instability and Light-Induced Spatial Bifurcation of HgI_2 and External Electric Field Experiments in Two-Dimensional Gel Media, *J. Phys. Chem.* 95, 9 (1991), 3866-3873.

[15] Müller, S. C., and Polezhaev, A. A. Complexity of Precipitation Patterns: Comparison of Simulation with Experiment, *Chaos* 4 (1994) 631-636.

[16] Al-Ghoul, M., and Sultan, R., Front Propagation in Patterned Precipitation 1. Simulation of a Migrating $Co(OH)_2$ Liesegang Pattern, *J. Phys. Chem. A* 105 (2001), 8053-8058.

[17] Nenniger, J. E., Kridotis, A., Chomiak, J., Longwell, J. J. P., and Sarofim, A. F., Characterization of a Toroidal Well Stirred Reactor, *Twentieth International Symposium on Combustion* 20, 1 (1985), 473-479.

[18] Benkhelifa, H., Legrand, J., Legentilhomme, P. and Montillet, A., Study of the Hydrodynamic Behaviour of the Batch and Continuous Torus Reactor in Laminar and Turbulent Flow Regimes by Means of Tracer Methods, *Chem. Eng. Sci.* 55, 10 (2000), 871-1882.

[19] Argawal, Sh., and Nigam, K. D. P. Modelling of a Coiled Tubular Chemical Reactor, *Chem. Eng. Jour.* 84, 3 (2001), 437-444.

[20] Shu, J., Lakshmanan, V. J., and Dodson, C. E., Hydrodynamic Study of a Toroidal Fluidized Bed Reactor, *Chemical Engineering and Processing: Process Intensification* 39, 6 (2000), Pages 499-506.

[21] Kirkpatrick, F. H., Woods, G. M., Weed, R. I., and La Celle, P. L., Fractionation of Spectrin by Differential Precipitation with Calcium, *Archives of Biochemistry and Biophysics* 175, 1 (1976), 367–372.

[22] Sultan, R., and Sadek, S., Patterning Trends and Chaotic Behavior in Co^{2+}/NH_4OH Liesegang Systems, *J. Phys. Chem.* 100 (1996), 16912-16920.

[23] Karam, T., El-Rassy, H., Zaknoun, F., Moussa, Z., and Sultan, R., Liesegang Banding and Multiple Precipitate Formation in Cobalt Phosphate Systems, *Chem. Phys. Lett*. 525-526 (2012**)**, 54-59.

[24] Matalon, R., and Packter, A. The Liesegang Phenomenon I. Sol Precipitation and Diffusion, *J. Colloid. Sci.* 10 (1955), 46.

[25] S. Wolfram, Mathematica software, version 7.

Rabih Fayez Sultan, Ph.D., Professor: American University of Beirut, Department of Chemistry, P.O. Box 11-0236, 1107 2020 Riad El Solh, Beirut, Lebanon (*rsultan@aub.edu.lb*). The author gave a presentation of this paper during one of the conference sessions.

Huria Ibrahim, B.Sc. (MA student): American University of Beirut, Department of Chemistry, P.O. Box 11-0236, 1107 2020 Riad El Solh, Beirut, Lebanon (*hsi01@mail.aub.edu*).

Dalia Ezzeddine, B.Sc. (M.Sc. student): American University of Beirut, Department of Chemistry, P.O. Box 11-0236, 1107 2020 Riad El Solh, Beirut, Lebanon (*dme34@mail.aub.edu*).

Controlled dynamical system for lowering vibrations of longitudinal forces in railway couplers of multiple-unit railway trains

Jacek Jackiewicz

Abstract: The work presents a technical solution designed for modern, multiple-unit railway-trains, which move at high speeds and have one low-floor to increase the comfort of travelers. In the multiple-unit train without an appropriate control system, braking forces, as well as tractive forces of each unit-vehicle of this train cannot appear with proper values at the same time. In most cases, the time-varying external forces acting on each unit-vehicle can be a source of the generation of unfavorable braking or acceleration waves. Therefore, the proposed solution uses suitable cruise control, coupled with a simple active eliminator of longitudinal vibrations in such type of railway-train, in which each unit-vehicle has its traction motor. Moreover, during braking, the action of the energy recovery system of each unit-vehicle of the train is under the simultaneous influence of cruise control.

1. Introduction

In the multiple-unit train, railway couplers have a meaningful effect on the longitudinal train stability, as well as its dynamics. Since the railway couplers have high stiffness at relatively small inertia compared to the large inertia of each body of the unit-vehicle, in the absence of hydraulic damping in the couplers mechanical vibrations of high frequencies can be easily generated.

Let look at a simplified 2D model of two screw-coupled railway-vehicles illustrated in Fig. 1. In this figure, the designation, F, denotes the propelling force, while the following denotations: R_1, R_2, R_3, and R_4 represent reactions at the track due to lateral force created at buffers. Coupler rotations of this type of connection of two carriages or wagons create lateral in-train forces generated by longitudinal in-train forces. Generated in such way lateral in-train forces become a more and more significant safety issue closely associated with the level of their values. Runnings off the rails of tracks caused by excessive lateral in-train forces have been reported many times.

A the beginning of the 1950s the French National Railway Company began works to develop a high-speed train. During one of the tests carried out in 1955, a disaster happened [1]. On the line, Bordeaux–Hendaye, a train with a locomotive type BB 9104 reached a top speed of circa 331 km/h. However, when trying to break a speed record, the track was displaced sideways by lateral in-train forces generated by its movements. Moreover, the overhead, as well as the traction line, were torn

down. The main reason for this catastrophe has been an unstable run of the prototype of the high-speed train.
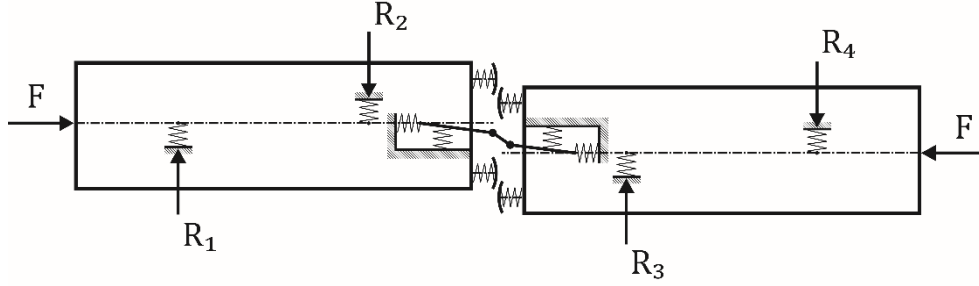
Figure 1. Simplified 2D model of two screw-coupled railway-vehicles.

2. Modeling of longitudinal dynamics of multiple-unit railway-trains

A system of differential equations can describe the longitudinal dynamic behavior of multiple-unit railway-train. After assuming that there is no vertical or lateral movement of each unit-vehicle of the considering train, the established equations of the system for modeling and simulation of this motion-type behavior have a much simpler structure. The application of two-dimensional models, shown in Fig. 2 and considered as multibody systems composed of interconnected rigid bodies, allows developing the governing differential equations for the considering here problem. Moreover, Fig. 2 depicts the differences in the structure of railway-trains with Jacobs' bogies and also with standard train bogies. Jacobs' bogie supports the ends of two adjacent separate unit-vehicles of the train (see lower drawing). However, each bogie, which belongs to any selected unit-vehicle of the train with the standard arrangement, supports the only one unit-vehicle (see upper drawing). The Jacobs idea provides for a reduced number of bogies supporting the train. Nevertheless, this idea has disadvantages associated with higher axle burdens as well as a more complex design (see [2]).

Approaches based on the Newton–Euler equations or the Euler-Lagrange equations are methods of developing equations of motion. For the body i in a multibody system, the Euler-Lagrange equations take the following form:

$$\frac{d}{dt}\left(\frac{\partial L}{\partial \dot{q}_i}\right) - \frac{\partial L}{\partial q_i} + \frac{\partial D}{\partial \dot{q}_i} = Q_i, \tag{1}$$

where $L \overset{\text{def}}{=} -V$ is called the Lagrangian, wherein T is the total kinetic energy and V is the total potential energy of the entire system. Besides, q_i ($i = 1,2, \dots, \text{m}$) are the independent generalized coordinates necessary to describe the system motion at any instant, Q_i ($i = 1,2, \dots, \text{m}$) are the generalized non-conservative forces associated with q_i ($i = 1,2, \dots, \text{m}$), and D is the energy dissipation due to viscous friction. The symbol, m, indicate the number of degrees of freedom of the multibody system.

The shown in Fig. 2a train-model consists of three separate unit-vehicles with the masses: m_i^A, which are connected by the stiffness and damping couplers. Note that k_i^A ($i = 1,2$) and b_i^A ($i = 1,2$) are the stiffness coefficients and the damping coefficients, respectively. In turn, tractive forces of electric or hybrid traction systems, assigned to each unit-vehicles of the train, are denoted by F_i^A ($i = 1,2,3$). Therefore, in a two-dimensional setup written in terms of Cartesian coordinates, the kinetic energy T_A, the potential energy V_A, and the energy dissipation D_A become

$$T_A = \tfrac{1}{2}m_1^A \dot{x}_1^2 + \tfrac{1}{2}m_2^A \dot{x}_2^2 + \tfrac{1}{2}m_3^A \dot{x}_3^2 \,, \tag{2a}$$

$$V_A = \tfrac{1}{2}k_1^A (x_1 - x_2)^2 + \tfrac{1}{2}k_2^A (x_2 - x_3)^2 \,, \tag{2b}$$

$$D_A = \tfrac{1}{2}b_1^A (\dot{x}_1 - \dot{x}_2)^2 + \tfrac{1}{2}b_2^A (\dot{x}_2 - \dot{x}_3)^2 \,. \tag{2c}$$

There are three independent generalized coordinates here, x_1, x_2, and x_3. Let use Eq. (1) along with Eq. (2) three-times once with x_1, once with x_2 and once with x_3. So, the three Euler–Lagrange equations are

$$m_1^A \ddot{x}_1 + c_1^A (\dot{x}_1 - \dot{x}_2) + k_1^A (x_1 - x_2) = F_1^A - R_1^A \,, \tag{3a}$$

$$m_2^A \ddot{x}_2 - b_1^A \dot{x}_1 + (b_1^A + b_2^A)\dot{x}_2 - b_2^A \dot{x}_3 - k_1^A x_1 + (k_1^A + k_2^A)x_2 - k_2^A x_3 = F_2^A - R_2^A, \tag{3b}$$

$$m_3^A \ddot{x}_3 + b_2^A (\dot{x}_3 - \dot{x}_2) + k_2^A (x_3 - x_2) = F_3^A - R_3^A \,. \tag{3c}$$

(a)

(b)
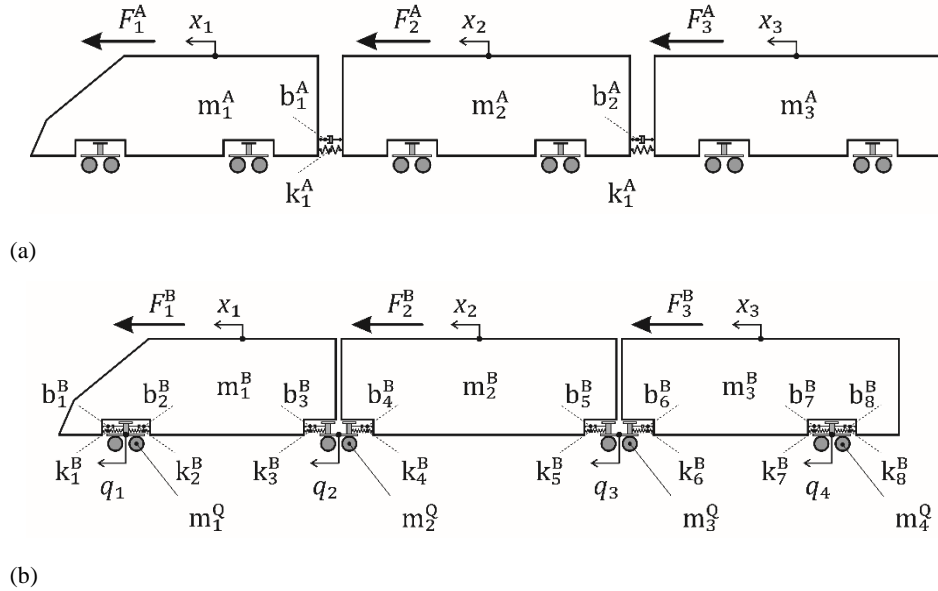
Figure 2. Models of multiple-unit railway trains.

In the above system of equations, R_i^A ($i = 1,2,3$) are summary forces of the resistance to motion.

Similarly, to describe the motion of the rigid body elements of railway-train model illustrated in Fig. 2b, let first determine the kinetic energy T_B, the potential energy V_B, and the energy dissipation D_B

$$T_B = \tfrac{1}{2}\mathrm{m}_1^B \dot{x}_1^2 + \tfrac{1}{2}\mathrm{m}_2^B \dot{x}_2^2 + \tfrac{1}{2}\mathrm{m}_3^B \dot{x}_3^2 + \tfrac{1}{2}\mathrm{m}_1^Q \dot{q}_1^2 + \tfrac{1}{2}\mathrm{m}_2^Q \dot{q}_2^2 + \tfrac{1}{2}\mathrm{m}_3^Q \dot{q}_3^2 + \tfrac{1}{2}\mathrm{m}_4^Q \dot{q}_4^2 \,, \tag{4a}$$

$$\begin{aligned} V_B &= \tfrac{1}{2}\mathrm{k}_1^B (x_1 - q_1)^2 + \tfrac{1}{2}\mathrm{k}_2^B (q_1 - x_1)^2 + \tfrac{1}{2}\mathrm{k}_3^B (x_1 - q_2)^2 + \tfrac{1}{2}\mathrm{k}_4^B (q_2 - x_2)^2 + \\ &+ \tfrac{1}{2}\mathrm{k}_5^B (x_2 - q_3)^2 + \tfrac{1}{2}\mathrm{k}_5^B (q_3 - x_3)^2 + \tfrac{1}{2}\mathrm{k}_7^B (x_3 - q_4)^2 + \tfrac{1}{2}\mathrm{k}_8^B (q_4 - x_3)^2 \,, \end{aligned} \tag{4b}$$

$$\begin{aligned} D_B &= \tfrac{1}{2}\mathrm{b}_1^B (\dot{x}_1 - \dot{q}_1)^2 + \tfrac{1}{2}\mathrm{b}_2^B (\dot{q}_1 - \dot{x}_1)^2 + \tfrac{1}{2}\mathrm{b}_3^B (\dot{x}_1 - \dot{q}_2)^2 + \tfrac{1}{2}\mathrm{b}_4^B (\dot{q}_2 - \dot{x}_2)^2 + \\ &+ \tfrac{1}{2}\mathrm{b}_5^B (\dot{x}_2 - \dot{q}_3)^2 + \tfrac{1}{2}\mathrm{b}_5^B (\dot{q}_3 - \dot{x}_3)^2 + \tfrac{1}{2}\mathrm{b}_7^B (\dot{x}_3 - \dot{q}_4)^2 + \tfrac{1}{2}\mathrm{b}_8^B (\dot{q}_4 - \dot{x}_3)^2 \,, \end{aligned} \tag{4c}$$

Because the train bogies have the masses: m_i^Q ($i = 1,2,3,4$), this model has as much as seven degrees of freedom. Furthermore, since it is not a significant problem to derive the differential equations of motion for the second railway-train model, it will be here skipped preserving the compactness of the presented description.

Although each unit-vehicle of the train is subjected to various external loads, only these loads related solely to the longitudinal direction are considered here. The resistance forces acting on each unit-vehicle, while the train is moving on along a straight line, occur as the result of wheel-rail friction, and bearing friction, and, moreover, are independent of the unit-vehicle speed but are functions of its type. Despite occurring the velocity-dependent resistance forces due to track deflection, it is generally assumed that they are to be constant. Based on Davis' relationship [3, 4], the sum, of both rolling and wind resistances acting on the unit-vehicle i, is given as

$$R_i = A_i + B_i v + C_i v^2, \tag{5}$$

where $A_i \overset{\text{def}}{=} (\mathbb{A}_i + \mathbb{B}_i \eta_i)W_i$ and $B_i \overset{\text{def}}{=} \mathbb{C}_i W_i$, wherein W_i is the weight of the vehicle, v its speed, $\mathbb{A}_i$ the rolling resistance coefficient, $\mathbb{B}_i$ bearing resistance coefficient, $\mathbb{C}_i$ the flange resistance (in curved track), C_i the aerodynamic resistance coefficient, and η_i denotes the number of axles. Note that the subscript of each symbol, i, indicates the number assigned to the unit-vehicle.

Sample coefficient values of Davis's constants for the unit-vehicles, which compose the train are given in [3].

3. Applications of train dynamics models and computer simulation implementations

Simulating dynamic systems means solving systems of differential equations, such as given by Eq. (3). The numerical integration of differential equations is a universal way to solve them. A software package of Scilab, called Xcos, for modeling and simulation of explicit and implicit dynamical systems comes with a variety of numerical solvers which can be used to integrate the differential equations describing,

considering here, dynamic systems. Xcos provides functionalities to establish the proper control strategy by simulating testing systems not only in open but also in closed loops.

The posed task is to design a cruise controller to bring the train smoothly up to speed 50 m/s followed by a step back down to 0 m/s utilizing an electric or hybrid traction system, which allows the possibility of the energy recovery. The shown in Fig. 3 model of the controller system generates both the traction force, F_1^A, and the motor regenerative braking force (also represented by F_1^A) directly, by neglecting the dynamics with which one of the selected train motors (or all of them) creates the torque applied to the wheels, as well as, by neglecting the way of the creation of forces at wheel/track interfaces. The introduced subsystem block mimics the longitudinal train-dynamics, represented by Eq. (3), to make the Xcos model of the cruise controller more understandable.
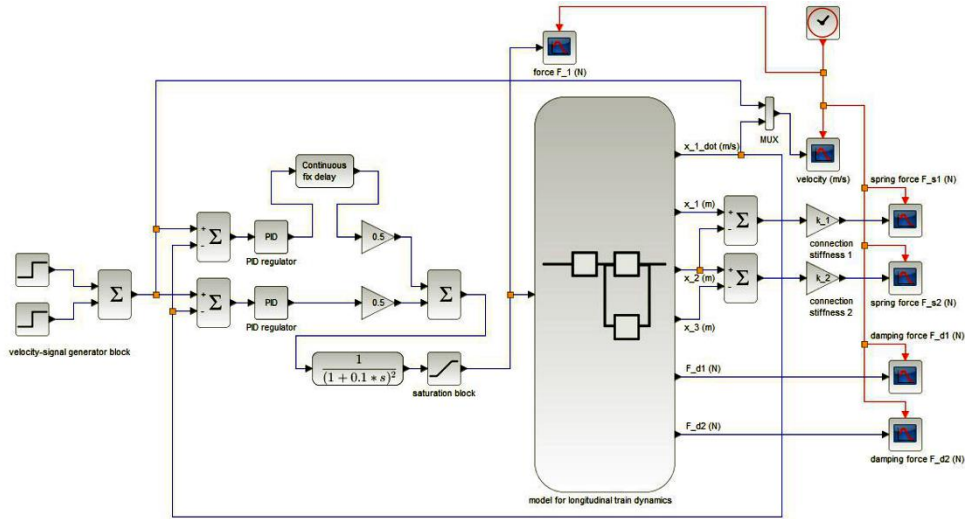
Figure 3. Cruise control system of the multiple-unit railway train.

During the computer simulations, the relationship between coupler forces and traction forces is analyzed, based on under two kinds of operating conditions. Both passive and active vibration damping allow lowering vibrations of longitudinal forces in railway couplers of multiple-unit railway trains. The use, of viscous dampers with the damping coefficients: b_1^A and b_2^A, provides to passively reduce vibrations (see Figs 2, 4, and 5). In turn, the application of active damping ensures to reduce vibrations, and above all lowering the dynamic force values in elastic coupler-elements with the stiffness coefficients: k_1^A and k_2^A as well as in damping coupler-elements with the damping coefficients: b_1^A and b_2^A by the appropriate tuning of values of both traction and braking forces as a result of the selection of values of coefficients: a_1, a_2 and a_3, which take values between 0 and 1 (Fig. 5).

Two separate scenarios of simulation tests are adopted. The first of them, which is implemented by the use of the subsystem shown in Fig. 4, is when the only first unit-vehicle of the multiple-unit railway train has a performing motor enabling the train to be accelerated and braked (i.e., $F_1^A \neq 0, F_2^A = 0, F_3^A = 0$). The second of them, which is implemented by the use of the subsystem shown in Fig. 5, is when all unit-vehicles of the multiple-unit railway train have performing motors (i.e., $F_1^A \neq 0, F_2^A \neq 0, F_3^A \neq 0$).
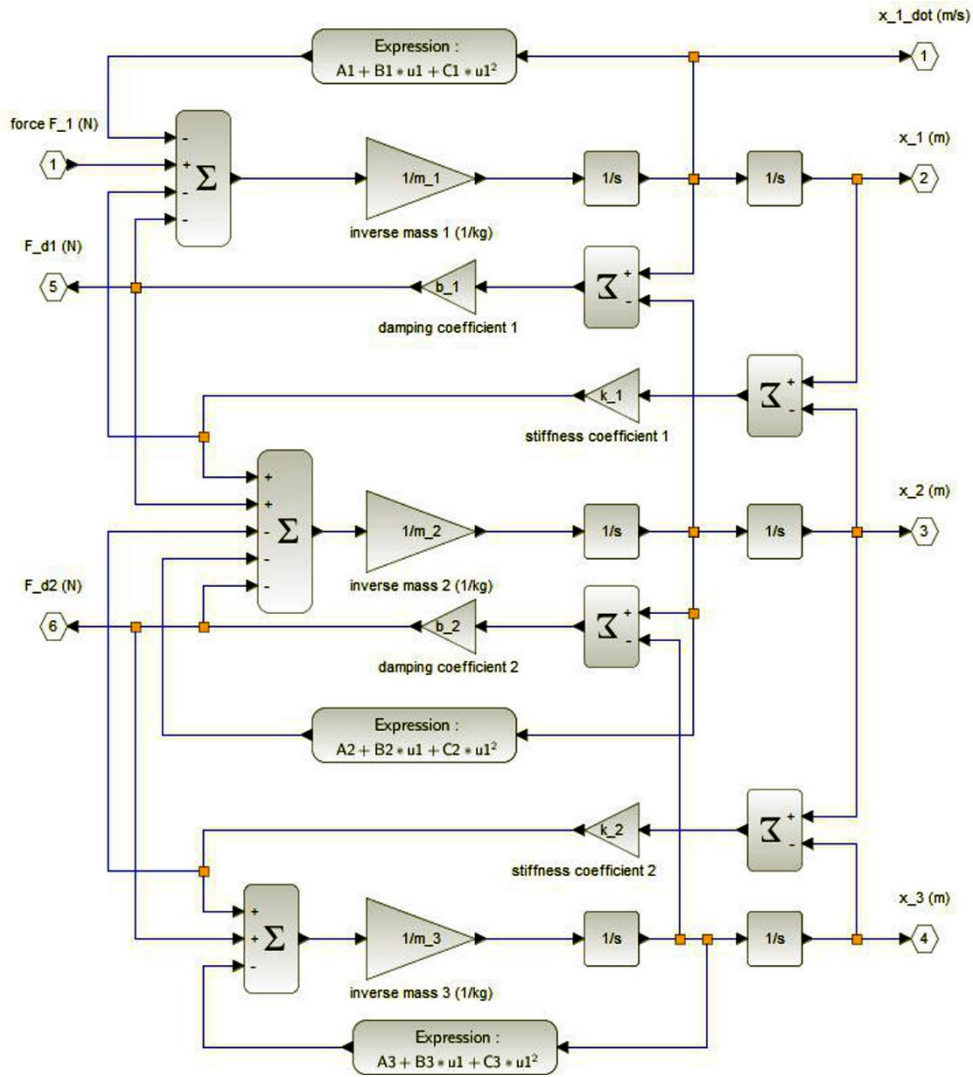
Figure 4. Subsystem block for the longitudinal train-dynamics with only passive vibration damping.
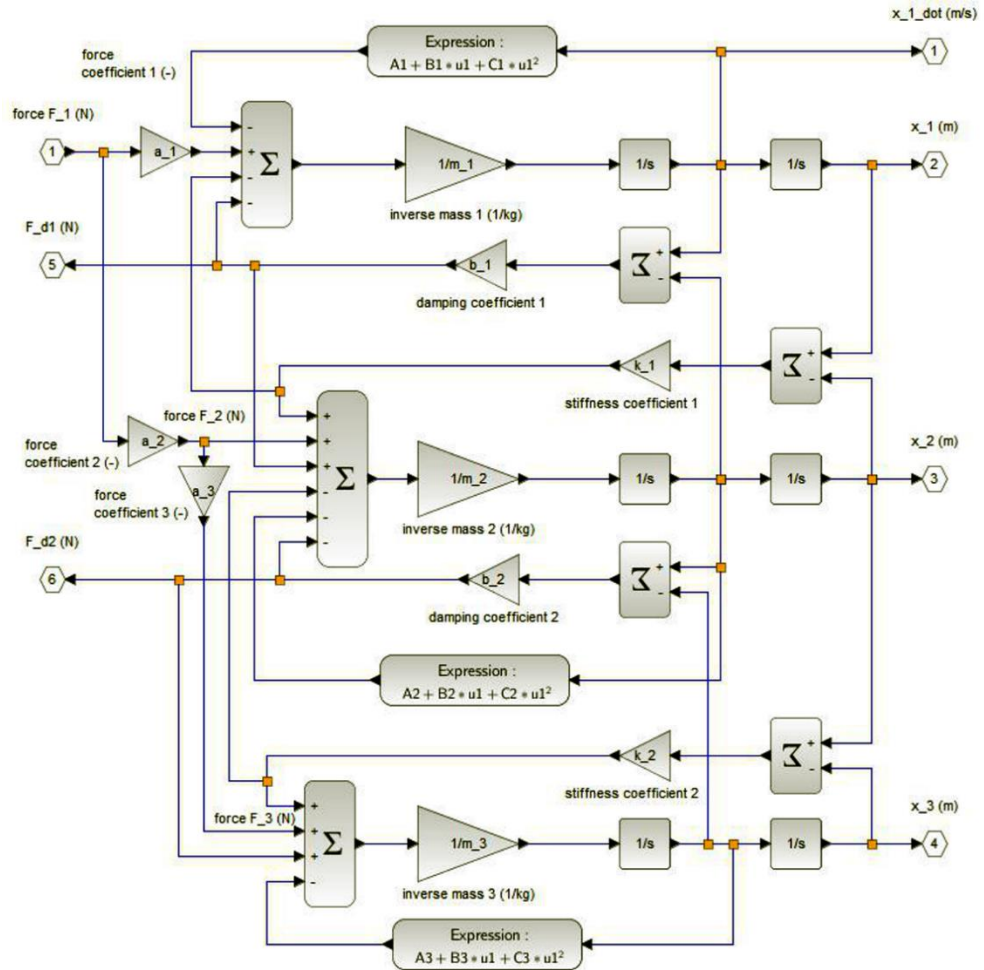
Figure 5. Subsystem block for the longitudinal train-dynamics with both passive and active vibration damping.

The computational results for both Xcos simulation scenarios are depicted in Figs 6, 7, 8, and 9.

177
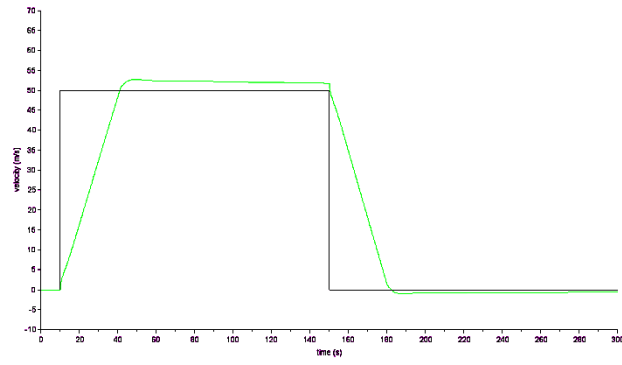
(a)
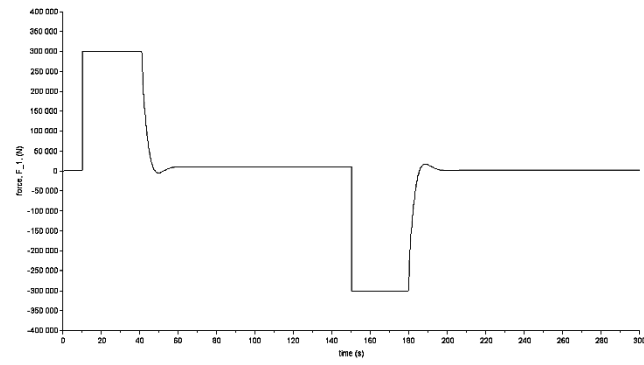
(b)
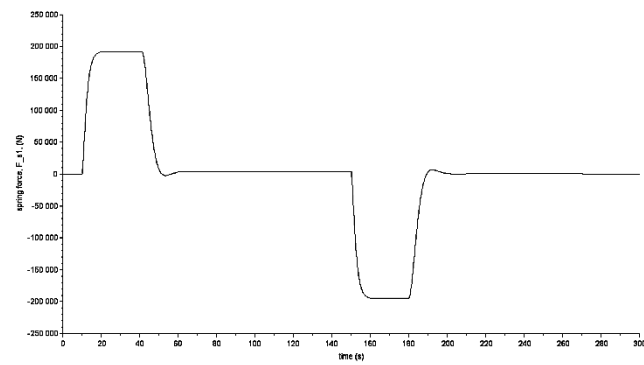
(c)

Figure 6. Computational results for the first scenario: (a) velocity of the train vs. time, (b) traction force, F_1, vs. time, (c) spring force, F_s1, vs. time.
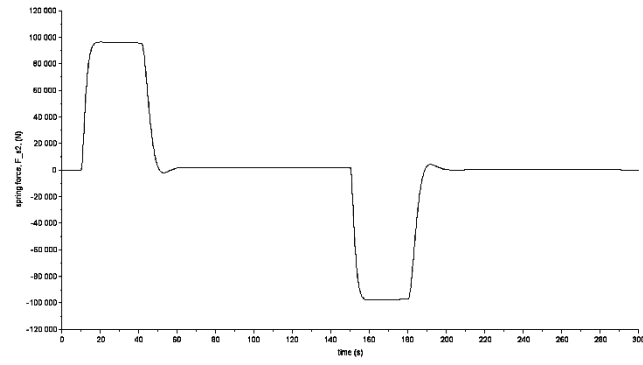
(d)
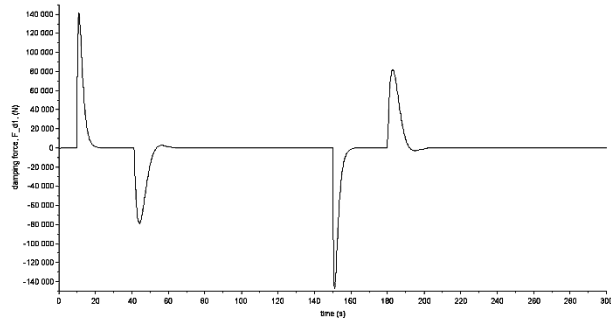
(e)
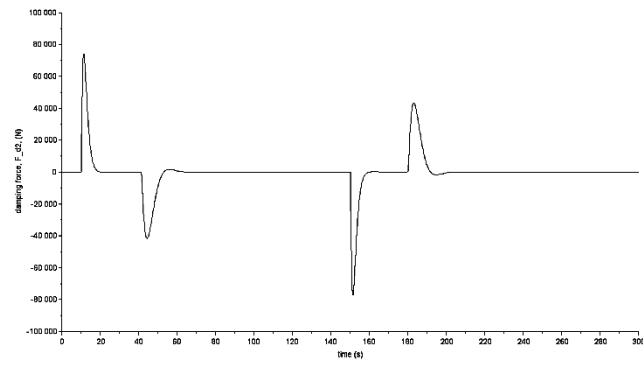
(f)

Figure 7. Computational results for the first scenario: (d) spring force, F_s2, vs. time, (e) damping force, F_d1, vs. time, (f) damping force, F_d2, vs. time (continuation of Fig. 6).

179
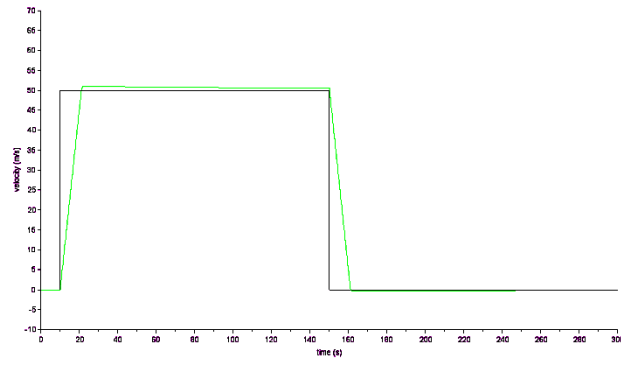
(a)
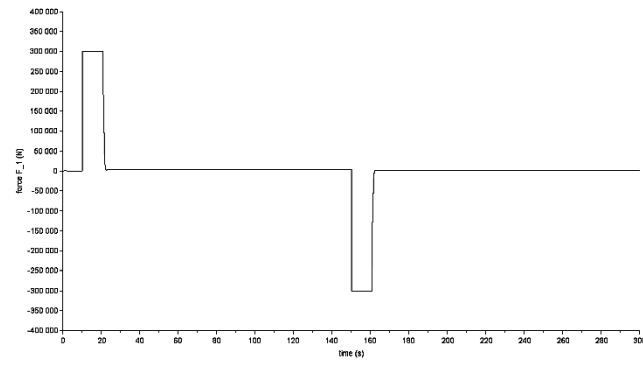
(b)
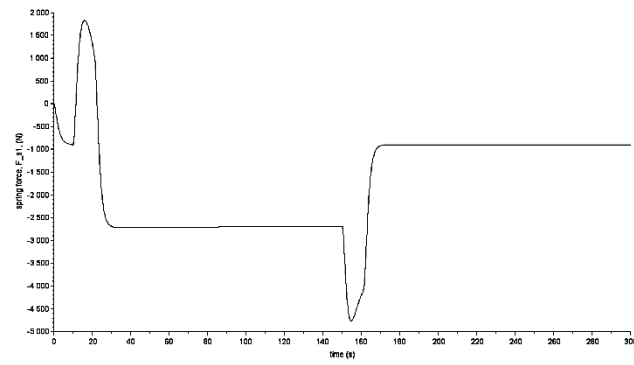
(c)

Figure 8. Computational results for the second scenario: (a) velocity of the train vs. time, (b) traction force, F_1, vs. time, (c) spring force, F_s1, vs. time.
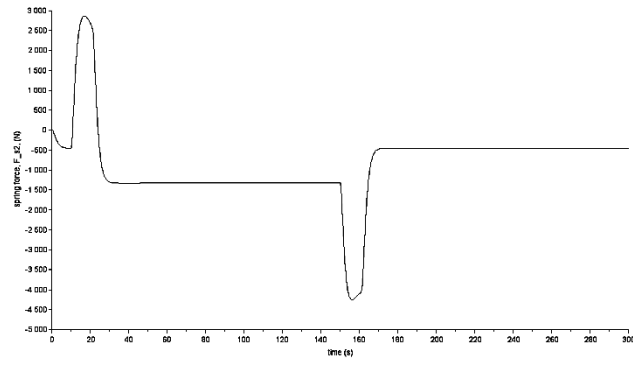
(d)
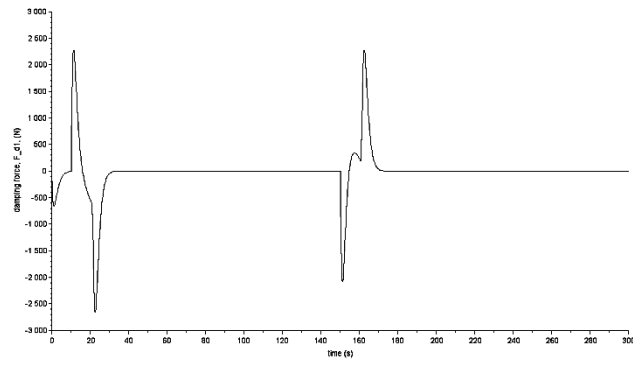
(e)
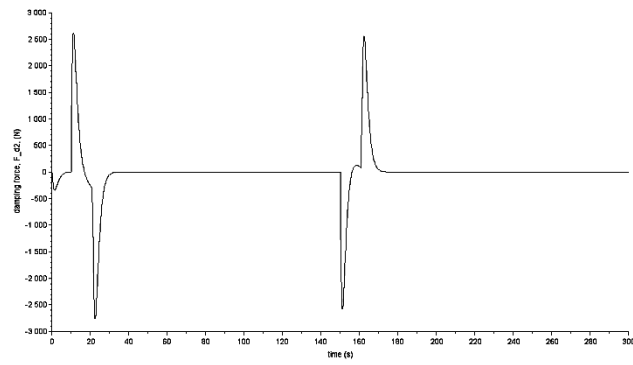
(f)

Figure 9. Computational results for the first scenario: (d) spring force, F_s2, vs. time, (e) damping force, F_d1, vs. time, (f) damping force, F_d2, vs. time (continuation of Fig. 8).

4. Conclusions

By applying the original method for lowering vibrations of longitudinal forces in railway couplers of multiple-unit railway trains, the dynamic forces transmitted through the couplers have been reduced approximately 20-times. As a consequence of that, it seems that the problems associated with the material fatigue of railway couplers become less significant in such a case.

The standard PID regulator is here applied in its double coupled system. The settings of the PID regulator constitute a compromise between the possibility of obtaining simultaneously the low overshoot and the close to zero value of the steady-state error.

Because the dynamic system considered here is nonlinear, the self-tuning control system should be applied [6].

References

[1] Knothe K., Stichel S. *Rail Vehicle Dynamics*. Springer International Publishing AG, Cham, 2017.

[2] http://www.railway-technical.com/trains/rolling-stock-index-l/bogies.html.

[3] Garg V.K., Dukkipati R.V. *Dynamics of railway vehicle systems*. Academic Press, Toronto-Orlando-San Diego-New York-London-Montreal-Sydney-Tokyo, 1984.

[4] Arsene S., Sebeșan I. Analysis of the resistance to motion in the passenger trains hauled by the locomotive LE 060 EA 5100kW. INCAS Bulletin 6 (2014) 13–21.

[5] Spiryagin M., Cole C., Sun Y.Q., McClanachan M., Spiryagin V., McSweeney T. *Design and simulation of rail vehicles*. Taylor & Francis Group, Boca Raton, 2014.

[6] Jackiewicz J. Optimal control of automotive multivariable dynamical systems. In: Awrejcewicz J. (Ed.) *Dynamical systems in theoretical perspective*. Springer International Publishing AG, Cham, 2018, pp 151–168.

Jacek1 Jackiewicz1, Associate Professor: Institute of Technology, Faculty of Mathematics, Physics & Technical Sciences: Kazimierz Wielki University, Chodkiewicza 30, 85-064 Bydgoszcz, Poland (jacek.jackiewicz@ukw.edu.pl).

Adaptive, nonlinear synchronization of a Duffing oscillator with unknown parameters

Jacek Kabziński

Abstract: For many years, the Duffing oscillator was investigated intensively as a benchmark of a chaotic system which demonstrates all phenomena of chaos. Contemporarily, oscillating systems that exhibit Duffing-like behavior are present in many areas: MEMS, laser technique, wireless power harvesters, and many others. Therefore, the problem of controlling a Duffing system becomes more and more practical. A general tracking control problem is solved for a chaotic system (Duffing oscillator) with unknown parameters. The additional requirement that the tracking error must remain inside an imposed hard constraint is considered. Barrier Lyapunov functions (BLF) approach is selected to solve the problem and different BLFs are compared. Several system properties are investigated and the influence of design parameters is discussed.

1. Introduction

The Duffing oscillator [1] has been investigated intensively for many years. It is commonly recognized as a fundamental benchmark of a chaotic system which is able to demonstrate all phenomena of chaos. In modern engineering, oscillating systems that exhibit Duffing-like behavior are present in many areas: MEMS [2], laser technique [3], wireless power harvesters [4] and numerous others. Controlling a Duffing system becomes a practical problem. In practical applications, it is usually desirable to suppress a chaotic motion of a Duffing oscillator to avoid the fracture or degradation of the mechanism. The control aim is usually to navigate the trajectory of a chaotic system to a periodic one, and such a task, formulated as a general tracking problem, is the main topic of this contribution. However, the approach presented here may be as well applied to other tasks, such as chaos synchronization or generation of chaos – "choaotification" [5].

The tracking problem for chaotic systems was investigated intensively and many control techniques were applied. Some classical results applicable to Duffing oscillators are described in [5, 6]. Among many others, the adaptive control techniques based on the backstepping [7] approach are used and recommended [8,9,10,11]. Some distinct nonlinear approaches such as phasor control [12] or fuzzy modular control [13], have been reported recently.

The common drawback of these solutions is that they do not offer any possibility to impose hard constraints on the tracking error. Any design technique includes design parameters which may be used

to shape the system trajectories and the error dynamics, but it is impossible to be sure that the error will remain inside the pre-specified interval for any dynamic conditions. For practical tracking systems, especially microscale mechanisms, respecting hard constraints is a matter of safe operation or failure. Therefore, in this contribution, an adaptive tracking problem for an unknown Duffing oscillator with hard tracking error constraints imposed a priori is formulated and solved.

The proposed solution is based on the adaptive backstepping design with the application of barrier Lyapunov functions (BLF). Control Lyapunov functions of this type were introduced and investigated in recent papers [14-17], mostly for systems with multiple state or output constraints. Here this strategy was adopted for a chaotic Duffing oscillator with unknown parameters. Similar nonlinear control techniques were successfully applied in some previous and contemporary works of the author [18-22]. In this contribution, two BLFs are compared and the influence of design parameters is investigated.

1.1. Problem statement

The Duffing's equation was formulated by Georg Duffing in 1918 [1] to describe the motion of a mechanical system with harmonic excitation and a nonlinear restoring force:

$$
\begin{aligned}
\dot{x}_1 &= x_2, \\
\dot{x}_2 &= -px_2 - p_1x_1 - p_2x_1^3 + q\cos(\omega t) + u,
\end{aligned}
\tag{1}
$$

where t is time, ω - external force frequency, q- it's amplitude, p, p_1, p_2 are real constants. The variable u represents the control – external force added to the periodic excitation. For $p_1 > 0$, the Duffing oscillator can be interpreted as a forced oscillator with a spring whose restoring force is $R = -p_1x_1 - p_2x_1^3$. When $p_2 > 0$, we have a 'hardening spring', and when $p_2 < 0$, we have a 'softening spring', although this interpretation is valid only for small x. For $p_1 < 0$, the Duffing oscillator describes the dynamics of a point mass in a double well potential, and it can be a model of a periodically forced steel beam deflected towards the two magnets.

Because the Duffing oscillator (1) with unknown, constant parameters is considered, eq. (1) may be expressed as

$$
\begin{aligned}
\dot{x}_1 &= x_2, \\
\dot{x}_2 &= f + u,
\end{aligned}
\tag{2}
$$

where

$$
f = -px_2 - p_1x_1 - p_2x_1^3 + q\cos(\omega t) = [p \quad p_1 \quad p_2 \quad q] \begin{bmatrix} -x_2 \\ -x_1 \\ -x_1^3 \\ \cos(\omega t) \end{bmatrix} = A^T \xi.
\tag{3}
$$

The function ξ is known and unknown parameters A will be approximated by the adaptive parameters $\hat{A}$. The error of adaptation will be denoted by $\tilde{A} = A - \hat{A}$.

The control aim is to follow a smooth, desired trajectory $x_{1d}, \dot{x}_{1d}$ in such a way that the tracking error $e_1 = x_{1d} - x_1$ tends to zero asymptotically and the hard constraints are fulfilled. The symmetric constraints imposed on the tracking error are considered:

$$|e_1(t)| \leq \Delta_{e1}. \tag{4}$$

2. Barrier Lyapunov function approach

A barrier Lyapunov function (BLF) is a continuous, positive definite scalar function $V(x)$, defined with respect to the system $\dot{x} = f(x)$ on an open region D containing the origin, has continuous first-order partial derivatives at every point of D, is such that $V(x) \to \infty$ as x approaches the boundary of D, and satisfies: $\exists M, \forall t > 0 \ V(x(t)) < M$ along any system trajectory starting inside D. Usually it is assumed that D is a hyperrectangle defined by $D := \{x: |x_i| \leq \Delta_{xi}\}$. The following corollary can be easily proved [15]:

Corollary 1. Consider a smooth dynamical system $\dot{z} = f(t, x, w)$, with the state variables $z = [x \ w]^T$. Let $V_i(x_i)$ be a BLF satisfying $V_i(x_i) \to \infty$ if $|x_i| \to \Delta_{xi}$. Let $V = \sum_{i=1}^{\dim(x)} V_i(x_i) + w^T Q w$ for any positive definite matrix Q. If the inequality $\dot{V} = \frac{\partial v^T}{\partial z} f \leq 0$ holds anywhere in the set $S = \{(x, w): |x_i| \leq \Delta_{xi}\}$, then any trajectory which fulfills the initial constraints $\forall i \ |x_i| \leq \Delta_{xi}$ remains in S for any t.

2.1. Selection of a BLF

The commonly accepted form of a single variable BLF corresponding to the interval $D = (-\Delta, \Delta)$ is a logarithmic BLF [14-17]:

$$V(\Delta, x) = \frac{1}{2} \ln \frac{\Delta^2}{\Delta^2 - x^2}. \tag{5}$$

In this contribution, we introduce two different BLFs:

$$V_A(\Delta, x) = \frac{1}{2} \ln \frac{\Delta^2 e^{x^2}}{\Delta^2 - x^2}, \quad V_B(\Delta, x) = \frac{\Delta^2}{\pi} \tan\left(\frac{\pi}{2} \frac{x^2}{\Delta^2}\right) \tag{6}$$

Each function possess this attractive feature that for any constant x, $-\Delta < x < \Delta$

$$\lim_{\Delta \to \infty} V_A(\Delta, x) = \lim_{\Delta \to \infty} V_B(\Delta, x) = \frac{1}{2} x^2, \tag{7}$$

so, for increasing bound Δ a barrier Lyapunov function is, in a certain sense, transformed into quadratic Lyapunov function (a standard control Lyapunov function in case of unconstraint design) and the closed-loop system properties may be changed smoothly from the bounded to unbounded case, although the nature of this transformation is different for both functions, as it is illustrated in fig. 1-2.
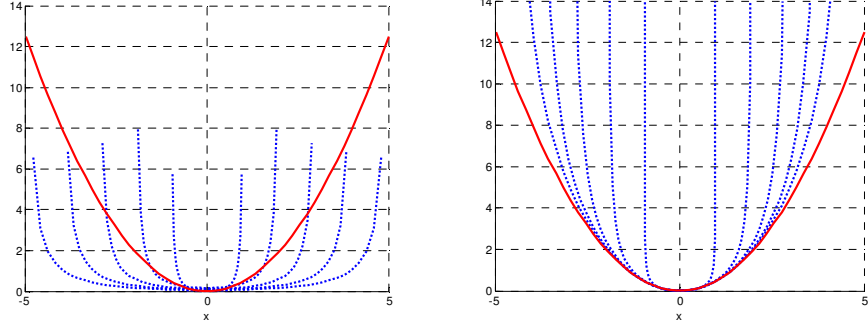
Figure 1. Barrier Lyapunov functions (dotted) for $\Delta = 1, \dots, 5$ and quadratic Lyapunov function (solid) - $V_A(\Delta, x)$ (left) and $V_B(\Delta, x)$ (right)
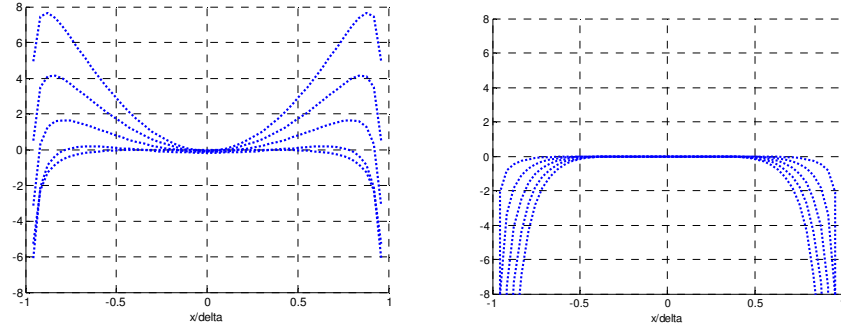
Figure 2. $\frac{1}{2}x^2 - V_A(\Delta, x)$ - (left) and $\frac{1}{2}x^2 - V_B(\Delta, x)$ (right) for $\Delta = 1, \dots, 5$ as a function of $\frac{x}{\Delta}$.

.

The derivative of each function (6) or (7) along a trajectory $x(t)$ possesses a similar form:

$$\dot{V}_*(\Delta, x) = x\dot{x}\varphi_*(\Delta, x), *= A, B, \quad \varphi_A(\Delta, x) = 1 + \frac{1}{\Delta^2 - x^2}, \quad \varphi_B(\Delta, x) = 1 + \tan^2\left(\frac{\pi}{2\Delta^2}x^2\right). \tag{8}$$

Both functions $\varphi_*(\Delta, x)$, $*= A, B$ are strictly positive.

2.2. Control algorithm

The tracking error dynamics is given by the equation

$$\dot{e}_1 = \dot{x}_{1d} - \dot{x}_1 = \dot{x}_{1d} - x_2. \tag{9}$$

The state variable x_2 will be a virtual control for the tracking error. The desired trajectory for x_2 will be denoted by x_{2d} and the error between the desired and the actual value by $e_2 = x_{2d} - x_2$. Hence, the tracking error dynamics may be represented as

$$\dot{e}_1 = \dot{x}_{1d} - x_{2d} + e_2. \tag{10}$$

In order to satisfy the tracking error constraints $|e_1| < \Delta_{e1}$, one the BLFs $V_1(\Delta_{e1}, e_1) = V_*(\Delta_{e1}, e_1)$, $* = A, B$ is applied during the first stage of backstepping. The system derivative is given by:

$$\dot{V}_1 = e_1(\dot{x}_{1d} - x_{2d} + e_2)\varphi_*(\Delta_{e1}, e_1). \tag{11}$$

The choice

$$x_{2d} = \dot{x}_{1d} + k_1 e_1, \tag{12}$$

where k_1 is a positive design parameter results in:

$$\dot{V}_1 = (-k_1 e_1^2 + e_2 e_1)\varphi_*(\Delta_{e1}, e_1), \tag{13}$$

$$\dot{e}_1 = \dot{x}_{1d} - x_{2d} + e_2 = e_2 - k_1 e_1, \tag{14}$$

$$\dot{x}_{2d} = \ddot{x}_{1d} + k_1 \dot{e}_1 = \ddot{x}_{1d} + k_1 e_2 - k_1^2 e_1. \tag{15}$$

The derivative of the desired trajectory $\dot{x}_{2d}$ is available for control purposes. The dynamics of e_2 is described by:

$$\dot{e}_2 = \dot{x}_{2d} - \dot{x}_2 = k_1 e_2 - k_1^2 e_1 + \ddot{x}_{1d} - f - u. \tag{16}$$

A smart way to smooth the trajectories is to introduce the constraint on the second tracking error $|e_2(t)| \leq \Delta_{e2}$, although increasing Δ_{e2} transforms the problem smoothly into the unconstrained case. The Lyapunov function for the second stage of backstepping is selected as

$$V_2(e_1, e_2) = V_1(\Delta_{e1}, e_1) + V_*(\Delta_{e2}, e_2) + \frac{1}{2}\tilde{A}^T \Gamma^{-1}\tilde{A}, \tag{17}$$

where $*$ indicates the same Lyapunov function (A or B) as it was selected in the first loop and the positive definite matrix Γ is selected by the designer. The derivative of the Lyapunov function along the system trajectory is

$$\dot{V}_2 = (-k_1 e_1^2 + e_2 e_1)\varphi_*(\Delta_{e1}, e_1) + e_2\varphi_*(\Delta_{e2}, e_2)(\dot{x}_{2d} - A^T \xi - u) + \tilde{A}^T \Gamma^{-1}\dot{\tilde{A}}. \tag{18}$$

The control u is chosen to cancel unnecessary components and to introduce a stabilizing factor:

$$u = \dot{x}_{2d} - \hat{A}^T \xi + k_2 e_2 + e_1 \frac{\varphi_*(\Delta_{e1}, e_1)}{\varphi_*(\Delta_{e2}, e_2)}, \tag{19}$$

where $k_2 > 0$ is the design parameter. The application of this control law reduces () to

$$\dot{V}_2 = -k_1 e_1^2 \varphi_*(\Delta_{e1}, e_1) - k_2 e_2^2 \varphi_*(\Delta_{e2}, e_2) - \tilde{A}^T\left(\varphi_*(\Delta_{e2}, e_2)e_2 \xi - \Gamma^{-1}\dot{\hat{A}}\right). \tag{20}$$

The simplest adaptive law to cancel the last, unknown term is

$$\dot{\tilde{A}} = \varphi_*(\Delta_{e2}, e_2)e_2 \Gamma\xi \Rightarrow \dot{\hat{A}} = -\varphi_*(\Delta_{e2}, e_2)e_2 \Gamma\xi. \tag{21}$$

<u>Corollary 2.</u> Consider the reference trajectory, the closed loop error system (14), (16) with the adaptation laws (21) and control (19), under all assumptions formulated above. Consider any trajectory

with initial conditions fulfilling $|e_1(0)| \leq \Delta_{e1}, |e_2(0)| \leq \Delta_{e2}$, then the following properties hold along this trajectory:

1. The variables $e_1, e_2, \tilde{A}$ remain inside a compact set and the constraint $|e_1(t)| \leq \Delta_{e1}, |e_2(t)| \leq \Delta_{e2}$ is satisfied.

2. All closed loop signals are bounded.

3. The tracking errors e_1, e_2, converge to zero asymptotically.

Indeed, as $V_{20} := V_2(e_1(0), e_2(0))$ is bounded and $\dot{V}_2 \leq 0$, $V_2 \leq V_{20}$ along the considered trajectory, the corollary 1 yields that $|e_1(t)| \leq \Delta_{e1}, |e_2(t)| \leq \Delta_{e2}$. Moreover $\|\tilde{A}\| \leq \sqrt{\frac{2V_{20}}{\lambda_{min}(\Gamma^{-1})}}$, where $\lambda_{min}(*)$ denotes the smallest eigenvalue of the symmetric matrix $*$. Therefore, the adaptive parameters $\hat{A}$ and the state variables are bounded, and hence, the control u is bounded. The tracking error asymptotic convergence may be obtained by demonstrating that $\ddot{V}_2$ is bounded and making use of the Barbalat's lemma [18].

Note that the error e_2 is not the gap between $\dot{x}_{1d}$ and x_2, but between $x_{2d} = \dot{x}_{1d} + k_1 e_1$ and x_2. Therefore, design parameter k_1 influences the error e_2 directly, and so the selection of Δ_{e2} must be done taking some feasibility conditions into account. The initial error value $e_2(0)$ fulfils

$$e_2(0) = \dot{x}_{1d}(0) + k_1[x_{1d}(0) - x_1(0)] - x_2(0) \tag{22}$$

and therefore depends on the initial conditions, the desired trajectory and the selected design parameter k_1. The constraint Δ_{e2} must be carefully chosen with a sufficient margin with respect to $|e_2(0)|$. Moreover, for any t $|x_2 - \dot{x}_{1d}| \leq k_1 \Delta_{e1} + \Delta_{e2}$, so the increase of the design parameter k_1 improves the convergence of the tracking error e_2, but also enlarges the obtained bound for $|x_2 - \dot{x}_{1d}|$.

3. Numerical experiments

The Duffing oscillator with parameters $p = 0.4, p1 = -1.1, p2 = 1, q = 2.1, \omega = 1.8$, is considered. The control aim is to synchronize the output with a limit cycle described by:

$$x_{1d} = cos(2.5t), \ x_{2d} = \dot{x}_{1d} \tag{23}$$

It is assumed that only the sign of the parameters is known, so the initial values of the estimated parameters are ∓ 1. The system starts at the point $x_1(0) = 1.07$, $x_2(0) = 0$ - outside the desired trajectory. The uncontrolled system demonstrates chaotic behavior, while the typical controlled case with $V_A(\Delta, x)$ and the constraint $\Delta_{e1} = 0.1, \Delta_{e2} = 0.2$ is presented in fig. 3.

The first experiment demonstrates the influence of the position constraint Δ_{e1}, while Δ_{e2} is sufficiently big. The plots are presented in fig.4. The tracking errors are bounded by the stabilizing feedbacks and by the influence of BLFs. For both values $\Delta_{e1} = 0.2, 0.1$ the tracking error is (almost) inside the narrower constraint. For $\Delta_{e1} = 0.2$ it is mostly due to the action of adaptive, stabilizing feedback. For

$\Delta_{e1} = 0.1$ the impact of BLFs is higher, as the trajectory moves closer to the constraint. The narrower constraint $\Delta_{e1} = 0.1$ results in slightly higher values of control and faster movement if the system is close to the constraint. The BLF $V_A(\Delta, x)$ (with logarithm) provides more rapid reaction then $V_B(\Delta, x)$ (with tangent) – what is understandable in context of the plots from fig. 1.
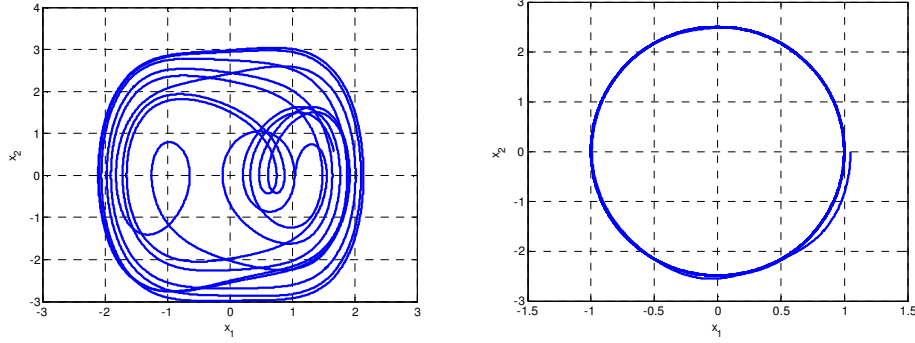
Figure 3. Trajectories of the uncontrolled (left) and controlled (right) Duffing oscillator.
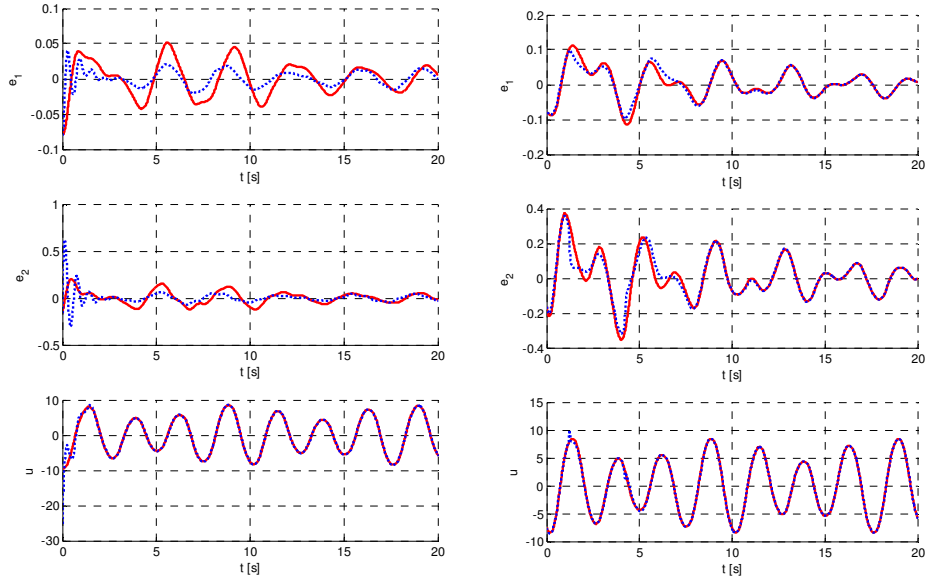
Figure 4. Tracking errors and control for $\Delta_{e2} = 2$ and $\Delta_{e1} = 0.2$ (solid), $\Delta_{e1} = 0.1$ (dotted). $V_A(\Delta, x)$ (left) and $V_B(\Delta, x)$ (right) BLFs are used.

The next experiment is performed to demonstrate the influence of the velocity constraint Δ_{e2}. The plots are presented in fig. 5. More restrictive constraint Δ_{e2} diminishes the tracking error e_2, what is obvious,

but also provides smoother and less-oscillatory trajectory of the position error e_2. Again, the influence of BLF $V_A(\Delta, x)$ (with logarithm) is stronger then $V_B(\Delta, x)$ (with tangent).
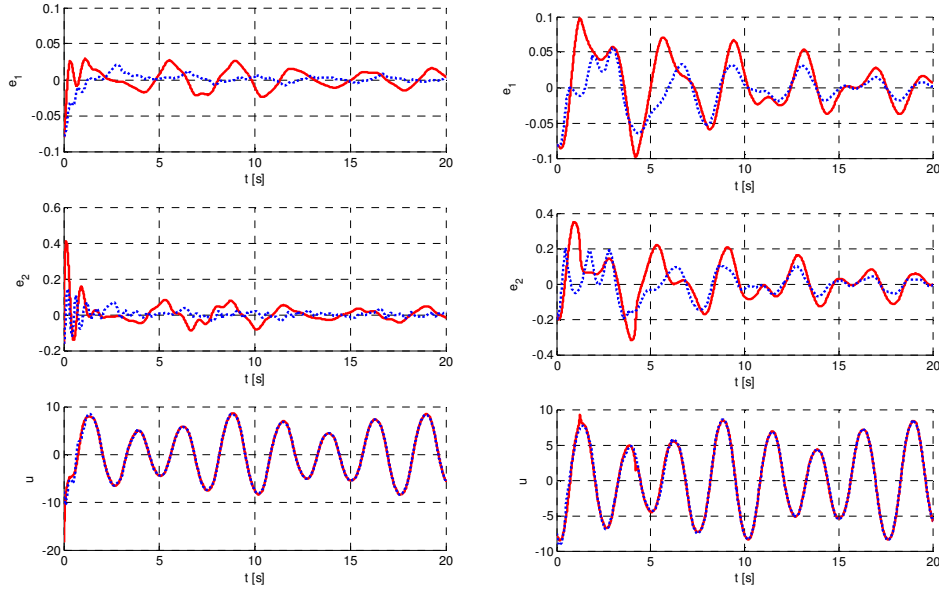
Figure 5. Tracking errors and control for $\Delta_{e1}= 0.1$ and $\Delta_{e2}= 1$ (solid), $\Delta_{e2}= 0.2$ (dotted). $V_A(\Delta, x)$ (left) and $V_B(\Delta, x)$ (right) BLFs are used.

Finally, the Duffing oscillator was synchronized with first two state variables of the Arneodo chaotic system

$$\begin{aligned}
\dot{x}_{1A} &= x_{2A} \\
\dot{x}_{2A} &= x_{3A} \\
\dot{x}_{3A} &= 7.5x_{1A} - 3.8x_{2A} - x_{3A} - x_{1A}^2.
\end{aligned} \tag{24}$$

The output of (24) was scaled to get $x_{1d} = 0.1x_{1A}, \dot{x}_{1d} = 0.1x_{2A}$. The controller was designed with parameters $k_1 = k_2 = 5, \Delta_{e1}= 0.1, \Delta_{e2}= 0.5$. The remaining settings were the same as in the previous examples. The tracking of the trajectories is illustrated in fig. 6 while the signals in the closed-loop system are plotted in fig. 7. The tracking is sufficiently accurate, the tracking errors are kept inside the predefined constraints, control signal is moderate, and the adaptive parameters are bounded (see fig. 8).
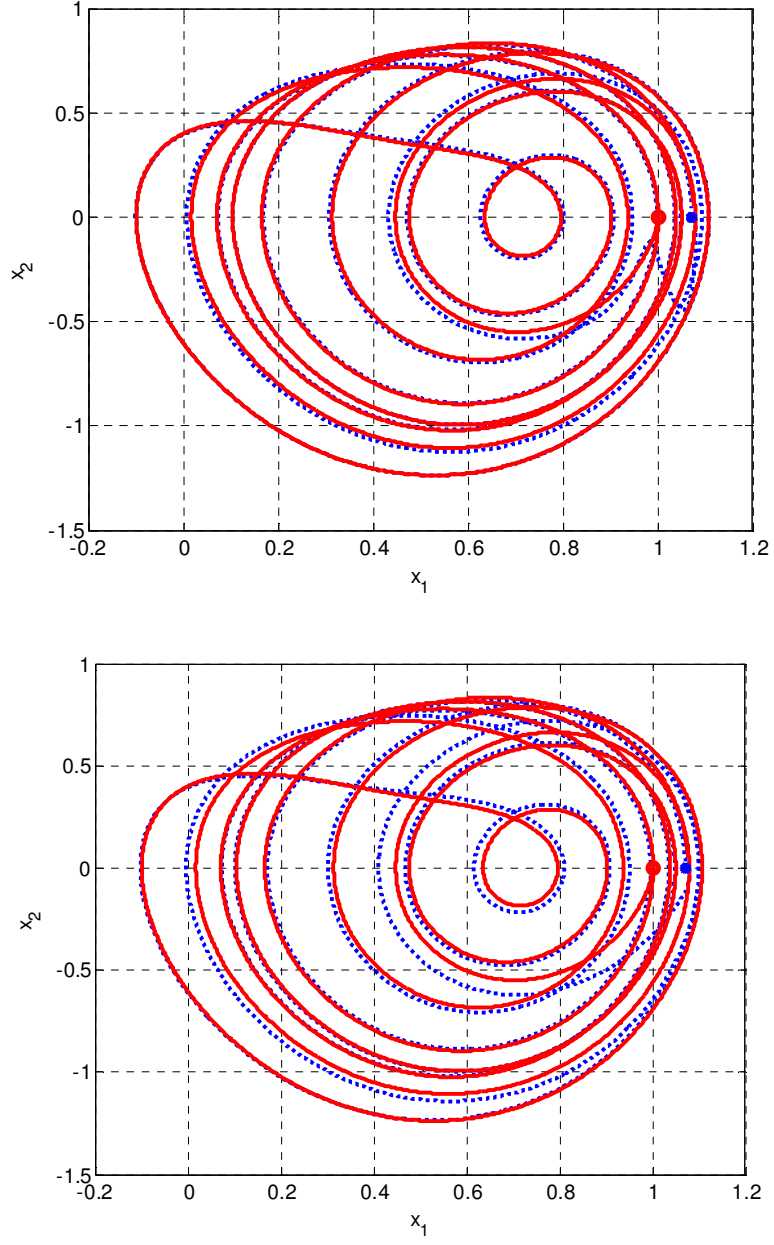
Figure 6. Trajectories of Arneodo system (solid) and the Duffing oscillator (dotted) $\Delta_{e1} = 0.1$ and $\Delta_{e2} = 0.5$. $V_A(\Delta, x)$ (upper) and $V_B(\Delta, x)$ (lower) BLFs are used.
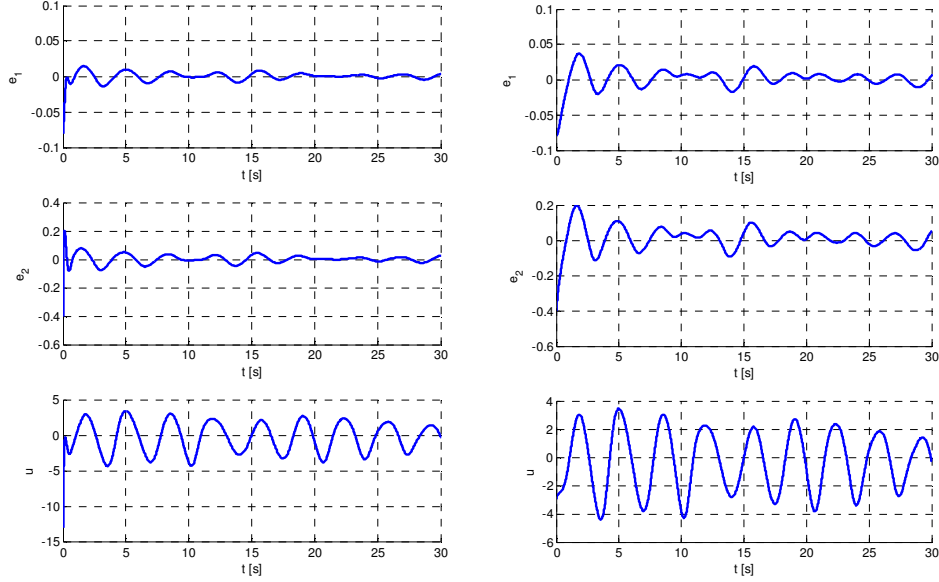
Figure 7. Tracking errors and control – tracking the Arneodo system for $\Delta_{e1} = 0.1$ and $\Delta_{e2} = 0.5$. $V_A(\Delta, x)$ (left) and $V_B(\Delta, x)$ (right) BLFs are used.

4. Conclusions

The proposed approach allows to suppress the chaotic motion of a completely unknown Duffing oscillator and to preserve hard constraints imposed on the tracking errors. Both tested BLFs provide satisfactory results. The one containing logarithmic function results in more aggressive control near the constraint, the one containing tangent function results in slightly smaller control values. Without any doubt, the control system must be tuned properly to the particular application. The design parameters: control gains k_1, k_2, adaptive gain Γ and tracking error bounds Δ_{e1}, Δ_{e2} must be designed appropriately. Values proposed in the discussed examples were selected to demonstrate the system features clearly and are not optimal. The "responsibility" of each design parameter is clear but also interactions among them influence the final choice.

It is noticeable that even small changes of control result in important changes of trajectories - it is not surprising with a chaotic system. Even numerical inaccuracies cause the errors to oscillate (with small amplitude) instead of approaching zero asymptotically. Therefore any practical realization of the controller must be done with proper care and take numerical and real-life aspects into account.

The simplest adaptive law was used in this study, but the adaptive parameters remain bounded. In spite of this, for real-life applications, robust adaptive laws [18] are strongly recommended.

The main drawback of the proposed approach is that the constraints are imposed on the tracking errors and not on the original state variables itself. Another approach based on a special nonlinear state transformation allows to formulate constraints for state variables directly but results in more complicated control [22].
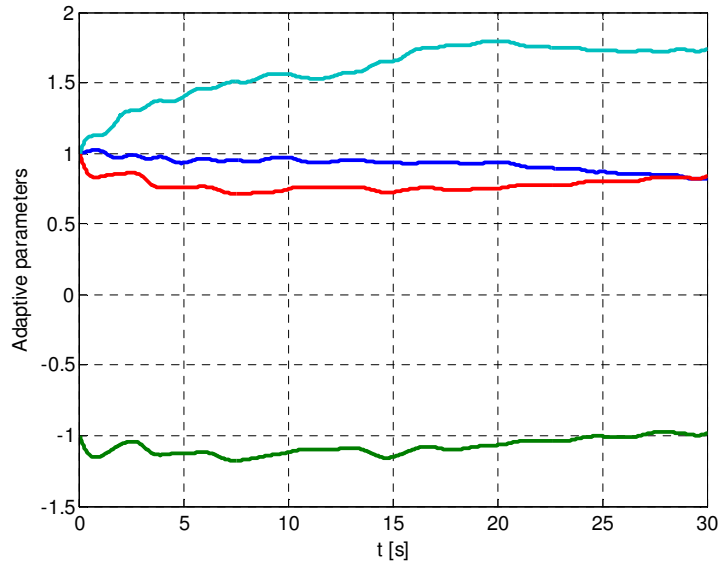
Figure 8. Adaptive parameters while tracking the Arneodo system ($\Delta_{e1} = 0.1$ and $\Delta_{e2} = 0.5$. $V_B(\Delta, x)$ BLFs are used).

References

[1] G. Duffing "Erzwungene Schwingungen bei veränderlicher Eigenfrequenz und ihre Technische Bedeutung" Sammlung Vieweg. Vieweg & Sohn, Braunschweig, 1918.

[2] J. F. Rhoads, S. W. Shaw, and K. L. Turner. Nonlinear Dynamics and Its Applications in Micro- and Nanoresonators. Journal of Dynamic Systems, Measurement, and Control, 132(3):034001, 2010.

[3] U. Hofmann, J. Janes, and H.-J. Quenzer. High-Q MEMS Resonators for Laser Beam Scanning Displays. Micromachines, 3(2), pp. 509–528, 2012.

[4] X. Wang and A. Mortazawi, "Duffing resonator circuits for performance enhancement of wireless power harvesters," *Microwave Symposium (IMS), 2015 IEEE MTT-S International*, Phoenix, AZ, 2015, pp. 1-4.do

[5] Huaguang Zhang, Derrong Liu, Zhilian Wang "Controlling Chaos – Supression, Synchronization and Chaotification" Sprinrer Verlag, 2009

[6] B. R. Andrievskii and A. L. Fradkov "Control of chaos: methods and applications", in Avtomatica I Telemekhanica, no.5, 2003, pp. 3-45.

[7] M. Krstic , I. Kanellakopoulos, and P.V. Kokotovic, "Nonlinear and Adaptive Control Design", New York: Wiley, 1995.

[8] A. M. Harb, A. A. Zaher, A. A. Al-Qaisia "Recursive backstepping control of chaotic Duffing oscillators", Chaos, Solitions & Fractals, 34, 2007, pp.639-645.

[9] Y. J. Cao. "A nonlinear adaptive approach to controlling chaotic oscillators" Physics Letters A, 270(3-4):171–176, 2000.

[10] X. Dong, G. Chen, and L. Chen. "Controlling the uncertain Duffing oscillator" In 1997 1st International Conference, Control of Oscillations and Chaos (Cat. No.97TH8329), pages 419–422, 1997.

[11] J. Kabziński, "Adaptive control of Duffing oscillator with unknown input gain," *Methods and Models in Automation and Robotics (MMAR), 2010 15th International Conference on*, Miedzyzdroje, 2010, pp. 234-239.

[12] T. von Wantoch, H. Röck, F. Koschmieder, W. Benecke, "Adaptive phasor control of a Duffing oscillator with unknown parameters" Preprints of the 19th World Congress The International Federation of Automatic Control Cape Town, South Africa. August 24-29, 2014, pp. 1308-1313

[13] Sung-Hoon Yu, Hyo Seok Kang, Yong-Tae Kim, Chang-Ho Hyun, and Mignon Park, "Fuzzy Adaptive Modular Design of Uncertain Chaotic Duffing Oscillators", International Journal of Control, Automation, and Systems (2014) 12(1), pp.188-194

[14] K. Ngo, Z. Jiang, "Integrator backstepping using barrier functions for systems with multiple state constraints", Proc. of the 44th IEEE Conf. Decision and Contr. Eur. Contr. Conf., (2005), pp.8306-8312

[15] K.P. Tee, S.S. Ge, and E.H. Tay, "Barrier Lyapunov functions for the output-constrained nonlinear systems", Automatica, vol. 45, no. 4, (2009), pp.918-927

[16] B.B. Ren, S.S. Ge, K.P. Tee, and T.H. Lee, "Adaptive neural control for output feedback nonlinear systems using a barrier Lyapunov function", IEEE Trans. Neural Networks, vol. 21, no. 8, (2010), pp. 1339-1345

[17] K.P. Tee, S.S. Ge, "Control of nonlinear systems with partial state constraints using a barrier Lyapunov function", International Journal of Control, vol. 84, no. 12, (2010), 2009-2023

[18] J. Kabziński and P. Mosiołek, Projektowanie nieliniowych układów sterowania (Nonlinear Control Design), I. Warszawa: PWN SA, 2018.

[19] J. Kabziński, "Adaptive tracking control of a Duffing oscillator with hard error constraints," in *2016 21st International Conference on Methods and Models in Automation and Robotics (MMAR)*, 2016, pp. 1176–1181.

[20] J. Kabziński, Synchronization of an uncertain duffing oscillator with higher order chaotic systems, Int. J. Appl. Math. Comput. Sci., Vol. 28, No 4, pp. 625-634, 2018

[21] J. Kabziński and P. Mosiołek, Adaptive, nonlinear control of a third-order Duffing–Holmes type chaotic oscillator, in *2019 24th International Conference on Methods and Models in Automation and Robotics (MMAR)*, 2019

[22] J. Kabziński and P. Mosiołek, Adaptive control of motion with hard constraints, based on nonlinear state transformation, (to appear) 2019

Jacek Kabziński,

Institute of Automatic Control, Lodz University of Technology,

Stefanowskiego 18/22, 90-924 Lodz, Poland,

jacek.kabzinski@p.lodz.pl

Application of the Drazin inverse of matrices to analysis of the pointwise completeness and the pointwise degeneracy of the descriptor linear systems

Tadeusz Kaczorek

Abstract: The Drazin inverse of matrices is applied to analysis of the pointwise completeness and the pointwise degeneracy of the descriptor linear continuous-time and discrete-time systems. It is shown that: 1) The descriptor linear continuous-time system is pointwise complete if and only if the initial and final states belong to the same subspace. 2) The descriptor linear discrete-time system is not pointwise complete if its system matrix is singular. 3) System obtained by discretisation of continuous-time system is always not pointwise complete. 4) The descriptor linear continuous-time system is not pointwise degenerated in any nonzero direction for all nonzero initial conditions. Considerations are illustrated by example of descriptor linear electrical circuit.

1. Introduction

A dynamical system described by homogenous equation is called pointwise complete if every final state of the system can be reached by suitable choice of its initial state. A system, which is not pointwise complete is called pointwise degenerated. The pointwise completeness and pointwise degeneracy of linear continuous-time systems with delays have been investigated in [2, 3, 8-11], the pointwise completeness of linear discrete-time cone systems with delays in [11] and of fractional linear systems in [1, 6-8]. The pointwise completeness and pointwise degeneracy of standard and positive hydrid systems described by the general model have been analyzed in [4] and of positive linear systems with state-feedbacks in [5].

In this paper the Drazin inverse of matrices will be applied to analysis of the pointwise completeness and the pointwise degeneracy of the descriptor linear continuous-time and discrete-time systems.

The paper is organized as follows. In section 2 the basic definitions and theorems concerning descriptor linear continuous-time and discrete-time systems and the Drazin inverse of matrices are recalled. The pointwise completeness of descriptor linear continuous-time and discrete-time systems is investigated in section 3 and the pointwise degeneracy in section 4. Concluding remarks are given in section 5. The considerations are illustrated by linear electrical circuit.

The following notation will be used: $\Re$ - the set of real numbers, $\Re^{n \times m}$ - the set of $n \times m$ real matrices, $\Re_+^{n \times m}$ - the set of $n \times m$ real matrices with nonnegative entries and $\Re_+^n = \Re_+^{n \times 1}$, I_n - the $n \times n$ identity matrix. ImP is the image of the operator (matrix) P.

2. Autonomous descriptor linear systems and their solutions

Consider the autonomous descriptor continuous-time linear system

$$E\dot{x} = Ax, \quad \dot{x} = \frac{dx}{dt} \tag{2.1}$$

where $x = x(t) \in \Re^n$ is the state vector and $E, A \in \Re^{n \times n}$.

It is assumed that $\det E = 0$ but the pencil (E, A) is regular, i.e.

$$\det[Es - A] \neq 0 \text{ for some } s \in C \text{ (the field of complex numbers)} \tag{2.2}$$

Assuming that for $c \in \Re \; \det[Ec - A] \neq 0$ and premultiplying (2.1) by $[Ec - A]^{-1}$ we obtain

$$\bar{E}\dot{x} = \bar{A}x, \tag{2.3a}$$

where

$$\bar{E} = [Ec - A]^{-1}E, \quad \bar{A} = [Ec - A]^{-1}A, \tag{2.3b}$$

The equations (2.1) and (2.3a) have the same solution x.

Definition 2.1. A matrix $E^D \in \Re^{q \times n}$ is called the Drazin inverse of E if it satisfies the conditions

$$\bar{E}\bar{E}^D = \bar{E}^D\bar{E}, \tag{2.4a}$$

$$\bar{E}^D\bar{E}\bar{E}^D = \bar{E}^D, \tag{2.4b}$$

$$\bar{E}^D\bar{E}^{q+1} = \bar{E}^q, \tag{2.4c}$$

where q is the index of E defined as the smallest nonnegative integer satisfying the condition

$$rankE^q = rankE^{q+1}. \tag{2.5}$$

Theorem 2.1. Let

$$P = \bar{E}\bar{E}^D, \tag{2.6a}$$

$$Q = \bar{A}\bar{E}^D, \tag{2.6b}$$

then

$$P^k = P \text{ for } k = 2, 3, \dots \tag{2.7a}$$

$$PQ = QP = Q, \tag{2.7b}$$

$$P\bar{E}^D = \bar{E}^D, \tag{2.7c}$$

$$Px = x. \tag{2.7d}$$

Proof is given in [8].

Theorem 2.2. The solution of the equation (2.3a) has the form

$$x(t) = e^{\bar{A}\bar{E}t}\,\bar{E}\bar{E}^D w \tag{2.8}$$

where $w \in \mathfrak{R}^n$ is any vector and $x(0) \in \operatorname{Im} \bar{E}\bar{E}^D = \operatorname{Im} P$.

Proof is given in [8].

Consider the autonomous descriptor discrete-time linear system

$$Ex_{i+1} = Ax_i, \quad i = 0,1,... \tag{2.9}$$

where $x_i \in \mathfrak{R}^n$ is the state vector and $E, A \in \mathfrak{R}^{n \times n}$.

It is assumed that $\det E = 0$ and

$$\det[Ez - A] \neq 0 \text{ for some } z \in C \tag{2.10}$$

Choosing $c \in \mathfrak{R}$ such that $\det[Ec - A] \neq 0$ and premultiplying (2.9) by $[Ec - A]^{-1}$ we obtain

$$\bar{E}x_{i+1} = \bar{A}x_i, \tag{2.11}$$

where $\bar{E}$ and $\bar{A}$ defined by (2.3b).

Theorem 2.1 is also valid for the discrete-time systems.

Using the Drazin inverse $\bar{E}^D$ of the matrix E we may find the solution x_i of the equation (2.11) by the use of the following Theorem.

Theorem 2.3. The solution of the equation (2.11) has the form

$$x_i = [\bar{E}\,\bar{A}]^i\,\bar{E}^D Ev = Q^i x_0, \quad i = 1, 2,... \tag{2.12}$$

where $v \in \mathfrak{R}^n$ is any vector and $x_0 \in \operatorname{Im} \bar{E}\bar{E}^D = \operatorname{Im} P$, the matrices P and Q are defined by (2.6).

Proof is given in [8].

3. Pointwise completeness of descriptor linear systems

In this section conditions for the pointwise completeness of descriptor continuous-time and discrete-time linear systems will be established.

3.1. Continuous-time systems

Definition 3.1. The descriptor continuous-time linear system (2.1) is called pointwise complete for $t = t_f$ if for final state $x_f = x(t_f) \in \mathfrak{R}^n$ there exists an initial condition $x(0) \in \operatorname{Im} P$ such that

$$x_f = x(t_f) \in \operatorname{Im} P, \tag{3.1}$$

where P is defined by (2.6a).

Theorem 3.1. The descriptor system (2.1) is pointwise complete for any $t = t_f$ and every $x_f \in \Re^n$ if and only if the condition (3.1) is satisfied.

Proof. Note that $\det e^{Qt} \neq 0$ and $[e^{Qt}]^{-1} = e^{-Qt}$ for any t. From (2.8) for $t = t_f$ we have

$$x(0) = e^{-Qt_f} x_f. \tag{3.2}$$

Therefore, for every x_f there exists $x(0) \in \operatorname{Im} P$ such that $x_f = x(t_f)$. $\square$

Example 3.1. Consider the descriptor linear electrical circuit shown in Figure 3.1 with given resistances R_1, R_2, R_3, inductances L_1, L_2, L_3 and source voltages e_1, e_2.
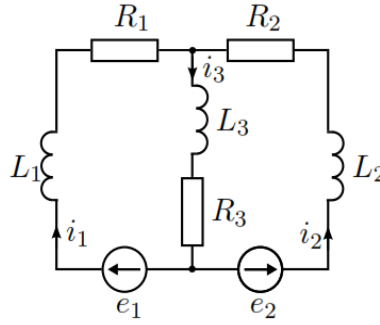
Fig. 3.1

Using Kirchhoff's laws we may write the equations

$$e_1 = R_1 i_1 + L_1 \frac{di_1}{dt} + R_3 i_3 + L_3 \frac{di_3}{dt},$$

$$e_2 = R_2 i_2 + L_2 \frac{di_2}{dt} + R_3 i_3 + L_3 \frac{di_3}{dt}, \tag{3.3}$$

$$i_1 + i_2 - i_3 = 0,$$

which can be written in the form

$$E \frac{d}{dt} \begin{bmatrix} i_1 \\ i_2 \\ i_3 \end{bmatrix} = A \begin{bmatrix} i_1 \\ i_2 \\ i_3 \end{bmatrix} + B \begin{bmatrix} e_1 \\ e_2 \end{bmatrix}, \tag{3.4a}$$

where

$$E = \begin{bmatrix} L_1 & 0 & L_3 \\ 0 & L_2 & L_3 \\ 0 & 0 & 0 \end{bmatrix}, \quad A = \begin{bmatrix} -R_1 & 0 & -R_3 \\ 0 & -R_2 & -R_3 \\ 1 & 1 & -1 \end{bmatrix}, \quad B = \begin{bmatrix} 1 & 0 \\ 0 & 1 \\ 0 & 0 \end{bmatrix}. \tag{3.4b}$$

The assumption (2.2) for the electrical circuit is satisfied, since the matrix E is singular $(\det E = 0)$ and

$$\det[Es - A] = \begin{vmatrix} L_1 s + R_1 & 0 & L_3 s + R_3 \\ 0 & L_2 s + R_2 & L_3 s + R_3 \\ -1 & -1 & -1 \end{vmatrix} = [L_1 (L_2 + L_3) + L_2 L_3] s^2 +$$

$$[R_1 (L_2 + L_3) + R_2 (L_1 + L_3) + R_3 (L_1 + L_2)] s + R_1 (R_2 + R_3) + R_2 R_3. \tag{3.5}$$

Therefore, the electrical circuit is a descriptor linear continuous-time system.

Note that the matrix A defined by (3.4b) is nonsingular and we may choose in (2.2) $s = 0$. In this case we obtain

$$\bar{E} = [-A]^{-1} E = \frac{1}{R_1 (R_2 + R_3) + R_2 R_3} \begin{bmatrix} L_1 (R_2 + R_3) & -L_2 R_3 & L_3 R_2 \\ -L_1 R_3 & L_2 (R_1 + R_2) & L_3 R_1 \\ L_1 R_2 & L_2 R_1 & L_3 (R_1 + R_2) \end{bmatrix} \tag{3.6}$$

$$\bar{A} = [-A]^{-1} A = -I_3 \tag{3.7}$$

and

$$\bar{E}^D = \begin{bmatrix} e_{d,11} & e_{d,1} & e_{d,13} \\ e_{d,21} & e_{d,22} & e_{d,23} \\ e_{d,31} & e_{d,32} & e_{d,33} \end{bmatrix} \frac{1}{\Delta_L^2}, \tag{3.8}$$

$$P = \bar{E}\bar{E}^D = \begin{bmatrix} L_1 (L_2 + L_3) & -L_2 L_3 & L_2 L_3 \\ -L_1 L_3 & L_2 (L_1 + L_3) & L_1 L_3 \\ L_1 L_2 & L_1 L_2 & L_3 (L_1 + L_2) \end{bmatrix} \frac{1}{\Delta_L^2}, \tag{3.9}$$

$$Q = \bar{A}\bar{E}^D = -\bar{E}^D, \tag{3.10}$$

where

$$e_{d,11} = L_1 (L_2^2 R_1 + L_3^2 R_1 + L_2^2 R_3 + L_3^2 R_2 + 2L_2 L_3 R_1),$$

$$e_{d,12} = -L_2 (L_3^2 R_1 + L_3^2 R_2 - L_1 L_2 R_3 + L_1 L_3 R_2 + L_2 L_3 R_1),$$

$$e_{d,13} = L_3 (L_2^2 R_1 + L_2^2 R_3 + L_1 L_2 R_3 - L_1 L_3 R_2 + L_2 L_3 R_1),$$

$$e_{d,21} = -L_1 (L_3^2 R_1 + L_3^2 R_2 - L_1 L_2 R_3 + L_1 L_3 R_2 + L_2 L_3 R_1),$$

$$e_{d,22} = L_2 (L_1^2 R_2 + L_1^2 R_3 + L_3^2 R_1 + L_3^2 R_2 + 2L_1 L_3 R_2),$$

$$e_{d,23} = L_3 (L_1^2 R_2 + L_1^2 R_3 + L_1 L_2 R_3 + L_1 L_3 R_2 - L_2 L_3 R_1),$$

$$e_{d,31} = L_1 (L_2^2 R_1 + L_2^2 R_3 + L_1 L_2 R_3 - L_1 L_3 R_2 + L_2 L_3 R_1),$$

$$e_{d,32} = L_2(L_1^2 R_2 + L_1^2 R_3 + L_1 L_2 R_3 + L_1 L_3 R_2 - L_2 L_3 R_1),$$

$$e_{d,33} = L_3(L_1^2 R_2 + L_2^2 R_1 + L_1^2 R_3 + L_2^2 R_3 + 2L_1 L_3 R_3),$$

$$\Delta_L = L_1(L_2 + L_3) + L_2 L_3.$$

The solution of the equation (3.4a) for $B = 0$ satisfies the condition

$$\begin{bmatrix} i_1(t_f) \\ i_2(t_f) \\ i_3(t_f) \end{bmatrix} = e^{Qt_f} \begin{bmatrix} i_1(0) \\ i_2(0) \\ i_3(0) \end{bmatrix} \in \operatorname{Im} P . \tag{3.11}$$

Therefore, the descriptor electrical circuit is poinwise complete.

From the above considerations we have the following conclusion.

Conclusion 3.1. In descriptor linear electrical circuit for $B = 0$ by suitable choice of initial conditions (currents in coils and voltages on capacitors) belonging to $\operatorname{Im} P$ it is possible to obtain in a given time t_f the desired values of currents in coils and voltages on capacitors belonging also to $\operatorname{Im} P$.

3.2. Discrete-time systems

Definition 3.2. The descriptor discrete-time linear system (2.9) is called pointwise complete for $i = q$ if for every final state $x_q \in \Re^n$ there exists an initial condition $x_0 \in \operatorname{Im} P$ such that $x_q = x_f \in \operatorname{Im} P$.

Theorem 3.2. The descriptor discrete-time linear system (2.9) is not pointwise complete for any $i = q$ and every x_f .

Proof. From (2.12) for $i = q$ we have $x_q = Q^q x_0$. Hence for given x_q it is possible to find x_0 if and only if $\det Q \neq 0$. Note that $\det Q = \det \bar{A} \det \bar{E}^D = 0$ since $\det \bar{E}^D = 0$ for any singular matrix E [8]. $\square$

Now we shall show that by Euler type discretization from pointwise complete continuous-time system (2.1) we obtain corresponding discrete-time system (2.9) which is not pointwise complete for any $i = q$.

Let $x_i = x(ih)$, $i = 0, 1, ...,$ $h > 0$ and

$$\dot{x}(t) \approx \frac{x_{i+1} - x_i}{h} \tag{3.12}$$

Then from (2.1) and (3.12) we have

$$E \frac{x_{i+1} - x_i}{h} = Ax_i, \quad i = 0,1,...,$$ (3.13)

and

$$Ex_{i+1} = (E + hA)x_i, \quad i = 0,1,...,$$ (3.14)

Note that

$$\det\left[Ec_1 - (E + hA)\right] = \det\left[h\left(E \frac{c_1 - 1}{h} - A\right)\right] = h^n \det\left[Ec_2 - A\right] \neq 0$$ (3.15)

for $h > 0$ and $c_2 = \dfrac{c_1 - 1}{h}$

If and only if $\det\left[Ec_1 - A\right] \neq 0$.

Therefore, the pencil of the corresponding discrete-time system (3.14) is regular if and only if the pencil of the continuous-time system (2.1) is regular.

By Theorem 3.1 the descriptor continuous-time system (2.1) is pointwise complete and the corresponding discrete-time system (3.14) by Theorem 3.2 is not pointwise complete. Therefore, we have the following theorem.

Theorem 3.3. The system obtained by the discretisation of continuous-time system is always not pointwise complete.

4. Pointwise degeneracy of descriptor linear systems

In this section conditions for the pointwise degeneracy of descriptor continuous-time and discrete-time linear systems will be established.

4.1. Continuous-time systems

Definition 4.1. The descriptor continuous-time linear system (2.1) is called pointwise degenerated in the direction $v \in \Re^n$ for $t = t_f$ if there exists nonzero vector v such that for all initial conditions $x(0) \in \operatorname{Im} P,$ the solution of (2.1) satisfies the condition

$$v^T x_f = 0,$$ (4.1)

where $x_f = x(t_f)$.

Theorem 4.1. The descriptor continuous-time linear system (2.1) is not pointwise degenerated in any nonzero direction $v \in \Re^n$ for all nonzero initial conditions $x(0) \in \operatorname{Im} P.$

Proof. Note that $\det e^{Qt_f} \neq 0$ for any matrix $Q = \bar{A}\bar{E}^D$ and all t_f. Substitution of $x_f = e^{Qt_f} x(0)$ into $v^T x_f$ yields

$$v^T x_f = v^T e^{Qt_f} x(0) \neq 0 \tag{4.2}$$

for all nonzero initial conditions $x(0) \in \mathrm{Im}\,P$. $\square$

Example 4.1. (Continuation of Example 3.1).

Consider the descriptor linear electrical circuit shown in Figure 3.1 with given the resistances, inductances and source voltages. The electrical circuit is described by the equation (3.4).

The matrix (3.10) of the descriptor electrical circuit is singular since

$$\det Q = 0 \tag{4.3}$$

but the matrix e^{Qt_f} is nonsingular.

Therefore, by Theorem 4.1 the descriptor electrical circuit is not pointwise degenerated in any nonzero direction $v \in \Re^3$ for all nonzero initial conditions.

4.2. Discrete-time systems

Definition 4.2. The descriptor discrete-time linear system (2.9) is called pointwise degenerated in the direction $v \in \Re^n$ for $i = q_f$ if there exists nonzero vector v such that for all initial conditions $x_0 \in \mathrm{Im}\,P$, the solution of (2.9) satisfies the condition

$$v^T x_q = 0. \tag{4.4}$$

Theorem 4.2. The descriptor discrete-time linear system (2.9) is pointwise degenerated in the direction $v \in \Re^n$ if and only if

$$\det Q = 0. \tag{4.5}$$

Proof. Note that $v^T Q = 0$ if and only if (4.5) holds. In this case

$$v^T x_q = v^T Q^q x_0 = 0 \quad \text{for all } x_0 \in P. \tag{4.6}$$

Therefore, the descriptor system (2.9) is pointwise degenerated in the direction $v \in \Re^n$ if and only if the condition (4.5) is satisfied. $\square$

5. Concluding remarks

The Drazin inverse of matrices has been applied to analysis of the pointwise completeness and the pointwise degeneracy of the descriptor linear continuous-time and discrete-time systems. It has been shown that:

1) The descriptor linear continuous-time system is pointwise complete if and only if the initial and final states belong to the same subspace (Theorem 3.1).

2) The descriptor linear discrete-time system is not pointwise complete if its system matrix is singular (Theorem 3.2).

3) The system obtained by discretisation of continuous-time system is always not pointwise complete (Theorem 3.3).

4) The descriptor linear continuous-time system is not degenerated in any nonzero direction for all nonzero initial conditions (Theorem 4.1).

Considerations have been illustrated by example of descriptor linear electrical circuit.

The considerations can be easily extended to fractional linear systems.

References

1. Busłowicz M., Pointwise completeness and pointwise degeneracy of linear discrete-time systems of fractional order. Zeszyty Naukowe Pol. Sląskiej, Automatyka, no. 151, 2008, pp. 19-24.

2. Busłowicz M., Kociszewski R., Trzasko W., Pointwise completeness and pointwise degeneracy of positive discrete-time systems with delays. Zeszyty Naukowe Pol. Sląskiej, Automatyka, no. 151, 2008, pp.55-56.

3. Choundhury A.K., Necessary and sufficient conditions of pointwise completeness of linear time-invariant delay-differential systems. Int. J. Control, vol. 16, no. 6, 1972, pp. 1083-1100.

4. Kaczorek T.,Pointwise completeness and pointwise degeneracy of standard and positive hydrid linear systems described by the general model. Archives of Control Sciences, vol. 2, 2010, pp. 121-131.

5. Kaczorek T., Pointwise completeness and pointwise degeneracy of standard and positive linear systems with state-feedbacks. Journal of Automation, Mobile Robotics and Ingelligent Systems, vol. 4, no. 1, 2010, pp. 3-7.

6. Kaczorek T., Selected Problems of Fractional Systems Theory, Springer, Berlin 2011.

7. Kaczorek T. and Busłowicz M., Pointwise completeness and pointwise degeneracy of linear continuous-time fractional order systems, Journal of Automation, Mobile Robotics and Intelligent Systems, vol. 3, no. 1, 2009, pp. 8-11.

8. Kaczorek T. and Rogowski K., Fractional Linear Systems and Electrical Circuits, Springer 2015.

9. Olbrot A., On degeneracy and related problems for linear constant time-lag systems, Ricerche di Automatica, vol. 3, no. 3, 1972, pp. 203-220.

10. Popov V.M., Pointwise degeneracy of linear time-invariant delay-differential equations, Journal of Differential Equation, vol. 11, 1972, pp. 541-561.

11. Trzasko W., Busłowicz M. and Kaczorek T., Pointwise completeness of discrete-time cone-systems with delays. Int. Proc. EUROCON 2007, Warsaw, pp. 606-611.

Tadeusz Kaczorek, Bialystok University of Technology, Faculty of Electrical Engineering, Wiejska 45D, 15-351 Białystok, e-mail: kaczorek@ee.pw.edu.pl

The influence of asymmetric electrodes on the non-planar dynamics of a parametrically excited nonlinear microbeam

P. N Kambali, T. Mintz, K. Mora, E. Buks and O. Gottlieb

Abstract: An initial-boundary value problem describing the three dimensional motion of a parametrically excited nonlinear microbeam in an asymmetric dual gap configuration is investigated asymptotically and numerically to study the influence of imperfections on its spatio-temporal dynamics. The analytical and numerical investigation of the non-planar dynamics reveals coexisting period doubled and quasiperiodic solutions corresponding to saddle-node and secondary Hopf instabilities in the slowly varying evaluation equations. The results are also compared with measurements from an experiment with asymmetric electrode gaps demonstrating that a planar model with parametric excitation cannot predict the documented bias in the observed frequency response of a nonlinear microbeam with an imperfect electrode configuration.

1. Introduction

Electrodynamically excited nano- and micro-mechanical resonators [1, 8] consist of configurations and structural elements which make use of one of their resonance frequencies. Their applications include atomic force microscopy [2], mass sensing [7] etc. These devices are mechanical structures (eg:electrodes and beams) consisting of various configurations which include both single element and multi-element arrays [3, 4] that are excited electrodynamically along in-plane direction [8], out-of-plane direction or both directions [3]. Majority of theoretical studies in literature assume that electrodes and beams are symmetrically spaced for both single and multi-element arrays. Thus in this work we study the influence of an imperfect configuration with asymmetric gaps between the electrodes (Fig.1) and investigate the bifurcation structure resulting from spatio-temporal effects of the asymmetrical gap configuration on a non-planar, nonlinear micro-beam-string response.

2. Problem Formulation

2.1. Initial-Boundary-Value Problem

We consider a fixed-fixed microbeam of length L, width B, thickness H separated from two side electrodes by distances G_1 and G_2 on either side respectively as shown in Fig. 1 (a). Following [5] we show a general view of electrostatically excited microbeam with assymetricaly

placed side electrodes in Fig. 1 (b). The experimental frequency and phase measurements are depicted in Fig. 1 (c). Following [6] we derive an initial-boundary value problem describing the three-dimensional motion of a parametrically excited microbeam with asymmetric electrodes.The equations of motions and boundary conditions for a microbeam with nonlinear damping and nonlinear stiffness can be written as

$$\rho A U_{tt} - \left[N U_x + E A \Big[U_x + \frac{1}{2} \big(V_x^2 + W_x^2 \big) \Big] + D A \big(U_{tx} + V_x V_{tx} + W_x W_{tx} \big) \right]_x = 0 \quad (1)$$

$$\rho A V_{tt} - \left[N V_x + E A V_x \Big[U_x + \frac{1}{2} \big(V_x^2 + W_x^2 \big) \Big] + D A V_x \big(U_{tx} + V_x V_{tx} + W_x W_{tx} \big) \right]_x$$
$$+ \Big[E I_z V_{xxx} + D I_z V_{txxx} \Big]_x = Q_V \quad (2)$$

$$\rho A W_{tt} - \left[N W_x + E A W_x \Big[U_x + \frac{1}{2} \big(V_x^2 + W_x^2 \big) \Big] + D A W_x \big(U_{tx} + V_x V_{tx} + W_x W_{tx} \big) \right]_x$$
$$+ \Big[E I_y W_{xxx} + D I_y W_{txxx} \Big]_x = Q_W \quad (3)$$

$$U(0,t) = V(0,t) = W(0,t) = U(L,t) = V(L,t) = W(L,t) = 0, U_x(0,t)$$
$$= V_x(0,t) = W_x(0,t) = U_x(L,t) = V_x(L,t) = W_x(L,t) = 0, \quad (4)$$

where $A = BH$ cross sectional area of the beam, ρA is the mass per unit length of the beam, E is the Young's modulus, N is the pretension, $I_y = HB^3/12$ and $I_z = BH^3/12$ denotes the moment of inertia, D is Kelvin-Voigt viscoelastic damping constatnt . The forcing Q_V along y direction is a combination of an electrostatic force [6] and a linear damping force, whereas the forcing Q_W along z direction is a linear damping force. Q_V and Q_W are given by

$$Q_V = \frac{\epsilon_0 B}{2} V_f{}^2 \Big[\frac{1}{(G_1 - V)^2} - \frac{1}{(G_2 + V)^2} \Big] - C V_t, \quad Q_W = -C W_t \quad (5)$$

where $V_f = V_{ac} \cos(\omega_{ac} t)$, $\epsilon_0 = 8.854 \times 10^{-12}$ is permittivity of free space. We non-dimensionlize the governing equations with the variables $u = U/L$, $v = V/L$, $w = W/L$, $\tau = t/T_s$ and $s = x/L$, where $T_s^2 = (\rho A L^2/N)$. Subsequently, we neglect inertia and damping terms in the longitudinal direction to yield the following coupled integro-differential equations of motions

$$v_{\tau\tau} - \Big[1 + \alpha C_1(v_s, w_s, \tau) + \delta C_{1,\tau}(v_s, v_{\tau s}, w_s, w_{\tau s}, \tau) \Big] v_{ss} + \beta_1 v_{ssss} + \mu_1 \delta v_{\tau ssss} = Q_v \quad (6)$$

$$w_{\tau\tau} - \Big[1 + \alpha C_1(v_s, w_s, \tau) + \delta C_{1,\tau}(v_s, v_{\tau s}, w_s, w_{\tau s}, \tau) \Big] w_{ss} + \beta_2 w_{ssss} + \mu_2 \delta w_{\tau ssss} = Q_w \quad (7)$$

where $C_1 = \frac{1}{2} \int_0^1 \big(v_s^2 + w_s^2 \big) ds$, $C_{1,\tau} = \int_0^1 \big(v_s v_{\tau s} + w_s w_{\tau s} \big) ds$ are the quadratic integro-differential terms and the forcing Q_v and Q_w are written as

$$Q_v = \frac{\eta_{ac}}{\gamma_1^2 \gamma_2^2} \Big(1 + \cos(2\Omega_{ac}\tau) \Big) \Big[\frac{(\gamma_2 + v)^2 - (\gamma_1 - v)^2}{1 + a_1 v + a_2 v^2 + a_3 v^3 + a_4 v^4} \Big] - \nu v_\tau, \quad Q_w = -\nu w_\tau \quad (8)$$

The corresponding non-dimensional boundary conditions are as follows

$$u(0,\tau) = v(0,\tau) = w(0,\tau) = u(1,\tau) = v(1,\tau) = w(1,\tau) = 0, u_s(0,\tau) = v_s(0,\tau)$$

$$= w_s(0,\tau) = u_s(1,\tau) = v_s(1,\tau) = w_s(1,\tau) = 0, \quad (9)$$

Note that the denominator in Eqn. (8) is a fourth-order polynomial with coefficients $a_1 = 2\frac{1-\Gamma}{\gamma_2}$, $a_2 = \frac{1-4\Gamma+\Gamma^2}{\gamma_2^2}$, $a_3 = 2\frac{\Gamma-1}{\gamma_1\gamma_2^2}$, $a_4 = \frac{1}{\gamma_1^2\gamma_2^2}$, $\Gamma = \frac{\gamma_2}{\gamma_1}$. The non-dimensionalized parameters in Eqns. (6)-(8) are defined as

$$\beta_1 = \frac{EI_z}{NL^2}, \beta_2 = \frac{EI_y}{NL^2}, \mu_1 = \frac{I_z}{AL^2}, \mu_2 = \frac{I_y}{AL^2}, \alpha = \frac{EA}{N}, \delta = \frac{D}{L}\sqrt{\frac{\alpha}{\rho E}}, \nu = \frac{C}{\rho A\omega_s}, \eta_{ac} =$$

$$\frac{1}{4}\frac{\epsilon_0 B}{LN}V_{ac}^2, \Omega_{ac} = \frac{\omega_{ac}}{\omega_s}, \omega_s = \sqrt{\frac{N}{\rho AL^2}}, \gamma_n = \frac{G_n}{L}. \quad (10)$$
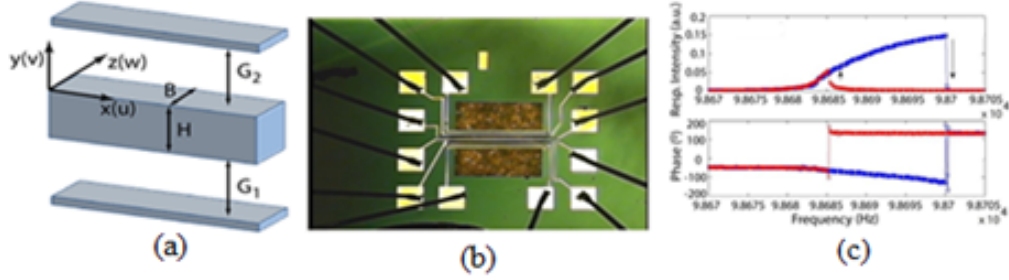
Figure 1. : (a) Definition sketch of the dynamical system (b) General view of the sample (c) Experimental frequency and phase measurements of a microbeam

2.2. Modal Dynamical System

We premultiply Eqn. (6) by denominator in Eqn. (8) and derive the modal dynamic equations of a microbeam by applying Galerkin's method [6]. We rescale the amplitudes by the nondimensional gap γ_1 as $x = q(\tau)/\gamma_1$, $y = p(\tau)/\gamma_1$ and time τ by natural frequency ω_q as $t = \omega_q\tau$. Thus the rescaled equations of motion are

$$\mathbb{M}(x)\left(\ddot{x} + x + \left(\delta_{11} + \delta_{12}x^2\right)\dot{x} + \delta_{12}xy\dot{y} + \alpha_1x^3 + \alpha_1y^2x\right) = \eta\left[1 + \cos(2\Omega t)\right](h_1 + h_2x) \quad (11)$$

$$\ddot{y} + k_2y + \left(\delta_{21} + \delta_{22}y^2\right)\dot{y} + \delta_{22}xy\dot{x} + \alpha_2y^3 + \alpha_2x^2y = 0 \quad (12)$$

where $\mathbb{M}(x) = 1 + \bar{a}_1 x + \bar{a}_2 x^2 + \bar{a}_3 x^3 + \bar{a}_4 x^4$ and the rescaled parameters are thus defined as

$$\delta_{11} = \frac{\nu + \delta\mu_1 k_4}{\omega_q}, \ \delta_{12} = \frac{\delta k_3 I_2 \gamma_1^2}{\omega_q}, \ \alpha_1 = \frac{\alpha k_3 I_2 \gamma_1^2}{2\omega_q^2}, \ \eta = \frac{2\eta_{ac}(\Gamma + 1)}{\gamma_1 \gamma_2^2 \omega_q^2}, \ \Omega = \frac{\Omega_{ac}}{\omega_q},$$

$$h_1 = \frac{(\Gamma - 1)}{2} I_4, \ h_2 = I_5, \ k_2 = \frac{w_p^2}{J_1 w_q^2}, \ \delta_{21} = \frac{\nu + \delta\mu_2 J_4}{J_1 \omega_q},$$

$$\delta_{22} = \frac{\delta J_2 J_3 \gamma_1^2}{J_1 \omega_q}, \ \alpha_2 = \frac{\alpha J_2 J_3 \gamma_1^2}{2 J_1 \omega_q^2}, \ \bar{a}_1 = a_1 I_{22} \gamma_1, \ \bar{a}_2 = a_2 I_{33} \gamma_1^2,$$

$$\bar{a}_3 = a_3 I_{44} \gamma_1^3, \ \bar{a}_4 = a_4 I_{55} \gamma_1^4, \ \omega_q = \sqrt{k_3 + k_4 \beta_1}, \ w_p = \sqrt{J_2 + J_4 \beta_2} \qquad (13)$$

3. Analysis of Results

3.1. Asymptotic Analysis

We assume small displacements which are the functions of multiple time scales as $x = \sum_{j=1}^{3} \epsilon^j x_j(T_0, T_1, T_2) + \bigcirc(\epsilon^4)$ and $y = \sum_{j=1}^{3} \epsilon^j y_j(T_0, T_1, T_2) + \bigcirc(\epsilon^4)$ where, $T_0 = t$, $T_1 = \epsilon t$, and $T_2 = \epsilon^2 t$. We also assume small excitation ($\eta = \epsilon\hat{\eta}$), small damping ($\delta_{11} = \epsilon^2 \hat{\delta}_{11}$, $\delta_{21} = \epsilon^2 \hat{\delta}_{21}$) and substitute them into Eqns. (11) and (12). We apply the reconstitution multiple-scales method [6] to Eqns. (11) and (12) to deduce complex modulation equations for both spatial 3D and planar 2D configurations. The polar form of modulation equations for spatial 3D configuration are as follows

$$\epsilon a_t = [\bar{r}_1 + \bar{r}_2 \cos(2\phi_1) - \bar{r}_3 \sin(2\phi_1)]\epsilon a + \bar{r}_5 \epsilon^3 a^3 + [\bar{r}_7 \sin 2(\phi_2 - \phi_1)$$
$$- \ \bar{r}_8 \cos 2(\phi_2 - \phi_1)]\epsilon^3 b^2 a \qquad (14)$$

$$\epsilon a \phi_{1t} = [\epsilon^2 \sigma_1 - \bar{r}_4 - \bar{r}_2 \sin(2\phi_1) - \bar{r}_3 \cos(2\phi_1)]\epsilon a - \bar{r}_6 \epsilon^3 a^3 - [\bar{r}_7 \cos 2(\phi_2 - \phi_1)$$
$$+ \ \bar{r}_8 \sin 2(\phi_2 - \phi_1) + \bar{r}_9]\epsilon^2 b^2 a \qquad (15)$$

$$\epsilon b_t = [\bar{s}_1 + \bar{s}_2 \cos(2\phi_2) - \bar{s}_3 \sin(2\phi_2)]\epsilon b + \bar{s}_5 \epsilon^3 b^3 + [\bar{s}_7 \sin 2(\phi_2 - \phi_1)$$
$$- \ \bar{s}_8 \cos 2(\phi_2 - \phi_1)]\epsilon^3 b a^2 \qquad (16)$$

$$\epsilon b \phi_{2t} = [\epsilon^2(\sigma_1 + \sigma_2) - \bar{s}_4 - \bar{s}_2 \sin(2\phi_2) - \bar{s}_3 \cos(2\phi_2)]\epsilon b - \bar{s}_6 \epsilon^3 b^3 + [\bar{s}_7 \cos 2(\phi_2 - \phi_1)$$
$$+ \ \bar{s}_8 \sin 2(\phi_2 - \phi_1) - \bar{s}_9]\epsilon^3 b a^2 \qquad (17)$$

where $\phi_1(t) = \epsilon^2 \sigma_1 t - \theta_1(t)$, $\phi_2(t) = \epsilon^2(\sigma_1 + \sigma_2)t - \theta_2(t)$ The polar form of modulation equations for Planar 2D configuration are

$$a_t = \left[\bar{r}_1 + \bar{r}_2 \cos(2\phi) - \bar{r}_3 \sin(2\phi)\right]a + \epsilon^2 \bar{r}_5 a^3 \qquad (18)$$

$$a\phi_t = \left[\epsilon^2 \sigma_1 - \bar{r}_4 - \bar{r}_2 \sin(2\phi) - \bar{r}_3 \cos(2\phi)\right]a - \epsilon^2 \bar{r}_6 a^3 \qquad (19)$$

where $\phi(t) = \epsilon^2 \sigma_1 t - \theta(t)$.

The comparison of non-planar frequency response of a microbeam plotted by slow varying evolution equations (solid blue line) and by numerical method (blue dots and red circles)
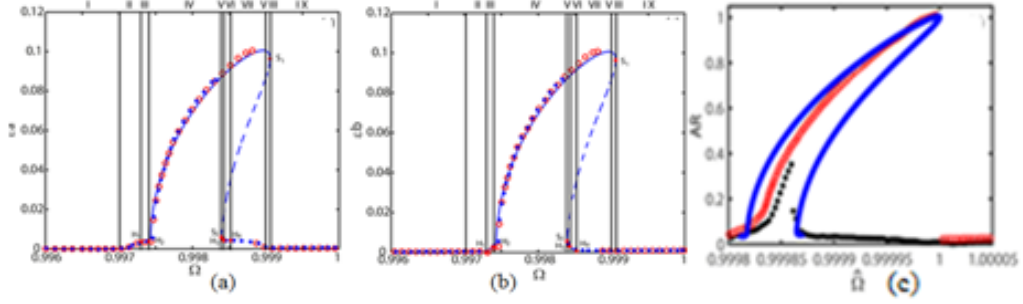
Figure 2. Non-planar frequency response (a) In-plane (b) Out-of-plane (c) Comparison of non-planar frequency response with experimental measurements

along in-plane and out-of-plane directions are shown in Fig. 2 (a) and (b). The in-plane and out-of-plane frequency response in Fig. 2 reveals nine different bifurcation regions. In Fig. 2 region I and IX depict a unique stable trivial solution. In region II the trivial solution becomes unstable. Region III is bounded by two Hopf bifurcation points H1 at $\Omega = 0.997297$ and H2 at $\Omega = 0.9974$ and it has two solutions, a unstable trivial solution and a unstable nontrivial solution. In region IV the nontrivial solution becomes stable and trivial solution remains unstable. Region V depicts one stable nontrivial solution for maximum amplitude, two nontrivial, stable and unstable solutions for minimum amplitude separated by a saddle node point S2 at $\Omega = 0.998396$ and a unstable trivial solution. Region VI is bounded by a supercritical Hopf bifurcation point H3 at $\Omega = 0.998424$ and a subcritical Hopf point H4 at $\Omega = 0.998516$. In this region there exist four solutions which include a stable nontrivial solution with a maximum amplitude, two unstable nontrivial solutions with minimum amplitude and an unstable trivial solution. Region VII shows a stable nontrivial and a unstable trivial solution. In region VIII a stable nontrivial solution loses its stability at a saddle node bifurcation point S1 at $\Omega = 0.999059$ and becomes unstable, this region also has a stable trivial solution.

We consider a AuPd microbeam with length $L = 500\mu$m, width $H = 1.75\mu$m, and thickness$B = 165$ nm developed by Mintz [5] and depicted in Fig. 1 (b). Subsequently, we estimate the linear and nonlinear parameters of a parametrically excited microbeam by comparison of the asymptotic results with the experimental measurements dipicted in Fig. 1 (c). The comparisons between experimental results with asymptotic results (both planar 2D and spatial 3D) using estimated parameters demonstarte that a 2D palnar model with parametric excitation cannot portray the documented bias in the observed frequency response of the microbeam whereas a spatial model that exhibits a 1:1 internal resonance

between coupled in and out-of-plane transverse modes enables an accurate prediction of the biased response. The comparison of non-planar frequency response of a microbeam plotted by slow varying evolution equations (solid blue line) with experimental measurements (black dots and red circles) are shown inFig. 2 (c)

3.2. Numerical Analysis

Numerical analysis of the dynamical system shows the existence of stable period-doubled solutions (Fig. 3 (a),(b) and (c)) in regions IV, V, VI (maximum amplitude), VII and quasiperiodic solutions corresponding to Hopf points in regions III (between H_1 and H_2) and VI (between H_3 and H_4) (Fig. 3, (e) and (f)).
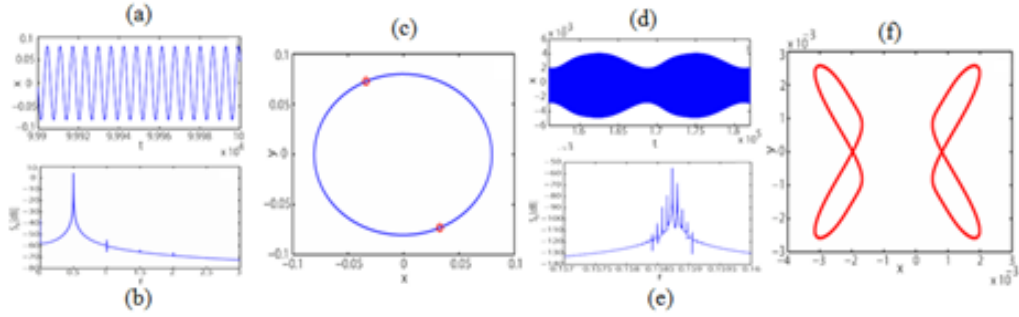
Figure 3. (a), (b), (c) Time history, Power spectra and Phase plane with Poincar overlaid points for $\Omega = 0.998$ in region IV of Fig. 2 (a) and (b). (d) (e), (f) Time history, Power spectra and Poincar map for $\Omega = 0.99735$ in region III of Fig. 2 (a) and (b).

4. Conclusions

In this work we formulated an initial-boundary value problem describing the three dimensional motion of a parametrically excited nonlinear microbeam in an asymmetric dual gap configuration and was investigated asymptotically and numerically to study the influence of imperfections on its spatio-temporal dynamics. The analytical and numerical investigation of the non-planar dynamics reveals coexisting period doubled and quasiperiodic solutions corresponding to saddle-node and secondary Hopf instabilities in the slowly varying evaluation equations. The results were also compared with measurements from an experiment with asymmetric electrode gaps demonstrating that a planar model with parametric excitation cannot predict the documented bias in the observed frequency response of a nonlinear microbeam with an imperfect electrode configuration whereas a spatial model that exhibits a 1:1 internal resonance between coupled in and out-of-plane transverse modes enables an

accurate prediction of the biased response. This study can be utilized to design a resonator for multi-functional sensing and actuation [2].

Acknowledgments

References

[1] GUTSCHMIDT, S., AND GOTTLIEB, O. Nonlinear dynamic behavior of a microbeam array subject to parametric actuation at low, medium and large dc-voltages. *Nonlinear Dynamics 67* (2012), 1–36.

[2] HORNSTEIN, S., AND GOTTLIEB, O. Nonlinear multimode dynamics and internal resonances of the scan process in noncontacting atomic force microscopy. *J. Applied Physics 112* (2012), 074314.

[3] KAMBALI, P. N., SWAIN, G., PANDEY, A. K., BUKS, E., AND GOTTLIEB, O. Coupling and tuning of modal frequencies in dc biased mems arrays. *Applied Physics Letters 107* (2015), 063104.

[4] KAMBALI, P. N., TORRES, F., BARNIOL, N., AND GOTTLIEB, O. Nonlinear multi-element interactions in an elastically copied microcantilever array subject to electrodynamic excitation. *Nonlinear Dynamics* (2019), DOI:10.1007/s11071–019–05074–7.

[5] MINTZ, T. Nonlinear dynamics and stability of a microbeam array subject to parametric excitation. *MSc Thesis, Technion-Israel Institute of Technology* (2009).

[6] MORA, K., AND GOTTLIEB, O. Parametric excitation of a micro-beam-string with asymmetric electrodes multimode dynamics and the effect of nonlinear damping. *J. Vibration and Acoustiics 139* (2017), 0409031.

[7] VIDAL-AVAREZ, G., AGUSTI, J., TORRES, F., ABADAL, G., BARNIOL, N., LLOBET, J., SANSA, M., FERNANDEZ, M., PEREZ, F., SNA PAULO, A., AND GOTTLIEB, O. Top-down silicon microcantilever with coupled bottom-up silicon nanowire for enhanced mass resolution. *Nanotechnology 26* (2015), 1–9.

[8] ZAITSEV, S., SHTEMPLUCK, O., BUKS, E., AND GOTTLIEB, O. Nonlinear damping in a micromechanical oscillator. *Nonlinear Dynamics 67* (2012), 859–883.

P. N Kambali, Ph.D.: Department of Mechanical Engineering, , Technion-Israel Institute of Technology, Haifa, Israel. (*kprashant@campus.technion.ac.il*). The author will give presentation of this paper during one of the conference sessions.

T. Mintz, M.Sc.: Department of Mechanical Engineering, Technion-Israel Institute of Technology, Haifa, Israel. (*haelavot@gmail.com*).

K. Mora, Ph.D.: Department of Electrical Engineering, University of Paderborn, Paderborn, Germany (*kmora@math.uni-paderborn.de*).

E. Buks, Ph.D: Department of Electrical Engineering,, Technion-Israel Institute of Technology, Haifa, Israel. (*eyal@ee.technion.ac.il*).

O. Gottlieb, Ph.D.: Department of Mechanical Engineering,, Technion-Israel Institute of Technology, Haifa, Israel. (*oded@technion.ac.il*).

Dynamics of a spherical robot in cases of periodical control actions and oscillations of the underlying surface

Yury Karavaev, Alexander Kilin, Alexey Borisov

Abstract: The dynamics of a spherical robot of combined type is investigated. The spherical robot is set in motion by moving the position of the center of mass and by generating variable gyrostatic momentum. Problems of stabilizing the rolling of the spherical robot using periodic control actions are considered within the framework of a nonholonomic model. A mathematical model is presented which describes the movement of the spherical robot on an oscillating flat surface. The results of numerical modeling of the motion of the spherical robot for various combinations of control actions and parameters of plane oscillations are discussed.

1. Introduction

In recent studies of nonholonomic systems the problems of moving a Chaplygin sleigh and Chaplygin top by small periodic control actions are considered. The results confirm the possibility of constant acceleration (speedup) of the wheeled vehicle due to the periodic change in the mass distribution [1, 2], as well as acceleration of the Chaplygin top with the help of an internal rotor [4].

This paper presents the results of the study of the dynamics of a real spherical robot of combined type in the case of control using small periodic oscillations. The spherical robot is set in motion by controlled change of the position of the center of mass and by generating variable gyrostatic momentum [3, 7, 8].

We demonstrate how to use small periodic controls for stabilization of the spherical robot during motion. The results of numerical simulation are obtained for various initial conditions and control parameters that ensure a change in the position of the center of mass and a variation of gyrostatic momentum.

The problem of the motion of a spherical robot of combined type on a surface that performs flat periodic oscillations is also considered. The results of numerical simulation are obtained for different initial conditions, control actions and parameters of oscillations. Possible modes of motion of the spherical robot on the oscillating plane are discussed.

2. Equations of motion of a spherical robot of combined type

Consider a spherical robot of combined type rolling without slipping on a horizontal absolutely rough plane (Fig. 1). To describe the dynamics of the spherical robot, we define two coordinate systems: a fixed (inertial) coordinate system $O\alpha\beta\gamma$ with unit vectors $\boldsymbol{\alpha}$, $\boldsymbol{\beta}$, $\boldsymbol{\gamma}$, and a moving coordinate system $Ce_1e_2e_3$ with unit vectors $\boldsymbol{e}_1$, $\boldsymbol{e}_2$, $\boldsymbol{e}_3$, attached to the pendulum so that the unit vector $\boldsymbol{e}_1$ is perpendicular to the plane of rotation of the pendulum and the unit vector $\boldsymbol{e}_3$ is directed along its symmetry axis.
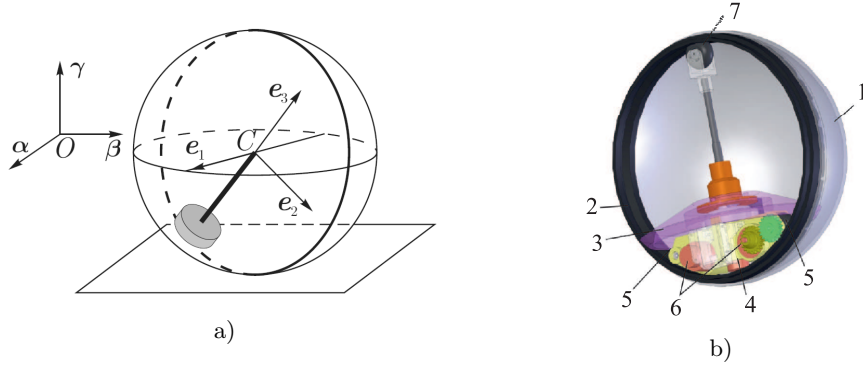
Figure 1. A schematic model of a spherical robot of combined type (a) and a 3D model of prototype (b)

This scheme can be implemented with various designs in practice. For example, by modification of the famous pendulum mechanism installing the rotor on it. But the simplest design is realized in the case of installation of the wheeled platform with rotor inside the spherical shell. Figure 1b shows a three-dimensional model of the proposed design of a spherical robot of combined type. In this figure, a wheeled platform moves inside the spherical shell — 1 along the rim — 2. The platform is driven by two wheels — 5 with individual drive motors — 6, synchronized by the control system. The profile of the drive wheels, as well as the material from which they are made, ensure that they roll without slipping around the rim. The contact of the driving wheels with the rim is provided by a spring-loaded roller — 7. A rotor — 3 actuated by an motor with a gearbox — 4, ensures the rotation of the spherical robot relative to the vertical axis.

The origin of the moving coordinate system is at the geometric center of the shell C (see Fig. 1). In what follows, all vectors are referred to the moving coordinate system $Ce_1e_2e_3$. The position of the system is given by the coordinates of the center of the sphere $\mathbf{r} = (x, y, 0)$ in the fixed reference frame, by the angle of rotation ϑ of the pendulum about the axis $\boldsymbol{e}_1$, by the angle of rotation φ of the rotor relative to the axis $\boldsymbol{e}_3$ and by the orthogonal

matrix of rotation $\mathbf{Q}$ of the moving coordinate system relative to the fixed one. The columns of the matrix $\mathbf{Q}$ are the coordinates of the fixed vectors $\boldsymbol{\alpha}$, $\boldsymbol{\beta}, \boldsymbol{g}$, referred to the moving coordinate system $C\boldsymbol{e_1 e_2 e_3}$: $\mathbf{Q} = (\boldsymbol{\alpha}, \boldsymbol{\beta}, \boldsymbol{g})$.

The absence of slipping at the point of contact of the shell with the plane is described by the nonholonomic constraint

$$\boldsymbol{F} = \boldsymbol{v} - R_s \boldsymbol{\Omega} \times \boldsymbol{g} = 0,$$

where $\boldsymbol{v}$ and $\boldsymbol{\Omega}$ are the velocity of the center and the angular velocity of rotation of the shell, respectively, R_s is the radius of the shell, and $\boldsymbol{\gamma} = (\gamma_1, \gamma_2, \gamma_3)^T$ is the unit vector of the fixed reference frame in the direction of the vertical axis.

The kinetic and the potential energy of the sphere-pendulum system can be represented in the following form:

$$T = \frac{1}{2} m_s \boldsymbol{v}^2 + \frac{1}{2}(\boldsymbol{\Omega}, \mathbf{I}_s \boldsymbol{\Omega}) + \frac{1}{2} m_b v_b^2 + \frac{1}{2}(\boldsymbol{\omega}, \mathbf{I}_{bc} \boldsymbol{\omega}), \quad U = -m_b R_b \mathrm{g}(\boldsymbol{\gamma}, \boldsymbol{e_3}),$$

where m_s and $\mathbf{I}_s = \mathrm{diag}(I_s, I_s, I_s)$ are the mass and the central tensor of inertia of the spherical shell, m_b and $\mathbf{I}_{bc} = \mathrm{diag}(I_{bc1}, I_{bc1}, I_{bc3})$ are the mass and the central tensor of inertia of the pendulum, respectively, and the velocity of the center of mass of the pendulum $\boldsymbol{v}_b$ and its angular velocity $\boldsymbol{\omega}$ are given by

$$\boldsymbol{v}_b = \boldsymbol{v} - R_b \boldsymbol{\omega} \times \boldsymbol{e_3}, \qquad \boldsymbol{\omega} = \boldsymbol{\Omega} + \boldsymbol{e_1} \dot{\vartheta} + \boldsymbol{e_3} \dot{\varphi},$$

where R_b is the distance from the center of the sphere to the center of mass of the pendulum.

The equations governing the dynamics of the system considered can be written in the form of the d'Alembert–Lagrange equations of the second kind in quasi-velocities with undetermined multipliers and forcing actions. As shown in [8], the equations of motion for the variables $\dot{\varphi}$, $\dot{\vartheta}$, $\boldsymbol{\Omega}$, $\boldsymbol{g}$ decouple from the complete system and take the following form:

$$
\begin{aligned}
&\Big(\boldsymbol{e_3}, \mathbf{I}_b(\dot{\boldsymbol{\Omega}} + \ddot{\varphi}\boldsymbol{e_3})\Big) = K_\varphi, \\
&\Big(\boldsymbol{e_1}, \mathbf{I}_b(\dot{\boldsymbol{\Omega}} + \ddot{\vartheta}\boldsymbol{e_1}) + \boldsymbol{\Omega} \times ((\mathbf{I}_s + \mathbf{I}_b)\boldsymbol{\Omega} + \dot{\varphi}\mathbf{I}_b \boldsymbol{e_3}) - \\
&\qquad\qquad - m_b R_b R_s \boldsymbol{e_3} \times \Big((\dot{\boldsymbol{\Omega}} + \dot{\vartheta}\boldsymbol{e_1} \times \boldsymbol{\Omega}) \times \boldsymbol{g}\Big) + m_b R_b \mathrm{g}\boldsymbol{g} \times \boldsymbol{e_3}\Big) = K_\vartheta, \\
&(\mathbf{I}_s + \mathbf{I}_b)\dot{\boldsymbol{\Omega}} + \ddot{\vartheta}\mathbf{I}_b \boldsymbol{e_1} + \ddot{\varphi}\mathbf{I}_b \boldsymbol{e_3} + (\boldsymbol{\Omega} + \dot{\vartheta}\boldsymbol{e_1}) \times ((\mathbf{I}_s + \mathbf{I}_b)\boldsymbol{\Omega} + \dot{\vartheta}\mathbf{I}_b \boldsymbol{e_1} + \dot{\varphi}\mathbf{I}_b \boldsymbol{e_3}) + \qquad (1) \\
&+ (m_s + m_b)R_s^2 \boldsymbol{g} \times ((\dot{\boldsymbol{\Omega}} + \dot{\vartheta}\boldsymbol{e_1} \times \boldsymbol{\Omega}) \times \boldsymbol{g}) - m_b R_b R_s \Big(\boldsymbol{e_3} \times ((\dot{\boldsymbol{\Omega}} + \dot{\vartheta}\boldsymbol{e_1} \times \boldsymbol{\Omega}) \times \boldsymbol{g}) + \\
&+ \boldsymbol{g} \times ((\dot{\boldsymbol{\Omega}} + \ddot{\vartheta}\boldsymbol{e_1}) \times \boldsymbol{e_3} + (\boldsymbol{\Omega} + \dot{\vartheta}\boldsymbol{e_1}) \times ((\boldsymbol{\Omega} + \dot{\vartheta}\boldsymbol{e_1}) \times \boldsymbol{e_3}))\Big) + m\mathrm{g}R_b \boldsymbol{g} \times \boldsymbol{e_3} = 0 \\
&\dot{\boldsymbol{g}} = \boldsymbol{g} \times (\boldsymbol{\Omega} + \dot{\vartheta}\boldsymbol{e_1}),
\end{aligned}
$$

where $\mathbf{I}_b = \mathrm{diag}(I_{b1}, I_{b1}, I_{b3}) = \mathrm{diag}(I_{bc1} + m_b R_b^2, I_{bc1} + m_b R_b^2, I_{bc3})$ is the tensor of inertia of the pendulum relative to the center of the sphere, K_θ is the moment of external forces (control action) which defines the rotation of the pendulum in the given plane, and K_φ is the moment of external forces which defines the rotation of the rotor about its symmetry axis (the rod of the pendulum). Supplementing equations (1) with kinematic relations describing the motion of the center of the spherical robot and the rotation of the moving axes relative to the fixed axes, we obtain a closed system of equations that completely describes the rolling of the spherical robot on the plane.

The control of a spherical robot of combined type with a feedback stabilizing the given partial solutions of the free system is considered in [5, 6]. In the approach considered, the feedback depends on the current position and the velocities of the spherical robot, does not depend on the specific type of trajectory, and involves specifying the control torques K_ϑ and K_φ.

The results of simulation of the motion of the spherical robot of combined type using feedback, as presented in [5, 6], confirm the possibility of stabilizing the spherical robot. However, the question of choosing and verifying the values of the coefficients $\tilde{k}_\vartheta$ and $\tilde{k}_\varphi$ remains open. The results of experimental investigations of the proposed algorithm show that the control actions for stabilization are similar to periodical oscillations [3, 7].

3. Motion in the case of periodically oscillating control actions

Consider the influence of control actions in the form of periodic oscillation on the stability of motion. Periodic control actions are provided by periodic rotations of the rotor of the pendulum, which are specified as

$$\dot{\varphi}(t) = \begin{cases} 0, & t < 0.1 \\ 0.05 \left(\sin\left(10.0\,\pi\,t\right)\right)^3, & t \geq 0.1. \end{cases} \tag{2}$$

Taking into account the smooth acceleration from the initial rest position of the pendulum, the motion along the straight line is realized by the deviation of the pendulum in the form

$$\dot{\theta}(t) = \begin{cases} 0, & t < 0.055 \\ 0.314 \left(\sin\left(10.0\,\pi\,t - 0.55\,\pi\right)\right)^2 & 0.055 < t \leq 0.105 \\ 0.314, & t > 0.105. \end{cases} \tag{3}$$

Depending on the initial conditions in the process of movement, the spherical robot will perform various oscillations. Consider the most illustrative examples for different initial conditions, which we define as follows:
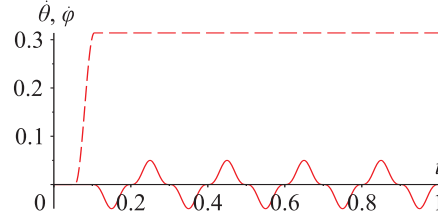
Figure 2. Graphical representation of control actions for the spherical robot.

| a) | b) | c) |
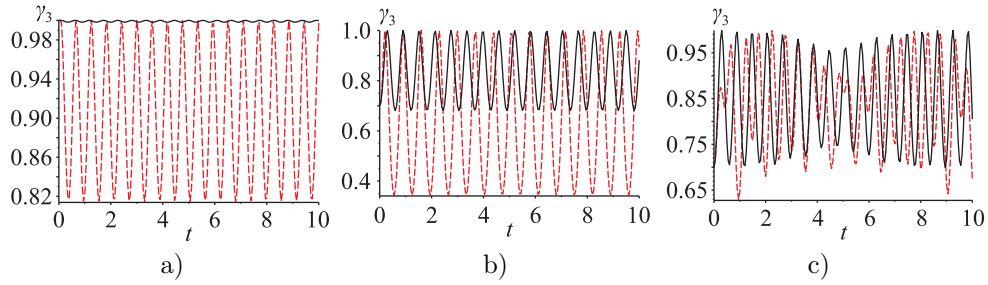
Figure 3. Oscillations of a spherical robot during its motion by control actions (3) and initial conditions: a) IC_1, b) IC_2, c) IC_3. The evolution of the component γ_3 by control action $\dot{\varphi} = 0$ is shown as dashed line, and the solid line corresponds to control action (2).

IC_1: $\boldsymbol{a} = (1, 0, 0)$, $\boldsymbol{b} = (0, 1, 0)$, $\boldsymbol{g} = (0, 0, 1)$;

IC_2: $\boldsymbol{a} = (1, 0, 0)$, $\boldsymbol{b} = (0, 0.7, -0.714)$, $\boldsymbol{g} = (0, -0.714, 0.7)$;

IC_3: $\boldsymbol{a} = (0.7, 0, 0.714)$, $\boldsymbol{b} = (0, 1, 0)$, $\boldsymbol{g} = (-0.714, 0, 0.7)$.

Figure 3 shows the results of numerical simulation of the system (1) with regard to (3) and various initial conditions for the mass-geometric parameters of a real spherical robot: $R_s = 0.150$ m, $m_s = 1.625$ kg, $\mathbf{I}_s = \mathrm{diag}(25.27 \cdot 10^{-3}, \ 20.73 \cdot 10^{-3}, \ 25.27 \cdot 10^{-3})$ kg·m^2, $R_r = 0.087$ m, $m_r = 2.46$ kg, $I_r = 5.64 \cdot 10^{-3}$ kg·m^2, $m_b = 3.25$ kg, $\mathbf{I}_b = \mathrm{diag}(31.88 \cdot 10^{-3}, \ 30.59 \cdot 10^{-3}, \ 8.76 \cdot 10^{-3})$ kg·m^2.

The results obtained and presented in Fig. 3 show that, regardless of the initial conditions, small periodic oscillations contribute to the stabilization of the motion of a spherical robot, while, for example, the constant rotation of the rotor leads to significant deviations of the trajectory [7]. In practice, such small periodic oscillations of control actions can be used to stabilize motion in the case of deviations caused by obstacles, deviations of geometric dimensions, and uncertainties.

4. Dynamics of the spherical robot rolling on a periodically oscillating underlying surface

Consider the problem of motion of the spherical robot on a periodically oscillating underlying surface (Fig. 4). Oscillations of the surface are realized by the angular velocity of the plane $\boldsymbol{\Omega}(t)$.
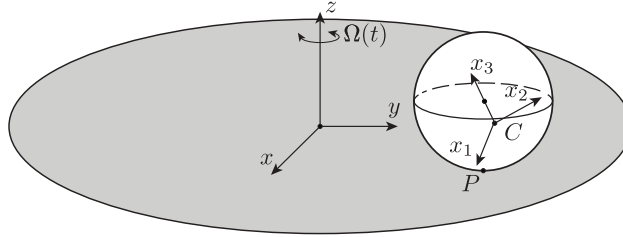
Figure 4.   The model of a spherical robot rolling on an oscillating plane.

The nonholonomic constraint in the case of a rotating underlying plane is

$$\boldsymbol{f} = \boldsymbol{v} + \boldsymbol{\omega} \times \boldsymbol{r} - \Omega(t)\boldsymbol{\gamma} \times \boldsymbol{R} = 0, \quad \boldsymbol{R} = x\boldsymbol{\alpha} + y\boldsymbol{\beta}, \tag{4}$$

where $\boldsymbol{r}$ is the radius vector of the contact point from the center of mass position.

After reduction the system under consideration takes the form in variables $\boldsymbol{\omega}$, $\boldsymbol{\gamma}$, $\boldsymbol{R}$:

$$\tilde{\mathbf{I}}\dot{\boldsymbol{\omega}} = (\tilde{\mathbf{I}}\boldsymbol{\omega} + \boldsymbol{K}) \times \boldsymbol{\omega} + m\boldsymbol{r} \times (\dot{\boldsymbol{r}} \times \boldsymbol{\omega}) + m\Omega(t)\boldsymbol{r} \times (\dot{\boldsymbol{R}} \times \boldsymbol{\gamma}) - m\Omega(t)(\boldsymbol{\omega}, \boldsymbol{\gamma})\boldsymbol{R} \times \boldsymbol{r} +$$
$$+ m\dot{\Omega}(t)\boldsymbol{r} \times (\boldsymbol{R} \times \boldsymbol{\gamma}) + mg\boldsymbol{\gamma} \times \boldsymbol{r}, \tag{5}$$
$$\dot{\boldsymbol{\gamma}} = \boldsymbol{\gamma} \times \boldsymbol{\omega}, \quad \dot{\boldsymbol{R}} = \boldsymbol{R} \times (\boldsymbol{\omega} - \Omega(t)\boldsymbol{\gamma}) + \boldsymbol{r} \times \boldsymbol{\omega} - (\boldsymbol{\omega}, \boldsymbol{c} \times \boldsymbol{\gamma})\boldsymbol{\gamma},$$

where $\boldsymbol{K} = (K_1, K_2, K_3)$ is the gyrostatic moment and $\boldsymbol{c} = (c_1, c_2, c_3)$ is the displacement of the center of mass relative to the geometrical center of the sphere.

Consider the results of numerical simulation of the system (5) for various control actions given by the gyrostatic moment: without any control, with constant gyrostatic moment and by periodical gyrostatic moment.

Results of simulations for different actions $\boldsymbol{K}$ by $\Omega(t) = \sin(t)$:

The results presented in Fig. 3 show that, regardless of the initial conditions, small periodic oscillations contribute to the stabilization of the motion of the spherical robot.

Conclusions

In conclusion, we present the most important problems obtained in this work and plans for the future in the study of the rolling of a spherical robot in the case of small periodic control actions or on the surface performing small oscillations:
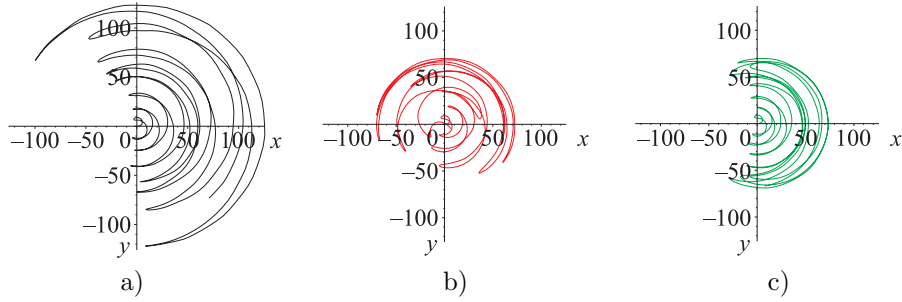
Figure 5. Trajectories of the spherical robot moving on an oscillating plane in the case of: a) $K(t) = 0$, b) $K(t) = (0, 0, 1)$, c) $K = (0, 0, 0.5 \cdot sin(2 \cdot t))$.

1. Small periodic oscillations contribute to the stabilization of the motion of a spherical robot keeping the desired direction of motion of the robot.

2. In addition to oscillations of the underlying surface in the horizontal plane, oscillations along the vertical should also be considered. Taking them into account will allow modeling more complex dynamic behavior.

3. Future research will be aimed at developing an algorithm for calculation of control actions to compensate for the influence of the oscillating underlying surface.

References

[1] BIZYAEV, I., BORISOV, A., AND KUZNETSOV, S. Chaplygin sleigh with periodically oscillating internal mass. *EPL 119*, 6 (2017), 60008.

[2] BIZYAEV, I., BORISOV, A., AND MAMAEV, I. The chaplygin sleigh with parametric excitation: Chaotic dynamics and nonholonomic acceleration. *Regul. Chaotic Dyn. 22*, 8 (2017), 955–975.

[3] BORISOV, A., KILIN, A., KARAVAEV, Y., AND KLEKOVKIN, A. Stabilization of the motion of a spherical robot using feedbacks. *Appl. Math. Model. 69* (2019), 583–592.

[4] Borisov, A., Kilin, A., and Pivovarova, E. Speedup of the chaplygin top by means of rotors. *Dokl. Phys. 64*, 3 (2019), 120–124.

[5] Ivanova, T., Kilin, A., and Pivovarova, E. Controlled motion of a spherical robot with feedback. i. *J. Dyn. Control Syst. 24*, 3 (2018), 497–510.

[6] Ivanova, T., Kilin, A., and Pivovarova, E. Controlled motion of a spherical robot with feedback. ii. *J. Dyn. Control Syst. 25*, 1 (2019), 1–16.

[7] Kilin, A., and Karavaev, Y. Experimental research of dynamic of spherical robot of combined type. *Russ. J. Nonl. Dyn. 11*, 4 (2015), 721—734.

[8] Kilin, A., Pivovarova, E., and Ivanova, T. Spherical robot of combined type: Dynamics and control. *Regul. Chaotic Dyn. 20*, 6 (2015), 716–728.

Yury Karavaev, Ph.D.: Kalashnikov Izhevsk State Technical University, 426069 Izhevsk, Studencheskaya str, 7, Russia (*karavaev_yury@istu.ru*). The author gave a presentation of this paper during one of the conference sessions.

Alexander Kilin, Professor: Udmurt State University, 426034 Izhevsk, Universitetskaya str., 1, Russia (*aka@rcd.ru*).

Alexey Borisov, Professor: Moscow Institute of Physics and Technology, 141701 Dolgoprudny, Institutskiy per., 9, Russia (*borisov@rcd.ru*).

Ultrasensitive mass sensing using a single cantilever coupled with a computational cantilever

Yuki Kasai, Hiroshi Yabuno, Takeshi Ishine, Yasuyuki Yamamoto, Sohei Matsumoto

Abstract: Mass sensing based on the eigenmode shift of coupled cantilevers achieves very high sensitivity. In this method, identical cantilevers and the weaker coupling stiffness between them enable higher sensitivity. However, the sensitivity is restricted because the identity of cantilevers and the coupling stiffness depend on machining accuracy. To maximize the sensitivity, we propose completely identical weakly coupled cantilevers using a single cantilever and a digital computer. The digital computer calculates the dynamics of one of the conventional coupled cantilevers and the effect of coupling. Then, the calculated effect of coupling moves the single cantilever's supporting point. The system enables us to set the physical parameters of the cantilever whose dynamics is calculated and the coupling stiffness appropriately. In addition, to use even in viscosity environments, we apply the self-excited oscillation with a steady-state amplitude proposed in our previous work to the coupled cantilevers. We realized the identical coupled cantilevers and their arbitrary coupling stiffness in the experiment using the prototype system with a macro-cantilever. Furthermore, we achieved ultrasensitive mass sensing.

1. Introduction

Recently, various MEMS sensors using eigenmode shift of coupled microresonators have been investigated [7, 9, 15, 16, 17]. In the field of mass sensing, Spletzer, et al. developed the sensitive mass sensor using weakly coupled cantilevers [10]. This method improved the sensitivity when compared with the conventional methods using eigenfrequency shift of a single cantilever [3, 8, 14]. Theoretical analysis of sensors based on the eigenmode shift shows that weaker coupling stiffness between cantilevers realizes higher sensitivity [10]. However, because the coupling between the cantilevers is usually established by the overhang between them, the ultimate weakness is not mechanically realized due to the limitation of machining accuracy. Furthermore, in practical systems, the physical parameters in the cantilever pairs have slight differences due to the machining accuracy, despite the assumption that they are identical in theory. For weak coupling stiffness, the electrical coupling was proposed, which is tunable arbitrary coupling stiffness [5, 6, 11, 12]. On the other hand, any methods for the identity of the cantilevers had not proposed.

To realize both the weak coupling and the identity, we proposed the concepts of "virtual coupled cantilevers" in our previous study [4]. In this concept, the dynamics of one of the coupled cantilevers and the effect of coupling are calculated by a digital computer in real-time; these are called "virtual cantilever" and "virtual coupling". The other "real cantilever" with a mass to be measured is vibrated by the coupling effect. In this way, the physical parameters of the virtual cantilever in the digital computer can be set for those of the real cantilever. Also, the virtual coupling can be ultimate weakness without the restriction of machining accuracy.

In addition, we produce the self-excited oscillation with stable steady amplitude [1, 2, 13] to the virtual coupled cantilevers. The self-excited oscillation enables us to use the mass sensor in high viscosity environments. The amplitude control realizes the mass sensing based on the linear theory by decreasing the influence of the cantilever's nonlinearity. It prevents the accuracy of the mass sensor from decreasing.

In this study, we examine the processing time and the error of the real-time calculation using in the system proposed in [4] and show the validity of the system method by showing the experimental results whose parameters are different from those in [4].

2. Theoretical summary of the virtual coupled cantilevers

We introduce the discretized model of two coupled cantilevers in the conventional study [10] as Fig. 1, where m is the equivalent mass of cantilevers, Δm is the mass to be measured, k is the equivalent stiffness of cantilevers, k_c is the equivalent stiffness of coupling part, c is the viscosity damping coefficient, and Δx is the actuation at the supporting point. The absolute displacements of the cantilever-1 and 2 are denoted by x_1 and x_2, respectively. The conventional coupled cantilevers [10] is implemented by two real cantilevers coupled through an overhang part. On the other hand, the cantilever-1 and the coupling part of the virtual coupled cantilevers [4], which are enclosed by the dashed lines in Fig. 1, are implemented by a real-time calculation. The cantilever-1 and 2 in Fig.1 correspond to the virtual and real cantilever in our previous research [4], respectively. The dimensionless equation of motion for the coupled cantilevers are expressed as

$$
\begin{cases}
\dfrac{\mathrm{d}^2 x_1^*}{\mathrm{d}t^{*2}} + 2\gamma \dfrac{\mathrm{d}x_1^*}{\mathrm{d}t^*} + (1+\kappa)x_1^* - \kappa x_2^* = \Delta x^* & (1) \\[2ex]
(1+\delta)\dfrac{\mathrm{d}^2 x_2^*}{\mathrm{d}t^{*2}} + 2\gamma \dfrac{\mathrm{d}x_2^*}{\mathrm{d}t^*} - \kappa x_1^* + (1+\kappa)x_2^* = \Delta x^*, & (2)
\end{cases}
$$

where x^* and t^* are the dimensionless displacement $x^* = x/L$ (L is the representative displacement) and the dimensionless time $t^* = Tt = \sqrt{k/m}\,t$ (T is the representative time),
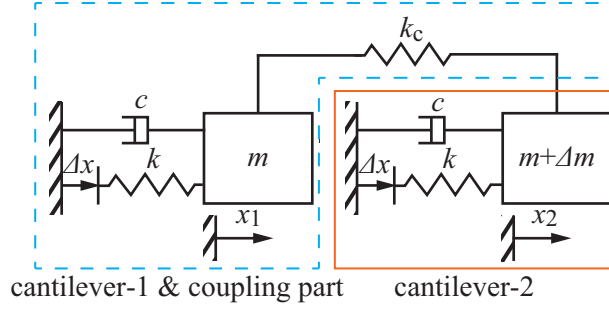
Figure 1. Analytical model corresponding to the two coupled cantilevers for mass sensing. m is the equivalent mass of cantilevers, Δm is the mass to be measured, k is the equivalent stiffness of cantilevers, k_c is the equivalent stiffness of coupling part, c is the viscosity damping coefficient, and Δx is the actuation at the supporting point. The absolute displacements of the cantilever-1 and 2 are denoted by x_1 and x_2, respectively. Reproduced from [4], with the permission of AIP Publishing.

respectively. The parameters, δ, γ and κ, are the mass ratio, the damping ratio and the coupling ratio, respectively. These dimensionless parameters can be expressed in terms of the dimensional parameters of the coupled cantilevers model as

$$\delta = \frac{\Delta m}{m}, \ 2\gamma = \frac{c}{\sqrt{mk}}, \ \kappa = \frac{k_c}{k}. \tag{3}$$

Based on the studies about the mass sensor using weakly coupled cantilevers [10, 13], the 1st eigenmode of coupled cantilevers is expressed as

$$\boldsymbol{p_1} \approx \left[\begin{array}{c} 1 - \frac{\delta}{2\kappa} \\ 1 \end{array} \right] \tag{4}$$

under the assumption of $\delta \ll \delta/\kappa \ll 1$. We can observe the 1st eigenmode from the amplitude ratio of the coupled cantilevers oscillated in 1st mode. The mode shift is in proportion to the mass ratio δ. The proportionality constant of the eigenmode shift is $1/2\kappa$. Therefore, we can improve the sensitivity of the mass sensor using coupled cantilevers by decreasing the coupling ratio κ.

In our previous research [4], in order to realize mass sensing based on the linear theory in viscosity environments, we produced the self-excited oscillation with stable steady amplitude [2] in the virtual coupled cantilevers. We can realize the nonlinear dynamics inspired by the Rayleigh oscillator with a limit cycle in the coupled cantilevers by setting the actuation Δx as

$$\Delta x^* = \beta_l \frac{\mathrm{d}x_2^*}{\mathrm{d}t^*} - \beta_n \left(\frac{\mathrm{d}x_2^*}{\mathrm{d}t^*} \right)^3, \tag{5}$$

where β_l and β_n are the dimensionless linear and nonlinear feedback gains, respectively. When the linear feedback gain β_l is set slightly larger than twice damping ratio 2γ, we can compensate for viscosity and produce self-excited oscillation in the coupled cantilevers. The nonlinear feedback realizes stable steady amplitude of self-excited cantilevers as shown in [2]. Larger nonlinear feedback gain makes amplitude smaller, which prevents the measurement accuracy from decreasing.

In the virtual coupled cantilevers we proposed [4], the cantilever-1 and the coupling part, which are enclosed by the dashed lines in Fig. 1, was implemented by the real-time calculation and the actuation to the cantilever-2, which is enclosed by the solid lines in Fig. 1. This method enables us to change the physical parameters of the cantilever-1 and the coupling part. In order to obtain the dynamics of the cantilever-1, we solve Eqs. (1) and (5) by using the fourth-order Runge-Kutta method. The coupling between the cantilevers is implemented by the feedback actuation Δx_c. According to the conventional study [4], the equation of motion of a single cantilever is expressed as

$$(1+\delta)\frac{\mathrm{d}^2 x_2^*}{\mathrm{d}t^{*2}} + 2\gamma\frac{\mathrm{d}x_2^*}{\mathrm{d}t^*} + x_2^* = \Delta x_c^*, \tag{6}$$

where Δx_c^* is the dimensionless feedback actuation ($\Delta x_c^* = \Delta x_c/L$). We set the feedback actuation Δx_c^* as

$$\begin{aligned}
\Delta x_c^* &= \kappa\left(x_1^* - x_2^*\right) + \Delta x^* \\
&= \kappa\left(x_1^* - x_2^*\right) + \beta_l\frac{\mathrm{d}x_2^*}{\mathrm{d}t^*} - \beta_n\left(\frac{\mathrm{d}x_2^*}{\mathrm{d}t^*}\right)^3
\end{aligned} \tag{7}$$

so that the dynamics of the single cantilever will correspond to that of cantilever-2. Equation (6) is equivalent to the equation of motion of the cantilever-2 expressed by Eq. (2) when we apply the feedback actuation Eq. (7).

3. Experiment

For mass sensing experiments, we built the virtual coupled cantilevers using a macro cantilever as a prototype system. Figure 2 shows the experimental apparatus of the virtual coupled cantilevers. The cantilever-2, whose dimensions are 210mm × 15mm × 0.3mm, is made of a phosphor bronze sheet. The mass m is 7.758g. When we measure mass of a sample, we fix it on the cantilever-2 using a double sided tape. The laser displacement sensor (KEYENCE Corp.: IL-S025) measures the displacement of the cantilever-2 x_2. Digital Signal Processor (DSP) (dSPACE GmbH: DS1104) calculates the displacement of the cantilever-1 x_1 by using the fourth-order Runge-Kutta method in real-time as mentioned bellow. From the result, the feedback actuation to the cantilever-2 through the piezo actuator (TOKIN Corp.: AHB700C801FD0LF), which is based on the feedback actuation Eq. (7)
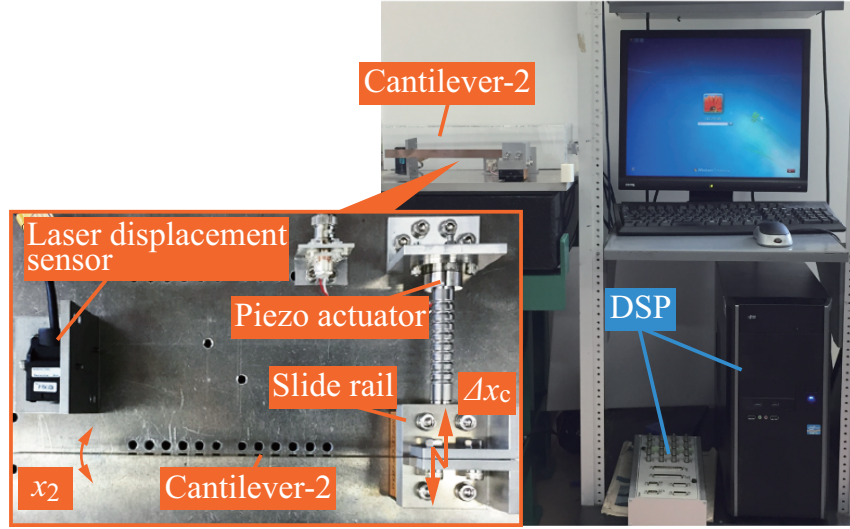
Figure 2. Experimental apparatus. When we measure mass of a sample, we fix it on the cantilever-2 using a double sided tape. The laser displacement sensor measures the displacement of the cantilever-2 x_2. Digital Signal Processor (DSP) calculates the displacement of the cantilever-1 x_1. The cantilever-2 moves smoothly in the excitation direction because it is on the slide rail. Reproduced from [4], with the permission of AIP Publishing.

for the effect of coupling, the linear feedback, and the nonlinear feedback, is determined in DSP. The cantilever-2 moves smoothly in the excitation direction because it is on the slide rail (THK CO., LTD.: LSP2050).

For the application of Runge-Kutta method, we set the state valuables as

$$
\boldsymbol{X^*} = \begin{bmatrix} x_1^* \\ \dot{x_1^*} \\ x_2^* \\ \dot{x_2^*} \end{bmatrix}, \tag{8}
$$

where x_2^* and $\dot{x_2^*}$ are the displacement and the velocity of cantilever-2 measured by the laser

displacement sensor, respectively. Equations (1) and (2) can be rewritten as

$$
\frac{d}{dt^*} \boldsymbol{X}^* = \begin{bmatrix} 0 & 1 & 0 & 0 \\ -(1+\kappa) & -2\gamma & \kappa & \beta_l \\ 0 & 0 & 0 & 1 \\ \kappa & 0 & -(1+\kappa) & -2\gamma+\beta_l \end{bmatrix} \boldsymbol{X}^* - \begin{bmatrix} 0 \\ \beta_n \dot{x_2}^3 \\ 0 \\ \beta_n \dot{x_2}^3 \end{bmatrix}
$$

$$
- \frac{\delta}{1+\delta} \begin{bmatrix} 0 & 0 & 0 & 0 \\ 0 & 0 & 0 & 0 \\ 0 & 0 & 0 & 0 \\ \kappa & 0 & -(1+\kappa) & -2\gamma+\beta_l \end{bmatrix} \boldsymbol{X}^* + \frac{\delta}{1+\delta} \begin{bmatrix} 0 \\ 0 \\ 0 \\ \beta_n \dot{x_2}^3 \end{bmatrix} . \qquad (9)
$$

By solving Eq. (9), we can obtain the dynamics of cantilever-1. However, we cannot solve it because the mass ratio δ is unknown. Therefore, we solve Eq. (9) under the approximation of $\delta = 0$. The order of the error from the actual model due to this approximation is $O(h^{*2}\delta)$, where h^* is the step-size of the numerical calculation. In this research, the orders of both the step-size h^* and the mass ratio δ are 10^{-3}. Therefore, the error due to the approximation of $\delta = 0$ is small enough to ignore. Thus, we use the solution of Eq. (9) with $\delta = 0$ as the displacement and the velocity of cantilever-1. On the other hand, we do not use those of cantilever-2 calculated because we can get the measurement data of the laser displacement sensor in real-time.

We consider the processing time of our system to verify that it is fast enough to realize the virtual coupled cantilevers without a delay. The laser displacement sensor measures every 1ms. The A/D converter of the DSP takes 9ns to convert the displacement signal from the laser displacement sensor into digital signals. We set the step size of real-time calculation as 1ms. Therefore, the order of the processing time of the system is millisecond. On the other hand, the period of the cantilever-2 is 0.255 seconds. Therefore, the processing time is fast enough to ignore the influences of the delay derived from the processing of the system.

In order to calculate the dynamics of the coupled cantilevers, we solve the equation of motion of cantilevers, i.e., Eq. (9), by using the fourth-order Runge-Kutta method. We set the representative time T and the dimensionless damping ratio γ to solve Eq. (9). These parameters derive from the physical parameters of the cantilever-2. The representative time T accords with the inverse of the cantilever-2's angular frequency. We measured the period of the cantilever-2 by Fast Fourier transform analysis and obtained the inverse of angular frequency. We set the representative time T as the inverse of angular frequency obtained (4.057×10^{-2}). The dimensionless damping ratio of the cantilever-1 accords with that of the cantilever-2. We can obtain the dimensionless damping ratio from the envelope curve of a free oscillation wave and the eigenfrequency of the cantilever-2. We described the envelope

curve of the free oscillated cantilever-2 from the experimentally measured time history and obtained the dimensionless damping ratio of the cantilever-2. We set the dimensionless damping ratio of cantilever-1 to be same as that of cantilever-2 (8.65×10^{-4}).

4. Experimental behavior of coupled cantilevers including a virtual cantilever

We measured the amplitude of the virtual coupled cantilevers applied the amplitude control method expressed as Eq. (5). Figure 3 is the time histories of the cantilever-2's displacement when the virtual coupled cantilevers have no additional mass, i.e., $\delta = 0$. The horizontal and vertical axes represent time and displacement of the cantilever-2, respectively. Figure 3 (a) shows the cantilever-2's displacement with the linear feedback only. Figures 3 (b) and (c) show the displacement with the linear and nonlinear feedbacks when the nonlinear feedback gain is set as $\beta_n = 0.02$ and $\beta_n = 0.04$, respectively. We observed almost same time histories of cantilever-1 because the two cantilevers oscillate in accordance with Eq. (4). The cantilever-2 is self-excited by the linear feedback. Figure 3 (a) shows the amplitude
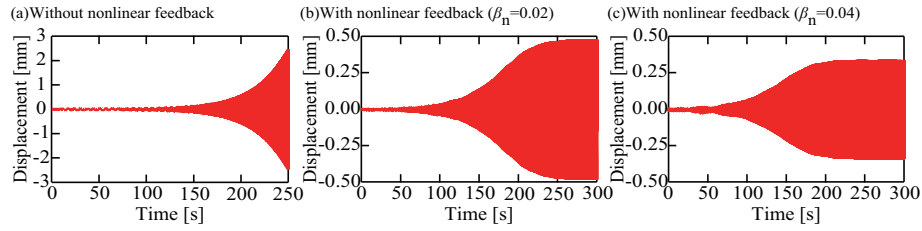
Figure 3. Time histories of cantilever-2's displacement. (a) without nonlinear feedback gain ($\beta_n = 0$), (b) with nonlinear feedback gain ($\beta_n = 0.02$), (c) with nonlinear feedback gain ($\beta_n = 0.04$). The horizontal and vertical axes represent time and displacement of the cantilever-2, respectively.

of the cantilever-2 grows with time when the nonlinear feedback does not apply to the cantilevers. On the other hand, Figs. 3 (b) and (c) show the amplitude of cantilever-2 does not grow unbounded, but reach the finite stable steady amplitude by the effect of the nonlinear feedback. Furthermore, we can observe higher nonlinear feedback realizes lower amplitude of the cantilever. The application of the self-excited oscillation and the amplitude control to the virtual coupled cantilevers leads to the same behaviors as the real coupled cantilevers [2].

We performed the mass sensing of ten mass samples ranging from 0.010g to 0.001g with two different coupling ratios κ (0.010 and 0.005). We carried out the measurement ten times per a sample. Figure 4 presents the mass sensing results. The horizontal and vertical axes
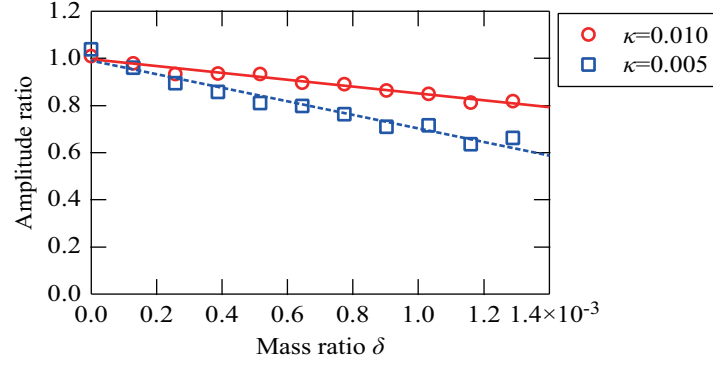
Figure 4. Relationship between the amplitude ratio and mass ratio δ. The horizontal and vertical axes represent the mass ratio δ and the amplitude ratio, respectively. The red circles and the blue squares represent the averaged ratio of the cantilever-1's amplitude to cantilever-2's when their coupling stiffness κ are 0.010 and 0.005, respectively. The red solid line and the blue dashed line represent the regression lines corresponding to the red circles and the blue squares, respectively.

represent the mass ratio δ and the amplitude ratio, respectively. The red circles and the blue squares represent the averaged ratio of the cantilever-1's amplitude to cantilever-2's when their coupling stiffness κ are 0.010 and 0.005, respectively. The red solid line and the blue dashed line represent the regression lines corresponding to the red circles and the blue squares, respectively. The amplitude ratio of the virtual coupled cantilevers is in proportion to the mass ratio δ. In addition, the rate of the amplitude ratio shifts is larger when we set the coupling ratio κ to be smaller. Therefore, weaker coupling stiffness realizes higher sensitivity. These results experimentally confirmed the theoretical analysis of amplitude ratio shown as Eq. (4).

5. Conclusion

In this paper, we examined the effect of the processing time and the error of the real-time calculation in the mass sensing using the virtual coupled cantilevers proposed in our previous study. From the theoretical and experimental approaches, we confirmed that they do not affect the accuracy of the measurement results. We experimentally showed that nonlinear feedback avoids the unbounded amplitude growth of the self-excited oscillation and the higher nonlinear feedback gain realizes the self-excited oscillation with smaller steady state amplitude. Tuning the weakness of the virtual coupling as different values, we preformed mass sensing to verify that the weaker coupling leads to higher sensitive mass sensing. The

virtual coupled cantilevers can achieve ultrasensitive mass sensing because they can realize identical cantilevers and the weak coupling stiffness between them.

Acknowledgments

References

[1] Endo, D., Yabuno, H., Higashino, K., Yamamoto, Y., and Matsumoto, S. Self-excited coupled-microcantilevers for mass sensing. *Appl. Phys. Lett. 106*, 22 (2015), 223105.

[2] Endo, D., Yabuno, H., Yamamoto, Y., and Matsumoto, S. Mass sensing in a liquid environment using nonlinear self-excited coupled-microcantilevers. *J. Microelectromech. Syst. 27*, 5 (2018), 774–779.

[3] Gupta, A., Akin, D., and Bashir, R. Single virus particle mass detection using microresonators with nanoscale thickness. *Appl. Phys. Lett. 84*, 11 (2004), 1976–1978.

[4] Kasai, Y., Yabuno, H., Ishine, T., Yamamoto, Y., and Matsumoto, S. Mass sensing using a virtual cantilever virtually coupled with a real cantilever. *Appl. Phys. Lett. 115*, 6 (2019), 063103.

[5] Manav, M., Phani, A. S., and Cretu, E. Mode localized mems transducers with voltage-controlled linear coupling. *J. Micromech. Microeng. 27*, 5 (2017), 055010.

[6] Manav, M., Reynen, G., Sharma, M., Cretu, E., and Phani, A. Ultrasensitive resonant mems transducers with tuneable coupling. *J. Micromech. Microeng. 24*, 5 (2014), 055005.

[7] Okamoto, H., Kitajima, N., Onomitsu, K., Kometani, R., Warisawa, S.-i., Ishihara, S., and Yamaguchi, H. High-sensitivity charge detection using antisymmetric vibration in coupled micromechanical oscillators. *Appl. Phys. Lett. 98*, 1 (2011), 014103.

[8] Ono, T., Li, X., Miyashita, H., and Esashi, M. Mass sensing of adsorbed molecules in sub-picogram sample with ultrathin silicon resonator. *Rev. Sci. Instrum. 74*, 3 (2003), 1240–1243.

[9] Spletzer, M., Raman, A., Sumali, H., and Sullivan, J. P. Highly sensitive mass detection and identification using vibration localization in coupled microcantilever arrays. *Appl. Phys. Lett. 92*, 11 (2008), 114102.

[10] Spletzer, M., Raman, A., Wu, A. Q., Xu, X., and Reifenberger, R. Ultrasensitive mass sensing using mode localization in coupled microcantilevers. *Appl. Phys. Lett. 88*, 25 (2006), 254102.

[11] THIRUVENKATANATHAN, P., YAN, J., WOODHOUSE, J., AZIZ, A., AND SESHIA, A. Ultrasensitive mode-localized mass sensor with electrically tunable parametric sensitivity. *Appl. Phys. Lett. 96*, 8 (2010), 081913.

[12] THIRUVENKATANATHAN, P., YAN, J., WOODHOUSE, J., AND SESHIA, A. A. Enhancing parametric sensitivity in electrically coupled mems resonators. *J. Microelectromech. Syst. 18*, 5 (2009), 1077–1086.

[13] YABUNO, H., SEO, Y., AND KURODA, M. Self-excited coupled cantilevers for mass sensing in viscous measurement environments. *Appl. Phys. Lett. 103*, 6 (2013), 063104.

[14] YANG, J., ONO, T., AND ESASHI, M. Mechanical behavior of ultrathin microcantilever. *Sens. Actuators. A. Phys. 82*, 1-3 (2000), 102–107.

[15] ZHANG, H., LI, B., YUAN, W., KRAFT, M., AND CHANG, H. An acceleration sensing method based on the mode localization of weakly coupled resonators. *J. Microelectromech. Syst. 25*, 2 (2016), 286–296.

[16] ZHAO, C., WOOD, G. S., XIE, J., CHANG, H., PU, S. H., CHONG, H. M., AND KRAFT, M. A sensor for stiffness change sensing based on three weakly coupled resonators with enhanced sensitivity. In *Micro Electro Mechanical Systems (MEMS), 2015 28th IEEE International Conference on* (2015), p. 881.

[17] ZHAO, C., WOOD, G. S., XIE, J., CHANG, H., PU, S. H., AND KRAFT, M. A force sensor based on three weakly coupled resonators with ultrahigh sensitivity. *Sens. Actuators. A. Phys. 232* (2015), 151–162.

Yuki Kasai, B.E. (M.E. student): University of Tsukuba/Graduate school of System and Information Engineering/Nonlinear Mechanical Systems Laboratory, 1-1-1 Tennodai, Tsukuba, Ibaraki, Japan (*s1920782@s.tsukuba.ac.jp*). The author gave a presentation of this paper during one of the conference sessions.

Hiroshi Yabuno, Ph.D., Professor: University of Tsukuba/Graduate school of System and Information Engineering/Nonlinear Mechanical Systems Laboratory, 1-1-1 Tennodai, Tsukuba, Ibaraki, Japan (*yabuno@esys.tsukuba.ac.jp*).

Takeshi Ishine, B.E.: University of Tsukuba/School of Science and Engineering/Nonlinear Mechanical Systems Laboratory, 1-1-1 Tennodai, Tsukuba, Ibaraki, Japan (*it3939241084@gmail.com*).

Yasuyuki Yamamoto, Ph.D.: Fluid Property Standards Group, Research Institute for Engineering Measurement, National Metrology Institute of Japan(NMIJ), National Institute of Advanced Industrial Science and Technology(AIST), 1-1-1 Umezono, Tsukuba, Ibaraki, Japan (*yamamoto-yasu@aist.go.jp*).

Sohei Matsumoto, Ph.D.: Research Center for Ubiquitous MEMS and Micro Engineering, National Institute of Advanced Industrial Science and Technology (AIST), 1-2-1 Namiki, Tsukuba, Ibaraki, Japan (*sohei.matsumoto@aist.go.jp*).

Improving functionality of absorber/harvester system by a smart adaptive suspension

Krzysztof Kecik, Rafal Rusinek

Abstract: In this work, a vibration absorber/harvester is designed and the interaction between its vibration absorption ability and harvesting capability is investigated. The special designed pendulum is mounted to the oscillator leads to the autoparametric system. In order to increase the effectiveness, the adaptive smart suspension consisting of the magnetorheological damper and shape memory spring is applied. The smart elements can improve or worsen effecivness of vibration mitigation as well as energy harvesting. However, the unstable zones can be easy reduced by a MR damper.

1. Introduction

Unwanted vibration have been one of the major problems for engineers. The harmful vibration caused in a resonance condtion existing in multifarious engineering applications. Buldings, bridges, towers and offshore rigs can execute large amplitude oscillations when the frequencies of excitation are close to their natural frequencies. This phenomenon can be amplified by geometric and material nonlinearity. To suppress the unwanted motions, passive, semi-active, active and hybrid control strategies were investigated in the literature [3, 8, 13]. Therefore, the civil structures demand special requirements of vibration mitigation or isolation. The basis way for achiving these requirments is the stiffness or/and damping control. The common method that changes the stiffness and damping is an use of components with controllable properties like magnetorheological (MR) damper and shape memeory alloy (SMA) spring. Combining stiffness element with a damping is common way to avoid unwanted vibrations.

On the other hand, the vibration energy that has attracted a lot of attention lately, is a renewable sustainable energy. The large amplitude vibration can be used to effective energy harvesting. The harvested energy could be accumulated to operate small devices such as microelectromechanical systems (MEMS), various type of actuators or wireless sensors [9, 15]. An example of this could be bridges, tunnels or buildings where sensors are required to assess continually the vibration levels whilst at the same time, being powered by those same vibrations [10, 11]. A typical vibration energy harvesting system consists of the excited mechanical system and the transducer which converts the vibration energy into electric one.

The effectiveness of harvester depends greatly on transducer mechanism and nonlinearity of the system.

The aim of this paper is to control of the non-linear dynamics and recovered power from the absorber/harvester system by the smart adaptive suspension.

2. Absorber/harvester model

2.1. Equations of motion

In this section the absorber/harvester is proposed. The system is based on modification of the model presented in the paper [4]. It consists of the host structure (I), the tuned mass damper (II) with the maglev harvester. The maglev harvester uses magnetic levitation effect. The detail description of the system can be found in papers [4, 5]. The classical suspension of the tuned mass damper has been changed into the adaptive smart suspension consists of the MR damper and the SMA spring.

Figure 1. Model of absorber/harvester system (a), and the maglev harvester (b).

The equations of motion governing the motion of the system derives from the Lagrange's equation of the second kind and given as [4]:

$$(m_1 + m_2 + m_3)\ddot{x} + (m_2 s + m_3(z + r))[\ddot{\varphi}sin\varphi + \dot{\varphi}^2 cos\varphi] + m_3(2\dot{r}\dot{\varphi}sin\varphi - \ddot{r}cos\varphi)$$
$$+F_{MR} + k_{SMA}x + k_2 x = k_2 x_0 sin(\omega t), \tag{1}$$

$$(I_0 + m_3(z + r)^2)\ddot{\varphi} + (\ddot{x} + g)[m_2 s + m_3(z + r)]sin\varphi + 2m_3\dot{\varphi}\dot{r}(z + r) + c_2\dot{\varphi} = 0, \tag{2}$$

$$m_3\ddot{r} - m_3[\ddot{x}cos\varphi + \dot{\varphi}^2(z + r)] - m_3 g cos\varphi + c_3\dot{r} + k_3 r + k_4 r^3 + \alpha i = 0, \tag{3}$$

$$L\dot{i} + (R_L + R_C)i - \alpha\dot{r} = 0, \tag{4}$$

where m_1, m_2, m_3 are masses of the oscillator, the pendulum and the magnet. Parameter k_2 is stiffness of the excitation linear spring, c_2 is the pendulum's pivot damping, s is the pendulum gravitation centre, I_0 is the pendulum momentum inertia, z is the initial position of the magnet. Parameters x_0 and ω are the kinematic amplitude and frequency of excitation. The k_{SMA} means SMA spring which depends on the phase transformation state. The term F_{MR} is the force in the MR damper. The maglev harvester can be treated as mechanical suspension consisting of the linear damper c_3 (friction) and the strong nonlinear spring with the stiffness k_3 and k_4. The harvester electrical circuit includes the coil (with the inductance L and resistance R_C), and the resistor load R_L. The mechanical and electrical systems are coupled by the transduction (electromechanical) factor α. The system has four degrees of freedom, namely: x for the host structure, φ for the tuned mass damper, r for the magnet and i for the recovered current.

2.2. Smart absorber/harvester suspension

The adaptive suspension of the absorber/harvester system consists of the SMA spring and the MR damper. Shape Memory Alloy (SMA) is one of most promising material with an enormous growth in usage [7, 14]. SMAs are naturally classified as metallic materials with high damping capacity, consequence of a hysteretic behavior related to phase transformations of the material. The SMA material characterizes the unique property of "shape effect"(simple and double), super elasticity and biocompatibility.

In this work, the simplified mathematical Ikuta's model [1, 2] was applied to describe the behaviour of the theoretical stiffness of the SMA spring. The model is a function of applied temperature and phases change. The SMA spring stiffness during heating is

$$k_{SMA(A)} = k_{min} + [(k_{max} - k_{min}) - \frac{k_{max} - k_{min}}{1 + e^{((\beta/(A_f - A_s))(T - ((A_f + A_s)/2)))}}], \tag{5}$$

and colling

$$k_{SMA(M)} = k_{min} + [(k_{max} - k_{min}) - \frac{k_{max} - k_{min}}{1 + e^{((\beta/(M_s - M_f))(T - ((M_f + M_s)/2)))}}], \tag{6}$$

where:

- $k_{SMA(A)}$, $k_{SMA(M)}$ are stiffness of the SMA spring during heating and cooling,

- k_{min}, k_{max} are minimum and maximum stiffness of the SMA spring,

- M_s, M_f, A_s and A_f are martensite and austenitic start and finish temperatures,

- T is the SMA spring temperature,

- β is the coefficient ($\beta = 6.2$).

The coefficient β is adapting transformation temperature obtained from the Differential Scaling Calorimeter method [2].

The stiffness-temperature relationship of the simplified Ikuta's model is presented in Fig.2 (a). The red line means transformation in austenitic phase (heating process), while the blue line in martensite (cooling process). The phase transformation temperatures obtained were M_s=56.8^{o}C (martensite start) and M_f=24.8^{o}C (martensite finish) during cooling and A_s=30.4^{o}C (austenite start) and A_f=61.5^{o}C (austenite finish) during heating.

(a) (b)
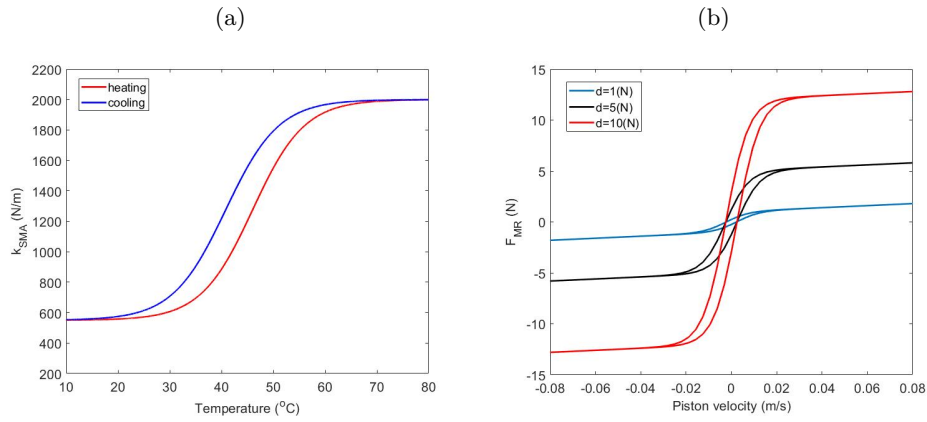
Figure 2. Theoretical stiffness of the SMA spring as a function of the temperature (a), obtained for parameters: k_{min}=550N/m, k_{max}=2000N/m (a). The force-velocity characteristics of the MR damper for c_1=10Ns/m (b).

It can be observed that the stiffness increased 3.6 times at the end of heating when is compared with the initial value. If temperature is higher than 60°C the stiffness tends to stabilize, due to the fact that from this point the crystalline structure (fully austenitic phase). Similarly, stabilization of stiffness can be obtained at temperatures below 25°C when the SMA spring gets fully martensitic.

The second smart element is the MR damper. The design and applications of the MR devices have been an area of recent interest due to the controllable characteristics of the MR material. They are controlled in terms of the applied current, which almost simultaneously changes the magnetic field and thus the shear viscosity of the damper. When it is not activated, the MR fluid behaves like a free flowing liquid, with a consistency similar to that of typical oil.

In our research, the MR damper can described by the modified Bingham's model [6]

$$F_{MR} = dtanh(e_1\dot{x} + e_2x) + c_1\dot{x}, \qquad (7)$$

where c_1 is the viscous damping coefficient, d is the force coefficient related to the rheological behaviour produced by the fluid, x and $\dot{x}$ are the piston displacement and velocity of the MR damper. The constant values e_1 and e_2 are assumed 100 and 0.25. They describe the hysteresis shape and are usually obtained by the curve fittings. Attitude of the MR damper in force-velocity curves in Fig. 2(b) are presented. The relationship shows hysteresis loops whose shapes vary according to the applied d parameter. The hysteresis is due to the difference between the accelerating and decelerating paths of the force-velocity curve.

3. Results and Discussion

The proposed smart suspension provides an important new tool for an engineer. The modification of the stiffness or damping gives possibility to control and improve vibration mitigation as well as energy harvesting. The set of equations 1-4 is solved numerically, and the various bifurcation scenarios by mens of pseudo-arclength continuation method is analysed.

The unstable solutions are marked by the dashed line, while the solid line denotes the stable solutions. The bifurcation point are labelled: PD (period doubling bifurcation) and NS (Neimark-Sacker bifurcation). The semi-trivial solution (pendulum in a rest) loss of the stability caused by the PD bifurcation, while the parametric instability in the main parametric resonance is caused by the NS bifurcation. The simulation data were taken from laboratory rig: m_1=0.45kg, m_2=0.3kg, m_3=0.1kg, k_2=1kN/m, k_3=200N/m, k_4=180kN/m^3, c_1=10Ns/m, c_2=0.125Nms/rad, c_3=0Ns/m, z=0.1m, L=1.46H, R_C=R_L=1.1$k\Omega$, α=30V/A.

3.1. Frequency response under SMA spring

In order to check the amplitude excitation influence on the system response for the martensite and austenite phases, the heating and cooling of the SMA spring was applied. The results were compared for the fully martensite phase (T=20°C). The activated temperature changes the SMA spring stiffness according to equations Eqs. 5-6.

The resonance curves of the oscillator, the pendulum and the recovered current for a system with the SMA spring in three different temperatures are presented in Figs. 3(a)-(c), respectively. Firstly, the system with the SMA spring at 20°C that correspond to the spring stiffness k_{SMA}=550N/m (green curve) is analysed. Then, it is heated to 40°C (black curve) and heating for the fully austenit phase is applied. Next, cooling from fully austenit phase to the temperature of 40° (blue curve) was applied. We observe one wide resonance region from $\omega \approx$15−52rad/s. The vibration mitigation region is clearly observed in the frequency

range of $\omega \approx 16.5-32.5$rad/s. In this region the oscillator's amplitude is significantly reduced. However, in the frequency range of $\omega \approx 32.5-52$rad/s the unstable region can appears. [12]. This region is dangerous for the vibration absorbers [12]. Increasing of temperature causes
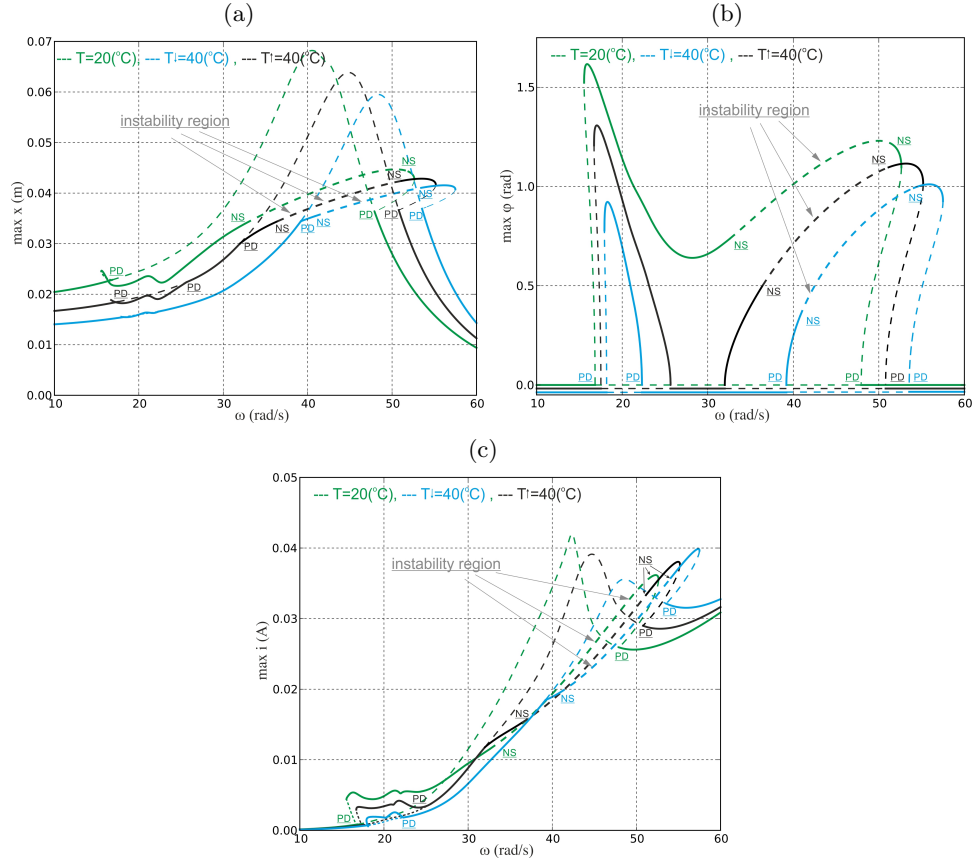
Figure 3. Frequency response of the oscillator (a), the pendulum (b) and the recovered current (c). The green color means response for temperature $T=20^oC$ (550N/m), blue for $T=40^oC$ (1220N/m, cooling), and black $T=40^oC$ (880N/m, heating).

that the main resonance curve divided into two separate curves (blue color in Fig.3(b)). The resonance frequency range became narrowed, and the oscillation of the main system and the pendulum are reduced. Unfortunately, the vibration mitigation is also significantly decreased (Fig. 3(a)). Increasing of the temperature reduces the recovered current for low frequency range and improves in higher frequencies (Fig. 3(c)). The maximal recovered current was at the level $i_{max}=0.04$A, what corresponds power $P=1.76$W (for 40^oC), while for temperature $T=20^oC$ the maximal recovered energy is 1.36W.

3.2. Frequency response under MR damper

To change the dynamics of the absorber/harvester system the second option based on the MR damper is proposed. The damping force F_{MR} can only be commanded by the input voltage adjusted to the MR damper, therefore this is simply to implementation in the real structures. Additionally, the unstable region can be controlled by proper value of the damping force.

Introducing damping force d to the system, we reduced the amplitudes of the oscillator (Fig. 4(a)) and pendulum (Fig. 4(b)), but the vibration mitigation effect still exists in the wide range. The analysis shows that increase of d causes smal reduce the resonance region. Moreover, reduction of the unstable area in the main resonance region is observed. This
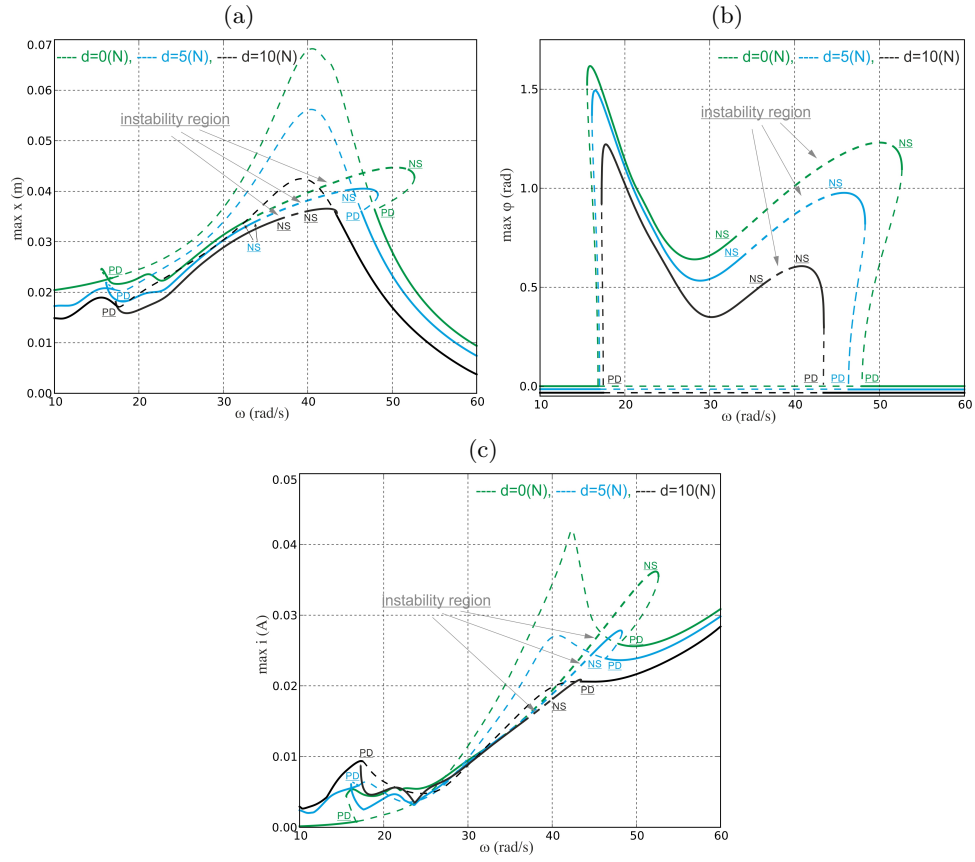
Figure 4. Frequency response for the oscillator (a), the pendulum (b), and the recovered current (c) obtained for k_{SMA}=550N/m. The green color means response for d=0N, blue line for d=5N and black for d=10N.

is a very important result from a practical point of view, because the parameter d can be

used to the dynamics control of the vibration absorber without decrease its efficiency. For parameter d=0N the unstable region appears in the frequency range of $\omega \approx 32.5-52$rad/s (green line), but for d=10N (black line) the instability is located for $\omega \approx 36.5-40$rad/s. Interesting situation is observed for the recovered current response (Fig. 4(c)). For frequency $\omega >50$rad/s increase of d to 10N causes decreasing of i_{max} about 77% to power P_{max}=0.45W (for d=5N, P_{max}=0.58W). However, for lower ω (<23rad/s) activation of the MR damper causes increasing in the recovered current. For d=0N the current is $i_{max} \approx 5$mA (30mW), for d=5N, $i_{max} \approx 6$mA (40mW), and for d=10N, $i_{max} \approx 9.5$mA (90mW). This suggest, that MR damper can improve energy harvesting effect.

4. Conclusions

The dynamic response, bifurcation analysis and control of a pendulum vibration absorber system with added the harvester device, operating under the parametric resonance conditions are discussed in the paper. The system originally designed to vibration mitigation allows energy recovery. The modification of the pendulum absorber by adding the harvester can influence on the response of mechanical parts. All subsystems are coupled by the electromechanical transduction coefficients. Additionally, the moment of inertia and the gravity centre of the pendulum changes as a result of the motion of the magnet. This can lead to unwanted vibration and the unstable regions.

The SMA spring analysis shows that an increase of the temperature causes modification of the resonance curve shape. It is divided into two separate resonance curves (Fig. 3). The vibration mitigation region is significantly reduced. However, the unstable region under the SMA spring is similar. Comparing result for the same temperature (40°C) during heating and cooling the best results obtained if the SMA spring is heating. Then, the maximal recovered power was on the level 1.76W.

The MR damping analysis shows that an increase of the MR parameter damping practically does not reduce the mitigation effect. Furthermore, it can be improving by the reduction of unstable regions. The recovered energy generally decreases if the MR damper is activated. However, for the lower frequency range the MR damper slightly increases energy harvesting efficiency.

In next step the proposed suspension will be implemented in the real laboratory system. The different algorithms to control will be proposed and tested. The description to find the compromise region between vibration mitigation and energy harvesting will be found.

Acknowledgments

References

[1] HOLANDA, S., SILVA, A., ARUJO, C., AND AQUINO, A. Study of the complex stiffness of a vibratory mechanical system with shape memory alloy coil spring actuator. *Shock and Vibration*, ID 162781 (2014), 1–11.

[2] IKUTA, K., TSUKAMOTO, M., AND HIROSE, S. Mathematical model and experimental verification of shape memory alloy for designing micro actuator. *Micro Electro Mechanical Systems (MEMS) Proceedings. An Investigation of Micro Structures, Sensors, Actuators, Machines and Robots. IEEE*, 3986925 (1991), 103–108.

[3] JIN, X., CHAN, M., AND HUANG, Z. Minimization of the beam response using inerter-based passive vibration control configurations. *International Journal of Mechanical Science*, 119 (2016), 80–87.

[4] KECIK, K. Assessment of energy harvesting and vibration mitigation of a pendulum dynamic absorber. *Mechanical Systems and Signal Processing 106* (2018), 198–209.

[5] KECIK, K., MITURA, A., LENCI, S., AND WARMINSKI, J. Energy harvesting from a magnetic levitation system. *International Journal of Non-Linear Mechanics 94* (2017), 200–206.

[6] KECIK, K., MITURA, A., SADO, D., AND WARMINSKI, J. Magnetorheological damping and semi-active control of an autoparametric vibration absorber. *Meccanica 8*, 49 (2014), 1887–1900.

[7] LAGOUDAS, D. *Shape Memory Alloys: Modeling and Engineering Applications.* Springer, New York, 2008.

[8] LEE, Y., VAKAKIS, A., BERGMAN, L., MCFARLAND, D., AND KERSCHEN, G. Suppressing aeroelastic instability using broadband passive targeted energy transfers, part 1: Theory. *AIAA Journal 3*, 45 (2007), 693–711.

[9] MURALT, P. Ferroelectric thin fims for micro-sensors and actuators: a review. *Journal of Micromechanics and Microengineering*, 10 (2000), 13646.

[10] PUCCINELLI, D., AND HAENGGI, M. Wireless sensor networks: applications and challenges of ubiquitous sensing. *Circuits and Systems Magazine, IEEE 5*, 3 (2005), 19–31.

[11] SODANO, H., INMAN, D., AND PARK, G. A review of power harvesting from vibration using piezoelectric materials. *The Shock and Vibration Digest 36*, 3 (2004), 197–205.

[12] Warminski, J., and Kecik, K. Instabilities in the main parametric resonance area of mechanical system with a pendulum. *Journal of Sound Vibration 322*, 3 (2009), 612–628.

[13] Yan, Z., Ragab, S., and Haji, M. Passive control of transonic utter with a nonlinear energy sink. *Nonlinear Dynamicse 1*, 9 (2018), 577–590.

[14] Yovaraja, M., and Senthil, K. M. Experimental studies on sma spring based dynamic vibration absorber for active vibration control. *European Journal of Scientific Research 2*, 77 (2012), 240–251.

[15] Zhou, W., Liao, W., and Li, W. Ferroelectric thin fims for micro-sensors and actuators: a review. *Smart Structures and Materials, Proceedings of SPIE*, 5763 (2000).

Krzysztof Kecik, Ph. D., D. Sc., Eng.: Lublin University of technology and Department of Applied Mechanics, Nadbystrzycka 36, 20-618 Lublin, Poland (*k.kecik@pollub.pl*). The author gave a presentation of this paper during one of the conference sessions.

Rafal Rusinek, Ph. D., D. Sc., Eng.: Lublin University of technology and Department of Applied Mechanics, Nadbystrzycka 36, 20-618 Lublin, Poland (*r.rusinek@pollub.pl*).

Rapid vibro-acoustic optimisation of laminated composites

Matthias Klaerner, Steffen Marburg, Lothar Kroll

Abstract: Lightweight and stiff composites are sensitive the propagation of structure-borne sound, but simultaneously offer a broad spectrum for adjusting material behaviour. Stiffness and damping of composites are contradictory material properties related to the fibre orientation. Commonly, the composite design is based on FEA simulations requiring special modelling efforts. In contrast, the multi-dimensional optimisation of a laminate with numerous layers of different materials and orientations requires very fast numerical solutions for numerous repetitions. In this study, a complex but efficient vibro-acoustic model is presented. The FEA is extended by a strain energy-based modal damping approach for the layerwise accumulation of the anisotropic damping. In addition, the radiated sound power is determined by a velocity-based approach directly from steady state simulations of the structure avoiding complex multi-physical modelling. Moreover, the frequency dependent radiation is consolidated to a single scalar optimisation objective using a fast and efficient semi-analytic approach. Therefore, analytical formulations of amplification factors of the modal power contributions are introduced. This efficient simulation methodology is further applied to design a vibro-acoustically optimised composite part. The achieved results show the vibro-acoustic optimisation potential of thermoplastic composites compared to a steel reference case by pure material substitution as well as an additional laminate optimisation.

1. Introduction

The simulation-based design and optimisation of dynamically loaded and acoustically sensitive components is state-of-the-art and essentially includes the determination of the radiated sound power. Exact analytical solutions of the sound power are available for only a few simple geometries. Thus, numerical approximation methods are used but are computationally expensive due to fluid-structure-interactions. This typically includes the solution of both, structural and acoustical domains as well as the coupling in one or both directions. In addition, the boundary element method (BEM) is a very popular approach but it is limited for optimising huge problems in a wide frequency range [13].

Avoiding complex multi-physical models, different velocity-based approaches of the sound power P can be used instead for hard reflecting surfaces [8, 4]. These approximation methods are based on structural simulations only using the normal surface velocity for the intensity determination. Namely, there are the equivalent radiated sound power (ERP), the

weighted ERP (wERP), the lumped parameter model (LPM) as well as the volume velocity (PVV) [4, 8]. In addition, the kinetic energy or the related mechanical power of the vibrating system can be used as a qualitative measure of the sound radiation [10, 8]. All power levels L_W are further related to a reference value of 10^{-12} W as well as the energy level L_E of 10^{-12} J.

When solving such complex optimisation problems, an efficient simulation model is essential, but in contrast to the huge number of required frequency steps. As fibre-reinforced components with anisotropic stiffness and damping [1, 2] offer a wide range of variable material properties this implies numerous design parameters and leads to a multi-dimensional optimisation problem. Therein, the modal damping can be modelled with an energetic approximation [7]. Within this study, a new semi-analytic approach is presented to determine the sound power within the given frequency domain with only one simulation step per resonance for the estimation of the radiated sound power in the whole frequency range. Computationally expensive steady state simulations thus are significantly reduced.

2. Analytical description of the sound power contributions

2.1. Sound power contribution of a single mode

The determination by different sound power approaches require numerous frequency steps to represent the entire frequency range with sufficient accuracy [9]. Accordingly, the required frequency resolution is dependent on the modal attenuation, the considered frequency range and the distance to the adjacent modes. Thus, at least 50 to 500 frequency steps per resonance (see section 3).

As a reference for an analytical solution, the sound radiation of an oil pan was investigated. The power was determined with a high frequency resolution of 250 steps per eigenfrequency with biasing of $b_f = 2.5$ (Fig. 1, left). Thus, the narrow local extrema are well represented with a narrow frequency step size while the anti-resonances with only small contributions have a sufficiently accurate but coarse frequency resolution. The modal contributions were further isolated for P_{ERP}. Each eigenfrequency shows a similar frequency characteristic. The superposition of all modal contributions leads to the overall sound power in the frequency domain (Fig. 1, right).

Ensuring sufficient data for the identification of the functional approach in a wide frequency range, the sound power of the first eigenfrequency at 913 Hz has been investigated based on 2,000 narrow equidistant frequencies near and 1,000 additional more distant points within an order of magnitude of the frequency range (here 100–10,000 Hz in Fig. 2, left). The characteristics of the used approaches are equally detectable for each eigenfrequency whereas the differences can be associated to the different assumptions [4, 8]. Therein, kinetic energy
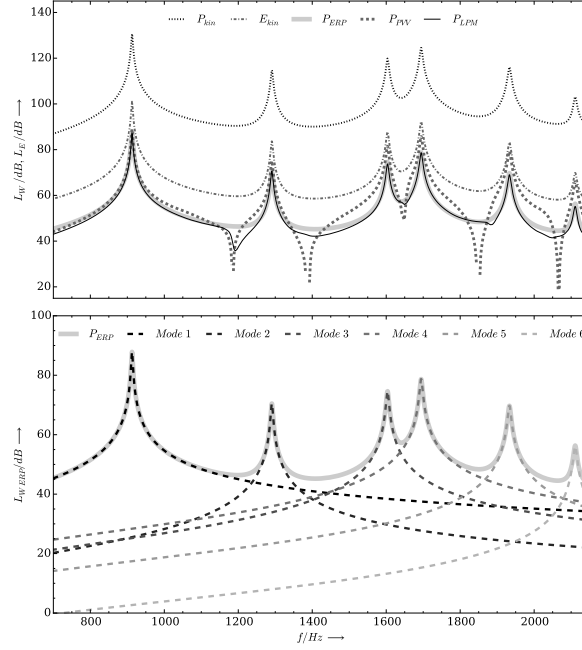
Figure 1. Radiated sound power of an oil pan: modes 1-6, determined with 250 frequency steps each (left) as well as modal contributions of P_{ERP} (right)

and ERP show a consistent frequency characteristic with symmetry to resonance. LPM and PVV correlate for the frequencies below resonance and slightly above. As the frequency increases, the less accurate PVV results in constant power levels, while the LPM converges to the ERP. Since the different local maxima are dependent on the underlying FEA results, the frequency responses are further normalised to their modal maximum $\hat{P}_k$ and $\hat{E}_k$ (Fig. 2, right).

In total, three different characteristic frequency profiles can be identified for which analytical descriptions are derived with the mode-specific frequency ratio $\eta_k = f/f_k$ and the modal damping D_k

$$V_{ERP_k} = \hat{P}_k \frac{4D_k^2 \eta_k^2}{(1-\eta_k^2)^2 + 4D_k^2 \eta_k^2} \qquad\qquad = \hat{P}_k \, V^\star \qquad (1)$$

$$V_{Ekin_k} = \hat{E}_k \frac{4D_k^2 \eta_k^2}{(1-\eta_k^2)^2 + 4D_k^2 \eta_k^2} \qquad\qquad = \hat{E}_k \, V^\star \qquad (2)$$

$$V_{PVV_k} = \hat{P}_k \frac{4D_k^2 \eta_k^4 (1-D_k^2)}{(1-\eta_k^2)^2 + 4D_k^2 \eta_k^2} \qquad\qquad = \hat{P}_k (1-D_k^2)\eta_k^2 \, V^\star \qquad (3)$$

$$V_{Pkin_k} = \hat{P}_k \frac{8\eta_k^3 C_{Pkin}}{(1-\eta_k^2)^2 + 4D_k^2 \eta_k^2} \qquad\qquad = \hat{P}_k \frac{2\eta_k C_{Pkin}}{D_k^2} \, V^\star \qquad (4)$$
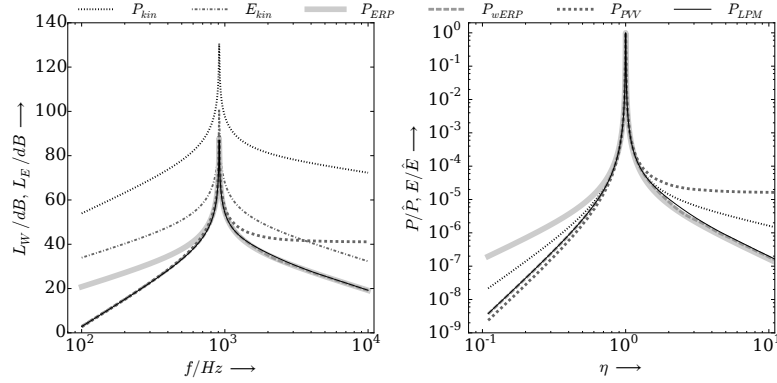
Figure 2. Radiated sound power of the first eigenfrequency of an oil pan: power and energy level (left) as well as power and energy normalised to maximum value (right)

similar to the various amplification factors of single-degree-of-freedom systems (e.g. in [3]) and using the abbreviations

$$V^{\star} = \frac{4D_k^2\eta_k^2}{(1-\eta_k^2)^2 + 4D_k^2\eta_k^2}, \qquad C_{Pkin} = \frac{2D_k^4 + (2D_k^2-1)(\sqrt{D_k^4 - D_k^2 + 1} - 1)}{\sqrt{(2D_k^2 + 2\sqrt{D_k^4 - D_k^2 + 1} - 1)^3}}. \qquad (5)$$

The modal characteristics are contrasted for selected approaches in Fig. 3. Due to the observed interactions of the individual monopole sources, the analytical description of the LPM model is not readily possible. Based on BESSEL-functions, those can be derived from ERP similar to the wERP.
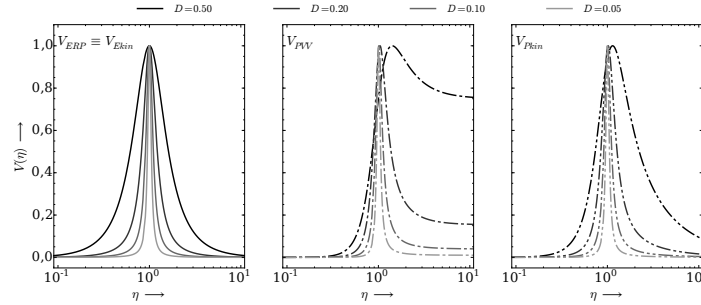
Figure 3. Frequency response of the amplification factors for the sound radiation power for different damping values

The defined amplification factors all have a maximum of 1 but with different locations (Table 1). As the variation of the location is significant only for high damping, the determination of the modal maxima at the undamped eigenfrequency is sufficient, c.f. [11].

244

Table 1. Maxima and its locations for the sound power amplification factors

	ERP, E_{kin}	PVV	P_{kin}
$\eta_{k,max}$	1	$\dfrac{1}{\sqrt{1-2D^2}}$	$\sqrt{2D^2-1+2\sqrt{D^4-D^2+1}}$
$V(\eta_{k,max})$	1	1	1

The determined function expressions and numerical simulations show a very good agreement. In addition, the deviations of LPM and wERP due to their transition from V_{PVV} to V_{ERP} are clearly visible.

2.2. Semi-analytical determination of the frequency-dependent sound power

The analytical descriptions are further used for a semi-analytical synthesis of the total radiated sound power. This can be understood as a superposition of the modal radiated sound power [5] similar to *radiation modes* e.g. [6, 14]. The whole process including finite element simulations (Abaqus 2017) as well as python routines, is shown in Fig. 4.

Figure 4. Velocity-based sound power approaches: FEM simulations, developed programme routines and transferred data as well as integration into iterative optimisation procedures

245

Accordingly, a numerical modal analysis for determining the eigenfrequencies f_k is followed by the determination of the modal damping D_k for anisotropic materials as well as the steady state analysis in modal space. Due to the semi-analytical approach only one frequency step per eigenfrequency is required. The velocity fields $\boldsymbol{v}_{\mu_k}$ and $\boldsymbol{v}_{\nu_k}$ are determined. From there, the maximum sound power within the resonance is calculated with certainty by either the ERP, the LPM or the PVV approach.

Fig. 5 illustrates the further process for the ERP exemplarily. Using the modal damping the amplification factors (1)–(4) give the modal frequency response $P_k(f)$ in the entire frequency range. The superposition of all modes then gives the total radiated power $P(f)$ or energy $E_{kin}(f)$ and can easily be determined with a high frequency resolution. Lastly, it shows very good agreement with a reference solution.

This process is extended by a vibro-acoustic optimisation with an average sound power or energy objective.
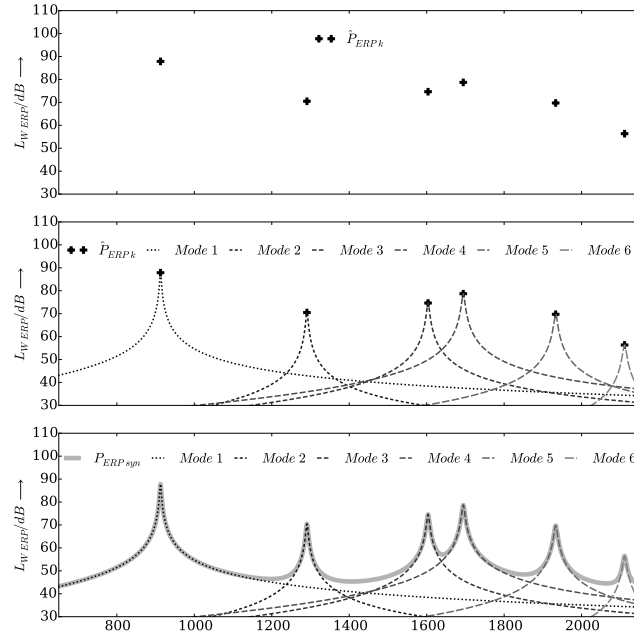
Figure 5. Radiated sound power (ERP) of the first six modes of the oil pan: power values at resonance; analytical solutions for the modal contributions; synthesis of the entire frequency response by superposition (from top to bottom)

3. Average sound power in the frequency domain

The radiation behaviour is frequency dependent. Resonance points produce significant contributions dominating the overall behaviour. This effect is significant for low damped materials and a low modal density. The variation of material or geometry parameters in optimization processes leads to a different number of modes that contribute within the considered frequency range $[f_l, f_u]$.

In order to evaluate different components and design variants, objective functions based on scalar values are implemented in numerical optimisation processes instead of the complex frequency-dependent power results [12, 15]. For the minimisation of the sound radiation, therefore, the average power within the considered frequency range (Fig. 6) is therefore based on

$$\bar{P} = \frac{1}{(f_u - f_l)} \int_{f_l}^{f_u} P(f)df. \tag{6}$$

For the determination of the limited integrals both analytical and numerical approaches are possible. The numerical integral approach is based on the midpoint rule. It applies to the average sound power

$$\bar{P} = \frac{1}{(f_u - f_l)} \sum_{n=1}^{N_f} (\mathrm{d}f_n P_n) \qquad \text{with} \tag{7}$$

$$\mathrm{d}f_1 = \frac{f_2 - f_1}{2}; \quad \mathrm{d}f_n = \frac{f_{n+1} - f_{n-1}}{2} \quad \text{for} \quad 1 < n < N_f; \quad \mathrm{d}f_{N_f} = \frac{f_{N_f} - f_{N_f-1}}{2}. \tag{8}$$

This averaging process can also be applied to non-equidistant frequency step sizes and combined with known A/B/C-weighting [8]. It also allows to evaluate narrowband analyses with scalars. In contrast, such scalar quantities are determined by normative methods of acoustics using octave band values by shifting fixed reference curves.
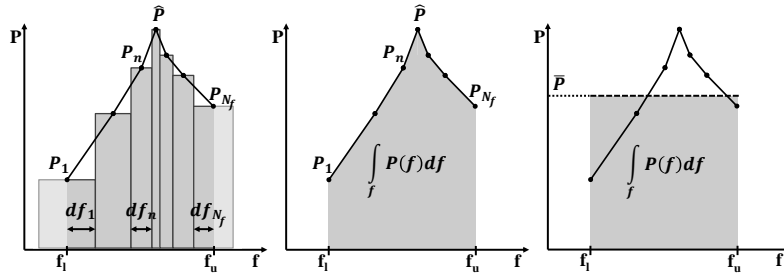
Figure 6. Integration in frequency domain for non-equidistant frequency steps (left); representative area (middle); mean sound power with equivalent representative area (right)

Based on the modal contributions of the radiated sound power, an analytical formulation of the mean power of a single mode was derived. The determination is based on the approaches of the amplification factors by integrating them in the frequency domain with the limits f_l, η_l and f_u, η_u with the assumptions $\eta > 0$ and $0 < D << 1$.

$$\bar{P}_{ERP} = \frac{-\hat{P}D}{\eta_u - \eta_l} \left[\frac{D}{2\sqrt{1+D^2}} \ln \left| \frac{\eta^2 + 2\eta\sqrt{1-D^2}+1}{\eta^2 - 2\eta\sqrt{1-D^2}+1} \right| \cdots \right.$$

$$\left. + \tan^{-1} \left(\frac{\sqrt{1-D^2}-\eta}{D} \right) - \tan^{-1} \left(\frac{\sqrt{1-D^2}+\eta}{D} \right) \right]_{\eta_l}^{\eta_u} \tag{9}$$

$$\bar{P}_{VV} = \frac{\hat{P}\,D}{\eta_u - \eta_l} \frac{1-D^2}{D^2-1} \left[\left[(2D^2-1)^2 + D^2 \right] \tan^{-1} \frac{\sqrt{1-D^2}+\eta}{D} \cdots \right.$$

$$+ \left[(2D^2-1)^2 - D^2 \right] \tan^{-1} \frac{\sqrt{1-D^2}-\eta}{D} \cdots$$

$$\left. + D\left(\sqrt{1-D^2}\frac{4D^2-3}{2} \cdot \ln \left| \frac{-\eta^2 + 2\eta\sqrt{1-D^2}-1}{\eta^2 + 2\eta\sqrt{1-D^2}+1} \right| + 4\eta(D^2-1) \right) \right]_{\eta_l}^{\eta_u} \tag{10}$$

$$\bar{P}_{kin} = \frac{2\hat{P}\,C_{Pkin}}{\eta_u - \eta_l} \left[\ln \left| \eta^4 + 2\eta^2(2D^2-1) + 1 \right| \cdots \right.$$

$$\left. - \frac{2(2D^2-1)}{\sqrt{1-(2D^2-1)^2}} \tan^{-1} \frac{\eta^2 + 2D^2 - 1}{\sqrt{1-(2D^2-1)^2}} \right]_{\eta_l}^{\eta_u} \tag{11}$$

These solutions are based on standard integrals (e.g. in [17]) as well as computer-algebra-systems. The analytical and numerical solutions were validated with different parameter ranges for D and η. The results agree with very good accuracy.

4. Application: composite optimisation

The whole system of structural FEA based sound power approximation with semi-analytic approaches has been applied to a laminate optimisation of the oil pan as a material substitution wherein the shape remains the same. In detail, a unidirectional glass-fibre-reinforced polypropylene thermoPre® material with anisotropic elastic and damping properties is used (table 2). To achieve an optimal lightweight design, the fibre orientations within the layup

Table 2. Material properties of unidirectional glass-fibre-reinforced polypropylene thermoPre® GF 47-PP-UD

elastic parameters				density	damping		
E_1/GPa	E_2/GPa	G_{12}/GPa	ν_{12}	$\varrho/g/cm^3$	$D_1/\%$	$D_2/\%$	$D_{12}/\%$
34.80	5.39	1.42	0.30	1.75	0.15	1.30	1.35

are varied. Due to manufacturing restrictions, symmetrical layups are practicable. For illustration, two independent fibre orientations φ_1 and φ_2 within an eight-layer laminate with $[\varphi_1, \varphi_2]_{2s}$-layup are used as optimisation parameters here. The layer thickness is chosen as 1.1142 mm for a mass-equivalent setup of 2.1 kg from the steel reference.

The sound power synthesis was implemented in the optimisation loop by complementary steps (Fig. 4, grey). First, the mean power $\bar{P}$ is determined as scalar optimisation objective from the frequency depended sound power estimations. The objective of the constraint optimisation problem

$$\Phi(\varphi_1^\star, \varphi_2^\star) = \min[\bar{P}(\varphi_1, \varphi_2)] \quad \text{with} \quad \varphi_1, \varphi_2 = [-90^\circ, 90^\circ] \tag{12}$$

is used to estimate a new parameter set with in any arbitrary deterministic or evolutionary optimisation algorithm.

For an all-encompassing overview of the objective, a full parameter study with a step size of 2° was performed. Fig. 7 shows the mean ERP. This complex and curvaceous objective function contains several local minima. Therefore, metaheuristics are typically used for the solution (e.g. [16]). In this case, the fibre orientations have been determined by a particle swarm optimisation. In addition, the changes in stiffness due to varying fibre orientations
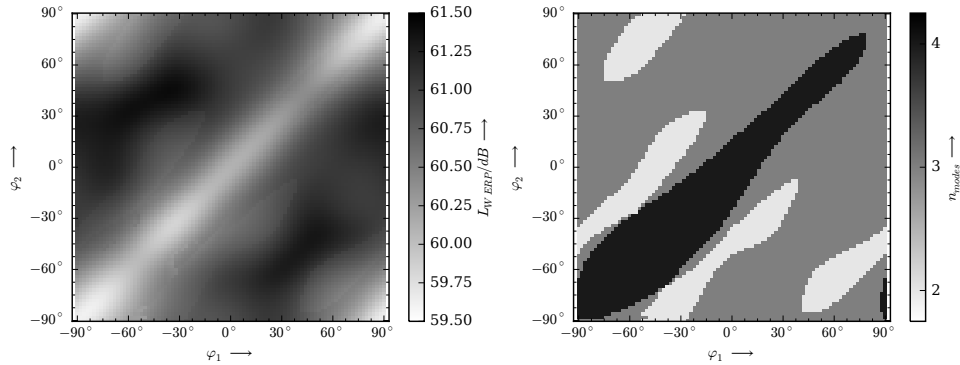
Figure 7. Mean radiated sound power (left) and number of contributing modes (right) of the oil pan from 100 to 2,000 Hz for a layup with varying fibre orientations $[\varphi_1, \varphi_2]_{2s}$

result in escalations of the number of contributing modes (Fig. 7, right). This causes changing sound power objectives, too. The results reflect the contradictory effects in stiffness and damping. A compliant layup may have lower eigenfrequencies and thus more contributing modes but offers significantly more damping. The global minimum is found for a laminate with a $[-82^\circ, -84^\circ]_{2s}$ layup.

To avoid imperfect solutions, stochastic optimisations such as the used particle swarm algorithms are helpful in finding the global optimum. Fig. 8 shows the development of the particles in the value range up to the global minimum. Using continuous model parameters, the global minimum was reached here for a $[-82.2°, -81.7°]_{2s}$ layup.
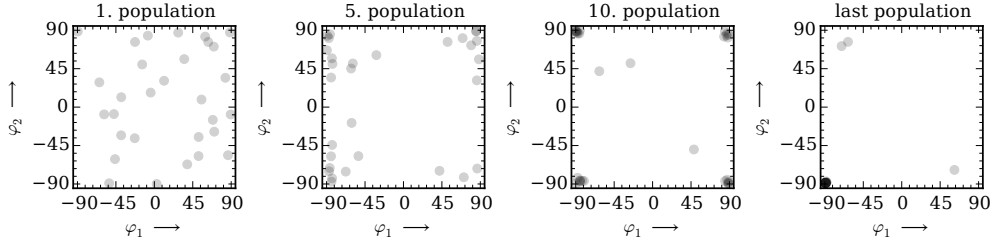
Figure 8. Parameter sets of a particle swarm optimisation of the mean radiated sound power

Regarding computational costs, the full parametric study with discrete fibre orientations of 2° accuracy required 8,281 simulation runs. In contrast, the particle swarm optimisation with continuous fibre orientations converged after 44 runs with 30 particles each and thus 1,320 runs in total.

5. Conclusions

In summary, the radiated sound power is an important objective for acoustic optimisation procedures of vibrating surfaces. Therefore, the known FEA-based approaches of the sound pressure, such as ERP, LPM or PVV, are helpful but still cause significant computational costs. Consequently, a huge number of frequency steps is required for a satisfying accuracy.

In this study, analytical formulations for a precise prediction of the frequency characteristics of the sound power of a single mode were derived. Therefore, only one frequency step per mode was evaluated to determine the modal contributions of the entire frequency range. A further super-positioning of all modal contributions achieves equivalent results but requires significantly less simulation runs compared to a full steady-state FEA with a high frequency resolution .

This semi-analytical approach has been successfully implemented and further applied to an optimisation problem. Therein, a laminate with two independent fibre orientations was optimised by minimising the radiated sound power of the component with a particle swarm optimisation. Due to numerous required simulation runs within any kind of multidimensional optimisation, the derived analytical formulations of the amplification factors are a key issue in accessing fast acoustic optimisation procedures.

Acknowledgments

References

[1] ADAMS, R. D., AND MAHERI, M. R. Dynamic flexural properties of anisotropic fibrous composite beams. *Composites Science and Technology 50*, 4 (1994), 497–514.

[2] BERTHELOT, J.-M. Damping analysis of laminated beams and plates using the Ritz method. *Composite Structures 74*, 2 (2006), 186–201.

[3] DRESIG, H., AND HOLZWEISSIG, F. *Dynamics of Machinery: Theory and Applications.* Springer Berlin Heidelberg, Berlin, Heidelberg, 2010.

[4] FRITZE, D., MARBURG, S., AND HARDTKE, H.-J. Estimation of radiated sound power: A case study on common approximation methods. *Acta Acustica United with Acustica 95* (2009), 833–842.

[5] HAMBRIC, S. A., SUNG, S. H., AND NEFSKE, D. J., Eds. *Engineering vibroacoustic analysis, methods and applications.* Wiley, 2016.

[6] HESSE, C., PAPANTONI, V., ALGERMISSEN, S., AND MONNER, H. Frequency-independent radiation modes of interior sound radiation: Experimental study and global active control. *Journal of Sound and Vibration 401* (2017), 204 – 213.

[7] KLAERNER, M., WUEHRL, M., KROLL, L., AND MARBURG, S. Modelling and fea-simulation of the anisotropic damping of thermoplastic composites. *Advances in Aircraft and Spacecraft Science 3*, 3 (2016), 331–349.

[8] KLAERNER, M., WUEHRL, M., KROLL, L., AND MARBURG, S. Fea-based methods for optimising structure-borne sound radiation. *Mechanical Systems and Signal Processing 89* (2017), 37–47.

[9] KLAERNER, M., WUEHRL, M., KROLL, L., AND MARBURG, S. Accuracy of vibro-acoustic computations using non-equidistant frequency spacing. *Applied Acoustics 145* (2019), 60–68.

[10] KOOPMANN, G. H., AND FAHNLINE, J. B. *Designing Quiet Structures.* Academic Press, London, 1997.

[11] LAMANCUSA, J. S., AND ESCHENAUERT, H. A. Design optimization methods for rectangular panels with minimal sound radiation. *AIAA Journal 32(3)* (1994), 472–479.

[12] MARBURG, S., BEER, H.-J., GIER, J., HARDTKE, H.-J., RENNERT, R., AND PERRET, F. Experimental verification of structural-acoustic modelling and design optimisation. *Journal of Sound and Vibration 252*, 4 (2002), 591–615.

[13] MARBURG, S., AND NOLTE, B., Eds. *Computational Acoustics of Noise Propagation in Fluids - Finite and Boundary Element Methods.* Springer-Verlag, Berlin, Heidelberg, 2008.

[14] MOHEIT, L., AND MARBURG, S. Numerical methods for vibro-acoustics and aeroacoustics: Infinite elements and their influence on normal and radiation modes in exterior acoustics. *Journal of Computational Acoustics* (2017), 1650020.

[15] SHEPHERD, M. R., AND HAMBRIC, S. A. Minimizing the acoustic power radiated by a fluid-loaded curved panel excited by turbulent boundary layer flow. *The Journal of the Acoustical Society of America 136*, 5 (2014), 2575–2585.

[16] ULKE-WINTER, L., AND KROLL, L. Holistic criteria-based optimization of filament wound high pressure vessels. *CIRP Journal of Manufacturing Science and Technology 18* (2017), 173–178.

[17] ZEIDLER, E., Ed. *Springer-Taschenbuch der Mathematik: Begründet von I.N. Bronstein und K.A. Semendjaew Weitergeführt von G. Grosche, V. Ziegler und D. Ziegler Herausgegeben von E. Zeidler.* Springer Fachmedien Wiesbaden, Wiesbaden, 2013.

Matthias Klaerner, Dipl.-Ing.: Chemnitz University of Technology, Institute of Lightweight Structures, 09107 Chemnitz, Germany (*matthias.klaerner@mb.tu-chemnitz.de*). The author gave a presentation of this paper during one of the conference sessions.

Steffen Marburg, Prof. Dr.-Ing.: Technical University of Munich, Gerhard Zeidler Endowed Professorship for Vibroacoustics of Vehicles and Machines, Boltzmannstr. 15/I, 85748 Garching, Germany (*steffen.marburg@tum.de*).

Lothar Kroll, Univ.-Prof. Dr.-Ing. habil. Prof. h. c. Dr. h. c. Prof.: Chemnitz University of Technology, Institute of Lightweight Structures, 09107 Chemnitz, Germany (*lothar.kroll@mb.tu-chemnitz.de*).

Influence of the shoe type on the ground reaction forces

Małgorzata Klepczyńska, Bartłomiej Zagrodny, Wiktoria Wojnicz,
Michał Ludwicki, Jan Awrejcewicz

Abstract: The aim of this work was to estimate a relationship between the type of the footwear and ground reactions. Differences in medio-lateral, anterior-posterior and vertical reactions are compared for different shoe-types for male and female volunteers. Each of the participants gait was recorded in case of different shoes and without them, also stabilograms were analyzed. Results revealed differences in ground reaction forces for different shoe-types and its influence on static stability.

1. Introduction

The concept of gait measurement can have various approaches, depending on the used method. One of the way is to record ground reaction forces/pressure distribution during locomotion [1], [2]. For this purpose, a dynamometric platform or pedobarographic forceplates are used [1–4].

Over the years, different types of footwear were created depending on activity and in order to facilitate foot. A differences between shoes are i.e.: sole thickness and its shape, height of the heel, presence of additional elements, geometry and used materials etc. According to research project, conducted by [5], which aim was to present the relation between well-fitted sports shoes and pain/discomfort reduction. Good assistance at store level in shoe selection has a great influence on orthopedic condition, heel's stability and grip, which give shock absorption and prevent sliding, vertical or horizontal movement. This leads to reduced risk of pain, fractures and overloads and also extends the life span of shoe.

Coordination between postural and locomotive mechanisms is essential to provide effective locomotion. Maintaining constant speed requires continuous renewing of energy – dissipated during center of pressure (COP) movements, limbs swing, friction and drag [6]. The energy is recovered by production of driving and support forces by alternating lower limb work. Under the movement, stability conditions are disturbed. It refers to initial swing phase, when a lower limb pushes off and area of support is reduced. Decreasing periods of double support phase, along with increased speed of gait, can influences balance. With regard to biomechanics, improper transmission of acceleration from limbs to trunk can also affect stability control [6], [7].

As soon as the heel strikes the ground, elastic structures of ankle joint absorbs the energy. Exchange of energy is low and only a small part of it can be reused in loading response (LR) phase.

Rest is dissipated as a sound and heat. Some kinds of soles may influence energy absorption and its further transformation [1]. Knee joint is subjected to inner, bending moment, which results in release of power, while the energy comes from concentric work of knee flexors and elastic strain energy of ligaments. Contrary to knee joint, a hip joint is affected by inner, erectile moment, produced by concentric work of hip extensors, which generates power [1], [8].

An objective of this work is to determine the relationship between different types of footwear and ground reaction and its characteristics – varying between sexes and shoe types. The scope of the research contained measurement of three components of ground reaction forces, center of pressure (COP) deviations due to changing shod type, basic body measurements and preparation of questionnaire, which investigated physical activity habits.

2. Materials and methods

2.1. Participants

The study group contained 12 people of both sexes, aged 22-27: 7 women and 5 men. They were asked to fill in the questionnaire, provided by the researcher, which scope of questions concerned: the age and sex of the subject, the trauma of the musculoskeletal system and its area, the time of undertaking physical activity, the type of physical activity most frequently undertaken and the type of footwear most frequently worn. Anthropometric measurements consisted of several steps, in which the mobility of the motor system was tested globally by the physiotherapist. Only participants, whose results were in range of norm (range of motion, faulty posture) were taken a part in measurements. Their anthropometric data are presented in Table 1a and b. The study was conducted in the Laboratory of Biomechanics, in the Department of Automation, Biomechanics and Mechatronics at the Lodz University of Technology. The respondents, whose health status foreclosed proper testing or did not agree with terms of participation, were excluded from the study, as well as those, whose measurement results indicated faulty postures. Research was organized according to Helsinki Regulations, all volunteers were informed in detail about aim and scope of the experiment, all of them sign a form of conscious agreement.

Table 1a. Female volunteers basic anthropometric data.

Volunteer	Body mass [kg]	Height [cm]	Age [years]
1	56.5	168	22
2	82	165	22
3	58	170	22
4	57.5	164,5	22
5	92	172	24

Volunteer	Body mass [kg]	Height [cm]	Age [years]
6	53	165	24
7	53	168	25
EX	64.57	167.50	23.00
SD	15.72	2.84	1.29

Table 1b. Male volunteers basic anthropometric data.

Volunteer	Body mass [kg]	Height [cm]	Age [years]
1	76	183	26
2	75.5	171	22
3	85	180	25
4	94	187	24
5	82	182	25
EX	82.5	180.6	24.4
SD	7.58	5.94	1.52

2.2. Materials

For reaction forces recording, the Steinbichler force platform (SFP Active 3D, Steinbichler GmbH force platform) with dedicated software were used. Gait measurements and center of pressure (COP) movement were recorded in following variants: for women: barefoot, shoes with flat, profiled sole, high-heels and for men: barefoot, suit shoes and sports shoes. Each subject was asked to bring his/her own shoes, which were then classified as suitable for the experiment according to the proper range of stiffness and heel height. The subject was asked to walk through the dynamometric platform with preferred, comfortable speed. Reaction forces of the right limb were recorded. In order to avoid their intentional adjustment of footsteps, the force plate was masked on the gait-path. From all trials only three correct (with whole foot placed close to the center of the force platform) were chosen for further analysis. After the correct series of passes in the given footwear, the subject was asked to stand freely with both feet on the platform, so that they did not go beyond its edge and not to move for 30 sec. At that time, the COP transitions were recorded for each shoe-type.

3. Results

3.1. Ground reaction forces

Obtained results are presented in form of graphs with average values with standard deviations in case of each graph: medio-lateral, anterior-posterior and vertical direction, separately for male and female participants and shoe-types.

3.1.1. Anterio-posterior reaction

In the case of female anterior-posterior reaction for barefoot gait (Fig. 1a.a) the first peak is low, rounded and corresponding to the moment of the heel striking the ground. After that, a sudden decrease of forces to the average value of about -75 N appeared. Then the phase of loading response (LR) is visible, with the mid stance (MST) point around 1.35 sec. The force rises to the average value of about 120 N, then drops down to toe off point around 1.75 sec. The largest deviations from the mean value were recorded near the first peak - in some of the studied women it took the shape of a sharp peak. Before the start of the LR phase, in some of the examined women, a temporary decrease and increase in the value of the acting force was noted, which may result, for example, from imbalance and attempt to stabilize the heel during loading. Also, a large difference in value was observed in the area of the second peak and just before the toe-off phase — some of the women had values up to 150 N.
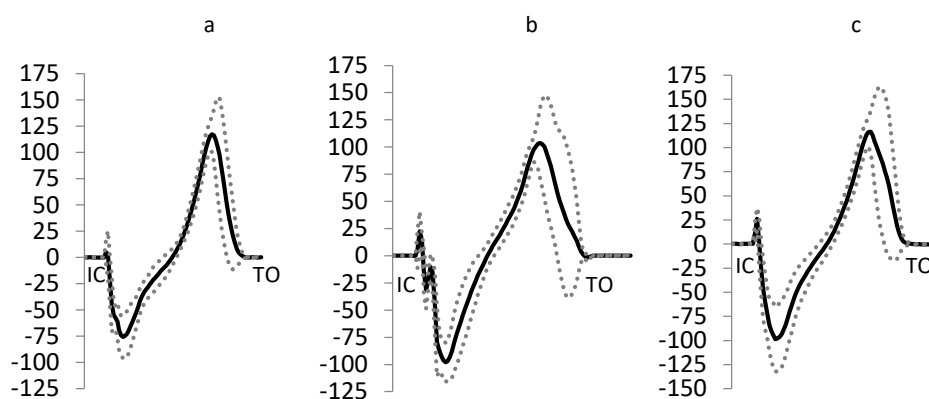
Figure 1a. Ground reaction force, female, anterio-posterior direction, a) barefoot b) highheels c) sport – shoes; description in text; horizontal axis – support phase, vertical – force [N].
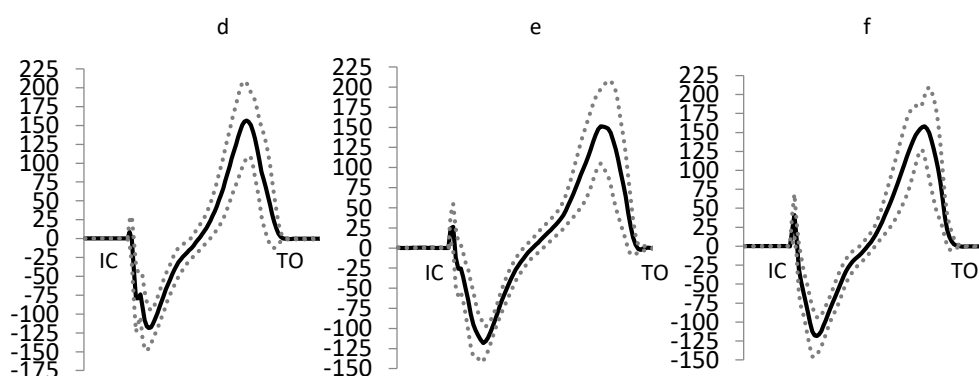
Figure 1b. Ground reaction force, male, anterio-posterior direction, d) barefoot e) suit f) sport – shoes; description in text; horizontal axis – support phase, vertical – force [N].

Similarly to the previous characteristics, for the high-heels (Fig. 1a.b), there is a sharp peak associated with the heel strike on the ground, then the curve drops sharply and rises until the beginning of the LR phase, which reaches an average value of -100 N. The MST point was reached a little earlier, in comparison to remaining shoes - before 1.35 sec. The next visible peak reaches the value of approximately 100 N. The values of extreme peaks are lower than for shoes with a flat, profiled sole (Fig. 1a.c). The variation in values among the examined group is particularly evident in the LR, heel-off (up to 150 N) and toe-off (about -40 N) phases. The total support phase is slightly extended to approx. 0.8 sec.

In case of sport-shoes (Fig. 1a.c female), the measurement begins with a sharp force peak during heel contact to the ground. The decrease in the force direction is smooth up to the value of -100 N. The increase in the force value is almost linear, up to the value of approx. 115 N. In the case of sports footwear, the greatest deviations from the average value, are located in the LR phase and between heel-off and toe-off phases. The highest values exceed -125 N and 150 N. Moreover, the curve appears smoothed without additional sways.

Fig, 1b.d (male, barefoot) shows small, but evident peak at the beginning of stance phase. Then a rapid drop in values occurs, until it reaches the approx. -125 N. What is more, a noticeable increase and drop in values at the beginning of LR phase is visible. Then values increase rapidly with marked MST phase around 1,30 sec - as well as in female group. At heel-off phase, the highest, obtained value of force was 150 N. Just like among the examined group of females, beginning of LR and heel-off phase showed the highest difference in values.

Suit type of footwear (Fig. 1b.e), presents some additional fluctuations of force and higher deviations from mean values – significant between IC and LR phase as well as heel-off phase. As well as in case of other types of footwear, measurement begins with rounded peak (25 N) directed upwards. Some of the male subjects present the value above 50 N. At the beginning of the LR phase, force reaches the value -125 N and at the end of the phase 150 N.

The characteristics of gait in sports footwear (Fig. 1b.f) is smooth and begins with sharp, positive peak with a value up to 50 N. Additional fluctuations, like in case of suit shoes, are not visible. The lowest value (approx. -125 N) is followed by the beginning of LR phase. The highest value stands for the end of LR phase - above 150 N. Differences among the group in sports shoes are significant, as in the other footwear - especially in the IC, LR and heel-off phases. In some of the examined males, the first positive peak reached a value up to 75 N.

3.1.2. Medio-lateral direction

For female barefoot (Fig. 2a.a) right after the initial contact (IC) phase (0.9 sec.), a sudden drop in vales of acting force is noticeable - reaching the value around -10 N - the lateral side of the heel is loaded. A

rapid increase in values indicates the COP movement towards metatarsals and beginning of MST phase. However, force hardly exceeds the value of 0 N, which suggests load positioning on the lateral edge of the foot – COP approximates to middle foot, but the load is finally directed more laterally. A further decrease in the force value to -25 N means the displacement of COP over the head of the 5th metatarsal bone. In the case of a barefoot support phase, this is the most weighted point on the foot. The value of the force increases again to positive values, showing the beginning of the heel-off and toe-off phases. For COP medial movement (and MST phase), some of the female subjects achieved positive values - over 5N. The lowest achieved values, under the load of head of the 5th metatarsal bone were approximately -33 N.
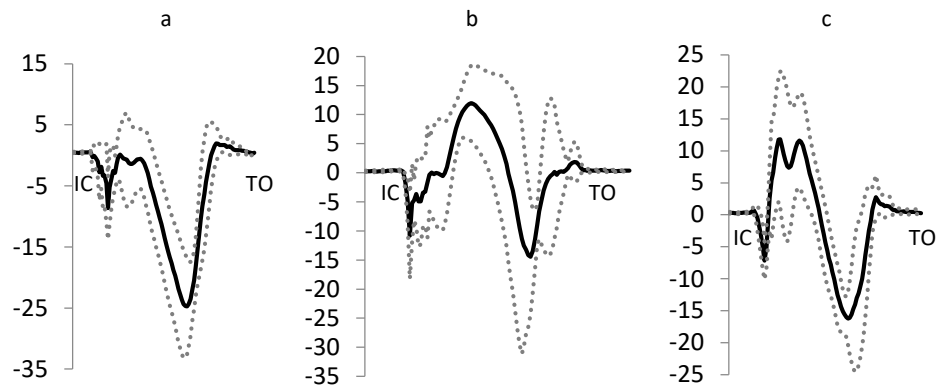
Figure 2a. Ground reaction force, female, medio-lateral direction, Fy: a) barefoot b) high-heels c) sport - shoes; description in text; horizontal axis – support phase, vertical – force [N].
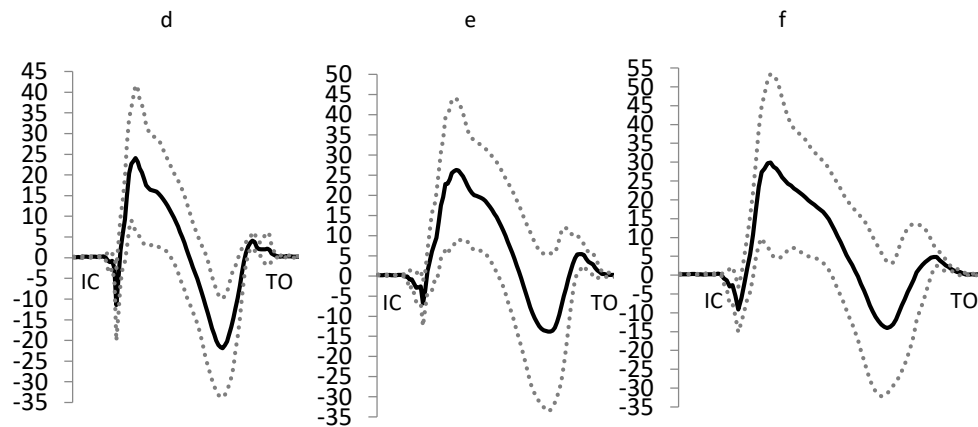
Figure 2b. Ground reaction force, male, medio-lateral direction, d) barefoot e) suit f) sport – shoes; description in text; horizontal axis – support phase, vertical – force [N].

The medio-lateral component for gait in high-heels (Fig. 2a.b) is the most diversified from all presented characteristics. The point of maximum lateral heel load is over -10 N and is the lowest of measured gaits. The increase in force values during the LP phase was non-uniform and many irregularities were registered. The maximum medial load was over 10 N - the graph in this area is arranged in the shape of a smooth hump. Loading attached to head of 5th metatarsal bone has reached the lowest value from the examined footwear - approx. -15 N. The values representing the heel-off and toe-off phases are similar for all examined types of footwear. The greatest variation in the values occurred during LP phase and before the start of the heel-off phase. The average values of the obtained curve for high-heels suggests more medial foot loading.

In the case of gait in sports footwear (Fig. 2a.c), the value of the maximum lateral heel load was lower than -5 N. While moving the COP towards the metatarsal bones, the highest values were registered above 10 N, with characteristic two humps before the COP was moved over the head of 5th metatarsal bone (below -15N). The values before the heel-off and toe-off phase were similar to those for other footwear. For the sports footwear examination, it can be said that the deflection of COP in the medio-lateral direction was evenly distributed. The largest differences in values for individual subjects were found in the LR phase. It is important to note, that characteristics of medio-lateral component of gait was strongly diversified, as is demonstrated by standard deviation curves.

For male volunteers, in case of barefoot gait (Fig. 2b.d) right after the IC phase, a sudden drop to less than -10 N is visible – the lateral side of the heel is fully loaded. While the LR phase begins, the values of force rise to positive value approx. 25 N – it suggest, that COP is moved above the medial side of metatarsal. Then a hump-like drop in values is noticed, below -20 N – the head of 5th metatarsal is loaded. A renewed increase in values, above 0 N indicates movement of COP towards head of 1st metatarsal and beginning of heel-off phase.

Figure 2b.e, which shows the measurement of the same medio-lateral component for suit shoes presents irregularities. The maximal load of the lateral side of heel stand at -5 N, which is the highest value of all presented types of footwear. An acting force during COP movement towards metatarsals reaches its maximal value around 25 N. Then an extended decrease in force values occurs, to approx. -15N – higher than for barefoot or flat shoes. For suit shoes, toe-off phase has the highest recorded value, up to 5 N. For the suit type footwear, the largest irregularities were recorded over the entire time of the support phase.

A characteristic feature of the medio-lateral component for sports footwear (Fig. 2b.f) is a rapid, partially linear decrease in values of acting force, during COP movement towards head of 5th metatarsal bone. For remaining types of footwear, the decrease is hump-shape. For the lateral side of the heel, load values are approx. -10 N, and for the head of 5th metatarsal bone is -15 N. Before the toe-off phase, the

force reaches 5 N. The largest deviations of the measured force values concern the COP movement over the metatarsus - the extreme value is about 55 N and 5 N – and before the toe-off phase.

3.1.3. Vertical reaction force

Figure 3a.a presents the average values for women barefoot measurement. On the graph a characteristic peak at the beginning of single support phase - initial slope (UP) is presented. However, it should be mentioned, that not each subject presented such a wave. Two peaks related to LR phase are evident and located approx. 600 N and above 650 N. Second peak reached higher value. This suggests, that push-off phase was launched stronger in comparison with beginning of LR phase. The drop in acting force estimated almost 500 N.
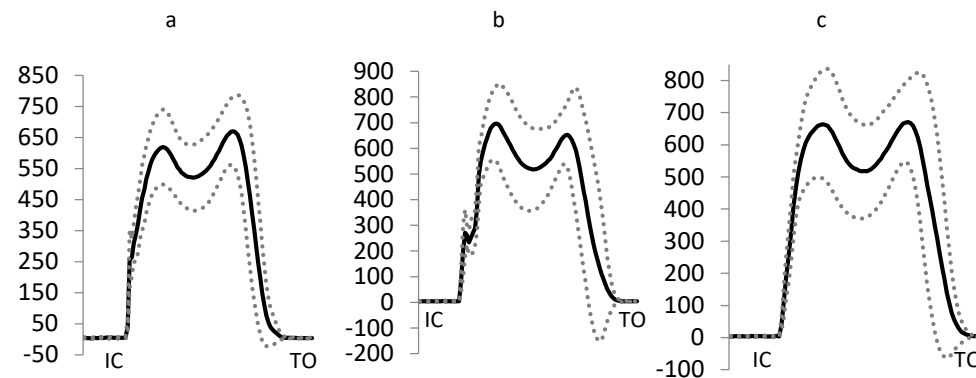
Figure 3a. Ground reaction force, female, vertical direction, a) barefoot b) high-heels c) sport - shoes; description in text; horizontal axis – support phase, vertical – force [N].
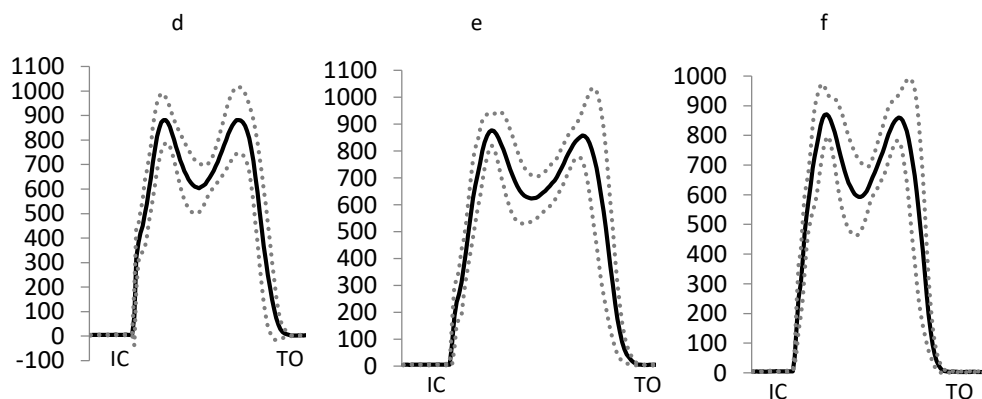
Figure 3b. Ground reaction force, male, vertical direction, d) barefoot e) suit f) sport - shoes; description in text; horizontal axis – support phase, vertical – force [N].

High-heels measurement (Fig. 3a.b) was the most non-uniform. On the front edge of graph, a sharp and clear-cut UP peak was visible - present in all examined females. This may indicate, that heel centering on the ground was difficult for all women. The curve showed also higher values of the first peak – 700 N, while the second one reaches the value of approx. 650 N. It suggests strong heel load before the LR phase and lighter push-off. A drop in acting force was approx. 500 N as well.

The graph showing the measurement in sports footwear for women (Fig. 3a.c) showed the smoothest line without any irregularities on the first slope. The UP waves and curve was not present. The curve seems quite symmetrical - peak values are similar and amount to over 650 N. The second peak seemed to be more narrow due to the first one, same as in case of flat shoes, with profiled sole. The drop in acting force was close to 500 N as well. However, characteristics of vertical component for sports shoes, for both sexes were smooth, the graph for females was more rounded and smoother.

In comparison to female characteristics, each male measurement (apart from suit shoes) demonstrated equal level of registered peaks – average at the level below 900 N. Curves obtained on the basis of the average values of the measurements did not show the specific UP waves – by analyzing the standard deviation on the graph, it can be seen that these waves appeared among male subjects, especially when measuring barefoot and suit type footwear (Fig. 3b.d and Fig. 3b.e). An elevating slope (Fig. 3b.d) of barefoot measurement, showed temporary irregularities. Two, peak values, in opposition to female group were equal and reached the force value up to 900 N. The drop in values, standing to MST phase went to 600 N.

In case of suit shoes (Fig. 3b.e), second peak has slightly lower value than the first one and some irregularities were found on the elevating slope. During MST phase, values approximated 600 N. The highest deviations in values were located around second peak (above 1000 N). What is more, representation for the suit shoes seemed to be more widen, indicating on extended stance phase.

As in the women's group, the graph for sports footwear was the smoothest (Fig. 3b.f). For sports footwear, the lowest, registered values are in the main part of MST phase – below 600 N. The both peaks are equal and reaches the value up to 900 N as well. Also the largest deviations from the mean value were recorded when the foot was placed flat on the platform (MST phase).

3.2. Stabilogram

The Table 2 shows the average values of amplitude of COP displacements, measured for each subject in static state. The values are delivered with standard deviation for both sexes. Minimal and maximal values for each footwear and both sexes are also presented. The amplitude was calculated in two directions on the basis of stabilogram: medio-lateral (M-L) and anterior-posterior (A-P).

Table 2. Average values of COP displacement for different sexes and shoe-types.

FOOTWEAR	Barefoot				Flat				High-heels		Suit		Sport			
COG DIRECTION	M-L		A-P		M-L		A-P		M-L	A-P	M-L	A-P	M-L		A-P	
SEX	F	M	F	M	F	M	F	M	F	F	M	M	F	M	F	M
MEAN ± SD [mm]	12,94 ± 4,10	13,92 ± 3,54	11,67 ± 4,45	9,47 ± 2,94	12,27 ± 4,18	14,68 ± 3,46	11,19 ± 4,29	10,02* ± 2,47	16,77* ± 4,33	13,17* ± 3,58	11,44 ± 2,56	9,51 ± 0,86	13,59 ± 4,46	15,50* ± 3,56	9,94 ± 2,31	9,30 ± 1,99
MIN. VALUE [mm]	8,99	9,40	7,03	5,76	6,99	11,53	7,37	7,00	12,18	9,27	9,00	8,09	8,25	11,09	7,08	7,19
MAX. VALUE [mm]	20,81	18,56	17,12	12,32	19,15	20,44	19,44	13,62	23,88	19,46	14,98	10,33	19,69	20,61	13,82	12,33

For medio-lateral movement of COP, among female subjects, the lowest, average value was obtained in case of flat shoes with profiled sole – 12.27 ± 4.18 mm. The highest, average value of COP displacement in medio-lateral direction concerned high-heels – 16.77 ± 4.33 mm. Average displacement in sport footwear were second highest – 13.59 ± 4,46 mm. The minimal, registered value of COP deflections in M-L direction, among examined females was 6.99 mm (flat shoes), while the maximal – 23.88 mm (high heels). For anterior-posterior movement of COP, among female subjects, the lowest average value was obtained for sports shoes – 9.94 ± 2.31 mm. The highest average value of COP displacement in anterior-posterior direction concerned also high-heels – 13.17 ± 3.58 mm. Average displacement in flat shoes with profiled sole and barefoot were similar. The minimal, registered value of COP displacement in A-P direction, among examined females was 7.03 mm for barefoot measurement, while the maximal – 19,46 mm – for high-heels. For medio-lateral movement of COP, among male subjects, the lowest, average value was obtained in case of suit shoes – 11.44 ± 2.56 mm. The highest values of COP deflections in medio-lateral direction concerned sports footwear – 15.50 ± 3.56 mm. Average displacement in flat shoes were the second highest – 14.68 ± 3.46 mm. The minimal, registered value of COP displacement in M-L direction, among examined males was 11.09 mm – for barefoot measurement, while the maximal – 20,61 mm – for sports footwear. For anterior-posterior movement of COP, among male subjects, the lowest average value was obtained for sports footwear – 9.30 ± 1.99 mm. The highest average value of COP displacement in anterior-posterior direction concerned flat shoes with profiled sole, however, the difference was not significant – 10.02 ± 2.47 mm. The minimal, registered value of COP deflections in A-P direction, among examined males was 5.76 mm for barefoot measurement, while the maximal was 13.62 mm for flat shoes.

4. Discussion and conclusions

The graphs presenting A-P component, for both, women and men started with positive peak, which is the smallest for barefoot measurements. This may be explained as a way of contact the heel on the ground. However, this phenomenon is common in case of loose or bad fitted shoe [9]. The foot moves backwards in relation to shoe. The lowest values were recorded for barefoot measurement.

The highest values of first peak were recorded for sports and flat shoes, for both sexes. Those types of footwear were usually laced-up, so the respondent might not put them on tight enough. What is more, most of the responders pointed out those kind of footwear as mainly worn. The footwear used for the study, belonged to the subjects. It is likely that it could be deformed as a result of normal, everyday use. What's more, all-day use of a given pair of shoes imposes it's change of shape to maintain comfort. Considerations about flat, profiled shoes, focus on irregularities and amplitude values among females and males. However, the values of A-P component are not the highest obtained. The proceed of suppression and loading response is strongly marked, in comparison with barefoot. What is more, the

values of recorded force are close to barefoot, which indicates on lack of amortization. Feminine gait is seem characterized by smaller, light steps. The construction of flat, profiled shoes resemble man-like style, so it may affect gait pattern. Simultaneously, this type of foot wear was chosen as mostly worn, so the gait could be more confident. What is more, this type of footwear obtained the lowest values of COP swings in medio-lateral direction among females. It is clearly shown on graphs for M-L force component, where outstanding movement of COP are not visible. In case of males, registered anterior-posterior COP swings were the highest. Majority of male participants brought shoes with springs at both sides, which are responsible for sudden bounce of the foot [10]. Gait in flat, profiled shoes seems to be more smooth, in comparison to barefoot, however it does not show any significant amortization abilities – the values of suppression and push-off are even higher, than those for barefoot – unlike than expected. In their study, Isabel Sacco et al. [3] presented a strong differences between shod and barefoot gait among diabetic neuropathic and healthy patients. Focusing on healthy subjects, Sacco noticed that gait in any footwear shows higher values of vertical component of ground reaction force at IC phase and higher propulsive force. She suggests, that smaller values in case of barefoot measurement were related to precautious gait. Sacco also admits, that the results are in opposition to the common opinion, that any shoes reduces ground shocks. What is more, in the previous study, they observed lower values of peaks in case of hard-sole shoes. It was also found the lowest values for barefoot measurement in his study of mechanical comparison of barefoot and shod running. They have suggested, that this phenomenon is related to neural-mechanical adaptation of body in order to reduce external stress under repetitive movements [11]. It can lead to opinion, that gait kinematics, changed in response to different footwear conditions can be caused by neurosensory mechanism, which founds wearing shoes as interaction between foot and material. In other study researchers examine the effect of footwear motion on foot relative motion during walking and running. For the measurement two types of sandals (with hard and soft sole) were used. A control, barefoot measurement was registered as well [12]. The differences between sole types were not significant. The push-off phase, abduction and adduction of the foot, in case of shoes were restricted. Authors considerate if footwear limits natural foot motion. They conclude, that too restricted footwear can lead to pain and discomfort.

In presented study, the most characteristic are the high-heels results. At the beginning of measurement in M-L component, a visible irregularity stands for problems with centering lifted heel on the ground. Extended second part of the apparent LP phase, toe-off phase and relatively low value of heel-off phase are visible on the graph. It might correspond to pronation and plantar flexion, where the body weight hinges on forefoot and COG is moved to the front. Registered COP swings for high-heel shoes showed maximal values in both directions. The M-L force component confirms this statement by registered irregularities. Those may originate from single support phase, where - in case of high-heel - area of support is reduced.

A characteristic, delayed hump (in M-L component), which occurs in MST phase may stand for sudden ground positioning the front part of the shoe – medial part of the forefoot is loaded, while the swing phase of the opposite lower limb had started. Conversely to other types of shoes, values of push-off are smaller than for suppression phase in vertical component. In case of high-heels the proper LP phase does not occur – the foot is not in a proper position to carry on the load, so the virtual COP movement is set between lifted heel and forefoot – no energy from lifting the heel can be recovered (vertical component). It should be mentioned, that all females, apart from one, claimed that they are not used to high-heels and presented difficulties in walking at the beginning of the measurement. In study [13] of long-term and short-term high-heels users found out, that walking in high-heels enlarges vertical component of ground reaction force. Author refer to other study, which explains that phenomenon by increased muscle work on tendon-aponeurosis complex [4], analyzed the influence of lifted heel on gait as well. They took into consideration several heel heights. The results are similar to presented in this work. The values of vertical component of ground reaction force presents the smaller second peak – the push-off phase was diminished, due to bare foot.

The anterior-posterior component presented problem of stabilization of heel on the ground and increased pressure at the beginning of LR phase. The characteristic of medio-lateral component differed from presented in this work, however both showed that loading on the head of 5th metatarsal bone was higher in case of barefoot [4]. Melvin in his doctoral thesis analyzed the effect of heel height on several variables [9]. The overview of papers, presented in his thesis, shows findings, similar to this work. Other authors, mentioned by Melvin, indicate, that lifted heel enlarged values for vertical and anterior-posterior ground reaction force. What is more, medio-lateral component increased in values due to heel height. Also it was mentioned, that greater load was located on medial side of the foot and reduced on lateral side. It is important to indicate an interesting fact - UP-peak appeared only in barefoot and high-heel measurement. It might suggest, that this element is present in case of gait with firm and point heel strike.

Gait in suit shoes seems to be similar, but smoother than in case of barefoot. The values do not differ from rest of shoe types. The COP swings among men received the smallest, recorded values in medio-lateral direction. However, swings in anterior-posterior direction are low as well. The M-L force component show lowest lateral movement and extension of loading response phase. The push-off values are lower than suppression. It can result from foot design, which is stiffer and imposes slower movement. It should be mentioned, that suit shoes were not pointed as often worn.

The general outcome from measuring the sports footwear for males and females is that the gait was smooth and uniform. Ground reaction was reduced only partially. Female subjects were the most stable in anterior-posterior direction in sports shoes. Male subjects had the lowest values of COP swings for anterior-posterior direction, but the highest in medio-lateral direction. Gait in sports shoes

among men was smooth as well and all the disturbances are faded out. The M-L component for both sexes, present highest medial COG movements, leading rapidly to head of 5th metatarsal bone. However, the push-off phase is not that strong, which also indicates equal peaks from vertical component. In next work, authors took into consideration changes in stiffness in heel lifts of sport shoes [14]. The study consists of measuring plantar pressure distribution, COG position and ground reaction force for three types of heel lifts, characterized by different stiffness – it does not influence anterior-posterior COP movements – due to barefoot. However, the heel height of 2.5 cm affects COP visibly. What is more, peak pressure for sport, lifted shoes in metatarsal area was 1/3 higher than in case of barefoot and the highest values were obtained for wedge of medium stiffness. This one decreased values of A-P component, kept unchanged first peak and pit of M-L component, but decreased the second peak and kept the vertical component unchanged – due to barefoot measurement.

A review of several papers of walk differences between barefoot and shod gait in general, was made by [15]. Some interesting results are distinguished, which are in accordance with those, obtained in this work. Analysis of vertical component of force for barefoot measurement showed, that the first peak was smaller (due to the second one) in case of subject, who habitually wear shoes. What is more, there was a reduced drop force values (MST phase) for bare foot measurement in opposition for shod gait. This can lead to the assumption, that for barefoot, forces were more evenly distributed in time. Authors also compared results of habitually barefoot subject – their plantar pressure at heel and metatarsals were reduced. The same results appeared in case, where the foot was placed flatter on the ground in order to increase its friction. From the investigation of stability, it came out, that less space for forefoot width (narrow ball of shoe) indicates less support and simultaneously - worse stability, which can lead to injury, and worsened stability again. It showed, that shoes can limit the movement and functions of the foot.

It can be stated, that footwear influences gait pattern and ground reaction, despite of sexes. The differences were strongly visible in anterior-posterior and medio-lateral component of ground reaction force. High-heeled shoes had the greatest influence on gait, which proved to be the most unstable and loading for medial and fore part of the foot. The variations were visible in ground reaction as well as stability measurements. Any significant deviations were not obtained in case of suit and flat shoes with profiled soles, however the values for flat shoes indicate on robust achievement of critical phase points (suppression, push-off). The differences could come from shoe design. Sports shoes evened the gait by reducing its regularities, caused by external shock. In case of vertical component – sports shoes unify suppression and push-of phase, which can come from its design. Sports shoes evened the gait by reducing its regularities, caused by external shock. In case of vertical component – sports shoes unify suppression and push-of phase, which can come from its design. According to COP swing amplitude, barefoot was not the most stable environment. In the majority of data, any footwear (apart from high-

heels) obtained better stability results. The difference was in case of sports shoes, where medio-lateral swings were higher, but anterior-posterior swings were smaller. Other important factors, which influence gait pattern are degree of wear and habituation to given type of footwear.

Acknowledgements

References

[1]   Levine D., Richards J. and Whittle M. H., *Whittle. Analiza chodu*. Elsevier Urban & Partner, 2012.

[2]   Hayot C., Sakka S. and Lacouture P. Contribution of the six major gait determinants on the vertical center of mass trajectory and the vertical ground reaction force. *Human Movement Science* 32, 2 (2013), 279–289.

[3]   Sacco C., Akashi P. M. and Hennig E. M. A comparison of lower limb EMG and ground reaction forces between barefoot and shod gait in participants with diabetic neuropathic and healthy controls. *BMC Musculoskeletal Disorders* 11, (2010), 24.

[4]   Świtoński E. and Głowacka-Kwiecień A. Analiza chodu w obuwiu o różnej wysokości i kształcie obcasa. *Aktualne Problemy Biomechaniki* 3, (2009), 11–24.

[5]   Ersson et al., Shoe Research Project Gävle. 2001. http://shoedoc.se/ [Online: 2019-09-02].

[6]   Błaszczyk J.W., *Clinical Biomechanics (in Polish)*. Warszawa: PZWL, 2004.

[7]   Yamasaki T., Nomura T. and Sato S. Phase reset and dynamic stability during human gait. *Bio Systems* 71, 1–2 (2003), 221–232.

[8]   Gage J.R., Deluca P.A. and Renshaw T.S. Gait Analysis: Principles and Applications. *JBJS* 77, 10 (1995), 1607.

[9]   Melvin J. M. A. *The effects of heel height, shoe volume and upper stiffness on shoe comfort and plantar pressure*. Ph.D. thesis, University of Salford, 2014, Nester C.J.

[10]   Fried D.A. Shoes That Don't Hurt. https://stage.trafford.com/Bookstore/BookDetail.aspx?BookId=SKU-000152574. [Online: 2019-09-02].

[11]   Divert C., Mornieux G., Baur H., Mayer F. and Belli A. Mechanical comparison of barefoot and shod running. *International Journal of Sports Medicine* 26, 7 (2005), 593–598.

[12]   Morio C., Lake M. J., Gueguen N., Rao G. and Baly L. The influence of footwear on foot motion during walking and running. *Journal of Biomechanics* 42, 13 (2009), 2081–2088.

[13]   Cronin N. J., Barrett R.S. and Carty C.P. Long-term use of high-heeled shoes alters the neuromechanics of human walking. *Journal of Applied Physiology (Bethesda, Md.: 1985)* 112, 6 (2012), 1054–1058.

[14]   Hessas S., Behr M., Rachedi M. and Belaidi I. Heel lifts stiffness of sports shoes could influence posture and gait patterns. *Science & Sports* 33, 2 (2018), e43–e50.

[15] Franklin S., Grey M.J., Heneghan N., Bowen L. and Li F.-X. Barefoot vs common footwear: A systematic review of the kinematic, kinetic and muscle activity differences during walking. *Gait & Posture* 42, 3 (2015), 230–239.

Małgorzata Klepczyńska, Łódź University of Technology, Department of Automation, Biomechanics and Mechatronics, 1/15 Stefanowski Street (building A22), 90-924 Łódź, Poland

Bartłomiej Zagrodny*, Ph.D: Łódź University of Technology, Department of Automation, Biomechanics and Mechatronics, 1/15 Stefanowski Street (building A22), 90-924 Łódź, Poland (*bartlomiej.zagrodny@p.lodz.pl*). The author gave a presentation of this paper during one of the conference sessions.

Wiktoria Wojnicz, Ph.D. DSc: Gdańsk University of Technology, Department of Mechanics and Mechatronics, Faculty of Mechanical Engineering, postal address, ZIP code City, Country (*wiktoria.wojnicz@pg.edu.pl*).

Michał Ludwicki, Ph.D.: Łódź University of Technology, Department of Automation, Biomechanics and Mechatronics, 1/15 Stefanowski Street (building A22), 90-924 Łódź, Poland (*michal.ludwicki@p.lodz.pl*).

Jan Awrejcewicz, Professor: Łódź University of Technology, Department of Automation, Biomechanics and Mechatronics, 1/15 Stefanowski Street (building A22), 90-924 Łódź, Poland (*jan.awrejcewicz@p.lodz.pl*).

Application of the wheel-flat detection algorithm using advanced acoustic signal analysis

Paweł Komorski, Grzegorz M. Szymański, Tomasz Nowakowski,
Małgorzata Orczyk

Abstract: Urban rail communication is one of the most attractive public modes of transport. There are plenty of advantages for the community and environment of using this kind of transport. Furthermore, vibroacoustic comfort and noise annoyance aspects during urban rail vehicles operations are significant topics for passengers and city dwellers. These problems are also important for rail fleet managers and city authorities. Therefore, dynamic interaction between wheel and rail during vehicle passage should be kept in good technical condition. On the other side, the impact noise is the one of the most annoying noise emitted by urban rail vehicles inside the cities. The flat spots (wheel-flats) on the wheel or rail surfaces are one of the main causes of increasing rolling noise level. The main aim of the article is to present the novel approach of the wheel-flat detection algorithm using advanced acoustic signal analysis. The measurement equipment was placed in the near field of track in one of the tram depots. Several measured cases are distinguished by high impact noise level. The wheel-flat detection system is described by implementation of different kind of frequency and time processing methods on measured acoustic data.

1. Introduction

Vibroacoustic comfort during public rail transportation is an important issue for passengers as well as for city authorities and rail vehicle operators. Low acoustic climate around the rail infrastructure is also significant for inhabitants. Several researches have shown the annoying car and light rail vehicle noise problem in Poznan city [5, 7, 9, 11]. Considering only the public light rail transportation, the rolling noise is the most significant component of the urban rail noise [2, 12]. Dynamic interaction between rail and wheel surface is the main cause of it [8, 11, 13]. One of the rolling noise examples is the impact noise which is the result of passing through rail joints/crossroads or the occurrence of wheel/rail flats on rolling surfaces [6, 14]. It is characterized by sudden and short-time vibroacoustic signal increase which can be uncomfortable and annoying for passengers or inhabitants.

The article is a continuation of the previously presented texts [4, 6] with another proposition of application the wheel-flat detection algorithm using advanced acoustic signal analysis. Acoustic measurements during trams pass-by tests were carried out and few trams were had wheel-flats. Based on experimental research, envelope analysis and Hilbert transform, the wheel-flat detection system was elaborated.

2. Basic theoretical aspects

The Hilbert transform usage has many advantages in the processing and analysis different kind of signals. It allows to determinate the real and imaginary parts of an analytic function [3, 10]. The analytic signal is created by implementing the Hilbert transform which enables to elaborate the instantaneous magnitude (so-called envelope) of the original time signal. Furthermore, the frequency analysis can be done by knowing the instantaneous phase of the analytic signal. The infinite Hilbert transform equation (Eq. 1) is described below [1, 3, 10]:

$$H[x(t)] = \tilde{x}(t) = \frac{1}{\pi}^* \int_{-\infty}^{\infty} \frac{x(\tau)}{t-\tau} d\tau \tag{1}$$

where: $x(t)$ is a real measured signal in time domain, τ is a time before the transformation, t is a time after the transformation and * denotes the Cauchy's principal value.

3. Experimental research methodology

3.1. Measurements assumptions

The experimental part of the research included the acoustic measurements during so-called pass-by tests. Exterior measurements were made on the area of Franowo tram depot (Poznan, Poland) when all vehicles were returning from service. The tram's speed was about 20 km/h. The main aim of the measurements was to record impact noise caused by wheel-flat and compared it to normal tram noise (emitted by vehicles in good technical condition, without wheel-flats) using advanced acoustic signal analysis.

3.2. Measurement points

Three microphones were used to acoustic measurements, located about 2 m from the track. The shame of the measurement position was shown in Fig. 1.
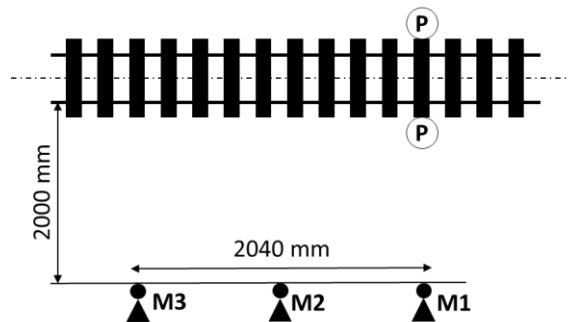
Figure 1. The scheme of measuring position in the pass-by test; M – Microphones, P – Photocells [4]

All electroacoustic transducers were spread along the track at a distance of 2.04 m which is the length of each tram wheel circumference [4]. It means one full wheel rotation period during passage will be made at this distance. However, after some signals processing and analysis, it was proved that using only one measurement microphone will be also enough to elaborate the wheel-flat detection system. The photocells were also used during acoustic measurements. Based on signal recorded between transmitter-receiver photocells, the speed of tram's ride was calculated.

3.3. Measurement devices

Measurement devices from a Brüel&Kjær Sound and Vibration company were used to record synchronously tram noise in the pass-by test. The equipment connection scheme (with all device names) was shown in Fig. 2.
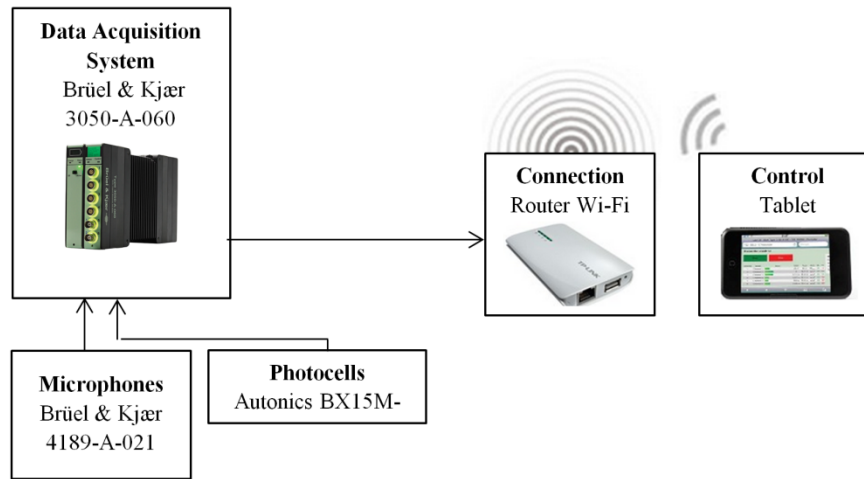
Figure 2. The measuring equipment scheme [4]

The main data acquisition system was called B&K type 3050-A-060. Tablet was used to control and monitor measurement process. All three microphones were calibrated before the sound recording.

3.4. Parameters of acoustic signals recording

Acoustic signals recording were conducted constantly in a full measurement spectrum of 25.6 kHz, with sampling frequency of 65536 samples per second. The signals were recorded synchronously in all measurement points and channels. Duration of signals was dependent on the speed and length of the tram passing through the measurement cross section, and was about 5-7 s.

4. Results

4.1. Main analysis

In Figure 3 there are shown two time history samples (measured by microphone M3) which were used to further signal processing and analysis. First recorded sample showed tram noise without impact noise, where vehicle was in good technical condition. While second measured signal depicted tram noise with the instantaneous sound pressure increase (above 2 Pa) caused by wheel-flat.
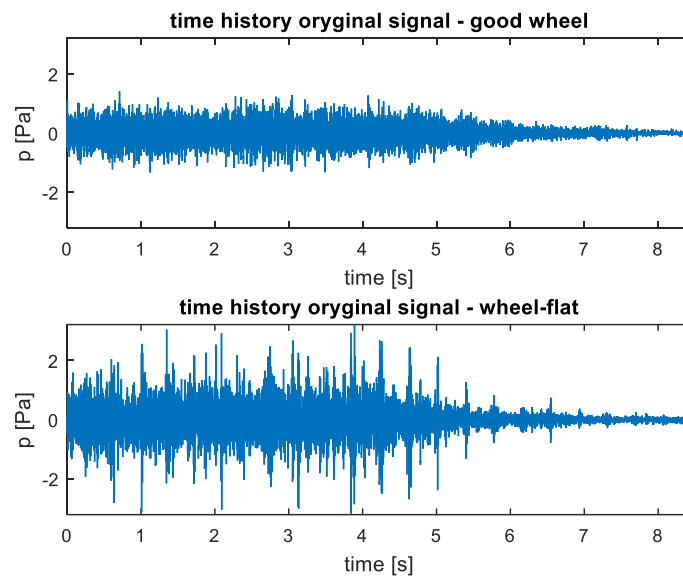
Figure 3. Two measured tram noise samples

Next signal processing step was to calculate the SPL (Sound Pressure Level) spectra using the main FFT (Fast Fourier Transformation) and Welch spectral assumptions. The results are shown in Fig. 4. The SPLs were higher in the wheel-flat spectrum while the signals frequency content was similar. However, after more detailed analysis, the main frequency differences were found between 500-1000 Hz which is marked as the resonance frequency span.
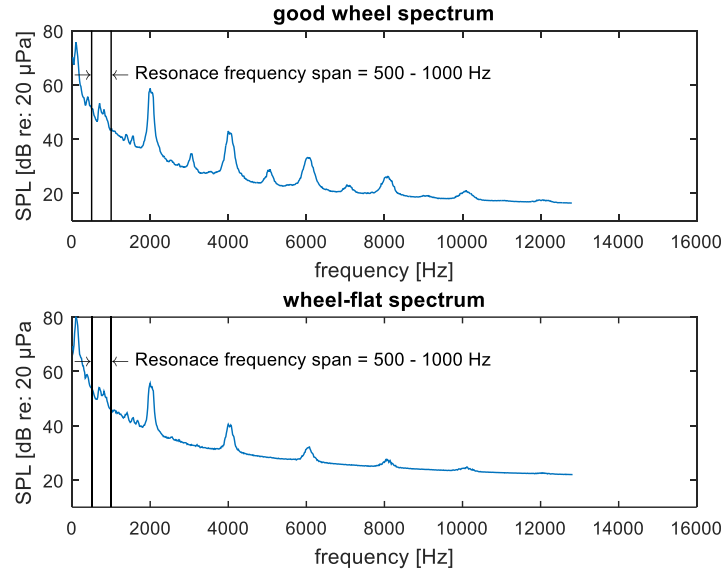
Figure 4. The SPL spectra of two different tram noise samples

After finding the resonance frequency span, the time signal filtering process was carried out. Then, the envelope time signals were calculated. The results are shown in Fig. 5. Periodic amplitude increases caused by impact noise can be observed in second example. That was the main difference between good and damage wheels during trams passage. In this case limit sound pressure amplitude should be set on approximately 0.5 Pa. This value ought to be elaborated by algorithm users based on statistics and observation of the envelope signal parameter. It is a first example of the wheel-flat detection algorithm which uses an acoustic time signal and the Hilbert transform.

Calculation only in frequency domain is another efficient way to detect wheel-flats in rail vehicles. In this case, a specter analysis of time signal envelope using the FFT algorithm was conducted [6]. In Figure 6 the envelope spectrum of the SPLs was shown. Corresponding frequency bands to possible wheel rotation frequencies (with a 10% boundary resulting from any changes from the expected wheel diameter) were found and marked.
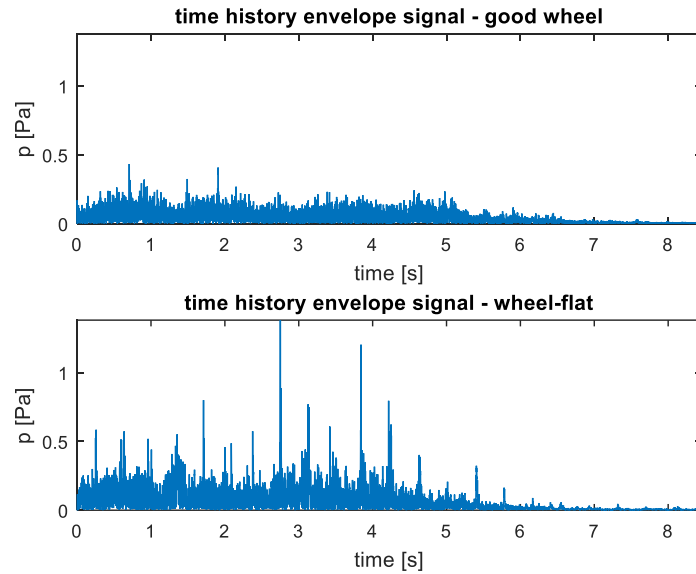
Figure 5. Time history envelope signals
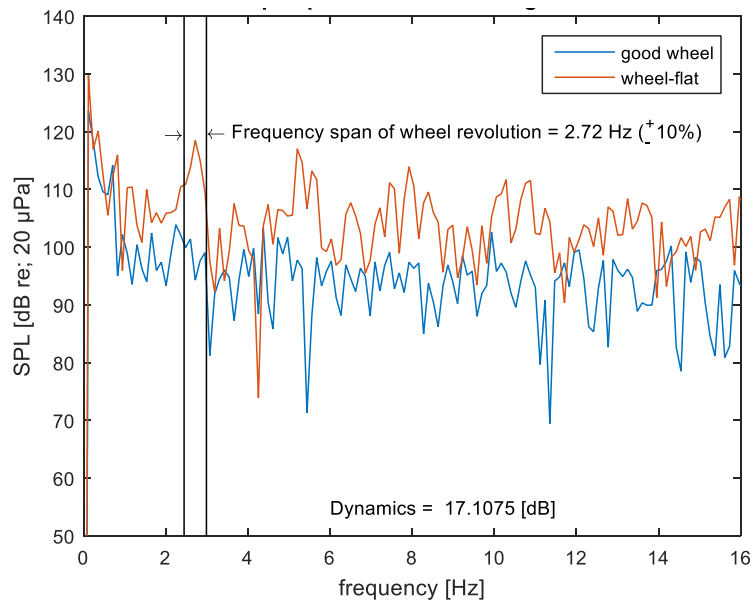
Figure 6. Envelope spectra of two sound pressure levels

Also the dynamics of changes between two analyzed signals was depicted which is equal to about 17 dB. It is a significant difference that indicates a positive result from application of the wheel-flat detection algorithm using advanced acoustic signal analysis.

4.2. The wheel-flat detection algorithm

Finally, the wheel-flat detection algorithm using advanced acoustic signal analysis was elaborated (Fig. 7). Firstly, the acoustic measurements during pass-by tests have to be carry out. An important aspect is the tram speed criterion which ought to be higher than 15 km/h.
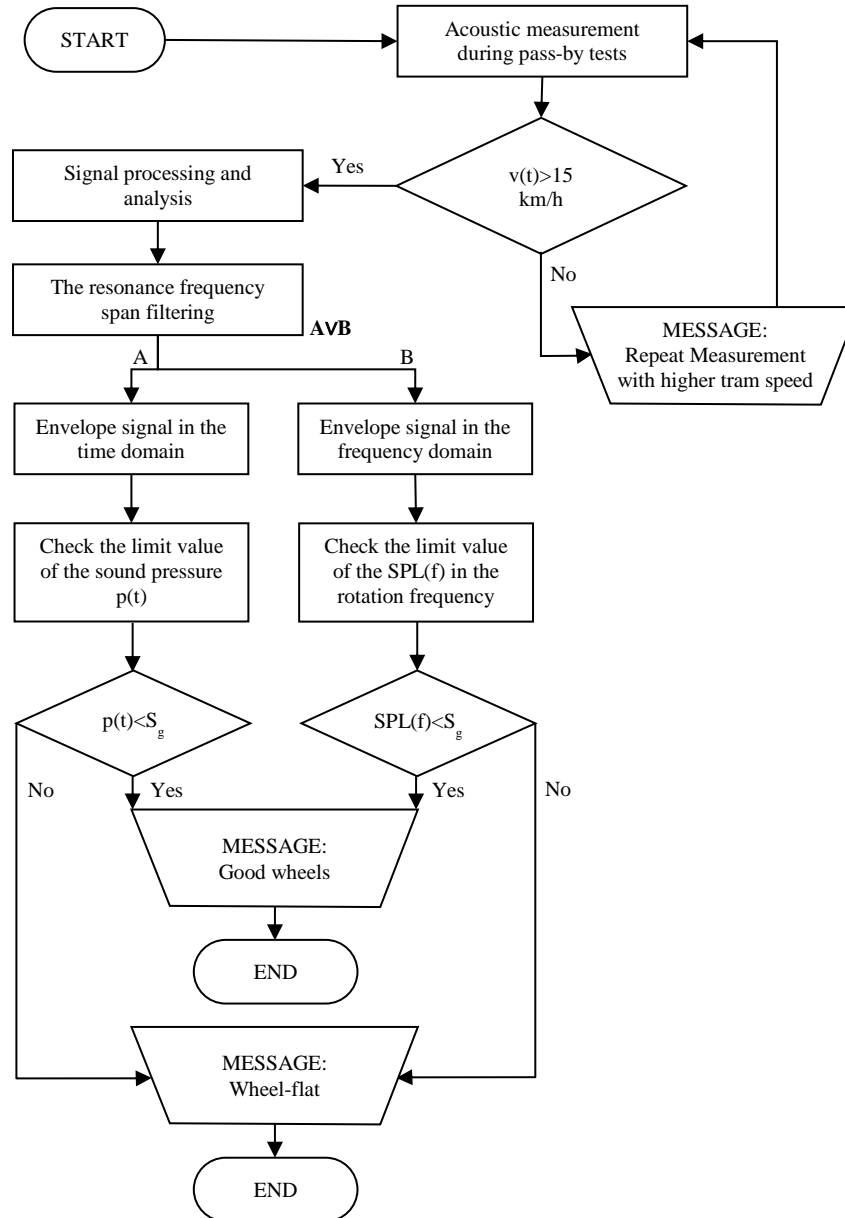
Figure 7. The wheel-flat detection algorithm based on advanced acoustic signal analysis

Signal analyses were made to noise samples recorded when trams passed by approximately at a speed of 20 km/h. Thus, authors assumed that trams speed cannot be lower than 15 km/h. When the velocity criterion is completed, the signal processing and analysis can be started. The resonance frequency span has to be founded. Therefore, the acoustic signals have to be filtered according to proper frequency band. Then, the user can choose his own algorithm method to wheel-flat detection. It is based on envelope signals analysis in time or frequency domains. In both methods, the limit value (marked by S_g) should be estimated by previously statistics research and observation. If the amplitudes are lower than the limit values, the trams wheels are in good technical condition and there is a lack of the wheel-flat. Otherwise, the wheel-flat was detected and the fleet operator is informed about it.

5. Conclusion

The article is a continuation of the vibroacoustic signals analysis and processing in order to vehicle wheel-flats detection using different kind of mathematical methods. Here, the aim was accomplished using the Hilbert and fast Fourier transforms applying on acoustic signals. The algorithm is similar to the one described in [6] which is based only on vibration signals processing and that is the main difference. Significant advantage is the low tram speed criterion which is equal to above 15 km/h. While in the [4] the tram speed has to be more than 30 km/h. Also the number of measuring points seems to be lower than in the [4]. Probably, only one microphone located at an appropriate distance from the track axis could be used in proposed method.

The elaborated wheel-flat detection system can be applied on various tram or railway depots. The system is not expensive to produce and apply. Furthermore, it can significant facilitate the vehicle service process, effectively informing an operator about the problem of damaged wheel rolling surfaces which cause uncomfortable impact noise and has influence on the higher vehicle and infrastructure wear.

References

[1] Cempel C., Vibroacoustic condition monitoring (Ellis Horwood Series in Mechanical Engineering), Ellis Horwood, Warsaw 1993, ISBN: 978-0139317187.

[2] Chiacchiari L., Thompson D., Squicciarini G., Ntotsios E., et al., Rail roughness and rolling noise in tramways, in: *Journal of Physics: Conference Series*, 2016.

[3]   Feldman M., Hilbert transform in vibration analysis. Mechanical Systems and Signal Processing, nr 25(3), 2011, p. 735–802, DOI: 10.1016/j.ymssp.2010.07.018.

[4]   Komorski P., Nowakowski T., Szymanski G.M., Tomaszewski F., Application of Time-Frequency Analysis of Acoustic Signal to Detecting Flat Places on the Rolling Surface of a Tram Wheel, in: Awrejcewicz, J. (Ed.), *Dynamical Systems in Applications*, Springer International Publishing, Łódź 2018, p. 205–215.

[5]   Makarewicz R., Kokowski P., Gołębiewski R., Mapa akustyczna miasta Poznania wraz z programem ochrony środowiska przed hałasem. Program Ochrony przed Hałasem (POH), Poznań 2008.

[6]   Nowakowski T., Komorski P., Szymanski G.M., Tomaszewski F., Wheel-flat detection on trams using envelope analysis with Hilbert transform. Latin American Journal of Solids and Structures, nr 16(1), 2019, p. 1–16, DOI: 10.1590/1679-78255010.

[7]   Nowakowski T., Komorski P., Tomaszewski F., The efficiency of tram articulations compared to vibroacoustic emissions. Archives of Transport, nr 44(4), 2017, p. 55–63, DOI: 10.5604/01.3001.0010.6161.

[8]   Pallas M.A., Lelong J., Chatagnon R., Characterisation of tram noise emission and contribution of the noise sources. Applied Acoustics, nr 72(7), 2011, p. 437–450, DOI: 10.1016/j.apacoust.2011.01.008.

[9]   Sandrock S., Griefahn B., Kaczmarek T., Hafke H., et al., Experimental studies on annoyance caused by noises from trams and buses. Journal of Sound and Vibration, nr 313(3–5), 2008, p. 908–919, DOI: 10.1016/j.jsv.2007.12.003.

[10] Skudrzyk E., The Foundations of Acoustics, Springer Vienna, Vienna 1971, ISBN: 978-3-7091-8257-4.

[11] Staśkiewicz T., Firlik B., Out-of-round tram wheels - current state and measurements. Archives of Transport, nr 45(1), 2018, p. 93–103, DOI: 10.5604/01.3001.0012.0946.

[12] Thompson D.J., Railway Noise And Vibration: Mechanisms, Modelling and Means of Control, ed. 1st, Elsevier, Southampton 2008, ISBN: 9780080914435.

[13] Thompson D.J., On the relationship between wheel and rail surface roughness and rolling noise. Journal of Sound and Vibration, nr 193(1), 1996, p. 149–160, DOI: 10.1006/jsvi.1996.0254.

[14] Wu T.X., Thompson D.J., On the impact noise generation due to a wheel passing over rail joints. Journal of Sound and Vibration, nr 267(3), 2003, p. 485–496, DOI: 10.1016/S0022-460X(03)00709-0.

Pawel Komorski, Ph.D.: Poznan University of Technology, Institute of Combustion Engines and Transport, Department of Rail Vehicles, Piotrowo 3 Street, 61-131 Poznan, Poland (pawel.komorski@put.poznan.pl).

Grzegorz M. Szymanski, Professor (Assistant): Poznan University of Technology, Institute of Combustion Engines and Transport, Department of Rail Vehicles, Piotrowo 3 Street, 61-131 Poznan, Poland (*grzegorz.m.szymanski@put.poznan.pl*).

Tomasz Nowakowski, M.Sc. (Ph.D. Student): Poznan University of Technology, Institute of Combustion Engines and Transport, Department of Rail Vehicles, Piotrowo 3 Street, 61-131 Poznan, Poland (tomasz.*zb.nowakowski@doctorate.put.poznan.pl*).

Malgorzata Orczyk, Ph.D.: Poznan University of Technology, Institute of Combustion Engines and Transport, Department of Rail Vehicles, Piotrowo 3 Street, 61-131 Poznan, Poland (*malgorzata.orczyk@put.poznan.pl*).

Complex vibrations of flexible beam NEMS elements, taking into account Casimir's forces under additive white noise

V.A. Krysko-jr, J. Awrejcewicz, I.V. Papkova

Abstract: A mathematical model of the vibrations of the sensing element NEMS in the form of a flexible size-dependent rigidly clamped beam connected to the electrode at a distance h_0 is developed. A transverse uniformly distributed alternating load and additive white noise act on the beam. Geometric nonlinearity is taken into account according to the theory of Kármán. The equations of motion of an element of a mechanical system, as well as the corresponding boundary and initial conditions, are derived based on both the Hamilton principle a modified couple stress theory taking into account the Euler-Bernoulli hypothesis. It was revealed that the size-dependent parameter significantly affects the dynamics of the beam under the action of a transverse alternating load and additive white noise. The dynamic stability loss is investigated.

1. Formulation of the problem

In recent years, interest in physical phenomena, known under the general name "Casimir effect" has steadily increased. Quantum theory has shown that vacuum is an extremely dynamic, continuously changing substance, from virtually born and right there dying elementary particles [1]. The combination of these effects and the fact that a mechanical device often integrates directly with electronics provides both problems and opportunities for studying the dynamics of NEMS. We note a number of works in this direction.

The static and dynamic behavior of carbon nanotube-based switches using the van der Waals interaction is described in [2, 3]. The influence of the Van der Waals forces and the Casimir forces on the stability of electrostatic torsion of NEMS accelerometers was studied in [4].

A study of the influence of self-affine roughness in terms of the retraction parameters for NEMS switches taking into account the Casimir force was carried out in [5]. A theoretical analysis of the influence of the Casimir forces on the nonlinear behavior of nanoscale electrostatic accelerometers is given in [6]. The study of the forces of Casimir and van der Waltz in cantilever beams is the subject of studies of references [7-10]. An analysis of the influence of the Casimir force on the instability of retraction in micro-membranes was described in [11] and various forms of plates were studied in [12, 13]. The electrostatic instability of nanobeams with allowance for the forces of Casimir and Van der Wals was investigated in [14]. In paper [15], a numerical algorithm is proposed that can predict the

static and dynamic behavior of circular NEMS devices under the influence of electrostatic and Casimir forces. Analytical modeling of the retracting instability of a CNT probe with van der Waals force was analyzed in [16], whereas Casimir effects are discussed in [17-19]. Zhang et al. [19], considered the theoretical details of Casimir effects, as well as experimental observations and applications were reported.

The study of the dynamic instability of a cantilever actuator made of a conductive cylindrical nanowire with a circular cross section, at the presence of Casimir power was carried out in [20]. The nano-beam is modeled on the basis of the nonlocal gradient theory of deformation and the Euler – Bernoulli hypothesis taking into account the Casimir forces in [21]. Jia and Yang [22] investigated the retracting instability of microswitches under combined electrostatic and intermolecular forces and axial residual stress, taking into account the force nonlinearity and geometric nonlinearity that arises from the extension of the middle plane. Theoretical formulations are based on the theory of the Bernoulli-Euler beam and geometric non-linearity of the Theodore von Kármán type. These solutions were confirmed by direct comparisons with experimental and other existing results. A parametric study was carried out taking into account the combined effects of geometric non-linearity, the ratio of the gap to the thickness of the structure, the Casimir force, the axial residual stress and the composition of the material with retracting instability.

Nayfeh [23] presented a nonlinear model of electric drive microbeams taking into account the electrostatic effect of the air gap condenser, the restoring force of the microbeam, and the axial load applied to the microbeam.

The boundary-value problem that describes the static deflection of a micro-object under the influence of electrostatic force due to constant polarizing voltage was solved. The eigenvalue problem, which described the vibration of a microsphere around its statically deflected position, was solved numerically for eigenfrequencies and modes. A comparison of the results obtained by this model with the experimental results showed excellent agreement, thus checking the model. The results indicated that the inability to take into account the extension of the midplane in the recovery effort of the micropulses leads to an underestimation of the stability limits. It was also demonstrated that the ratio of the width of the air gap to the thickness of the beam can be configured to expand the region of the linear relationship between the polarization voltage of the direct current and the fundamental natural frequency. This fact and the ability of the nonlinear model to accurately predict the natural frequencies for any constant polarization voltage allow developers to use a wider range of polarized DC voltages in the resonators. A review of the literature showed that the issue of the dynamics of beams under Casimir's action, vibration load and additive white noise was not considered.

In the classical theory of elasticity, the work of deformation and the strain energy depend on the stress tensor and do not depend on the rotation vector due to material independence. However, the rotation vector gradient can be a significant factor in the equations of state. Based on the modified couple stress theory presented by Yang et al. [24], the strain energy density is a function of both the stress tensor (conjugate to the strain tensor) and the curvature tensor (conjugate to the moment stress tensor). In one or another deformed isotropic linear elastic material located in the region Ω, the strain energy Π is expressed by the formula:

$$\Pi = \int_{\Omega} (\sigma_{ij}\,\varepsilon_{ij} + m_{ij}\eta_{ij})d\Omega \quad (i,j = 1,2,3) \tag{1}$$

where: σ_{ij} is a Cauchy stress tensor, ε_{ij} is a stress tensor, m_{ij} represents the deviator component of the moment stress tensor, and η_{ij} symmetric curvature tensor. These tensors are determined by the formulas:

$$\sigma_{ij} = \lambda tr(\varepsilon_{ij)}I + 2\mu\varepsilon_{ij}, \tag{2}$$

$$\varepsilon_{ij} = \frac{1}{2}[\nabla u + (\nabla u)^T], \tag{3}$$

$$m_{ij} = 2l^2\mu\chi_{ij}, \tag{4}$$

$$\eta_{ij} = \frac{1}{2}\left[\nabla\varphi + \left(\nabla_\varphi\right)^T\right], \tag{5}$$

where: u — vector moving, λ = Eν/(1+ν) (1-2ν) и μ = E/2 (1+ν) — Lamé constants, E, ν are respectively Young's modulus and Poisson's ratio for the beam material, φ — this is a rotation vector, presented as $\varphi_{i=}\frac{1}{2}rot(u_i)$. l — this is a parameter of the length scale of the material, understood as a property of the material, characterizing the effect of moment stress [24]. The material length scale parameter related to the microstructures of the material is designed to interpret the size effect in a non-classical model of Bernoulli-Euler beams.

From the analysis of equations (3) and (5) it follows that the stress tensor ε_{ij} and symmetric curvature tensor η_{ij} are symmetric, and therefore it follows from equations (2) and (4) that the stress tensor σ_{ij} and the deviator component of the moment stress tensor m_{ij} also symmetrical. Considered structure represents a beam located at a distance of h_0, a two-dimensional region of space R^2 with a Cartesian coordinate system, introduced as follows: in the body of the nanobalk, a cast line, called the midline, is fixed: $z = 0$, axis OX is directed from left to right along the midline, axis OZ – down, perpendicular to OX. In the indicated coordinate system, a structure of two beams, as a two-dimensional region Ω determined by in the following way:

$$\Omega = \left\{(x,z)\,|\,x \in [0,a], -\frac{h}{2} \le z \le \frac{h}{2}\right\} \text{ (Fig. 1); } 0 \le t \le \infty .$$
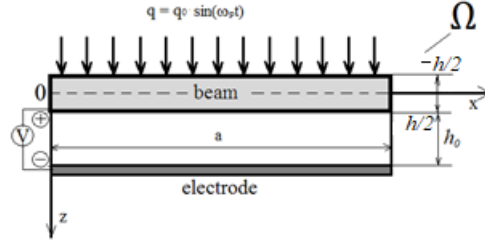
Fig. 1 Computational scheme.

At getting equations size-dependent beams connected to the electrode at a distance h_0, the following hypotheses are used:

- single-layer beam, isotropic, Hooke's law holds;
- the longitudinal size of the beams significantly exceeds their transverse dimensions;
- the beam axis is a straight line, the Euler-Bernoulli kinematic model is used, the normal stresses at sites parallel to the axis are negligible;
- the load acts in the direction of the OZ axis and external forces do not change their direction during beam deformation;
- geometric nonlinearity is taken into account in the form of von Kármán.

According to the Hamilton principle, we have

$$\int_{t_0}^{t_1} (\delta K - \delta \Pi + \delta' W) dt = 0.$$

(7)

Here K, Π are the kinetic and potential energy, respectively, $\delta' W$ is the work of external forces. Using the methods of calculus of variations, a system of differential equations of the theory of flexible beams is obtained taking into account the modified couple stress theory of elasticity [24]:

$$-\left(\frac{1}{12} + \bar{D}_1\right)\frac{\partial^4 \bar{w}}{\partial \bar{x}^4} + L_1(\bar{u}, \bar{w}) + \left(\frac{h_0}{h}\right)^2 L_2(\bar{w}, \bar{w}) - \frac{\partial^2 \bar{w}}{\partial \bar{t}^2} + \bar{q}(t) + \frac{\bar{q}_k}{(1-\bar{w})^4} = 0,$$

$$\left(\frac{h}{a}\right)^2 \frac{\partial^2 \bar{u}}{\partial \bar{x}^2} + \left(\frac{h_0}{h}\right)^2 \left(\frac{a}{h}\right)^2 L_3(\bar{w}, \bar{w}) - \frac{\partial^2 \bar{u}}{\partial \bar{t}^2} = 0,$$

(8)

where: $L_1(\bar{u}, \bar{w}) = \frac{\partial^2 \bar{u}}{\partial \bar{x}^2}\frac{\partial \bar{w}}{\partial \bar{x}} + \frac{\partial^2 \bar{w}}{\partial \bar{x}^2}\frac{\partial \bar{u}}{\partial \bar{x}}$; $L_2(\bar{w}, \bar{w}) = \frac{3}{2}\frac{\partial^2 \bar{w}}{\partial \bar{x}^2}\left(\frac{\partial \bar{w}}{\partial \bar{x}}\right)^2$; $L_3(\bar{w}, \bar{w}) = \frac{\partial^2 \bar{w}}{\partial \bar{x}^2}\frac{\partial \bar{w}}{\partial \bar{x}}$. The boundary and initial conditions should be added to the system of nonlinear partial differential equations (8). The dimensionless quantities are introduced as follows:

$$\bar{x} = \frac{x}{a}; \quad \bar{w} = \frac{w}{h_0}; \quad \bar{u} = \frac{ua}{h_0^2}; \quad \bar{t} = t\sqrt{\frac{D_0}{\rho h a^4}}; \quad \bar{q} = \frac{a^4}{E h_0 h^3}q; \quad D_0 = \frac{Evh^3}{(1+v)(1-2v)}; \quad \bar{q}_k = \frac{\hbar c \pi^2 a^4}{240 D_0 h_0^5};$$

$$\bar{D}_1 = \gamma \frac{(1-2v)}{2v}; \quad \gamma = \frac{l^2}{h^2}.$$

We have used the following notation: t - time; w – deflection, u – function axis movements x; h – beam thickness; h_0 – the distance between the electrode and nanobalk; q_0 – amplitude of load, v – Poisson's ratio, E – elastic modulus, l – size dependent parameter, ρ – density plate material, a – radius, $\hbar$ - Planck constant.

The system of nonlinear partial differential equations reduces to the Cauchy problem by the finite difference method with approximation of the second order of accuracy. The Cauchy problem is solved by methods of the Runge-Kutta type (4th, 6th, 8th order of accuracy) and the Newmark method [25], [26].

2. Numerical results

Consider the vibrations of a rigidly clamped at both ends of the nanobeam under the action of the Casimir force, an alternating load $q = q_0\sin(\omega_p t)$ and white additive noise [27], [28]:

$$\overline{w}(0,\overline{t}) = \overline{w}(1,\overline{t}) = u(0,\overline{t}) = u(1,\overline{t}) = \frac{\partial w(0,\overline{t})}{\partial \overline{x}} = \frac{\partial \overline{w}(1,\overline{t})}{\partial \overline{x}} = 0 , \qquad (9)$$

with zero initial conditions: $\overline{w}(\overline{x})|_{t=0} = 0, \ \overline{u}(\overline{x})|_{t=0} = 0, \ \dfrac{\partial \overline{w}(\overline{x})}{\partial \overline{t}}\bigg|_{t=0} = 0, \ \dfrac{\partial \overline{u}(\overline{x})}{\partial \overline{t}}\bigg|_{t=0} = 0 , \qquad (10)$

Geometric and physical parameters of nanobeams: length $a = 4 \cdot 10^{-7}$m, thickness $h = 4 \cdot 10^{-9}$m, density $\rho = 19320$ kg/m^3 and Young's modulus $E = 1{,}224 \cdot 10^7$ kgF/m^2 (gold), Poisson's modulus $v = 0.44$, size-dependent parameter $l = 0.5$, distance between electrode and beam $h_0 = 6 \cdot 10^{-9}$ m.

Microbeam geometric parameters: length $a = 4 \cdot 10^{-4}$ m, thickness $h = 4 \cdot 10^{-6}$ m, size-dependent parameter $l = 0$, distance between electrode and beam $h_0 = 6 \cdot 10^{-6}$ m.

Beam is in a vacuum ($\varepsilon = 0$).

Case study 1.

Vibrations of a nanobeam under impact with an account of only the forces of Casimir. In this case, the periodic vibrations exhibit natural frequency ω_0. Table 1 shows the Fourier power spectra for the size-dependent parameter $\gamma = 0$ without white noise ($w_n = 0$) and taking into account white noise ($w_n = 5$). The presence of white noise leads the system to chaotic vibrations at the natural frequency ω_0 and independent frequency $\omega_1 = 7.1942$.

Consider the vibrations of microbeams ($\gamma = 0$) under the action of the Casimir force and transverse uniformly distributed load $q = q_0\sin(\omega_p t)$ without white noise ($w_n = 0$). Table 2 presents the Fourier power spectra. Under action of the Casimir force and lateral load, the microbeam vibrates at a frequency ω_p and independent frequency ω_1 and their linear combinations $\omega_2 = \omega_p - \omega_1$. Taking into account the size-dependent parameter leads to a purification of the power spectrum in the region of the frequency of natural vibration. When the additive white noise load is taken into account

in the power spectrum of the microbeam, the noise features are observed at low frequencies; for a nano-beam with the same loading parameters, an increase of the noise component in the power spectrum is observed.

Table 1. Fourier Power Spectra

$w_n = 0, \gamma = 0$	$w_n = 5, \gamma = 0$

$w_n = 0, \gamma = 0, q_0 = 5, \omega_p = \omega_0 = 22.366$	$w_n = 0, \gamma = 0.5, q_0 = 5, \omega_p = \omega_0 = 22.366$
$w_n = 5, \gamma = 0, q_0 = 5, \omega_p = \omega_0 = 22.366$	$w_n = 0.5, \gamma = 0.5, q_0 = 5, \omega_p = \omega_0 = 22.366$
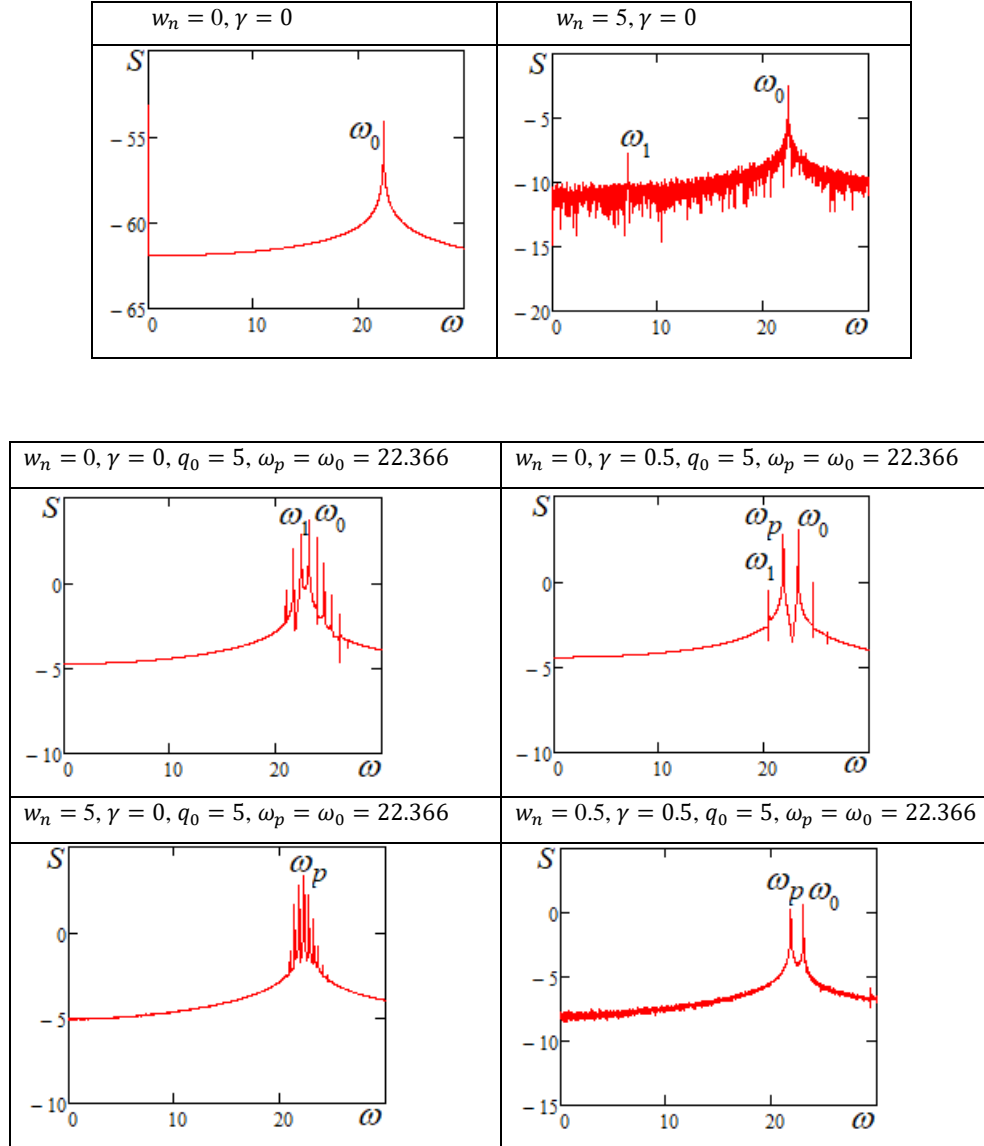
Table 2. Maximum deflection dependencies of the amplitude versus the driving load $w_{max}(q_0)$ and scales of vibrations

$w_n = 0, \gamma = 0$	$w_n = 5, \gamma = 0$
$w_n = 0, \gamma = 0.5$	$w_n = 5, \gamma = 0.5$

	periodic vibrations with ω_p		subharmonic vibrations $\frac{\omega_p}{2n}$, where $n \in N$
	subharmonic vibrations with $\frac{\omega_p}{2}$		chaotic vibrations
	Quasi-periodic vibrations with 2 frequencies		subharmonic vibrations $\frac{\omega_p}{3}$
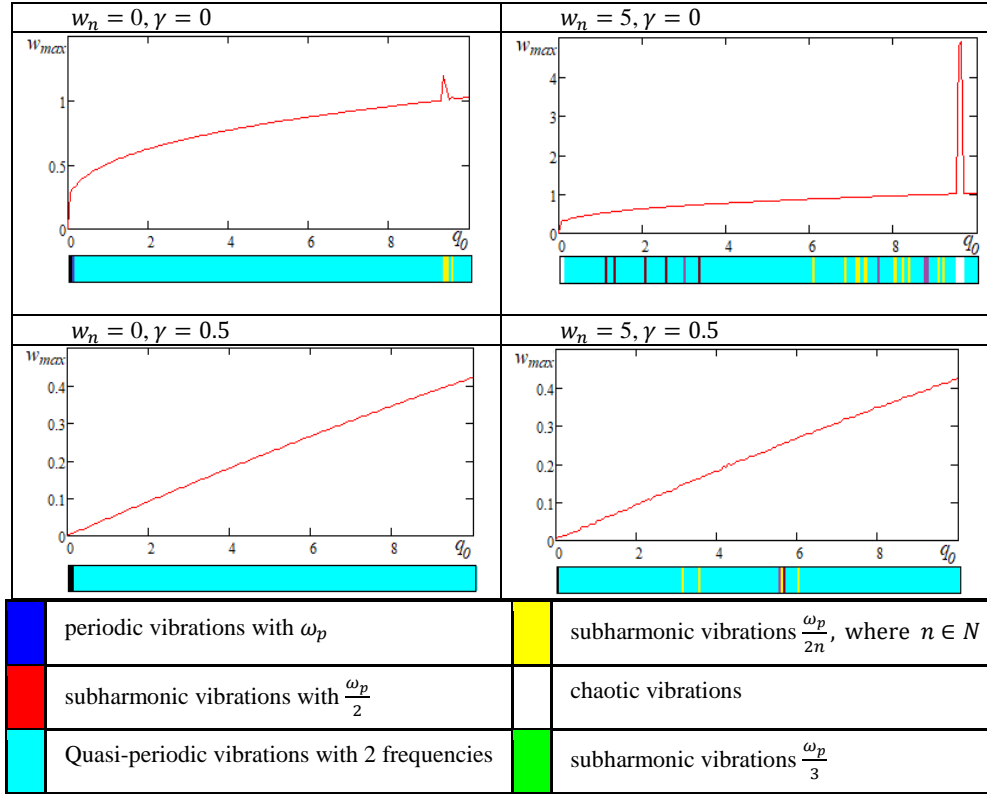
A general analysis of the study of vibrations of micro- and nano-beams taking into account the additive white noise of a transversely alternating load yields the following results: Table 3 presents the dependences of the maximum deflection in the center of the beam on the amplitude of the driving load $w_{max}(q_0)$ and character scales vibrations. In the range $q_0 \in (0; 9.4)$ beam exhibits vibrations at two independent frequencies, i.e. forcing load frequency ω_p and frequency ω_1. The first Lyapunov exponent is zero, and the rest are negative. With increasing load $q_0 \in [9.4; 9.6)$ there is a dynamic loss of stability, in which the signal exhibits subharmonic $\omega_p/23$ with a sharp increase in deflection, and a sharp change character of vibration (all Lyapunov exponents are close to zero (Le1 $= -58 \cdot 10^{-5}$, Le2 $= -61 \cdot 10^{-4}$, Le3 $= -57 \cdot 10^{-4}$, Le4 $= -11 \cdot 10^{-3}$). Spectrum of the Lyapunov exponents was calculated Jacobian method [29]. When taking into account the noise load, the nature of vibrations under changes: using the range of chaotic vibrations $q_0 \in (0; 0.1)$ - hyperchaos (Le1 $= 18 \cdot 10^{-4}$, Le2 $= 1.7494 \cdot 10^{-5}$, Le3 $= -39 \cdot 10^{-2}$, Le4 $= -46 \cdot 10^{-2}$). At the load $q_0 \in [0.1; 9.7)$, the microbeam vibrates at two independent frequencies. At frequencies $k\omega_p/2^n$ the periodicity windows appear, where $k, n \in$

N. At load $q_0 \in [9.7; 9.8)$ the dynamic loss of stability occurs, sharp increase deflection and transition from quasiperiodicity to hyperchaos takes place (Le1 = $48 \cdot 10^{-4}$, Le2 = $11 \cdot 10^{-3}$, Le3 = $-31 \cdot 10^{-2}$, Le4 = $-78 \cdot 10^{-2}$). Increase of the size dependent parameter implies changes within the whole interval $q_0 \in (0; 9.4)$.

3. Conclusions

A mathematical model of the nonlinear dynamics of the MEMS / NEMS beam element under the action of the Casimir force, under uniformly distributed alternating load and additive white noise is developed. The governing PDEs are yielded by the Hamilton principle for the Euler-Bernoulli kinematic model and the modified couple stress theory. For the first time, the phenomenon of stability loss with a transverse alternating load MEMS / NEMS is detected. As a dynamic criterion for the loss of stability, the Lyapunov approach is used by analyzing the spectrum of Lyapunov exponents. For microbeams, it was found that with a loss of stability, hyperchaotic oscillations are observed (the two highest Lyapunov exponents are positive). When the size-dependent parameter is taken into account in the equations, the amplitude of the oscillations and the nature of the vibrations at high loads decrease. It was revealed that the additive noise field inversely depends on the ratio of the amplitude of the driving load to the intensity of the noise field q_0/w_n.

Acknowledgments

References

[1]   Casimir, H.B.G., On the attraction between two perfectly conducting plates. *Proceedings of the Koninklijke Nederlandse Akademie van Wetenschappen* 51 (1948) 793-795.

[2]   Dequesnes, M., Rotkin, S., Aluru, N., Calculation of pullin voltages for carbon-nanotube-based nanoelectromechanical switches. *Nanotechnology* 13(11) (2002) 120.

[3]   Dequesnes, M., Tang, Z., Aluru, N., Static and dynamic analysis of carbon nanotube-based switches. *Journal of Engineering Materials and Technology* 126(3) (2004) 230-237.

[4]   Guo, J.-G., Zhao, Y.-P., Influence of van der Waals and Casimir forces on electrostatic torsional actuators. *J. Microelectromech. Syst*. 13(6) (2004) 1027–1035.

[5]   Palasantzas, G., De Hosson, J.T.M., Pull-in characteristics of electromechanical switches in the presence of Casimir forces: Influence of self-affine surface roughness. *Phys. Rev. B*. 72(11) (2005) article id.115426.

[6]   Lin, W.-H., Zhao, Y.-P., Nonlinear behavior for nanoscale electrostatic actuators with Casimir force. *Chaos, Solitons & Fractals* 23(5) (2005) 1777–1785.

[7]   Ramezani, A., Alasty, A., Instability of nanocantilever arrays in electrostatic and van der Waals interactions. *J. Phys. D: Appl. Phys*. 42(22) (2009) article id. 225506.

[8]   Ramezani, A., Alasty, A., Akbari, J., Closed-form solutions of the pull-in instability in nano-cantilevers under electrostatic and intermolecular surface forces. *Int. J. Solids Struct*. 44(14-15) (2007) 4925–4941.

[9]   Ramezani, A., Alasty, A., Akbari, J., Closed-form approximation and numerical validation of the influence of van der Waals force on electrostatic cantilevers at nano-scale separations. *Nanotechnology* 19(1) (2008) 015501.

[10]   Ramezani, A., Alasty, A., Combined action of Casimir and electrostatic forces on nanocantilever arrays. *Acta Mech*. 212(3-4) (2010) 305–317.

[11]   Batra, R., Porfiri, M., Spinello, D., Effects of Casimir force on pull-in instability in micromembranes, *Europhysics Letters* 77(2) (2007) 20010.

[12]   Batra, R., Porfiri, M., Spinello, D., Reduced-order models for microelectromechanical rectangular and circular plates incorporating the Casimir force. *Int. J. Solids Struct*. 45(11-12) (2008) 3558–3583.

[13]   Batra, R., Porfiri, M., Spinello, D., Vibrations and pull-in instabilities of microelectromechanical von Kármán elliptic plates incorporating the Casimir force. *J. Sound Vib*. 315(4-5) (2008) 939-960.

[14]   Zand, M.M., Ahmadian, M., Dynamic pull-in instability of electrostatically actuated beams incorporating Casimir and van der Waals forces. *J. Mech. Eng. Sci*. 224 (2010) 2037–47.

[15]   Wang, Y.-G., Lin, W.-H., Li, X.-M., Feng, Z.-J., Bending and vibration of an electrostatically actuated circular microplate in presence of Casimir force. *Appl. Math. Modelling*. 35(5) (2011) 2348–2357.

[16]   Koochi, A., Fazli, N., Rach, R., Modeling the pull-in instability of the CNT-based probe/actuator under the Coulomb force and the van der Waals attraction. *Latin American J. Solids Struct*. 11(8) (2014) 1315–1328.

[17]   Rodriguez, A.W., Capasso, F., Johnson, S.G., The Casimir effect in microstructured geometries. *Nat. Photonics*. 5(4) (2011) 211–221.

[18]   Berman, D., Krim, J., Surface science, MEMS and NEMS: progress and opportunities for surface science research performed on, or by, microdevices. *Prog. Surf. Sci*. 88(2) (2013) 171–211.

[19]   Zhang, W.-M., Yan, H., Peng, Z.-K., Meng, G., Electrostatic pull-in instability in MEMS/ NEMS: A review. *Sens. Actuators A: Physical*. 2014 (214) 187–218.

[20]   Keivani, M., Mardaneh, M., Koochi, A., Rezaei, M., Abadyan, M, On the dynamic instability of nanowire-fabricated electromechanical Actuators in the Casimir regime: Coupled effects of surface energy and size dependency. *Physica E: Low-dimensional Systems and Nanostructures*. 76 (2016) 60–69

[21]   Amin Vahidi-Moghaddam, Arman Rajaei, Ramin Vatankhah, Mohammad Reza Hairi-Yazdi. Terminal sliding mode control with non-symmetric input saturation for vibration suppression of electrostatically actuated nanobeams in the presence of Casimir force. *Applied Mathematical Modelling*, 60 (2018) 416-434.

[22]   Jia, X.L., Yang, J., Kitipornchai, S., Pull-in instability of geometrically nonlinear micro-switches under electrostatic and Casimir forces. *Acta Mech*. 218(1-2) (2011) 161-174.

[23]   Abdel-Rahman, E.M., Younis, M.I., Nayfeh, A.H., Characterization of the mechanical behavior of an electrically actuated microbeam. *Journal of Micromechanics and Microengineering* 12(6) (2002) 759, DOI: 10.1088/0960-1317/12/6/306

[24] Yang, F., Chong, A.C.M., Lam, D.C.C., Tong, P., Couple stress based strain gradient theory for elasticity. *Int J Solids Struct*. 39(10) (2002) 2731–2743

[25] Krysko, V.A., Awrejcewicz, J., Papkova, I.V., Saltykova, O.A., Krysko, A.V., On reliability of chaotic dynamics of two Euler-Bernoulli beams with a small clearance. *International Journal of Non-Linear Mechanics* 104 (2018) 8-18.

[26] Krysko, A.V., Awrejcewicz, J., Zakharova, A.A., Papkova, I.V., Krysko, V.A., Chaotic vibrations of flexible shallow axially symmetric shells. *Nonlinear Dynamics* 91(4) (2018) 2271-2291.

[27] Awrejcewicz, J., Krysko, A.V., Papkova, I.V., Zakharov, V.M., Erofeev, N.P., Krylova, E.Yu., Mrozowski, J., Krysko, V.A., Chaotic dynamics of flexible beams driven by external white noise. *Mechanical Systems and Signal Processing* 79 (2016) 225-253

[28] Awrejcewicz, J., Krysko, A.V., Papkova, I.V., Erofeev, N.P., Krysko, V.A., Chaotic dynamics of structural members under regular periodic and white noise excitations Lecture Notes in Computer Science 2017, 10187 LNCS, 25-32

[29] Eckmann, J.-P., Ruelle, D., Ergodic theory of chaos and strange attractors. *Rev. Mod. Phys*. 57 (1985) 617–656.

[30] Sato, S., Sano, M., Sawada, Y., Practical methods of measuring the generalized dimension and the largest Lyapunov exponent in high dimensional chaotic systems. *Prog. Theor. Phys*. 77 (1) (1987) 1-5.

Vadim A. Krysko-jr, PhD student: Department of Automation, Biomechanics and Mechatronics, Lodz University of Technology, 1/15 Stefanowskiego Str., 90-924 Lodz, Poland; Department of Mathematics and Modeling, Saratov State Technical University, Politehnicheskaya 77, 410054 Saratov, Russian Federation (vadimakrysko@gmail.com).

Jan Awrejcewicz, Professor: Lodz University of Technology, Faculty of Mechanical Engineering, Department of Automation, Biomechanics and Mechatronics, 1/15 Stefanowskego Str., 90-924 Lodz, Poland (jan.awrejcewicz@p.lodz.pl);

Irina V. Papkova Associate Professor: Department of Mathematics and Modeling, Saratov State Technical University, Politehnicheskaya 77, 410054 Saratov, Russian Federation (ikravzova@mail.ru);

Flexural waves propagation in piezoelectric metamaterial beam

Marcela Machado, Adriano Fabro, Braion Barbosa de Moura

Abstract: In this paper, we analysed a piezoelectric metamaterial to focus on flexural waves in beams modelled by using the spectral element method. The piezoelectric metamaterial is applied in cases of attenuation and control of waves, as well as, adopted in the designing process of the piezo-lens used to trace the waves trajectories in large frequency bands. The configuration considered of a periodic array of piezoelectric patches incorporated to a beam undergoing transverse motion. The periodic arrangement of shunted patches provides the beam with attenuation properties which depend on the resonant behaviour of the shunts. A numerical model predicts the flexural wave behaviour of the beam for different shunting configurations.

1. Introduction

Metamaterials are designed materials developed properties previews required. By assembling multiple individual elements constructed into repeating patterns a required behaviour could be projected. Their potential applications include an invisibility cloak, vibration, acoustic control in structures, and metadevices [24]. Phononic crystal (PC) [5, 10, 19, 11] is a typical metamaterial that the materials has a periodic distribution of elastic constant or mass density. Because of the periodic distribution, it is found that when an elastic wave propagates through PC a stop-band or bandgap is formed in its transmission. The metamaterial in engineering application has increased in the last few years due to the improvement the manufacturing process. The inclusion of electronic sensors, e.g. piezoelectric sensor (piezo), into the structure allowed us to monitor and control the vibration in of systems [8, 3, 9, 17, 7]. The application of the piezoelectric-sensors with shunt circuits in metamaterial with an emphasis on reducing vibrations or creating bandgaps [2, 1, 25, 23, 20].

An alternative to the Finite element method, that in some application requires a large number of finite elements, is the Spectral element method (SEM) [4, 12]. In this method, the element shape functions is obtained from the analytical solution of governing differential equations and the dynamic system solution written in the frequency domain. This feature reduces significantly the number of elements required in the structure model and b improves the accuracy of the dynamic system solution. Therefore, a single element is sufficient to model any continuous and uniform part of the structure [15]. A few spectral element have

been developed, like as rod , beam, plates, etc [4, 12, 6, 13, 14, 16], and there are on going researches proposing new and improved elements. Lee and Kim [21, 22] developed a spectral element coupling the Euler-Bernoulli beam with a piezoelectric layer, and active piezoelectric, respectively. Park et al.[18] presented a spectral element formulation for one and two coupled piezoelectric wafer.

Aiming the metastructure designed using the piezoelectric, this paper proposes a spectral element beam coupled with a piezo-shunt and presents a study of the vibration response and flexure wave propagation of the metamaterial. The transfer matrix is estimated from the dynamic stiffness of a unit cell of the periodic assembly and used to estimate the attenuation properties of a beam through the dispersion diagram and illustrate the proposed vibration control strategy for various shunting configurations.

2. Spectral element beam piezoelectric-shunt

The coupled structure composed by the beam and a piezo layer illustrated in fig 1 was based on the study presented by [21].

(a)
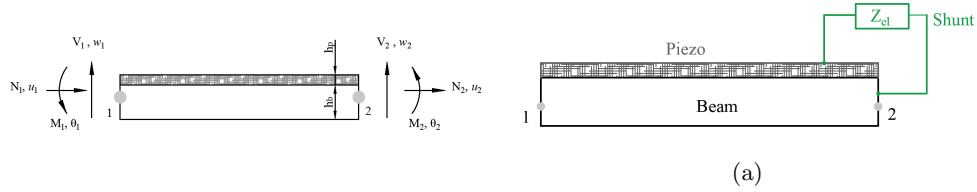
Figure 1. Two node spectral beam-piezoelectric element (a), and beam-piezoelectric-shunt element (b).

The structural dynamic equations of motion consider a beam coupled with a piezo layer, both with uniform density and thickness, the shear deformations in both layers neglected, and the rotational inertia has no influence. The transverse displacement $w(x,t)$ is the same for both layers, and the applied voltage is uniform along the piezo. There is a perfect continuity in the coupling interactions, which does not slip in the interface, relying on the understanding that the linear elasticity and piezoelectricity theories are applicable. For perfect boundary conditions, the geometry of Fig. 1 provides the kinematics relation as:

$$u_p = u_b - \frac{h_b + h_p}{2}\theta. \tag{1}$$

where u_p and u_b are the axial displacement of the neutral axes of the base beam and the piezo layer, respectively; h_b and h_p are the high cross-section beam and piezoelectric layer, respectively; and $\theta = \partial\omega/\partial x$ is rotational angle. The electromechanical model of the coupling

beam and piezoelectric patch is based on the stress-charge form of the constitutive equations for a piezoelectric material,

$$\begin{Bmatrix} \sigma \\ \mathtt{E} \end{Bmatrix} = \begin{bmatrix} C_{11}^D & -h_{31} \\ -h_{31} & \beta_{33}^S \end{bmatrix} \begin{Bmatrix} \epsilon \\ D \end{Bmatrix}. \tag{2}$$

where σ is the mechanical stress, ϵ the mechanical strain, D is the electrical displacement (charge/area in the beam vertical direction) and $\mathtt{E}$ is the electrical field (voltage/length along the vertical direction). C_{11}^D is the elastic stiffness, β_{33}^S is the dielectric constant, and h_{31} is the piezoelectric constant. The elementary beam nodal displacements are vertical w and the rotation of the cross section ϕ, where the rotation is derived from the transverse deformation as $\phi = \partial w / \partial x$. As the changes in the beam are of shear V and bending moment M. Fig. 1(a) shows the two-node coupled element with nodal forces and displacements. By using the constitutive relation and assuming D as a constant, the strain energy of the two-layer beam is derived after integrating over its base, the potential kinetic energy that applying into the Hamilton's principle the axial-bending coupled equation of motion can be described as

$$EIw''' + \rho\,A\ddot{w} = -\alpha\ddot{u}_b' + \beta\,u_b''' + \gamma\ddot{w}'',$$
$$EIu_b'' - \rho\,A\ddot{u}_b = -\alpha\ddot{w}' + \beta\,w'''. \tag{3}$$

where

$$\rho\,A = \rho_b A_b + \rho_p A_p, \qquad EA = E_b A_b + E_p A_p, \qquad EI = E_b I_b + C_{11}^D I_p + \frac{1}{4} E_p A_p h^2$$
$$\alpha = \frac{1}{2}\rho_p A_p h, \qquad \beta = \frac{1}{2} E_p A_p h, \qquad \gamma = \frac{1}{4}\rho_p A_p h^2$$
$$h = h_b + h_p, \qquad E_p = C_{11}^D - \frac{h_{31}^2}{\beta_{33}^S}. \tag{4}$$

The parameters E, A, I and ρ (for each layer) are the Young's modulus, the cross-sectional area, the area moment of inertia about the neutral axis, and the mass density, respectively; α, β, and γ denotes the axial-bending coupling, which tends to zero if no coupling is applied. The Hamilton principle also provides the boundary conditions related to the mechanical and piezo variable, where the nodal forces is given as

$$N = EAu_b' - \beta\,w'' - bd_{31}E_pV(t),$$
$$M = \bar{\theta} = EIw'' - \beta\,u_b' + \frac{1}{2}hbd_{31}E_pV(t),$$
$$V = \bar{w} = -EIw''' - \alpha\ddot{u}_b'' - \gamma\ddot{w}'. \tag{5}$$

where d_{31} is the piezo constant defined by $d_{31} = h_{31}/(E_p\beta_{33}^s)$.

2.1. Spectral element analysis

The spectral element assumption is that the beam vibration and the applied voltage are spectral expressed as

$$w(x,t) = \sum_n^{\text{N}} \hat{W}(x, \omega_n) e^{i\omega_n t}; \qquad u_b(x,t) = \sum_n^{\text{N}} \hat{U}(x, \omega_n) e^{i\omega_n t}; \qquad V(t) = \sum_n^{\text{N}} \hat{V}(\omega_n) e^{i\omega_n t}.$$

(6)

where ω_n is the frequency and $\hat{W}$, $\hat{U}$ and $\hat{V}$ are the spectral components of w, u_b, and V, respectively; and N is the total number of spectral components. By substituting Eq. 4 into Eq. 6 leads to a coupled two ordinary differential equations for $\hat{W}$ and $\hat{U}$,

$$EI\hat{W}'''' - \omega^2 \rho \, A\hat{W} = \omega^2 \left(-\gamma \hat{W}'' + \alpha \hat{U}' \right) + \beta \hat{U}'''$$

$$EA\hat{U}'' + \omega^2 \rho \, A\hat{U} = \omega^2 \alpha \, W' + \beta \hat{W}''''$$

(7)

The general solutions for $\hat{W}$ and $\hat{U}$ can be obtained in the forms of,

$$\hat{W}(x) = \sum_{i=1}^{3} \left(A_i e^{\frac{k_i x}{L}} + A_{2i} e^{-\frac{k_i x}{L}} \right) = [\mathbf{N}(x)] \, \mathbf{A},$$

$$\hat{U}(x) = \sum_{i=1}^{3} \left(B_i e^{\frac{k_i x}{L}} + B_{2i} e^{-\frac{k_i x}{L}} \right) = [\mathbf{N}(x)] \, \mathbf{B}.$$

(8)

where,

$$[\mathbf{N}(x)] = [e^{\frac{k_1 x}{L}}, e^{\frac{k_2 x}{L}}, e^{\frac{k_3 x}{L}}, e^{-\frac{k_1 x}{L}}, e^{-\frac{k_2 x}{L}}, e^{-\frac{k_3 x}{L}}],$$

$$\{\mathbf{A}\} = A_1, A_2, A_3, A_4, A_5, A_6, \qquad \{\mathbf{B}\} = B_1, B_2, B_3, B_4, B_5, B_6.$$

(9)

In Eq. 8, $k_i (i = 1, 2, 3)$ are the wave numbers of the from,

$$\left(\beta^2 - EAEI \right) k^6 + \omega^2 L^2 \left(2\alpha\beta - \rho AEI - \gamma EA \right) k^4 + \omega^2 L^4 \left(\alpha^2 \omega^4 + \rho A \left(EA - \gamma \omega^2 \right) \right) k^2 + \omega^4 L^6 \rho \, A^2 = 0.$$

(10)

and in Eq. 10 is the six[th] term polynomial representing the dispersion relation that gives the relation between wave number and frequency. The relations between the coefficients A_i and B_i of Eq.9 can be obtained as

$$B_i = (-1)^i \left\{ \frac{L^4 \rho A \omega^2 + L^2 \gamma \omega^2 k_i^2 + EI k_i^4}{L k_i (L^2 \alpha \omega^2 - \beta k_i^2)} \right\} A_i = \lambda_i(\omega) \, A_i \quad (i = 1, \, 2, \, \ldots 6)$$

(11)

or

$$\{\mathbf{B}\} = [diagonal(\lambda_i)] \, \mathbf{A}.$$

The spectral nodal displacements can be expressed in terms of A_i by using Eq. 8, which give us the relation $\{\mathbf{x}\} = [\mathbf{Q}]\,\mathbf{A}$. The vector $\mathbf{x}$ is the spectral nodal displacements defined by

$$\{\mathbf{x}\} = \left\{ \hat{U}_1 \quad \hat{W}_1 \quad \hat{\Theta}_1 \quad \hat{U}_2 \quad \hat{W}_2 \quad \hat{\Theta}_2 \right\}^T. \tag{12}$$

The spectral displacement components of Eq. 9 can be represented in terms of the spectral nodal displacement vector $\{\mathbf{x}\}$, as

$$\hat{W}(x) = [\mathbf{N}(x)]\,[\mathbf{Q}]^{-1}\,\mathbf{x},$$
$$\hat{U}(x) = [\mathbf{N}(x)\,[diagonal\,(\lambda_i)]\,\{\mathbf{Q}\}^{-1}\,\mathbf{x}. \tag{13}$$

By substituting Eq.8 into the spectral representations and relate force-displacement, the spectral components of the nodal forces and moments can be expressed in terms of A_i as

$$\{\mathbf{f}\} = [\mathbf{P}]\,\{\mathbf{A}\} = \left[\hat{N}_1 - \hat{N}^e \quad \hat{Q}_1 \quad \hat{M}_1 + \hat{M}^e \quad \hat{N}_2 + \hat{N}_2^e \quad \hat{Q}_2 \quad \hat{M}_2 - \hat{M}^e \right]^T. \tag{14}$$

The forces $\hat{N}^e$ and $\hat{M}^e$ are the nodal spectral components of piezo-electrical induced axial force and bending moment defined by

$$\hat{N}^e = b d_{31} E_p \hat{V}, \qquad \hat{M}^e = \frac{1}{2} h b d_{31} E_p \hat{V}. \tag{15}$$

The relation between spectral nodal displacement and force is given by the coefficients A_i, that is defined by

$$\{\mathbf{f}\} = [\mathbf{P}]\,[\mathbf{Q}]^{-1}\,\{\mathbf{x}\} = [\mathbf{S}]\,\{\mathbf{x}\}. \tag{16}$$

where $\mathbf{S}$ is the frequency-dependent spectral element matrix or dynamic stiffness matrix. The explicit expressions for $\mathbf{P}$ and $\mathbf{Q}$ are listed herein as [21]

$$[\mathbf{P}] = \frac{1}{L^3} \begin{bmatrix} p_{11} & p_{11} & p_{12} & p_{12} & p_{13} & p_{13} \\ p_{21} & -p_{21} & p_{22} & -p_{22} & p_{23} & -p_{23} \\ p_{31} & p_{31} & p_{32} & p_{32} & p_{33} & p_{33} \\ -e^{k_1}p_{11} & -e^{-k_1}p_{11} & -e^{k_2}p_{12} & -e^{-k_2}p_{12} & -e^{k_3}p_{13} & -e^{-k_3}p_{13} \\ -e^{k_1}p_{21} & -e^{-k_1}p_{21} & -e^{k_2}p_{22} & -e^{-k_2}p_{22} & -e^{k_3}p_{23} & -e^{-k_3}p_{23} \\ -e^{k_1}p_{31} & -e^{-k_1}p_{31} & -e^{k_2}p_{32} & -e^{-k_2}p_{32} & -e^{-k_3}p_{33} & -e^{k_3}p_{33} \end{bmatrix}$$

$$\tag{17}$$

$$[\mathbf{Q}] = \begin{bmatrix} \lambda_1 & -\lambda_1 & \lambda_2 & -\lambda_2 & \lambda_3 & -\lambda_3 \\ 1 & 1 & 1 & 1 & 1 & 1 \\ \frac{k_1}{L} & \frac{-k_1}{L} & \frac{k_2}{L} & \frac{-k_2}{L} & \frac{k_3}{L} & \frac{-k_3}{L} \\ e^{k_1}\lambda_1 & -e^{-k_1}\lambda_1 & e^{k_2}\lambda_2 & -e^{-k_2}\lambda_2 & e^{k_3}\lambda_3 & -e^{-k_3}\lambda_3 \\ e^{k_1} & e^{-k_1} & e^{k_2} & e^{-k_2} & e^{k_3} & e^{-k_3} \\ \frac{e^{k_1}k_1}{L} & \frac{-e^{-k_1}k_1}{L} & \frac{e^{k_2}k_2}{L} & \frac{-e^{-k_2}k_2}{L} & \frac{e^{k_3}k_3}{L} & \frac{-e^{-k_3}k_3}{L} \end{bmatrix} \qquad (18)$$

where,

$$p_{1i} = k_i L(\beta \ k_i - EAL\lambda_i), \qquad p_{2i} = L^2\omega^2\gamma \ k_i + EIk_i^3 - L^3\omega^2\alpha\lambda_i - L\beta \ k_i^2\lambda_i,$$

$$p_{3i} = k_i L(L\beta\lambda_i - EIk_i).$$

2.2. Single-resonance shunt

Airoldi and Ruzzene [1] present the governing equations of the RL-shunted piezo patch scheme used in this paper. Fig.2 shows the shunt circuit and its equivalent, in (a) The RL-shunt circuit of a transducer piezo, and (b) the sketch of resonant electronic components circuit.

(a)   (b)
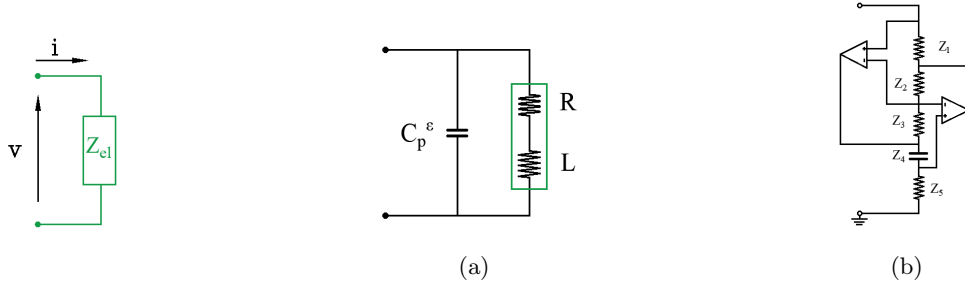
Figure 2. Shunt circuit. a) Equivalent RL-shunt circuit of a transducer piezo; b) Sketch of resonant electronic components circuit.

The equivalent circuit of a piezoelectric transducer is, according to its inherent capacitance C_p^ε at constant strain, shunted through a resistor-inductor in series. The electrical admittance of the piezo patch is given by:

$$Y_{el} = Y_p + Y_{su}, \qquad (19)$$

where $Y_{el} = 1/Z_{el}$ is the equivalent admittance of the piezo, and $Y_{el} = 1/Z_{su}$ is the admittance of the shunting circuit, with $Z_{su} = R + i\omega L$, R is the resistor, and L the inductance.

The impedance Z_{el} is defined as,

$$Z_{el}(\omega) = \frac{R + i\omega L}{\left(1 - \omega^2 L C_p^\varepsilon\right) + i\omega R \, C_p^\varepsilon}. \tag{20}$$

The global electromechanical equation of motion that coupling the beam with the piezo shunt in the spectral domain is expressed by

$$\mathbf{S}(\omega)\mathbf{x} - \mathbf{S}_{sh}(\omega)\mathbf{v}(\omega) = \mathbf{f} \tag{21}$$

$$i\omega\mathbf{S}_{sh}(\omega)\mathbf{x} + i\omega C_p^\varepsilon \mathbf{v}(\omega) = \mathbf{i}(\omega). \tag{22}$$

where $\mathbf{x}$ is the generalized nodal displacement, $\mathbf{f}$ the generalized force, $\mathbf{i}$ is the current in the spectral domain,and $\mathbf{v}$ the voltage. By condensing Eqs. 21 and 22 we have the generalized spectral equation expressed by

$$\left[\mathbf{S}(\omega) + \omega^2 \mathbf{S}_{sh}^2(\omega)\left(\frac{1}{i\omega + Z_{el}^{-1}}\right)\right]\mathbf{x} = \mathbf{f}. \tag{23}$$

By considering these elements involved the impedance relations, we can express the shunted part $[\mathbf{Z}(\omega)]$ in a matrix form as,

$$\mathbf{Z}(\omega) = \begin{bmatrix} N_{e1} & N_{e1} & N_{e1} & N_{e1} & N_{e1} & N_{e1} \\ 0 & 0 & 0 & 0 & 0 & 0 \\ M_{e1} & M_{e1} & M_{e1} & M_{e1} & M_{e1} & M_{e1} \\ -N_{e2} & -N_{e2} & -N_{e2} & -N_{e2} & -N_{e2} & -N_{e2} \\ 0 & 0 & 0 & 0 & 0 & 0 \\ M_{e2} & M_{e2} & M_{e2} & M_{e2} & M_{e2} & M_{e2} \end{bmatrix}. \tag{24}$$

where

$$N_{e1} = N_{e2} = \frac{Z_t^2 i\omega Z_{ef} b d_{31} E_p}{1 + i\omega C_p^\varepsilon Z_{ef}}, \qquad M_{e1} = M_{e2} = \frac{Z_t^2 i\omega Z_{ef} h b d_{31} E_p}{2 + 2i\omega C_p^\varepsilon Z_{ef}}.$$

3. Numerical analysis

The numerical simulation analyse the dynamic response and flexural wave propagation of a simple beam, a beam coupled with the piezo, and the beam coupled with the piezo shunt. The material and geometrical properties for the beam are Young's modulus 71.0 GPa, density of 2700 kg/m^3, width of 12.7 mm, and thickness of 2.86 mm. The piezo material and geometrical properties are Young's modulus of 64.9 GPa, density of 7600 kg/m^3, width of 12.7 mm, and thickness of 0.762 mm, piezoelectric constant $d_{31} = -172$ m/V $\times$ 10^{-12}, dielectric constant of $\beta_{33}^S = -5.6788$ m/V $\times$ 10^{-12}, elastic stiffness of $C_{11}^D = 74.0$ GPa.

Tuning frequency [Hz]	Resistor [\Omega]	Capacitance [nF]
556	$Z_1 = 780, Z_2 = 680, Z_3 = 120, Z_5 = 2594$	$Z_4 = 100$
1101	$Z_1 = 2500, Z_2 = 680, Z_3 = 120, Z_5 = 2594$	$Z_4 = 100$
1831	$Z_1 = 4380, Z_2 = 1680, Z_3 = 500, Z_5 = 2594$	$Z_4 = 100$

Table 1. Setting of electrical components of the shunted electric circuit.

The total length of both is $L = 0.25$ m. The circuit shunt, fig. 2(b), design to the resonant tuning frequencies of 556 Hz, 1101 Hz, and 1831 Hz is displayed in Table 3.

This association of inductors, capacitors, and other influencers can promote an impedance resonance at a frequency necessary to influence the desired structure. However, high-amplitude resonances, which are limited to a small frequency range, rely exclusively on high values of R to increase bandwidth, but reduce the overall efficiency of the electromechanical energy conversion, and hence the mechanism of attenuation. Fig. 3 shows the impedance resonance, vibrating at the designed resonant circuit shunt.

| (a) | (b) | (c) |
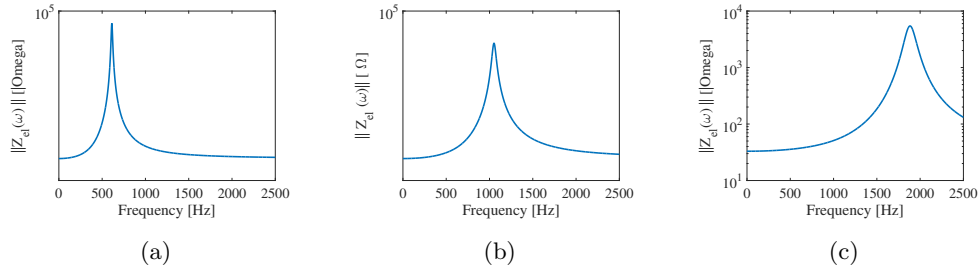
Figure 3. Electrical impedance (Z_{el}) of the resonant circuit tuned to vibrating at a) 556 Hz; b)1101 Hz; and c)1831 Hz.

Fig. 4 (a-c) shows the comparison among the single beam (yellow line), coupled beam-piezo (blue line), and coupled beam-piezo-shunt (orange line) tuned at 556, 1101, and 1831 Hz. It is assumed a clamped boundary condition. The coupled beam presented a shift in relation to the simple beam because of the piezo mass and stiffness. In each tunning shunt, resonance happened a resonance attenuation that demonstrates the efficient of the piezo shunt to vibration control.

Fig. 5 presents the real part of wavenumber related to the positive going flexural wavenumber. This is obtained from a single SE, assuming it is a periodic unit cell, rewriting the dynamic stiffness as a transfer matrix under the Bloch-Floquet framework. They clearly show a locally resonant behaviour around the shunt tuning frequencies 556 Hz, 1101 Hz and
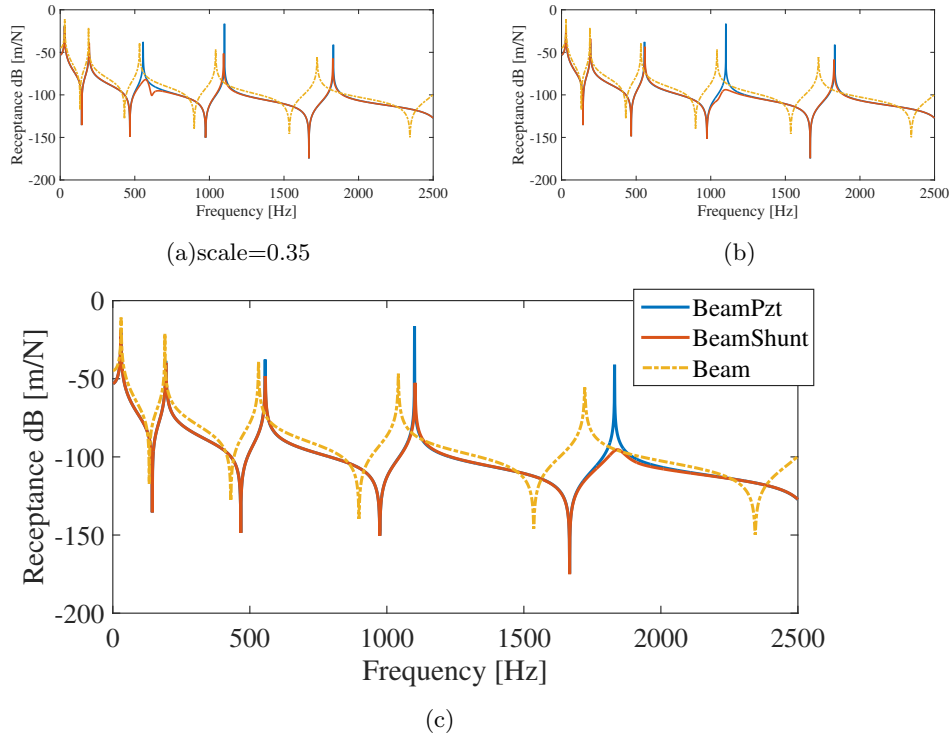
Figure 4. FRFs comparison among single beam (yellow line), coupled beam-piezo (blue line), and coupled beam-piezo-shunt (orange line) tuned at a) 556 Hz; b)1101 Hz; and c)1831 Hz.

1831 Hz, similarly to the dispersion curves shown by Airoldi and Ruzzene [1]. The longitudinal modes, not presented here, show a similar behaviour for each respective shunt tuning frequency.

4. Comments and final remarks

This paper presents a dynamic analysis of a beam system with a piezo coupling and a shunt configuration. The effects that geometric coupling includes oscillation in the through FRFs, which show that the resonance peaks have changed with the associated frequencies. The impact of coupling the beam with piezo shunted demonstrated by FRF comparisons present an attenuated at 556, 1101, and 1831 Hz, same of the shunt impedance resonance. The flexural wavenumber follows some attenuation as the FRFs. Thus, the piezoelectric association with the shunt configuration in the structure can result in vibration attenuation either at the FRF and wavenumber.
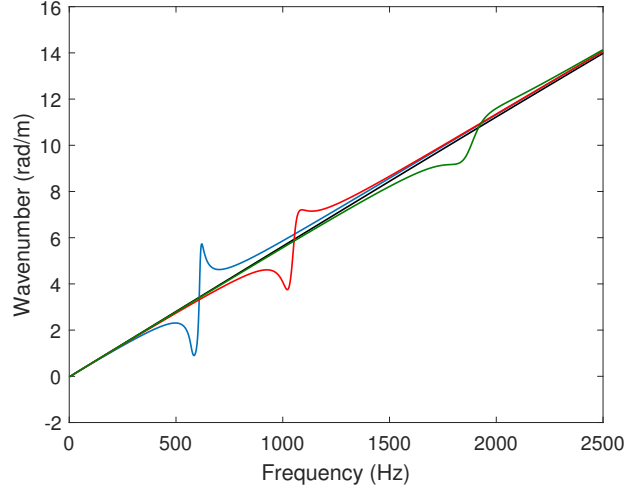
Figure 5. Real part of the bending wavenumber for the coupled beam-piezo (black line), coupled beam-piezo-shunt tuned at 556 Hz (blue line), b) 1101 Hz (red line) and c) 1831 Hz (green line).

Acknowledgments

References

[1] AIROLDI, L., AND RUZZENE, M. Design of tunable acoustic metamaterials through periodic arrays of resonant shunted piezos. *New Journal of Physics 13* (2011), Art. no. 113010.

[2] CASADEI, F., RUZZENE, M., DOZIO, L., AND CUNEFARE, K. A. Broadband vi- bration control through periodic arrays of resonant shunts: Experimental investigation on plates. *Smart Material and Structure 19* (2010), Art. no. 015002.

[3] DOSCH, J. J., INMAN, D. J., AND GARCIA, E. A self-sensing piezoelectric actuator for collocated control. *Journal of Intelligent Material Systems and Structures 3* (1992), 166–185.

[4] DOYLE, J. F. *Wave propagation in structures : spectral analysis using fast discrete Fourier transforms*, second ed. Mechanical engineering. Springer-Verlag New York, Inc., New York, 1997.

[5] EL-NAGGAR, S. Dependency of the photonic band gaps in two-dimensional metallic photonic crystals on the shapes and orientations of rods. *Optical Engineering 51*, 1 (2012), 68001–68008.

[6] GOPALAKRISHNAN, S. *Wave propagation in materials and structures.* CRC Press, 2016.

[7] GRIPP, J. A. B., AND RADE, D. A. Vibration and noise control using shunted piezo-electric transducers: A review shunt circuit flexible structure. *Mechanical Systems and Signal Processing 112* (2018), 359–383.

[8] HAGOOD, N. W., AND VON FLOTOW, A. Damping of structural vibrations with piezo-electric materials and passive electrical networks. *Journal of Sound and Vibration 146*, 2 (1991), 242–268.

[9] HALIM, D., AND MOHEIMANI, S. O. Experimental implementation of spa- tial h- control on a piezoelectric-laminate beam. *IEEE/ASME Trans. Mechatronics 9(1)* (2002), 346–356.

[10] KUSHWAHA, M., HALEVI, P., AND MARTÍNEZ, G. Theory of acoustic band structure of periodic elastic composites. *Physical Review B 49*, 1 (1994), 2313–2322.

[11] LAUDE, V., ACHAOUI, Y., BENCHABANE, S., AND KHELIF, A. Evanescent bloch waves and the complex band structure of phononic crystals. *Physical Review B 80(092301)*, 1 (2009), 1–4.

[12] LEE, U. *Spectral Element Method in Structural Dynamics.* BInha University Press, 2004.

[13] MACHADO, M., ADHIKARI, S., AND SANTOS, J. A spectral approach for damage quan- tification in stochastic dynamic systems. *Mechanical Systems and Signal Processing 88* (2017), 253–273.

[14] MACHADO, M., ADHIKARI, S., AND SANTOS, J. D. Spectral element-based method for a one-dimensional damaged structure with distributed random properties. *Journal of Brazilian Society of Mechanical Sciences and Engineering 40* (2018), 214–226.

[15] MACHADO, M., KHALIJ, L., AND FABRO, A. Dynamic analysis of a composite struc- ture under random excitation based on the spectral element. *International Journal of Nonlinear Sciences and Numerical Simulation 1* (2019), 1–12.

[16] MACHADO, M. R., APPERT, A., AND KHALIJ, L. Spectral formulated modelling of an electrodynamic shaker. *Mechanics Research Communications 97* (2019), 70–78.

[17] MOHEIMANI, S. O., FLEMING, A. J., AND BEHRENS, S. Dynamics, stability, and control of multivariable piezoelectric shunts. *IEEE/ASME Trans. Mechatronics 9(1)* (2004), 87–99.

[18] Park, H. W., Kim, E. J., Lim, K. L., and Sohn, H. Spectral element formulation for dynamic analysis of a coupled piezoelectric wafer and beam system. *Computers and Structures 88(9-10)* (2010), 567–580.

[19] Sigalas, M., and Economou, E. Elastic and acoustic wave band structure. *Journal of Sound and Vibration 158*, 1 (1992), 377–382.

[20] Sugino, C., Ruzzene, M., and Erturk, A. Design and analysis of piezoelectric metamaterial beams with synthetic impedance shunt circuits. *EEE/ASME Transactions on Mechatronics 23(5)* (2018), 2144–2155.

[21] U., L., and J., K. Dynamics of elastic-piezoelectric two-layer beams using spectral element method. *International Journal of Solids and Structures 37* (2000), 4403–4417.

[22] U., L., and J., K. Spectral element modeling for the beams treated with active constrained layer damping. *International Journal of Solids and Structures 38* (2001), 5679–5702.

[23] Yi, K., Collet, M., Ichchou, M., and Li, L. Flexural waves focusing through shunted piezoelectric patches. *Smart Materials and Structures 25(7)* (2010), 567–580.

[24] Zheludev, N., and Kivshar, Y. From metamaterials to metadevices. *Nature Material 11* (2012), 917–924.

[25] Zhou, W., Wu, Y., and Zuo, L. Vibration and wave propagation attenuation for metamaterials by periodic piezoelectric arrays with high-order resonant circuit shunts. *Smart Materials and Structures 24(6)* (2015), Art. no.065021.

Marcela Rodrigues Machado, Ph.D.: University of Brasilia/Department of Mechanical Engineering/Group of Dynamic Systems, UnB-Campus Universitário Darcy Ribeiro-ENM-Bloco G. CEP:70910-900- Asa Norte - Brasília-DF-Brazil (*mromarcela@gmail.com*). The author gave a presentation of this paper during one of the conference sessions.

Adriano Todorovic Fabro, Ph.D.: University of Brasilia/Department of Mechanical Engineering/Group of Dynamic Systems, UnB-Campus Universitário Darcy Ribeiro-ENM-Bloco G. CEP:70910-900- Asa Norte - Brasília-DF-Brazil (*fabro@unb.br*).

Braion Barbosa de Moura, M.Sc. student: University of Brasilia/Department of Mechanical Engineering/Group of Dynamic Systems, UnB-Campus Universitário Darcy Ribeiro-ENM-Bloco G. CEP:70910-900- Asa Norte - Brasília-DF-Brazil (*braionmoura@hotmail.com*).

Bond Graph Modeling and Simulation of Left Ventricle of Human Heart

Mohit Makkar, Saransh Jain

Abstract:

To ensure proper functioning of the left ventricle of Human Heart, it is very important to know about its functioning in detail and how other muscles of heart are affecting it. Bond graphs are ideally suited to the modeling of non-linear, multi-energy systems. Biophysical and physiological systems like left ventricle belong to this category. The bond graph model for the anatomy of blood around the left ventricle is studied in detail and using this model, suitable results were obtained for different cases like varying afterload conditions. Various parameter and variables were analzed with respect to the volume of blood in left ventricle and pressure inside it. The results obtained are clearly depicting the mechanism of the left ventricle and looked very promising. A careful study about the constant values has really made the results equivalent to actual results. The model has therefore cast a significant influence over the prediction of performance of left ventricle.

1. Introduction

Heart is the most vital organ of the human body. Every part of the human body is connected to heart for its functioning and energy needs. The function of heart is to supply oxygen and important nutrients to different parts of the body through blood. The left ventricle is one of four chambers (two atria and two ventricles) in the human heart. It receives oxygenated blood from the left atrium via the mitral valve, and pumps it into the aorta via the aortic valve. Starting from the mechanisms of contraction in the cardiac muscle at the contractile proteins level from the microscopic level up to the muscular and ventricular level and finally reach the hemodynamic part of the left ventricle and its arterial load, the left ventricle involves multi physics and multi domains. To ensure proper functioning of the left ventricle, it is very important to know about its functioning in detail and how other muscles of heart are affecting it. The idea of presenting a feasible and easy model representing most of the mechanisms was a challenging task.

Bond Graph modeling has a natural place in these developments. Bond graphs (BGs) are ideally suited to the modeling of nonlinear, multi-energy systems. Thus, their is huge expectation to use BGs in this domain as such physiological systems are always nonlinear and

multi- energy systems[3]. BGs may in many cases provide more intuitive solutions than other methods of graphical modeling.

Researchers like [12] presented design of a linear passive model of the human systemic arterial tree. [9] analyzed the time-varying ratio of instantaneous pressure, *P(t)*, to instantaneous volume, *V(t)*, in the canine left ventricle. [8] presented a study on a supported heart preparation indicating that the thesis on *E(t)* is also valid for different physiological conditions. [10] worked on Pressure-volume relationship of the left ventricle of the dog. They found consistently that as long as the contractile state was stable, the end-diastolic pressure-volume relationship curve is largely independent of the loading conditions and mode of contraction. [6] explained mechanisms related to the pattern of vascular impedance in human systemic arteries. Increasing aortic pressure/volume relationships were expressed as input impedance. [7] explained the use of the pressure-volume diagram in evaluating cardiac performance.

Most of the work on modeling and simulation of left ventricle relates to accurate measurement of pressure and volume of blood at anytime during a heartbeat. To take into account the mechanical, chemical, hydraulic and electrical phenomena, the bond graph approach seems to be a relevant alternative. Upcoming sections will describe the modeling phenomena taking care that every single mechanism being discussed in detail.

2. MODEL OF THE LEFT VENTRICLE

The function of left ventricle can broadly divided into four stages. The four stage development of the model is as follows:

2.1. Modeling of the Cross Bridges

A sacromere is the basic unit of heart muscle. They appear as dark and light bands. Sacromeres are composed of two long fibrous proteins myosin and actin. Myosin has a long, fibrous tail and a globular head, which binds to actin. The actin-myosin attached together is called a cross bridge [2]. The attached cross bridges act as spring. The stored energy of these springs is supplied to the muscles and the force produced in the muscle is called muscle force. This stored energy will be represented by a C-element in the bond graph. [4]. The bond graph model for this chemical cross bridge cycle is shown in Fig.1. The general equation for C1 and C2 will be:

Figure 1. Bond graph model of chemical cycle

$$e = f(q). \tag{1}$$

Here, R represents the reaction mechanism. X_A is the ratio of attached cross bridges and X_D is the ratio of detached cross bridges. If all the cross bridges are attached the value of X_A will be 1 and value of X_D will be 0 or if all the bridges are detached then value of X_A will be 0 and of X_D will be 1. The speed of attached and detached cross bridges has rate constants X_a and X_d respectively. The two C-elements are for $X_A(q)$ and $X_D(q)$. For $C1$, the flow is the rate of change of detached cross bridges $\frac{dX_D}{dt}$ and effort (e) is the chemical potential of detached cross bridges (μ_D). For $C2$, the flow is the rate of change of attached cross bridges $\frac{dX_A}{dt}$ And effort (e) is the chemical potential of attached cross bridges (μ_A).). From Nernst formula [11]:

$$\frac{dX_D}{dt} = K_d(t)X_A(t)^\beta - K_a(t)X_D(t), \tag{2}$$

$$\mu_D = A_D + B_D Tln(X_D). \tag{3}$$

A_D and $B_D$re constant with time(t) and B_D is a function of temperature (T).

$$\frac{dX_A}{dt} = K_A(t)X_D(t)^\beta - K_d(t)X_A(t), \tag{4}$$

$$\mu_A = A_A + B_A Tln(X_A). \tag{5}$$

At any point of time $X_A + X_D = 1$ and $-\frac{dX_D}{dt} = \frac{dX_A}{dt}$ A_a and B_a are constant with time *(t)* and B_a is a function of temperature (T). The states *(q)* of the two C-elements are X_A and X_D respectively for *C1* and *C2* β in equation 2 is the order of the forward reaction accounting for the speed of the reaction. For each beat time (t),K_a and K_d are as follows: if $t >= 0$ and $t <= t_{amax}$ then:

$$F1 = 1 + \alpha(l_m - 1), \tag{6}$$

$K_{amax} = K_{amaxn}$ and

$$K_a(t) = F1(K_{amax} * sin(\pi\frac{t}{t_{amax}}))^{\alpha_1}, \tag{7}$$

Else: $K_a(t) = K_{amin}$. And if $t >= t_{dmax}$ and $t <= t_{count}$ then:

$$K_{d1}(t) = (K_{dmax} * sin(\pi\frac{t - t_{dmax}}{t_{cont} - t_{dmax}}))^{\alpha_2}. \tag{8}$$

Else:

$$K_{d1}(t) = K_{dmin}. \tag{9}$$

$$fi = \frac{(X_a - 10^{-6})^3}{10^{-5} + (X_a - 10^{-6})^3},$$ (10)

$K_d = K_{d1} * fi.$

t_{amax} and t_{dmax} are the attachment and detachment times of the cross bridges. t_{cont} is the time of contraction and α_1, α_2 are the partial orders of reaction. All these values are kept constant. Fi and $F1$ are the correcting coefficients, l_m is the length of muscle.

2.2. Chemo-Mechanical Transaction Model

The muscle fibres in the left ventricle contribute to the muscle force but here it was assumed that mechanical energy of muscle is coming from an equivalent muscle with an equivalent length L_m. The transaction here is shown by a new element called 2PC [1], the two port capacitor which is responsible for the representation of two-port node in bond graphs. For the ventricle side, the 2PC will provide an elastic potential energy and will behave like a variable spring (dynamic compliance). On the other side, it will receive and store a concentration of attached acto-myosin cross bridges from the chemical cycle. The representation of the 2PC in bond graph is shown in Fig.2:- The direction of half arrows is pointed towards the 2PC
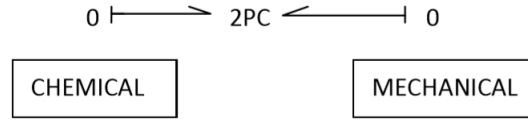
Figure 2. Bond graph model of chemo-mechanical transduction

showing that in this direction of energy, the C-element is storing energy and in opposite direction it will be giving its energy [4]. The general equation of such element in nonlinear conditions [7] is:

$$\frac{e1}{e2} = \frac{f1(q1, q2)}{f2(q1, q2)}.$$

On chemical side the effort ($e1$) of the 2PC model will be chemical potential(μ_A):

$$\mu = (A_a + B_b(T)ln(X_A))\beta(L_m),$$ (11)

and the flow will be $\frac{dX_A}{dt}$:

$$\frac{dX_A}{dt} = K_a(t)X_D(t) - K_d(t)X_A(t)^\beta.$$ (12)

The state q1 is X_A itself. On mechanical side the effort ($e2$) will be muscle force (F_m):

$$F_m = E_x(X_A)E_a'(l_m) + (1 - E_x(X_A)E_r'(L_m)).$$ (13)

The flow is rate of change of length of muscle $\frac{dL_m}{dt}$, and State (q2) of the element will be length of muscle (L_m). The general form for the energy of muscle will be:

$$E_m = E_m(l_m, X_A) \tag{14}$$

Power(P):

$$\begin{aligned}
P &= \frac{dE_m}{dt} \\
&= \frac{\partial E_m}{\partial l_m}\frac{\partial l_m}{\partial t} + \frac{\partial E_m}{\partial X_A}\frac{\partial X_A}{\partial t} \\
&= f_m v_m + \mu_A \dot{X}_A.
\end{aligned} \tag{15}$$

From the Maxwell equation, we can get

$$\frac{\partial f_m}{\partial X_a} = \frac{\partial \mu_a}{\partial l_m}. \tag{16}$$

From the above two equations this can be reckoned that

$$f_m = \frac{\partial E_m}{\partial l_m}, \tag{17}$$

and

$$\mu_A = \frac{\partial E_m}{\partial X_A}. \tag{18}$$

From the experiments [4], muscle force found to be:

$$f_m = E_x\left(X_A\right)E_a'\left(l_m\right) + \left(1 - E_x\left(X_A\right)E_r'\left(l_m\right)\right), \tag{19}$$

where E_x is the active state function of X_A, E_a' and E_r' are the active and passive force-length curves measured experimentally. Integrating the muscle force with respect to length of muscle will give the energy equation:

$$E_m = E_x\left(X_A\right)E_a\left(l_m\right) + \left(1 - E_x\left(X_A\right)E_r(l_m\right), \tag{20}$$

$$E_a'\left(l_m\right) = \frac{dE_a(l_m)}{dl_m}, \tag{21}$$

$$E_r'\left(l_m\right) = \frac{dE_r(l_m)}{dl_m}. \tag{22}$$

Now we know that:

$$\begin{aligned}
\mu_A &= \frac{\partial E_m}{\partial X_A} \\
&= E_X'(E_a\left(l_m\right) - E_r\left(l_m\right)).
\end{aligned} \tag{23}$$

On comparing the two equations for μ_A we get:

$$E'_X = A_a + B_a\left(T\right)\ln\left(X_A\right). \tag{24}$$

On integration:

$$E_x = A_a X_A + B_a\left(T\right)X_A(\ln\left(X_A\right)-1), \tag{25}$$

and

$$\beta = E_a\left(l_m\right) - E_r\left(l_m\right). \tag{26}$$

The reaction order β is thus length-dependent and expressing the reverse Maxwell coupling [5]:

$$\beta = \left(e_a - e_r\right)\left[\left(\frac{l_m{}^5}{5} - l_m{}^4\right)l_o + 2l_m{}^3 l_o{}^2 - 2l_m{}^2 * l_0{}^3 + l_m l_0{}^4\right]. \tag{27}$$

From the experimental data [8], the following functions have been chosen for $E'_a(L_m)$ and $E'_r(L_m)$:

$$E'_a\left(l_m\right) = e_a\left(l_m - l_o\right)^4 \; and \tag{28}$$

$$E'_r\left(l_m\right) = e_r\left(l_m - l_o\right)^4. \tag{29}$$

Here e_a, e_r and L_o are constants.

2.3. Mechano-Hydraulic Transduction Model

This model describes how the mechanical energy of left ventricle wall is transformed into hydraulic energy. Here, ventricular wall is thus acting as a pure transducer i.e. a device transducing pressure and flow. The transduction of mechanical energy in to hydraulic energy can be seen in Fig3. The constitutive relations for this TF-element are:
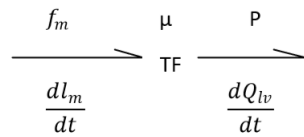
Figure 3. Bond graph of Mechano-Hydraulic stage

$$\frac{dQ_{lv}}{dt} = \mu\frac{dl_m}{dt}. \tag{30}$$

Also,

$$f_m = \mu P_{lv}/N. \tag{31}$$

2.4. Modeling of Hemodynamics

In bond graph, the pulmonary pressure is regarded as a constant pressure and represented by source of effort(S_e) element. Mitral valve and aortic valve are resistance (R) element with variable resistance. For both valves if $\Delta P > 0$, then R will be very small(R_{pass}) to let the fluid pass else R will be that high (R_{blo})) that it will completely chokes the blood flow. Capacity of left ventricle will be represented by a C element. The bond graph of the hemodynamic mechanism is show in Fig.4: C afterload (C_{al}) and R afterload(R_{al}) are
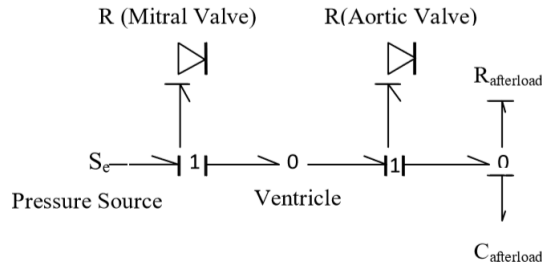
Figure 4. 5.Bond graph model of hemodynamics

accounting for storage and losses respectively when the blood is pumped to the aorta.

2.5. Bond Graph Model of Complete System

Combining the bond graph models of hemodynamic and the ventricle capacitance, the causalled and numbered bond graph of the complete system with two information bonds will be as shown in Fig.5. Bond 19 is to take out some flow from the ventricle in case to evade the extra volume in high throughput experiments. After derivation of equation from the BG, the Pressure in left ventricle (P_{lv}) will be:

$$P_{lv} = \frac{N\,(l_m - l_o)^4}{nAl_m^{n-1}} \left\{ e_a(A_a X_A + B_a\,(T)\,X_A(\ln\,(X_A) - 1)) \right. \tag{32}$$
$$\left. + e_r(1 - (A_a X_A + B_a\,(T)\,X_A(\ln\,(X_A) - 1)))\right\}$$

Rate of change of volume ($\frac{dQ_{lv}}{dt}$) of left ventricle will be:

$$\frac{dQ_{lv}}{dt} = \left(\frac{SE - P_{lv}}{R_{mv}}\right) - \left(\frac{P_{lv} - C_{al}}{R_{av}}\right) - CFP * \left(\frac{SE - P_{lv}}{R_{mv}}\right). \tag{33}$$

Rate of change of attached cross bridges ($\frac{dX_A}{dt}$) will be:

$$\frac{dX_A}{dt} = K_a\,(t)\,X_D\,(t) - K_{d1}\,(t)\,X_A(t)^\beta. \tag{34}$$
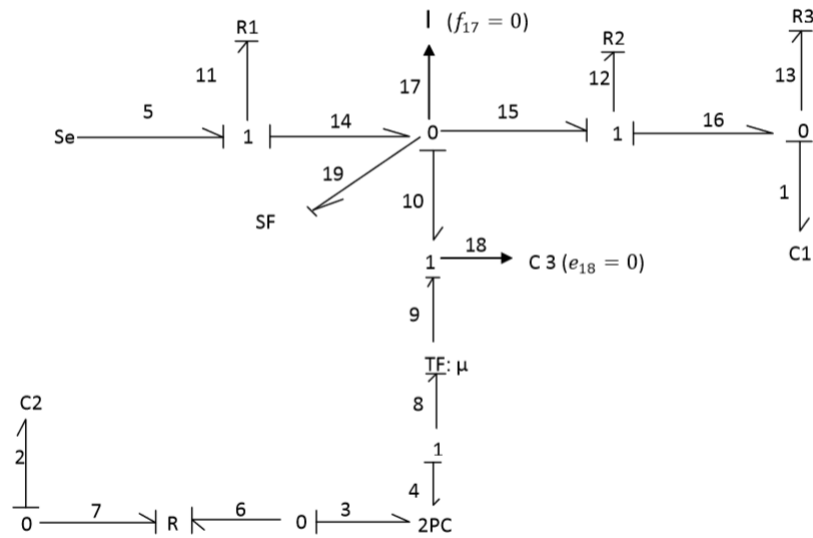
Figure 5. Causalled and numbered bond graph for equation derivation

Rate of change of detached cross bridges ($\frac{dX_D}{dt}$) will be:

$$\left(\frac{dX_D}{dt}\right) = K_{d1}(t)X_A(t)^\beta - K_a(t)X_D(t). \tag{35}$$

Rate of change of aortic volume ($\frac{dQ_{aor}}{dt}$) will be:

$$\frac{dQ_{aor}}{dt} = \left(\frac{P_{lv} - C_{al}Q_{aor}}{R_{av}}\right) - \left(\frac{C_{al}Q_{aor}}{R_{al}}\right). \tag{36}$$

Rate of change of length of muscle ($\frac{dL_m}{dt}$) will be:

$$\frac{dl_m}{dt} = \frac{1}{nAl_m^{n-1}}\left\{\left(\frac{SE - P_{lv}}{R_{mv}}\right) - \left(\frac{P_{lv} - C_{al}}{R_{av}}\right) - CFP*\left(\frac{SE - P_{lv}}{R_{mv}}\right)\right\}. \tag{37}$$

3. RESULTS AND DISCUSSION

The differential equations depicting rate of change of Volume, Pressure, Muscle length etc. were derived from Bond Graph Model and solved using MATLAB.Limited results are shown here for analysis. At t = 0, the value of pressure depends on the initial conditions of ventricular volume, length of muscle and other variables. After the completion of one beat time, it is at the stage of starting of systole. At t = 1 sec, the isovolumic compression will start, hence very steep rise in the left ventricle pressure as shown in Fig.6. Once the
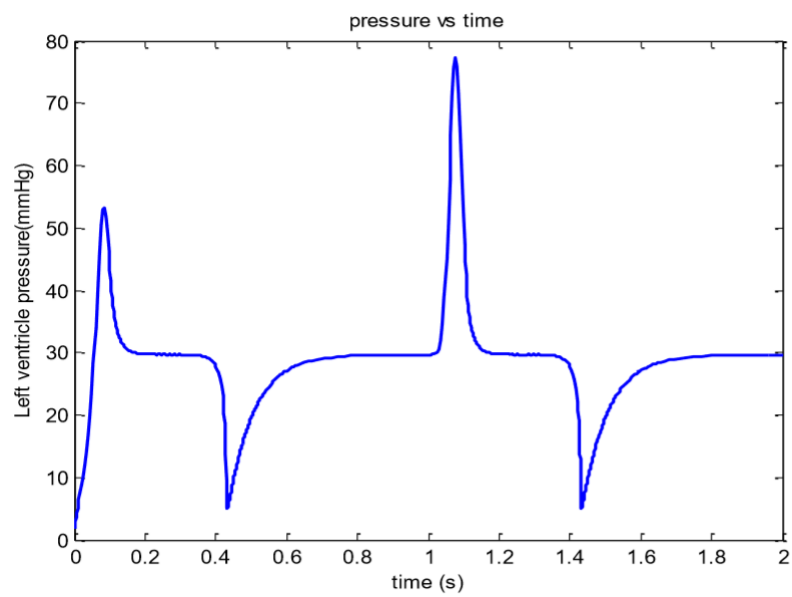
Figure 6. Pressure-time loop of left ventricle
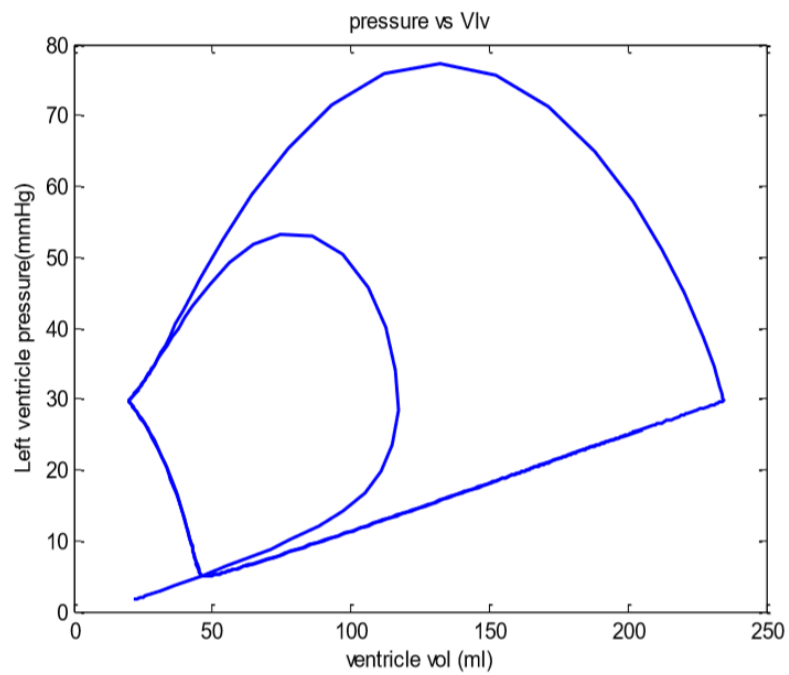
Figure 7. Pressure- Volume curve
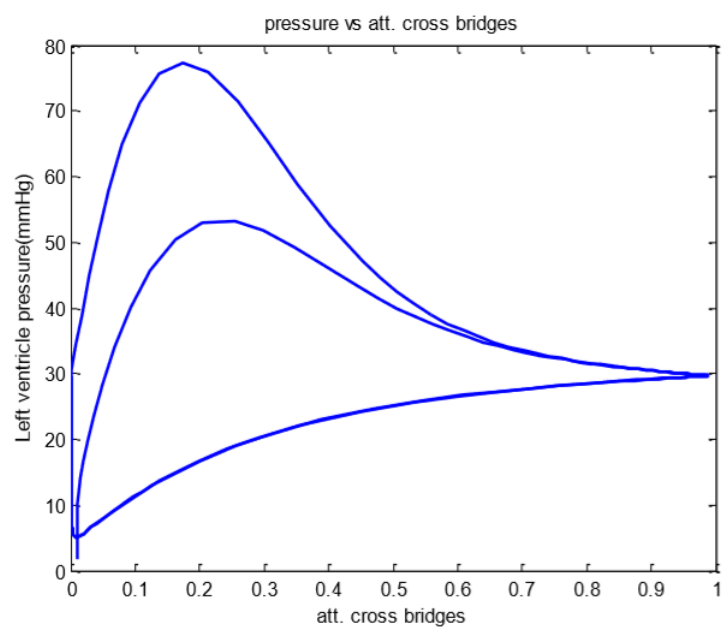
Figure 8. Pressure-Attached Cross bridges cycle
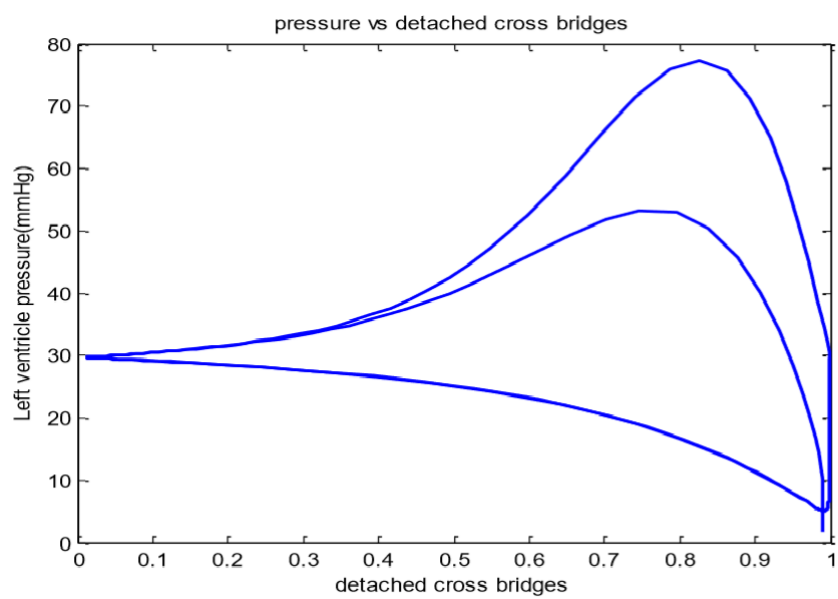
Figure 9. Pressure-detached cross bridges curve
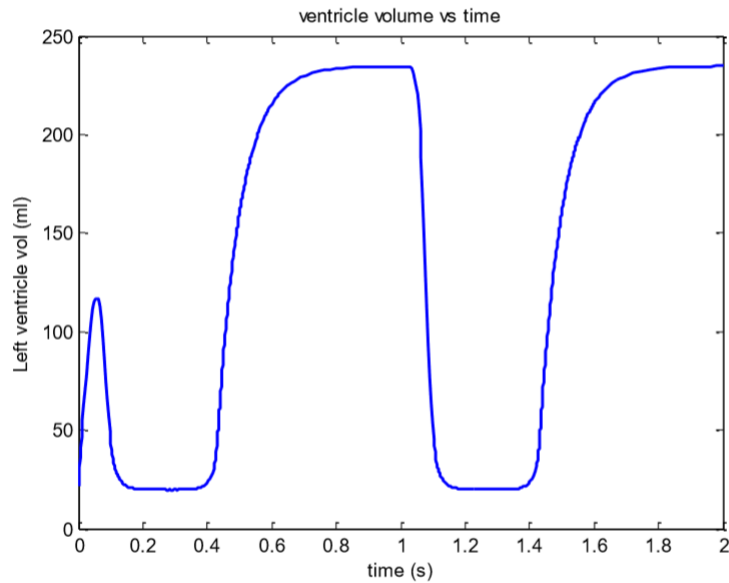
Figure 10. Volume-time curve

mitral valve opens due to pressure difference, the ventricle starts filling physiologically. The Pressure-Volume curve is depicting this phenomena in Fig.7.

In Fig.8, the pressure starts to build up because the valves are closed at this point of time. The aortic valve opens but the attachment reaction is continued. Ventricle contracts to its maximum but does not affect the reduction in pressure.

As reckoned, the pressure-detached cross bridges curve must be the mirror image of the pressure-attached cross bridges curve. Fig.9 and

Length of muscle is directly proportional to volume of ventricle. The length of muscle keeps on increasing in corresponding time of every beat and this is also the same case in volume, So this phenomena is shown in volume-time curve in Fig10. As length of muscle and volume of ventricle are directly proportional to each other hence Fig 11 should be no more than overlapping lines for every beat.

When the attached cross bridges are at 0 after the initial beat, the volume rise in systole and also attached cross bridges raise to 1, just in the case of length of muscle and attached cross bridges. Then detaching starts but this process should be isovolumic hence the curve should be horizontal until the opening of mitral valve till X_a again reaches to 0 but this is slightly tilted upwards due to the impact of non consumption of the full flow and impact of previous beats leads to slight rise in the volume as shown in Fig. 12.
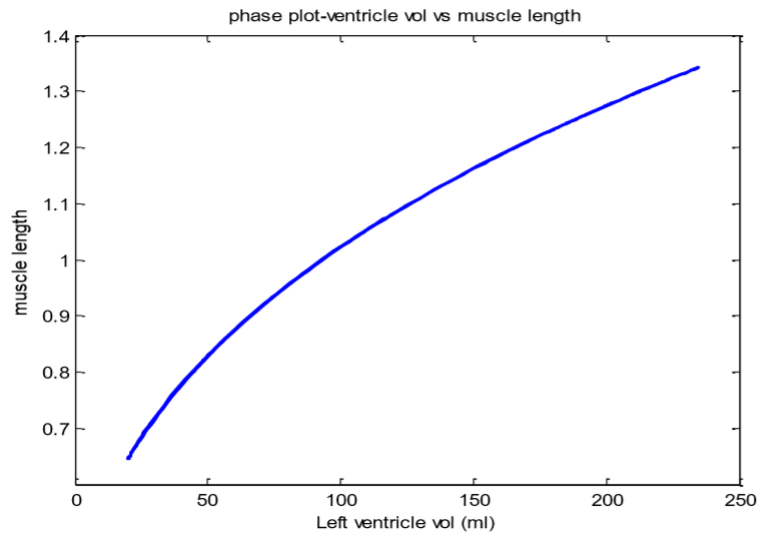
Figure 11. Volume-length of muscle curve.
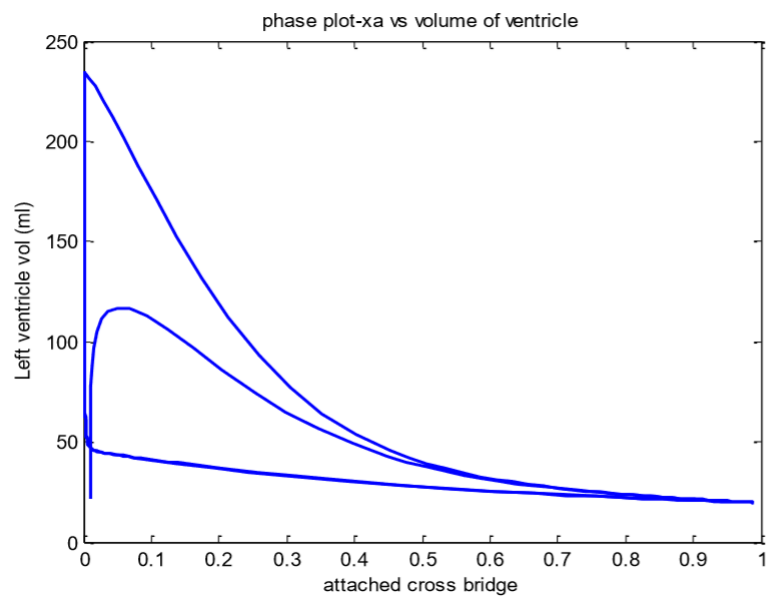
Figure 12. Volume-attached cross bridges curve

3.1. CASE 2- When after load conditions are being altered

In this section the aortic pressure in being altered by altering the values of C and R. If afterload is increased by increasing aortic pressure, and if the preload and entropy are held constant, this will result in a smaller stroke volume and an increase in end-systolic volume. If afterload is reduced by decreasing aortic pressure, the opposite occurs - stroke volume and ejection fraction increase, and endsystolic volume decreases. The value of $C_{afterload}$ and $R_{afterload}$ are both raised and lowered from the given standard value. The higher values of afterload conditions gave the same pattern but magnitude of pressure and volume are changing. The reason for this is that both C and R elements are used for storing and consuming the flow respectively. The similar results were obtained for different afterload conditions. Even the volume of ventricle is also not influenced by the afterload conditions because once the flow is passed to the aorta, it should not come back in to the ventricle and should have been consumed in the given time till next ejection.

4. Conclusion

The required goal was to be able to adapt approaches of lumped parameter and to avoid the use of the partial models with derivative or finite elements. This model illustrates well the advantage of the bond graphs with respect to other modeling techniques. Bond graph allows a simpler comprehension of the studied system and it can develop the coherency among several structural levels. the most important points emerging from the work are: 1. The natural representation of the results of the interactions between the geometrical shapes of the ventricle muscle with other factors. 2. The point of maximum pressure rise is isovolumic as is clear from the simulation that maximum ones of pressure are always reached at the same moment of each cycle for any initial condition.

The structure of this model is coherent with the observations. The model presented in this paper is able to reproduce the effects of apparent resistance and deactivation during the experiments of high flow.

References

[1] DRZEWIECKI, G. M., LI, J. K., AND LI, J. K. *Analysis and assessment of cardiovascular function: with 106 figures.* Springer Science & Business Media, 1998.

[2] HUXLEY, A. F. Muscle structure and theories of contraction. *Prog. Biophys. Biophys. Chem 7* (1957), 255–318.

[3] LEFÈVRE, J., LEFÈVRE, L., AND COUTEIRO, B. A bond graph model of chemo-

mechanical transduction in the mammalian left ventricle. *Simulation Practice and Theory 7*, 5-6 (1999), 531–552.

[4] LeFèvre, J., Lefèvre, L., and Couteiro, B. A bond graph model of chemo-mechanical transduction in the mammalian left ventricle. *Simulation Practice and Theory 7*, 5-6 (1999), 531–552.

[5] LeFèvre, L., LeFèvre, J., and Barreto, J. Introduction of functional and higher-order elements in bond graphs. *SIMULATION SERIES 27* (1994), 29–29.

[6] O'rourke, M. F., and Avolio, A. P. Pulsatile flow and pressure in human systemic arteries. studies in man and in a multibranched model of the human systemic arterial tree. *Circulation Research 46*, 3 (1980), 363–372.

[7] Sagawa, K. Cardiovascular interaction. *Cardiac contraction and the pressure-volume relationship* (1988).

[8] Suga, H., and Sagawa, K. Instantaneous pressure-volume relationships and their ratio in the excised, supported canine left ventricle. *Circulation research 35*, 1 (1974), 117–126.

[9] Suga, H., Sagawa, K., and Shoukas, A. A. Load independence of the instantaneous pressure-volume ratio of the canine left ventricle and effects of epinephrine and heart rate on the ratio. *Circulation research 32*, 3 (1973), 314–322.

[10] Suga, H., and Yamakoshi, K. Left ventricle as a compression pump. *European journal of cardiology 4* (1976), 97–103.

[11] Wahl, D. A short history of electrochemistry- part i. *Galvanotechnik 96*, 7 (2005), 1600–1610.

[12] Westerhof, N., Bosman, F., De Vries, C. J., and Noordergraaf, A. Analog studies of the human systemic arterial tree. *Journal of biomechanics 2*, 2 (1969), 121–143.

Mohit Makkar, Assistant Professor: Mechanical-Mechatronics Engineering Department, The LNM Institute of Information Technology, Jaipur. , Gram Rupa ki Nangal, Post-Sumel, Via-Jamdoli, Jaipur 302031- India (*mohit.makkar@lnmiit.ac.in*). .

Saransh Jain, UG Student: Mechanical-Mechatronics Engineering Department, The LNM Institute of Information Technology, Jaipur. , Gram Rupa ki Nangal, Post-Sumel, Via-Jamdoli, Jaipur 302031- India (*saransh.j1997@gmail.com*). The author gave a presentation of this paper during one of the conference sessions.

Dynamics assessment of mechanically induced solid phase transitions in shape memory alloys via nonlocal thermomechanical coupling

Adam Martowicz, Sławomir Kantor, Jan Pawlik, Jakub Bryła, Jakub Roemer

Abstract: The work deals with presentation of the properties and applications of the developed nonlocal model of shape memory alloys (SMA), which is dedicated for simulations of dynamic processes of mechanically induced solid phase transitions. To date, many various phenomenological, macroscopic, microscopic and the free energy based constitutive models have been proposed for SMA, however, none of them is able to reliable capture the complexity of SMA physical behavior in a comprehensive manner. The authors of the present work employ peridynamics to alternatively nonlocally formulate thermomechanical coupling in the modeled SMA, considering, therefore, its advantageous characteristics. Particularly, the phenomenon of superelasticity is investigated and the related phase transitions in SMA are studied. The elaborated peridynamic model of SMA is validated using the experimental data gathered with a fatigue testing machine and a high-speed infrared camera. With reference to the authors' recently published work, the newly proposed solution extends the functionalities of the former nonlocal SMA model, taking into account the influence of the temperature. As confirmed with the numerical results provided, the new capability allows for studying dynamic problems more conveniently, not being limited by the necessity of satisfying the condition of isothermal phase transition.

1. Introduction

Growing demands regarding functionality and effectiveness of various engineering solutions require applications of materials and structures which exhibit extraordinary properties. Shape memory alloys (SMA) stand for a such group of materials (known as *smart materials* or *intelligent materials*) [1]. The usable properties of SMA directly reflect the thermomechanical phenomena which can be experimentally observed when applying mechanical and thermal excitations. Reversible solid phase transitions in SMA enable their unique behavior. Specifically, the characteristics of SMA result from the *martensitic transition*, which indicates the two-way martensite–austenite phase transition. Consequently, the following effects occur in SMA: *one-way* and *two-way memory effects* as well as *superelasticity* (also referred to as *pseudoelasticity*). The above mentioned effects are of high practical importance, since SMA can both memorize one or two arbitrarily set geometric shapes and withstand extraordinary strains not allowed for other metallic materials, i.e., up to the level of 8% [2-5].

Complexity of the SMA behavior is a challenge when developing new computational tools, which are dedicated for description the properties of this type of smart materials. To date, many various phenomenological, macroscopic, microscopic and the free energy based constitutive models have been proposed for SMA, however, none of them is able to reliable capture the physic of SMA in a holistic manner [2,3,6,7].

Taking into account the promising capabilities of SMA, the authors of the present work continue their previous efforts made towards more physical modeling of SMA [3,8,9]. In particular, the work deals with presentation of the properties and applications of the developed nonlocal model, which is dedicated for simulations of dynamic processes of mechanically induced solid phase transitions. The newly proposed solution extends the functionalities of the former nonlocal SMA model, taking into account temperature and the respective thermomechanical coupling observed for the phenomena of superelasticity.

The overall motivation of the work is investigation on the application of SMA based components for passive control of dynamic properties of gas foil bearings (GFB) [10-12]. The inherent hysteretic properties of SMA allows for mechanical energy dissipation and, therefore, assures efficient reduction of mechanical vibrations. Consequently, to properly address the modelled issue, it is necessary for a model to handle both mechanical and thermal material properties, including the respective couplings between the operational parameters defined for the two mentioned above physical domains. It should be emphasized that thermal management is critical for correct operation of GFB. Hence, a reliable computational framework, which is intended for the studies on the GFB's properties, requires thermomechanical analysis to be taken into consideration. In particular, the authors take an advantage of the introduction of a nonlocal approach [13]. The peridynamics (PD) is proposed to model the phenomenon of superelasticity and the relevant martensite-austenite phase transitions in SMA [14]. By doing so, the introduced integral based formulation of PD allows for convenient handling various types of model nonlinearities including: material properties, geometry and boundary conditions. Nonlocal interactions, i.e., long-range interactions, which are considered in a numerical model, lead to its more physical responses, being less influenced by the structure of the model itself. Moreover, lack of spatial partial derivatives in the governing equation, amongst others, reduces numerical errors and aids to avoid ambiguities at the boundaries of various model domains.

The following sections of the work cover: presentation of the fundamental mathematical formulas describing the properties of SMA and PD (Sections 2 and 3, respectively), introduction to the proposed theory of nonlocal thermomechanical coupling dedicated for investigation of mechanically induced solid phase transitions in SMA (Section 4) as well as presentation of an exemplary outcome from the numerical simulation and experimental validation (Section 5). Final Section 6 summarizes the work and provides the authors' main conclusions.

2. Phase transitions in SMA – analytical description

Although the characteristic solid phase transitions in SMA primarily apply to nanoscale – where the geometric changes regarding crystal structure of the material occur – the respective projection of this physical nature of SMA is directly observed at macroscale, e.g., via the already mentioned ability to memorize geometric shapes. Fortunately, the behavior of SMA components can be modelled making use of macroscopic and phenomenological models.

Fig. 1 illustrates the phenomenon of superelasticity in SMA. This mechanically induced effect is addressed by the authors of the present work to introduce a nonlocal model of the thermomechanical coupling present in SMA. The reversible solid phase transitions, i.e., the change from austenite to the deformed version of martensite while the stress growth, and adequate reverse transition observed for the mechanical relaxation, can be achieved at a constant temperature. The kinetics of phase transition depends on the characteristics temperatures: A_s, A_f, M_s, M_f. These material properties respectively denote the temperatures at which the austenite ($A_\blacksquare$) and martensite ($M_\blacksquare$) phases start ($\blacksquare_s$) and finish ($\blacksquare_f$) developing. Change of the ambient temperature results in the shifts of the stresses at which respective forward or backward martensitic phase transitions occur (please see the four skewed solid lines in Fig. 1). Fig. 2 presents a hysteretic stress-strain relationship for an SMA material.
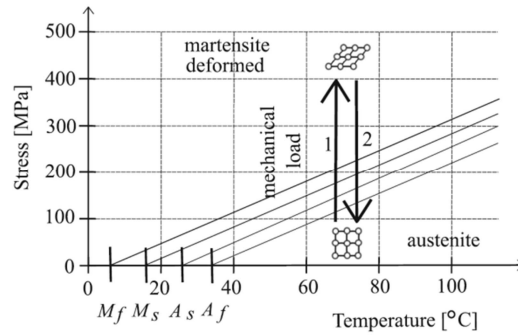
Figure 1. Effect of superelasticity in SMA – change of the characteristic temperatures [3].
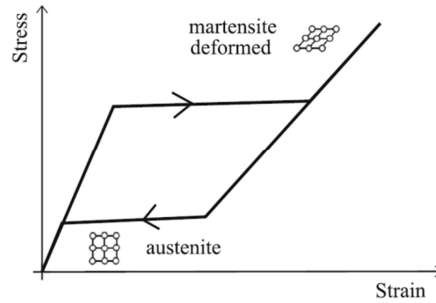
Figure 2. Effect of superelasticity in SMA – hysteretic stress-strain relationship [3].

The description of macroscopic behavior of an SMA component can be handled via analytical formulas [1,2,6]. The phenomenological approaches which are based on the Gibbs free energy concept are of particular concern due to their convenient description of both the material properties of an SMA specimen and its current state present under given mechanical and thermal load.

To model the kinetics of the martensitic phase transition in SMA, we may introduce after Lagoudas the following definition of the total specific Gibbs free energy G [15]

$$G\left(\bar{\bar{\sigma}}, T, \xi, \bar{\bar{\varepsilon}}^t\right) = -\frac{1}{2\rho} \mathbf{C}_{ijkl}\sigma_{ij}\sigma_{kl} - \frac{1}{\rho}\sigma_{ij}\left[\alpha_{ij}(T - T_0) + \bar{\bar{\varepsilon}}^t\right] +$$

$$+c\left[(T - T_0) - T\ln\left(\frac{T}{T_0}\right)\right] - s_0 T + u_0 + \frac{1}{\rho}f(\xi) \tag{1}$$

where:

- $\bar{\bar{\sigma}}$ (σ_{ij}, σ_{kl}) – second order Cauchy stress tensor (following the Einstein summation notation),
- T, T_0 – temperature and reference (ambient) temperature,
- $\xi \in [0,1]$ – martensitic volume fraction,
- $\bar{\bar{\varepsilon}}^t$ – second-order transformation strain tensor,
- ρ – mass density,
- $\mathbf{C}_{ijkl}$ – fourth-order elastic compliance tensor,
- α_{ij} – second-order thermal expansion coefficient tensor,
- c – specific heat,
- s_0 – specific entropy at the reference state,
- u_0 – specific internal energy at the reference state,
- $f(\xi)$ – the transformation hardening function – declares elastic strain energy originating from the interactions between various variants of the martensitic phase, including the interactions with the surrounding phases.

Eq. 1 evolves to the following expression for a one-dimensional (1-D) thermomechanical case considered in the present study

$$G(\sigma, T, \xi, \varepsilon^t) = -\frac{1}{2\rho}C\sigma^2 - \frac{1}{\rho}\sigma[\alpha(T - T_0) + \varepsilon^t] +$$

$$+c\left[(T - T_0) - T\ln\left(\frac{T}{T_0}\right)\right] - s_0 T + u_0 + \frac{1}{\rho}f(\xi) \tag{2}$$

where the parameters: C, s_0 and u_0 are declared as functions of the martensitic volume fraction ξ, i.e.,

$C = C^A + \xi(C^M - C^A) = C^A + \xi\Delta C = \frac{1}{E^A} + \xi\left(\frac{1}{E^M} - \frac{1}{E^A}\right),$ $\qquad s_0 = s_0^A + \xi(s_0^M - s_0^A) = s_0^A + \xi\Delta s_0,$

$u_0 = u_0^A + \xi(u_0^M - u_0^A) = u_0^A + \xi\Delta u_0.$ E^A and E^M are respectively the Young's moduli.

The total strain for the model of an SMA component equals

$$\varepsilon = C\sigma + \varepsilon^t + \alpha(T - T_0). \tag{3}$$

considering

$$\dot{\varepsilon}^t = \Lambda\dot{\xi}, \text{ for } \dot{\xi} \neq 0 \tag{4}$$

$$\Lambda = \sqrt{\frac{3}{2}}H. \tag{5}$$

H is the maximum uniaxial transformation strain. Under varying external mechanical load the entropy of the model is a non-decreasing parameter, which is assured by the Clausius–Planck inequality

$$\sigma\dot{\varepsilon}^t - \rho\frac{\partial G}{\partial \xi}\dot{\xi} \geq 0. \tag{6}$$

Considering Eq. 4 and the partial derivative $\frac{\partial G}{\partial \xi}$

$$\frac{\partial G}{\partial \xi} = -\frac{1}{2\rho}\Delta C\sigma^2 - \frac{1}{\rho}\Lambda\sigma - T\Delta s_0 + \Delta u_0 + \frac{1}{\rho}\frac{\partial}{\partial \xi}\big(f(\xi)\big) \tag{7}$$

in Eq. 6 leads to the expression

$$\Pi\big(\sigma, T, \xi, \dot{\xi}\big)\dot{\xi} \geq 0 \tag{8}$$

where

$$\Pi = \frac{1}{2}\Delta C\sigma^2 + \rho\Delta s_0 T + \begin{cases} \sqrt{6}H\sigma + \rho\Delta s_0\big(M_s - M_f\big)\xi - \frac{1}{4}\rho\Delta s_0\big(3M_s + A_f + A_s - M_f\big), \dot{\xi} > 0 \\ \sqrt{6}H\sigma + \rho\Delta s_0\big(A_f - A_s\big)\xi - \frac{1}{4}\rho\Delta s_0\big(M_s + 3A_f - A_s + M_f\big), \dot{\xi} < 0 \end{cases} \tag{9}$$

Kinetics of the phase transition in SMA is determined based on the conditionally defined value of the transformation function Φ

$$\Phi = \begin{cases} \Pi - Y, \dot{\xi} > 0 \\ -\Pi - Y, \dot{\xi} < 0 \end{cases} \tag{10}$$

with

$$Y = \frac{1}{4}\rho\Delta s_0\big(M_s + M_f - A_f - A_s\big). \tag{11}$$

The contribution of martensite is growing (i.e., ξ increases) if the stress σ grows and the condition $\Phi\big(\dot{\xi} > 0\big) > 0$ is satisfied. Conversely, the parameter ξ is gradually reduced when the stress σ decreases and $\Phi\big(\dot{\xi} < 0\big) > 0$.

3. Fundamentals of PD

Below, the theory of PD is briefly presented. Fig. 3 visualizes the nonlocal interactions present between the parts of the modelled solid body (referred to as *particles*) [14]. The space around an actual central particle localized at the position **x** and considered for the above mentioned interactions is the horizon, usually marked as H. All parts of the neighboring particles lying at the positions $\hat{\mathbf{x}}$ within the horizon H and of given volume $V_{\hat{\mathbf{x}}}$ interact with the central particle.
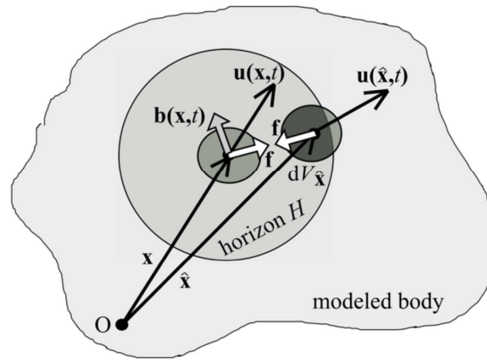
Figure 3. Definition of horizon and long-range force interactions in bond-based variant of PD [3].

Due to long-range interactions the governing equation takes the integral based form

$$\rho \ddot{\mathbf{u}}(\mathbf{x}, t) = \int_H \mathbf{f}(\mathbf{u}(\hat{\mathbf{x}}, t) - \mathbf{u}(\mathbf{x}, t), \hat{\mathbf{x}} - \mathbf{x}) dV_{\hat{\mathbf{x}}} + \mathbf{b}(\mathbf{x}, t) \tag{12}$$

$\mathbf{u}(\hat{\mathbf{x}}, t)$ and $\mathbf{u}(\mathbf{x}, t)$ respectively denote the particle displacements. $\mathbf{b}(\mathbf{x}, t)$ is the external force volumetric density. The elastic properties of the modeled body are defined with the function $\mathbf{f}$, which in general, depends on both the relative particle displacement and their relative position.

Having considered in the present study a simplified 1-D numerical PD model of a prismatic rod made of SMA the following equation of motion for the i-th degree of freedom may be first formulated for a metallic material

$$m_i \ddot{u}_i^t = 2 \sum_{\substack{j=-N \\ j \neq 0}}^{N} \beta_{i,j} \gamma_i \frac{EA}{L} \frac{u_{i+j}^t - u_i^t}{|j| N^2} + F_i \tag{13}$$

The fraction $\frac{EA}{L}$ constitutes the resultant stiffness coefficient k. j denotes each of $2N$ neighboring particles. The auxiliary parameters γ_i and $\beta_{i,j}$ assure correct fractions of the considered volumes of the central and neighboring particles respectively at the rod's edges and boundaries of the horizon. For more detailed description the reader is kindly asked to study the work [3]. Based on the above introduced PD model, in the following section an adequate model for SMA is derived.

4. PD based nonlocal formulation for thermomechanical coupling for modeling phase transitions in SMA

To derive a nonlocal model of SMA intended for simulations of mechanically induced solid phase transitions, the theory of thermoelasticity has been considered

$$\rho\ddot{\mathbf{u}} = \mu\nabla^2\mathbf{u} + (\lambda + \mu)\nabla\nabla\cdot\mathbf{u} + \mathbf{f} - \gamma\nabla T$$
$$\frac{1}{\kappa}\dot{T} = \nabla^2 T - \eta\nabla\cdot\dot{\mathbf{u}} + \frac{Q}{\kappa} \tag{14}$$

where λ, μ – the Lame constants, γ, κ and η are thermal and thermomechanical properties. Making the substitution $\theta = T - T_0$, where θ is the relative temperature, the parameter θ can be found via the thermal diffusion equation, which contributes to Eq. 14

$$\theta_i^{t+1} = \Delta t(\kappa\nabla^2\theta_i^t - \kappa\eta\nabla\cdot\dot{u}_i^t + Q_i^t) + \theta_i^t. \tag{15}$$

The wave equation (the former formula in Eq. 14) takes the following analytical form for a 1-D case with the thermomechanical interactions involved

$$\rho\frac{\partial^2 u}{\partial t^2} = E\frac{\partial^2 u}{\partial x^2} + b - \gamma\nabla T \tag{16}$$

Considering the wave equation (Eq. 16) and the definition of the total strain in SMA given by Eq. 3, the PD model defined via Eq. 13 takes the final form

$$m_i\ddot{u}_i^t = 2\sum_{\substack{j=-N \\ j\neq 0}}^{N}\beta_{i,j}\gamma_i\frac{k^A}{\alpha_E\xi_i+1}\frac{u_{i+j}^t-u_i^t}{|j|N^2} + \frac{F_M^*\xi_i+\alpha E^A A}{\alpha_E\xi_i+1}\theta + F_i \tag{17}$$

where: $k^A = \frac{E^A A}{L}$, $\alpha_E = \frac{E^A}{E^M} - 1$, $F_M^* = \sqrt{\frac{2}{3}}HE^A A$. Below, exemplary numerical results are briefly reported to show capabilities of the elaborated PD model of an SMA material.

5. Numerical simulation and experimental validation

A straightforward 4-degree-of-freedom numerical model of an SMA rod of the total length 4mm has been used to study the properties of the presented approach. The elaborated PD SMA model has been validated with the experimental data gathered during tests carried out using a fatigue testing machine. The numerically and experimentally registered hysteretic stress-strain and the simulated force-elongation relationships are shown in Fig. 4 and Fig. 5. The temporal courses for the above mentioned parameters found for the entire period of the experimental test are presented in Fig. 6.

The curve, which is obtained from the experiments exhibits fluctuations. The process of solid phase transitions is spontaneous. Similarly, the transitions between identified subsequent phases of the material behavior – with reference to the subsequent pieces of the hysteretic stress-strain relationship – are smooth. Thermomechanical coupling has been effectively handled by the model.
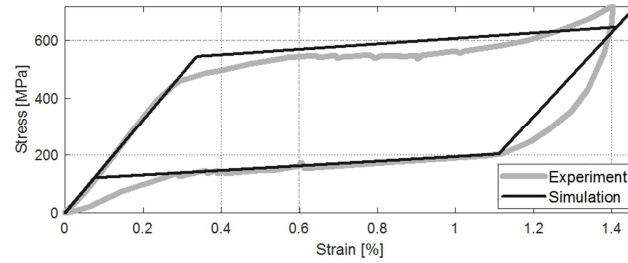
Figure 4. Hysteretic stress-strain relationship for the experimentally validated model of SMA.
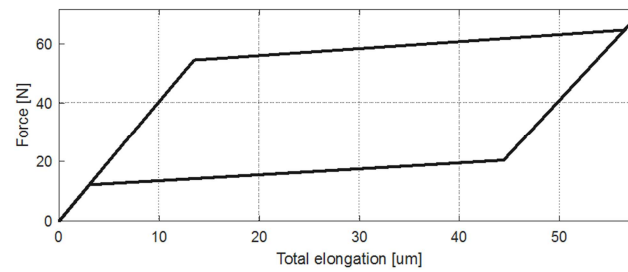
Figure 5. Force vs. total elongation curve for the experimentally validated model of SMA.
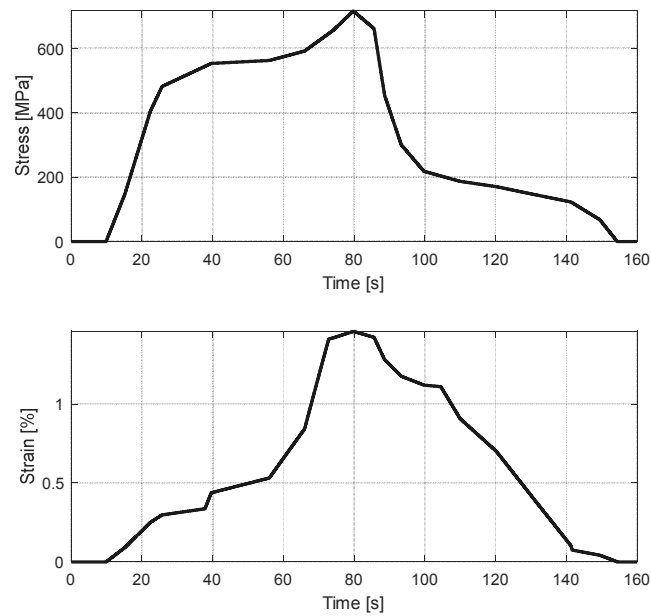
Figure 6. Temporal courses of stress and strain in modeled SMA.

6. Summary and final conclusions

In the paper the authors present the preliminary results provided by the elaborated model of SMA undergoing mechanically induced solid phase transitions. Specific demanded properties of SMA have been effectively handled via nonlocal modeling, To derive a nonlocal model of SMA the theory of both PD and thermoelasticity have been considered and briefly discussed.

As confirmed with the numerical results, the available capability of the PD SMA model allows for studying dynamic problems more conveniently, not being limited by the necessity of satisfying the condition of isothermal phase transition. The authors of the present work advantageously employ PD to alternatively nonlocally formulate thermomechanical coupling in the modeled SMA. Particularly, the phenomenon of superelasticity has been investigated and the related phase transitions in SMA have been studied. As confirmed with the experiments the phenomena of phase transitions in SMA are reversible and exhibit hysteretic nature.

References

[1] Lagoudas, D. *Shape memory alloys: modeling and engineering Applications.* Springer, Berlin, 2008.

[2] Auricchio, F., Bonetti, E., Scalet, G., and Ubertini, F. Theoretical and numerical modeling of shape memory alloys accounting for multiple phase transformations and martensite reorientation. *International Journal of Plasticity* 59 (2014), 30–54.

[3] Martowicz, A., Bryła, J., Staszewski, W.J., Ruzzene, M., and Uhl, T. Nonlocal elasticity in shape memory alloys modeled using peridynamics for solving dynamic problems. *Nonlinear Dynamics* 97, 3 (2019), 1911–1935.

[4] Rusinek, R., Warminski, J., Weremczuk, A., and Szymanski, M. Analytical solutions of a nonlinear two degrees of freedom model of a human middle ear with SMA prosthesis. *International Journal of Non-Linear Mechanics* 98 (2018), 163–172.

[5] Bryła, J., and Martowicz, A. Shape memory materials as control elements used in a dot Braille actuator. *Mechanics and Control* 33, 4 (2014), 83–89.

[6] Cisse, C., Zaki, W., and Zineb, T.B. A review of modeling techniques for advanced effects in shape memory alloy behavior. *Smart Materials and Structures* 25, 10 (2016), 103001.

[7] Auricchio, F., and Taylor, R.L. Shape-memory alloy: modeling and numerical simulations of the finite-strain superelastic behavior. *Computer Methods in Applied Mechanics and Engineering* 143 (1997), 175–194.

[8] Martowicz, A., Staszewski, W.J, Ruzzene, M., and Uhl, T. *Nonlocal elasticity theory for solving dynamic problems via peridynamics.* In: Awrejcewicz J., et al. (eds.) Mathematical and Numerical

Aspects of Dynamical System Analysis. 14th Conference Dynamical Systems—Theory and Applications—DSTA 2017, Łódź, Poland, 11–14 December 2017, (2017), 345–356.

[9] Martowicz, A., Pieczonka, Ł., Bryła, J., and Roemer, J. *Handling nonlinearities in metallic materials and structures using nonlocal elasticity.* Proceedings of 24th International Conference on Nonlinear Elasticity in Materials, Kraków, Poland, 24–28 June 2019, (2019).

[10] Nalepa, K., Pietkiewicz, K., and Żywica, P. Development of the foil bearing technology. *Technical Sciences* 12 (2009), 230–240.

[11] Lubieniecki, M., Roemer, J., Martowicz, A., Wojciechowski, K., and Uhl, T. A multi-point measurement method for thermal characterization of foil bearings using customized thermocouples. *Journal of Electronic Materials* 45, 3 (2016), 1473–1477.

[12] Howard, S., Dellacorte, C., Valco, M., Prahl, J., and Heshmat, H. Steady-state stiffness of foil air journal bearings at elevated temperatures. *Tribology Transactions* 44, 3 (2001), 489–493.

[13] Kunin, I.A. Inhomogeneous elastic medium with non-local interactions. *Journal of Applied Mechanics and Technical Physics* 8, 3 (1967), 60–66.

[14] Silling, S.A. Reformulation of elasticity theory for discontinuities and long-range forces. *Journal of the Mechanics and Physics of Solids* 48 (2000), 175–209.

[15] Lagoudas, D.C., Bo, Z.C., and Qidwai, M.A. A unified thermodynamic constitutive model for SMA and finite element analysis of active metal matrix composites. *Mechanics of Composite Materials and Structures* 3, 2 (1996), 153–179.

Adam Martowicz, Ph.D.: AGH University of Science and Technology, Department of Robotics and Mechatronics, al. A. Mickiewicza 30, 30-059 Krakow, Poland (adam.martowicz@agh.edu.pl). The author gave a presentation of this paper during one of the conference sessions.

Sławomir Kantor, M.Sc. (Ph.D. student): AGH University of Science and Technology, Department of Robotics and Mechatronics, al. A. Mickiewicza 30, 30-059 Krakow, Poland (slawomir.kantor@agh.edu.pl).

Jan Pawlik, M.Sc. (Ph.D. student): AGH University of Science and Technology, Department of Robotics and Mechatronics, al. A. Mickiewicza 30, 30-059 Krakow, Poland (jan.pawlik@agh.edu.pl).

Jakub Bryła, M.Sc. (Ph.D. student): AGH University of Science and Technology, Department of Robotics and Mechatronics, al. A. Mickiewicza 30, 30-059 Krakow, Poland (jakbryla@agh.edu.pl).

Jakub Roemer, Ph.D.: AGH University of Science and Technology, Department of Robotics and Mechatronics, al. A. Mickiewicza 30, 30-059 Krakow, Poland (jroemer@agh.edu.pl).

Investigation of piezoelectric and multiple electromagnetic hybrid vibration energy harvester

Rajarathinam Murugesan, Vinoth Krishnan, Aravindan Muralidharan Shaikh Faruque Ali

Abstract: This study presents a hybrid transduction based vibration energy harvester for achieving sufficient power across a wide band of frequencies. In the energy harvesting device, a cantilever beam with an unimorphed macro fiber composite patch is used to harvest piezoelectric energy and a spring-magnet mass system moving within a solenoid hung in different places of the cantilever is used to harvest electromagnetic energy out of motion in a magnetic field. The present study analyzes the implications of the number of electromagnetic subsystems on the total harvested power of the hybrid system and the saturation trends for various steel mass and hanging magnet mass under constant input energy have been reported. The results show that the maximum total power harvested by the hybrid harvester saturates after a particular number of electromagnetic subsystems. Also, it is observed that the optimal number of electromagnetic subsystems is found to be inversely proportional to the mass of the electromagnetic subsystem and percentage of tuned steel mass.

1. Introduction

Micro powered sensors are used in several applications like health monitoring of civil, mechanical, automobile and aerospace structures, environmental monitoring, medical remote sensing, military field and so on. Most of the sensors are deployed in remote locations. Powering these sensors using batteries is a costly affair for both technological as well as the environmental aspect. Moreover, manual access to remote locations for battery replacement is costly, time-consuming and unsafe [7]. The above stated reasons motivated to seek an alternative and reliable power source for wireless nodes from the ambient energy resources. Generating micro scale electrical power from ambient energy resources is known as energy harvesting. In this study, vibration is taken to be the ambient energy source. The aim of this research field is to power small electronic components by converting the vibration energy available in the environment into useful electrical energy. The energy in mechanical vibrations can be tapped mostly using piezoelectric (PE) and electromagnetic (EM) transductions based harvesting devices. In piezoelectric transduction, the piezoelectric element is stressed through external vibrations to generate electrical power [8] and in the electromagnetic transduction, mechanical system imparts motion to the magnets through the solenoid to generate electrical power [4].

In general, the vibration based energy harvester is broadly classified into two types based on their harvested power's frequency bandwidth namely narrow band and broadband harvesters. Narrow band, single frequency based resonance harvesting devices generate maximum power only at the resonance and the efficiency of energy conversion drops drastically as the excitation frequency moves away from resonance [2]. In reality, ambient vibration sources are random. Hence, from the point of view of practical applications, narrow band linear systems are inefficient. To overcome this drawback, the researchers focused on different approaches for harvesting broadband energy such as multi-modal [12], resonance tuning [3], nonlinear [5] and hybrid [10] harvesting techniques.

This manuscript proposes a novel design of modified multi-frequency based hybrid harvester that can generate power at a broad band of frequencies. The proposed harvesting device consists of a cantilever beam having MFC patch in unimorph configuration and multiple spring-magnetic masses suspended at different places of cantilever beam along with solenoid arrangements. In addition, lumped masses (steel masses) are also attached on the beam at the respective positions of hanging magnetic masses. This harvester will generate the power from both piezoelectric and electromagnetic tranductions simultaneously and hence it shall be termed as a hybrid harvester.

Most of the research, the beam based energy harvester are modeled as a simplified lumped mass model by using maximum kinetic energy principle and first mode assumption [9, 10]. But modeling the proposed harvester using a single mode will not be a correct approximation of the physical reality since the effect of multiple electromagnetic harvesters cannot be built into the system with the first mode assumption. Hence the finite element model of the harvester is developed in this analysis to obtain the power response of the proposed harvester system.

In this paper, an electromechanically coupled finite element beam model along with electromagnetic harvester model is presented for predicting the electrical power output of the piezoelectric and electromagnetic parts of the hybrid energy harvester. The present work reports the saturation characteristics of the total harvested power with the number of electromagnetic subsystems at various values of hanging mass and tuning percentages of lumped mass. The remainder of the article is organized as follows: Section 2 deals with the finite element modeling of the proposed harvester. Results of numerical simulations are reported in Section 3. Finally, the concluding remarks of current work have been explained in Section 4.

2. Design and Modeling of the Hybrid Harvester

Figure 1 illustrates the schematic diagram of proposed hybrid energy harvester (MHH). It is composed of a cantilever beam with a Macro Fiber Composite (MFC) patch, springs, permanent magnets, solenoid and extra steel masses. The MFC patch is attached on the upper surface of the cantilever beam near its fixed end. Permanent magnets are suspended at different places of the cantilever beam with a linear elastic spring. The solenoids are placed along the axis of motion of the each permanent magnet. Additionally, lumped mass are also attached on the beam, which are exactly positioned along the axis of each spring as shown in Fig. 1. Here, the piezoelectric harvesting part of the hybrid harvester (PHH) comprises the cantilever beam with MFC and the electromagnetic harvesting part of the hybrid harvester (EHH) consists of spring-magnetic mass with solenoid arrangement. In this study, EHH attached at the free end of the cantilever beam is kept undisturbed and the number of intermediate EHHs are increased from 1 to $m-1$ harvesters such that total number of harvesters is m. It has been noted that in each increment the distance between the EHH is equal and also there is no EHH at the fixed end.
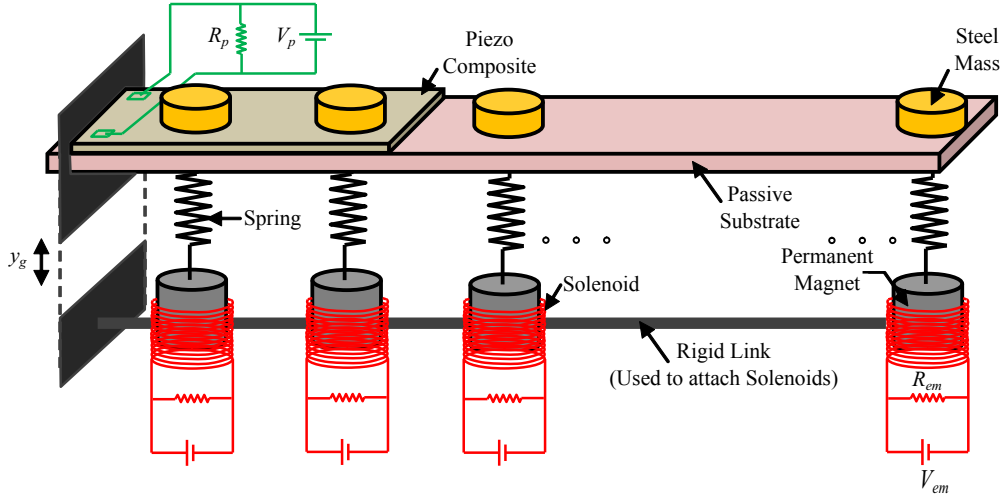
Figure 1. Schematic of the proposed hybrid energy harvester.

When a host structure undergoes vibrations, the system generates power from both piezoelectric and electromagnetic mechanisms due to direct piezoelectric effect and electromagnetic induction respectively. The PE and each of the EM harvesters are connected to separate external resistances, R_p and R_{em} respectively. In Fig. 1, V_p and V_{em} denote voltages generated by the PHH and EHH respectively. y_g denotes the support motion.

2.1. Formulation of finite element model

In this analysis, the beam is divided into two parts where the part with MFC is modelled as a composite beam and the part without MFC is modelled as a homogeneous beam. Each electromagnetic harvester is modelled as a single degree of freedom system. The Euler Bernoulli's beam theory is assumed for the modelling of the cantilever beam. where, the co-ordinate directions X, Y and Z are considered along the length, thickness and width of the beam respectively.

The degrees of freedom considered for the beam are deflection (w), slope (θ) and voltage (V). The displacements and voltages corresponding to the EHH subsystem are also taken to be the degrees of freedom of the system. Finite element method has been implemented in this study to discretize the domain of the cantilever beam. The deflection and slope of each element in the beam are expressed using Hermite cubic interpolation shape functions as given below

$$w(x) = w_1 N_1 + \theta_1 N_2 + w_2 N_3 + \theta_2 N_4 \tag{1}$$

where, w_1, θ_1 are deflection and slope at node 1 and w_2, θ_2 are deflection and slope at node 2. The shape functions N_1, N_2, N_3 and N_4 are given as

$$
\begin{aligned}
N_1 &= 1 - 3\left(\frac{x}{L_e}\right)^2 + 2\left(\frac{x}{L_e}\right)^3; \qquad N_2 = -x\left(1 - \frac{x}{L_e}\right)^2; \\
N_3 &= 3\left(\frac{x}{L_e}\right)^2 - 2\left(\frac{x}{L_e}\right)^3; \qquad N_4 = -x\left[\left(\frac{x}{L_e}\right)^2 - \frac{x}{L_e}\right]
\end{aligned}
\tag{2}
$$

where, L_e is the length of element and x is the axial location in element. For the region of the beam with MFC, the electric potential is treated as an electrical degree of freedom in addition to the displacement degrees of freedom. The interpolating shape function for the electric potential varying along the length and thickness of the beam element is taken as follows [6]

$$V(x,z) = N_5 V_1 + N_6 V_2; \qquad N_5 = \left(\frac{1}{2} + \frac{z}{h}\right)\left(1 - \frac{x}{L_e}\right); \qquad N_6 = \left(\frac{1}{2} - \frac{z}{h}\right)\left(\frac{x}{L_e}\right) \tag{3}$$

where, V_1 and V_2 are voltages at the two nodes of element and N_5, N_6 are shape functions. h is the thickness of MFC in the element, and z is the location in thickness direction of the element. The element stiffness matrix with respect to deflection and slope is expressed as [1]

$$K_{ij} = -\int_v D_{11} \frac{d^2 N_i}{dx^2}\frac{d^2 N_j}{dx^2} dxdydz; \qquad i,j = 1,2,3,4 \tag{4}$$

where, D_{11} is material parameter, and equal to Young's Modulus for isotropic beam. The element mass matrix is expressed as [1]

$$M_{ij} = -\int_v \rho N_i N_j dxdydz; \qquad i,j = 1,2,3,4 \tag{5}$$

where, ρ is the density of element. The elements of coupling matrix is given as [1]

$$\theta_{ij} = -\int_v e_{13} z \frac{dN_i}{dz} \frac{d^2 N_j}{dx^2} dx dy dz; \qquad i = 5, 6, \qquad j = 1, 2, 3, 4 \tag{6}$$

where, e_{13} is the piezoelectric constant. The element permittivity matrix is given as [1]

$$\varepsilon_{ij} = -\int_v \varepsilon_{33}^s \frac{dN_i}{dz} \frac{dN_j}{dz} dx dy dz; \qquad i, j = 5, 6 \tag{7}$$

where, ε_{33}^s is the permittivity of piezoelectric material. As mentioned above, the mechanical and electrical degrees of freedom for the beam element are

$$d_0 = \{w_1 \quad \theta_1 \quad w_2 \quad \theta_2\}^T; \qquad V_0 = \{V_1 \quad V_2\}^T \tag{8}$$

The element stiffness and matrices matrix for beam with MFC is obtained by expanding Eqs. (4), (5) and rewriting them in a compact form as follows

$$\begin{aligned}
K_e &= \frac{EI}{L_e^3} \begin{bmatrix} 16 & 6L_e & -12 & 6L_e \\ 6L_e & 4L_e^2 & -6L_e & 2L_e^2 \\ -12 & -6L_e & 12 & -6L_e \\ 6L_e & 2L_e^2 & -6L_e & 4L_e^2 \end{bmatrix} \\
M_e &= \frac{\rho A L_e}{420} \begin{bmatrix} 156 & 22L_e & 54 & -13L_e \\ 22L_e & 4L_e^2 & 13L_e & -3L_e^2 \\ 54 & 13L_e & 156 & -22L_e \\ -13L_e & -3L_e^2 & -22L_e & 4L_e^2 \end{bmatrix}
\end{aligned} \tag{9}$$

where, E is the Young's modulus, A is the area, and I is the moment of inertia of beam element. The section modulus of the beam with MFC region is calculated by equivalent area method to locate the neutral axis of the transformed section. Also, for the beam with MFC patch, the mass per unit length (ρA) will be taken as the weighted average of the mass per unit length of both MFC and beam material.

Similarly, the stiffness (K_{EH}) and mass (M_{EH}) matrix for the electromagnetic harvesters are given below

$$K_{EH} = \begin{bmatrix} k_{EH} & -k_{EH} \\ -k_{EH} & k_{EH} \end{bmatrix}; \qquad M_{EH} = \begin{bmatrix} m_s & 0 \\ 0 & m_m \end{bmatrix} \tag{10}$$

where, k_{EH}, m_m and m_s are the stiffness of spring element, mass of the permanent magnet and the steel mass placed on the beam respectively. By expanding Eq. (6) and Eq. (7), the

element coupling matrix (θ_e) and permittivity matrix (ε_e) are given by

$$\theta_e = \begin{bmatrix} \dfrac{e_{31}bt_p}{4L_e} & \dfrac{e_{31}bt_p}{4L_e} & -\dfrac{e_{31}bt_p}{4L_e} & 0 \\[2ex] -\dfrac{e_{31}bt_p}{2L_e} & 0 & \dfrac{e_{31}bt_p}{4L_e} & 0 \end{bmatrix}^T \quad ; \quad \varepsilon_e = \begin{bmatrix} -\dfrac{\varepsilon_{33}^s bL_e}{3t_p} & -\dfrac{\varepsilon_{33}^s bL_e}{6t_p} \\[2ex] -\dfrac{\varepsilon_{33}^s bL_e}{6t_p} & -\dfrac{\varepsilon_{33}^s bL_e}{3t_p} \end{bmatrix} \tag{11}$$

where, b is width of the MFC element, t_p is thickness of the MFC element.

The whole beam is discretized into n beam elements. The global stiffness matrix (K_G) and mass matrix (M_G) of the system are obtained by the assembly of individual element stiffness and mass matrices considering the structural and electrical degrees of freedom. The assembled global stiffness and mass matrices will be of size $(2n + 2) \times (2n + 2)$. m additional degrees of freedom corresponding to the electromagnetic harvesters are added in the assembled global mass and stiffness matrices which makes the final size of the matrices to $(2n + 2 + m) \times (2n + 2 + m)$. The index mm corresponds to the position of added electromagnetic harvester.

$$K_G = \begin{bmatrix} k_{e1} & \cdot & \cdot & \cdot & \cdot & \cdot & \cdot & \cdots & \cdot \\ \cdot & k_{e1}+k_{e2} & \cdot & \cdot & \cdot & \cdot & \cdot & \cdots & \cdot \\ \cdot & \cdot & \cdot & \cdot & \cdot & \cdot & \cdot & \cdots & \cdot \\ \cdot & \cdot & \cdot & k_{emm}+k_{EH} & \cdot & \cdot & -k_{EH} & \cdots & \cdot \\ \cdot & \cdot & \cdot & \cdot & \cdot & \cdot & \cdot & \cdots & \cdot \\ \cdot & \cdot & \cdot & \cdot & \cdot & k_{en}+k_{EH} & \cdot & \cdots & -k_{EH} \\ \cdot & \cdot & \cdot & -k_{EH} & \cdot & \cdot & k_{EH} & \cdots & \cdot \\ \vdots & \vdots & \vdots & \vdots & \vdots & \vdots & \vdots & \vdots & \vdots \\ \cdot & \cdot & \cdot & \cdot & \cdot & -k_{EH} & \cdot & \cdot & k_{EH} \end{bmatrix} \tag{12}$$

$$M_G = \begin{bmatrix} m_{e1} & \cdot & \cdot & \cdot & \cdot & \cdot & \cdot & \cdots & \cdot \\ \cdot & m_{e1}+m_{e2} & \cdot & \cdot & \cdot & \cdot & \cdot & \cdots & \cdot \\ \cdot & \cdot & \cdot & \cdot & \cdot & \cdot & \cdot & \cdots & \cdot \\ \cdot & \cdot & \cdot & m_{emm}+m_s & \cdot & \cdot & \cdot & \cdots & \cdot \\ \cdot & \cdot & \cdot & \cdot & \cdot & \cdot & \cdot & \cdots & \cdot \\ \cdot & \cdot & \cdot & \cdot & \cdot & m_{en}+m_s & \cdot & \cdots & \cdot \\ \cdot & \cdot & \cdot & \cdot & \cdot & \cdot & m_m & \cdots & \cdot \\ \vdots & \vdots & \vdots & \vdots & \vdots & \vdots & \vdots & \vdots & \vdots \\ \cdot & \cdot & \cdot & \cdot & \cdot & \cdot & \cdot & \cdot & m_m \end{bmatrix} \tag{13}$$

The assembled global coupling matrix (θ_G) is of the size $(2n + 2 + m) \times (n + 1 + m)$. It has to be noted that the diagonal zero terms of coupling matrix correspond to region where the

MFC patch is not present. The assembled permittivity matrix will have non zero terms only at the positions where MFC layer is present and rest of elements of the matrix will all be zero. The assembled coupling (θ_G) and permittivity (ε_G) matrices look like

$$\theta_G = \begin{bmatrix} \theta_{e1} & . & . & . & 0 & \dots & 0 \\ . & \theta_{e1}+\theta_{e2} & . & . & 0 & \dots & 0 \\ . & . & . & . & 0 & \dots & 0 \\ . & . & . & \theta_{ej} & 0 & \dots & 0 \\ 0 & 0 & 0 & 0 & 0 & \dots & 0 \\ \vdots & \vdots & \vdots & \vdots & \vdots & \vdots & 0 \\ 0 & 0 & 0 & 0 & 0 & 0 & 0 \end{bmatrix} ; \varepsilon_G = \begin{bmatrix} \varepsilon_{e1} & . & . & . & 0 & \dots & 0 \\ . & \varepsilon_{e1}+\varepsilon_{e2} & . & . & 0 & \dots & 0 \\ . & . & . & . & 0 & \dots & 0 \\ . & . & . & \varepsilon_{ej} & 0 & \dots & 0 \\ 0 & 0 & 0 & 0 & 0 & \dots & 0 \\ \vdots & \vdots & \vdots & \vdots & \vdots & \vdots & 0 \\ 0 & 0 & 0 & 0 & 0 & 0 & 0 \end{bmatrix}$$
$$(14)$$

where, j represents the last node of MFC patch from the fixed end of the beam. The potential degree of freedom defined at each node makes the adjacent piezoelectric elements insulated from each other and as a result, single potential does not exist between the elements. In actual scenario, a single continuous electrode is pasted over the MFC which gives a single potential V_s. The coupling matrix should hence be converted to a vector so that a single voltage value is obtained. This is done by adopting the potential constrained from [11], which is given as follows

$$\theta_G V = \theta_G \begin{bmatrix} 1 & 1 & 1 & 1 & 1 & 1 \end{bmatrix}^T_{n+1,1} V_s = \hat{\theta} V_s \qquad (15)$$

$\hat{\theta}$ is the coupling matrix which gives a single potential. Similarly the permittivity matrix ε_G also changes accordingly as follows

$$\varepsilon_G V = \begin{bmatrix} 1 & 1 & 1 & 1 & 1 \end{bmatrix}_{1,n+1} \begin{bmatrix} 1 & 1 & 1 & 1 & 1 \end{bmatrix}^T_{n+1,1} V_s = n C_{pe} V_s = C_p V_s \qquad (16)$$

The assembled vector of mechanical degrees of freedom are given as

$$d = \left\{ w_1 \quad \theta_1 \quad w_2 \quad \theta_2 \dots w_{2n+2} \quad \theta_{2n+2} y_{EH_m} \right\}^T_{2n+2+m,1} \qquad (17)$$

The boundary condition at the fixed end are taken to be $w_1{=}0$ and $\theta_1{=}0$.

2.2. Harmonic analysis

The electromechanical coupling dynamics of the system given below is then solved by harmonic analysis.

$$M_G\{\ddot{d}\} + C\{\dot{d}\} + K_G\{d\} - \hat{\theta}_G V_s = \{F\}$$
$$\hat{\theta}_G^T\{\ddot{d}\} + C_p \dot{V}_s + \frac{V_s}{R_p} = 0 \qquad (18)$$

Assuming the amplitude of excitation force, $F=F_o e^{i\omega t}$ and responses $d=d_0 e^{i\omega t}$, $V_s=V_f e^{i\omega t}$ the Eq. (18) becomes

$$[-\omega^2 M_G + K_G + i\omega C]\{d_0\} - [\hat{\theta}_G]V_f = \{F_0\}$$
$$\left[i\omega \hat{\theta}^T\right]\{d_0\} + \left[i\omega C_p + \frac{1}{R_p}\right]V_f = 0$$

$$(19)$$

where, $F_0=\omega\sqrt{\frac{2E_{in}}{M}}\left[M_G \cdot I_{(2n+2+m)\times(2n+2+m)}\right]$; E_{in} is the input energy amplitude, which is considered to be constant in this analysis; $M=m_b + \sum_{i=1}^{m}\left(m_{si}+m_{mi}\right)$. m_b, m_s and m_m are mass of the beam, steel and hanging magnet mass respectively. The solution of the above set equations gives the steady state amplitudes of displacements and voltage generated by the PHH as a function of excitation frequency. The steady state power of PHH is given by

$$P_{PHH} = \frac{|V_f|^2}{2R_p} \qquad (20)$$

For the electromagnetic harvester, the voltage shall be obtained as

$$V_{em_m} = -\sum_{j=1}^{m}\theta_{em}i\omega d_{0rem_j}; \quad j = 1, 2, 3, \ldots, m \qquad (21)$$

where, d_{0rem} is the relative displacement between the magnet and solenoid. The steady state amplitudes of power corresponding to EHH subsystems are given as follows

$$P_{EHH_m} = \left|\frac{V_{em_m}}{R_{em}+R_c}\right|^2 \frac{R_{em}}{2} \qquad (22)$$

Finally, the total power of the system is obtained by the sum of individual power magnitudes generated by each subsystem.

3. Results and discussion

In this section, the simulated results of multiple electromagnetic hybrid energy harvester are presented for an energy input of 10mJ. The energy level is chosen such that the beam deformation is well within its elastic limit. Studies in the present work are simulated within frequency range of 1Hz to 10Hz. The optimal load resistance of the piezoelectric circuit (R_p) is approximated to be $\frac{1}{\omega_1 C_p}$ [13] and that of the electromagnetic circuit (R_{em}) is approximately equal to the internal resistance (R_c) of the solenoid [14]. The important parameters used for the analysis are given in Table 1.

In this analysis, the lumped masses are tuned to various percentages of m_s=40gm such that it linearly increases along with increase in the number of EHH subsystems but bounded within $m_m + (\eta\%)m_m$; η is varied from 0% to 50%. The hanging mass, m_m is varied from 5gm

Table 1. Description of parameters and their values

Symbol	Description	Value
L	Length of the beam	1000 mm
b	Width of the beam	32 mm
t_b	Thickness of the beam	5 mm
E	Young's modulus of the beam	70 GPa
t_p	Thickness of the MFC	0.3 mm
c^E	Young's modulus of the MFC	15.857 GPa
C_p	Electrical capacitance of the MFC	177.07 nF
B_r	Residual magnetic flux density	1.1 T
R_{em}	Load resistance of the EM circuits	60 Ω
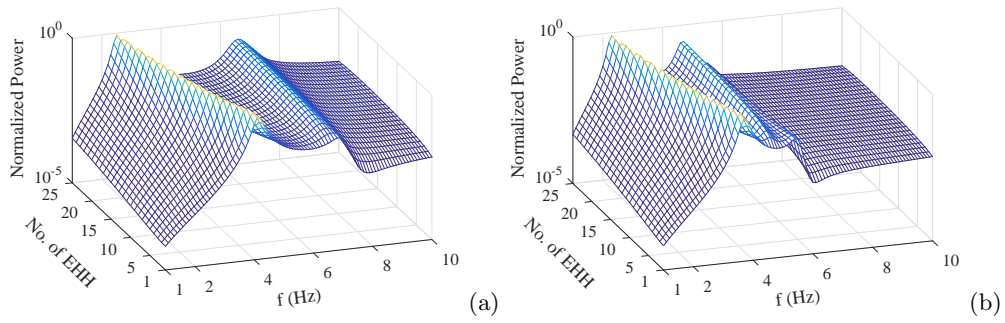
Figure 2. Variation of normalized power of the hybrid harvester with frequency and number of electromagnetic harvesters for 10% tuning of lumped mass and (a) 10gm of hanging mass, (b) 20gm of hanging mass.
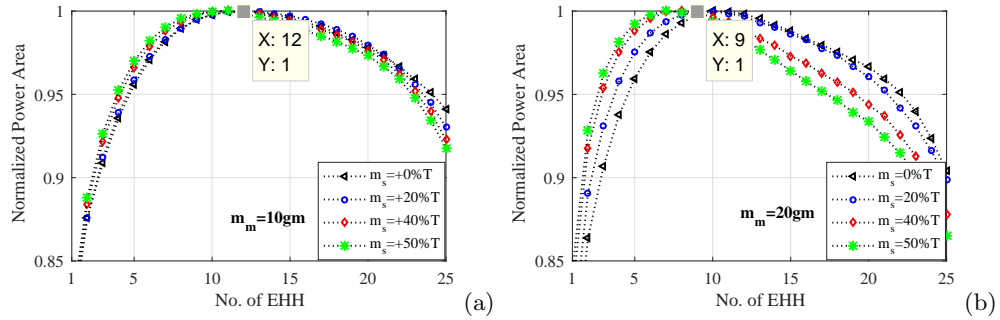
Figure 3. Variation of normalized power area of the hybrid harvester with number of electromagnetic harvesters for various percentages of tuning of lumped mass and (a) hanging mass, m_m=10g (b) m_m=20g.

to 40gm. Numerical simulations have been carried out to probe the feasibility of determining the optimal number of EHH subsystems to be introduced into the system such that sufficient

power is obtained in the considered frequency band for a given energy level.

Figure 2 shows the normalized power of HH as a function of excitation frequency and the number of electromagnetic subsystems for an input energy amplitude of 10mJ given at the base. It is implied from the figure that with the increase in the values of m_m, the bandwidth of the total harvested power reduces significantly. The reason for the above stated observation shall be attributed to the dominant role of m_m in shifting the resonant frequencies of the system towards each other as opposed to the effect of percentage tuning of m_s. Also, the resonant peaks in a given frequency range tend to diverge with the increase in the number of EHH subsystems. Hence, with m_m being a parameter, the hybrid harvester can be designed to generate broadband power which is unachievable in single resonance based harvesters.

To quantify the power harnessing potential of the harvester with increase in the number of EHH in the considered frequency, the metric of normalized power area has been considered in this analysis. The area under the power curve is a representation of the energy that can be harvested within the frequency zone [15]. Figures 3(a) and (b) show the variation of the normalized power area with various % of tuned lumped mass with respect to hanging mass of values of 10gm and 20gm respectively. Figure indicates that with the increase in the number of electromagnetic harvesters, the area under the power curve increases to a maximum and then decreases. The number of EHH subsystems at which normalized power area reaches the maximum shall be taken to be the optimal number for given set of parameters. The optimal number of EHH subsystems decreases with increase in the values of m_m for various tuning percentages of m_s.

For a given tuning percentage of m_s, the normalized power area of the hybrid harvester
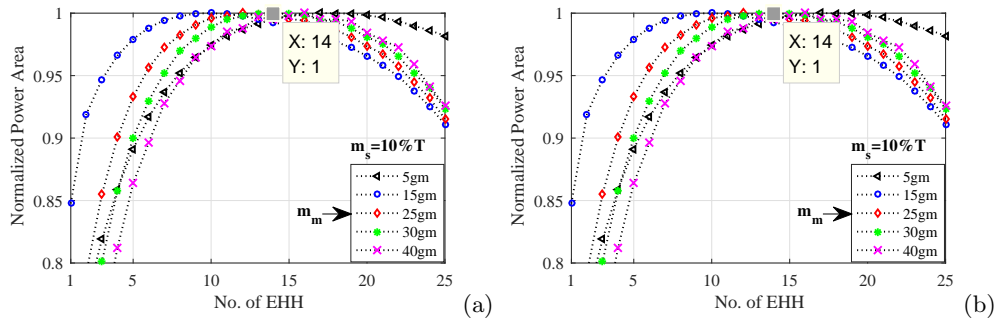
Figure 4. Variation of normalized power area of the hybrid harvester with number of electromagnetic harvesters for various values of hanging mass and (a) 10% tuning of lumped mass (b) 50% tuning of lumped mass.

becomes maximum at an optimum number of EHH subsystems similar to the case of varying m_m. From Fig. 4, it can be observed that the number of EHH subsystems for obtaining maximum power area also decreases with the increase in % of tuned lumped mass. It has been noted from Figs. 4(a) and (b) that at very small values of m_m, the optimal value occurs at much larger number of EHH subsystems and hence becomes physically infeasible. From all the cases considered in the study, it can be inferred that the variation in m_m prominently affects the bandwidth of the system while the variation in the tuning percentage of m_s influences the optimal number of EHH subsystems of the system for a given energy level.

4. Conclusions

This article analyses the evolution of broadband characteristics of coupled piezoelectric and multiple electromagnetic hybrid energy harvester with change in the values of selective parameters. Effects of the number of electromagnetic subsystems on the total harvested power of the hybrid harvester are assessed numerically for a constant input energy amplitude. The results show that the normalized power area of the hybrid harvester attains a maximum value at an optimum number of the electromagnetic subsystems. The routes to reaching an optimum number is discussed with respect to the variation in tuning percentage of tuned lumped mass and hanging magnetic mass. The present study shows that the harvesting system can be designed to achieve broadband power at a minimum possible number of electromagnetic subsystems with the proper selection of the parameter values.

References

[1] ALLEN, D. H., AND HAISLER, W. E. *Introduction to aerospace structural analysis.* John Wiley & Sons, New York, USA, 1985.

[2] BEEBY, S. P., TORAH, R., TUDOR, M., GLYNNE-JONES, P., O'DONNELL, T., SAHA, C., AND ROY, S. A micro electromagnetic generator for vibration energy harvesting. *Journal of Micromechanics and microengineering 17*, 7 (2007), 1257.

[3] CHENG, Y., WU, N., AND WANG, Q. An efficient piezoelectric energy harvester with frequency self-tuning. *Journal of Sound and Vibration 396* (2017), 69–82.

[4] FAN, K., CAI, M., LIU, H., AND ZHANG, Y. Capturing energy from ultra-low frequency vibrations and human motion through a monostable electromagnetic energy harvester. *Energy 169* (2019), 356–368.

[5] FAN, K., ZHANG, Y., LIU, H., CAI, M., AND TAN, Q. A nonlinear two-degree-of-freedom electromagnetic energy harvester for ultra-low frequency vibrations and human body motions. *Renewable energy 138* (2019), 292–302.

[6] HUMAR, J. L. *Dynamics of structures.* A Balkema Publishers, Tokyo, 2002.

[7] MAAMER, B., BOUGHAMOURA, A., EL-BAB, A. M. F., FRANCIS, L. A., AND TOUNSI, F. A review on design improvements and techniques for mechanical energy harvesting using piezoelectric and electromagnetic schemes. *Energy Conversion and Management 199* (2019), 728–747.

[8] MADINEI, H., KHODAPARAST, H. H., FRISWELL, M., AND ADHIKARI, S. Minimising the effects of manufacturing uncertainties in mems energy harvesters. *Energy 149* (2018), 990–999.

[9] PRIYA, S., AND INMAN, D. J. *Energy harvesting technologies*, vol. 21. Springer, 2009.

[10] RAJARATHINAM, M., AND ALI, S. F. Energy generation in a hybrid harvester under harmonic excitation. *Energy Conversion and Management 155* (2018), 10–19.

[11] SURABHI, A. Finite element beam model for piezoelectric energy harvesting using higher order shear deformation theory. *All Theses* (2014).

[12] UPADRASHTA, D., AND YANG, Y. Trident-shaped multimodal piezoelectric energy harvester. *Journal of Aerospace Engineering 31*, 5 (2018), 1–9.

[13] XUE, H., HU, Y., AND WANG, Q. M. Broadband piezoelectric energy harvesting devices using multiple bimorphs with different operating frequencies. *IEEE transactions on ultrasonics, ferroelectrics, and frequency control 55*, 9 (2008), 2104–2108.

[14] YANG, B., LEE, C., XIANG, W., XIE, J., HE, J. H., KOTLANKA, R. K., LOW, S. P., AND FENG, H. Electromagnetic energy harvesting from vibrations of multiple frequencies. *Journal of Micromechanics and Microengineering 19*, 3 (2009), 1–8.

[15] ZHOU, S., CAO, J., WANG, W., LIU, S., AND LIN, J. Modeling and experimental verification of doubly nonlinear magnet-coupled piezoelectric energy harvesting from ambient vibration. *Smart Materials and Structures 24*, 5 (2015), 1–13.

Rajarathinam Murugesan, Ph.D: Department of Applied Mechanics, Indian Institute of technology Madras, Chennai-600036, Tamil Nadu, India (*rajmiitm@gmail.com*).

Vinoth Krishnan, M.Sc.: Department of Applied Mechanics, Indian Institute of technology Madras, Chennai-600036, Tamil Nadu, India (*am18m007@smail.iitm.ac.in*).

Aravindan Muralidharan, M.Sc. (Ph.D. student): Department of Applied Mechanics, Indian Institute of technology Madras, Chennai-600036, Tamil Nadu, India (*aravindanm24@gmail.com*). The author gave a presentation of this paper during one of the conference sessions.

Shaikh Faruque Ali, Associate Professor: Department of Applied Mechanics, Indian Institute of technology Madras, Chennai-600036, Tamil Nadu, India (*sfali@iitm.ac.in*).

Optimization of the actuator/sensor placement for active vibration control of a funnel shaped piezoelectric structure

Tamara Nestorović, Kevin Hassw, Atta Oveisi

Abstract: Placement of piezoelectric actuators and sensors implemented in the form of thin piezoelectric films plays an important role in active vibration control of structures, since after applying they remain permanently integrated with a structure. In this work a funnel shaped structure inlet of the magnetic resonance imaging (MRI) tomopraph is analysed and a balanced optimization of the actuator/sensor placement is performed based on H_2 and H_∞ norms. The applied procedure is a global one, seeking for optima across the entire domain of the structure. A thorough study of the mesh refinement influence with respect to the eigenfrequency analysis was performed in order to obtain a reliable numeric finite element (FE) model for the optimization purposes. The material parameter optimization was performed as well. Based on placement indices optimal placement study was performed under consideration of several eigenmodes of interest. The optimization was performed for individual modes as well as for simultaneous consideration of multiple modes. A software in the loop approach with recurrent communication in each iteration of the optimization between the numerical simulation FE software and optimization tool designed in Python was implemented through the evaluation of the placement indices for candidate locations over the entire curved surface of the structure. Depending on support conditions the optimal locations of piezoelectric are proposed.

1. Introduction

Active vibration control gains more and more importance both in research and engineering applications. Especially related to smart structures and systems, active control becomes an indispensable part of a smart system. Magnetic resonance imaging tompograph is an example of a system with high potential for implementation of active vibration and noise control using multifunctional materials – piezoelectric films integrated with the structure in the form of actuators and sensors for the vibration suppression. The main problem during diagnostic treatment of patients in MRI is a high noise level the patients have to undergo [5]. Beside the noise coming from the cylindrical body of an MRI tomograph, the secondary source of noise is the funnel shaped inlet. This noise is the consequence of the transmitted vibrations from the tomograph body, which in turn induce additional secondary noise. Thus the reduction of the secondary vibration of the funnel shaped MRI inlet can contribute to

an overall noise reduction. In addition to negative influence on patients (anxious condition due to noise, hearing deterioration or temporary hearing lost [6, 1]), the resolution and the quality of the scanning images can be influenced by vibration as well [8]. For an efficient vibration suppression the placement of piezoelectric actuators and sensors plays a decisive role. Since the piezoelectric transducers glued in form of thin films remain permanently on the surface of the structure, their proper placement is particularly important.

2. Methodology

Considerable savings can be achieved by model-based optimization of the piezoelectric actuator/sensor positions. For a funnel shaped geometry, the form of the MRI tomograph inlet, the optimization procedure represents a special challenge, since opposite to plane plate-like structures, the optimization procedure requires not only iterative change of the pure geometric parameter(s) defining the location of the actuators/sensors having fixed geometry, but it also requires at the same time iterative change of the actuator/sensor geometry itself, i.e. its adaptation to the shape of the curved surface of the funnel in contact with an actuator or a sensor. Model-based optimization of the actuator/sensor placement in this research is a global one and it is performed based on finite element (FE) models of the funnel shaped MRI tomograph inlet in Abaqus CAE. The optimality criteria are based on placement indices, which are defined later in this paper. The values of the placement indices are evaluated over the entire considered geometry, so the method is global and thus enables finding global optima in contrast to gradient methods (which, depending on initial guess, may be trapped in the neighborhood of a local optimum) or other optima search methods (which narrow the search region). Each time when a user sends a command to Abaqus CAE from GUI (graphical user interface), a Python script is generated and updated. This Python script is passed through the interpreter to the kernel. These procedures are saved in Abaqus in terms of an .rpy-file. In addition, a sequence of commands which are run from GUI of the Abaqus CAE are saved in a .jln-file. The .jnl-file serves as a main modulus for programming in Python [4, 3]. The parameters which define the position and the geometry of the actuators/sensors and which are altered iteratively, are defined within a Matlab script (.m-file), they are saved in Python files and finally imported by the Abaqus model. All parameters relevant for the Python files are clearly arranged within the Matlab script, and they are updated after each iteration without having to invoke GUI from Abaqus CAE. In addition, the calculation and graphical representation of the placement indices are performed in Matlab in order to specify optimal positions. After performing modal analysis in Abaqus for a specified actuator/sensor placement Matlab reads in iteratively in the loop the next set of parameters. Previous parameters are overwritten in the Python by the current ones,

which are then sent to Abaqus for calculation. After having performed the modal analysis for a specified actuator/sensor position, Abaqus generates text files (.txt) with produced results. The .txt-files are updated after each calculation of a new position and they contain the results for each selected placement within the loop. After passing through all candidate placement locations, the generated text files are read in Matlab and used there for further calculation of the placement indices matrix, in order to specify optimal placement [4, 3].

3. Development of a state space model in modal coordinates

Starting point for obtaining the state space representation of the model is a system of equations of motion in matrix form (1), which can be obtained from FE modelling or through system identification.

$$\mathbf{M}\ddot{\mathbf{q}} + \mathbf{D_d}\dot{\mathbf{q}} + \mathbf{K}\mathbf{q} = \mathbf{F} \tag{1}$$

Vector $\mathbf{q}$ contains all degrees of freedom (dofs) of the system: mechanical dofs – generalized displacements and electric dofs – electrical charges or potentials. The total force force vector

$$\mathbf{F} = \mathbf{F_E} + \mathbf{F_C} = \bar{\mathbf{E}}\bar{\mathbf{f}}(t) + \bar{\mathbf{B}}\bar{\mathbf{u}}(t) = \mathbf{B_0}\mathbf{u} \tag{2}$$

consists of the part $\mathbf{F_E}$ which represents the vector of external forces and $\mathbf{F_C}$ control forces. Matrix $\bar{\mathbf{E}}$ defines the position of generalized external forces $\bar{\mathbf{f}}(t)$ and $\bar{\mathbf{B}}$ is related to the control parameters, i.e. it defines the positions of the control inputs $\bar{\mathbf{u}}(t)$ (actuators). These information are contained within the unified input matrix $\mathbf{B_0}$ and the total vector of inputs $\mathbf{u}$ consisting both of external and control inputs. The output equation (3)

$$\mathbf{y} = \mathbf{C_{0q}}\mathbf{q} + \mathbf{C_{0v}}\dot{\mathbf{q}} \tag{3}$$

relates the system outputs (measurements) $\mathbf{y}$ with the vector of generalized displacements $\mathbf{q}$ through the corresponding output matrix $\mathbf{C_{0q}}$ and with the vector of generalized velocities $\dot{\mathbf{q}}$ through the output matrix $\mathbf{C_{0v}}$. These matrices are obtained through the FE modelling and their elements are sensor placement dependent [2]. The solution of the eigenvalue problem for the system of equations (1) results in eigenfrequencies ω_i and eigenvectors (eigenmodes) φ_i, which form the spectral matrix $\mathbf{\Omega}$ and the modal matrix $\mathbf{\Phi}$, respectively:

$$\mathbf{\Omega} = diag(\omega_1, \omega_2, ..., \omega_n); \qquad \mathbf{\Phi} = \begin{bmatrix} \varphi_1 & \varphi_2 & ... & \varphi_n \end{bmatrix}. \tag{4}$$

Applying transformation $\mathbf{q} = \mathbf{\Phi}\mathbf{q_m}$ to system (1) and the output equation (3) and the orthogonality property of the mass $\mathbf{M_m} = \mathbf{\Phi^T}\mathbf{M}\mathbf{\Phi} = diag(m_i)$ and the stiffness $\mathbf{K_m} = \mathbf{\Phi^T}\mathbf{K}\mathbf{\Phi} = diag(m_i\omega_i^2)$ matrices with respect to modal matrix, as well as the assumption of

the proportional (Rayleigh) damping, results in decoupled system of equations of motion and the output equation in modal coordinates $\mathbf{q_m}$, respectively:

$$\ddot{\mathbf{q}}_\mathbf{m} + 2\mathbf{Z\Omega}\dot{\mathbf{q}}_\mathbf{m} + \mathbf{\Omega}^2\mathbf{q}_\mathbf{m} = \mathbf{B_m}\mathbf{u}; \qquad \mathbf{y} = \mathbf{C_{mq}}\mathbf{q}_\mathbf{m} + \mathbf{C_{mv}}\dot{\mathbf{q}}_\mathbf{m} \tag{5}$$

with: $\mathbf{\Omega}^2 = \mathbf{M_m^{-1}K_m}$, $\mathbf{Z} = diag(\zeta_i)$, $\mathbf{B_m} = \mathbf{\Phi^T B_0}$, $\mathbf{C_{mq}} = \mathbf{C_{0q}\Phi}$, $\mathbf{C_{mv}} = \mathbf{C_{0v}\Phi}$, where ζ_i represents the damping ratio of the corresponding eigenform. The damping ratio can be obtained from experimental modal analysis. In this work it is assumed to be 0.01.

Further transformation of the system (5) yields a state space model:

$$\dot{\mathbf{x}} = \mathbf{A}\mathbf{x} + \mathbf{B}\mathbf{u}, \quad \mathbf{y} = \mathbf{C}\mathbf{x} \tag{6}$$

$$\mathbf{A} = \begin{bmatrix} \mathbf{0} & \mathbf{\Omega} \\ -\mathbf{\Omega} & -\mathbf{Z\Omega} \end{bmatrix}, \ \mathbf{B_m} = \begin{bmatrix} \mathbf{0} \\ B_m \end{bmatrix}, \ \mathbf{C} = \begin{bmatrix} \mathbf{C_{mq}} & \mathbf{C_{mv}} \end{bmatrix}, \ \mathbf{x} = \begin{bmatrix} \mathbf{\Omega q_m} \\ \dot{\mathbf{q}}_\mathbf{m} \end{bmatrix} \tag{7}$$

The modal state space representation can be applied to mode shape i in a similar way.

$$\mathbf{A_{mi}} = \begin{bmatrix} 0 & \omega_i \\ -\omega_i & -2\zeta_i\omega_i \end{bmatrix}, \ \mathbf{B_{mi}} = \begin{bmatrix} 0 \\ b_{mi} \end{bmatrix}, \ \mathbf{C_{mi}} = \begin{bmatrix} \frac{c_{mqi}}{\omega_i} & c_{mvi} \end{bmatrix}, \ \mathbf{x_i} = \begin{bmatrix} \omega_i\mathbf{q}_{\mathbf{m}i} \\ \dot{\mathbf{q}}_{\mathbf{m}i} \end{bmatrix} \tag{8}$$

Matrices $\mathbf{A_{mi}}$, $\mathbf{B_{mi}}$ and $\mathbf{C_{mi}}$ are calculated for each position of the actuator/sensor pair and for each einenform i. These matrices are used to form the transfer functions according to the H_2 and H_∞ norms, in order to determine the optimal actuator/sensor placement [7, 2]. Here $\mathbf{B_{mi}}$ contains electric potential of the actuator and $\mathbf{C_{mi}}$ electric potential of the sensor:

$$\mathbf{B_{mi}} = \begin{bmatrix} 0 \\ \varphi_i^{(a)} \end{bmatrix}, \quad \mathbf{C_{mi}} = \begin{bmatrix} 0 & \varphi_i^{(s)} \end{bmatrix} \tag{9}$$

where $\varphi_i^{(a)}$ represents the sum of all electric potentials of the nodes at the upper side of the actuator surface and $\varphi_i^{(s)}$ the sum of all electric potentials of the nodes at the upper side of the sensor surface in FE model for each modeshape i.

4. Placement index and objective function

Based on the modal reduced-order state space model of the funnel-shaped inlet of the MRI tomograph, optimal positions of actuators and sensors are determined for first three eigenforms based on H_2 and H_∞ norms. Exact evaluation of these norms would require a high computational effort, especially when applied to full order FE models. Therefore a reduced order state space model is used. This approach can also be used for large structures of higher model orders [7]. In this work for determination of the optimal actuator/sensor placement

4

on a curved surface of the funnel both norms are evaluated both for the actuator and sensor positions as well as for all corresponding eigenforms considered both separately (mode shapes 1, 2, 3) and simultaneously (modes 1-2 and 1-3).

The transfer function based on the state space model (8) for each mode shape i is calculated in the following way:

$$\mathbf{G_i}(\omega) = \mathbf{C_{mi}}(j\omega\mathbf{I} - \mathbf{A_{mi}})^{-1}\mathbf{B_{mi}} \tag{10}$$

Approximate calculation of the H_2 norm results in:

$$\|\mathbf{G_i}\|_2 \approx \frac{\|\mathbf{B_{mi}}\|_2\|\mathbf{C_{mi}}\|_2}{2\sqrt{\zeta_i\omega_i}} = \frac{\|\mathbf{B_{mi}}\|_2\|\mathbf{C_{mi}}\|_2}{\sqrt{2\Delta\omega_i}} \approx \sigma_i\sqrt{2\Delta\omega_i} \tag{11}$$

Here $\mathbf{B_{mi}}$ represents the input matrix and $\mathbf{C_{mi}}$ the output matrix of the reduced state space model. ζ_i is the damping ratio of the corresponding mode shape i and $\Delta\omega_i = 2\zeta_i\omega_i$ represents a frequency segment around the resonant frequency. σ_i is the Hankel singular value for the corresponding mode shape i [2]. The H_∞ norm of the transfer function for a single mode shape i is calculated in the following way:

$$\|\mathbf{G_i}\|_\infty \approx \frac{\|\mathbf{B_{mi}}\|_2\|\mathbf{C_{mi}}\|_2}{2\zeta_i\omega_i} = \frac{\|b_{mi}\|_2\|c_{mi}\|_2}{2\zeta_i\omega_i} \tag{12}$$

The H_2 norm of the structure in the state space form is calculated as:

$$\|\mathbf{G}\|_2 \approx \sqrt{\sum_{i=1}^{n}\|\mathbf{G_i}\|_2^2} \tag{13}$$

with n being the number of mode shapes, $i = 1, ..., n$. The H_∞ norm of the structure represented in the state space fomr is calculated as:

$$\|\mathbf{G}\|_\infty \approx max\|\mathbf{G_i}\|_\infty \tag{14}$$

For iteratively changing positions of the actuators and sensors the norms of the transfer functions and therefore the norm of their sum can be calculated:

$$\|\mathbf{G_i}\|_{2,\infty} \approx \sqrt{\sum_{j=1}^{p_{a,s}}\|\mathbf{G_{ij}}\|_{(2,\infty)}^2}, \quad \text{for a single eigenform } i \text{ out of } n, \, i = 1, ..., n \tag{15}$$

$$\|\mathbf{G}\|_{2,\infty} \approx \sqrt{\sum_{j=1}^{p_{a,s}}\|\mathbf{G_j}\|_{(2,\infty)}^2}, \quad \text{for entire structure} \tag{16}$$

where p_a represents the number of possible actuator candidate locations and p_s of the sensor candidate locations. Generally the number of actuators and sensors is not necessarily equal.

In this work colocated actuator/sensor pairs $p_a = p_s$ are considered [7, 2]. With $j = 1, ..., p_a$ and $k = 1, ..., p_s$ the input and output matrices have the following form.

$$\mathbf{B_{mi}} = \begin{bmatrix} \mathbf{B_{mi}^1} & \mathbf{B_{mi}^2} & \dots & \mathbf{B_{mi}^j} & \dots & \mathbf{B_{mi}^{p_a}} \end{bmatrix}, \quad \mathbf{C_{mi}} = \begin{bmatrix} \mathbf{C_{mi}^1} \\ \mathbf{C_{mi}^2} \\ \dots \\ \mathbf{C_{mi}^k} \\ \dots \\ \mathbf{C_{mi}^{p_s}} \end{bmatrix} \tag{17}$$

For each eigenform, $\mathbf{B_{mi}^j}$ represents a (2×1)-block for a corresponding actuator position j and $\mathbf{C_{mi}^k}$ represents a (1×2)-block for each corresponding sensor position k, see (9). In this way the H_2 and H_∞ norms can be calculated for each corresponding actuator and each corresponding sensor related to each corresponding eigenform.

$$\|\mathbf{G_i}\|_{2,\infty}^2 \approx \sum_{j=1}^{p_a} \|\mathbf{G_i^j}\|_{(2,\infty)}^2, \quad \text{for an actuator} \tag{18}$$

$$\|\mathbf{G_i}\|_{2,\infty}^2 \approx \sum_{k=1}^{p_s} \|\mathbf{G_i^k}\|_{(2,\infty)}^2, \quad \text{for a sensor} \tag{19}$$

Here i is the corresponding eigenform and j are the actuator positions, where $j = 1, ..., p_a$ (p_a is the number of selected actuator positions) and $k = 1, ..., p_s$ (p_s is the number of selected sensor positions). For each eigenform the corresponding norms for corresponding actuator/sensor positions have to be calculated first. For the H_2 norm of the eigenform i for the corresponding actuator position j and the corresponding sensor position k applies:

$$\|\mathbf{G_i^j}\|_2 \approx \frac{\|\mathbf{B_{mi}^j}\|_2 \|\mathbf{C_{mi}}\|_2}{2\sqrt{\zeta_i \omega_i}}, \quad \|\mathbf{G_i^k}\|_2 \approx \frac{\|\mathbf{B_{mi}}\|_2 \|\mathbf{C_{mi}^k}\|_2}{2\sqrt{\zeta_i \omega_i}} \tag{20}$$

The H_∞ norm is calculated in a similar way:

$$\|\mathbf{G_i^j}\|_\infty \approx \frac{\|\mathbf{B_{mi}^j}\|_2 \|\mathbf{C_{mi}}\|_2}{2\zeta_i \omega_i}, \quad \|\mathbf{G_i^k}\|_\infty \approx \frac{\|\mathbf{B_{mi}}\|_2 \|\mathbf{C_{mi}^k}\|_2}{2\zeta_i \omega_i} \tag{21}$$

Using previously calculated norms the placement indices can be evaluated. The placement indices are defined for the H_2 and H_∞ norms for each eigenform i and for each actuator candidate location j and the sensor candidate location k where $j = 1, ..., p_a$ and $k = 1, ..., p_s$:

$$\eta_{i(2,\infty)}^j = \frac{\|\mathbf{G_i^j}\|_{(2,\infty)}}{\|\mathbf{G}\|_{(2,\infty)}}, \quad \eta_{i(2,\infty)}^k = \frac{\|\mathbf{G_i^k}\|_{(2,\infty)}}{\|\mathbf{G}\|_{(2,\infty)}} \tag{22}$$

$\mathbf{G_i^j}$ und $\mathbf{G_i^k}$ are the transfer functions for all possible actuator/sensor candidate locations. The placement indices can be organized in the form of a placement matrix for actuator/sensor

positions, where $p = p_a$ for the actuator positions and $p = p_s$ for the sensor positions:

$$\mathbf{N}_{(2,\infty)} = \begin{bmatrix} \eta^1_{1(2,\infty)} & \eta^2_{1(2,\infty)} & \cdots & \eta^{j,k}_{1(2,\infty)} & \cdots & \eta^p_{1(2,\infty)} \\ \eta^1_{2(2,\infty)} & \eta^2_{2(2,\infty)} & \cdots & \eta^{j,k}_{2(2,\infty)} & \cdots & \eta^p_{2(2,\infty)} \\ \vdots & \vdots & \vdots & \vdots & \vdots & \vdots \\ \eta^1_{i(2,\infty)} & \eta^2_{i(2,\infty)} & \cdots & \eta^{j,k}_{i(2,\infty)} & \cdots & \eta^p_{i(2,\infty)} \\ \vdots & \vdots & \vdots & \vdots & \vdots & \vdots \\ \eta^1_{n(2,\infty)} & \eta^2_{n(2,\infty)} & \cdots & \eta^{j,k}_{n(2,\infty)} & \cdots & \eta^p_{n(2,\infty)} \end{bmatrix} \tag{23}$$

The row elements correspond to eigenforms $i = 1, ..., n$ (n is the number of the eigenforms). The column elements correspond to each candidate location j and k. For actuators $j = 1, ..., p$ with $p = p_a$ (p_a is the number of possible actuator candidate locations) and for sensors $k = 1, ..., p$ with $p = p_s$ (p_s is the number of possible sensor candidate locations). For the objective function based on H_2 norm the placement indices are calculated as:

$$\eta^{j,k} = \sqrt{\sum_{i=1}^{n} (\eta^{j,k}_i)^2} \tag{24}$$

Index i denotes corresponding mode shapes, with $i = 1, ..., n$. For an actuator at position $j = 1, ..., p_a$ and for a sensor at position $k = 1, ..., p_s$, placement indices are calculated according to the H_∞ norm in the following way:

$$\eta^{j,k} = max(\eta^{j,k}_i) \tag{25}$$

For placement indices $\eta^{j,k}$ calculated based on both the H_2 and the H_∞ norm, the placement of the actuators and sensors is considered individually. For the simultaneous placement of actuators and sensors the placement indices for actuator of sensor are determined as:

$$\eta^{jk}_i = \frac{\|\mathbf{G}^{jk}_i\|}{\|\mathbf{G}^i_m\|} \tag{26}$$

Index i again corresponds to an eigenform, $i = 1, ..., n$. $\mathbf{G}^{jk}_i$ represents the transfer function for the eigenform i under simultaneous consideration of the actuator at position j and of the sensor at position k [7, 2].

5. Analyses and results

The model of the funnel shaped inlet of an MRI tomograph (represented in Fig. 1) is used as a starting point for various analyses preceding the optimization procedure for the actuator/sensor placement. The CAD geometry of the funnel (Fig. 1, right) represents the real

funnel (Fig. 1, left). The funnel geometry is complex (consisting of a flat and a curved part) and cannot be completely described analytically, which would be required for the parametrization of the actuator/sensor location and geometry. Nevertheless, for the optimal placement in this work only the curved surface of the funnel is relevant, and the analytical description of the curved surface as well as the parametrization of the actuator/sensor geometry and position was possible. In addition, the material properties of the funnel had to be adjusted in accordance with the mesh refinement and convergence of the material parameters through the FE simulations in order to obtain the model which will accurately describe structural behaviour and electro-mechanical properties of the piezoelectric patches implemented as actuators and sensors.
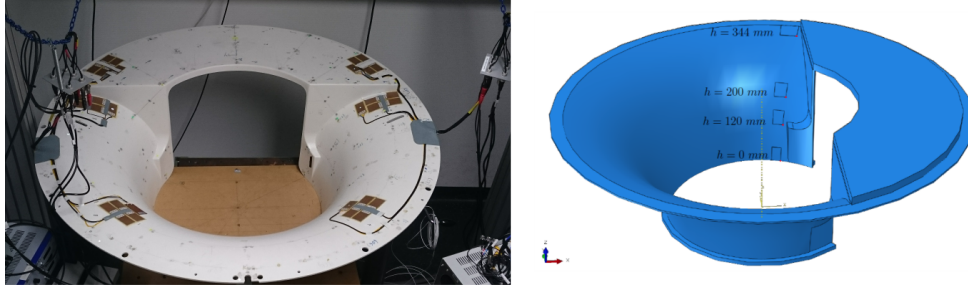
Figure 1. The funnel shaped inlet of an MRI tompograph (left) and its CAD model with exemplary positions of piezo patches at different heights (right).

The optimization procedure strongly depends on selected properties of the FE model used to obtain the reduced state space model. Therefore a thorough mesh convergence study and material parameter analyses were conducted. A starting point for this investigation is the aforementioned CAD model, with radius of the larger base of the funnel of $596mm$. For the mesh convergence study an initial model with isotropic material properties is adopted. The funnel consists of PVC (Polyvinylchlorid) and ABS (Acrylnitril-Butadien-Styrol). The model analyses are initiated with following material properties of a typical hard PVC with density $\rho_{\mathrm{PVC}} = 1465 \ \frac{kg}{m^3}$, elasticity modulus $E_{\mathrm{PVC}} = 3500 \ MPa$ and Poisson's ratio $\nu_{\mathrm{PVC}} = 0.4$. Geometry of the piezo-patches used for actuators and sensors varies with position on a curved surface in the height direction of the funnel (z-direction). All the transducers have constant curvature of $6°$ in xy- and xz-plane.

For the mesh convergence study 19 models of the funnel were considered, while determining first 10 eigenfrequencies for each of the models. The FE mesh was refined in regular steps, mesh size reduction of 10 A.G.S. (*Approximate Global Size*) per model, till no significant difference between the calculated eigenfrequencies of the two subsequent models was observed.

In that case the mesh was further refined in smaller steps (5 A.G.S. per model). In order to determine optimal meshing, the eigenfrequency error was observed. Subsequently only first three eigenfrequencies were considered for the mesh optimization purpose, since they could be compared with experimentally determined once, used as reference. The optimal meshing was adopted by computing the error between the eigenfrequencies of different models and their comparison. The mesh was adopted as optimal when the difference between the converging eigenfrequencies of the subsequent models lies under 5%. Similar convergence study was performed with respect to frequency response functions (FRFs) as well as the material parameters. The analyses resulted in a model with following material parameters adopted based on the similar criterion that the difference between the converging eigenfrequencies of the subsequent models lies under 5%: $\rho_{op} = 1230 \, \frac{kg}{m^3}, \quad E_{op} = 4000 \, MPa, \quad \nu = 0.4.$

According to procedure for determining placement indices and optimal placement described in Section 4 the optimization of actuator/sensor placement was performed on the curved surface of the MRI funnel. In the global procedure a total number of 600 candidate locations were considered and the placement indices were determined. The parametrization of the position for actuators and sensors was performed using two parameters: the height of a transducer in z-direction and the angle in radial direction in planes parallel to xy-plane at corresponding height. For each of the considered first three eigenforms of the funnel the placement indices were determined in following cases: for an actuator and for a sensor according to the H_2 and the H_∞ norms for individually considered mode shapes and for simultaneously considered mode shapes 1–2 and 1–3 both for an actuator and for a sensor and both according to the H_2 and the H_∞ norms. Due to a limited space in the following only selected results of the optimization are represented by plots showing the placement indices in a colour scale. Positions with highest values of the placement indices represent favourable placement for a given criterion. Fig. 2 represents the placement indices for individually considered mode shape 2 for the actuator (left) and the sensor placement (right).

The influence of the boundary conditions was also investigated. Different boundary conditions result in different mode shapes (Fig. 3) and influence in turn also the results of the optimal placement. In Fig. 4 the placement indices based on H_∞ norm are represented for individual consideration of the second eigenmode for a sensor in the case of clamped (left) and free boundary condition (right). Besides the boundary conditions which influence the mode shapes, the optimal placement depends also on selection of the eigenmodes of interest, i.e. if individual eigenmodes are considered, or multiple modes simultaneously. Selected results for simultaneous consideration of several modes are represented in Fig. 5.
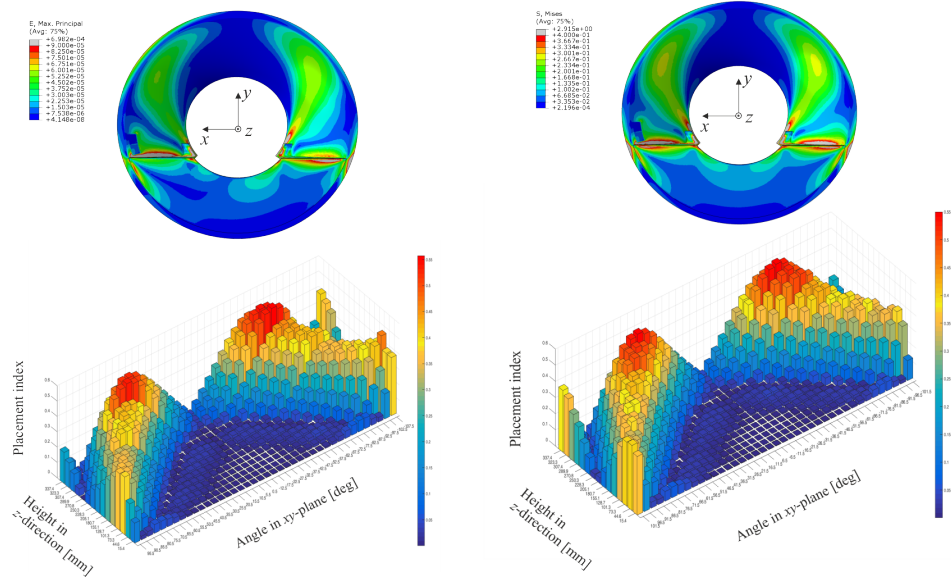
Figure 2. Placement indices at candidate locations for optimal placement of an actuator (left) and a sensor (right) based on the H_2 norm under consideration of the 2nd mode shape.
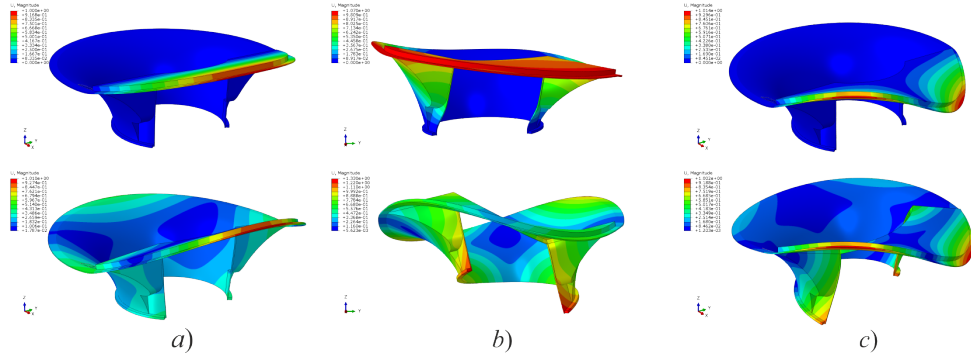
Figure 3. Comparison of the first three mode shapes for different boundary conditions: upper - clamped, lower - free; a) first mode, b) second mode, c) third mode.

6. Conclusions

In this work the optimization of the actuator/sensor placement on a funnel shaped inlet of the MRI tomograph was performed based approximate calculation of the H_2 and H_∞ norms. Applying the procedure described in Section 4, under consideration of single modes and simultaneous consideration of the first three eingenmodes of the funnel, the following
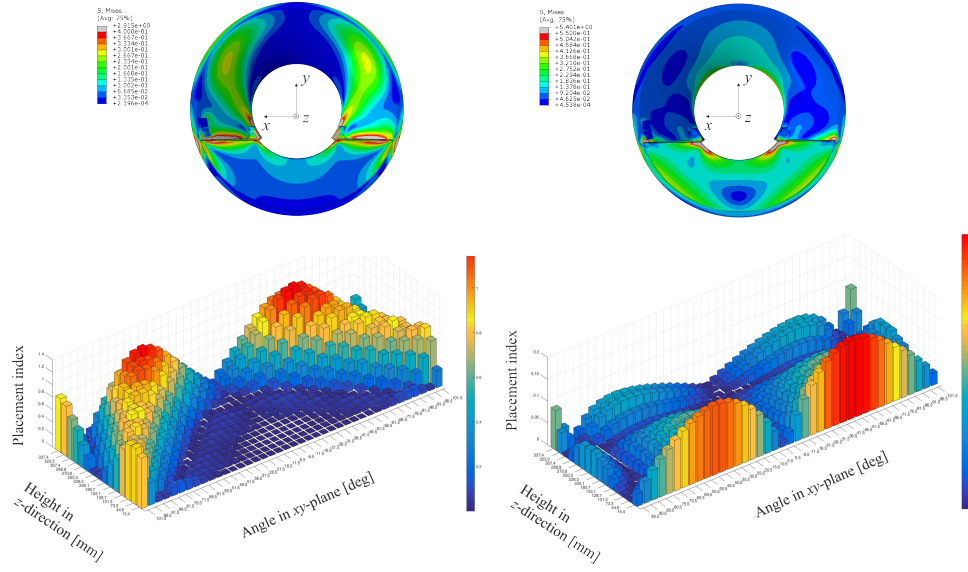
Figure 4. Placement indices at candidate locations for optimal placement of a sensor based on the H_∞ norm under consideration of the 2nd eigenform; boundary conditions: left - clamped, right - free.
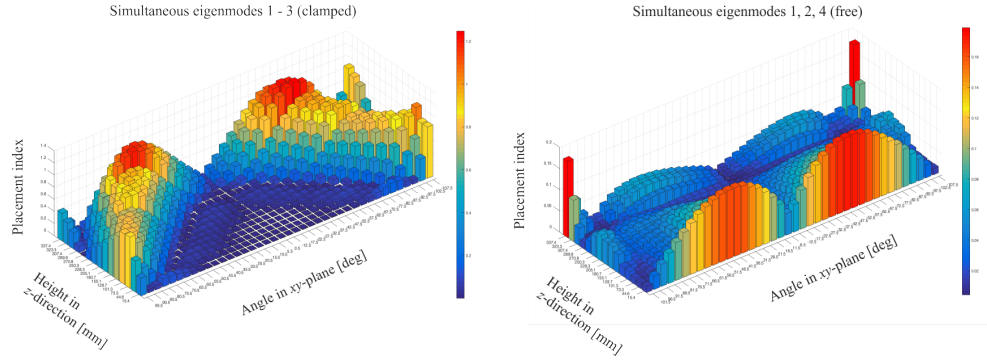
Figure 5. Placement indices for simultaneous consideration of eigenmodes using H_∞ norm for an actuator: left – modes 1–3 (clamped); right – modes 1,2,4 (free).

results for the optimal placement of actuators/sensors placed side by side are obtained.

$$h_{op1,2_f} = 337, 4 \ mm \tag{27}$$

$$\phi_{op1_f} = -107, 5° \text{ for the actuator}, \quad \phi_{op1_f} = -101, 5° \text{ for the sensor} \tag{28}$$

$$\phi_{op2_f} = 101, 5° \text{ for the actuator}, \quad \phi_{op2_f} = 95, 5° \text{ for the sensor} \tag{29}$$

$$h_{op3,4_f} = 15, 4 \ mm \tag{30}$$

$$\phi_{op3_f} = -52, 5° \text{ for the actuator}, \quad \phi_{op3_f} = -46, 5° \text{ for the sensor} \tag{31}$$

$$\phi_{op4_f} = 46, 5° \text{ for the actuator}, \quad \phi_{op4_f} = 40, 5° \text{ for the sensor} \tag{32}$$

Optimal placement results depend on the number of considered eigenmodes of interest, boundary conditions, but in preliminary consideration also the meshing has to be carefully performed.

References

[1] Edelstein, W., Mallozzi, R., Hedeen, R., El-Hamamsy, S.-A., Miller, M., Thompson, P., Ackermann, R., Amm, B., Fura, J., Radziun, M., Dean, D., Mansell, S., Purgill, D., and Vavrek, R. Low noise MRI scanner. *Grant Application number US 09/676,945* (2002).

[2] Nestorović, T., and Trajkov, M. Optimal actuator and sensor placement based on balanced reduced models. *Mechanical Systems and Signal Processing 36* (2013).

[3] Oveisi, A., Sukhairi, T. A., and Nestorović, T. Finite element-based software-in-the-loop for offline post-processing and real-time simulations. *Structural Engineering and Mechanics, Vol. 67, No. 6, pp. 643-658* (2018).

[4] Puri, G. *Python Scripts for ABAQUS: Learn by Example*, 1st ed. Gautam M. Puri, Charleston, South Carolina, 2011.

[5] Rutt, B. Safety issues in MRI. *The 11th Scientific Meeting of the International Society for Magnetic Resonance in Medicine* (2003).

[6] Takamori, H., Katsunuma, A., Sakakura, Y., Hamamura, Y., Ogo, Y., and Katayama, R. Quiet MRI with novel acoustic noise reduction. *Magnetic Resonance Materials in Physics, Biology and Medicine 13, pp. 139-144* (2002).

[7] Trajkov, M., and Nestorović, T. Optimal placement of piezoelectric actuators and sensors for smart structures. *15th International Conference on Experimental Mechanics ICEM 15, Porto Portugal* (2012).

[8] Wu, Y., Bowen, C., Mechefske, C., and Rutt, B. Gradient-induced acoustic and magnetic field fluctuation in a 4T whole-body MR imager. *Magnetic Resonance in Medicine 44, pp. 532-536* (2000).

Tamara Nestorović, Prof. Dr.-Ing.: Ruhr-Univeristät Bochum/Faculty of Civil and Environmental Engineering/Institute of Computational Engineering/Mechanics of Adaptive Systems, Universitätsstr. 150, 44801 Bochum, Germany (*tamara.nestorovic@rub.de*). The author gave a presentation of this paper during one of the conference sessions.

Kevin Hassw, M.Sc.: Ruhr-Univeristät Bochum/Faculty of Civil and Environmental Engineering/Institute of Computational Engineering/Mechanics of Adaptive Systems, Universitätsstr. 150, 44801 Bochum, Germany (*kevin.hassw@rub.de*).

Atta Oveisi, M.Sc.: Ruhr-Univeristät Bochum/Faculty of Civil and Environmental Engineering/Institute of Computational Engineering/Mechanics of Adaptive Systems, Universitätsstr. 150, 44801 Bochum, Germany (*atta.oveisi@rub.de*).

On the use of transmissibility to estimate vibro-acoustic responses in operational conditions

Miguel Neves, Dmitri Tcherniak, Hugo Policarpo, Nuno Maia

Abstract: This work briefly reviews the concepts of displacement transmissibility, acoustic transmissibility as well as vibro-acoustic transmissibility used to relate responses from some parts with their counterpart. One application where the concept appears naturally is the Operational Transfer Path Analysis (OTPA). It is based solely on operational measurements, not requiring any Frequency Response Functions (FRFs), thus significantly reducing the complexity of the measurement campaign and reducing the measurement time. The OTPA method has advantages depending on the conditions of the problem. Here, the authors are concerned with the influence of the stiffness values of the vibration source (excitation) mounts on the response inside the structurally connected acoustic cavity. In this article, the authors conclude that if the stiffness of the mounts approaches zero, the OTPA contributions coincide with the baseline ones independently of having cross talk or not. If the mount stiffness approaches infinity, the contributions coincide with the OTPA contributions obtained when the indicator signals are measured on the passive side of the mount. Therefore, placing the indicator accelerometers on the active side of the mounts are advantageous as this will produce a lesser error than when they are placed on the passive side of the mounts. Placing the indicator accelerometers on the both sides of the mount produces no cross-talk error. These results illustrate in which conditions the contributions from conventional TPA and OTPA compare.

1. Introduction

The use of transmissibility in structural dynamics may be regarded from several points of view and have different and useful applications. Pioneer attempts to extend the vibration transmissibility, from Single Degree-of-Freedom (SDOF) systems to Multiple Degree-of-Freedom (MDOF), are described e.g. in [1-4]. The generalization to MDOF is found e.g. in [5] relating two sets of response positions in matrix form.

In acoustics and vibro-acoustics, a multipoint transmissibility can be set as in [6] using a discrete acoustic transmissibility to measure a wall pressure spectrum, and as in [7], where scalar transmissibility is considered of high potential for operational modal analysis, model updating [8] and structural health monitoring [9].

When technical difficulties arise in measuring operational responses at some co-ordinates of the structure (e.g. at inaccessible co-ordinates), the transmissibility matrix evaluated beforehand, by measuring a few responses, can help in overcoming those difficulties [10].

Vibration excitation forces can be estimated from measured responses [11-15]. The same can be achieved through the use of force transmissibility [16]. As mentioned in [17], expression relating force transmissibility and displacement transmissibility are not identical for MDOF systems [18].

Several applications of the transmissibility approach have been developed, e.g. the dynamic response estimation [19], damage detection [20, 21], operational modal analysis [22], evaluation of unmeasured FRFs [23], and force identification [24,25]. As in transfer path analysis (TPA) the measurement of transfer functions may often be time consuming and error-prone, several authors sought for easier and more reliable ways through the use of the transmissibility matrix extracted from operational measurements (see Tcherniak [26,27] and Tcherniak et al. [28, 29]).

In acoustics, few publications are fully dedicated to transmissibility, but many cover its applications, like e.g. OTPA. Among the ones dedicated to transmissibility, let us mention the works of Devrient et al. [30], Kletschkowski [31], Weber et al. [32], Guedes and Neves [33], and Guedes [34]. In [35], the acoustic multipoint transmissibility is developed for noise source identification and reconstruction.

Recently, a renewed interest for faster TPA methods [36] has driven to the use of operational data with the transmissibility concept. Several related methods have been named as Operational TPA [37], blocked-force TPA, Operational Path Analysis with eXogenous inputs (OPAX), Gear Noise Propagation, in situ Source Path Characterization and Virtual Acoustic Prototyping. Meanwhile, literature has also been produced on the limitations and drawbacks of these methods, see e.g. [38], including issues in the estimation of transmissibility, or errors due to coupling between path inputs, etc.

In this paper, the generalized concepts for vibration and acoustic transmissibility are described in section 2. The extension to vibro-acoustic transmissibility between MDOFs is described in the section 3. In section 4, the authors elaborate on the operational conditions and signal processing with the objective of reducing errors. Finally, in section 5, the authors present the main conclusions.

2. Fundamentals

The concept of vibration transmissibility and acoustic transmissibility between MDOFs is briefly reviewed in this section. For a detailed description, the authors recommend reading [18, 23, 35].

2.1. Vibration transmissibility in MDOF dynamic systems

For a linear viscoelastic solid, the structural (subscript 's') response may be given by

$$[M_s]\{y^{\cdot\cdot}(t)\} + [C_s]\{y^{\cdot}(t)\} + [K_s]\{y(t)\} = \{f_s(t)\} \tag{1}$$

where $[M_s]$, $[C_s]$ and $[K_s]$ are the mass, damping and stiffness matrices, respectively; $\{y\}$ is the nodal displacement vector; the dots are for its time derivatives; t is time and $\{f_s\}$ is the applied excitation load vector.

For a harmonic excitation load the steady-state response can be obtained from

$$\big[[K_s] + i\omega[C_s] - \omega^2[M_s]\big]\{Y(\omega)\} = \{F_s(\omega)\} \quad\Leftrightarrow\quad [Z_s(\omega)]\{Y(\omega)\} = \{F_s(\omega)\} \tag{2}$$

where $[Z_s(\omega)]$ is the dynamic stiffness matrix and ω is the excitation frequency. The receptance matrix $[H_s(\omega)]$ may be obtained as

$$\{Y(\omega)\} = [Z_s(\omega)]^{-1}\{F_s(\omega)\} = [H_s(\omega)]\{F_s(\omega)\} \tag{3}$$

The generalization to MDOF requires the definition of some sets of DOFs. The sets U and K are composed by coordinates where the responses are measured and the set A by coordinates where loads can be applied (may include DOFs from other sets). These sets can be unions spatially separated subsets.

From Eq. (3) the amplitudes $\{Y_U\}$ and $\{Y_K\}$ are described by

$$\begin{cases} \{Y_U\} = [H_{s\,UA}]\{F_{sA}\} \\[4pt] \{Y_K\} = [H_{s\,KA}]\{F_{sA}\} \end{cases} \tag{4}$$

where $[H_{sUA}]$ is the truncated FRF matrix to the sets of DOFs U and A (representing the respective co-ordinates). To obtain the respective transmissibility matrix, from Eq. (4), one can use the pseudo-inverse of $[H_{sKA}]$, i.e.

$$\{Y_U\} = [H_{sUA}] \cdot ([H_{sKA}]^+)\{Y_K\} = \left[T_{UK}^{A\,(s)}\right]\{Y_K\} \tag{5}$$

Note that the pseudo-inversion requires the set K to be larger or equal than the set A.

2.2. Acoustic pressure transmissibility

In a similar way, an acoustic system of linear dynamic inviscid and non-flowing fluid (subscript 'f') may be modelled in the frequency-domain (i.e. steady-state case) using the following equation

$$\big[[K_f] + i\omega[C_f] - \omega^2[M_f]\big]\{P(\omega)\} = \{F_f(\omega)\} \;\; or \;\; [Z_f(\omega)]\{P(\omega)\} = \{F_f(\omega)\} \tag{6}$$

where $[K_f]$, $[C_f]$ and $[M_f]$ are the acoustic stiffness, acoustic damping and acoustic mass matrices, respectively; $\{P(\omega)\}$ is the sound pressure amplitude vector in steady-state; and $\{F_f(\omega)\}$ is the force vector associated with the internal sound sources and/or imposed velocities. As $[Z_f(\omega)]\{P(\omega)\} = \{F_f(\omega)\}$, the steady-state pressure $\{P(\omega)\}$ is given by

$$\{P(\omega)\} = [Z_f(\omega)]^{-1}\{F_f(\omega)\} = [H_f]\{F_f(\omega)\} \tag{7}$$

where $[H_f]$ is the frequency-response matrix in the acoustic system.

The domain is divided in the four sets of coordinates: 1) the set of known coordinates K (where pressure can be measured); 2) the set of known coordinates U (where the pressure amplitudes are unknown or to be estimated); 3) the unknown set of coordinates S (where sources are located); and 4) the set C representing the remaining coordinates. Note that the sets can be unions of subsets spatially separated.

Assuming that no sources exist other than the ones in set S, i.e. $\{F_{fK}(\omega)\}$, $\{F_{fU}(\omega)\}$ and $\{F_{fC}(\omega)\}$ are zero, then Eq. (7) can be written as

$$\begin{Bmatrix} P_K \\ P_U \\ P_S \\ P_C \end{Bmatrix} = \begin{bmatrix} H_{fKS} \\ H_{fUS} \\ H_{fSS} \\ H_{fCS} \end{bmatrix} \{F_{fS}\} \tag{8}$$

From Eq. (8), one can obtain an expression relating $\{P_U(\omega)\}$ with $\{P_K(\omega)\}$. The acoustic pressure transmissibility matrix between sets U and K, assuming the sources acting only in set S, is given by

$$\{P_U(\omega)\} = [H_{fUS}] \cdot [H_{fKS}]^+ \{P_K(\omega)\} = \left[T_{UK}^{S\,(f)}\right]\{P_K(\omega)\} \tag{9}$$

where $\left[T_{UK}^{S\,(f)}\right]$ has dimensions $n_U \times n_K$, respectively the number of coordinates in sets U and K. It requires that n_K be greater or equal than n_S. This matrix may have ill-conditioning problems that shall be taken into account.

A disadvantage of existing Operational Acoustic Modal Analysis (OAMA) [29] is that non-measured acoustic sources must be pure white noise. But, in operation one advantage of the transmissibility functions is that they can be measured without the knowledge of the excitation forces.

3. Vibro-acoustic transmissibility

In the coupled model the pressures at solid-fluid interface are considered as in the last term of the following equation for the structural part

$$\left[[K_s] + i\omega[C_s] - \omega^2[M_s]\right]\{Y(\omega)\} = \{F_s(\omega)\} - [A]\{P(\omega)\} \tag{10}$$

where matrix [A] is the coupling matrix that in this case transfers the pressure from the acoustic fluid to the structure (for a detailed description on the formulation aspects, see [39]).

The following fluid-structure interface condition is used

$$\frac{\partial p}{\partial n} = -\rho \ddot{y}_n \tag{11}$$

which is expressed in the acoustic fluid part by adding the influence of the displacement at the boundary (last term in Eq. (12))

$$\left[[K_f] + i\omega[C_f] - \omega^2[M_f]\right]\{P(\omega)\} = \{F_f(\omega)\} - \omega^2\rho[A]^t\{Y(\omega)\} \tag{12}$$

Combining the modified structural Finite Element (FE) model of Eq. (10) with the modified acoustic FE model of Eq. (12), one obtains the following Eulerian FE/FE model for an interior coupled vibro-acoustic system [39]

$$\left(\begin{bmatrix} K_s & A \\ 0 & K_f \end{bmatrix} + i\omega\begin{bmatrix} C_s & 0 \\ 0 & C_f \end{bmatrix} - \omega^2\begin{bmatrix} M_s & 0 \\ -\rho A^t & M_f \end{bmatrix}\right)\begin{Bmatrix} Y(\omega) \\ P(\omega) \end{Bmatrix} = \begin{Bmatrix} F_s(\omega) \\ F_f(\omega) \end{Bmatrix} \tag{13}$$

This coupled system model the Fluid-Structure Interaction (FSI) and may be expressed as

$$([K^{FSI}] + i\omega[C^{FSI}] - \omega^2[M^{FSI}])\{X(\omega)\} = \{F^{FSI}\} \Leftrightarrow \{X(\omega)\} = [H^{FSI}]\{F^{FSI}\} \tag{14}$$

From Eq. (14), it is possible to relate some displacement responses on a new set A (that defines coordinates where displacements are of interest), as well as some pressures responses on a new set B (that defines coordinates where pressures are of interest), i.e.

$$\{Y_A(\omega)\} = \left[H_{AA}^{FSI}\right]\{F_A(\omega)\} \tag{15a}$$

$$\{P_B(\omega)\} = \left[H_{BA}^{FSI}\right]\{F_A(\omega)\} \tag{15b}$$

Finally, pressure responses can be related to displacement responses as

$$\{P_B(\omega)\} = \left[H_{BA}^{FSI}\right]\left[H_{AA}^{FSI}\right]^{-1}\{Y_A(\omega)\} = \left[T_{BA}^{FSI}\right]\{Y_A(\omega)\}, \tag{16}$$

which defines the corresponding vibro-acoustic transmissibility $\left[T_{BA}^{FSI}\right]$.

4. On the noise source contributions from conventional TPA and Operational TPA

Identifying and understanding noise sources and noise propagation paths is an important aspect in industries like in automotive Noise, Vibration, and Harshness (NVH). A typical problem in NVH source-path-receiver involves the noise and vibration at sensitive locations (driver's ears, steering wheel, etc.), which are instrumented by receivers (microphones and accelerometers).

The noise sources, e.g. the engine and the ventilation fan, can be considered two uncorrelated sources. In this work, the considered *noise propagation paths* from the engine to the cabin are essentially two *structure borne* paths (through two engine mounts) and one *air-borne* path (the fan

takes the air-borne path to reach the receivers). The TPA estimates *contributions* from each source and propagation paths.

4.1. Conventional TPA and Operational TPA

Although this study can be generalized to multiples receivers, we consider the simple case where only one receiver exist. In the conventional TPA approach, one has u_n ($n=1,...,N$) noise or vibration sources (or paths) to be characterized. The C_n contributions of n-th source to the total noise Y (at the receiver position) is

$$Y = \sum_{n=1}^{N} C_n \tag{17}$$

where each contribution C_n is estimated as

$$C_n = H_{Yn} U_n \tag{18}$$

Here, the capital letters denote the complex Fourier spectra of the corresponding physical quantities in time domain that are denoted by small letters.

The contribution C_n is a product of H_{Yn}, the FRF, and U_n, the operational source strength. The FRFs can be measured in the lab (when the machine is not under operation), but it is not possible or at least difficult to measure the source strength U_n in operation. This lead to the use of indirect methods.

The most usual indirect method is the matrix inversion method. In this method, indicator sensors (indicated by v) are placed near the sources (indicated by u), and the FRFs between the sources and the indicators are measured to form the indicator-to-source matrix $[H_{VU}]$.

When the machine is under operation, the signals from the indicator sensors $\{\tilde{V}\} = \{\tilde{V}_1, \tilde{V}_2, ..., \tilde{V}_{N_V}\}^T$ are measured (where $\sim$ stands for measured). Based on the relation

$$\{\tilde{V}\} = [H_{VU}]\{U\} \tag{19}$$

where $\{U\} = \{U_1, U_2, ..., U_{N_U}\}^T$, the operational source strength is estimated as

$$\{U\} = [H_{VU}]^{-1}\{\tilde{V}\} \tag{20}$$

This inversion requires that the number of the indicator sensors N_V be greater or equal to the number of sources N_U.

The conventional TPA method involves a set of FRFs to be measured, which is a time consuming process. This, a faster technique is of major interest. One answer to this problem is the so-called Operational TPA.

OTPA is based solely on operational measurements (conducted when the machine is in operation) and does not require any FRFs. On the one hand, it significantly reduces the complexity of

the measurement task as well as its measurement time. On the other hand, OTPA has been criticized as it may provide incorrect results in some situations.

OTPA is based on the concept of transmissibility and it can be directly derived from the conventional TPA. In what follows, one analyses its basis in order to identify some of its drawbacks and possibly find how to circumvent them.

Rewriting (19) in matrix notation

$$Y = \{H_{Y1} \quad H_{Y2} \quad \dots \quad H_{YN}\}\{U_1, U_2, \dots U_N\}^T = \{H_{YU}\}^T\{U\} \tag{21}$$

and substituting Eq. (20) into Eq. (21) yields

$$Y = \{H_{YU}\}^T[H_{VU}]^{-1}\{\tilde{V}\} = \left\{T_{YV}^{(U)}\right\}^T\{\tilde{V}\} \tag{22}$$

Thus, the estimated response Y can be expressed as a linear combination of the indicator responses $\{\tilde{V}\}$.

The OTPA method postulates that if the indicator sensors are placed in a vicinity of noise sources the conventional TPA contributions C_n can be approximated by

$$C_n \approx S_n = T_{Yn}^{(U)}\tilde{V}_n \tag{23}$$

where S_n is the OTPA contribution from the n-th source/path, and T_{Yn} is the corresponding element of the transmissibility matrix. This vicinity requirement is based on empirical evidence, but the problem can be more complex as it will be discussed in the next section.

4.2.   On reducing OTPA error in the structural path

Here, let us consider, as in Fig. 1a, a structural path where the forces acting across the mounts (energy source) are $\{U\} = \{F_1, F_2\}^T$. The indicator accelerometers are placed on the passive side of the mounts, close to the mount connection interfaces, and so $\{\tilde{V}\} \equiv \{X_p\}$, where $\{X_p\}$ denotes the displacement at the passive side of the mounts.

The FRF matrices are

$$[H_{VU}] \equiv \left[H_{X_pF}\right] = \begin{bmatrix} H_{11} & H_{12} \\ H_{21} & H_{22} \end{bmatrix} \tag{24}$$

$$\{H_{YU}\} \equiv \{H_{YF}\} = \left\{H_{YF_1} \quad H_{YF_2}\right\}^T \tag{25}$$

In order to discuss the influence of the cross terms, H_{12} and H_{21}, on the OTPA contributions S_n, one replaces in Eq. (24) the original matrix $\left[H_{X_pF}\right]$ by the new one $\begin{bmatrix} H_{11} & \varepsilon H_{12} \\ \varepsilon H_{21} & H_{22} \end{bmatrix}$. The factor ε reflects the level of cross-talk between the sources and indicator sensors, i.e. $\varepsilon = 0$ means no cross-

talk and $\varepsilon = 1$ means full cross-talk. Substituting Eq.s (24) and (25) in Eq. (22) and considering Eq. (23), one obtains the expressions for S_1 and S_2, which after expanding in Taylor series around $\varepsilon = 0$, yields the following OTPA contributions:

$$S_1 = C_1 + \left(-\frac{H_{21}H_{YF_2}F_1}{H_{22}} + \frac{H_{12}H_{YF_1}F_2}{H_{11}}\right)\varepsilon + O(\varepsilon^2) \tag{26}$$

$$S_2 = C_2 + \left(\frac{H_{21}H_{YF_2}F_1}{H_{22}} - \frac{H_{12}H_{YF_1}F_2}{H_{11}}\right)\varepsilon + O(\varepsilon^2) \tag{27}$$

The OTPA contributions will have an error of order ε, which in structure borne case will depend on the frequency and can be quite significant. However, it is clear from Eq. (26) and Eq. (27) that the sum of the OTPA contributions differs from the baseline by a term of order ε^2.

a)   b)   c)
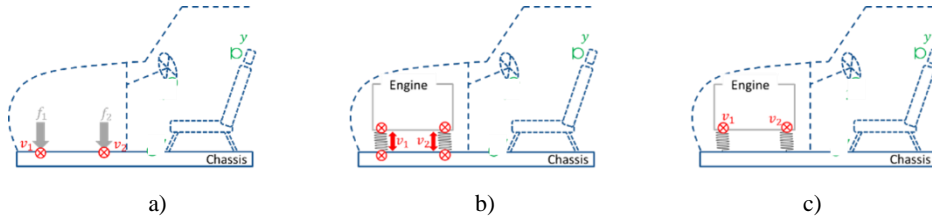
Figure 1. Setup illustrations on measuring operational mount deformation with accelerometers placed: a) on the passive side of the mounts and close to the mount connection interfaces; b) on *both* sides of the mount; and c) on the active sides of the mounts.

The following question arises from the above results: can we devise a measurement setup that eliminates or reduces the OTPA error due to the cross-talk?

As observed, OTPA produces correct results if there is no cross-talk, i.e. if $[H_{VU}]$ is diagonal. Also, the operational forces acting through the mounts are expressed by $F_i = K_i\Delta X_i$, where K_i is the stiffness and ΔX_i is the operational deformation of the i-th mount. In matrix notation,

$$\{F\} = \begin{bmatrix} K_1 & 0 \\ 0 & K_2 \end{bmatrix}\begin{Bmatrix} \Delta X_1 \\ \Delta X_2 \end{Bmatrix} = [K]\{\Delta X\} \tag{28}$$

Solving for $\{\Delta X\}$ one obtains

$$\{\Delta X\} = [K]^{-1}\{F\} = \begin{bmatrix} 1/K_1 & 0 \\ 0 & 1/K_2 \end{bmatrix}\{F\} \tag{29}$$

One can notice that if the vector $\{\Delta X\}$ is declared as the vector of indicator signals, $\{\tilde{V}\} \equiv \{\Delta X\}$, matrix $[K]^{-1}$ becomes the $[H_{VU}]$ matrix, and it is diagonal. So, if one can devise a sensor that measures ΔX_i, and use such sensors for measuring the indicator signals, the $[H_{VU}]$ will be diagonal, and the OTPA method will provide exact contributions.

In principle, one can suggest that it is rather easy to implement such a sensor by placing accelerometers on *both* sides of the mount (see Fig. 1b), and subtracting one's readings from another. In this case, the OTPA contributions of each mount will be correct.

In automotive industry, many mounts connecting substructures are soft; for these mounts the vibration magnitude of the active side X_a can be much higher than of its passive counterpart X_p.

One can expect that, in the case of such soft mounts, placing the indicator accelerometers on the active sides of the mounts (see Fig. 1c), will produce almost correct OTPA contributions. Let us quantify them as $\{\tilde{V}\} \equiv \{X_a\}$. Constructing $\{\tilde{V}\}$ from the already introduced components,

$$\{\tilde{V}\} \equiv \{X_a\} = \{X_p\} + \{\Delta X\} = \left(\left[H_{X_pF}\right] + [K]^{-1}\right)\{F\} \tag{30}$$

For the sake of simplicity, the indices of $\left[T_{YV}^{(U)}\right]$ will be omitted in the following text, and the transmissibility matrix will be simply denoted as $[T]$. One can readily derive the respective transmissibility matrix [T] (in this case a vector) as:

$$\{T\} = \frac{1}{det}\begin{Bmatrix} H_{YF_1}K_1 + H_{YF_1}H_{22}K_1K_2 - \varepsilon\,H_{YF_2}H_{21}K_1K_2 \\ H_{YF_2}K_2 + H_{YF_2}H_{11}K_1K_2 - \varepsilon H_{YF_1}H_{12}K_1K_2 \end{Bmatrix}^T \tag{31}$$

where $det = 1 + H_{11}K_1 + H_{22}K_2 + H_{11}H_{22}K_1K_2 - \varepsilon^2\,K_1K_2$. Then the corresponding OTPA contributions S are

$$S_1' = C_1 + \frac{(F_2H_{YF_1}K_1 + F_2\,H_{YF_1}H_{22}K_1\,K_2)H_{12} - (F_1H_{YF_2}K_2 + F_1H_{YF_2}H_{11}K_1K_2)H_{21}}{1 + H_{11}K_1 + H_{22}K_2 + H_{11}H_{22}K_1K_2}\varepsilon\, + O(\varepsilon^2)$$

$$S_2' = C_2 + \frac{-(F_2H_{YF_1} + F_2H_{YF_1}H_{22}K_1K_2)H_{12} + (F_1H_{YF_2}K_2 + F_1H_{11}H_{YF_2}K_1K_2)H_{21}}{1 + H_{11}K_1 + H_{22}K_2 + H_{11}H_{22}K_1K_2}\varepsilon\, + O(\varepsilon^2) \tag{32}$$

It is difficult to interpret expressions in Eq. (32), but one can observe that they are similar in the sense that, if there is no cross-talk then $S_1' = C_1$ and $S_2' = C_2$. Also, if the contributions summed up, the terms of the order of ε cancel out, and

$$S_1' + S_2' = C_1 + C_2 + O(\varepsilon^2) \tag{33}$$

Another interesting property of S'_1 and S'_2 is that:
- if the stiffness of these mounts approaches zero, the OTPA contributions coincide with the baseline ones, even for $\varepsilon \neq 0$:

$$\lim_{\substack{k_1 \to 0 \\ k_2 \to 0}} S_1' = C_1 \;\text{ and }\; \lim_{\substack{k_1 \to 0 \\ k_2 \to 0}} S_2' = C_2 \tag{34}$$

- if the stiffness of these mounts approaches infinity, the contributions coincide with the OTPA contributions obtained when the indicator signals are measured on the passive side of the mount:

$$\lim_{\substack{k_1 \to \infty \\ k_2 \to \infty}} S_1' = S_1 \quad \text{and} \quad \lim_{\substack{k_1 \to \infty \\ k_2 \to \infty}} S_2' = S_2 \qquad (35)$$

5. Conclusions

The formulations for vibration, acoustic as well as their extension to the vibro-acoustic transmissibility problem were presented. Some considerations have been done to the application of these concepts with respect to OAMA, TPA and OTPA.

A real advantage of OTPA is the use of transmissibility matrices that can be estimated without measuring FRFs. In this work, the authors analysed the conditions where the sum of the OTPA contributions may differ from the baseline (conventional TPA) in the presence of a cross-talk factor ε and conclude that for small values of ε they differ by a term of order ε^2.

Answering to a question on how to devise a measurement setup that eliminates or reduces the OTPA error due to cross-talk, it is clear for the given examples that placing the indicator sensors on the active side of the mounts is advantageous. Indeed, this configuration will produce a smaller error than when they are placed on the passive side of the mounts. The best option is to place the indicator sensors on both sides of the mounts, as it produces no cross-talk.

Acknowledgments

References

[1]   Snowdon, J.C., Mechanical four-pole parameters: transmission matrices, Report TM76-122, Pennsylvania State University, Applied Research Lab, 1976.

[2]   Vakakis, A.F., Dynamic analysis of a unidirectional periodic isolator, consisting of identical masses and intermediate distributed resilient blocks, Sound and Vibration 103,1 (1985), 25-33.

[3]   Liu, W., Ewins, D.J., Transmissibility Properties of MDOF Systems, Proceedings of 16th International Operational Modal Analysis Conference (IMAC XVI), Santa Barbara, California (1998), 847-854.

[4]   Varoto, P.S., McConnell, K.G., Single Point vs Multi Point Acceleration Transmissibility Concepts in Vibration Testing, Proceedings of 12th International Modal Analysis Conference (IMAC XVI), Santa Barbara, California, USA, (1998), 83-90.

[5]   Maia, N.M.M., Silva, J.M.M., Ribeiro, A.M.R., The Transmissibility Concept in Multi-Degree-of-Freedom Systems, Mechanical Systems and Signal Processing 1, 15,(2001), 129-137.

[6]   Curlinf, L.L.R., Païdoussis, M.P., A discrete method for the acoustic transmissibility of a pressure transducer-in-capsule arrangement, Mechanical Systems and Signal Processing 9, 3, (1995), 225–241.

[7]   Devriendt, C., Guillaume, P., Identification of modal parameters from transmissibility measurements, Sound and Vibration 314, (2008), 343–356.

[8]   Steenackers, G., Devriendt, C., Guillaume, P., On the use of transmissibility measurements for finite element model updating, Sound and Vibration 303, (2007),707–722.

[9] Devriendt, C., Presezniak, F., Sitter, G., K. Vanbrabant, T. D., Troyer, S. Vanlanduit, P. Guillaume, Structural health monitoring in changing operational conditions using transmissibility measurements, in: Proceedings of International Conference on Structural Engineering Dynamics (ICEDyn 2009), Ericeira, Portugal, (2009).

[10] Maia, N.M.M., Almeida, R.A.A., Urgueira, A.P.V., Understanding Transmissibility Properties, in: Proceedings of 26th Intern. Modal Analysis Conference (IMAC XXVI), Orlando, Florida, USA, (2008).

[11] Hillary, B., Indirect Measurement of Vibration Excitation Forces, Ph.D. thesis, Imperial College of Science, Technology and Medicine, Dynamics Section, London, UK, 1983, Supervisor: D.J. Ewins.

[12] Stevens, K.K., Force Identification Problems – an overview, Proceedings of the 1987 SEM Spring Conference on Experimental Mechanics, Houston, TX, USA, (1987).

[13] Mas, P., Sas, P., Wyckaert, K, Indirect force identification based on impedance matrix inversion: a study on statistical and deterministic accuracy, Proceedings of 19th International Seminar on Modal Analysis, Leuven, Belgium, (1994),1049-65.

[14] Dobson, B.J., Rider, E., A review of the indirect calculation of excitation forces from measured structural response data, Proceedings of the Institution Mechanical Engineers, Part C, Journal of Mechanical Engineering Science, 204, 2, (1990), 69-75.

[15] Zhang H., Schulz M.J. and F. Feruson, Structural Health Monitoring Using Transmittance Functions, Mechanical Systems and Signal Processing, 13, 5, (1999), 765-787.

[16] Maia, N.M.M., Fontul, M., Ribeiro, A.M.R. Transmissibility of Forces in Multiple-Degree-of-Freedom Systems, Proceedings of ISMA 2006, Noise and Vibration Engineering, Leuven, Belgium, (2006).

[17] Maia, N.M.M., Urgueira, A.P.V., Almeida, R.A.B., Whys and Wherefores of Transmissibility, in: Dr. Francisco Beltran-Carbajal (ED.), Vibration Analysis and Control - New Trends and Developments, InTech, (2011), 187-216.

[18] Lage, Y.E., Neves, M.M., Maia, N.M.M., Tcherniak, D., Force Transmissibility versus Displacement Transmissibility, Sound and Vibration, 333, 22, (2014), 5708-5722.

[19] Law, S.S., Li, J., Ding, Y., Structural response reconstruction with transmissibility concept in frequency domain, Mechanical Systems and Signal Processing 25, 3, (2011), 952–968.

[20] Maia, N.M.M., Urgueira, A.P.V., Almeida, R.A.B., An Overview of the Transmissibility Concept and Its Application to Structural Damage Detection, Topics in Modal Analysis I, Volume 5, Proceedings of the Society for Experimental Mechanics Conference 30, (2012), 137-15.

[21] Sampaio, R.P.C., Maia, N.M.M., Ribeiro, A.M.R., Silva, J.M.M., Damage detection using the transmissibility concept, Proceedings of the 6th International Congress on Sound and Vibration (ICSV 6), Copenhagen, (1999), 2559–2568.

[22] Devriendt, C, De Sitter, G, Guillaume, P, An operational modal analysis approach based on parametrically identified multivariable transmissibilities, Mechanical Systems and Signal Processing, 24, 5, (2010), 1250–1259.

[23] Urgueira, A.P.V., Almeida, R.A.B., Maia N.M.M., On the use of the transmissibility concept for the evaluation of frequency response functions. Mechanical Systems and Signal Processing 25, 3, (2011), 940–951.

[24] Neves, M.M.; Maia, N.M.M., Estimation of Applied Forces Using The Transmissibility Concept, Proceedings of the International Conference on Noise and Vibration Engineering (ISMA 2010), Leuven, Belgium, (2010), 3887-3897.

[25] Lage, Y.E., Maia, N.M.M.; Neves, M.M.; Ribeiro, A.M.R., Force identification using the concept of displacement transmissibility, Sound and Vibration, 332, 7, (2013), 1674-1686.

[26] Tcherniak, D., Application of Transmissibility Matrix method to structure borne path analysis, Proceedings of NAG/DAGA conference, Rotterdam, Holland, (2009).

[27] Tcherniak, D., Application of operational noise path analysis to systems with rotational degrees of freedom, in: Sas, P., Bergen, B. (Eds.), Proceedings of the International Conference on Noise and Vibration Engineering (ISMA 2010), Leuven, Belgium, (art. no. 528), (2010), 3943-3952.

[28] Tcherniak, D.,Schuhmacher, A.P., "Application of Transmissibility Matrix Method to NVH Source Contribution Analysis", Proceedings of the 27th International Modal Analysis Conference (IMAC XXVII), Orlando, Florida, (2009).

[29] Vaitkus, D., Tcherniak, D., Brunskog, J., Application of vibro-acoustic operational transfer path analysis, Applied Acoustics, 154, (2019), 201-212.

[30] Devriendt, C., Presezniak, F., De Sitter, G., Operational acoustic modal analysis using transmissibility measurements, in Proceedings of the ICSV 16, edited by M. Pawelczyk and D. Bismor, 5-9 July,(2009), Krakow, Poland.

[31] Kletschkowski, T., Inverse noise source identification in an aircraft cabin. University of Applied Sciences, Hamburg, 2013.

[32] Weber, M., Kletschkowski, T., Sachau, D., Identification of noise sources by means of inverse finite element method using measured data. In Acoustics'08, Paris, 2008.

[33] Guedes, C., Neves, M.M., A model-based acoustic source localization using the mdof transmissibility concept, in Proceedings of Euroregio 2016, Porto, 2016.

[34] Guedes, C., Localização de fontes acústicas em interiores de avião usando o conceito de transmissibilidade. M.Sc. thesis (in Portuguese), Instituto Superior Técnico, Universidade de Lisboa, (2016), Supervisor: Miguel Matos Neves.

[35] Neves, M.M., Guedes, C., Multipoint transmissibility concept to estimate pressures at locations of difficult access, in Proceedings of Simpósio de Acústica e Vibrações, IteCons, Coimbra, (2017).

[36] Van der Seijs, M.V., Klerk, M., Rixen, D., General framework for transfer path analysis: History, theory and classification of techniques, Mechanical Systems and Signal Processing, 68-69, (2016), 217-244.

[37] De Sitter, G., Devriendt, C., Guillaume, P., Pruyt, E., Operational transfer path analysis, Mechanical Systems and Signal Processing, 24, 2, (2010), 416–431.

[38] Gajdatsy, P., Janssens, K., Desmet, W., Van der Auweraer, H., Application of the Transmissibility Concept in Transfer Path Analysis, Mechanical Systems and Signal Processing, 24, 7, (2010), 1963-1976.

[39] Desmet, W, Vandepitte, D., Finite Element Method in Acoustics, in ISAAC 13- International, Seminar on Applied Acoustics, Leuven, (2002).

Miguel Matos Neves, Ph.D.: IDMEC, Instituto Superior Técnico, Universidade de Lisboa, Av. Rovisco Pais, 1049-001, Lisboa, Portugal (miguel.matos.neves@tecnico.ulisboa.pt)

Dmitri Tcherniak, Research Engineer, Brüel & Kjær Sound & Vibration Measurement A/S, Nærum, Denmark (dmitri.tcherniak@bksv.com)

Hugo Policarpo, Ph.D.: Faculdade de Ciências e Tecnologia, Universidade Nova de Lisboa, 2829-516 Caparica, Portugal and IDMEC, Instituto Superior Técnico, Universidade de Lisboa, Av. Rovisco Pais, 1049-001, Lisboa, Portugal (hugo.policarpo@tecnico.ulisboa.pt)

Nuno Maia, Professor: IDMEC, Instituto Superior Técnico, Universidade de Lisboa, Av. Rovisco Pais, 1049-001, Lisboa, Portugal (nuno.manuel.maia@tecnico.ulisboa.pt) The author gave a presentation of this paper during one of the conference sessions.

On the influence of external stochastic excitation on linear oscillators with subcritical self-excitation applied to brake squeal

Minh-Tuan Nguyen-Thai, Paul Wulff, Nils Gräbner, Utz von Wagner

Abstract: A characteristic of linear systems with self-excitation is the occurrence of non-normal modes. Because of this non-normality, there may be a significant growth in the vibration amplitude at the beginning of the transient process even in the case of solely negative real parts of the eigenvalues, i.e. asymptotic stability of the trivial solution. If such a system is excited additionally with white noise, this process is continually restarted and a stationary vibration with dominating frequencies and comparably large amplitudes can be observed. Similar observations can be made during brake squeal, a high-frequency noise resulting from self-excitation due to the frictional disk-pad contact. Although commonly brake squeal is considered as a stable limit cycle with the necessity of corresponding nonlinearities, comparable noise phenomena can in the described model even observed in a pure linear case when the trivial solution is asymptotically stable.

1. Introduction

In a lot of applications, including but not limited to cutting machines, bridges under wind, and disk brakes, self-excited vibrations may appear as an unwanted phenomenon that reduces the effectiveness of the machines, causes inconvenience or even leads to destruction. In linear analysis, a self-excited system is usually modeled as a system of homogeneous linear ordinary differential equations (ODE) which may be obtained for a general continuous system by discretization and linearization. As a consequence, a trivial solution exists. The most popular criterion to determine, whether harmful vibrations happen or not is based in that type of mathematical models on the stability of the trivial solution. If the trivial solution is asymptotically stable, any difference between the initial state and the trivial solution is reduced to a negligible amount after a period of time called the transient process. The common disinterest in the transient process is supported by the fact that it is usually so short that it is far less representative for the behavior of the system than the steady state. However, the importance of the transient process is remarkable when there is an appearance of transient growth: vibration amplitudes may increase at the beginning of the transient process even when the largest Lyapunov exponent is negative. Transient growth is of more interest in fluid dynamics to study turbulence [1, 2]. In the field of mechanics, some studies led by Hoffmann show that transient growth may cause beating

[3] or initiate stick-slip [4] in friction-induced vibration problems. So far, this phenomenon is known from literature although probably not aware to many engineers in this field.

In reality, there may be sources for additional external forces in the self-excited systems so that their governed ODE are not homogeneous. Instead, white noise excitation, for example, can be added to the mathematical models. In this case, stability analysis of the trivial solution alone is not enough to characterize the behavior of the system. The asymptotic stability of the respective homogeneous system only means that the stochastic process in case of Gaussian white noise excitation is not drifting away. The result is a Gaussian probability density distribution around zero. But asymptotic stability together with the maximum Lyapunov exponent does not say anything about how likely large deviations from zero are.

These deviations may be important, noting the fact that harmful phenomena may occur even with small vibration amplitudes: the amplitudes of mechanical parts during brake squeal [5, 6] – a type of uncomfortable noise with kHz-frequency that may happen when an automotive mechanical brake system is activated – lie in the micrometer range. Therefore, the effect of stochastic excitation on linear systems, especially systems with the above-mentioned transient growth, should be studied.

By comparing a normal and a non-normal system with same maximum real part of the eigenvalues, the reason for transient growth is introduced, and then the effect of stochastic excitation on such equations examined.

2. Non-normality and transient growth in linear systems with self-excitation

2.1. Properties of an EDKN system

Consider a system of two linear ordinary differential equations for self-excited vibrations, which is in its basic structure similar to those, which are obtained from minimum models for brake squeal [4, 7]. These equations are written in the form

$$\ddot{\mathbf{x}} + (\mathbf{K} + \mathbf{N})\mathbf{x} = \mathbf{0} \,, \tag{1}$$

where $\mathbf{x}$ is a 2-by-1 vector representing in mechanical systems displacements or angles, $\mathbf{K}$ is a 2-by-2 symmetric positive definite matrix (stiffness matrix) and $\mathbf{N}$ is a 2-by-2 skew-symmetric matrix representing the self-excitation (circulatory matrix). If linear damping is added to the model, its equations read [4]

$$\ddot{\mathbf{x}} + \mathbf{D}\dot{\mathbf{x}} + (\mathbf{K} + \mathbf{N})\mathbf{x} = \mathbf{0} \,, \tag{2}$$

where $\mathbf{D}$ is a 2-by-2 symmetric positive definite matrix (damping matrix). In general, minimal brake squeal models may have equations of motions, where the mass matrix is not an identity matrix (e.g. in [8]), i.e. they read as

$$\mathbf{M\ddot{x}} + \mathbf{D\dot{x}} + (\mathbf{K} + \mathbf{N})\mathbf{x} = \mathbf{0} ,\tag{3}$$

where $\mathbf{M}$ is the 2-by-2 symmetric positive definite mass matrix.

A system governed by Eq. (3) is called an MDKN system [9], implying that its equations include four matrices denoted by these four letters. The special case Eq. (2) of this with mass matrix being identity matrix $\mathbf{E}$ can be called an EDKN system. Any MDKN system whose matrix $\mathbf{M}$ is a diagonal matrix with all diagonal elements equal to each other can be easily written in the form of an EDKN system by multiplying to the left of its equations the inverse matrix of $\mathbf{M}$. The positive definite assumptions for $\mathbf{M}$, $\mathbf{D}$ and $\mathbf{K}$ can be reduced to positive semi-definite for generalization, but it is not the case considered in this paper. The appearance of $\mathbf{N}$ originates from non-conservative circulatory forces and may result in instability of the trivial solution, which is in linear brake squeal models considered to be the mechanism of squeal. Even in the case of asymptotically stable trivial solution, a system with non-vanishing $\mathbf{N}$ is a system with self-excitation in which it can be called more specifically a system with subcritical self-excitation. Without $\mathbf{N}$, we have the well-known MDK system which has always an asymptotically stable trivial solution provided that $\mathbf{M}$, $\mathbf{D}$ and $\mathbf{K}$ are all symmetric positive definite.

2.2. Non-normality and transient growth

The basic effect of transient growth for non-normal systems is known from literature also with application to friction induced vibrations [3, 4]. Nevertheless it shall be repeated here as an introduction of the considered systems and the effects resulting from additional stochastic excitation to be described in section 3.

To visualize the concept of non-normality and transient growth, consider an EDKN system whose matrices are chosen as

$$\mathbf{D} = \begin{bmatrix} 0.1 & -0.01 \\ -0.01 & 0.1 \end{bmatrix}, \quad \mathbf{K} = \begin{bmatrix} 1 & -0.5 \\ -0.5 & 1 \end{bmatrix}, \quad \mathbf{N} = \begin{bmatrix} 0 & -n \\ n & 0 \end{bmatrix},\tag{4}$$

where n is a real parameter, and a corresponding EDK system

$$\mathbf{\ddot{x}} + \alpha\mathbf{D\dot{x}} + \mathbf{Kx} = \mathbf{0} ,\tag{5}$$

where α is chosen so that both systems have the same maximum real part of the eigenvalues. For simplicity purposes, all the parameters including the time are considered as dimensionless in the following.

As long as the trivial solution is asymptotically stable (subcritical self-excitation) and its characteristic polynomial has no repeated roots, the general real solution of it has the form

$$\mathbf{x}(t) = C_1 \mathbf{u}_1 e^{-\lambda_1 t} \cos(\omega_1 t) + C_2 \mathbf{u}_2 e^{-\lambda_2 t} \cos(\omega_2 t) + C_3 \mathbf{u}_3 e^{-\lambda_1 t} \sin(\omega_1 t) + C_4 \mathbf{u}_4 e^{-\lambda_2 t} \sin(\omega_2 t) , \tag{6}$$

where λ_1, λ_2, ω_1 and ω_2 are positive values. The Euclidean norms of modal vectors $\mathbf{u}_i$ (i = 1, 2, 3, 4) are chosen as 1. C_1, C_2, C_3 and C_4 are coefficients to be determined from the initial condition.

If we consider the initial condition

$$\mathbf{x}(0) = \mathbf{x}_0 = \begin{bmatrix} x_{10} & x_{20} \end{bmatrix}^T , \quad \dot{\mathbf{x}}(0) = \mathbf{0} , \tag{7}$$

with

$$\| \mathbf{x} \|_2 = x_{10}^2 + x_{20}^2 = 1 , \tag{8}$$

both C_3 and C_4 are equal to zero while C_1 and C_2 can be found by solving the linear algebraic equations

$$\mathbf{U}\mathbf{c} = \mathbf{x}_0 \tag{9}$$

where

$$\mathbf{U} = \begin{bmatrix} \mathbf{u}_1 & \mathbf{u}_2 \end{bmatrix}, \quad \mathbf{c} = \begin{bmatrix} C_1 & C_2 \end{bmatrix}^T . \tag{10}$$

Varying n, one gets different pairs of $\mathbf{u}_1$, $\mathbf{u}_2$ and different angles between them. When the angle is close to $\pi/2$, the Euclidean norm of $\mathbf{c}$ always stay near 1. In contrast, when the angle close to 0 or π and with appropriate initial conditions, either C_1 or C_2 or both can take a value much higher than 1, i.e. the initial modal vectors can be much larger than the vector of initial conditions. We can say that the latter case shows a strong *non-normality* and a system with this characteristic is called a *non-normal system*. The explanation of the concept of non-normality can also be found in [10]. As a result of the large initial vectors, a non-normal system may have a transient growth: even when the system is exponentially stable, its vibration amplitude initially increases before decaying to zero (Fig. 1a). This behavior cannot be seen in a typical MDK system (Fig. 1b). The maximum real part of the eigenvalues for both systems is approximately –0.0324 and the initial conditions are as described in Eq. (7), with x_{10} = 0 and x_{20} = 1. It should be noted that whether transient growth occurs or not also depends on the choice of the initial conditions as described in [3].
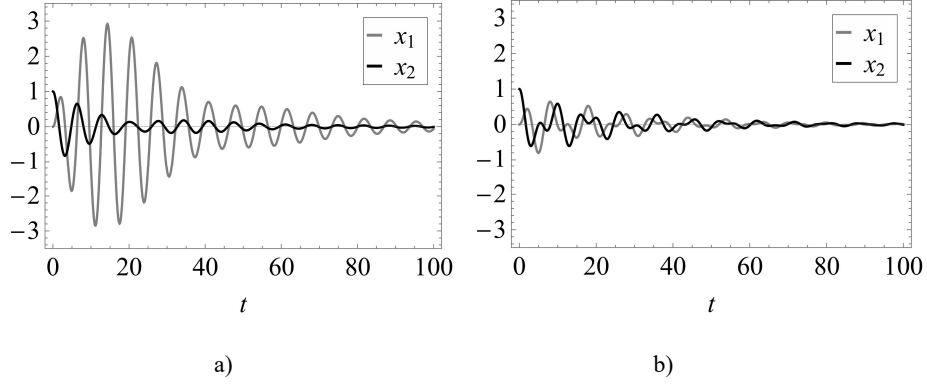
Figure 1. a) Transient growth and subsequent decaying vibration of an EDKN system (2)

with $n = 0.48$.

b) Decaying vibration without transient growth of an EDK system (5) when $n = 0$, $\alpha = 0.72$.

3. Comparison of vibrational behavior EDK and EDKN systems subjected to external stochastic excitation

In the operation of real systems, may they contain self-excitation or not, it can be expected, that small external disturbances are present, which are in the following modeled by Gaussian white noise. As we consider linear systems with Gaussian white noise most of the following steps can be performed analytically with well-known relations.

The governing ODEs in this case become inhomogeneous by adding white noise to the right-hand side of equation (2) and (5)

$$\ddot{\mathbf{X}}_t + \mathbf{D}\dot{\mathbf{X}}_t + (\mathbf{K} + \mathbf{N})\mathbf{X}_t = \boldsymbol{\sigma}\xi_t \,, \tag{11}$$

$$\ddot{\mathbf{X}}_t + \alpha\mathbf{D}\dot{\mathbf{X}}_t + \mathbf{K}\mathbf{X}_t = \boldsymbol{\sigma}\xi_t \,. \tag{12}$$

Herein ξ_t is a scalar Gaussian white noise with zero mean and the 2-by-1 vector $\boldsymbol{\sigma}$ contains their intensity coefficients. The considered equations now form a system of linear stochastic differential equations (SDE). In the following we use stationary probability density functions p (PDF) for comparing the two systems under consideration. The probability density function can either be calculated using numerical integration (Monte-Carlo simulation) or by solving the corresponding Fokker-Planck equation. In both cases, (11) and (12) are rewritten as a first-order system

$$d\mathbf{Q}_t = \mathbf{A}\mathbf{Q}_t + \mathbf{g}\,dW_t \,, \tag{13}$$

$$d\mathbf{Q}_t = \mathbf{A}'\mathbf{Q}_t + \mathbf{g}\,dW_t \tag{14}$$

respectively, where $\mathbf{Q}_t$ is the vector of the random state processes

$$\mathbf{Q}_t = \begin{bmatrix} \mathbf{X}_t \\ \dot{\mathbf{X}}_t \end{bmatrix}. \tag{15}$$

W_t is the Wiener process corresponding to ξ_t, and the other matrices are determined as follows

$$\mathbf{A} = \begin{bmatrix} \mathbf{0} & \mathbf{E} \\ -(\mathbf{K}+\mathbf{N}) & -\mathbf{D} \end{bmatrix}, \quad \mathbf{A}' = \begin{bmatrix} \mathbf{0} & \mathbf{E} \\ -\mathbf{K} & -\alpha\mathbf{D} \end{bmatrix}, \tag{16}$$

$$\mathbf{g} = \begin{bmatrix} 0 \\ 0 \\ \boldsymbol{\sigma} \end{bmatrix}. \tag{17}$$

The diffusion matrix is defined as

$$\mathbf{B} = \mathbf{g}\mathbf{g}^T. \tag{18}$$

To save space, the equations from now on are only written for $\mathbf{A}$, but they also hold for $\mathbf{A}'$. In order to find a PDF $p(\mathbf{q})$ of the stationary process $\mathbf{Q}_t$, the stationary Fokker-Planck equation associated with Eq. (13) and (14)

$$\sum_{i=1}^{4} \frac{\partial}{\partial q_i}\left[p(\mathbf{q})\sum_{j=1}^{4} a_{ij}q_j \right] - \frac{1}{2}\sum_{i=1}^{4}\sum_{j=1}^{4} \frac{\partial^2}{\partial q_i \partial q_j}\left[p(\mathbf{q})b_{ij} \right] = 0 \tag{19}$$

has to be solved, where a_{ij} and b_{ij} are the elements in row i and column j of matrix $\mathbf{A}$ and matrix $\mathbf{B}$, respectively.

Since we have a linear system with Gaussian excitation, the corresponding solution is also Gaussian. Following [11], the solution has the form

$$p(\mathbf{q}) = \mathbf{N}\ (\boldsymbol{\mu} = \mathbf{0}, \boldsymbol{\Lambda}) = \frac{1}{(2\pi)^2 |\boldsymbol{\Lambda}|^{\frac{1}{2}}} \exp\left(-\frac{1}{2}\mathbf{q}^T(\boldsymbol{\Lambda})^{-1}\mathbf{q} \right) \tag{20}$$

with mean value vector $\boldsymbol{\mu} = \mathbf{0}$ due to missing asymmetry and covariance matrix $\boldsymbol{\Lambda}$. Hence, Eq. (19) yields to the following algebraic equation [12]

$$[(\mathbf{E} \otimes \mathbf{A}) + (\mathbf{A} \otimes \mathbf{E})]\,\mathrm{vec}(\boldsymbol{\Lambda}) + \mathrm{vec}(\mathbf{B}) = 0, \tag{21}$$

where $\otimes$ denotes the Kronecker product and $\mathrm{vec}(\cdot)$ denotes vectorization operator. For the results discussed later on, it is chosen that

$$\boldsymbol{\sigma} = \begin{bmatrix} 0 \\ 1 \end{bmatrix}. \tag{22}$$

Solving (21) for Λ and computing (20), one obtains $p(\mathbf{q})$. Marginal PDF p_{X_1} and p_{X_2} can then calculated by

$$p_{X_1}(x_1) = p_{Q_1}(q_1) = \int\limits_{-\infty}^{\infty} \int\limits_{-\infty}^{\infty} \int\limits_{-\infty}^{\infty} p(\mathbf{q}) \, dq_2 dq_3 dq_4 , \tag{23}$$

$$p_{X_2}(x_2) = p_{Q_2}(q_2) = \int\limits_{-\infty}^{\infty} \int\limits_{-\infty}^{\infty} \int\limits_{-\infty}^{\infty} p(\mathbf{q}) \, dq_1 dq_3 dq_4 . \tag{24}$$

In the following, corresponding results are discussed. Figure 2 shows time responses X_{1t} and X_{2t} obtained by Monte-Carlo simulation performed by using the Euler-Maruyama method. It can be observed, that the vibration amplitudes of X_{2t} of both cases are in a similar range, while for X_{1t} the EDKN system produces much higher amplitudes.

a)   b)
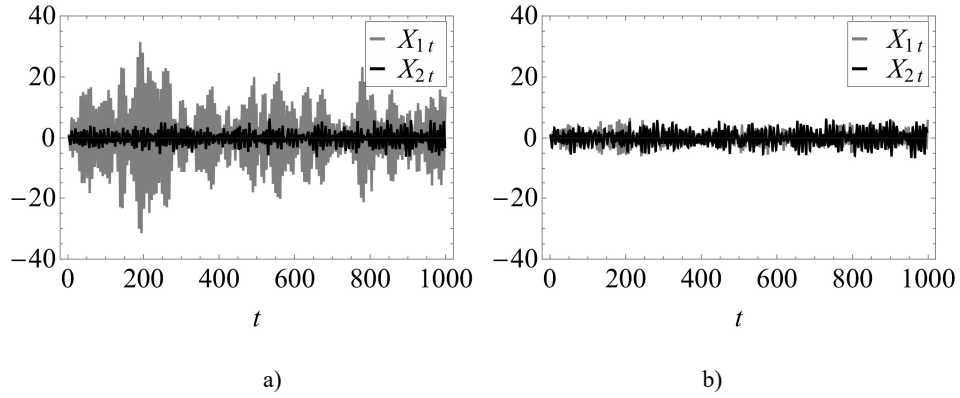
Figure 2. Time responses X_{1t} and X_{2t} for a) EDKN system and b) EDK system with same white noise excitation according to Eq. (22).

A similar behavior can be observed when considering the PDF. Figures 3 and 4 show the marginal PDF p_{X_1} and p_{X_2} for both EDKN and EDK system as analytical solution of the Fokker-Planck equation according to Eqs. (20) – (24) compared with Monte-Carlo simulation results. Again p_{X_1} is spreading much more for the EDKN system compared to the EDK system while p_{X_2} is comparable in both cases.
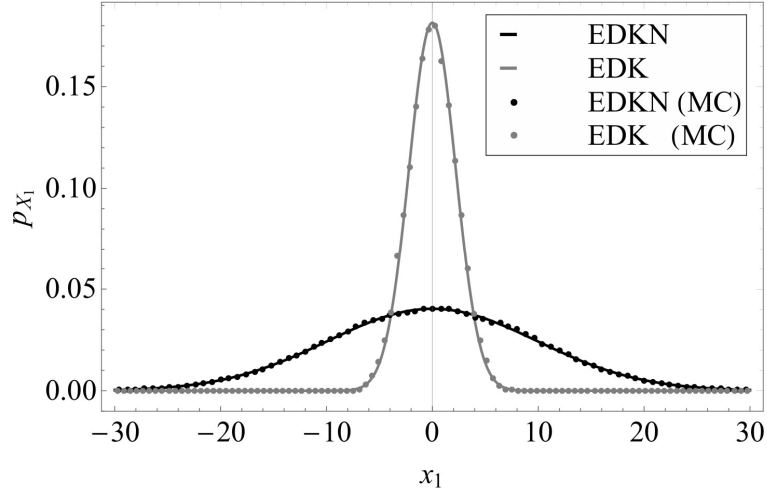
Figure 3. Marginal PDFs p_{X_1} of stochastically excited EDKN and EDK system respectively obtained from solving the Fokker-Planck equation (lines) and from Monte-Carlo simulation (dots).
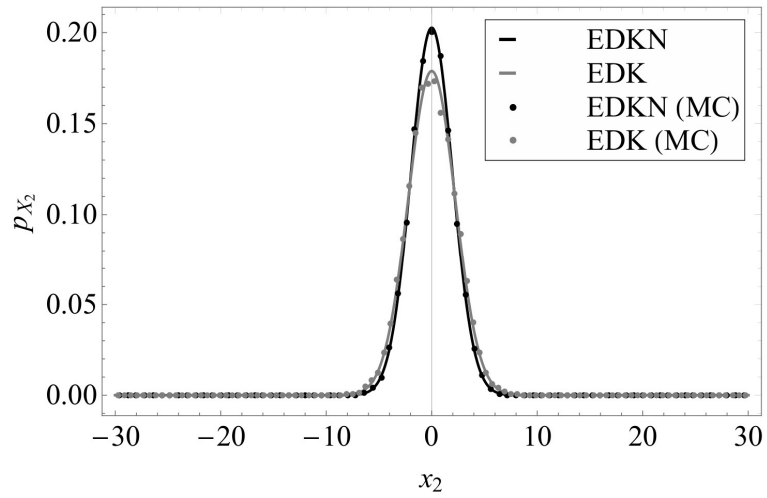

Figure 4. Marginal PDFs p_{X_2} of stochastically excited EDKN and EDK system respectively obtained from solving the Fokker-Planck equation (lines) and from Monte-Carlo simulation (dots).

Finally the frequency characteristic of the responses X_{1t} and X_{2t} for the EDKN system shall be considered by the absolute values of corresponding transfer functions $H_1(\Omega)$ and $H_2(\Omega)$ in the case of single excitation of the second equation in Eq. (2) which is in accordance with excitation Eq. (22). It can be seen, that for X_{1t} distinct vibrations can be expected with (as the two eigenfrequencies are close together) almost one single dominating frequency which is very close to the behavior observed in brake squeal (Fig. 5).
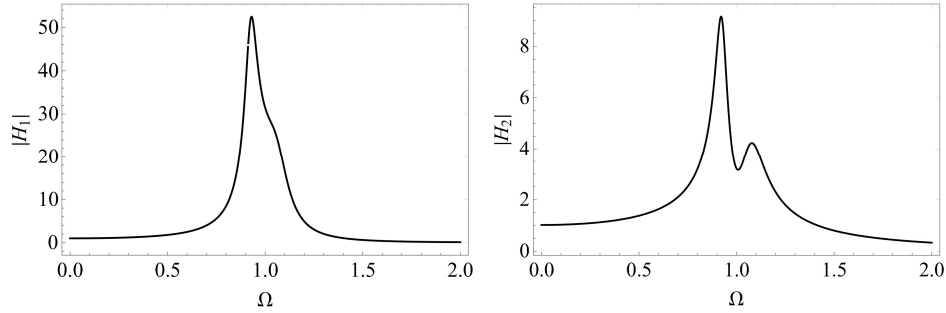
Figure 5. Transfer functions $\left|H_1(\Omega)\right|$ and $\left|H_2(\Omega)\right|$ for excitation according to (21).

4. Conclusions and outlook

In this paper a non-normal EDKN system with corresponding suitable system and initial condition parameters producing a negative maximum real part of the eigenvalues, i.e. a system with transient growth and sub-critical self-excitation, has been considered in comparison with an EDK system showing similar stability behavior. Stochastic excitation has been added to both systems to compare its effect in both cases. In a system without self-excitation and stable trivial solution this will result in vibrations according to the excitation level around the zero solution. In contrast to this, in a system with similar maximum real part of the eigenvalues but self-excitation, much larger vibrations may result as the transient growth behavior is continually restarted by the stochastic excitation. The resulting vibrations remember to what can be observed during brake squeal. This surprisingly happens for a linear system, with stable trivial solution only needing some external noise excitation to get comparably large responses, while general explanation of brake squeal is that of a stable limit cycle in a nonlinear system.

In future work, we intend to consider full MDGKN systems resulting from minimal models of brakes.

References

[1] Waleffe, F. Transition in shear flows. Nonlinear normality versus non-normal linearity. *Physics of Fluids* 7, 12 (1995), 3060-3066.

[2]   Cantwell, C. D., Barkley, D., and Blackburn, H. M. Transient growth analysis of flow through a sudden expansion in a circular pipe. *Physics of Fluids,* 22, 3 (2010), 034101.

[3]   Hoffmann, N., and Gaul, L. Non-conservative beating in sliding friction affected systems: transient amplification of vibrational energy and a technique to determine optimal initial conditions. *Mechanical Systems and Signal Processing,* 18, 3 (2004), 611-623.

[4]   Hoffmann, N. Transient growth and stick-slip in sliding friction. *Journal of applied mechanics,* 73, 4 (2006), 642-647.

[5]   Kinkaid, N. M., O'Reilly, O. M., and Papadopoulos, P. Automotive disk brake squeal. *Journal of Sound and Vibration*, 267, (2003), 105-166.

[6]   Cantoni, C., Cesarini, R., Mastinu, G., Rocca, G. and Sicigliano, R. Brake comfort - a review. *Vehicle Systems Dynamics,* 47, 8 (2009), 901-947.

[7]   Hamabe, T., Yamazaki, I., Yamada, K., Matsui, H., Nakagawa, S., and Kawamura, M. Study of a method for reducing drum brake squeal. *SAE Technical Paper* 1999-01-0144, (1999), https://doi.org/10.4271/1999-01-0144.

[8]   Popp, K., Rudolph, M.; Kröger, M. and Lindner, M. Mechanisms to generate and to avoid friction induced vibrations. *VDI-Bericht,* 1736, (2002), 1-15.

[9]   Hagedorn, P., Heffel, E., Lancaster, P., Müller, P. C., & Kapuria, S. (2015). Some recent results on MDGKN-systems. *ZAMM‐Journal of Applied Mathematics and Mechanics/Zeitschrift für Angewandte Mathematik und Mechanik*, 95, 7 (2015), 695-702.

[10] Blumenthal, R. *A systems view on non-normal transient growth in thermoacoustics*. Doctoral dissertation, Technische Universität München, 2015.

[11] Soong, T. T. *Mathematics in Science and Engineering: Vol. 103. Random Differential Equations in Science and Engineering*. Academic Press, New York, 1973.

[12] Martens, W. *On the solution of the Fokker-Planck-Equation for multi-dimensional nonlinear mechanical systems*. Doctoral dissertation, Technische Universität Berlin, Shaker, 2013.

Minh-Tuan Nguyen-Thai, Dr.: Hanoi University of Science and Technology, Department of Applied Mechanics, No. 1 Dai Co Viet, 112400 Hanoi, Vietnam (*tuan.nguyenthaiminh@hust.edu.vn*).

Paul Wulff, M.Sc.: Technische Universität Berlin, Chair of Mechatronics and Machine Dynamics, Institute of Mechanics, Einsteinufer 5, 10587 Berlin, Germany (*paul.wulff@tu-berlin.de*).

Nils Gräbner, Dr.: Technische Universität Berlin, Chair of Mechatronics and Machine Dynamics, Institute of Mechanics, Einsteinufer 5, 10587 Berlin, Germany (*nils.graebner@tu-berlin.de*).

Utz von Wagner, Professor: Technische Universität Berlin, Chair of Mechatronics and Machine Dynamics, Institute of Mechanics, Einsteinufer 5, 10587 Berlin, Germany (*utz.vonwagner@tu-berlin.de*). The author gave a presentation of this paper during one of the conference sessions.

Lyapunov function-based control of a DC/DC buck converter using Hybrid Systems formalism

Luz-Adriana Ocampo, Fabiola Angulo, David Angulo-Garcia

Abstract: In this paper we propose a switched control strategy for the buck converter based on Lyapunov functions and the Hybrid system framework. First, we introduce the differential inclusion describing the dynamics of the buck converter in the Hybrid systems formalism using the Krasovskii regularization. Then, a Lyapunov function is derived for the hybrid system, which naturally defines switching control surfaces that guarantee global stability of the system. With the aim of extending the degree of tuning of the Lyapunov-based switched control, we include a nonlinear term to the functions describing the switching manifolds, which preserves the stability features of the system allowing to further control transient behavior of the system. Finally, we show by means of numerical simulations that the proposed controller is robust to the switch position and can flexibly adjust the transient dynamics via a suitable selection of gains in the added nonlinear terms.

1. Introduction

Over the past years, DC/DC power converters have gained a lot of attention due to the increasing use in different technological applications [7, 2, 4]. The aim of a DC/DC converter is to take an unregulated DC input voltage and deliver a desired DC output voltage [6, 8]. To achieve this, power converters include different commuting elements (diodes, transistors, Mosfets), together with passive elements for signal filtering. The presence of commuting mechanisms, introduce topological changes in the dynamical equations driving the system's behavior. Hence, a suitable law governing the transitions between the dynamical regimes, generates the desired output signal.

Previous analysis performed in the buck converter have shown that the hybrid system's formalism can be applied for the design of switched control techniques achieving robust and global control [9]. However, this approach only guaranteed stabilization of the desired output signal with no control over the transient dynamics. The purpose of this paper is to extend that design to a more general type of control in which transient behavior can be also controlled.

To do so, we make use of the ideas presented in [13], where the dynamics and control of the boost converter is presented in the theoretical framework of hybrid systems, (see [5, 11]).
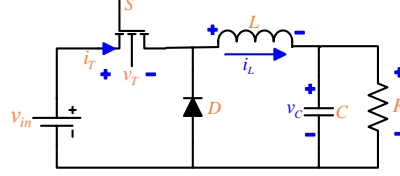
Figure 1. Schematic representation of the buck converter

This paper is organized as follows: In section 2, we present the model of the buck converter as a Hybrid system. Then in section 3 we demonstrate that a suitable choice of a Lyapunov function gives rise to a switched control action that guarantees global stability. Next we propose a modification of the resulting switched control via a nonlinear term in section 4, which allows to modify transient features of the system. Finally we show numerically that our proposed control successfully manages to drive to system to a desired operation point and that it is able to largely modify transient behavior.

2. Hybrid model of the buck converter

A schematic representation of the buck converter is shown in Figure 1. It consists of a capacitor (C), an inductor (L), a diode (D), a resistive load (R), a DC voltage source v_{in} and a MOSFET (switch, S). The voltage across the capacitor and the current through the inductor are denoted as v_C and i_L, respectively. The presence of commuting elements makes the system non-smooth and therefore we can study it from the Hybrid Systems framework. Both the diode and the switch can take the discrete values $D, S \in \{0, 1\}$ depending whether the diode/switch is ON (1) or OFF (0). With this in mind, three different topologies may arise, namely:

$$
\begin{aligned}
\text{when } S = 1 \text{ and } D = 0 \rightarrow \xi_1 : &\begin{cases} \frac{dv_C}{dt} = -\frac{v_C}{RC} + \frac{i_L}{C} \\ \frac{di_L}{dt} = -\frac{v_C}{L} + \frac{v_{in}}{L} \end{cases} \quad \text{with } i_L \geq 0 \\
\text{when } S = 0 \text{ and } D = 1 \rightarrow \xi_2 : &\begin{cases} \frac{dv_C}{dt} = -\frac{v_C}{RC} + \frac{i_L}{C} \\ \frac{di_L}{dt} = -\frac{v_C}{L} \end{cases} \quad \text{with } i_L > 0 \\
\text{when } S = 0 \text{ and } D = 0 \rightarrow \xi_3 : &\begin{cases} \frac{dv_C}{dt} = -\frac{v_C}{RC} \\ \frac{di_L}{dt} = 0 \end{cases} \quad \text{with } i_L = 0
\end{aligned}
\tag{1}
$$

It is worth noticing that a state corresponding to $S = 1$ and $D = 1$ has no physical meaning. Let $x = [v_C, \ i_L]^T$ represent the state space and $\Xi_1 = \{x \in \mathbb{R}^2 : \ i_L \geq 0\}$, $\Xi_2 = \{x \in \mathbb{R}^2 : \ i_L > 0\}$ and $\Xi_3 = \{x \in \mathbb{R}^2 : \ i_L = 0\}$ the algebraic restrictions for each topology of the system. The discontinuous nature of the vector fields defining the dynamics when

$S = 0$ requires a Krasovskii regularization operation [12, 5, 10]. After this operation the system takes the form of the differential inclusion $\dot{x} \in F_S(x) \ \forall x \in \tilde{\Xi}_S$, where F_S is the regularized field on each switch position and $\tilde{\Xi}_S$ is the regularization of the sets containing the algebraic restrictions to be applied depending on the switch position S. For $S = 0$, $\tilde{\Xi}_0 = \overline{\Xi_2 \cup \Xi_3}$; while for $S = 1$, $\tilde{\Xi}_1 = \overline{\Xi}_1$. Here the overline denotes the closure of the set. The regularization of the vector fields follows the ideas in [10] and results in:

For $S = 0$ the regularization is defined as

$$
F_0 \quad = \quad
\begin{cases}
\{\xi_2\} & \text{if } x \in \overline{\Xi}_2 \backslash \overline{\Xi}_3 \\
\mathcal{C}\left\{ \begin{bmatrix} -\frac{v_C}{RC} \\ -\frac{v_C}{L} \end{bmatrix}, \begin{bmatrix} -\frac{v_C}{RC} \\ 0 \end{bmatrix} \right\} & \text{if } x \in \overline{\Xi}_3
\end{cases}
$$

$$
= \quad
\begin{cases}
\left\{ \begin{bmatrix} -\frac{v_C}{RC} + \frac{i_L}{C} \\ -\frac{v_C}{L} \end{bmatrix} \right\} & \text{if } x \in \overline{\Xi}_2 \backslash \overline{\Xi}_3 \\
\{-\frac{v_c}{RC}\} \times \left[-\frac{v_c}{LC} : 0 \right] & \text{if } x \in \overline{\Xi}_3
\end{cases}
\tag{2}
$$

where $\mathcal{C}$ denotes the closed convex hull of the set and is composed by the elements resulting from the Cartesian product of $-\frac{v_c}{RC}$ and all the elements of the interval $\left[-\frac{v_C}{L} : 0 \right]$.

Similarly, for $S = 1$ regularization reads as

$$
F_1 = \{\xi_1\} \quad = \quad \left\{ \begin{bmatrix} -\frac{v_C}{RC} + \frac{i_L}{C} \\ -\frac{v_C}{RC} + \frac{v_{in}}{L} \end{bmatrix} \right\} \quad \text{if } x \in \overline{\Xi}_1
\tag{3}
$$

3. Control law based on Lyapunov function

As suggested in [13] for the Boost converter, one can propose a switched control which leads the dynamics governed by Eqs. (2) and (3) to a desired operation point $x^* = [v_C^*, i_L^*]$, with $v_C^* > 0$ and $i_L^* > 0$. For this we consider the Lyapunov Function Candidate:

$$
V(x) = (x - x^*)^T P(x - x^*) \quad \text{with} \quad P = \begin{bmatrix} P_{11} & 0 \\ 0 & P_{22} \end{bmatrix}
\tag{4}
$$

If we demonstrate that there is a choice of $S \in \{0, 1\}$ that guarantees that $\langle \nabla V(x), F_S \rangle < 0$, then we can make use of the Lyapunov function to generate a switching control law. We proceed to calculate the largest possible value of $\langle \nabla V(x), F_S \rangle$ in each set:

- For $S = 0$ and $x \in \overline{\Xi}_2 \backslash \overline{\Xi}_3$, we have:

$$
\langle \nabla V(x), \xi_2(x) \rangle = 2P_{11} (v_C - v_C^*) \left(-\frac{v_C}{RC} + \frac{i_L}{C} \right) + 2P_{22} (i_L - i_L^*) \left(-\frac{v_C}{L} \right)
\tag{5}
$$

- For $S = 0$ and $x \in \overline{\Xi}_3$, $F_0(x)$ is set-valued so we compute the largest possible value of the gradient in $\overline{\Xi}_3$. For simplicity in the notation we will define $f := \{-\frac{v_c}{RC}\} \times \left[-\frac{v_c}{LC} : 0\right]$, with this:

$$\max_f \langle \nabla V(x), f \rangle \quad = \tag{6}$$

$$= \begin{cases} 2P_{11}(v_C - v_C^*)\left(-\frac{v_C}{RC}\right) & \text{if } i_L \geq i_L^* \\ 2P_{11}(v_C - v_C^*)\left(-\frac{v_C}{RC}\right) + 2P_{22}(i_L - i_L^*)\left(-\frac{v_C}{L}\right) & \text{if } i_L < i_L^* \end{cases}$$

Given that $i_L^* > 0$, and each $x \in \overline{\Xi}_3$ is of the form $i_L = 0$, then the inequality $i_L \geq i_L^*$ never holds in $\overline{\Xi}_3$. Therefore, for $S = 0$ and $x \in \overline{\Xi}_3$ we finally have:

$$\max_f \langle \nabla V(x), f \rangle = 2P_{11}(v_C - v_C^*)\left(-\frac{v_C}{RC}\right) + 2P_{22}(i_L - i_L^*)\left(-\frac{v_C}{L}\right) \tag{7}$$

Also, it is worth noticing that since Eq. (7) was calculated for $i_L = 0$, Eq. (5) holds the information of both Eqs. (7) and (5).

- For $S = 1$ and $x \in \tilde{\Xi}_1$, we have:

$$\langle \nabla V(x), F_1(x) \rangle \quad = \quad \langle \nabla V(x), \xi_1(x) \rangle \tag{8}$$

$$= \quad 2P_{11}(v_C - v_C^*)\left(-\frac{v_C}{R} + \frac{i_L}{C}\right) + 2P_{22}(i_L - i_L^*)\left(-\frac{v_C}{L} + \frac{v_{in}}{L}\right)$$

Given the previous analysis, we can define the following functions

$$\gamma_1(x) \quad := \quad 2P_{11}(v_C - v_C^*)\left(-\frac{v_C}{RC} + \frac{i_L}{C}\right) + 2P_{22}(i_L - i_L^*)\left(-\frac{v_C}{L} + \frac{v_{in}}{L}\right) \tag{9}$$

$$\gamma_0(x) \quad := \quad 2P_{11}(v_C - v_C^*)\left(-\frac{v_C}{RC} + \frac{i_L}{C}\right) + 2P_{22}(i_L - i_L^*)\left(-\frac{v_C}{L}\right) \tag{10}$$

and the (largest) Lyapunov function derivative along the trajectory in the regularized set $x \in \tilde{\Xi}_S$ can be expressed in the simplified form

$$\max_{\xi \in F_S(x)} \langle \nabla V(x), \xi \rangle = \begin{cases} \gamma_1(x) & \text{if } S = 1 \\ \gamma_0(x) & \text{if } S = 0 \end{cases} \tag{11}$$

The changes in the sign of the functions γ_1 and γ_0 are used to defined the MOSFET state S. The following Lemma establishes the properties of γ_1 y γ_0 that demonstrates that $V(x)$ is a Lyapunov Control Function.

Lemma 1. *Let R, v_{in}, P_{11} and $P_{22} > 0$, $\frac{P_{11}}{C} = \frac{P_{22}}{L}$, $v_C^* < v_{in}$, $i_L^* = \frac{v_C^*}{R}$ and $A_x = \{x \in \mathbb{R}^2 : \gamma_S(x) = 0\}$. Then, for each $x \in \mathbb{R}^2 \backslash A_x$, exists an S such that $\gamma_S(x) < 0$.*

Proof of Lemma 1. We start by defining the sets $\tau_S = \{x \in \mathbb{R}^2 : \gamma_S(x) < 0\}$, delimited by $\omega_S = \{x \in \mathbb{R}^2 : \gamma_S(x) = 0\}$. With this, we proceed as follows:

i. We obtain the explicit expressions for τ_S. The set τ_1 is formed by the points in x such that $\gamma_1(x) < 0$. Using the fact that $\frac{P_{11}}{C} = \frac{P_{22}}{L}$ and solving for i_L in (9):

$$i_L < \frac{L}{P_{22}(v_{in} - v_C^*)} \left(\frac{P_{22}}{LR} v_C^2 - \frac{P_{22}}{L} \left(\frac{v_C^*}{R} + i_L^* \right) v_C + \frac{P_{22} v_{in} i_L^*}{L} \right). \tag{12}$$

Simplifying:

$$\tau_1 = \left\{ i_L < \frac{1}{v_{in} - v_C^*} \left(\frac{v_C^2}{R} - \left(\frac{v_C^*}{R} + i_L^* \right) v_C + i_L^* v_{in} \right) \right\} \tag{13}$$

Similarly, for τ_0 we solve $\gamma_0(x) < 0$. Using $\frac{P_{11}}{C} = \frac{P_{22}}{L}$ and solving for i_L in (10):

$$i_L \quad > \quad \frac{L}{P_{22} v_C^*} \left(-\frac{P_{22}}{LR} v_C^2 + \frac{P_{22}}{L} \left(\frac{v_C^*}{R} + i_L^* \right) v_C \right) \tag{14}$$

$$\tau_0 \quad = \quad \left\{ i_L > -\frac{v_C^2}{R v_C^*} + \left(\frac{1}{R} + \frac{i_L^*}{v_C^*} \right) v_C \right\} \tag{15}$$

ii. Then we demonstrate that $\tau_1 \cup \tau_0 = \{x : x \in \mathbb{R}^2 \backslash A_x\}$ when $v_C^* < v_{in}$. From (13) we have $\frac{1}{v_{in} - v_C^*} > 0$, meaning that ω_1 is an upward parabola in the (v_C, i_L) plane and τ_1 is the region below it. The opposite is true for ω_0, i.e, it is a downward parabola and τ_0 is the region above it. These two regions will span the desired set if and only if there is a unique intersection at A_x namely, $\omega_1 \cap \omega_0 = A_x$. Equating (13) and (15) we find the unique solution $(v_C, i_L) = (v_C^*, i_L^*)$, which turns out to be the operation point.

□

Lemma 1 and its proof can be used to obtain the position of the MOSFET as:

$$S = \arg \min_{S \in \{0,1\}} \max_{\xi \in F_S(x)} \langle \nabla V(x), \xi \rangle < 0 \quad \forall x \in \mathbb{R}^2 \backslash A_x \tag{16}$$

which is equivalent to:

$$S = \begin{cases} 1 & \text{if} \quad \gamma_1(x) < 0 \\ 0 & \text{if} \quad \gamma_0(x) < 0 \end{cases}. \tag{17}$$

4. Extended Control

In the previous section, we found a Lyapunov function which allows us to define a suitable switching control law defined by the behavior of the functions γ_0 and γ_1. This control law is robust both upon selection of the switch state S and initial conditions. Nonetheless, since the switching surfaces are fixed, the transient state of the system cannot be controlled. To solve this problem, we make use of a modified CLF with an additional nonlinear term. To do so we define the functions $\tilde{\gamma}_1$ and $\tilde{\gamma}_0$ designed in such a way that the commutation from q to $1 - q$ occurs only when $\tilde{\gamma}_q = 0$. The functions $\tilde{\gamma}_q$ are chosen according to Lemma 2 as proposed in [13]:

Lemma 2. *Let R, v_{in}, P_{11}, and $P_{22} > 0$; P_{11} and $P_{22} > 0$, $\frac{P_{11}}{C} = \frac{P_{22}}{L}$, $v_C^* < v_{in}$, Defining the functions $\tilde{\gamma}_q$ with $q \in \{0, 1\}$, for each $x \in \mathbb{R}^2$ as:*

$$\tilde{\gamma}_1(x) = \gamma_1(x) + K_1(v_C - v_C^*)^2 \tag{18}$$

$$\tilde{\gamma}_0(x) = \gamma_0(x) + K_0(v_C - v_C^*)^2. \tag{19}$$

If K_1 and $K_0 \in \left[0, \frac{2P_{11}}{RC}\right]$, then the following properties hold:

   a) For each $q \in \{0, 1\}$ and $x \notin A_x$, when $\tilde{\gamma}_q \geq 0$, then $\tilde{\gamma}_{1-q} < 0$.

   b) For each $q \in \{0, 1\}$ and $x \notin A_x$, when $\tilde{\gamma}_q \leq 0$, then $\tilde{\gamma}_q < 0$.

Proof Lemma 2. a) Analogously to the Proof of Lemma 1, from Eqs. (18) and (19) we can define the sets $\tilde{\tau}_q = \left\{x \in \mathbb{R}^2 : \tilde{\gamma}_q(x) < 0\right\}$, with limits $\tilde{\omega}_q = \left\{x \in \mathbb{R}^2 : \tilde{\gamma}_q(x) = 0\right\}$ for each $q \in \{0, 1\}$. In order to obtain the explicit expressions of $\tilde{\tau}_q$, we include the nonlinear terms in Eqs. (18) and (19) into Eqs. (12) and (14), respectively:

$$i_L < \frac{L}{2P_{22}\left(E - v_C^*\right)} \left[\begin{array}{l} -\left(\frac{-2P_{22}}{RL} + K_1\right)v_C^2 - \left[\frac{2P_{22}}{L}\left(\frac{1}{R} + i_L^*\right) - 2K_1 v_C^*\right]v_C \\ -\frac{2P_{22}i_L^* E}{L} + K_1 v_C^{*2} \end{array} \right] \tag{20}$$

$$i_L > \frac{-L}{2P_{22}v_C^*} \left[\begin{array}{l} -\left(\frac{-2P_{22}}{RL} + K_0\right)v_C^2 - \left[\frac{2P_{22}}{L}\left(\frac{v_C^*}{R} + i_L^*\right) - 2K_0 v_C^*\right]v_C \\ -K_0 v_C^* \end{array} \right] \tag{21}$$

Simplifying the inequalities (20) and (21), the sets $\tilde{\tau}_q$ take the form:

$$\tilde{\tau}_1 = \left\{ i_L < \frac{L}{\left(E - v_C^*\right)} \left[\begin{array}{l} \left(\frac{1}{R} - \frac{2P_{22}K_1}{L}\right)v_C^2 - \left[\left(\frac{1}{R} - i_L^*\right) - \frac{P_{22}K_1 v_C^*}{L}\right]v_C \\ -i_L^* E + \frac{2P_{22}K_1 v_C^{*2}}{L} \end{array} \right] \right\} \tag{22}$$

$$\tilde{\tau}_0 = \left\{ i_L > \frac{1}{v_C^*} \left[\begin{array}{l} \left(-\frac{1}{R} + \frac{2P_{22}K_0}{L} \right) v_C^2 + \left[\left(\frac{v_C^*}{R} + i_L^* \right) - \frac{P_{22}K_0 v_C^*}{L} \right] v_C \\ + \frac{2P_{22}K_0 v_C^*}{L} \end{array} \right] \right\} \tag{23}$$

Considering that $\frac{1}{v_{in}-v_C^*} > 0$ y $K_1, K_0 > 0$, from Eqs. (22) and (23) it is easy to see that $\tilde{\omega}_1$ and $\tilde{\omega}_0$ are upward parabolas if $K_1 < \frac{C}{2P_{11}R}$ and $K_0 > \frac{C}{2P_{11}R}$ respectively, and downward parabolas otherwise. It shall be noticed though, that the region $\tilde{\tau}_1$ is always the region below the parabola $\tilde{\omega}_1$ and $\tilde{\tau}_0$ is the region above the $\tilde{\omega}_0$. Finally, if we can demonstrate that $\tilde{\omega}_1 \cap \tilde{\omega}_0 = A_x$, then it implies that $\tilde{\tau}_1 \cup \tilde{\tau}_0 = x \in \mathbb{R}^2 \backslash A_x$. Some straightforward algebra leads to $\tilde{\omega}_1 \cap \tilde{\omega}_2 = \{(v_C^*, i_L^*)\}$ meaning that the only intersection point between the two parabolas is the desired operation point of the controller. With this, literal a) of the Lemma is demonstrated.

b) We start rearranging Eqs. (18) and (19) as:

$$\gamma_1(x) = \tilde{\gamma}_1(x) - K_1(v_C - v_C^*)^2 \text{ and } \gamma_0(x) = \tilde{\gamma}_0(x) - K_0(v_C - v_C^*)^2 \tag{24}$$

Since $K_1, K_0 > 0$, $\tilde{\gamma}_q(x) \leq 0$; it follows that $\gamma_q(x) < 0$ if $v_C \neq v_C^*$. Then, if $v_C = v_C^*$ and $i_L \neq i_L^*$, we have $\gamma_q(x) = \tilde{\gamma}_q(x)$. Therefore, as $\gamma_q(x) = \tilde{\gamma}_q(x)$ cannot be true beacause it would imply that $v_C = v_C^*$ and $i_L = i_L^*$, then also in this case $\tilde{\gamma}_q(x) = \gamma_q(x) < 0$. With this, the proof of con literal b is complete.

As a result of property a), if $x \notin A_x$, it follows that $\tilde{\gamma}_{1-q} < 0$. Also, due to property b) while $x \notin A_x$, we have $\tilde{\gamma}_q < 0$. These two properties, imply a control law that guarantees that $\tilde{\gamma}_q \leq 0$ for the any value of q and x, therefore the commutations are well defined. With this, we have defined a suitable control law for the robust stabilization from the properties derived in *Lemma 2*. □

From the modified control curves (19) and (18) it can be seen that as K_0 and K_1 approach to zero, the switching surfaces approach the original functions $\gamma_0(x)$ and $\gamma_1(x)$ respectively. Moreover, when K_0 and K_1 approach to the limit value of $\frac{2P_{11}}{RC}$, the switching surfaces $\tilde{\gamma}_q(x)$ tend to the straight line $2(i_L - i_L^*) = 0$. Therefore, the constants K_0 and K_1 can control the position of the commutation limits, adding an additional degree of freedom to the control.

Finally, we can write down the closed-loop Hybrid system in the following form:

$$
H = \begin{cases} \begin{bmatrix} \dot{x} \\ \dot{q} \end{bmatrix} \in \begin{bmatrix} F_q(x) \\ 0 \end{bmatrix} & (x,q) \in C \\[4mm] \begin{bmatrix} x^+ \\ q^+ \end{bmatrix} \in \begin{bmatrix} x \\ G_q(x) \end{bmatrix} & (x,q) \in D \end{cases} \tag{25}
$$

Where F_0 and F_1 are given by the regularization in Eqs. (2) and (3), respectively. Moreover, the component of the jump map G_q is written as:

$$
G_q = \begin{cases} 1 & \text{if} \quad q = 0, \ \tilde{\gamma}_0 \geq 0 \\ 0 & \text{if} \quad q = 1, \ \tilde{\gamma}_1 \geq 0 \end{cases}, \tag{26}
$$

and the flow set and jump set are respectively:

$$
C = \{(x,q) : x \in \{i_L \geq 0\}, \tilde{\gamma}_0 < 0, q = 0\} \cup \{(x,q) : x \in \{i_L \geq 0\}, \ \tilde{\gamma}_1 < 0, q = 1\} \tag{27}
$$

$$
D = \{(x,q) : x \in \{i_L \geq 0\}, \ \tilde{\gamma}_0 \geq 0, q = 0\} \cup \{(x,q) : x \in \{i_L \geq 0\}, \ \tilde{\gamma}_1 \geq 0, q = 1\} \tag{28}
$$

5. Numerical Simulations

In this section we present simulation results of the proposed control, showing robustness to initial conditions and the position of the switch as well as control of the transient state. This performance is obtained thanks to constants K_0 and K_1 which control the form and position of the commutation limits. The parameters used for the simulations are $v_{in} = 20$V, $C = 47\mu$F, $L = 20$mH, $R = 22\Omega$, $P_{11} = C/2$, $P_{22} = L/2$, $v_C^* = 11.03$V in correspondence to widely used values for the buck converter [3].

In Fig. 2 we show the evolution of the state variables for different initial conditions corresponding to two different initial switch positions. It can be seen from the time traces (Figs. 2(a)-(b)) that the solutions converge to the operation point $x^* = [11.03 \ 0.505]^T$. Moreover, we show in Fig. 2(c) the phase diagram together with the switching surfaces $\tilde{\gamma}_1$ and $\tilde{\gamma}_0$.

Finally, in Figs. 3 and 4, we illustrate the response of the system to changes in the operation point and input DC voltage, respectively. As observed from these figures, the switching surfaces adapt so that the desired output is reached, despite the changes in these two conditions.
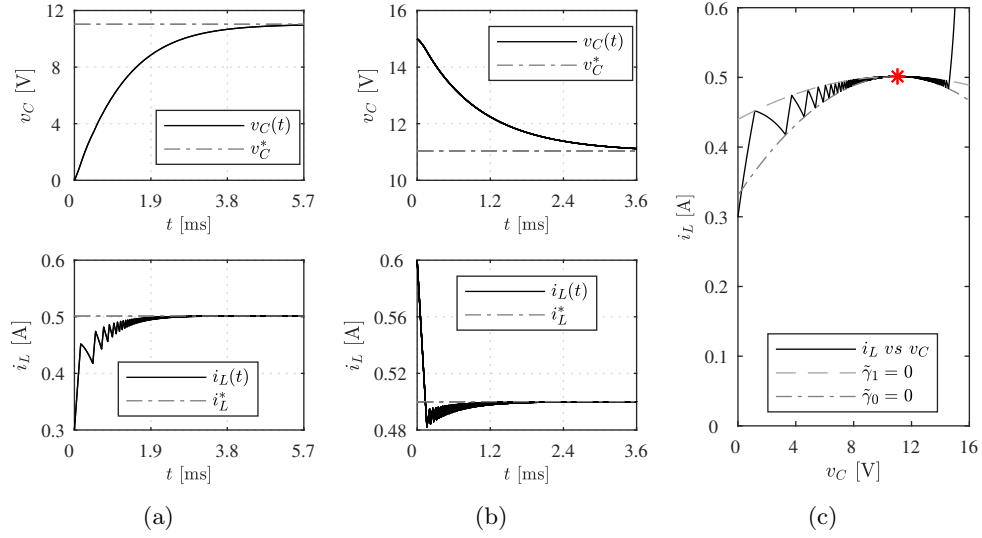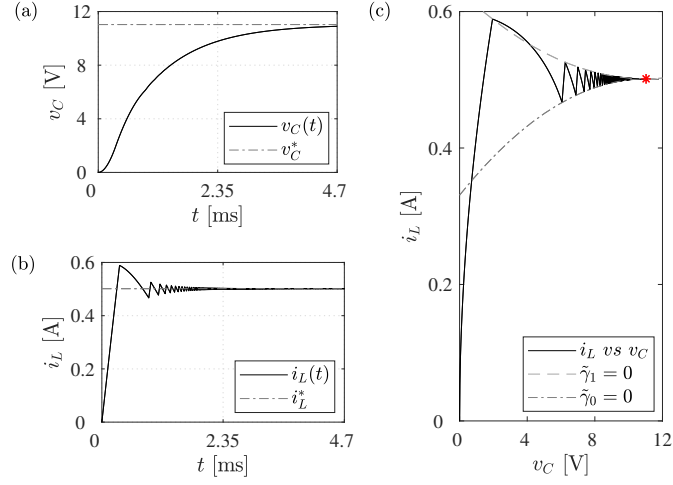
Figure 2. Time series of the state variables $(v_C(t),\, i_L(t))$ of the closed-loop hybrid system H with (a) $x_0 = [0,\, 0.3]^T$, $q_0 = 1$ and (b) $x_0 = [15,\, 0.6]^T$, $q_0 = 0$. (c) Phase diagram depicting the trajectories in (a) and (b), together with the switching surfaces $\tilde{\gamma}_1$ y $\tilde{\gamma}_0$. For this figure we used $K_0 = 0.03$, $K_1 = 0.05$ and $x^* = [11.03\ 0.505]^T$
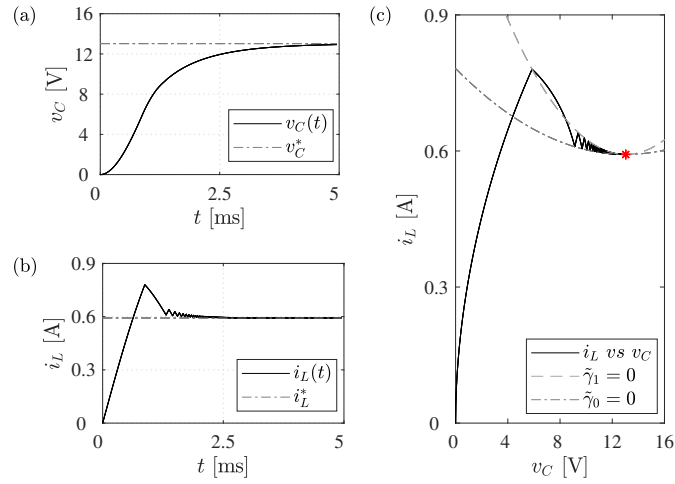
Figure 3. (a) Time series of the state variables $(v_C(t),\, i_L(t))$, of the closed-loop hybrid system H with $x_0 = [0\ 0]^T$, $q_0 = 1$ and $x^* = [13.03\ 0.59]^T$. (b) Trajectory in the phase plane for the solution in panel (a), together with the switching surfaces. For this figure $K_0 = 0.06$, $K_1 = 0.02$

Figure 4. (a) Time series of the state variables $(v_C(t), i_L(t))$ of the closed-loop system H with initial condition $x_0 = [0\ 0]^T$, $q_0 = 0$ and $x^* = [11.03,\ 0.505]^T$. (b) Trajectory in the phase plane of the solution in panel (a), together with the switching surfaces $\tilde{\gamma}_1$ and $\tilde{\gamma}_0$. For this figure $K_0 = 0.02$, $K_1 = 0.03$ and $v_{in} = 35$

6. Conclusions and future work

Here we have designed a switched control law based on Lyapunov functions, using the hybrid systems formalism for the DC/DC buck converter. To achieve this, we performed a differential inclusion on the system that captured all the dynamical regimes of the buck converter. Then, we proceeded to demonstrate that the proposed hybrid system can be controlled via a state dependent switching mechanism which guarantees globalstability. In order to control the form of switching surfaces, we proposed a modified switching mechanism that preserved the stability properties of the system. Finally, we showed by means of numerical simulations that indeed the controlled system is not only globally stable, but also robust to the switch position and reference and input voltages.

This technique shows a potential flexibility that can be exploited through the selection of the free parameters K_0 and K_1. This could allow to tune particular desired transient behavior, conferring a powerful benefit to our proposed design.

The numerical simulations presented were performed using parameter values reported in the literature. We propose as a next step to make the controller robust to changes in parameter values, apply it to more realistic buck power converters and compare its performance with other globally stable design techniques (see for instance [1] for a recent application).

Acknowledgments

References

[1] ANGULO-GARCIA, D., ANGULO, F., OSORIO, G., AND OLIVAR, G. Control of a dc-dc buck converter through contraction techniques. *Energies 11*, 11 (2018), 3086.

[2] CHEN, W., HUANG, A. Q., LI, C., WANG, G., AND GU, W. Analysis and comparison of medium voltage high power dc/dc converters for offshore wind energy systems. *IEEE Transactions on Power Electronics 28*, 4 (2013), 2014–2023.

[3] DEANE, J., AND HAMILL, D. Analysis, simulation and experimental study of chaos in the buck converter. In *Proc. IEEE PESC.* (Jun 1990), pp. 491–498.

[4] FERNANDEZ, L. M., GARCIA, P., GARCIA, C. A., AND JURADO, F. Hybrid electric system based on fuel cell and battery and integrating a single dc/dc converter for a tramway. *Energy Conversion and Management 52*, 5 (2011), 2183–2192.

[5] GOEBEL, R., SANFELICE, R. G., AND TEEL, A. R. *Hybrid Dynamical Systems: modeling, stability, and robustness*. Princeton University Press, 2012.

[6] KAZIMIERCZUK, M. K. *Pulse-width modulated DC-DC power converters*. John Wiley & Sons, 2015.

[7] LI, W., AND HE, X. Review of nonisolated high-step-up dc/dc converters in photovoltaic grid-connected applications. *IEEE Transactions on Industrial Electronics 58*, 4 (2011), 1239–1250.

[8] LUO, F. L., AND YE, H. *Advanced dc/dc converters*. crc Press, 2016.

[9] LUZ-ADRIANA, O., ANGULO, F., OSORIO, G., AND ANGULO-GARCIA, D. Hybrid control design of a dc/dc buck power converter. In *2019 4th IEEE Colombian Conference on Automatica Control (CCAC)* (2019), IEEE, p. In Press.

[10] SANFELICE, R. G., GOEBEL, R., AND TEEL, A. R. Generalized solutions to hybrid dynamical systems. *ESAIM: Control, Optimisation and Calculus of Variations 14*, 4 (2008), 699–724.

[11] SANFELICE, R. G., AND PRIEUR, C. Uniting two output-feedback controllers with different objectives. In *American Control Conference (ACC), 2010* (2010), IEEE, pp. 910–915.

[12] THEUNISSE, T. A., CHAI, J., SANFELICE, R. G., AND HEEMELS, W. M. H. Hybrid control of the boost converter: Robust global stabilization. In *52nd IEEE Conference on Decision and Control* (2013), IEEE, pp. 3635–3640.

[13] Theunisse, T. A., Chai, J., Sanfelice, R. G., and Heemels, W. M. H. Robust global stabilization of the dc-dc boost converter via hybrid control. *IEEE Transactions on Circuits and Systems I: Regular Papers 62*, 4 (2015), 1052–1061.

Luz-Adriana Ocampo, M.Sc. (Ph.D. student): Universidad Nacional de Colombia - Sede Manizales, Facultad de Ingeniería y Arquitectura, Departamento de Ingeniería Eléctrica, Electrónica y Computación, Percepción y Control Inteligente, Bloque Q, Campus La Nubia, Manizales, 170003 - Colombia (*laocampona@unal.edu.co*).

Fabiola Angulo, Ph.D.: Universidad Nacional de Colombia - Sede Manizales, Facultad de Ingeniería y Arquitectura, Departamento de Ingeniería Eléctrica, Electrónica y Computación, Percepción y Control Inteligente, Bloque Q, Campus La Nubia, Manizales, 170003 - Colombia (*fangulog@unal.edu.co*).

David Angulo-Garcia, Ph.D.: Instituto de Matemáticas Aplicadas, Grupo de Modelado Computacional & Dinámica y Complejidad de Sistemas, Universidad de Cartagena, Carrera 6 # 36 - 100. Cartagena - Colombia
(*dangulog@unicartagena.edu.co*).

Analysis of dynamical response of a Stewart platform operating in six degrees of freedom

Paweł Olejnik, Jan Awrejcewicz

Abstract: Stewart platforms belong to a wide range of forcing devices and form the basis for positions testing properties and dynamic responses of various objects (e.g., vehicles, machine parts, combat machines, moving components of production lines and others). Mechanical enforcement in the form of various functions of position, velocity or acceleration must be precise, because it serves as a reference point (dynamic reference) in the assessment of the response of objects placed on the platform table and subjected to excitation. This work describes several performance tests of the tested platform, as well as the reaction rate for selected forms of excitation is recorded. In LabVIEW environment, on the basis of the readings from the motion sensors, the time delays of the open control system were determined, the system was qualitatively evaluated and the time response characteristics of the dynamic response were presented.

1. Introduction

The main task of the original system prepared for the measurements and analysis of data is to check the capabilities of the vision system and 6-axis Stewart platform control system designed for generation of a dynamical reference signals for other objects placed on or attached to it. The results of the work allow to plan the applications to determine the capabilities of equipment. The work contains a description of the performed tests, i.e., methodology, the impact of the system parameters on the results and on the performance of the platform's positioning system. The detailed results are summarized at the end.

All tests were carried out in the context of estimating the system's performance in terms of the possibility of further development of algorithms, implementing a closed-loop control of the Stewart platform, the so-called hexapod. The task will be based on a visual observation of dynamical responding objects located on the platform subjected to excitation from six electromechanical actuators.

1.1. The experimental stand

The experimental laboratory stand consists of the following components:

a. six degrees of freedom Stewart platform [1-3];
b. PXI 1071 implementing the Stewart platform control via Parker TPDM 020202DLE5g controllers;
c. dedicated laptop with software enabling control of the platform;
d. 4 Basler acA2040-180km cameras;

e. PXIe 1085 with PXIe-8880 Xeon 8-Core controller, Win 7 (64-bit);

f. 4 PXIe-1435 Camera Link Frame Grabber cards for connecting cameras.

Figure 1. The laboratory test stand in the Department of Automation, Biomechanics and Mechatronics of Lodz University of Technology.
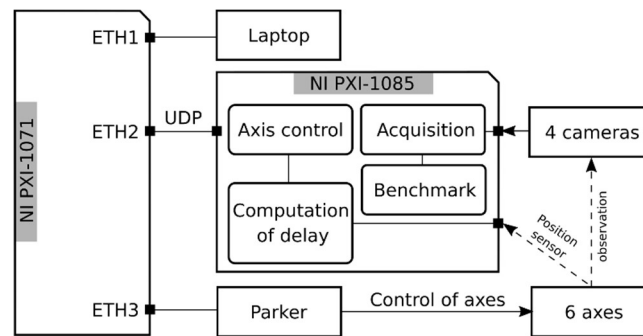
Figure 2. Block diagram of the mechatronic system installed on the laboratory stand.

Picture of laboratory stand and its mechatronic system with connections between the platform, NI components, sensors and software communicating over UDP protocol are presented in Fig. 1 and 2.

The scope of the work included conducting separate tests to check the technical capabilities of the investigated platform, while the following ones have been carried out:

a. delay of all cameras acquisition;

b. speed of all cameras acquisition;

c. platform response delay to control signals;

d. CPU load for image acquisition;

e. system performance while saving to the disk images from cameras;

f. CPU load while processing video algorithm.

1.2. LabVIEW programs

The tests enumerated in Sec. 1.1 are created with the use if virtual instruments in LabVIEW environment. They are consolidated in a project "Benchmark" the window of which is shown in Fig. 3.

a.   b.
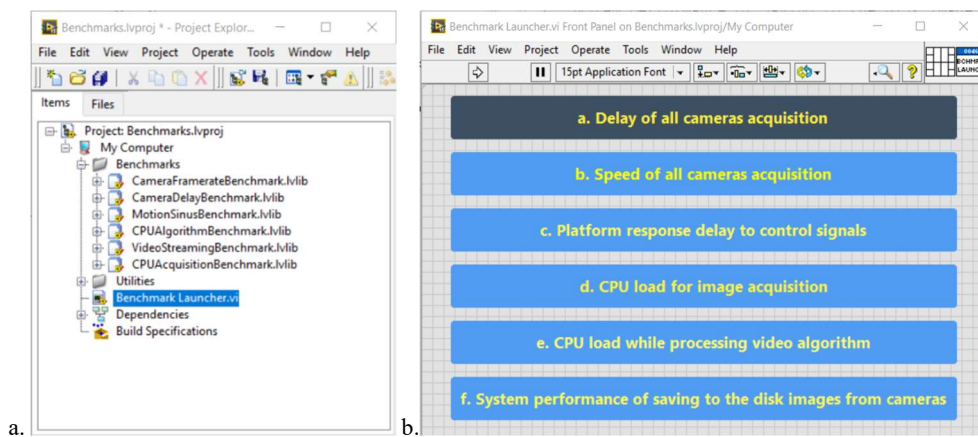
Figure 3. The LabVIEW project "Benchmarks" (a) including particular codes testing the platform (b). Launching the project a window containing shortcuts to run all the tests a-f is open.

2. Tests of the entire system

2.1. Delay of image acquisition from all cameras

The purpose of the test is to measure the delay in the image acquisition from all cameras, i.e., the difference between the actual time of change of the object observed by the cameras, and the time when the camera data representing the change will be available for processing in the controller program. The observed object is a LED diode, whose state is changed by a signal given from the myDAQ card.

Configuration No. 1:

a. the PXIe 8880 controller runs Windows 7 Professional SP1;

b. 4 Basler acA2040-180km cameras connected in full mode to PXIe 1435 frame grabbers (one camera to one PXIe 1435);

c. camera acquisition mode set as triggered automatically (all triggers from the Frame Grabber section: Acquisition Control set to OFF);

d. exposure time control mode (Exposure Control = "Free Run", Exposure Mode = "Manual");

e. exposure time no more than 5 ms;

f. each camera acquires the image with the maximum number of frames per second;

g. bit depth is 8 bits;

h. card with digital lines (myDAQ) connected to the PXIe 8880 controller via USB;

i. LED is connected to the digital output card;

j. configuration parameters can be changed using the NI MAX program.

The "Delay of all cameras acquisition" test starts from the main project "Benchmarks". The limit detection value of the LED status is set. We set the path for saving the results in the "Result Path" field and the number of test repetitions in the fields "WarmUp Repetitions" and "Test Repetitions". "Warm up repetitions" is the number of run test repetitions carried out before the actual test during which no results are collected, "Test repetitions" are test repetitions from which the results are recorded. Recommended values are "WarmUp Repetitions" = 5 and "Test Repetitions" = 50. After starting the program with the "Run" button, the screen area in which the brightness of the LED image is expected to change is confirmed with the ENTER button. The operation is repeated for all 4 cameras. The test stops automatically after the assumed number of repetitions.

The first tests were carried out on a simulated diode displayed on the monitor screen in the LabVIEW program. In this way, the time after which the cameras detected changes in the status of the indicator on the front panel of the application was measured. However, the results obtained were unreliable due to the long delays associated with updating the user panel in LabVIEW. Therefore, it was decided to eliminate the factor introducing additional delays and used 3 physical LEDs. A digital signal is generated in the running program. The binary state changes every 500 ms. Along with the signal, the program saves a moment of time when the on-off signal was sent to the diode.

Cameras were directed at diodes. At the time of detection of a change in the status of the LED, the program saves a moment of time at which the change was recorded by the camera. The program is designed in such a way that the time needed for performing the image processing algorithm required to detect a change in the diode's state does not affect the measured delay. The time difference between the real signal of the diode status change and its detection on the camera image is the delay in the acquisition of camera images. Tests were carried out at nominal camera parameters, i.e., image resolution – 2040x2040, color depth – 8 bits, maximum acquisition speed – 187 fps. The image was recorded simultaneously from 4 cameras. Front panel of the benchmark is shown in Fig. 4.

The test allowed to estimate an image acquisition delay. The average delay was 12 ms for each camera. Camera images were taken and processed in parallel, so camera delays do not add up – 12 ms is the average time to observe a change in status on all cameras.
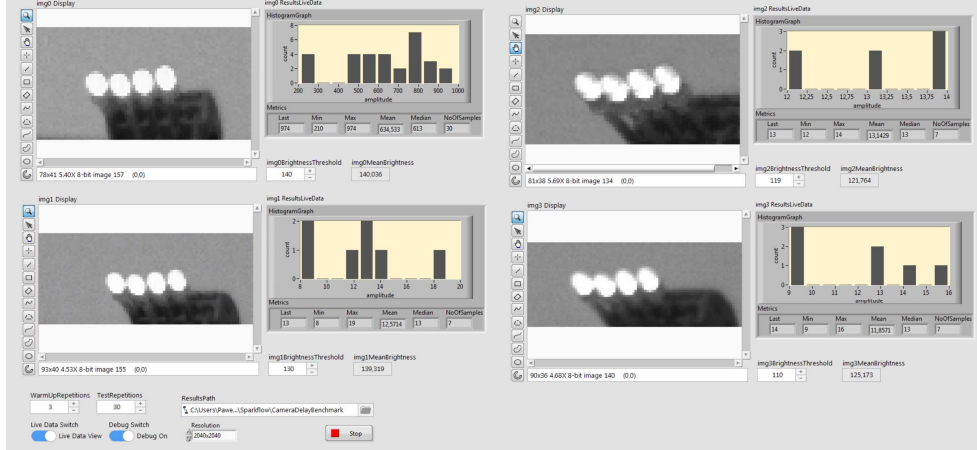
Figure 4. Front panel of the "Delay of all cameras acquisition" benchmark.

It should be noted that in the hardware configuration at the station, the camera clocks are not synchronized, i.e., the detection delays of the occurrence of the diode's change in state on each camera may differ from each other by the maximum time of acquisition of one image frame, i.e., by 5.35 ms.

2.2. Speed of image acquisition from all cameras

Measurement of image acquisition speed from cameras is based on the estimation of the number of frames processed in one second. The goal was to check if the resolution and bit depth of the acquired (processed) image affect the acquisition rate.

In the Configuration No. 2, a-f are repeated as in the Configuration 1, bit depth is 8, 10, 12 bits.

The "Speed of all cameras acquisition" test starts from the main project "Benchmarks". First, in the "Resolution" field, the desired image resolution recorded by cameras is selected. The display of camera images and the display of debug data using the "Live Data" and "Debug Data" switches are further disabled. One sets the path for saving the results in the "Result Path" field and the number of test repetitions in the fields "WarmUp Repetitions" and "Test Repetitions". "Warm up repetitions" is the number of run test repetitions carried out before the actual test during which no results are collected, "Test repetitions" are test repetitions from which the results are recorded. Recommended values are "WarmUp Repetitions" = 500 and "Test Repetitions" = 3000. After starting the program with the "Run" button the test stops automatically after the assumed number of repetitions.

Cameras carry out acquisitions with the maximum frame rate set by the manufacturer. The images from the cameras are sent to the PXIe controller and read in the test application. The number of frames per second is computed. The tests are conducted for three resolutions of the image taken from cameras: 2040x2040, 510x510 and 60x60 pixels and for three bit depths: 8 bit, 10 bit and 12 bit. The average number of frames acquired during 1 second of acquisition is written in Table 1.

Table 1. The average number of frames acquired during one second of acquisition.

	Frames per second (fps)		
Bit depth (bit)	2040x2040	510x510	60x60
8	187.06	187.04	187.04
10	75.20	75.20	75.20
12	37.70	37.70	37.70
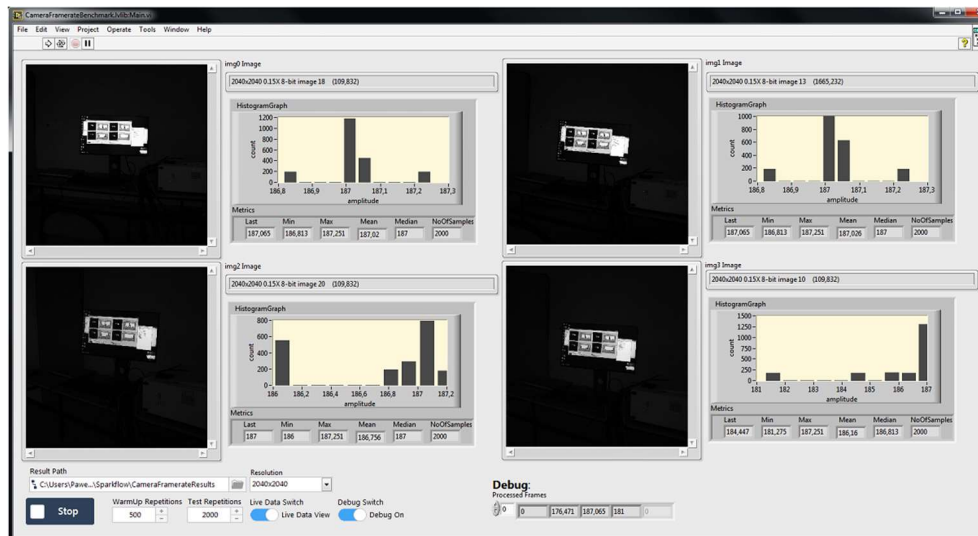
Figure 5. Front panel of the "Speed of all cameras acquisition" benchmark.

The obtained results show that changing the resolution has no effect on the speed of image acquisition. Increasing the bit depth causes the acquisition to slow down.

2.3. Delay of the Stewart platform response to control signals

The purpose of the test is to estimate the dynamic response delay of the investigated platform relatively to the given sinusoidal control signal. The measurement is performed using a rotary potentiometer energized from a battery.

Configuration No. 3 includes a computer with Vzero software controlling the platform, PXIe 8880 controller cooperating with Windows 7 Professional SP, benchmark project (c), enabling the task of external control signals using the UDP protocol and an analog sensor – a potentiometer connected to the analog input card (e.g., myDAQ) powered by a 1.8 V battery.

The "Platform response delay to control signals" test starts from the main project "Benchmarks". Next, the UDP communication parameters between the computer sending the control function and the platform controller are set, as well as the frequency and amplitude of the sinusoidal control signal, the

parameters of acquisition of angular rotation read from the myDAQ card, processing the voltage values read from the rotary potentiometer and the number of test repetitions are assumed. The test stand showing placement of the sensor is shown in Fig. 6.
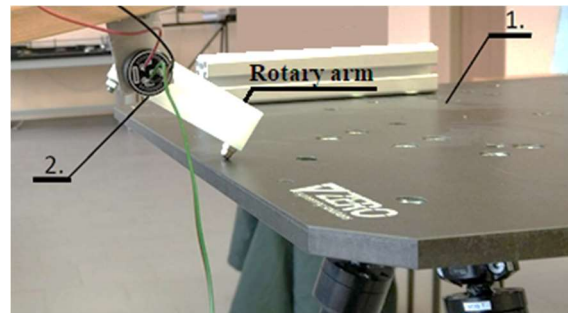
Figure 6. Front panel of the "Speed of all cameras acquisition" benchmark (1 – the table of the platform, 2 – rotary potentiometer measuring vertical displacement of the platform).

The test program generates a sinusoidal signal with a given amplitude and frequency, which is then sent as a signal controlling the position of the selected platform axis to the platform controller via the UDP protocol. At the same time, the program collects the signal measured with the rotary potentiometer. After the test, the program calculates the phase shift of both signals, displaying the time delay of the platform response to the control signal.

After 50 test iterations, an average platform delay of 12.04 ms is obtained. The total delay consists of the delay associated with UDP communication and the delay caused by dynamic limitations of the platform.
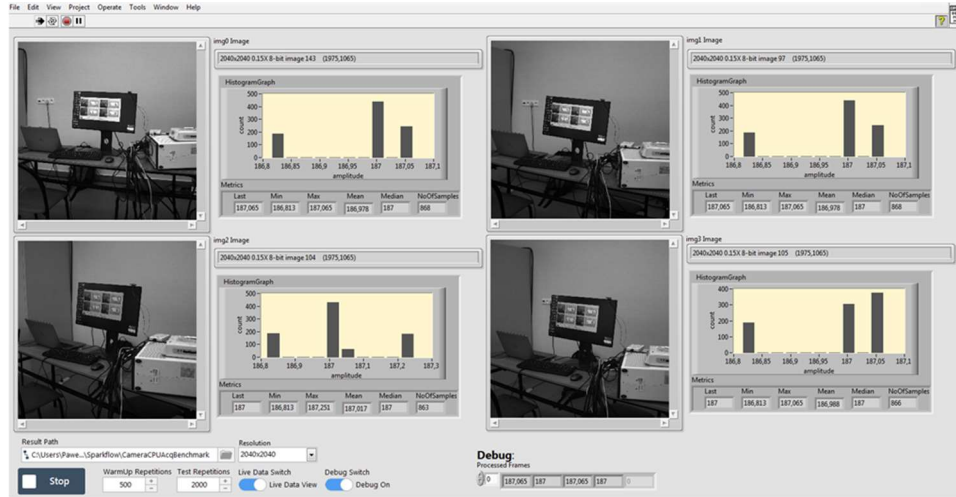
2.4. CPU load for image acquisition

This test is performed to check the load on the microprocessor unit during image acquisition from all cameras with the maximum frame rate set by the manufacturer.

In the Configuration No. 4, points a-g are repeated as in the Configuration No. 1.

The "CPU load for image acquisition" test starts from the main project "Benchmarks". First, in the "Resolution" field, the desired image resolution recorded by cameras is selected. The display of camera images and the display of debug data using the "Live Data" and "Debug Data" switches are further disabled. One sets the path for saving the results in the "Result Path" field and the number of test repetitions in the fields "WarmUp Repetitions" and "Test Repetitions". "Warm up repetitions" is the number of run test repetitions carried out before the actual test during which no results are collected, "Test repetitions" are test repetitions from which the results are recorded. Recommended values are

"WarmUp Repetitions" = 500 and "Test Repetitions" = 3000. After starting the program with the "Run" button the test stops automatically after the assumed number of repetitions.

**Figure 7.** Front panel of the "CPU load for image acquisition" benchmark.

Cameras record images in a continuous mode with the maximum frame rate set by the manufacturer (the image is not saved to the hard disk). The images from the cameras are sent to the PXIe 8880 controller and read in the test application. The number of frames per second is read and the processor load is checked during the tests.

As a result, the CPU load during image acquisition is insignificant and amounts to about 10% of the available resources for the images at 2040x2040 resolution and about 5% for the images at 60x60 pixels resolution. These results coincide with expectations. Due to the way the system performs image acquisition, the acquired data is transferred from Frame Grabber directly to the controller's RAM memory without the participation of the processor in data transfer.

The performance tests of the investigated system described above tend to build a more complex closed-loop position control system. The system will control an object moving on the Stewart platform's table. All the tests made possible to determine the time delays on the path: setting the reference value of the object's position on the platform, triggering platform position, measuring the position of the object on the platform using vision algorithms, correcting the position of the platform, checking the positioning error. Details are provided in the next section.

3.   Analysis of delays occurring in the system

Delays occurring in the system, based on the predicted algorithm of controlling the position of the ball rolling on the platform in a closed control loop are presented in the diagram in Fig. 7.
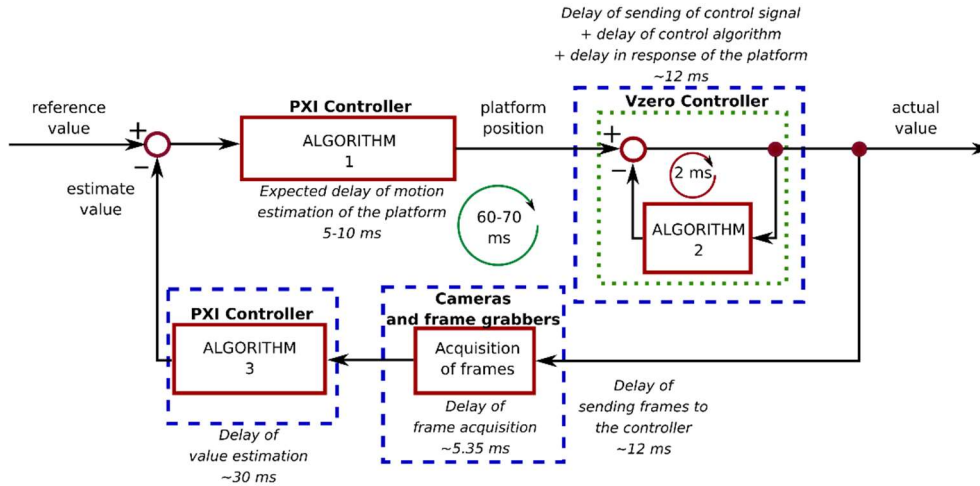
Figure 8. Diagram of position control of an object rolling on the platform. Algorithms are denoted as follows: 1) estimation of platform position to move the object on the platform; 2) control of Stewart platform; 3) estimation of position of the object based on vision procedures.

Expected execution times of individual code fragments, communication between subsystems and their response times can be determined as follows:

1. delays due to internal hardware restrictions of the platform controller and cameras;
2. delays resulting from the settings used, the algorithms used and the data transfer methods;
3. total delay of the closed control loop, assuming that the control can be performed only after the system moves to the reference position in space;
4. time delays in a closed control system include the time of:

   a. computations required by the platform's control algorithm,

   b. transmission and interpretation of the control signal by the platform controller,

   c. dynamic platform response,

   d. image collection by cameras,

   e. image transfer from cameras to the controller,

   f. image processing,

   g. computing the algorithm for determining the position of the object on the images.

The sum of the described delays is 60-70 ms. It is the time of signal propagation in the control system from the generation of the platform control signal, by changing the position of the platform to measure the location of the object. This approach to the control loop would be appropriate when testing the static properties of an object on a platform, where a stabilized state of the object would be required.

4. Conclusions

The presented Stewart platform manipulator constructed in the Department of Automation, Biomechanics and Mechatronics of Lodz University of Technology allows for a relatively fast realization of mechanical enforcement in the form of various functions of position, velocity or acceleration. The described performance tests performed under control of LabVIEW environment and NI hardware have revealed some restrictions, but also a big potential in terms of improvement of the dynamic response characteristics and reduction of time delays.

The tested system has various types of delays and each of them will be subject to a different reduction method. Delays resulting from the processing of algorithms will be subject to optimization of image processing algorithms and determining the movement of the platform. The selection of appropriate system performance parameters and algorithms may consist of: optimizing camera settings so that the controlled object occupies the largest part of the image frame; limiting the number of cameras needed to determine the position of the object; setting the lighting so that it is easier to distinguish the object (edges or markers) from the background by using the appropriate background, object and lighting colors.

Such settings and optimization of code performance should allow for significantly accelerating the operation of algorithms and reducing time delays. The minimum delay time resulting from algorithm processing is not easy to estimate and requires additional testing.

References

[1] Dasgupta, B., Mruthyunjaya, T.S. The Stewart platform manipulator: a review. *Mechanism and Machine Theory* 35(1), 2000, 15-40, doi: 10.1016/S0094-114X(99)00006-3.

[2] Huang, X. Liao, Q. Wei. S. Closed-form forward kinematics for a symmetrical 6-6 Stewart platform using algebraic elimination. *Mechanism and Machine Theory* 45(2), 2010, 327-334, doi: 10.1016/j.mechmachtheory.2009.09.008.

[3] Dudita F., Neagoe M., Gogu G. On the Kinematic Calibration of a Stewart Platform. In: Gogu G., Coutellier D., Chedmail P., Ray P. (eds) *Recent Advances in Integrated Design and Manufacturing in Mechanical Engineering*, 2003, pp. 117-128, Springer, Dordrecht.

Paweł Olejnik, Associate Professor: Department of Automation, Biomechanics and Mechatronics, 1/15 Stefanowski Street, 90-924 Łódz, Poland (*pawel.olejnik@p.lodz.pl*). The author gave a presentation of this paper during one of the conference sessions.

Jan Awrejcewicz, Professor: Department of Automation, Biomechanics and Mechatronics, 1/15 Stefanowski Street, 90-924 Łódz, Poland (*jan.awrejcewicz@p.lodz.pl*).

Design of a medium-scale test for the assessment of a resonant seismic barrier within the ReWarD Project

Antonio Palermo, Farhad Zeighami, Athanasios Vratsikidis, Zhibao Cheng, Dimitris Pitilakis, Alessandro Marzani

Abstract: The growing interest about meta-structures from the civil engineer community has led to the development of novel low frequency isolation systems for ground borne vibrations and seismic waves. Among those, the resonant Metabarrier, i.e., an array of meter-size resonators embedded in the ground around the structure, or a cluster of structures, to be protected, has been recently proposed. The metabarrier is designed to attenuate the surface ground motion induced by Rayleigh waves, with the potential ability to retrofit and shield existing vulnerable structures including historical buildings and cultural heritage sites. Additionally, it can be tuned to operate at specific frequencies ranges, for instance at the resonant frequencies of the structure. While the metabarrier conceptual design has been validated numerically and at small-scale laboratory tests, its engineering implementation still needs an on-field validation. Here we present the design of an experimental campaign, currently under development at the Euroseistest facility (`http://euroseisdb.civil.auth.gr`) within the framework of the ReWarD project (`https://site.unibo.it/reward/en`), meant at testing the performance of a medium-scale metabarrier. The barrier is designed according to the stratigraphy of the site exploiting dispersion curves and time history analysis developed within a Finite Element framework. The experimental test, designed according to such numerical indications, are expected to confirm a significant attenuation of the ground motion in the presence of the metabarrier.

1. Introduction

Periodic and resonant foundations and buried wave barriers designed to damp the propagation of seismic waves can represent a breakthrough for the safety and for the preservation of historic and strategic infrastructures including hospitals and power plants [1, 18, 21, 7, 9, 11, 19, 2, 20]. These structures, commonly defined as "seismic metamaterials" [3], base their seismic isolation capabilities on physical concepts well established in the domains of phononic crystals and resonant metamaterials [10]. Phononic crystals are periodic materials that can exhibit large band gaps, i.e. frequency regions where the propagation of waves with wavelengths in the order of material periodicity is hindered. For seismic scale applications, meter size phononic crystals made of cylindrical holes in sedimentary soil have

proved the possibility of reflecting seismic elastic energy, achieving attenuation of ground accelerations at a frequency range around 50 Hz [3]. More recently, a similar concept has been used to realize seismic lenses with large (100 m) gradient index able to reroute surface waves around buildings [5]. Although revolutionary in their conception, implementation of these systems at the low frequencies characteristic of seismic events (<30 Hz) requires very large structures, since the wavelengths of typical seismic waves can be of several meters or decameters. Complementary to phononic crystals, resonant metamaterials exploit an array of embedded locally resonant units to interact with propagating waves at a sub-wavelength scale. Therefore, for seismic waves characterized by long wavelengths, resonant metamaterials allow for the construction of more viable devices, i.e. of smaller and feasible spatial dimensions. On the basis of this paradigm, sub-wavelength structures, in the form of resonant metafoundations [4] or resonant metabarriers [11] have been proposed in recent years to isolate buildings and infrastructures from incoming seismic longitudinal and shear waves or to shield them from surface Rayleigh waves, respectively. The idea of a resonant metabarrier, in particular, is motivated by the fact that far from the epicenter surface waves can carry a significant portion of the earthquake energy [6] and that existing structures may be hard to be retrofitted with innovative foundation systems. The resonant metabarrier bases its operating principle on the interaction between purposely designed resonant units with surface waves in the low frequency regime (<10 Hz). The resonant units are passive devices (mass-stiffness resonators), placed atop of the soil or buried below the surface and excited by the vertical component of the Rayleigh wave motion. Once activated, their dynamic interaction with the soil redirects part of the surface elastic Rayleigh wave energy into the interior of the soil deposit as vertically polarized shear waves. The physics of these resonant systems has been predicted analytically and verified numerically at different wave scales, or in other words at different frequencies. Conversely, experimental proof of their working mechanism and attenuation capabilities are up to now limited to few table-top experimental tests [11]. Nonetheless, measurements at the geophysical scale have shown a reduction of the surface motion due to the resonance of forest trees [5], encouraging the realization of an experimental proof of the metabarrier concept in the Hz range. Indeed a full scale realization and test of a resonant barrier is still missing, probably due to its cost of realization as well as for the significant resonating mass needed to activate the wave conversion. In this work, we aim at making a further step towards the realization of this isolation system for seismic waves by testing the effectiveness of a resonant metabarrier at a medium-size scale for the first time, within a $50 - 100$ Hz frequency range, taking into account the inevitable variability in stiffness and strength of the soil and the resonators components. To such purpose the design of an experimental campaign under development at the Euroseistest TA facility [14] is here

presented. The barrier is designed according to the in-situ soil properties and the available operative frequency range of the measuring equipment. Multichannel Analysis of Surface Waves (MASW) technique will be used to excite the soil and to measure the soil response in the presence of the metabarrier or without it. The test setup is expected to confirm an attenuation of the ground motion in the presence of the metabarrier. In what follows we will describe the barrier arrangement and the site soil properties. In addition, we will provide numerical predictions of the expected performance of the barrier. Experimental evidences from the testing will be presented and discussed at the conference.

2. Metabarrier

The metabarrier consits of an array of resonators arranged in a regular square grid of 5×10 m, spaced apart of 0.5 m (see Fig. 1a).

The key element of the metabarrier is the resonator (see Fig. 1b). Resonators can be realized using simple construction materials (concrete, sand and steel). In this preliminary design phase, our prototype resonator consists in a PVC barrel (diameter 400 mm and height approximately 500 mm) filled with dry sand. The mass of the resonator can be thus varied up to 100 kg by pouring different amounts of dry sand within the barrel. The barrel is placed on a bed of 4 to 8 vertical steel springs kept between two 10 mm thick steel plates of planar dimensions 400×400 mm. By varying the number of springs, the overall stiffness of the resonator can be changed. The prototype resonator is designed to provide a surface wave attenuation between 50 and 55 Hz, well above the frequency range of the seismic action, but limiting the overall experimental cost. For a mass of 50 kg and a resonant frequency $f_r = 50$ Hz, the overall stiffness is $K_{tot} = 50 \cdot (2\pi f_r)^2 = 4934802 \ N/m$, i.e. approximately $4935 \ N/mm$.

The modular and tunable design of the resonator allows realizing metabarriers with different resonant frequencies (even once the resonators are in place). The resonant frequency of each resonator, once buried in the ground, will be evaluated to account also for the soil-structure-interaction (SSI) which should slightly lower the nominal resonant frequency. To this purpose, an operator can simply activate the resonator mass with a soft hammer stroke, record its motion with a single axis (vertical) accelerometer positioned on the top of the mass and measure its resonance frequency. Adjustments of the resonator frequency are achievable by varying the compaction of the soil below the resonator base, or varying the number/stiffness of some/all springs. Moreover, this flexible design approach of the resonator allows also building metabarriers characterized by lines of resonators with different resonant frequencies. This design strategy, known as rainbow trapping concept in the metamaterial community, can widen the attenuation frequency range of the barrier.
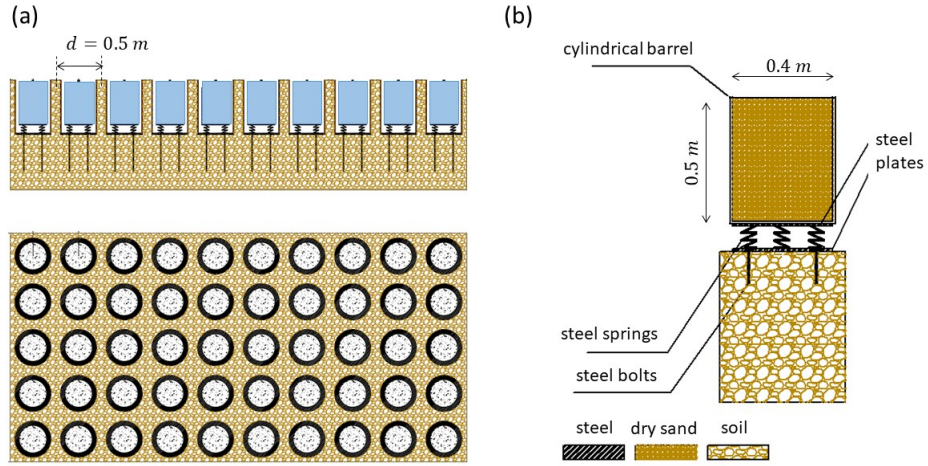
Figure 1. (a) Side view and top view of the 5×10 m array of resonators composing the metabarrier. (b) Schematic of a single resonator.

3. Site description

Previous analytical and numerical studies [11, 12, 13] indicate that the metabarrier isolation performance, both in terms of frequency width and wave amplitude decay, highly depends on the soil mechanical properties (e.g., mass density, longitudinal and shear bulk speeds). Hence, it is of paramount importance to have a detailed knowledge of the soil stratigraphy for a meaningful design of the barrier. The EUROSEISTEST site is the longest running valley-instrumentation project worldwide. The site is located in the centre of Mygdonian basin, Thessaloniki (Greece), in a high seismicity region, where the epicentral area of the destructive Magnitude 6.5 Volvi earthquake (1978) is included. The soil stratigraphy and dynamic properties of the site are already well-documented from previous extended geotechnical and geophysical surveys [16, 17, 14, 15]. Hence, the proposed site offers a unique opportunity to validate the effectiveness of the metabarrier. In Fig. 2, the longitudinal (a) and shear (b) bulk waves speed of the site versus the soil depth are given. The density of the soil is assumed to be $\rho = 1500\ kg/m^3$.

The depth-dependent speed profile is used to compute the surface waves dispersion curves supported by the soil. To such purpose, a 2D soil column (e.g. the model unit cell) of dimensions $d \times h = 0.5 \times 70$ m is modeled via Finite Element method in Comsol
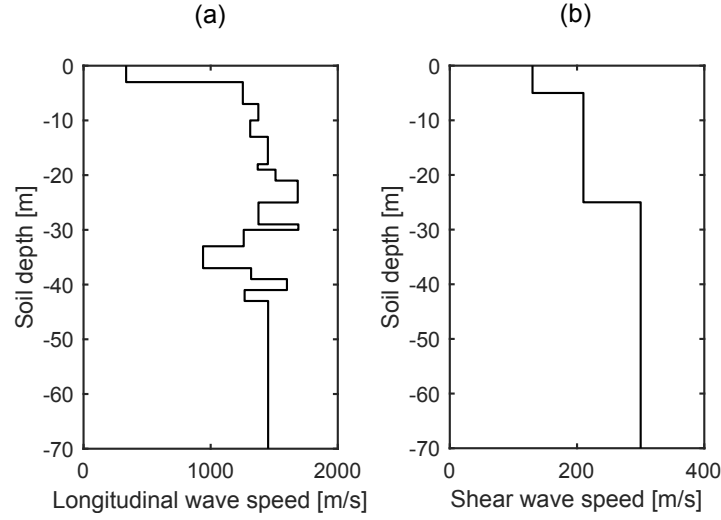
Figure 2. Longitudinal (a) and shear (b) bulk waves speed of the EUROSEISTEST site soil profile.

Multiphysics as shown in Fig. 3a. The 2D model with plane strain conditions suffices to capture the dynamics of vertically polarized surface waves, which are of interest for this study. The domain is discretized by quadrilateral elements with the maximum dimension of $d_{max} = 0.5$ m. Following the Wave Finite Element approach [8], Bloch-Floquet boundary conditions are applied to the vertical sides of the unit cell to extract the surface modes of a semi-infinite soil column. Fig. 3b displays the first three surface modes within the frequency range $10 - 70$ Hz as extracted from the frequency-wavenumber eigenproblem setup via the WFEM. As expected, due to the heterogeneous soil stratigraphy, multiple and dispersive surface modes are found.

4. Metabarrier numerical design via dispersion curve calculations

The analysis of the resonant metabarrier is performed numerically by extracting the barrier dispersion curve via WFEM. As a preliminary investigation we compute the soil column dispersive properties considering only the effect of the trench, which is needed to bury the resonators in the soil. The trench has dimensions 0.5×0.4 m as it is shown in Fig. 4a. Excluding the presence of the trench, the soil column computational model is unchanged and the surface wave dispersion extraction follows the same procedure as the pristine soil. Results of this procedure are displayed in Fig. 4b. The presence of a trench introduces two flat branches in the low frequency range, linked to the resonant behavior of the lateral
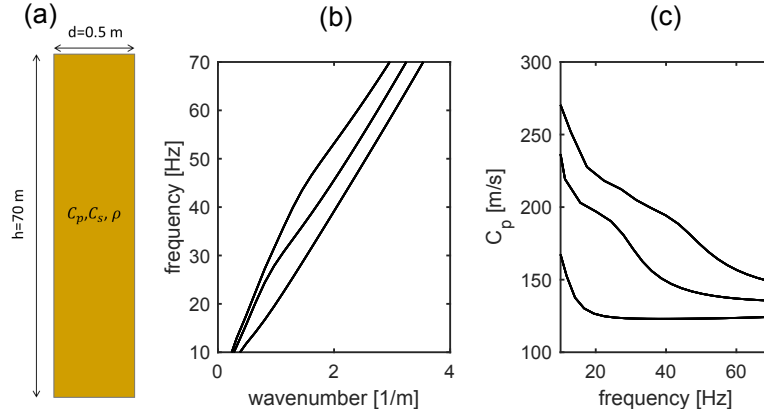
Figure 3. (a) Schematic of the reference soil model (RSM). (b) Dispersion curves for the RSM. (c) Longitudinal velocity vs. frequency.
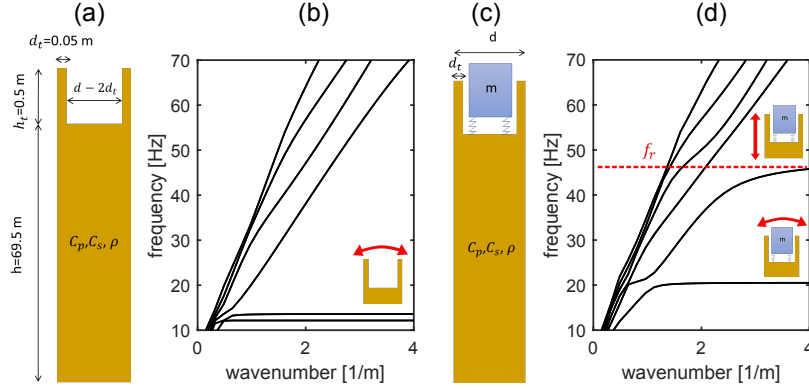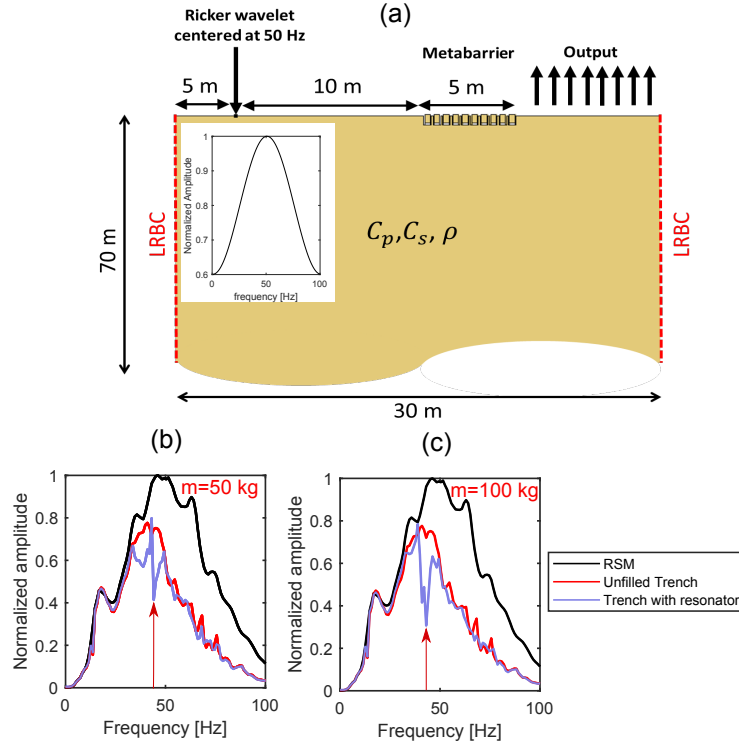

Figure 4. (a) Schematic of the soil model with the trench only and (b) its dispersion curves. (c) Soil model representation in presence of the resonator placed inside trench and (d) its corresponding dispersion curves.

cantilevered soil portions. In practice, these modes are prevented by utilizing stiffer material or retaining walls. Within the remaining frequency range no significant changes in the dispersion curve are found. For the metabarrier model, our 2D model (of unitary thickness $t = 1m$) utilizes a resonator with an equivalent mass per unit length so to correctly model the resonator density of the real metabarrier in its 3D configuration. This approach has been validated in our previous study [13]. The introduction of the resonators induces two flat branches around 20 Hz and 46 Hz, corresponding to the horizontal and vertical motion of the resonators (see Fig. 4d). Here, we remind that the interaction between resonances and surface waves in a homogeneous half space [11] leads to the nucleation of a clear band gap

where surface waves are redirected within the soil bulk. In heterogeneous or stratified soils no clear evidences of this phenomenon is found [12]. Nonetheless, the significant changes in the surface waves dispersion curve around the higher flat branches and in the frequency region above displayed in Fig. 4d suggest that large wave attenuation should be expected around and above 45 Hz due to the impedance mismatch between surface waves in soil and waves travelling within the barrier. In what follows, we verify this hypothesis by performing time transient analysis of surface waves travelling across a finite length resonant barrier embedded in a pristine soil.

## 5. Metabarrier assessment via time transient analysis

Time transient analysis are performed by means of FE simulations utilizing the 2D plane strain model shown in Fig. 5a. Bottom corners of model are restrained in horizontal and vertical directions, and low reflective boundary conditions (LRBCs) are applied at the lateral and bottom edges to prevent wave reflection phenomena from the boundaries. The model is discretized by triangular mesh elements with mesh sizes equal to 0.5 m. The domain has a dimension of 30×70 m and a velocity profile defined according to data in Fig. 2. Surface waves are generated via a point load applied at the model surface at a distance of 10 m from the barrier edge. The signal of choice is a Ricker Wavelet centred at 50 Hz, able to illuminate the whole frequency range of interest. The barrier counts 10 resonators with dimensions and spacing defined according to the schematic in Fig. 1. The output wavefield is evaluated as the averaged vertical displacement extracted over a grid of 11 points (i.e., equivalent to an array of physical sensors in the real scenarios) distributed over 10 m after the barrier. The output displacement of the pristine soil is used as a reference case, namely reference soil model (RSM). Fourier spectra of the averaged displacements for different test configurations are used to evaluate the attenuation performance of the barrier in terms of amplitude and frequency range. Two different scenarios are initially compared, a case with an array of unfilled trenches and the metabarrier case, i.e. an array of trenches equipped with resonators. In addition, two different resonators with overall masses of 50 and 100 kg, and nominal resonant frequency $f_r = 50$ Hz are considered. By comparing the spectrum of the unfilled trench configuration with that of the reference pristine soil, a significant reduction of amplitude in the frequency range > 40 Hz is noticed (see Fig. 5b). Reduction in the wave amplitude can be ascribed to the scattering induced by the trench which acts as a defect/discontinuity in the soil profile. This scattering becomes significant when the trench depth is comparable w.r.t. the depth of the surface wave profile. It follows that a trench designed to be effective for low frequency (e.g. <10 Hz) seismic waves would have a minimum depth of tens of meters.

Figure 5. (a) Schematic of the full 2D FE model used in numerical simulations. Frequency spectra of the reference soil model (RSM, black line), unfilled trench (red line) and trench (light purple line) considering resonators with nominal resonant frequency $f_r = 50$ Hz and (b) 50 kg and (c) 100 kg mass.

The addition of the resonators introduces a marked reduction in the spectrum amplitude around the resonator vertical frequency. A larger mass results in a larger amplitude and frequency width reduction as it can be comprehended by comparing Fig. 5b and c, in accordance with what observed on previous studies on the metabarrier [13]. This marked peak in frequency, could be further widened by using resonators of different nominal resonant frequency and exploiting the so-called rainbow trapping concept [7].

As a further study, we compare the attenuation performance of a barrier fully buried in the soil ('deep trench'), partially buried in the soil ('shallow trench') and placed directly over the soil surface ('no trench'). A reduction in the trench depth corresponds to a reduction in the energy scattered in the high frequency range, which is minimized for the case where no discontinuity in the soil profile is created ('no trench') as shown in Fig. 6.
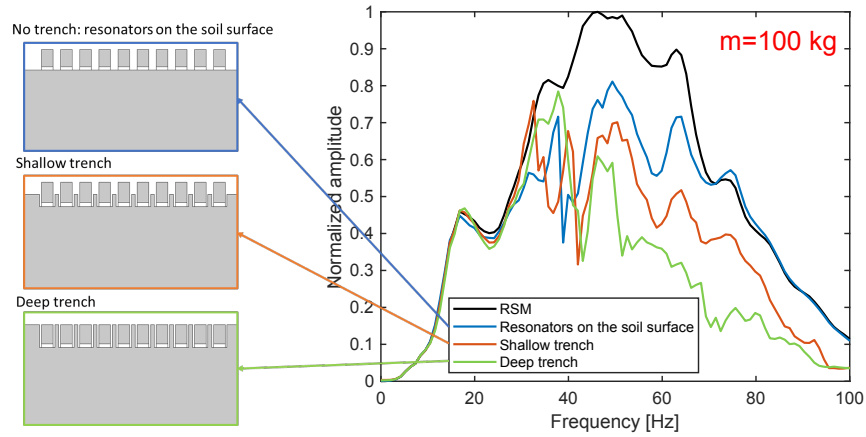
**Figure 6.** Effect of trench depth in attenuation performance of the barrier.
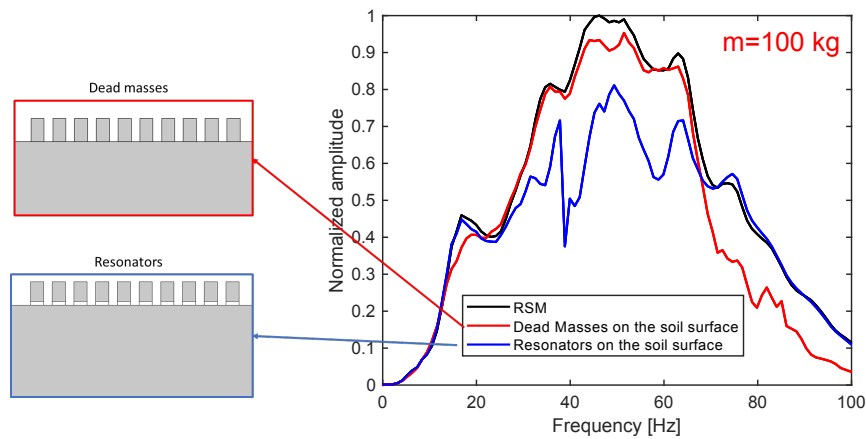
Figure 7. Surface barrier performance vs dead masses placed over the soil surface.

Finally, Fig. 7 compares the performance of this latter configuration to a companion equivalent arrangement of dead mass, to single out the contribution of the resonances in the attenuation performance of the barrier.

6. Discussion and conclusions

The metabarrier consists in a device located around the target which has to be protected from surface waves. Since it does not require any intervention on the existing structure, the metabarrier can represent not only an alternative to the traditional approaches for seismic

retrofitting of a cluster of structures but also a mean for a more viable strengthening of structures and infrastructures of prior importance for the public safety (schools, hospitals, power plants, etc.).
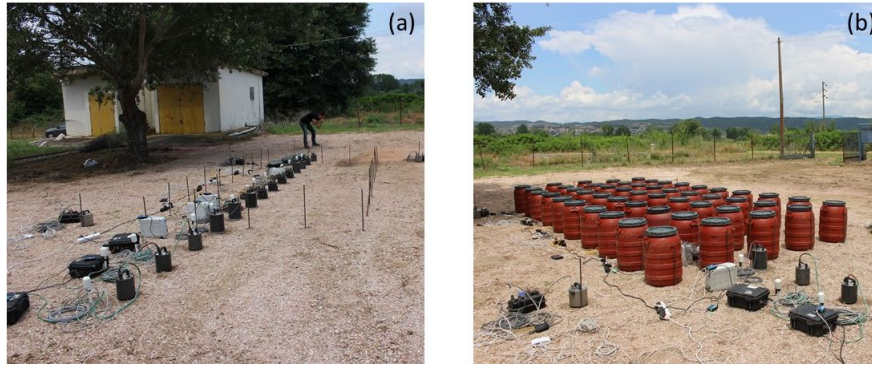
Figure 8. (a) On-field line measurement setup across barrier length. (b) Dead mass configuration atop soil surface (no trench).

The numerical investigations carried out in this work show that while a trench provides seismic attenuation due to scattering at frequencies related to the depth of the trench, the metabarrier exploits resonance to attenuate the seismic motion at frequencies related to the resonators characteristics (i.e. masses and springs).The study evidences that the dynamic coupling between the surface wave and the resonances of the distributed mass-spring isolation system is fundamental to activate the barrier wave attenuation mechanism (see Fig. 7). In particular, it is shown that a barrier of distributed resonator placed directly over the soil can both simplify the realization of the test (no excavation phase required) and clearly highlight the effect of the resonators on the attenuation spectrum. A first experimental campaign is currently under development to validate the numerical findings. In particular, at first the "dead mass" configuration atop the soil, i.e. the "no trench" case, is considered (see Fig. 8). The test aims confirming the numerical results predicted in Fig. 7 for the reference soil (RSM) and the dead mass case. Subsequently, the designed steel plates and springs will be put in place to allow the masses to resonate. A throughout description of the testing equipment, protocol and data processing will be presented during the conference.

Acknowledgments

References

[1] Bao, J., Shi, Z., and Xiang, H. Dynamic responses of a structure with periodic foundations. *Journal of Engineering Mechanics 138*, 7 (2011), 761–769.

[2] Basone, F., Wenzel, M., Bursi, O. S., and Fossetti, M. Finite locally resonant metafoundations for the seismic protection of fuel storage tanks. *Earthquake Engineering & Structural Dynamics 48*, 2 (2019), 232–252.

[3] Brûlé, S., Javelaud, E. H., Enoch, S., and Guenneau, S. Experiments on seismic metamaterials: Molding surface waves. *Phys. Rev. Lett. 112* (Mar 2014), 133901.

[4] Cheng, Z., and Shi, Z. Novel composite periodic structures with attenuation zones. *Engineering Structures 56* (2013), 1271 – 1282.

[5] Colombi, A., Roux, P., Guenneau, S., Gueguen, P., and Craster, R. V. Forests as a natural seismic metamaterial: Rayleigh wave bandgaps induced by local resonances. *Scientific Reports 6* (Jan 2016), 19238 EP –. Article.

[6] K.F. Graff. *Wave motion in elastic solids*. Dover, 1975.

[7] Krdel, S., Thom, N., and Daraio, C. Wide band-gap seismic metastructures. *Extreme Mechanics Letters 4* (2015), 111 – 117.

[8] Mace, B. R., and Manconi, E. Modelling wave propagation in two-dimensional structures using finite element analysis. *Journal of Sound and Vibration 318*, 4 (2008), 884–902.

[9] Miniaci, M., Krushynska, A., Bosia, F., and Pugno, N. M. Large scale mechanical metamaterials as seismic shields. *New Journal of Physics 18*, 8 (2016), 083041.

[10] P. A. Deymier. *Acoustic Metamaterials and Phononic Crystals*. Springer, 2013.

[11] Palermo, A., Krödel, S., Marzani, A., and Daraio, C. Engineered metabarrier as shield from seismic surface waves. *Scientific Reports 6* (Dec 2016), 39356 EP –. Article.

[12] Palermo, A., Krödel, S., Matlack, K. H., Zaccherini, R., Dertimanis, V. K., Chatzi, E. N., Marzani, A., and Daraio, C. Hybridization of guided surface acoustic modes in unconsolidated granular media by a resonant metasurface. *Phys. Rev. Applied 9* (May 2018), 054026.

[13] Palermo, A., Vitali, M., and Marzani, A. Metabarriers with multi-mass locally resonating units for broad band rayleigh waves attenuation. *Soil Dynamics and Earthquake Engineering 113* (2018), 265 – 277.

[14] Pitilakis, D., Dietz, M., Wood, D. M., Clouteau, D., and Modaressi, A. Numerical simulation of dynamic soilstructure interaction in shaking table testing. *Soil Dynamics and Earthquake Engineering 28*, 6 (2008), 453 – 467.

[15] PITILAKIS, D., ROVITHIS, E., ANASTASIADIS, A., VRATSIKIDIS, A., AND MANAKOU, M. Field evidence of ssi from full-scale structure testing. *Soil Dynamics and Earthquake Engineering 112* (2018), 89 – 106.

[16] PITILAKIS, K., RAPTAKIS, D., LONTZETIDIS, K., TIKA-VASSILIKOU, T., AND JONGMANS, D. Geotechnical and geophysical description of euro-seistest, using field, laboratory tests and moderate strong motion recordings. *Journal of Earthquake Engineering 3*, 3 (1999), 381–409.

[17] RAPTAKIS, D., CHVEZ-GARCA, F., MAKRA, K., AND PITILAKIS, K. Site effects at euroseistesti. determination of the valley structure and confrontation of observations with 1d analysis. *Soil Dynamics and Earthquake Engineering 19*, 1 (2000), 1 – 22.

[18] SHI, Z., CHENG, Z., AND XIANG, H. Seismic isolation foundations with effective attenuation zones. *Soil Dynamics and Earthquake Engineering 57* (2014), 143–151.

[19] SMITH, A., AND SMITH, C. *Book Title Book Title Book Title Book Title Book Title.* Publisher of the Book, City, 2015.

[20] SUN, F., XIAO, L., AND BURSI, O. S. Optimal design and novel configuration of a locally resonant periodic foundation (lrpf) for seismic protection of fuel storage tanks. *Engineering Structures 189* (2019), 147 – 156.

[21] YAN, Y., LASKAR, A., CHENG, Z., MENQ, F., TANG, Y., MO, Y., AND SHI, Z. Seismic isolation of two dimensional periodic foundations. *Journal of Applied Physics 116*, 4 (2014), 044908.

Antonio Palermo, Ph.D.: University of Bologna, Viale del Risorgimento 2, Italy (IT) (*antonio.palermo6@unibo.it*).

Farhad Zeighami, Ph.D. student: University of Bologna, Viale del Risorgimento 2, Italy (IT) (*farhad.zeighami3@unibo.it*).

Athanasios Vratsikidis, Ph.D. student: Aristotle University of Thessaloniki, 424 GR-54124 Thessaloniki, Greece (GR) (*avratsik@civil.auth.gr*).

Zhibao Cheng, Ph.D.: Beijing Jiaotong University, Beijing, China, 100044, China (CN) (*chengzb@bjtu.edu.cn*).

Dimitris Pitilakis, Associate Professor: Aristotle University of Thessaloniki, 424 GR-54124 Thessaloniki, Greece (GR) (*dpitilakis@civil.auth.gr*).

Alessandro Marzani, Ph.D.: University of Bologna, Viale del Risorgimento 2, Italy (IT) (*alessandro.marzani@unibo.it*). the author presented this contribution at the conference in the special session "Innovative strategies for vibration control and mitigation" organized by G. Failla and R. Santoro.

Alternative inverse kinematic calculation methods in velocity and acceleration level

Dóra Patkó, Ambrus Zelei

Abstract: Inverse kinematics calculation of manipulators is a common building block in most of the robotic control processes. However, the numerical implementation of the inverse kinematics calculation has several alternatives yielding certain advantages and disadvantages.

This paper compares two approaches. In the classical one, the joint position increment is stepwise calculated based on the local velocity vector of the desired trajectory. In contrast, the joint position increment is obtained from the error between the desired and the realized trajectory in some alternative methods. The two approaches are also distinguished on the acceleration level. Our analytical and numerical studies show the benefits and drawbacks of these inverse kinematics methods.

1. Introduction

Kinematic calculation of robotic manipulators is a fundamental task in robot control, involving many issues such as numerical efficiency [8, 10]. In case of *direct kinematics*, the position and orientation of the end-effector is determined based on the joint coordinates. If the joint space and the task space (or workspace), where the end-effector is moving, have different dimensions, there is no kinematic redundancy [6, 7, 5] (joint space is higher dimension than the task space for redundant manipulators). In other words, degrees of freedom (DoFs) of the manipulator exactly equals the necessary DoFs for performing the task. We consider non-redundant cases only.

In practice, the desired position of the end-effector (tool-center-point) is prescribed and we try to find the corresponding joint coordinate values. This mapping from the task space to the joint space is called *inverse kinematics*. Many methods exist in the literature to solve the inverse kinematic problem with different approaches. These methods can be categorized as geometric level approaches, velocity level approaches and acceleration level approaches. Acceleration level resolution methods of the inverse kinematic problem may improve the performance of redundant robots [4, 9] comparing to velocity level methods. There are alternatives for the position error compensation too [2, 1]. In this paper, our focus is on the accuracy and efficiency of different combination of approaches used for inverse kinematics.

1.1. The idea of auxiliary input in motion control

For the sake of easy formalization of the inverse kinematic alternatives, we apply the idea of the auxiliary input that is used in inverse dynamics control of robots [10, 11]. The idea is summarized briefly in this subsection based on the literature. To this end, let us consider the general form of the equation of motion of a robot given as

$$\mathbf{M}(\mathbf{q})\ddot{\mathbf{q}} + \mathbf{C}(\mathbf{q}, \dot{\mathbf{q}}) = \mathbf{H}(\mathbf{q})\mathbf{u} \, . \tag{1}$$

By chosing the control input according to

$$\mathbf{u} = \mathbf{H}^{-1}(\mathbf{q}) \left[\mathbf{M}(\mathbf{q})\tilde{\mathbf{v}} + \mathbf{C}(\mathbf{q}, \dot{\mathbf{q}}) \right] \, , \tag{2}$$

the closed loop system assumes the following linear form: $\ddot{\mathbf{q}} = \tilde{\mathbf{v}}$. The term $\tilde{\mathbf{v}}$ in (2) is an auxiliary input, which is typically chosen as $\tilde{\mathbf{v}} = \ddot{\mathbf{q}}^{\mathrm{d}} - \tilde{D}(\dot{\mathbf{q}} - \dot{\mathbf{q}}^{\mathrm{d}}) - \tilde{P}(\mathbf{q} - \mathbf{q}^{\mathrm{d}})$. This choice makes the error dynamics stable, when a desired trajectory $\mathbf{q}^{\mathrm{d}}(t)$ is tracked. This can be proven by substituting (2) into (1):

$$\mathbf{M}\ddot{\mathbf{q}} + \mathbf{C} = \mathbf{H}\mathbf{H}^{-1} \left[\mathbf{M} \left(\ddot{\mathbf{q}}^{\mathrm{d}} - \tilde{D}(\dot{\mathbf{q}} - \dot{\mathbf{q}}^{\mathrm{d}}) - \tilde{P}(\mathbf{q} - \mathbf{q}^{\mathrm{d}}) \right) + \mathbf{C} \right] \, , \tag{3}$$

which leads to the stable error dynamics

$$\ddot{\mathbf{q}} - \ddot{\mathbf{q}}^{\mathrm{d}} + \tilde{D}(\dot{\mathbf{q}} - \dot{\mathbf{q}}^{\mathrm{d}}) + \tilde{P}(\mathbf{q} - \mathbf{q}^{\mathrm{d}}) = 0 \, . \tag{4}$$

All in all, we can say that the auxiliary input $\tilde{\mathbf{v}}$ can be chosen arbitrarily depending on the control goal. The idea of the auxiliary input will be used in the subsequent sections.

2. Inverse kinematics calculation alternatives

Inverse kinematics is a fundamental process, when the task of the robot is transferred to the joint space from the workspace [6, 5, 10]. In case of a simple position trajectory tracking, the desired time history $\mathbf{r}^{\mathrm{d}}(t) \in \mathbb{R}^n$ of the tool-center-point (TCP) position (or end-effector position) is given in the workspace. The goal of the inverse kinematics calculation is to find the joint variables in $\mathbf{q} \in \mathbb{R}^n$ which satisfy the geometric equation for the position error $\mathbf{e}$

$$\mathbf{e}(\mathbf{q}, t) \quad = \quad \mathbf{0} \quad \text{with} \tag{5}$$

$$\mathbf{e}(\mathbf{q}, t) \quad = \quad \mathbf{r}(\mathbf{q}) - \mathbf{r}^{\mathrm{d}}(t). \tag{6}$$

The term $\mathbf{r}(\mathbf{q})$ in (6), which expresses the actual TCP position, depends on the joint coordinates and the geometry of the manipulator. The desired position $\mathbf{r}^{\mathrm{d}}(t)$ is purely time dependent. In the geometric level approach, (5) is solved directly with a proper non-linear root searching algorithm. Geometric solution is not typical in practice; the inverse kinematics is solved in velocity [12] or acceleration level [4, 9] as it is detailed in the followings.

2.1. The application of the idea of the auxiliary input on velocity level

By the time differentiation of (5), we obtain that the equation

$$\dot{\mathbf{e}}(\mathbf{q}, t) \quad = \quad \mathbf{0} \quad \text{with} \tag{7}$$

$$\dot{\mathbf{e}}(\mathbf{q}, t) \quad = \quad \dot{\mathbf{r}} - \dot{\mathbf{r}}^{\mathrm{d}} \tag{8}$$

must be satisfied in the velocity level approaches. Based on the system geometry, we know that the linear connection of the TCP position and the joint speed is

$$\dot{\mathbf{r}} = \mathbf{J}\dot{\mathbf{q}}, \tag{9}$$

where the Jacobian is $\mathbf{J}(\mathbf{q}) = \partial \mathbf{r}(\mathbf{q})/\partial \mathbf{q}$. Consequently, we can write that the commanded joint speed is

$$\dot{\mathbf{q}} = \mathbf{J}^{-1}\mathbf{v}_{\mathrm{v}}, \tag{10}$$

where $\mathbf{v}_{\mathrm{v}}$ is considered as an auxiliary input of the inverse kinematic control (such as $\tilde{\mathbf{v}}_{\mathrm{v}}$ in (2)). Based on (8), $\mathbf{v}_{\mathrm{v}} = \dot{\mathbf{r}}^{\mathrm{d}}$ is an obvious choice; however it does not guarantee the elimination of position error $\mathbf{e}$. Therefore there are many alternative possibilities.

In the followings, two alternatives are explained for the choice of $\mathbf{v}_{\mathrm{v}}$ with the possibility of the elimination of position errors.

2.1.1. Classical velocity level approach

By chosing the auxiliary input $\mathbf{v}_{\mathrm{v}}$ in (10) in such way that the TCP position error is maintained [12] ($\mathbf{v}_{\mathrm{v}} := \dot{\mathbf{r}}^{\mathrm{d}} - \kappa(\mathbf{r} - \mathbf{r}^{\mathrm{d}})$), we obtain the commanded joint velocity in the form:

$$\dot{\mathbf{q}} = \mathbf{J}^{-1}\left(\dot{\mathbf{r}}^{\mathrm{d}} - \kappa(\mathbf{r} - \mathbf{r}^{\mathrm{d}})\right). \tag{11}$$

Neglecting the digital effects, and by substituting (11) into (9), the TCP velocity can be expressed as:

$$\dot{\mathbf{r}} = \dot{\mathbf{r}}^{\mathrm{d}} - \kappa(\mathbf{r} - \mathbf{r}^{\mathrm{d}}), \tag{12}$$

which leads to a stable error (see (6)) dynamics governed by the following first order differential equation with the solution $\mathbf{e}(t) = \mathbf{B}\mathrm{e}^{-\kappa t}$:

$$\dot{\mathbf{e}} + \kappa\mathbf{e} = \mathbf{0}, \tag{13}$$

if $\kappa > 0$. The stability analysis in the presence of digital effect is detailed in Section 3.

2.1.2. An alternative velocity level approach

Again, the question is that how we choose the auxiliary input $\mathbf{v}_\mathrm{v}$ appearing in (10). As it is explained in papers [2, 1], the main idea in this approach is to define the auxiliary input in such way that the position error is eliminated immediately if it is possible.

For the sake of precise explanation, we introduce the actual value of variables in the specific time instances: $\mathbf{q}_i := \mathbf{q}(t_i)$, $\mathbf{r}_i := \mathbf{r}(\mathbf{q}(t_i))$ and $\mathbf{r}_i^\mathrm{d} := \mathbf{r}^\mathrm{d}(t_i)$. We also introduce the timestep $h := t_{i+1} - t_i$.

We consider the error $\boldsymbol{\delta}_i = \mathbf{r}_{i+1}^\mathrm{d} - \mathbf{r}_i$ between the actual TCP position in the current timestep t_i and the desired TCP position in the upcoming timestep t_{i+1}. The goal is to eliminate $\boldsymbol{\delta}_i$. We assume constant TCP velocity $\dot{\mathbf{r}}_i$, with which the desired TCP position of the upcoming timestep $\mathbf{r}_{i+1}^\mathrm{d}$ can be approximately reached (see Fig. 1 left panel):

$$\mathbf{r}_{i+1}^\mathrm{d} = \mathbf{r}_i + h\dot{\mathbf{r}}_i . \tag{14}$$

By solving (14) for $\dot{\mathbf{r}}_i$, one can see that the error $\boldsymbol{\delta}_i$ is approximately eliminated if the auxiliary input in the time instant t_i is chosen as $\mathbf{v}_{\mathrm{v},i} = (\mathbf{r}_{i+1}^\mathrm{d} - \mathbf{r}_i)/h$. With this, the commanded joint speed (see (10)) reads:

$$\dot{\mathbf{q}}_i = \mathbf{J}_i^{-1} \frac{\mathbf{r}_{i+1}^\mathrm{d} - \mathbf{r}_i}{h} . \tag{15}$$

After a single explicit Euler [3] time integration step ($\mathbf{q}_{i+1} = \mathbf{q}_i + h\dot{\mathbf{q}}_i$) we obtain the commanded joint position in the upcoming time instant as:

$$\mathbf{q}_{i+1} = \mathbf{q}_i + \mathbf{J}_i^{-1}(\mathbf{r}_{i+1}^\mathrm{d} - \mathbf{r}_i) . \tag{16}$$

The resulting error of the TCP position is depicted in Fig. 1 right panel. The commanded joint coordinates would give the exact TCP positioning of the end-effector in case of linear relation of the joint coordinates and the TCP position. However, if $\mathbf{r}(\mathbf{q})$ is nonlinear, a certain error $\mathbf{e}_{i+1}$ occures. This error is small in case of small timeteps h. The thorough convergence analysis is presented in Section 3.
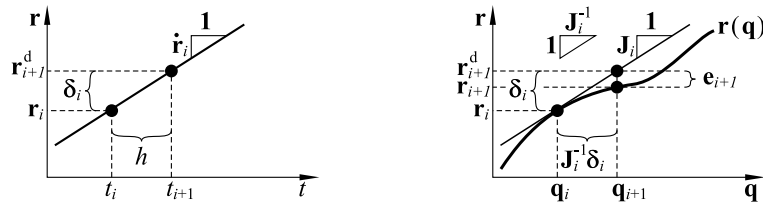
Figure 1. Left panel: sketch of the TCP velocity estimation. Right panel: sketch of the joint coordinate values and the TCP position after a single integration step.

2.2. The application of the idea of the auxiliary input on acceleration level

By the double time differentiation of (5), we obtain that the equation [4, 9]:

$$\ddot{\mathbf{e}}(\mathbf{q}, t) \;=\; \mathbf{0} \quad \text{with} \tag{17}$$

$$\ddot{\mathbf{e}}(\mathbf{q}, t) \;=\; \ddot{\mathbf{r}} - \ddot{\mathbf{r}}^{\mathrm{d}} \tag{18}$$

has to be satisfied in the acceleration level approaches. Similarly to (9), we know that the TCP acceleration can be expressed as

$$\ddot{\mathbf{r}} = \mathbf{J}\ddot{\mathbf{q}} + \dot{\mathbf{J}}\dot{\mathbf{q}} \,. \tag{19}$$

From (19), we express the commanded joint acceleration as

$$\ddot{\mathbf{q}} = \mathbf{J}^{-1}(\mathbf{v}_{\mathrm{a}} - \dot{\mathbf{J}}\dot{\mathbf{q}}), \tag{20}$$

where $\mathbf{v}_{\mathrm{a}}$ is again an auxiliary input of the inverse kinematic control. Based on (18), $\mathbf{v}_{\mathrm{a}} = \ddot{\mathbf{r}}^{\mathrm{d}}$ is an obvious choice. Since this choice does not guarantee the decaying of the position error $\mathbf{e}$, there are several alternatives. Two alternatives, which are capable of eliminating the position errors, are explained for the choice of $\mathbf{v}_{\mathrm{a}}$ in the followings.

2.2.1. Classical acceleration level approach

By chosing the auxiliary input $\mathbf{v}_{\mathrm{a}}$ in (20) in such way that the TCP position error is eliminated [4] ($\mathbf{v}_{\mathrm{a}} := \ddot{\mathbf{r}}^{\mathrm{d}} - \kappa_D(\dot{\mathbf{r}} - \dot{\mathbf{r}}^{\mathrm{d}}) - \kappa_P(\mathbf{r} - \mathbf{r}^{\mathrm{d}})$), we obtain the commanded joint acceleration

$$\ddot{\mathbf{q}} = \mathbf{J}^{-1}\left(\ddot{\mathbf{r}}^{\mathrm{d}} - \kappa_D(\dot{\mathbf{r}} - \dot{\mathbf{r}}^{\mathrm{d}}) - \kappa_P(\mathbf{r} - \mathbf{r}^{\mathrm{d}}) - \dot{\mathbf{J}}\dot{\mathbf{q}}\right) . \tag{21}$$

Neglecting the digital effects, and by substituting (21) into (19), the TCP acceleration in the workspace can be expressed as:

$$\ddot{\mathbf{r}} = \ddot{\mathbf{r}}^{\mathrm{d}} - \kappa_D(\dot{\mathbf{r}} - \dot{\mathbf{r}}^{\mathrm{d}}) - \kappa_P(\mathbf{r} - \mathbf{r}^{\mathrm{d}}) , \tag{22}$$

which leads to a stable error (see (6)) dynamics with $\kappa_P > 0$ and $\kappa_D > 0$ governed by the following second order differential equation with the stable solution:

$$\ddot{\mathbf{e}} + \kappa_D\dot{\mathbf{e}} + \kappa_P\mathbf{e} = \mathbf{0} \,. \tag{23}$$

The error dynamics is assymptotically stable, if $\kappa_P > 0$ and $\kappa_D > 0$. The detailed stability analysis, in the presence of digital effect, is detailed in Section 3.

2.2.2. An alternative acceleration level approach

The goal is the elimination of the position error by chosing the auxiliary input appearing in (20) properly. Similarly, as in Section 2.1.2, we consider the error $\boldsymbol{\delta}_i = \mathbf{r}_{i+1}^{\mathrm{d}} - \mathbf{r}_i$ between the actual and the desired TCP position. We assume constant TCP acceleration $\ddot{\mathbf{r}}_i$, with which the desired TCP position of the upcoming timestep $\mathbf{r}_{i+1}^{\mathrm{d}}$ can be reached (see Fig. 2):

$$\mathbf{r}_{i+1}^{\mathrm{d}} = \mathbf{r}_i + h\dot{\mathbf{r}}_i + \frac{1}{2}h^2\ddot{\mathbf{r}}_i \,. \tag{24}$$

By solving (24) for $\ddot{\mathbf{r}}_i$, one can see that the error $\boldsymbol{\delta}_i$ is approximately eliminated if the auxiliary input is chosen as $\mathbf{v}_{\mathrm{a},i} = 2(\mathbf{r}_{i+1}^{\mathrm{d}} - \mathbf{r}_i)/h^2 - 2\dot{\mathbf{r}}_i/h$. Knowing that $\dot{\mathbf{r}}_i = \mathbf{J}_i\dot{\mathbf{q}}_i$, and using the joint speed estimation $\dot{\mathbf{q}}_i \approx \mathbf{J}^{-1}(\mathbf{r}_{i+1}^{\mathrm{d}} - \mathbf{r}_i)/h$, the commanded joint speed (see (20)) reads:

$$\begin{aligned}
\ddot{\mathbf{q}}_i &= \frac{2\,\mathbf{J}_i^{-1}(\mathbf{r}_{i+1}^{\mathrm{d}} - \mathbf{r}_i)}{h^2} - \frac{2\dot{\mathbf{q}}_i}{h} - \mathbf{J}_i^{-1}\dot{\mathbf{J}}_i\dot{\mathbf{q}}_i = \\
&= \frac{2\,\mathbf{J}_i^{-1}(\mathbf{r}_{i+1}^{\mathrm{d}} - \mathbf{r}_i)}{h^2} - \frac{2\dot{\mathbf{q}}_i}{h} - \mathbf{J}_i^{-1}\dot{\mathbf{J}}_i\mathbf{J}^{-1}(\mathbf{r}_{i+1}^{\mathrm{d}} - \mathbf{r}_i) \,.
\end{aligned} \tag{25}$$

The time integration is performed in the following two steps (see Adams-Moulton family of numerical integrators in [3]):

$$\dot{\mathbf{q}}_{i+1} = \dot{\mathbf{q}}_i + h\ddot{\mathbf{q}}_i \,, \tag{26}$$

$$\mathbf{q}_{i+1} = \mathbf{q}_i + h(\dot{\mathbf{q}}_{i+1} + \dot{\mathbf{q}}_i)/2 \,. \tag{27}$$

After time integration, we obtain the commanded joint position in the upcoming time instant. Again, the nonlinearity of $\mathbf{r}(\mathbf{q})$ causes small errors in the TCP position. The smaller the timestep, the smaller the position error. The convergence analysis is detailed in Section 3.
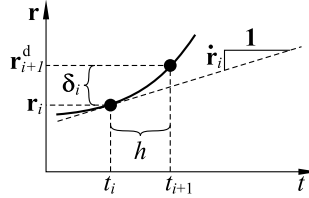


Figure 2. Sketch of the TCP acceleration estimation.

3. Case study examples with convergence analysis

The case study examples are shown in Fig. 3. For all case examples, the mapping of the commanded joint coordinates from the time instant t_i to t_{i+1} arises in the form:

$$\mathbf{q}_{i+1} = \mathbf{A}\mathbf{q}_i + \mathbf{b} \tag{28}$$

after linearizaton around an arbitrarily chosen point of the desired trajectory. Depending on the integration scheme and the formula for the auxiliary input $\mathbf{v}_\mathrm{v}$ or $\mathbf{v}_\mathrm{a}$, the coefficient matrix $\mathbf{A}$ and the vector $\mathbf{b}$ might change. The eigen-values of $\mathbf{A}$ defines the convergence of the inverse kinematic method, which are summarized in Section 3.4.
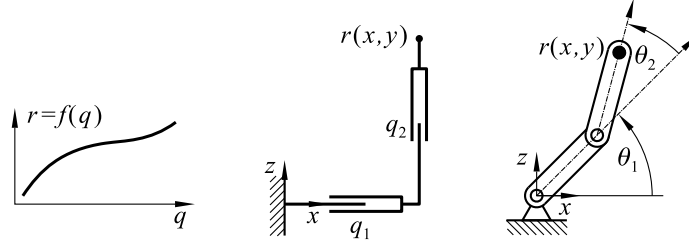
Figure 3. Case study examples: single DoF problem (in the left panel), Cartesian PP robotic arm (in the middle panel), RR robotic arm (in the right panel).

3.1. Case example: single DoF nonlinear system

The simplest (kinematically non-redundant) case example for testing the inverse kinematic methods is depicted in Fig. 3 left. A nonlinear connection of the single joint coordinate q and the TCP position r is given by $r = f(q)$.

3.1.1. Analytical study of the linearized mapping (single DoF example)

For the single DoF example, the mapping matrix $\mathbf{A}$ appearing in (28) is obtained for all four inverse kinematic approaches.

In the **classical velocity level** approach (abbreviated as cv), the numerical integration scheme was the second order Adams-Bashforth scheme [3]:

$$q_{i+1} = q_i + (3\dot{q}_{i+1} - \dot{q}_i)h/2 \,. \tag{29}$$

This integration scheme is applied on the commanded joint velocity defined in (11) with which, the mapping matrix is obtained in the form

$$\mathbf{A}_\mathrm{cv} = \begin{bmatrix} (2 - 3\kappa h)/2 & -h/2 \\ -\kappa & 0 \end{bmatrix} \,. \tag{30}$$

In the **alternative velocity level** approach (abbreviated as av), the numerical integration is already incorporated in (16), for which the mapping matrix is:

$$\mathbf{A}_\mathrm{av} = \begin{bmatrix} 0 \end{bmatrix} \,. \tag{31}$$

In the **classical acceleration level** approach (abbreviated as ca), the numerical integration scheme was the second order Adams-Bashforth scheme combined with the second order Adams-Moulton scheme [3]:

$$\dot{q}_{i+1} = \dot{q}_i + (3\ddot{q}_{i+1} - \ddot{q}_i)h/2 \,, \tag{32}$$

$$q_{i+1} = q_i + (\dot{q}_{i+1} + \dot{q}_i)h/2 \,. \tag{33}$$

This integration scheme is applied on the commanded joint acceleration defined in (21) with which, the mapping matrix reads

$$\mathbf{A}_{\mathrm{ca}} = \begin{bmatrix} (4 - 3\kappa_P h^2)/4 & (4h - 3\kappa_D h^2)/4 & -h^2/4 \\ -3/2\,\kappa_P h & (2 - 3\kappa_D h)/2 & -h/2 \\ -\kappa_P & -\kappa_D & 0 \end{bmatrix} \,. \tag{34}$$

In the **alternative acceleration level** approach (abbreviated as aa), the commanded acceleration is defined by (25), and the numerical integration scheme is defined in (26) and (27), with which the mapping matrix is:

$$\mathbf{A}_{\mathrm{aa}} = \begin{bmatrix} 0 & 0 \\ -2/h & -1 \end{bmatrix} \,. \tag{35}$$

3.1.2. Simulations (single DoF example)

In the test simulations (see Fig. 4) and also in the above analytical calculations, the desired trajectory $r^{\mathrm{d}}(t)$ and the joint space $\mapsto$ workspace mapping function $f(q)$ were:

$$r^{\mathrm{d}}(t) = a_0 + a_1 \sin \omega t \,, \tag{36}$$

$$f(q) = c + \sqrt{q} \tag{37}$$

with the parameter values $a_0 = 1.2\,\mathrm{m}$, $a_1 = 0.6\,\mathrm{m}$, $\omega = 0.28\,\mathrm{rad/s}$ and $c = 0.2\,\mathrm{m}$. The simulation was performed with an initial error as it is shown in Fig 4. The control parameters and the timestep were $\kappa = 5.5\,1/\mathrm{s}$, $\kappa_P = 110\,1/\mathrm{s}^2$, $\kappa_D = 6.5\,1/\mathrm{s}$ and $h = 0.12\,\mathrm{s}$ respectively.

3.2. Case example: two DoF linear system

A two dimensional problem is introduced for test purposes. The example PP manipulator, which is illustrated in Fig. 3 middle, consists of two perpendicular prismatic drive. The TCP position $\mathbf{r} = [x, y]^{\mathrm{T}}$ is given by the mapping $\mathbf{r}(\mathbf{q}) = \mathbf{f}(q_1, q_2)$:

$$\mathbf{r}(\mathbf{q}) = \begin{bmatrix} l + q_1 \\ l + q_2 \end{bmatrix} \,, \tag{38}$$

where l is a geometric parameter.
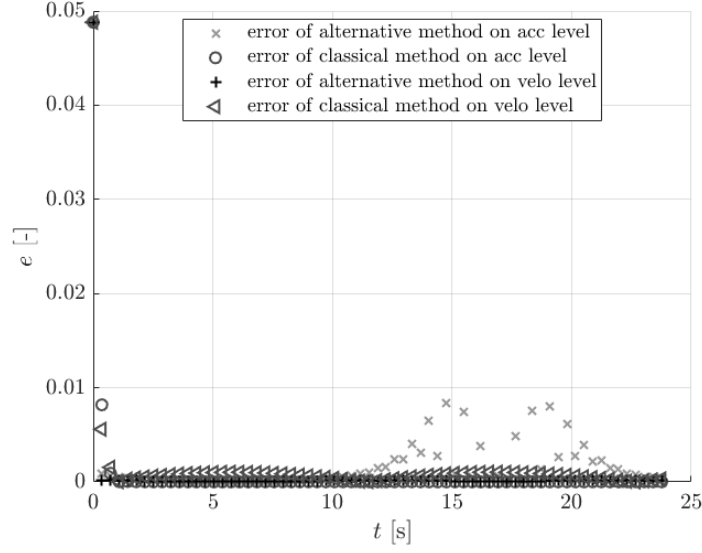
Figure 4. Position error for the 1 DoF case study example with stable parameters. Each inverse kinematics approach is reported here.

3.2.1. Analytical study of the linearized mapping (two DoF linear example)

The mapping matrices were obtained as it was explained in case of the single DoF example. Although, the size of the matrices are double because of the two DoFs:

$$
\mathbf{A}_{\mathrm{cv}} = \begin{bmatrix} (2-3\kappa h)/2 & 0 & -h/2 & 0 \\ 0 & (2-3\kappa h)/2 & 0 & -h/2 \\ -\kappa & 0 & 0 & 0 \\ 0 & -\kappa & 0 & 0 \end{bmatrix}, \tag{39}
$$

$$
\mathbf{A}_{\mathrm{av}} = \begin{bmatrix} 0 & 0 \\ 0 & 0 \end{bmatrix}, \tag{40}
$$

$$
\mathbf{A}_{\mathrm{ca}} = \begin{bmatrix} \frac{4-3\kappa_P h^2}{4} & 0 & \frac{4h-3\kappa_D h^2}{4} & 0 & -\frac{h^2}{4} & 0 \\ 0 & \frac{4-3\kappa_P h^2}{4} & 0 & \frac{4h-3\kappa_D h^2}{4} & 0 & -\frac{h^2}{4} \\ -\frac{3}{2}\kappa_P h & 0 & \frac{2-3\kappa_D h}{2} & 0 & -\frac{h}{2} & 0 \\ 0 & -\frac{3}{2}\kappa_P h & 0 & \frac{2-3\kappa_D h}{2} & 0 & -\frac{h}{2} \\ -\kappa_P & 0 & -\kappa_D & 0 & 0 & 0 \\ 0 & -\kappa_P & 0 & -\kappa_D & 0 & 0 \end{bmatrix}, \tag{41}
$$

$$
\mathbf{A}_{\mathrm{aa}} = \begin{bmatrix} 0 & 0 & 0 & 0 \\ 0 & 0 & 0 & 0 \\ -2/h & 0 & -1 & 0 \\ 0 & -2/h & 0 & -1 \end{bmatrix}. \tag{42}
$$

413

The eigen-values of the matrices of the two DoF linear example are the same as the single DoF example, but there are twice as many of them because of the eigen-value multiplicity.

3.2.2. Simulations (two DoF linear example)

Firstly, we performed simulation (see Fig. 5 and Fig. 6 left) with parameters which are intentionally out of the stable range; i.e. the norm of the corresponding eigenvalues of **A** are larger than 1. The control parameters and the timestep were $\kappa = 17\,1/\mathrm{s}$, $\kappa_P = 400\,1/\mathrm{s}^2$, $\kappa_D = 6\,1/\mathrm{s}$ and $h = 0.0628\,\mathrm{s}$ respectively.
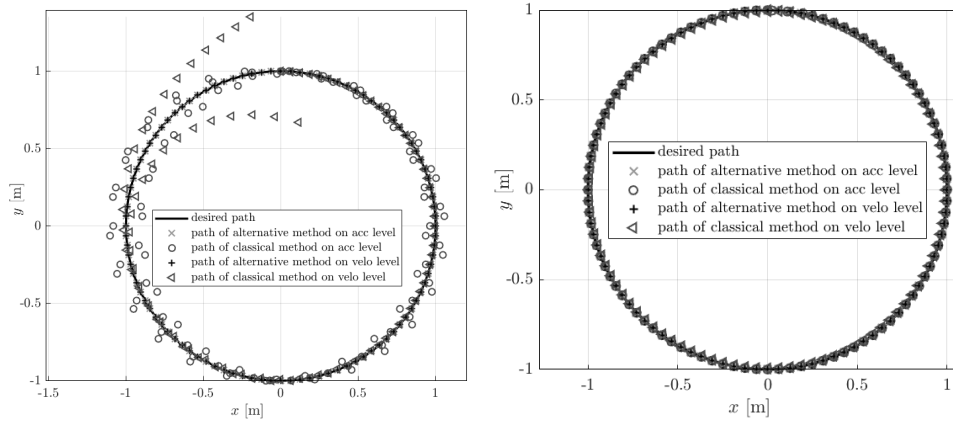
Figure 5. Left: Tracking of a test trajectory with badly tuned unstable parameters. Right: Tracking of a test trajectory with nearly optimal and stable parameters.
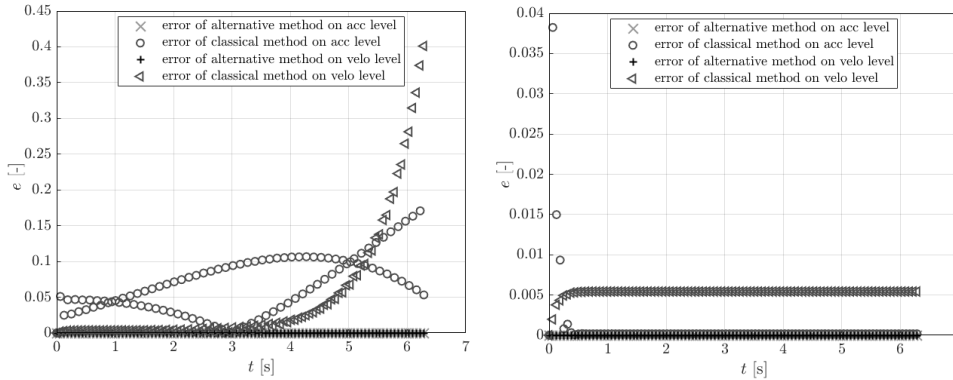
Figure 6. Left: Tracking error with badly tuned unstable parameters. Right: Tracking error with nearly optimal and stable parameters.

Secondly, the simulations were performed with stable parameters (see Fig. 5 and Fig. 6 right), with which the norm of the eigenvalues are smaller (or equal in alternative acceleration method) than 1. The timestep h was the same. The control parameters were $\kappa = 11.5\,1/\text{s}$, $\kappa_P = 365\,1/\text{s}^2$, $\kappa_D = 12.5\,1/\text{s}$ respectively.

3.3. Case example: two DoF nonlinear system

A two dimensional non-redundant problem with geometric nonlinearity is shown in Fig. 3 right. The example system is a planar RR manipulator, consists of two rigid bars and the driven joints. The TCP position $\mathbf{r} = [x, y]^\mathrm{T}$ is given by $\mathbf{r}(\mathbf{q}) = \mathbf{f}(q_1, q_2)$:

$$\mathbf{r}(\mathbf{q}) = \left[\begin{array}{c} l\cos(q_1) + l\cos(q_2) \\ l\sin(q_1) + l\sin(q_2) \end{array} \right], \tag{43}$$

where l is a the length of the bars.

After defining a statical point in the workspace, the analytical calculations were performed similarly as in the previous case examples, and the resulting mapping matrices were obtained in exactly the same form (see (39), (40), (41) and (42)). Consequently the eigenvalues and the stable parameter regions are the same too.

Firstly, we performed simulation (see Fig. 7 and Fig. 8) with unstable parameters. The control parameters and the timestep were $\kappa = 5\,1/\text{s}$, $\kappa_P = 61\,1/\text{s}^2$, $\kappa_D = 3.8\,1/\text{s}$ and $h = 0.2\,\text{s}$ respectively.

Secondly, the simulations were performed with stable parameters. The timestep h was the same. The control parameters were $\kappa = 3.25\,1/\text{s}$, $\kappa_P = 40\,1/\text{s}^2$, $\kappa_D = 4\,1/\text{s}$ respectively.
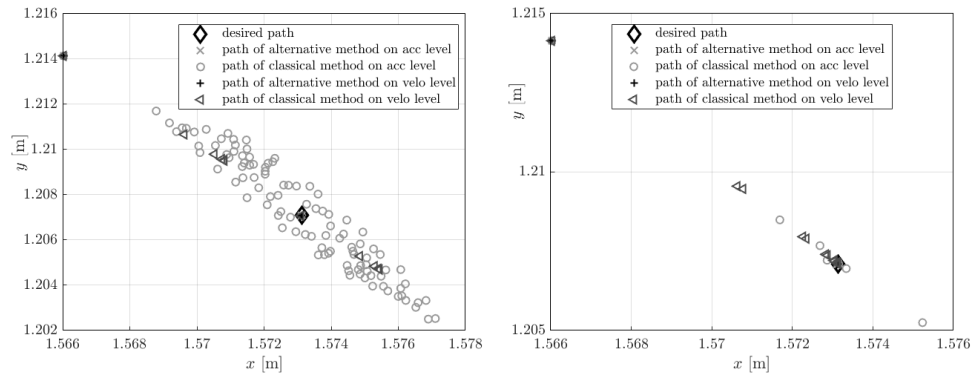

Figure 7. Left: Tracking of a test trajectory with badly tuned parameters. Right: Tracking of a test trajectory with nearly optimal and stable parameters.
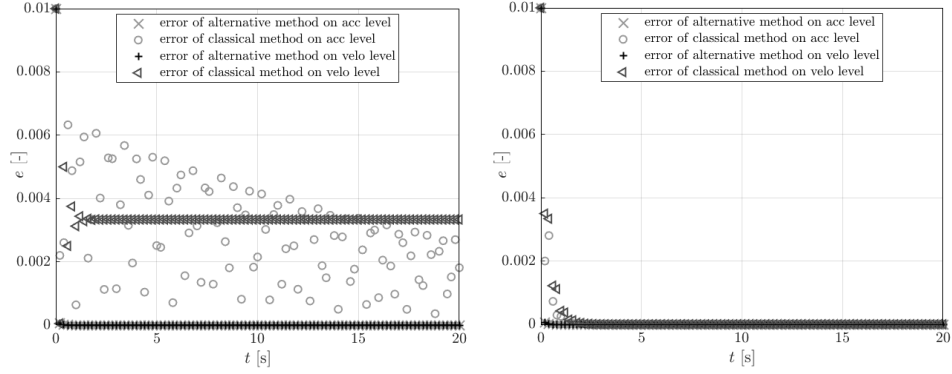
Figure 8. Left: Tracking error with badly tuned parameters. Right: Tracking error with nearly optimal and stable parameters.

3.4. Summary of the case examples

For all case examples, the same stability chart is obtained for the classical velocity and acceleration level approaches. These are reported in Fig. 9. The grey region is stable in the left panel for the classical velocity level approach. On the right panel, for different h values, different regions are plotted in the 2D space of the control parameters κ_P and κ_D.
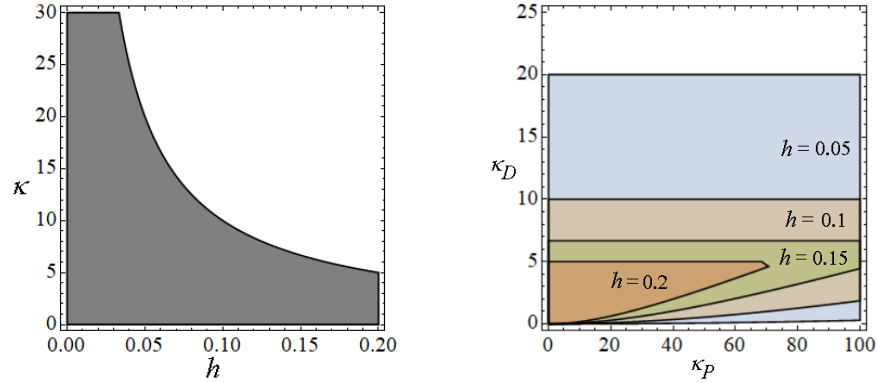
Figure 9. Left panel: stable region of the parameters $h[\text{s}]$ and $\kappa[1/\text{s}]$ in case of the classical velocity level methods. Right panel: stable region of the parameters $h[\text{s}]$, $\kappa_D[1/\text{s}]$ and $\kappa_P[1/\text{s}^2]$ in case of the classical acceleration level methods.

For all case examples, the eigenvalue(s) for the alternative velocity level approach is/are always 0 regardless any parameter. The set of eigenvalues for the alternative acceleration method always consists of 0 and -1 values.

In simulations, the alternative acceleration level invers kinematic methods behaved more favorably than expected based on the analytical calculations. The linear stability was marginal; however, the trajectory tracking error decayed because of the nonlinear effects.

4. Conclusion

In the literature, the classical velocity and acceleration level approaches are analysed. The alternative velocity level method is available in the literature too. As a novelty, the acceleration level alternative method was tested.

Based on the simulations, we observed that the trajectory tracking error in the velocity level is smaller for the alternative method comparing to the classical one. However, in acceleration level, the classical method performs better, since the alternative method is marginally stable only.

The stable control parameter ranges were defined by the linearization of the numerical inverse kinematics formulae. The simulations showed stable operation when the control parameters and the time step were chosen from the theoretically stable domain.

References

[1] BURRELL, T., MONTAZERI, A., MONK, S., AND TAYLOR, C. J. Feedback controlbased inverse kinematics solvers for a nuclear decommissioning robot. *IFAC-PapersOnLine 49*, 21 (2016), 177–184. doi:10.1016/j.ifacol.2016.10.541.

[2] BUSS, S. R. Introduction to inverse kinematics with jacobian transpose, pseudoinverse and damped least squares methods. Tech. rep., IEEE Journal of Robotics and Automation, 2004.

[3] BUTCHER, J. *Numerical Methods for Ordinary Differential Equations.* John Wiley and Sons, Ltd, Hoboken, San Francisco, Weinheim, Queensland, Milton, Singapore, Mississauga, 2008. ISBN 978-0-470-72335-7.

[4] DE LUCA, A., ORIOLO, G., AND SICILIANO, B. Robot redundancy resolution at the acceleration level. *Laboratory Robotics and Automation* (1992).

[5] FROM, P. J., AND GRAVDAHL, J. T. General solutions to functional and kinematic redundancy. In *Proceedings of the 46th IEEE Conference on Decision and Control* (New Orleans, LA, USA, 12-14 December 2007), pp. 1–8. ISSN: 0191-2216, doi:10.1109/CDC.2007.4434442.

[6] HOLLERBACH, J. M., AND SUH, K. C. Redundancy resolution of manipulators through torque optimization. *IEEE Journal of Robotics and Automation 3*, 4 (1987), 308–316. doi: 10.1109/JRA.1987.1087111.

[7] NAKAMURA, Y. *Advanced Robotics: Redundancy and Optimization.* Addison-Wesley, 1991.

[8] ORIN, D. E., AND SCHRADER, W. W. Efficient computation of the jacobian for robot manipulators. *The International Journal of Robotics Research 49*, 21 (1984), 66–75. doi:10.1177/027836498400300404.

[9] REITER, A., MÜLLER, A., AND GATTRINGER, H. On higher-order inverse kinematics methods in time-optimal trajectory planning for kinematically redundant manipulators. *IEEE Transactions on Industrial Informatics 14*, 12 (2018), 1681 – 1690. doi:10.1109/TII.2018.2792002.

[10] SICILIANO, B., AND KHATIB, O. *Handbook of Robotics.* Springer, 2008, ISBN: 978-3-540-38219-5.

[11] SPONG, M. W., AND VIDYASAGAR, M. *Robot Dynamics and Control.* John Wiley & Sons, 1989.

[12] WANG, J., LI, Y., AND ZHAO, X. Inverse kinematics and control of a 7-dof redundant manipulator based on the closed-loop algorithm. *InternationalJournalofAdvancedRoboticSystems 7*, 4 (2010), 1–10.

Dóra Patkó, B.Sc.: Budapest University of Technology and Economics, Muegyetem rkp. 3. Budapest, H-1111, Hungary (*patkodora@edu.bme.hu*).

Ambrus Zelei, Ph.D.: MTA-BME Research Group on Dynamics of Machines and Vehicles, Muegyetem rkp. 3. Budapest, H-1111, Hungary (*zelei@mm.bme.hu*). The author gave a presentation of this paper during one of the conference sessions.

Experimental evaluation of PLC based fractional order PI$^\lambda$D$^\mu$ temperature control in pipeline

Jakub Petryszyn, Jakub Możaryn, Stepan Ozana

Abstract: The following paper presents the experimental evaluation of the fractional-order PI$^\lambda$D$^\mu$ temperature control in the pipeline, using standard PLC Siemens S7-1200 controller. The control algorithm is based on the implementation of the Grünwald-Letnikov differ-integral Continuous Fraction Expansion approximation and tuned using the Interior-Point optimization method with the Integral Time Squared Error (ITSE) criterion. The PI$^\lambda$D$^\mu$ temperature control system wasevaluated using simulations, and experiments on the laboratory test stand. Based on the discussion of the results obtained during the simulation, Hardware-In-Loop, and experimental research, there are proposed further developments considering the accuracy and robustness of the PLC-based fractional order PI$^\lambda$D$^\mu$ control system.

1. Introduction

PID (Proportional-Integral-Derivative) algorithm is one of the most commonly used algorithms to control processes in the industry. It has a simple implementation, and there is a vast number of methods of tuning such a controller depending on the controlled process. This allowed to develop easy to use and intuitive tuning methods, which mostly meet required quality constraints [7].

The standard PID control system design is based on the integer order calculus. However, some systems, mostly in chemistry and pharmacist industry, can be precisely described by fractional-order equations [9, 10, 20]. In such situations, to model processes with higher accuracy, the non-integer calculus is used. In such cases, the PID algorithm can be insufficient.

The fractional order PID algorithm (FOPID), which is described as PI$^\Lambda$D$^\mu$, enables to use of non-integral derivatives and integrals. That increases the number of tuned parameters from 3 to 5 and allows to better match controller with the process. In [3, 4, 10] authors prove that fractional order PID outperforms in some applications integral order solution. There are alsoproposed different tuning methods for the FOPID controller which fulfil the control system design requirements e.g. optimization with integral criterions [4, 10], constrained min-max optimisation [1], swarm optimization [8], auto-tuning methods [11] or robust tuning methods [22]. Usually, PI$^\Lambda$D$^\mu$ algorithm istested and simulated in MATLAB/Simulink environments, for example, to control HVAC systems [18], water tanks [13] or nuclear power

plant [21]. Unfortunately, there is still a lack of tests on real-time systems, mostly because of the complicated implementation issues.

Nowadays, most production lines in small and medium companies are controlled by Programmable Logic Controllers (PLC). The main problem to solve and ensure the proper functionality of the automation system is tuning of controller parameters. Unlike e.g. Distributed Control Systems (DCS), solutions based on PLCs dont have wide support in terms of integration and operation of control algorithms.

This paper describes the results of implementing and tuning the fractional order PID algorithm on the laboratory test stand, where the controlled value is the temperature in the pipeline. In the test stand system, it is possible to impose additional disturbances, and checking the robustness of the proposed solution. The test stand is equipped with Siemens S7-1200 PLC controller, allowing for data acquisition. Therefore, the industrial implementation of the $PI^\Lambda D^\mu$ algorithm can be evaluated.

The article is organized as follows. In Section 2, basic fractional-order calculus definitions and numerical approximations are explained. Then, in Section 3, the laboratory test stand is described. In Section 4 the process identification is presented. In Section 5 the $PI^\Lambda D^\mu$ controller design and tuning are described. In Section 6 the PLC implementation of the $PI^\Lambda D^\mu$ controller is presented. In Section 7 experimental results for the $PI^\Lambda D^\mu$ controller, obtained during simulations and experiments, are demonstrated. Finally, concluding remarks are given.

2. Fractional order calculus definitions

2.1. Differ-integral operator

The fractional calculus generalizes the well-known integer order actions by using real numbers to differentiation and integration actions. The differ-integral operator is the combination of non-integral differentiation and integration operators of the function $f(t)$, defined as

$$\mathrm{Def_a}\, \mathfrak{D}^a_t f(t) = \begin{cases} \frac{\mathrm{d}^\alpha}{\mathrm{d}t^\alpha} & \alpha > 0 \\ 1 & \alpha = 0 \\ \int_a^b (\mathrm{d}\tau)^{-\alpha} & \alpha < 0 \end{cases} \tag{1}$$

where: α - integer order of the operation ($\alpha \in R$), a and b - time limits.

The differ-integral operator (1) acts as the integrator for $\alpha < 0$, as the derivative for $\alpha > 0$. It is defined, according to the Riemann-Liouville definition (RL definition) [12], as

$$^{RL}_a\mathfrak{D}^\alpha_t f(t) = \frac{\mathrm{d}^\alpha f(t)}{\mathrm{d}(t-a)^\alpha} = \frac{1}{\Gamma(m-\alpha)} \frac{\mathrm{d}^m}{\mathrm{d}t^m} \int_0^t f(\tau)(t-\tau)^{m-\alpha-1} \mathrm{d}\tau > 0 \tag{2}$$

The Laplace transform of (2) can be calculated as

$$L\left[_0 D_t^\alpha f(t)\right] = s^\alpha F(s) - \sum_{k=0}^{m-1} s^k \left[D^{\alpha-k-1} f(t)\right]_{t=0} \qquad (3)$$

2.2. Grünwald-Letnikov numerical approximation

There are many differ-integral operator definitions. The most commonly used are the Riemann-Liouville (RL definition) [12], the Caputo (C definition) [2], and the Grünwald–Letnikov definition (GL definition) [9, 10].

Because of easy numerical implementation in PLC controllers, the Grünwald–Letnikov definition of the numerical approximation of the differ-integral operator is used in the form

$$_a^{GL}\mathfrak{D}_t^\alpha f(t) = \frac{d^\alpha f(t)}{d(t-a)^\alpha} = \lim_{N\to\infty} \left[\frac{t-a}{N}\right] \sum_{j=0}^{N-1} (-1)^j \begin{pmatrix} \alpha \\ j \end{pmatrix} f\left(t - j\left[\frac{t-a}{N}\right]\right) \ t > 0, \qquad (4)$$

where: $m \in Z$ - integer number fulfilling dependence $m - 1 < \alpha < m$, $(\alpha \in N)$ and $\Gamma()$ - Euler function [6].

2.3. Oustaloup approximation of differ-integral operator

Because direct numerical implementation of the differ-integral operator (3) is hard to calculate, it is necessary to approximate it. The most commonly used approximation method in practical implementations is the Oustaloup filter in the form [10]

$$s^\alpha = K \prod_{i-1}^{N} \frac{s + \omega_i'}{s + \omega_i} \qquad (5)$$

where the filter coefficients are calculated using the following equations

$$\begin{cases} \omega_i'\left(\alpha, N, \omega_d, \omega_w\right) = \omega_d \omega_w \dfrac{(2i-1-\alpha)}{N} \\ \omega_i\left(\alpha, N, \omega_d, \omega_w\right) = \omega_d \omega_w \dfrac{(2i-1+\alpha)}{N} \\ K\left(\alpha, \omega_g\right) = \omega_g^\alpha \\ \omega_w\left(\omega_g, \omega_d\right) = \sqrt{\dfrac{\omega_g}{\omega_d}} \end{cases}, \qquad (6)$$

ω_d, ω_g - lower and higher bound frequencies ($\omega \in [\omega_d, \omega_g]$, N - the order of the approximation.

2.4. Discrete approximation methods of differ-integral

To implement the differ-integral operator in the digital controller (e.g. PLC), there are used different discrete approximation methods. The first common approximation method is the

Power Series Expansion (PSE) [13, 16] that implements directly GL differ-integral and has digital Finite Impulse Response (FIR) filter structure, based on the system outputs. Unfortunately, PSE approximation requires many values from previous steps of approximation, which increases the controllers hardware and memory minimal requirements. Another popular approximation is the Continued Fraction Expansion (CFE) [15, 16], which has Infinite Impulse Response (IIR) filter structure, containing both zeros and poles of the system. It requires previous outputs and inputs of the system, allowing for faster convergence and low order of the filter (not higher than 5).

$$
\begin{aligned}
\left(\omega\left(z^{-1}\right)\right)^{\pm\alpha} &= \left(\frac{1+a}{T}\right)^{\pm\alpha} \mathrm{CFE} \left(\frac{1-z^{-1}}{1+az^{-1}}\right)^{\pm\alpha}\bigg|_{p,q} = \left(\frac{1+a}{T}\right)^{\pm\alpha} \frac{P_p\left(z^{-1}\right)}{Q_q\left(z^{-1}\right)} \\
&= \left(\frac{1+a}{T}\right)^{\pm\alpha} \frac{P_0 + P_1 z^{-1} + P_2 z^{-2} + \cdots + P_p z^{-p}}{Q_0 + Q_1 z^{-1} + Q_2 z^{-2} + \cdots + Q_q z^{-q}}
\end{aligned}
\tag{7}
$$

where: a - argument that depends on the approximation method ($a = 0$ for Euler approximation and $a = 1$ for Tustin approximation), T - sampling time.

Since CFE provides better memory usage, it is implemented often in real systems with limited capacity. Digital devices as a PLC or a micro-controller, have to work with finite sampling time and it is crucial to choose its adequate value. The PLC with too short T cannot make all calculations in the real-time, but then too long T will cause the lower control quality.
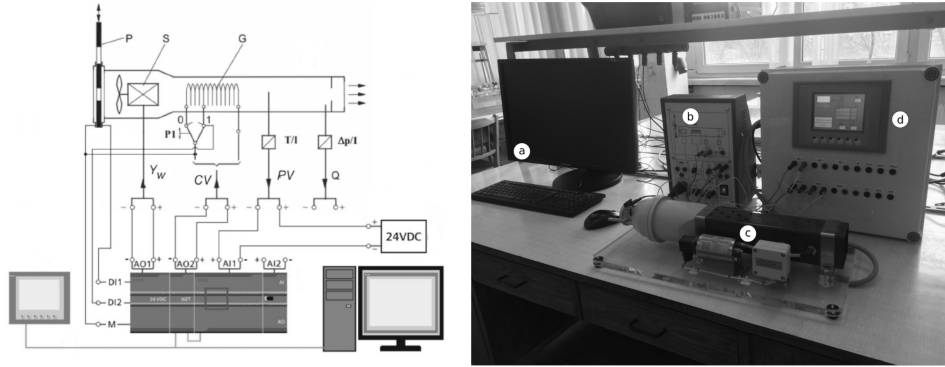
3. Laboratory test stand

The laboratory test stand (see Fig. 1) comprised a pipeline with a heater (G) in which an airflow is induced by the fan (S). The control system controlled the amount of the heat released by the heater (G) at the constant airflow. The power control signal of the heater (Y_G) and speed of the fan (Y_W) were standard current signals 4 - 20 mA generated by the PLC controller used in the closed-loop control system.

To measure the temperature there was used the T/I measuring transducer with the Pt100 resistant thermometer and additional linearization. The measurement range of the transducer was 25 °C - 75 °C.

To control the system, a PLC S7-1212c DC / DC / DC Siemens controller was used with the analog input and analog output module and a 24V power supply. The SIMATIC HMI KPT 600 panel and the desktop PC with the TIA-Portal software were used for the visualization and the controller implementation.

On the test stand it was possible to artificially induce following disturbances (see Fig. 1):

- The step change in the air inlet orifice (D1, change of the cross-section from 389 to 1661 mm^2).

- The step-change in the heater power (G) by adding or disconnecting additional resistance which changes the heater resistance from 100 Ω to 75 Ω (D2).

- The step-change of the fan speed through - (Y$_W$) signal.

Figure 1. The scheme of the process part of the temperature control system and the photo of the laboratory test stand: a) PC with the TIA-Portal software, b) the control interface, c) the pipeline with induced airflow and the heater, d) the industrial box with the PLC controller and the HMI panel for the process monitoring.

4. Process identification

The mathematical model of the process was approximated with the transfer function of the first-order lag system with a delay. The plant parameters were determined from the open-loop system step response using the secant method [5]. The following transfer function of the control object was identified

$$G_{ob}(s) = \frac{\Delta PV(s)}{\Delta CV(s)} = \frac{k_{ob}}{T_z s + 1} e^{-T_0 s} = \frac{0,765}{42,37s + 1} e^{-5,63s} \tag{8}$$

where: $y(s) = PV(s)$ - the process value, $u(s) = CV(s)$ - the control value, T_z - the first order lag time constant, T_0 - the delay time constant and k_{ob} - the process gain.

5. PI$^\lambda$D$^\mu$ controller design and tuning

5.1. Controller structure

The adopted PI$^\lambda$D$^\mu$ controller transfer function was in the following form

$$G_{\text{PI}^\lambda\text{D}^\mu}(s) = K_P + K_I s^\lambda + K_D s^\mu \tag{9}$$

where: K_P - the proportional gain, K_I - the integral time constant, K_D - the derivative time constant, $s^\lambda, s^\mu, \lambda < 0, \mu > 0$ - differ-integral operators.

5.2. Controller tuning

PI$^\Lambda$D$^\mu$ controller was tuned according to the method described in [10, 19, 17], assuming the controller transfer function in the form (9) and the process transfer function in the form

$$G_o(s) = \frac{1}{a_1 s^\alpha + a_2 s^\beta + a_3} \tag{10}$$

The chosen tuning method based on the Oustaloup approximation (5). It required to solve following set of equations

$$
\begin{cases}
K_p + \dfrac{K_I}{\omega_p^\lambda} \cos \dfrac{\pi\lambda}{2} + K_D \omega_p^\mu \cos \dfrac{\pi\mu}{2} = -\dfrac{a_1}{A_m} \omega_p^\alpha \cos \dfrac{\pi\alpha}{2} - \dfrac{a_s}{A_m} \omega_p^\beta \cos \dfrac{\pi\beta}{2} - \dfrac{a_3}{A_m} \\[2ex]
\quad -\dfrac{K_I}{\omega_p^\lambda} \sin \dfrac{\pi\lambda}{2} + K_D \omega_p^\mu \sin \dfrac{\pi\mu}{2} = -\dfrac{a_1}{A_m} \omega_p^\alpha \sin \dfrac{\pi\alpha}{2} - \dfrac{a_s}{A_m} \omega_p^\beta \sin \dfrac{\pi\beta}{2} \\[2ex]
\quad K_p + \dfrac{K_I}{\omega_g^\lambda} \cos \dfrac{\pi\lambda}{2} + K_D \omega_g^\mu \cos \dfrac{\pi\mu}{2} \\[2ex]
\quad = -a_1 \omega_g^\alpha \cos \left(\dfrac{\pi\alpha}{2} + \theta_m \right) - a_2 \omega_g^\beta \cos \left(\dfrac{\pi\beta}{2} + \theta_m \right) - a_3 \cos \theta_m \\[2ex]
\quad -K_I \dfrac{\sin \frac{\pi\lambda}{2}}{\omega_g^\lambda} + K_D \sin \dfrac{\pi\mu}{2} \omega_g^\mu \\[2ex]
\quad = -a_1 \omega_g^\alpha \sin \left(\dfrac{\pi\alpha}{2} + \theta_m \right) - a_2 \omega_g^\beta \sin \left(\dfrac{\pi\beta}{2} + \theta_m \right) - a_3 \sin \theta_m
\end{cases}
\tag{11}
$$

where: ω_p - the cut-off frequency, A_m - the gain margin, θ_m - the phase margin.

The following condition had to be fulfilled to calculate λ, μ, ω_p, ω_g

$$
\begin{aligned}
\left(\omega_g^{\lambda+\mu} - \omega_p^{\lambda+\mu}\right) &\left\{ a_1 \left[\omega_g^\alpha \cos\left(\frac{\pi\alpha}{2} + \theta_m\right) - \omega_p^\alpha \cos\frac{\pi\alpha}{2} \right] + \right. \\
&\quad a_2 \left[\omega_g^\beta \cos\left(\frac{\pi\beta}{2} + \theta_m\right) - \omega_p^\beta \cos\frac{\pi\beta}{2} \right] \\
&\quad \left. + a_3 \cos\left(\theta_m - \frac{1}{A_m}\right) \right\} \\
&+ \left(\operatorname{ctg}\frac{\pi\lambda}{2} + \cot\frac{\pi\mu}{2} \right) \left(\frac{\omega_p^\lambda \omega_g^\mu F_p}{A_m} + \omega_g^\beta \omega_p^\mu F_g \right) \\
&- \left(\frac{\omega_p^{\lambda+\mu} F_p}{A_m} + \omega_g^{\lambda+\mu} F_g \right) \operatorname{ctg}\frac{\pi\mu}{2} \\
&- \left(\omega_p^{\lambda+\mu} F_g + \frac{\omega_p^{\lambda+\mu} F_p}{A_m} \right) \operatorname{ctg}\frac{\pi\lambda}{2} = 0
\end{aligned}
\tag{12}
$$

where

$$
\begin{cases}
F_p = a_1 \omega_p^\alpha \sin\frac{\pi\alpha}{2} + a_2 \omega_p^\beta \sin\frac{\pi\beta}{2} \\
F_g = a_1 \omega_g^\alpha \sin\left(\frac{\pi\alpha}{2} + \theta_m\right) + a_2 \omega_g^\beta \left(\sin\frac{\pi\beta}{2} + \theta_m\right) + a_3 \sin\theta_m
\end{cases}
\tag{13}
$$

6. PLC implementaion of $\mathrm{PI}^\lambda \mathrm{D}^\mu$ controller

The process of implementing the $\mathrm{PI}^\lambda \mathrm{D}^\mu$ control algorithm (9) on PLC can be divided into three stages.

The first stage base on implementing the $\mathrm{PI}^\Lambda \mathrm{D}^\mu$ control algorithm and testing its performance in the MATLAB/Simulink environment. Theset of functions had been created to determine the parameters of the discrete CFE approximation.

While tuning the $\mathrm{PI}^\Lambda \mathrm{D}^\mu$ controller, the following conditions had been assumed:

- No steady-state error

- Gain margin: 10 dB

- Phase margin: 60 $^\circ$

There was used the Interior-Point optimization method [14] with the Integral Squared Time Error (ITSE) criterion, to fulfill the conditions (11)-(12) while calculating the controller parameters.

In result, the following $\mathrm{PI}^\Lambda \mathrm{D}^\mu$ controller transfer function was chosen

$$
G_{\mathrm{PI}^\Lambda \mathrm{D}^\mu}(s) = 2.142 + 0.856s^{-0.9851} + 29.626s^{0.7998}
\tag{14}
$$

In the second stage, the code for the PLC was created in the Structured Control Language (SCL). For this purpose, the extension Simulink PLC Coder[1] was used, which allowed creating code for PLC directly from the MATLAB code. In this stage, the CFE differ-integral approximation was used (See Section 2.4).

The last stage of the design was to simulate the algorithm in the PLC and to simulate a controlled object using MATLAB/Simulink (Hardware-In-the-Loop, HIL). For this purpose, it was necessary to transfer data between the Siemens PLC software (TIA-Portal) and the MATLAB/Simulink environment. An additional OPC UA server was used to enable data exchange between the simulated controller in PLCSim (part of the TIA-Portal software) and Simulink. Moreover, there was used NetToPLCsim [2] extension, allowing TCP / IP connections of simulated controllers. The preliminary results of the implementation tests practically coincided with the ones calculated in MATLAB only. This confirmed the effective implementation of the code from the MATLAB/Simulink environment to the Siemens S7-1200 PLC controller.

7. Laboratory tests

During laboratory tests, the designed and tuned $\mathrm{PI}^{\Lambda}\mathrm{D}^{\mu}$ controller was used in the laboratory test stand.

The step response of the control system with the $\mathrm{PI}^{\Lambda}\mathrm{D}^{\mu}$ controller, as well as the influence of disturbances, were examined.

The quality of the control system was analyzed in the time domain using the following indexes:

- Maximum error

$$e_{\max} = \max_{t}[e_{\mathrm{sp}}(t)] \tag{15}$$

where: $e_{\mathrm{sp}}(t) = y_{\mathrm{sp}}(t) - y(t)$

- Overshoot

$$\gamma = \left|\frac{e_2}{e_1}\right| 100\% \tag{16}$$

where e_1 and e_2 are the first two consecutive biggest errors with opposite signs, assuming as the zero level (baseline) the steady state value of the output signal $y(t)$ after the transient response.

---

[1]https://www.mathworks.com/products/sl-plc-coder.html
[2]http://nettoplcsim.sourceforge.net/ (it should be noted that it is necessary to use TIA-Portal V15)

- Transient response time T_R - it is the time between the moment of change of the set point $y_{\mathrm{sp}}(t)$, or introduction of disturbances $d(t)$ and the moment when error $e_{\mathrm{sp}}(k)$ reaches a fixed value inside a boundary $|0.05e_{\mathrm{sp\,max}}(t)|$.

The calculated control quality indexes for the control system with the $PI^{\Lambda}D^{\mu}$ controller aresummarized in Table 1 and showed in Fig. 2. It should be noted, that the plant implementation in the HIL simulation did not include disturbances.

a)

b)
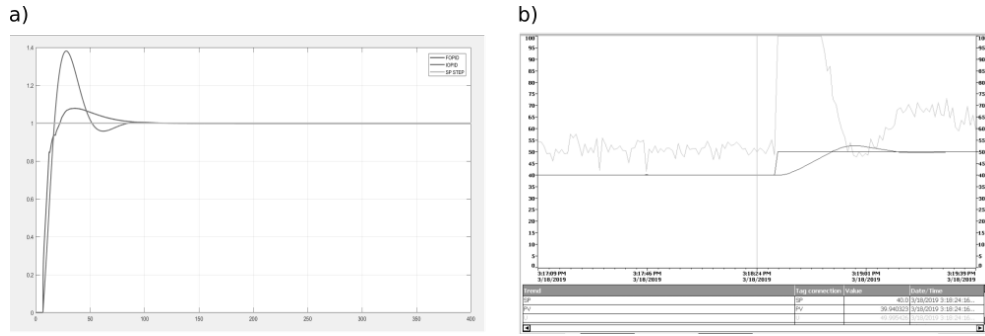
Figure 2. a) Simulated step response of the system with PID and $PI^{\Lambda}D^{\mu}$ controllers; b) the laboratory control system response to the set-point step change with the $PI^{\Lambda}D^{\mu}$ controller.

Table 1. Quality of the $PI^{\Lambda}D^{\mu}$ temperature control system

	HIL simulation			Laboratory stand		
	$e_{\max}$	γ	T_R	$e_{\max}$	γ	T_R
	[%]	[%]	[s]	[%]	[%]	[s]
Step SP change	1.00	8.50	87.00	10.00	15.00	45.00
Air inlet change	-	-	-	0.76	0.00	60.00
Heat power change	-	-	-	0.77	0.00	23.50
Fan speed change	-	-	-	0.70	0.00	23.00

The results gathered in Table 1 prove the successful implementation of the $PI^{\Lambda}D^{\mu}$ controller. Besides tracking the set-point the controller was robust to induced disturbances (air inlet change, heat power change, fan speed change). Comparing with the HIL simulation, the test stand implementation is characterized with shorter transient response times (T_R), higher maximum errors ($e_{\max}$) and higher overshoot (γ). It can be due to the problems with selecting the optimal controller settings for the system with a delay and the additional disturbances. Another problem is the numerical approximations used during the implementation. The simulated $PI^{\lambda}D^{\mu}$ controller tuning based the Oustaloup continuous approximation. However, because of implementation requirements, in the PLC controller,

the discrete approximation using CFE method was used. Therefore, there still exists the problem of interpreting of the optimized parameters for PLC.

8. Conclusions

The paper describes the experimental evaluation of the fractional-order $PI^\lambda D^\mu$ temperature control on the laboratory test stand, where the fractional order controller is implemented on standard PLC Siemens S7-1200 controller. For the approximation of the Grünwald-Letnikov differ-integral, the Continued Fraction Expansion (CFE) was used and implemented on the PLC controller. The proposed solution was tested using simulations, and experiments on the laboratory test stand.

The results obtained during the presented research, with the thermal-flow process, showed that to apply the proposed control algorithm, it is crucial to develop methods for tuning the controller to minimize the influence of input delays and disturbances. Therefore, the proposed future work will include the research on proper tuning methods of $PI^\lambda D^\mu$ controllers with CFE approximation of differ-integral.

References

[1] BESCHI, M., PADULA, F., AND VISIOLI, A. The generalised isodamping approach for robust fractional pid controllers design. *International Journal of Control 90*, 6 (2017), 1157–1164.

[2] CAPUTO, M. Linear model of dissipation whose q is almost frequency independent-ii. *Geophysical Journal International 13*, 5 (1967), 529–539.

[3] CHUNNA, Z., DINGYU, X., AND YANGQUAN, C. A fractional order pid tuning algorithm for a class of fractional order plants. *IEEE International Conference on Mechatronics and Automation 1* (2005), 216–221.

[4] EL-KHAZAL, R. Fractional-order $pi^\lambda d^\mu$ controller design. *Computers & Mathematics with Applications 66*, 5 (2013), 639–646.

[5] HABER, R., AND KEVICZKY, L. *Nonlinear System Identification : Input-output Modeling Approach.* Kluwer Academic Publishers, Boston, 1999.

[6] KACZOREK, T., AND ROGOWSKI, K. *Fractional linear systems and electrical circuits (in Studies in Systems, Decision and Control, vol 13)*. Springer, Cham, 2015.

[7] KOLAJ, W., MOZARYN, J., AND SYFERT, M. Plc-pidtuner: Application for pid tuning with simatic s7 plc controllers. In *2016 21st International Conference on Methods and Models in Automation and Robotics (MMAR)* (Aug 2016), pp. 306–311.

[8] KUMAR, A., AND KUMAR, V. Hybridized abc-ga optimized fractional order fuzzy pre-compensated fopid control design for 2-dof robot manipulator. *AEU - International Journal of Electronics and Communications 79* (2017), 219–233.

[9] LIU, F., AGRAWAL, O. P., MOMANI, S., LEONENKO, N. N., AND CHEN, W. Fractional differential equations 2012. *International Journal of Differential Equations 2013*, 1 (2013), 1–2.

[10] MONJE, C., CHEN, Y., VINAGRE, B., XUE, D., AND FELIU-BATLLE, V. *Fractional Order Systems and Control - Fundamentals and Applications*. Springer, London, 2010.

[11] MONJE, C. A., VINAGRE, B. M., FELIU, V., AND CHEN, Y. Tuning and auto-tuning of fractional order controllers for industry applications. *Control Engineering Practice 16*, 7 (2008), 798 – 812.

[12] MUNKHAMMAR, J. *Riemann-Liouville Fractional Derivatives and the Taylor-Riemann Series (B.Sc. Thesis)*. PhD thesis, Uppsala University/Department of Mathematics, 2004.

[13] MYSTKOWSKI, A., AND ZOLOTAS, A. Plc-based discrete fractional-order control design for an industrial-oriented water tank volume system with input delay. *Fractional Calculus and Applied Analysis 21*, 4 (2018), 1005–1026.

[14] NOCEDAL, J., AND WRIGHT, S. J. *Numerical Optimization (2nd ed.)*. Springer-Verlag, Berlin, New York, 2006.

[15] OPRZEDKIEWCZ, K., MITKOWSKI, W., AND GAWIN, E. The plc implementation of fractional-order operator using cfe approximation. *Advances in Intelligent Systems and Computing (Automation 2017. ICA 2017.) 550* (2017), 22–33.

[16] OPRZEDKIEWICZ, K., GAWIN, T., GAWIN, E., AND MITKOWSKI, W. Plc implementations of an elementary fractional order operator. *AUTSYM 2017* (2017).

[17] PADULA, F., AND VISIOLI, A. Tuning rules for optimal pid and fractional-order pid controllers. *Journal of Process Control 21* (2011), 69–81.

[18] PETRAS, I. Realization of fractional order controller based on plc and its utilization to temperature control. *Transfer inovacii 14* (2009), 34–38.

[19] PETRAS, I. Tuning and implementation methods for fractional-order controllers. *Fractional Calculus and Applied Analysis 15*, 2 (2012), 282–303.

[20] PODLUBNY, I. Fractional-order systems and pi$^\lambda$d$^\mu$-controllers. *IEEE Transactions on Automatic Control 44*, 1 (1999), 208–214.

[21] PUCHALSKI, B., DUZINKIEWICZ, K., AND RUTKOWSKI, T. Analysis of fractional order piλdμ power control of a nuclear reactor. *Informatyka, Automatyka, Pomiary w Gospodarce i Ochronie Środowiska (IAPGOŚ) 4* (2013), 63–68.

[22] VALRIO, D., AND DA COSTA, J. S. Tuning of fractional pid controllers with zieglernichols-type rules. *Signal Processing 86*, 10 (2006), 2771 – 2784. Special Section: Fractional Calculus Applications in Signals and Systems.

Jakub Petryszyn, B.Sc.: Warsaw University of Technology, Faculty of Mechatronic, Institute of Automatic Control and Robotics, ul. Sw. A. Boboli 8, 02-525, Warsaw, Poland (*01113987@pw.edu.pl*).

Jakub Możaryn, Ph.D.: Warsaw University of Technology, Faculty of Mechatronic, Institute of Automatic Control and Robotics, ul. Sw. A. Boboli 8, 02-525, Warsaw, Poland (*jakub.mozaryn@pw.edu.pl*). The author gave a presentation of this paper during one of the conference sessions.

Stepan Ozana, Ph.D.: VSB-Technical University of Ostrava, Faculty of Electrical Engineering and Computer Science, Department of Cybernetics and Biomedical Engineering, 17. Listopadu 2172/15, 708 00 Ostrava, Czech Republic (*stepan.ozana@vsb.cz*).

Theoretical and numerical analysis of different modes in a system of a "kicked" magnetic pendulum

Krystian Polczyński, Adam Wijata, Jan Awrejcewicz

Abstract: A non-linear magnetic pendulum system has been studied theoretically and numerically. The main component of the system is a pendulum equipped with a neodymium magnet, which is "kicked" by an alternating magnetic field form an electrical coil underneath. The current signal which flows through the coil is repeatedly switched on and off with a given frequency and a duty cycle. Switched on magnetic field introduces a two-well potential instead of a single-well gravitational one, what results in two stable fixed points and one saddle from a dynamical point of view. Describing the system with a discrete two-state equation, different modes of regular motion have been analyzed. The excitation signal parameters set has been identified for a special type of systems trajectory. Existence of different solutions has been examined in terms of switching signal parameters, that is a frequency and a duty cycle. Obtained numerical results from discrete as well as continuous simulative models have been justified against experimental data from a specially constructed laboratory stand.

1. Introduction

The content of the presented paper focuses on the behavior of an electro-magneto-mechanical system whose the main part is a pendulum. Recent years have shown a growing interest in that kind of systems, it is a result of searching for novel methods of excitation in mechanical engineering as well as pendulums are easy-to-built examples of strongly non-linear mechanical systems.

The experiment setup suggested by Duboshinsky [1–3] involves a pendulum with a magnet suspended above the inductance coil connected to an alternating current source. The orientation of solenoid is perpendicular to the pendulum. The system exhibits quantized modes regarding changes in the system's parameters such as frequency of current or length of the pendulum. The disturbances of these parameters can cause the jumps of system trajectory from one mode to another, those jumps imitate the "quantum jumps" of atomic physics. A similar experiment was conducted by J. Bethenod [2,4]. He reported the phenomenon of growing and sustained oscillations exhibited by a pendulum with a ferromagnetic bob embedded in vary inductance generated by a coil. The pendulum revealed different kinds of behavior in terms of electrical circuit's parameters. The steady-state of oscillations was obtained for an electrical circuit with a predominant reactance. Furthermore, with predominant resistance the oscillations decayed more rapidly than in the case when the coil was unexcited. Sustained oscillations of definite amplitude depended on the reactance of the coil, the voltage and the frequency

of excitation as well as internal damping of the mechanical system. Damgov and Popov [5] studied numerically and analytically a kick-excited, self-adaptive pendulum system. Attractor set of the system has been analyzed by multiple bifurcation diagram as well as complex dynamics, evolution and the fractal boundaries of the multiple attractor basins. Siahmakoun et al. [6] investigated experimentally and numerically a driven pendulum in the repulsive magnetic field. They obtained a different kind of attractors and their transformations regarding the system's parameters such as the distance between magnets and frequency of a driven force. Wojna et al. [7] studied a dynamics of a double pendulum driven by external torque, while the lower link of the pendulum has been equipped in a strong magnet acting on the other magnet fixed to the rig's frame. Chaotic and regular motion have been obtained numerically and experimentally and discussed. Numerous of presented regular motions have featured a multiperiodic form. The system of two coupled pendulums subjected to the alternating magnetic field has been examined by Polczyński et al. [8,9]. Numerical and experimental investigation justified the existence of not only a chaotic and regular motion but also quasi-periodicity. Computed basins of attraction have shown the richness of symmetric system's responses in terms of different initial conditions.

2. Experimental setup and physical model

In this section, we present the experimental rig which has been constructed in our department as well as its physical model with forces and moments of forces acting on it. The experimental rig and the physical model of the system are shown in Fig. 1a and Fig. 1b, respectively.
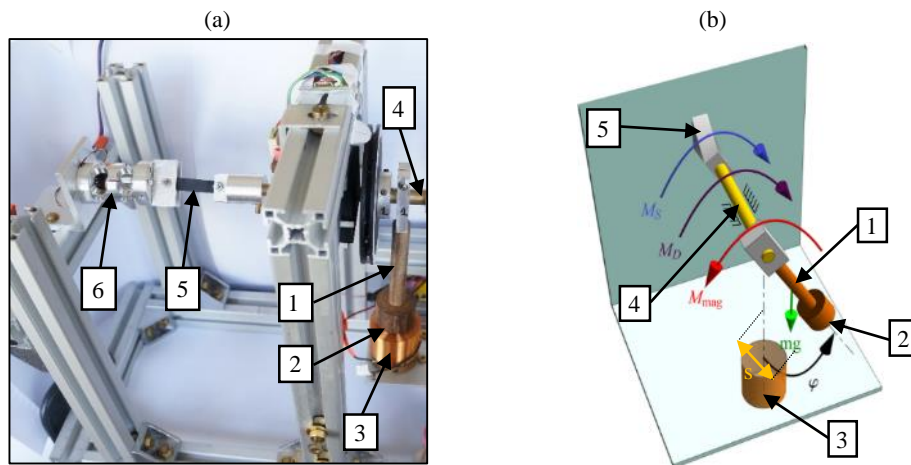
Figure 1. Experimental setup of a single magnetic pendulum (a) and its physical model (b) where: 1 – pendulum, 2 – neodymium magnet (not visible), 3 – electrical coil, 4 – brass pivot, 5 – rubber elastic element and 6 – torque transducer.

The main parts of the system are a single physical pendulum (1) equipped with a neodymium magnet (2) (not visible in Fig.1) at the end of the link and an electrical coil (3) placed underneath. The pendulum is fixed to a brass pivot (4) which is connected with an elastic rubber element (5). The other side of the mentioned element has been fixed to the stationary torque transducer (6). The pendulum's rod is subjected to a gravitational force mg and a torque M_{mag} being a result of repulsive magnetic forces coming from the electric coil. Force mg is put in a center of mass of the pendulum and distance between this center and the axis of rotation is denoted as s. The resistance of the motion is introduced as a torque M_D. It is a sum of all damping factors such as viscous friction, dry friction and internal damping of the elastic element. Moreover, stiffness of the elastic element induces a torque M_S.

The repulsive force generated by the coil is realized by a rectangular current waveform which flows inside the circuit. Fig. 2 pictures particular parameters which are regulated, that is the frequency $f = \frac{1}{\tau}$ and the duty cycle $w = \frac{\tau_{ON}}{\tau} \cdot 100\%$, current's amplitude I was set on 1A.
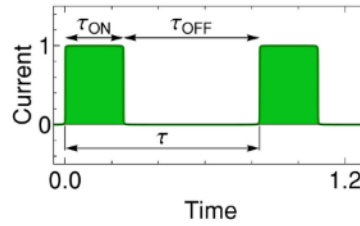
Figure 2. The rectangular current signal flows through the electric coil, where τ is a period of the signal, τ_{ON} is a time when the coil is powered and τ_{OFF} is a time when the coil is switched off.

Angular position of the pendulum has been measured by an incremental optical encoder HEDS-9040#J00, the smallest angular displacement which can be detected is 0.36°. LabVIEW software and NI USB-6341 device were used for the data acquisition process.

3. Mathematical modeling of the system

In this paper two approaches to the systems modeling are presented. The first approach is based on one non-autonomous ordinary differential equation (ODE) describing the system's motion, where the coil's current rectangular signal is modelled with a continuous approximation. The second approach assumes that the coil current signal is discrete, i.e. the coil is instantaneously switched on or off. In this case motion of the system is described with two different autonomous ODEs, which are switched between themselves accordingly to the set frequency and the duty cycle. In this section, we present the conceptions of these two approaches as well as a mathematical model of electromagnetic interaction. Some nomenclature in the section is based on work [5].

### 3.1. Electromagnetic interaction between a neodymium magnet and an electric coil

The electromagnetic interaction between the magnet and the coil has been investigated previously in our work [8]. The proposed mathematical model was based on experimental data of the torque generated by a steady magnetic field. The complexity of the mentioned model has encouraged us to develop a simpler model to accelerate numerical computation. The simpler model was yielded by the potential analysis. Mathematically, a character of the potential energy generated by the coil-magnet interaction in our system can be approximated by the Gaussian peak function. The mathematical formula used to describe the magnetic potential is as follows

$$V_G(\varphi) = a \exp\left(-\frac{\varphi^2}{b}\right), \tag{1}$$

where coefficient a, b are constant and depend on current amplitude. According to the mechanical definition of the potential, we can calculate torque M_{mag*} acting on the pendulum for steady coil's current as:

$$M_{mag*}(\varphi) = -\frac{\partial V_G}{\partial \varphi} = \frac{2a}{b} \exp\left(-\frac{\varphi^2}{b}\right) \varphi. \tag{2}$$

Fig. 3a depicts the potential of the system. In the case of the one-well potential the system is subjected only to gravitational and elastic element's forces. In the case of the powered coil the two-wells potential is obtained. One can notice that, the significant differences between these two kinds of potentials occur only in so-called "active zone", which is placed between angles $\pm\varphi_A$. Outside of the active zone, the influence of the electromagnetic interaction on the pendulum can be neglected. The experimental measurement and approximation (Eq. 2) of the torque M_{mag*} are shown in Fig. 3b.
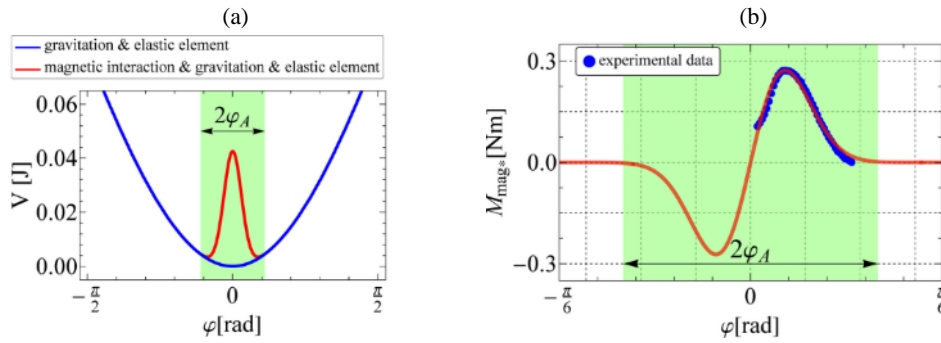
Figure 3. The one-well and two-well potentials of the system (a); The experimental measurement and approximation of the torque M_{mag*} (b).

3.2. Non-autonomous mathematical model

Taking into account the classical mechanics the governing equation of the system can be written as one ODE in a following way

$$J\ddot{\varphi} + c_e\dot{\varphi} + k_e\varphi + mgs \sin\varphi + T_s(\dot{\varphi}) - M_{mag*}I(t) = 0, \tag{3}$$

where J is the pendulum's moment of inertia, c_e and k_e denote viscous damping and stiffness of the elastic element. Term mgs stands for a torque of the gravitational force mg at arm s. Moreover, basing on the experimental measurements we decided to model the damping $T_s(\dot{\varphi})$ which comes from the rolling bearings with the following function:

$$T_s = \left[F_c + (F_s + F_c)\exp\frac{-(\dot{\varphi})^2}{v_s}\right]\tanh \varepsilon\dot{\varphi} + c\dot{\varphi}, \tag{4}$$

where F_c is the value of the simple Coulomb friction, v_s represents so-called Stribeck velocity and the F_s denotes the value of static friction when the pendulum does not move. Term c is viscous damping coefficient, whereas ε is a regularization parameter. Because, the magnetic interaction is possible only when the current flows through the coil, in Eq. 3 the value of M_{mag*} is multiplied by dimensionless current signal $I(t)$ (see Fig. 2) described by the following formula [8]

$$I(t) = \frac{1}{2}\left[1 + \frac{2}{\pi}\arctan\left(\epsilon \sin\left(2\pi f(t + t_0)\right) + i_0\right)\right], \tag{5}$$

where $i_0 = -\sin\left(\frac{\pi - \frac{2\pi w}{100}}{2}\right)$ and $t_0 = \frac{\pi - \frac{2\pi w}{100}}{2\pi f}$. Term w is a percentage duty cycle, f [Hz] stands for the frequency and ϵ is a regularization parameter.

3.3. Discrete mathematical model

The main goal of this approach is to eliminate the continues form of the current signal from the motion's equation. The goal can be achieved by dividing the motion into two different states. Each of the states is described by one autonomous ODE. The occurrences of the relevant states are related to times calculated on the basis of frequency and duty cycle of the current signal. The first state corresponds to the time when the coil is switched off and is governed by the following equation

$$J\ddot{\varphi} + c_e\dot{\varphi} + k_e\varphi + mgs \sin\varphi + T_s(\dot{\varphi}) = 0, \tag{6}$$

whereas the equation of the second state corresponding to the switched-on coil is as follows

$$J\ddot{\varphi} + c_e\dot{\varphi} + k_e\varphi + mgs \sin\varphi + T_s(\dot{\varphi}) - M_{mag*} = 0. \tag{7}$$

As a result, the continues coil current signal has been discretized. Parameters used in Eqs. 6 and 7 have the same description as parameters in the subsection 3.2. The trajectory of the motion is a set of solutions received in numerical integration of the Eqs. 6 and 7. The initial conditions employed to integration process have been taken from the last point of a preceding state's solution. The values of system's parameters were as follow: a=0.0425 [Nm rad], b=0.0181 [rad^2], J=6.787·10^{-4} [kgm^2],

mgs=5.800·10^{-2} [Nm], k_e=1.742·10^{-2} [Nm/rad], c_e=1.282·10^{-4} [Nms/rad], F_c=2.223·10^{-4} [Nm], F_s=4.436·10^{-4} [Nm], φ_A=0.3484 [rad], v_s=0.5374 [rad/s], c=7.369·10^{-5} [kg m2], ε=5.759 [-], ϵ=200 [-].

4. Experimental and numerical investigation of 1-period and one-side pendulum's oscillation

In this section, we present experimental and numerical investigations of one-side oscillations of the pendulum. By one-side oscillations, we mean oscillations of the pendulum without moving through the lower and upper equilibrium positions. Our studies focus on the influence of the duty cycle and frequency of the current signal on the motion. Experimentally, one can observed that for set constant frequency f exists a wide range of the duty cycle w for which the pendulum's oscillation does not change. Fig. 4 displays experimentally obtained phase plots of these same oscillations for various excitation signal's parameters.
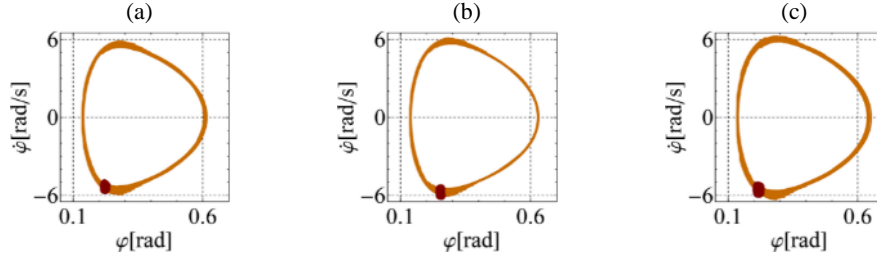
Figure 4. Experimental phase plots and Poincaré sections for a fixed frequency f=3.5 Hz but different duty cycles w: (a) 30%, (b) 60% and (c) 80%.

It is well visible that for a given frequency and different duty cycles it is possible to hold similar oscillations' amplitude, angular velocity and periodicity. In order to understand and explain this behavior we started our analysis from determining the initial conditions, which have to be fulfilled to achieved one-side oscillation. In Fig. 5 we can distinguish two states of pendulum's motion and characteristic points, which pendulum has to cross during oscillation. The first state starts when the pendulum is freely falling from the initial point ($\varphi_0, \omega_0=0$) to the point (φ_k, ω_k) where the coil is switched on what results in the magnetic barrier (blue arrows in Fig. 5a). We call this point "the kick", because the system is "kicked" to the higher energy state (green arrow in Fig. 5a). The system goes to the second state when the pendulum bounces from the magnetic barrier and goes away from it (red arrows in Fig. 5a). Fig. 5b depicts a phase plot of trajectory with colored line segments corresponding to the systems states. Taking into consideration the relations shown in Fig. 5, the 1-period motion can exist only for particular values of boundary conditions (φ_k, ω_k), which used as initial conditions in Eqs. 7 result in the trajectory which crosses the point ($\varphi_0, \omega_0=0$). The set of these values has been obtained numerically. Frist, a range of search was limited by boundaries following the motion scenario shown in Fig. 5:

(i)   the kick must be within the active zone,

(ii)   the minimum initial angle φ_0 cannot be smaller than φ_A (yellow line (2) in the Fig.6),

(iii)   the initial angle φ_0 cannot provide to potential well escape (blue line (1) in the Fig. 6).
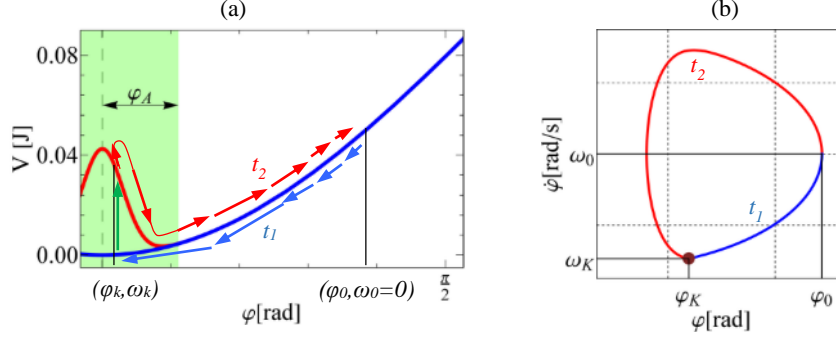

Figure 5. The potential plot (a) and phase plot (b) with characteristic points and stages during one-side pendulum's oscillation.

The obtained set of (φ_k,ω_k) and boundary lines are shown in Fig. 6. For each point (φ_k,ω_k) the time t_1 and t_2 (see Fig. 5a) of the motion's states have been computed. These times are related to the frequency and duty cycle of the current signal $I(t)$ in the following way: $f = 1/(t_1 + t_2)$ and $w = t_2/(t_1 + t_2)$. In Fig. 7, the line labeled as 3 shows the values of w and f that have been computed for the basic scenario shown in the Fig. 5a. However, since we have noticed before, that outside the active zone differences between two states are insignificant, switching off the coil (transition from state 2 to 1) can be performed anywhere outside the active zone. For those same (φ_k,ω_k) one can found the shortest time t_2 (spread from point (φ_k,ω_k) to some point before (φ_0,ω_0)) which corresponds to the minimum duty cycle w – line labeled as 1 in the Fig.7. The similar situation concerns calculating the longest time t_2 (spread from point (φ_k,ω_k) to point after (φ_0,ω_0)) what corresponds to the maximum w – line labeled as 2 in the Fig.7. In other words, the coil can be switched off just after the system leaves the active zone, or just before the system enters it.
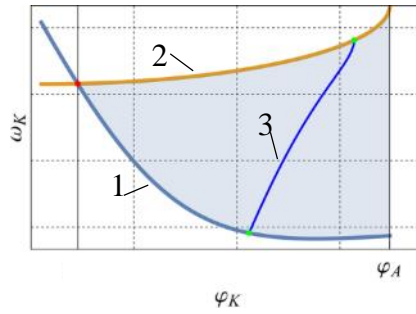
Figure 6.   (1), (2) – Boundary conditions; (3) – set of (φ_k,ω_k) fulfilling period-1 motion scenario.
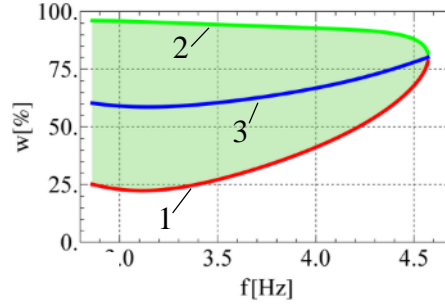
Figure 7. Range of w and f giving 1T and one-side oscillations; (1) – solution described in text; (2) – minimum *w*; (3) – maximum *w*.

Values of frequency and duty cycle get from the green area in Fig. 7 result in period-1 and one-well oscillating solution of the pendulum's motion. The comparison of numerical results to previously presented in Fig.4 solutions is shown in Fig. 8.
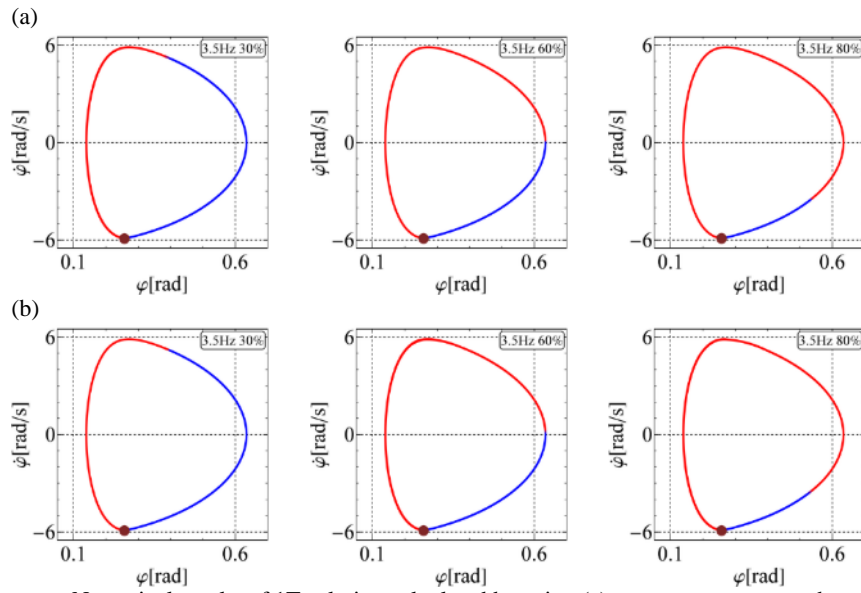
Figure 8. Numerical results of 1T solution calculated by using (a) non-autonomous mathematical model (Eq. 3) and (b) discrete mathematical model (Eqs. 6 and 7).

The comparison of the phase plots has justified that both non-autonomous and discrete models give those same solutions as experiment for fixed frequency 3.5 Hz and three different duty cycles. Numerical investigation have yielded that the amplitude of oscillations increases with decreasing frequency of current signal. Fig. 9 presents behavior of the system for different values of the frequency.
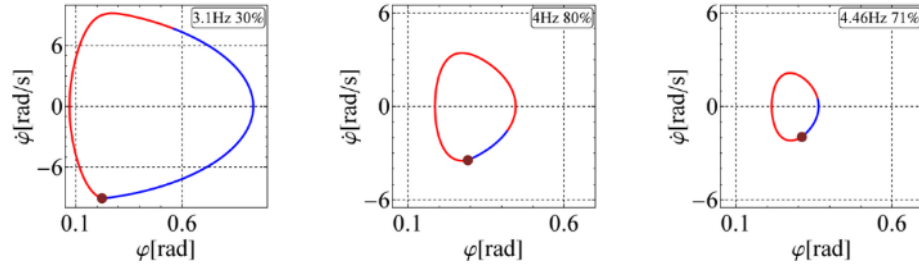
Figure 9. Influence of increasing frequency on oscillation amplitude.

5. Concluding remarks

The nonlinear one-degree-of-freedom system has been investigated numerically and experimentally. The system is composed of a single magnetic pendulum elastically coupled with a fixed base and excited by an alternating magnetic field. Two approaches of mathematical modeling of the system's motion have been presented as well as the model of magnetic interaction. The one-well oscillation has been analyzed in terms of parameters of the current signal: duty cycle and frequency. The numerical computation has yielded a range of duty cycles and frequencies for which the system exhibits period-1 motion. Both non-autonomous and discrete mathematical models provide similar results which are in good agreement with experiment. The work presents promising results which can be used to control so-called "kicked" systems. The future studies will concern more complicated scenarios of the 1-period motion.

References

[1] Penner, D.I., Doubochinski, D.B., Kozakov, M.I., Vermel', A.S., and Galkin, Y. V. Asynchronous excitation of undamped oscillations. *Soviet Physics - Uspekhi* 16 (1973), 158.

[2] Landa, P.S., *Nonlinear Oscillations and Waves in Dynamical Systems*. Springer Netherlands, Dordrecht, 1996.

[3] Doubochinski, D.B. and Tennenbaum, J. Theory and applications of the macroscopic quantization effect in nonlinearly-coupled vibrating systems, in: *1st Euro-Mediterranean Conference on Structural Dynamics and Vibroacoustics*, Marrakech, Marocco, 2013: pp. 23–26.

[4] Kesavamurthy, N. and Rao, G., A. study of Bethenod's phenomenon. *IEEE Transactions on Circuit Theory* 19 (1972), 215–218.

[5] Damgov, V. and Popov, I. "Discrete" Oscillations and multiple attractors in kick-excited systems. *Discrete Dynamics in Nature and Society* 4 (2000), 99–124.

[6] Siahmakoun, A., French, V.A., and Patterson, J. Nonlinear dynamics of a sinusoidally driven

pendulum in a repulsive magnetic field. *American Journal of Physics* 65 (1997), 393–400.

[7] Wojna, M., Wijata, A., Wasilewski, G., and Awrejcewicz, J. Numerical and experimental study of a double physical pendulum with magnetic interaction. *Journal of Sound and Vibration* 430 (2018), 214–230.

[8] Polczyński, K., Wijata, A., Awrejcewicz, J., and Wasilewski, G. Numerical and experimental study of dynamics of two pendulums under a magnetic field. *Proceedings of the Institution of Mechanical Engineers, Part I: Journal of Systems and Control Engineering* 233 (2019), 441–453.

[9] Polczyński, K., Wijata, A., Wasilewski, G., Kudra, G., and Awrejcewicz, J. Modelling and Analysis of Bifurcation Dynamics of Two Coupled Pendulums with a Magnetic Forcing, in: I. Kovacic, S. Lenci (Eds.), *IUTAM Symposium on Exploiting Nonlinear Dynamics for Engineering Systems*, Springer International Publishing, Cham, 2020: pp. 213–223.

Krystian Polczyński, M.Sc. (Ph.D. student): Lodz University of Technology, Department of Automation, Biomechanics and Mechatronics, 1/15 Stefanowskiego Str., 90-924 Łódź, Poland (*krystian.polczynski@edu.p.lodz.pl*). The author gave a presentation of this paper during one of the conference sessions.

Adam Wijata, M.Sc. (Ph.D. student): Lodz University of Technology, Department of Automation, Biomechanics and Mechatronics, 1/15 Stefanowskiego Str., 90-924 Łódź, Poland (*adam.wijata@edu.p.lodz.pl*).

Jan Awrejcewicz, Professor: Lodz University of Technology, Department of Automation, Biomechanics and Mechatronics, 1/15 Stefanowskiego Str., 90-924 Łódź, Poland, (*jan.awrejcewicz@p.lodz.pl*).

Stability and vibration of a two-member cantilever column with an integrated PZT rod

Jacek Przybylski, Krzysztof Kuliński

Abstract: This paper concerns the problem of transversal vibration a geometrically non-linear two-member column with a piezoceramic rod being a component of the structure. In the considered system, the external load applied to the column with an unintentional eccentricity and the internal piezo force are distributed among both members. The piezo rod is mounted discretely with an offset distance in regard to the host column what makes that the piezoelectric actuation may be effective in suppressing of prebuckling deflection in the whole range of the external load. Although the main role of the piezoelectric force generated by the actuator is the control of the column shape, it affects also the natural vibration frequency of the system. To analyze the problem a non-linear analytical model of the structure is developed on the basis of Hamilton's principle and solved with use of the perturbation method.

Performing adequate computations, the static deflection and internal axial force distribution modified by the electric field application are determined by changing column properties such as the offset distance and the eccentricity of the external load. In the dynamic analysis, the fundamental vibration frequency of the deflected column and the adequate modes are studied in relation to both the external load and the piezoelectric force. It has been proved that the natural vibration frequency, affected by the piezoelectric force, also depends on the matched column and rod materials, the ratio of the cross section of the rod to the host column and the direction of the electric field.

1. Introduction

The problem of stability and vibrations of beams and columns subjected to various types of external load with different types of support, cross-section dimensions, imperfections etc. is the subject of interest by many researchers. In those works, the problems are stated and formulated on the basis of both the classical analytical methods and the finite element method. Among physical models of the studied structures, two types of geometrical systems can be distinguished, i.e. the linear and non-linear systems. It is worth noting that linear systems do not exist in practice - each analyzed model has certain non-linear properties like imperfect rod/beam shape, non-homogeneous material, unideal mounting head assembly etc. The assumed linearity of the system results from application of abstract mathematical models, which simplify performed analysis. In mechanics, one of typical geometrically

non-linear structures consist of two or more parallely connected rods with different geometry of the cross-section, as well as the axial and bending rigidities.

The prebuckling behavior of the geometrically non-linear column, composed of two bars subjected to compression by means of the axial force was analyzed by Tomski [1]. In that paper the stability problem and its solution in regard to the slender two-member column was presented to show that the non-linear nature of the problem allows one to observe the straight and curvilinear static equilibrium of the system. Moreover, it was found that the bifurcation load value for a single member column is greater than that of a geometrically non-linear one. Numerical studies on the local and global instability and vibrations of a geometrically non-linear column subjected to Euler's load were discussed in [2]. Two-member column with a hinge and rotational spring located on one of the members in the specified distance from the support was investigated. The stated problem was formulated on the basis of Hamilton principle. It was proved that significant influence on column's instability and vibrations frequency had the localization of the hinge and rotational spring stiffness. Moreover, regardless of the spring stiffness, the closer the location of the hinge to the column's free end, the more stable system was observed. The influence of structural and geometrical parameters, the ways of applied loading, mounting conditions, prestress, etc. on the static and dynamic behavior of geometrically non-linear systems are widely discussed in [3-5].

In civil engineering and mechanics, a common solution to improve static and dynamic behavior of structures is prestressing of one or more their components. Prestress may be achieved via cables, turnbuckles, springs, electromagnets and "intelligent" materials – piezoelectric rods/patches, shape memory alloys (SMA) etc. The change in the frequency of vibrations and critical force in a beam made of carbon fiber with mounted pre-stretched SMA wires along the neutral axis of the system was the subject of interest of Baz *et al*. [6]. It was stated by Baz [6] that the appropriate use of reinforcement introduced by prestressed SMA wires increased the stiffness of the tested system and reduced its structural strength to buckling. With the use of the reinforcement, a shift in the basic forms of beam vibrations to higher frequency bands was observed in comparison to unreinforced beams. In addition, the system was discretized using the finite element method and the obtained results confirmed the validity of the experimental study. Ballas [7] made a numerical analysis of a simply supported Euler-Bernoulli beam with attached single sensor and actuator. The aim of the analysis was to actively control the first four vibration frequencies. Active control of the natural frequency of the cantilever beam using a piezoelectric polymer made of polyvinylidene fluoride was considered by Bailey and Hubbard [8]. The authors stated that if only the angular velocity of the beam's free end under the influence of vibrations is known, it is possible to control all forms of vibrations at the same time. Crawley and Luis [9] presented analytical methods and experimental tests of aluminum cantilever beams and graphite epoxy beams, where piezoactuators were mounted on the

top and bottom surface or embedded into the host beam structure. Experimental studies of the systems' dynamic response confirmed adopted analytical models. Moreover it was shown, as a part of experimental investigations, that embedding the piezoactuator inside the glass and epoxy-graphite laminate reduces its tensile strength by 20%. It should be noted that the stability and vibration control by means of piezoelectric actuation is an important problem from the optimization point of view. Significant influence on system's static and dynamic response has piezoactuator position, its cross-section dimensions, mounting method, voltage applied etc. The optimization of physical and theoretical intelligent structures with the use of piezoceramic materials was discussed in [10-12].

In this paper a slender geometrically non-linear two-member cantilever column subjected to eccentric partially follower force is investigated. One of the column members is made of piezoceramic material and is discretely mounted to the host column rods. The influence of the piezoelectric rod member offset location in regard to the host column neutral axis on static and dynamic system response is considered. Knowing that ideal axial loads do not exist in the practical engineering, the piezoceramic rod offset location is introduced to enhance the influence of piezoelectric force to counteract the bending moment resulting from the external eccentric load. A possibility of changing natural vibration frequency via the piezoelectric actuation is taken into considerations.

2. Problem formulation

In this study the slender two-member cantilever column is investigated. The host column member consists of two symmetrically mounted aluminum rods with regard to the z-axis as shown in Fig. 1b. The second member is a piezoceramic rod, which longitudinal axis is offset by distance $\overline{d}$ along z-axis in regard to the host column member neutral axis. The bottom end of the column is clamped making the displacements and rotations in any direction nulled. Both members are connected with ideally rigid mounting head on their top. External load is applied eccentrically, where eccentricity $\overline{e}$ is measured along z-axis as shown in Fig. 1a. Moreover, the external force direction is determined by follower force parameter η describing the relation between the direction of the external load and the tangent of bent column's end.

A stability and transversal vibrations problem of the column with piezoceramic rod shifted outside the contour of host member rods manifested by value $d = \overline{d}/L = 1/30$ is discussed. Implementation of the piezoceramic rod into the system allows induction of a compressive or a tensile internal piezoelectric force as a result of the applied electric field. The direction of that force is determined by the direction of the electric field vector. It is worth noticing that the piezo-rod assembled with the host column takes over some amount of the external force.
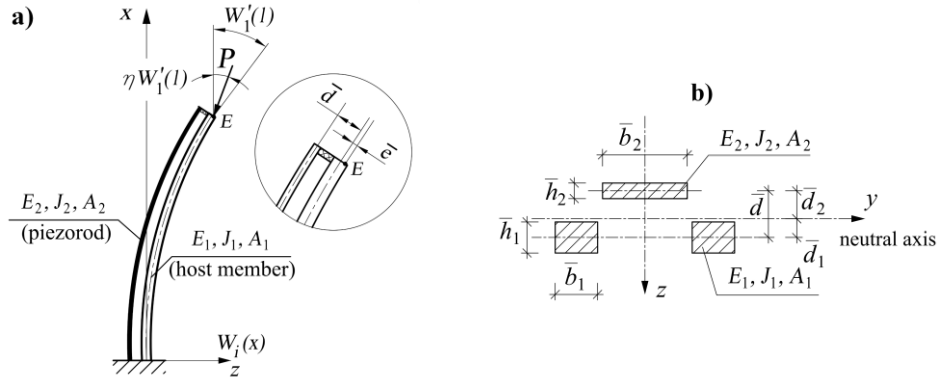
Figure 1. Cantilever two-member column subjected to partially follower force with eccentricity $\bar{e}$ (a), column's cross-section (b).

The Hamilton principle has been used for the problem's formulation. On the basis of the theory of moderately large deflections, which is a development of the non-linear von Karman theory, the deformation-displacement relationship and curvature of the i-th column's rod can be expressed as:

$$\varepsilon_i(x,t) = \frac{\partial U_i(x,t)}{\partial x} + \frac{1}{2}\left(\frac{\partial W_i(x,t)}{\partial x}\right)^2 \tag{1}$$

$$\kappa_i(x,t) = -\frac{\partial^2 W_i(x,t)}{\partial x^2} \tag{2}$$

where: $\varepsilon_i(x,t)$ denotes the mid-plane strain, $\kappa(x)$ is the curvature, $U(x,t)$, $W(x,t)$ are the axial and transverse displacements, respectively. The variation of the total mechanical energy may be presented as follows:

$$\delta \int_{t_1}^{t_2} \left\{ \frac{1}{2}\sum_{i=1}^{2}\int_0^L \rho_i A_i\left[\frac{\partial W_i(x,t)}{\partial t}\right]^2 dx - \frac{1}{2}\sum_{i=1}^{2}\left[\int_0^L E_i J_i \kappa_i^2 dx + \int_0^L E_i A_i \varepsilon_i^2 dx\right] - E_z A_2\left(e_{31}\int_0^L \varepsilon_2 dx + \frac{1}{2}\xi_{33}E_z\int_0^L dx\right) \right.$$
$$\left. - PU_1(x,t)\big|_{x=L} - P\bar{e}\frac{\partial W_1(x,t)}{\partial x}\bigg|_{x=L} - P\eta\frac{\partial W_1(x,t)}{\partial x}\bigg|_{x=L} W_1(x,t)\bigg|_{x=L} \right\} dt = 0, \qquad (i=1,2) \tag{3}$$

where: ρ_i denotes the volumetric mass density, A_i – i-th member cross-section area, E_i – Young's modulus, J_i – cross-section moment of inertia, e_{31} – piezoelectric constant, P – external load, e – eccentricity, η is the follower force parameter.

It is worth noting that when the piezoceramic rod is offset with regard to the neutral axis of the host column, the center of mass of the column's cross-section changes its initial location. According to that, the J_i parameter in Eq. (3) is described as:

$$J_i = \int_{A_i} z_i^2 dA_i = J_i^{(0)} \left\{ 1 + 12 \left[\beta^{i-1} A_{3-i} \overline{d} \left(h_i \sum_{i=1}^{2} \beta^{2-i} A_i \right)^{-1} \right]^2 \right\}, \quad (i = 1, 2) \tag{4}$$

where: $J_i^{(0)}$ denotes cross-section moment of inertia with respect to the centroidal axis, β is the relation of Young's modulus ($\beta = E_1/E_2$), $\overline{d}$ is the sum of distance between column members neutral axes in regard to the center of mass ($\overline{d} = \overline{d}_1 + \overline{d}_2$) and h_i is the i-th rod thickness.

After some mathematical manipulation of Eq. (3), taking into account that the virtual displacements $\delta U_i(x, t)$ and $\delta W_i(x, t)$ with respect to $i = 1, 2$ are arbitrary and independent in the range of $0 < x < $ L, one obtains a set of two equations describing column members' transversal vibrations motion and equations describing the strain invariance:

$$E_i J_i \frac{\partial^4 W_i(x,t)}{\partial x^4} - E_i A_i \frac{\partial}{\partial x} \left[\left\{ \frac{\partial U_i(x,t)}{\partial x} + \frac{1}{2} \left(\frac{\partial W_i(x,t)}{\partial x} \right)^2 \right\} \frac{\partial W_i(x,t)}{\partial x} \right] + (i-1) E_z A_2 e_{31} \frac{\partial^2 W_i(x,t)}{\partial x^2} + $$
$$+ \rho_i A_i \frac{\partial^2 W_i(x,t)}{\partial t^2} = 0 \tag{5}$$

$$E_i A_i \frac{\partial}{\partial x} \left(\frac{\partial U_i(x,t)}{\partial x} + \frac{1}{2} \left[\frac{\partial W_i(x,t)}{\partial x} \right]^2 \right) = 0 \qquad (i=1,2) \tag{6}$$

After double integration of Eq. (6), the equation describing the longitudinal displacements in i-th column's rods is:

$$U_i(x,t) = -\frac{S_i(t)}{E_i A_i} x - \frac{1}{2} \int_0^L \left[\frac{\partial W_i(x,t)}{\partial x} \right]^2 dx, \qquad (i=1,2) \tag{7}$$

where $S_i(t)$ is an internal longitudinal force depending on the members strain.

In the studied system the presence of the piezoceramic rod allows one to induce an additional tensile or compressive piezoelectric force as a result of the applied electric field. When the electric field vector and the polarization vector are parallel to each other and both vectors have the same direction, the internal compressive piezoelectric force is generated. Such force is a very effective tool for modification both the transversal displacements and the natural vibration frequency of the system. The piezoelectric force may be expressed by the electric field applied or by electric potential as follows:

$$F = \pm E_z A_2 e_{31} = \pm \frac{V}{h_2} A_2 e_{31} \tag{8}$$

where E_z denotes the electric field and V corresponds to the voltage applied. Sign (+) in Eq. (8) denotes the compressive piezoelectric force, whereas sign (-) describes tensile force, respectively. Geometrical boundary conditions of considered structure from Fig. 1a are:

$$W_i(x,t)\big|_{x=0} = 0, \qquad W_1(x,t)\big|_{x=L} = W_2(x,t)\big|_{x=L}, \qquad \frac{\partial W_i(x,t)}{\partial x}\bigg|_{x=0} = 0,$$

$$\frac{\partial W_1(x,t)}{\partial x}\bigg|_{x=L} = \frac{\partial W_2(x,t)}{\partial x}\bigg|_{x=L}, \quad U_i(x,t)\big|_{x=0} = 0, \quad U_2(x,t)\big|_{x=L} = U_1(x,t)\big|_{x=L} + \overline{d}\frac{\partial W_1(x,t)}{\partial x}\bigg|_{x=L}$$

$$\text{(9}_{\text{a-i}})$$

By performing necessary variational operations and integration by parts in Eq. (3) and successively introducing boundary conditions from Eq. (9$_{\text{a-i}}$) one obtains a set of natural boundary conditions necessary to solve Eqs. (5) and (7):

$$\sum_{i=1}^{2} E_i J_i \frac{\partial^2 W_i(x,t)}{\partial x^2}\bigg|_{x=L} - [S_2(t) - F]\overline{d} + P\overline{e} = 0 \tag{10}$$

$$\sum_{i=1}^{2} \left\{ E_i J_i \frac{\partial^3 W_i(x,t)}{\partial x^3}\bigg|_{x=L} + S_i(t)\frac{\partial W_i(x,t)}{\partial x}\bigg|_{x=L} \right\} - F\frac{\partial W_2(x,t)}{\partial x}\bigg|_{x=L} - P\eta\frac{\partial W_1(x,t)}{\partial x}\bigg|_{x=L} = 0 \tag{11}$$

$$\sum_{i=1}^{2} S_i(t) - F - P = 0, \qquad\qquad (i = 1,2) \tag{12}$$

In order to generalize the analysis, following dimensionless parameters are introduced:

$$\xi = \frac{x}{L}, \quad e = \frac{\overline{e}}{L}, \quad d = \frac{\overline{d}}{L}, \quad u_i(\xi,\tau) = \frac{U_i(x,t)}{L}, \quad w_i(\xi,\tau) = \frac{W_i(x,t)}{L}, \quad k_1^2(\tau) = \frac{S_1(t)L^2}{E_1 J_1},$$

$$k_2^2(\tau) = \frac{[S_2(t) - F]L^2}{E_2 J_2}, \quad p^2 = \frac{PL^2}{E_1 J_1 + E_2 J_2}, \quad f^2 = \frac{FL^2}{E_1 J_1 + E_2 J_2}, \quad \omega_i^2 = \frac{\rho_i A_i \Omega^2 L^4}{E_i J_i},$$

$$\omega^2 = \frac{\displaystyle\sum_{i=1}^{2} \rho_i A_i \Omega^2 L^4}{\displaystyle\sum_{i=1}^{2} E_i J_i}, \quad \mu^{(0)} = \frac{E_2 J_2^{(0)}}{E_1 J_1^{(0)}}, \quad \mu = \frac{E_2 J_2}{E_1 J_1}, \quad \tau = \Omega t, \quad \lambda^{(0)} = \frac{A_i L^2}{J_i^{(0)}}, \quad \lambda = \frac{A_i L^2}{J_i} \tag{13}$$

Taking into account Eq. (5) and assuming the dimensionless parameters described by Eq. (13), the dimensionless equation of motion of the i-th column member takes the form:

$$\frac{\partial^4 w_i(\xi,\tau)}{\partial \xi^4} \pm k_i^2(\tau)\frac{\partial^2 w_i(\xi,\tau)}{\partial \xi^2} + \omega_i^2 \frac{\partial^2 w_i(\xi,\tau)}{\partial \tau^2} = 0, \qquad (i = 1,2) \tag{14}$$

The axial force parameter k_i^2 may be expressed as:

$$k_i^2(\tau) = \lambda_i \left[\frac{\partial u_i(\xi,\tau)}{\partial \xi} + \frac{1}{2} \int_0^\xi \left(\frac{\partial w_i(\xi,\tau)}{\partial \xi} \right)^2 d\xi \right] \pm (i-1)(1+\mu^{-1})f^2 \tag{15}$$

Dimensionless longitudinal displacements on the basis of Eq. (7) are expressed as:

$$u_i(\xi,\tau) = \frac{-k_i^2}{\lambda_i} - \frac{1}{2} \int_0^\xi \left(\frac{\partial w_i(\xi,\tau)}{\partial \xi} \right)^2 d\xi \tag{16}$$

The solution to the problem is based on the small amplitude parameter perturbation method. According to that method, transversal and longitudinal displacements, axial forces and vibration frequency are expanded into power series with respect to the small amplitude parameter ε:

$$w_i(\xi,\tau) = w_{i0}(\xi) + \sum_{j=1}^N \varepsilon^j w_{ij}(\xi,\tau) + O(\varepsilon^N)$$

$$u_i(\xi,\tau) = u_{i0}(\xi) + \sum_{j=1}^N \varepsilon^j u_{ij}(\xi,\tau) + O(\varepsilon^N)$$

$$k_i^2(\tau) = k_{i0}^2 + \sum_{j=1}^N \varepsilon^j k_{ij}^2(\tau) + O(\varepsilon^N)$$

$$\omega_i^2 = \omega_{i0}^2 + \sum_{j=1}^N \varepsilon^j \omega_{ij}^2 + O(\varepsilon^N)$$

(17a-d)

The introduction of Eqs. (17a-d) into the general equation of motion (14) and longitudinal displacements (16) leads to an infinite sequence of these equations with increasing powers of small amplitude parameter ε, where the first two sets are:

$$O(\varepsilon^0): \quad \frac{d^4 w_{i0}(\xi)}{d\xi^4} + k_{i0}^2 \frac{d^2 w_{i0}(\xi)}{d\xi^2} = 0, \qquad u_{i0}(\xi) = \frac{-k_{i0}^2}{\lambda_i} \xi - \frac{1}{2} \int_0^\xi \left(\frac{dw_{i0}(\xi)}{d\xi} \right)^2 d\xi \tag{18a-b}$$

$$O(\varepsilon^1): \quad \frac{\partial^4 w_{i1}(\xi,\tau)}{\partial \xi^4} + k_{i0}^2 \frac{\partial^2 w_{i1}(\xi,\tau)}{\partial \xi^2} + \omega_{i0}^2 \frac{\partial^2 w_{i1}(\xi,\tau)}{\partial \tau^2} = -k_{i1}^2(\tau) \frac{\partial^2 w_{i0}(\xi)}{\partial \xi^2},$$

$$u_{i1}(\xi,\tau) = \frac{-k_{i1}^2(\tau)}{\lambda_i} \xi - \int_0^\xi \left(\frac{\partial w_{i0}(\xi)}{\partial \xi} \cdot \frac{\partial w_{i1}(\xi,\tau)}{\partial \xi} \right) d\xi \qquad (i=1,2)$$

(19a-b)

The equation with zero power of small amplitude parameter (Eqs. (18a-b)) describes the system's static behavior, whereas Eqs. (19a-b) under the first power of ε describe the dynamic response, respectively. In order to obtain the load-displacement relation, the solution of Eq. (18a) needs to be introduced into boundary conditions (9a-h)-(12) written in the nondimensional form. The obtained system of inhomogeneous linear algebraic equations with respect to integration constants cannot be

solved due to unknown parameter of the longitudinal force k_{i0}^2. The ninth, additional equation is determined by the condition (9$_i$), after the introduction of (13) and expansion (17). By grouping the members with zero power of the small parameter ε, a transcendental equation determining the relationship between dimensionless longitudinal forces (k_{i0}^2) in the column's rods is obtained, depending on the piezoelectric force (f^2) and external load (p^2).

As soon as the column's stability problem is solved, one proceeds to solve the problem of transversal vibrations on the basis of Eq. (19$_a$). The general solution of that equation consists of the sum of the general equation integral and the inhomogeneous equation integral. The solution is applied to boundary conditions (9)-(12), in which are introduced (13) and (17), then members with the first power of ε parameter are collected to separate the space with time variables. It should be noted that the frequency parameter ω_0 is not known at that moment, thus supplementary condition is derived on the basis of Eq. (19$_b$) introduced to (9$_i$). Both static and dynamic problem are solved numerically with the use of *Mathematica* code.

3. Exemplary results

To study the column's static and dynamic response, three different external load eccentricities (e = -0.01, 0, 0.01) and two different values of follower force parameter ($\eta = 0$ and $\eta = 0.50$) are taken into considerations. Dimensionless geometrical relations in column's cross-section are related to the column's host member thickness h_1 (see Fig. 1b). The following relations hold: $b_1 = (3/2)h_1$, $b_2 = 2b_1$, $h_2 = 0.5h_1$ and the total length of both column members is assumed as $L=30h_1$. The piezo-rod member is made of a piezoceramic material P-41 and on the basis of manufacturer's data [13] it has the following properties: $E_2 = 83.33$ GPa, $e_{31} = 8.333$ and $\rho_2 = 7450$ kg/m^3. In order to avoid the phenomenon of piezo-material depolarization, it is assumed that the maximum operational value of the electric field intensity should not exceed $E_{MAX} = 2000$ V/mm. Due to the fact that the highest influence of piezoelectric force on static column's response on the basis of [14] is obtained when the offset parameter is $d = 1/30$, that value is adopted to the presentation of numerical results. Remaining parameters required in the analysis are assumed as follows: $\mu^{(0)} = 0.148$, $\lambda_1^{(0)} = 10800$ and $\lambda_2^{(0)} = 43200$. An actual example of the discussed configuration may be a column in which the host member has the thickness equal to $h_1 = 7$ mm and according to that, the remaining dimensions of the rods would be: $b_1 = 10.5$ mm, $b_2 = 21$ mm, $h_2 = 3.5$ mm, $L = 210$ and $d = 7.0$ mm, respectively.

In Fig. 2a-c the influence of tensile/compressive piezoelectric force $f^2 = \pm 0.20p_c^2$ on vibration frequency ω of the conservative system with different load eccentricities is documented. The dashed line corresponds to the compressive piezo-force, the dashed-dot line denotes the tensile piezo-force and with the continuous lines the non-actuated system is distinguished.
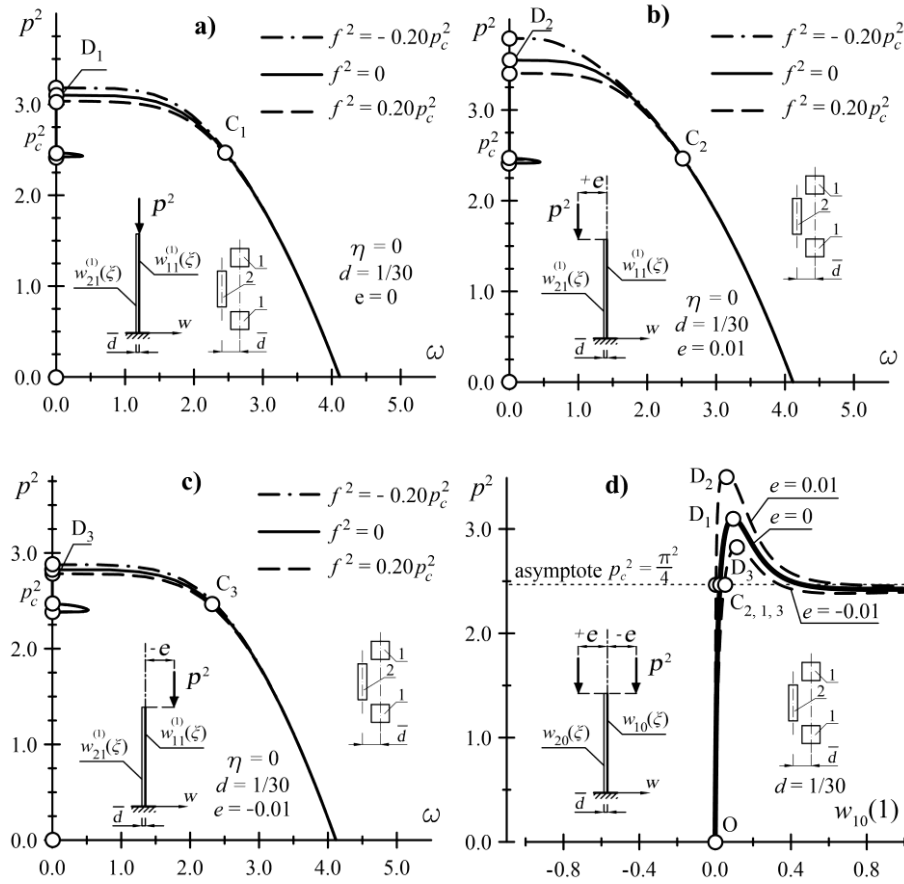
Figure 2. The first natural vibration frequency ω versus non-dimensional load p^2 (a, b, c), load-displacement relation (d); other parameters: $\eta = 0$, $d = 1/30$.

By mounting the piezoceramic rod at a distance $d = 1/30$ in regard to the host column member neutral axis, a strong influence of the load eccentricity on column's tip transversal displacement is observed (Fig. 2d). That impact is also clearly visible when the relation between internal forces is analyzed (see. [14]). Regardless of the eccentricity parameter value (e), the load-displacement curves, presented in Fig. 2d, cross the asymptote, exhibiting the level of critical buckling force at points C_i ($i = 1, 2, 3$), which are located under the limit points D_i ($i = 1, 2, 3$). Points D_i correspond to the maximum external load values at which the considered systems becomes unstable. It is worth noticing that analogical course of the load-displacement curves regarding the stability of geometrically nonlinear frames were presented by the Simitses and Vlahinos [15]. The presented numerical results in Fig. 2a-c prove that regardless of eccentricity parameter e, the greater the value of external load p^2, the lower the vibrations frequency ω of the non-actuated systems. As shown in Fig. 2a-c one may

notice that the second load-frequency curve starts beneath the $p_c{}^2$ point and ends at that point. That solution appears between local minimum in Fig. 2d and the critical buckling force. The influence of the piezoelectric force on the natural vibrations frequency increases with the growing external load value up to the limit point D_i. Then, with a rapid increase of the column's tip transversal displacement (Fig. 2d), the role of the piezoelectric force in modifying the vibration frequency decreases (Fig. 2a-c). Generation of the tensile piezo force increases system's natural frequency in regard to the non-actuated system, whereas compressive piezoelectric force acts in an opposite way. The intensity of vibrations control depends on points D_i location. The lower position of point D_i on the load-displacement curves, the higher range of frequency changes through piezo actuation is observed.

The influence of piezoactuation on the system's vibration frequency for the nonconservative load is presented in Fig. 3a-c, whereas the load-displacement relations for the non-actuated systems are shown in Fig. 3d. When the column is subjected to a partially follower force characterized by $\eta = 0.5$, the courses of the load-displacement curves only slightly changes in comparison to the system loaded by a force of the constant direction (compare Fig. 3d and Fig. 2d). In both cases, the load-frequency and load-displacement relationship curves strongly depend on the value of eccentricity e. The vibration frequency assume zero value in the non-actuated systems for the external load lower than that obtained in limit points denoted by D_i in Fig. 3d. The induction of piezoelectric force in the analyzed nonconservative systems allows one to only slight modification of the vibration frequency. Comparing to the Euler's load, the highest influence of piezoactuation on natural frequency ω is observed when deflection of the column is relatively small under relatively high value of external load p^2 (near the limit points D_i). The highest range of vibration frequency modification is observed for $e = 0$ (Fig. 3a) when $p^2 \approx 8.00$. Characteristic changes in the vibration frequency occurs for $e = -0.01$ (Fig. 3c) within the load range for which the force-displacement relation changes irregulary (Fig. 3d). For $p^2 \in \langle 6.33, 7.06 \rangle$, the tensile piezo-force diminishes frequency ω, whereas the compressive force increases the value of ω.

4. Conclusions

In this paper the static and dynamic response of a slender non-linear column with discretely mounted piezoceramic rod and subjected to the eccentric load has been analyzed. The rod operates as a piezoelectric transformer which under the applied electric field induces in the system an internal axial force. That force is used for control purposes of the column's deflection and it modifies also the natural vibration frequency of the structure. The thorough numerical analysis proved that the structure instability occurs due to buckling or at limit points what depends on the piezoceramic rod offset. The natural vibrations frequency may be modified significantly only in indicated ranges of the external load. Regardless of both the follower parameter η and eccentricity e, the greatest range of vibration
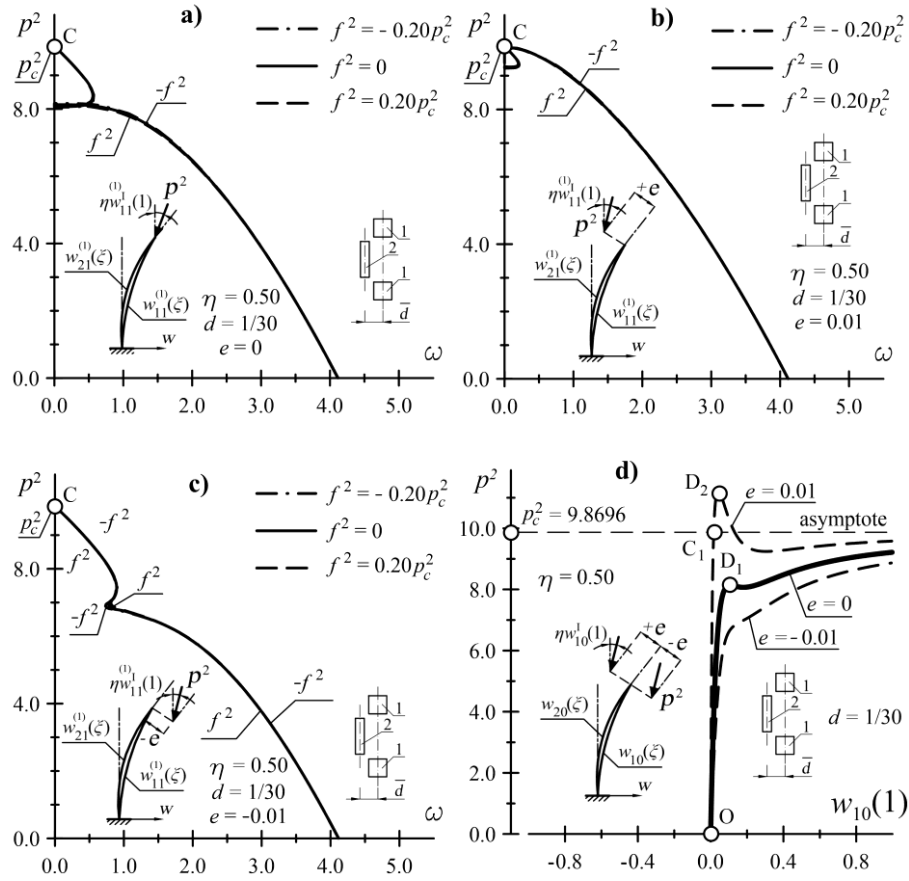
Figure 3. The first natural system's frequency ω versus non-dimensional load p^2 (a, b, c), load-displacement relation (d); other parameters: $\eta = 0.50$, $d = 1/30$.

frequency modification is obtained when the external load is slightly below given limit points of instability. It has been demonstrated also that the tensile piezoelectric force increases the natural vibration frequency of the system, whereas the compressive piezo-force decreases the frequency, respectively. The performed study reveals that the actuated piezoceramic rod integrated into the system may be successfully applicable for avoiding the resonance phenomenon in small structures.

References

[1]　Tomski L. Prebuckling behavior of compound column – direct nonlinear analysis, *Zeitschrift für angewandte Mathematik und Mechanik ZAMM* 65, 1 (1985), 59-61.

[2]　Sokół K. The local and global instability and vibration of a nonlinear column subjected to Euler's load, *Scientific research of the Institute of Mathematics and Computer Science* 9, 1, (2010), 187-194.

[3] Padovan J. Non-linear vibrations of general structures, *Journal of Sound and Vibration*72, (1980), 427-441.

[4] Eringen A. C. On the non-linear vibration of elastic bars, *Quarterly of Applied Mathematics* 9, 4, (1952), 361-369.

[5] Srinivasan A. V. Nonlinear vibrations of beams and plates, *International Journal of Non-Linear Mechanics* 1, 3, (1966), 179-191.

[6] Baz A., Poh S., Ro J. and Gilheany J. Control of the natural frequencies of nitinol-reinforced composite beams, *Journal of Sound and Vibration* 185, 1, (1995), 171-185.

[7] Balas M.J. Active control of flexible systems, *Journal of Optimization Theory and Applications* 25, 3, (1978), 415-436.

[8] Bailey T. and Hubbard J. E. Distributed piezoelectric-polymer active vibration control of a cantilever beam, *Journal of Guidance, Control, and Dynamics* 8, 5, (1985), 605-611.

[9] Crawley E. and De Luis L., Use of piezoelectric actuators as elements of intelligent structures, *American Institute of Aeronautics and Astronautics Journal* 25, 10, (1987), 1373-1385.

[10] Kang Y., Park H., Hwang W. and Han K. Optimum placement of piezoelectric sensor/actuator for vibration control of laminated beams, *American Institute of Aeronautics and Astronautics Journal* 34, 9, (1997), 1921-1926.

[11] Wankhade R. L. and Bajoria K. M., Numerical optimization of piezolaminated beams under static and dynamic excitations, *Journal of Science: Advanced Materials and Devices* 2, 2, (2017), 255-262.

[12] Yamada K., Enhancing efficiency of piezoelectric element attached to beam using extended spacers, *Journal of Sound and Vibration* 341, (2015), 31-52.

[13] http://www.annon-piezo.com/pztmaterials.asp (date accessed: 9th January 2017).

[14] Przybylski J. and Kuliński K. Shape enhancement of an eccentrically loaded column using piezoelectric actuator, *Engineering Structures* 189, (2019), 644-654.

[15] Simitses G. J. and Vlahinos, A. S. Elastic stability of rigidly and semirigidly connected unbraced frames. *Steel Framed Structures, Stability and Strength*, (1985), 115-152.

Jacek Przybylski, Professor: Czestochowa University of Technology, Institute of Mechanics and Machine Design Fundamentals, Dąbrowskiego 73 street, 42-200 Częstochowa, Poland (j.przybylski@imipkm.pcz.pl).

Krzysztof Kuliński, MSc. Eng. (Ph.D. student): Czestochowa University of Technology, Department of Technical Mechanics and Engineering Graphics, Akademicka 3 street, 42-200 Częstochowa, Poland (k.kulinski@bud.pcz.pl). The author gave a presentation of this paper during one of the conference sessions.

Investigation of energy harvesting in a 2DOFs portal frame by means of the positioning of the piezoelectric material

Rodrigo T. Rocha, Remei H. Junior, Wagner B. Lenz, Maurício A. Ribeiro, Angelo M. Tusset, Jose M. Balthazar, Elzbieta Jarzebowska

Abstract: In this work, a piezoelectric energy harvesting application will be considered using a two-degrees-of-freedom portal frame. The piezoelectric material will be considered as a linear device by using a capacitive mathematical model. The portal frame is a two-degrees-of-freedom structure considering a quadratic coupling in its coupling and set a 2:1 internal resonance between the first and second modes of vibration, which is a special condition of this kind of system due to the appearance of saturation phenomenon. As this phenomenon makes the system starts vibrating from the first mode and then, at steady state, vibrates into the second mode, the objective of this work is to verify the energy harvesting by considering the different positioning of a piezoelectric material, which are either to the supported beam or to the column. However, this portal frame is excited by a non-ideal DC motor with limited power supply. The results showed a considerably nonlinear behavior due to the non-ideal motor and, with the saturation phenomenon, it is more efficient to harvest energy by coupling the PZT on the column.

1. Introduction

The research about nonlinear dynamic systems has been increased substantially in the last decades. Mainly because such nonlinearities can make dynamic systems behave with unexpected behavior, presenting different responses depending on the excitation which is applied to such system.

External excitation in the environment, which provides kinetic energy (vibrations) in vibrating structures, are very common due to wind, vehicle traffic, and so on. However, there are some excitations which affect such structure and are affected by the vibration of the structure as well, and they are well-known by non-ideal excitations. Generally, they are small excitation sources, such as, for example, a DC motor or a crank-mechanism. The DC motor is one of the most used devices due to its non-ideality, for the mechanical output power depends on the motion of its armature and on the dynamics of its rotor, among other factors. In addition, these DC motors, when they have an orthogonal shaft coupled to its axis, it causes an imbalance, in which when used on a vibrating structure, they can affect each other, which is a non-ideal excitation source. Some non-ideal problems were studied in Refs. [1-3].

As such non-ideal excitation sources can cause high amplitudes of vibration and sometimes undesirable, it would be worthy to suppress them while transforming the mechanical energy from the

vibration into electrical energy. Among such possible energy harvesting devices which are can transform mechanical energy into electrical energy, the piezoelectric materials have been used as a common energy transducer due to their significant response for stimulus of different physical natures [4,5]. These materials were studied since last decade by several authors by considering a linear [6-8] and nonlinear materials [9-13]. An overview of the nonlinearities presented in the piezoelectric material was carried out in [14].

With that, some kind of structures in which can be found as buildings or bridges, they may have two particular degrees-of-freedom in which they are internally resonant with a ratio of 2:1. In addition, it is known that these kinds of structures are nonlinear due to geometry affecting directly the dynamics of them. One dynamic phenomenon which can happen, and it is quite dangerous is the saturation phenomenon [13,15]. This phenomenon happens when such a structure with 2:1 internal resonance is excited in resonance with the doubled natural frequency, in which such DOF will increase its amplitude of vibration until it saturates and then transfer the surplus energy to the other DOF. Sometimes, the structure was not supposed to move on such direction and then it can be quite dangerous. However, depending on the scale of the structure, it would be a good idea to harvest the surplus energy [13,15-21].

Therefore, this work presents the comparison of positioning a piezoelectric material as an energy harvesting device by using a two-degrees-of-freedom portal frame platform when the saturation phenomenon happens. In addition, the effect of the DC motor as an excitation source is taken into account.

In the following, the next section shows the mathematical and physical models to be studied and its governing equations of motion.

2. The 2:1 portal frame platform

The two-degrees-of-freedom portal frame system, represented by Fig. 1, consists of a supported beam of length L pinned to two columns with height h that are clamped in their bases. The beam and columns are considered as lumped masses, which are M and m, respectively, being that their motions are stated for two directions, vertical and horizontal directions. The coordinate q_1 is related to the horizontal displacement related to the sway mode of vibration, with natural frequency ω_1, while q_2 is the vertical displacement of related to the symmetric mode, with natural frequency ω_2. Both coordinates are related to the displacement of the mid-span of the beam (lumped mass M). The linear stiffness of the columns and the beam can be evaluated by a Rayleigh-Ritz procedure using cubic trial functions, which depend on the Young modulus E and the momentum of inertia I. Geometric nonlinearity is introduced by considering the shortening due to bending of the columns and of the beam.

As mentioned previously, two piezoelectric materials are coupled, one to a column and the other one to the supported beam of mass M. In this way, it is possible to evaluate the energy harvesting of both vertical and horizontal directions, i.e., verify if either the sway or the symmetric mode is the most efficient way to harvest energy. The piezoelectric material is considered as a nonlinear device proposed by (Tripplet and Quinn, 2009). The authors defined an approximation of the theoretical model to experimental results as $d(x) = \beta(1+\Theta|x|)$, where β is the linear piezoelectric strain coefficient and Θ is the nonlinear piezoelectric strain coefficient. Its representation is an RC circuit with capacitance C, resistance R, and electrical charge Q.

In this case, the excitation is given due to the non-ideal source on top of the mid-span of the supported beam. This source is an unbalanced DC electric motor with limited power supply composed of a moment of inertia J, eccentricity r, a shaft with a mass m_0 in its tip and with angular displacement θ. The torque of the motor is due to the resistive torque applied to the motor, which is represented by a function $H(\dot{\theta})$, and the driving torque is provided by the energy source, which is represented by $L(\dot{\theta})$. The function that defines the characteristic curve of the energy source of the motor as straight lines is $\Gamma(\dot{\theta}) = L(\dot{\theta}) - H(\dot{\theta}) = V_1 - V_2\dot{\theta}$, where V_1 is the voltage applied across the armature of the power supply and V_2 is a constant related to the kind of the motor to be utilized, which is directly related to the angular velocity [1,2,3]. As the latter constant is related to the angular velocity of the shaft of the motor, it has the most influence on the frequency of excitation of the system, then it is very important the choice of the right kind of DC motor. Therefore, depending on this value, the frequency of excitation provided by the motor can be set near resonance with the symmetric mode, which is the twice of the frequency of the sway mode, i.e., $\omega_n \approx \omega_2 + \sigma_2$ and $\omega_2 \approx 2\omega_1 + \sigma_1$, in which σ_1 and σ_2 are detuning factors. Such resonant conditions are set to saturation phenomenon appear.
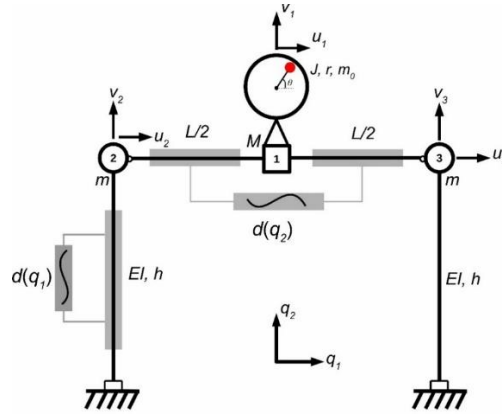
Figure 1. Portal frame physical system

Nodal displacements, shown in Fig. 1, are given by Eq. (1)

$$u_1 = q_1 \qquad u_2 = u_1 + \frac{B}{4} v_1^2 \qquad u_3 = u_1 - \frac{B}{4} v_1^2$$
$$v_1 = q_2 \qquad v_2 = -\frac{A}{2} u_1^2 \qquad v_3 = -\frac{A}{2} u_1^2 \qquad , \qquad (1)$$

where $A = 6/5h$ and $B = 24/5L$. The stiffness of the beam and column calculated by the Rayleigh-Ritz method are, respectively, $k_b = 48EI/L^3$ and $k_c = 3EI/h^3$.

The generalized coordinates are the displacements of the concentrated mass at the mid-span of the beam M. Using nodal displacements of Eq. (1), the kinetic energy is denoted by

$$T = \frac{1}{2} M \left(\dot{u}_1^2 + \dot{v}_1^2 \right) + \frac{1}{2} m \left(\dot{u}_2^2 + \dot{u}_3^2 + \dot{v}_2^2 + \dot{v}_3^2 \right) + \frac{1}{2} m_0 \left[\left(\dot{q}_1 + r\dot{\theta}\cos\theta \right)^2 + \left(\dot{q}_2 + r\dot{\theta}\sin\theta \right)^2 \right] + \frac{1}{2} J\dot{\theta}^2 , \quad (2)$$

in which, substituting the nodal displacements and eliminating higher-order terms that there is no contribution to the behavior of the system, it is obtained

$$T = \frac{1}{2} M \left(\dot{q}_1^2 + \dot{q}_1^2 \right) + \frac{1}{2} m \left(2\dot{q}_1^2 \right) + \frac{1}{2} m_0 \left[\left(\dot{q}_1 + r\dot{\theta}\cos\theta \right)^2 + \left(\dot{q}_2 + r\dot{\theta}\sin\theta \right)^2 \right] + \frac{1}{2} J\dot{\theta}^2 , \quad (3)$$

The potential energy of the system is given by the strain energy of the structure, the work of the weight of the masses of the beam and columns and by the electrical potential part of the piezoelectrics circuits with the contribution of the piezoelectric and the capacitor for each PZT layer, resulting in

$$U = \frac{1}{2} k_c \left(u_2^2 + u_3^2 \right) + \frac{1}{2} k_b \left(v_1 - \frac{v_2 + v_3}{2} \right)^2 + mg \left(v_2 + v_3 \right) + Mgv_1$$
$$- \frac{d(q_1)}{C_1} Q_1 \left(u_2 + v_2 \right) - \frac{d(q_2)}{C_2} Q_2 v_1 + \frac{1}{2} \left(\frac{Q_1^2}{C_1} + \frac{Q_2^2}{C_2} \right) , \quad (4)$$

Substituting Eq. (1) into Eq. (4), in terms of the general coordinates q_1, q_2, q_3, Q_1 and Q_2, the potential energy becomes

$$U = \left(k_c - mgA \right) q_1^2 + \frac{1}{2} k_b \left(q_2^2 + A q_2 q_1^2 \right) + Mgq_2$$
$$- \frac{d(q_1)}{C_1} Q_1 \left(q_1 + \frac{B}{4} q_2^2 \right) - \frac{d(q_2)}{C_2} Q_2 q_2 + \frac{1}{2} \left(\frac{Q_1^2}{C_1} + \frac{Q_2^2}{C_2} \right) , \quad (5)$$

Next, the dissipation energy of the system is considered by comprising the structural defined by a Rayleigh function and the resistance of the electrical circuits, which is denoted by

$$D = \frac{1}{2} c_1 \dot{q}_1^2 + \frac{1}{2} c_2 \dot{q}_2^2 + \frac{1}{2} R_1 \dot{Q}_1^2 + \frac{1}{2} R_2 \dot{Q}_2^2 , \quad (6)$$

The external excitation is given by the total torque of the DC motor, which is

$$\Gamma(\dot{\theta}) = L(\dot{\theta}) - H(\dot{\theta}) = V_1 - V_2\dot{\theta} , \quad (7)$$

Therefore, by applying Lagrange's function and Euler-Lagrange equation, the equations of motion of the system are given by

$$\left(2m + M + m_0\right)\ddot{q}_1 + c_1\dot{q}_1 + 2\left(k_c - mgA\right)q_1 + Ak_bq_1q_2 = \frac{d(q_1)}{C_1}Q_1 + m_0r\left(\dot{\theta}^2\sin\theta - \ddot{\theta}\cos\theta\right)$$

$$\left(M + m_0\right)\ddot{q}_2 + c_2\dot{q}_2 + k_bq_2 + \frac{Ak_b}{2}q_1^2 + Mg = \frac{d(q_1)}{2C_1}BQ_1q_2 + \frac{d(q_2)}{C_2}Q_2 - m_0r\left(\dot{\theta}^2\cos\theta - \ddot{\theta}\sin\theta\right)$$

$$\left(J + m_0r^2\right)\ddot{\theta} + m_0r\left(\ddot{q}_1\cos\theta - \ddot{q}_2\sin\theta\right) = V_1 - V_2\dot{\theta} \tag{8}$$

$$R_1\dot{Q}_1 - \frac{d(q_1)}{C_1}\left(q_1 + \frac{B}{4}q_2^2\right) + \frac{Q_1}{C_1} = 0$$

$$R_2\dot{Q}_2 - \frac{d(q_2)}{C_2}q_2 + \frac{Q_2}{C_2} = 0$$

Afterward, it is important to carry out a dimensionless process of the equations of motion of the system, becoming

$$x_1'' + \mu_1x_1' + x_1 + \alpha_1x_1x_2 = \delta_1\beta\left(1 + \Theta|x_1|\right)U_1 + \rho_1\left(\theta'^2\sin\theta - \theta''\cos\theta\right)$$

$$x_2'' + \mu_2x_2' + \omega_2^2x_2 + \alpha_2x_1^2 + G_2 = \delta_2\beta\left(1 + \Theta|x_1|\right)U_1x_2 + \delta_3\beta\left(1 + \Theta|x_2|\right)U_2 - \rho_2\left(\theta'^2\cos\theta + \theta''\sin\theta\right)$$

$$\theta'' + \rho_3\left(q_1''\cos\theta - q_2''\sin\theta\right) = \rho_4 - \rho_5\theta' \tag{9}$$

$$U_1' - \beta\left(1 + \Theta|x_1|\right)\left(\delta_4x_1 + \delta_5x_2^2\right) + \delta_4U_1 = 0$$

$$U_2' - \beta\left(1 + \Theta|x_2|\right)\left(\delta_6x_2\right) + \delta_6U_1 = 0$$

where

$$x_1 = \frac{q_1}{r} \qquad x_2 = \frac{q_2}{r} \qquad U_1 = \frac{Q_1}{q_0} \qquad U_2 = \frac{Q_2}{q_0} \qquad \tau = \omega_1t \qquad \omega_1 = \sqrt{\frac{2(k_c - mgA)}{2m + M + m_0}} \qquad d(x_{1,2}) = \frac{r}{q_0}d(q_{1,2})$$

$$\mu_1 = \frac{c_1}{\left(2m + M + m_0\right)\omega_1} \qquad \alpha_1 = \frac{Ak_br}{\left(2m + M + m_0\right)\omega_1^2} \qquad \rho_1 = \frac{m_0}{\left(2m + M + m_0\right)} \qquad \mu_2 = \frac{c_2}{\left(M + m_0\right)\omega_1}$$

$$\omega_2 = \frac{1}{\omega_1}\sqrt{\frac{k_b}{\left(M + m_0\right)}} \qquad \alpha_2 = \frac{Ak_br}{2\left(M + m_0\right)\omega_1^2} \qquad G_2 = \frac{Mg}{\left(M + m_0\right)\omega_1^2r} \qquad \rho_2 = \frac{m_0}{\left(M + m_0\right)} \qquad \rho_3 = \frac{m_0r^2}{\left(J + m_0r^2\right)}$$

$$\rho_4 = \frac{V_1}{\left(J + m_0r^2\right)} \qquad \rho_5 = \frac{V_2}{\left(J + m_0r^2\right)\omega_1} \qquad \delta_1 = \frac{q_0^2}{\omega_1^2r^2\left(2m + M + m_0\right)C_1} \qquad \delta_2 = \frac{Bq_0^2}{2\left(M + m_0\right)\omega_1^2rC_1}$$

$$\delta_3 = \frac{q_0^2}{\left(M + m_0\right)\omega_1^2r^2C_2} \qquad \delta_4 = \frac{1}{R_1C_1\omega_1} \qquad \delta_5 = \frac{Br}{R_1C_1\omega_1} \qquad \delta_6 = \frac{1}{R_2C_2\omega_1}$$

To calculate the harvested power of the considered system, Eqs. (10) are given as dimensional, dimensionless harvested power and the average power, respectively

$$P_{1,2} = R_{1,2} \dot{Q}_{1,2}^2$$
$$P_{1,2} = R_{0(1,2)} V_{1,2}'^2 \qquad , \tag{10}$$
$$P_{avg} = \frac{1}{T} \int_0^T P(\tau) d\tau$$

where $R_0 = R_{1,2}(\omega_1 q_0)^2$.

Next, Section 3 shows some numerical simulations neglecting the nonlinear piezoelectric contribution fixed in $\Theta = 0$.

3. Numerical simulations and discussions

The numerical simulations for this system were focused on the frequency-response of the system to find out about saturation phenomenon and the DC motor influences on the behavior of the system. For the numerical simulations, the parameters to be used are given in Tab. 1. Those parameters are considered to be fixed for the system with the exception when indicated.

Table 1. Parameters of the system

μ_1	μ_2	α_1	α_2	G_2	δ_1	δ_2	δ_3
0.0064	0.0183	0.443	0.3103	0.033	2.435	0.787	3.409

$\delta_4 = \delta_6$	δ_5	ρ_1	ρ_2	ρ_3	ρ_4	ρ_5	ω_2
0.146	0.067	0.02	0.01	1.0	1.0	Vary	1.9297

3.1. Frequency-response of the dynamic system

First of all, it is important to characterize the dynamic behavior of the system due to the non-ideal excitation source without any coupling of the piezoelectric material. As it is expected some nonlinear behavior in a region near resonance, the frequency-response of the system is plotted in Fig. 2 for the vertical motion (Fig. 2a) and horizontal motion (Fig. 2b). Note that the curves delight amplitude *versus* ρ_5 due to these parameters is directly related to the excitation frequency.

With the drawn plots, it is possible to see a softening behavior of the system due to the presence of the non-ideal motor, which is different from the common saturation phenomenon (as reported in [13,15]). In addition, saturation phenomenon still happens in a small region of $0.39 \leq \rho_5 \leq 0.491$, however, in a forward variation (black dots). This is totally different in a backward variation (red dots), as it is possible to see, saturation occurs in $0.209 \leq \rho_5 \leq 0.476$. Still, between $0.6 \leq \rho_5 \leq 0.7$, there is such phenomenon occurring, however, with a small potential. Note that this phenomenon occurred due to the increase of the amplitude of the horizontal motion (sway mode) while the excitation comes from the mid-span of the supported beam.

Even though the excitation source gives a rotational motion which affects the horizontal motion as well, it is possible to figure out that not always this excitation will affect the horizontal motion, only when there is resonance between the DC motor and the middle-beam, which is a condition of the saturation phenomenon. Then, a little bit after $\rho_5 > 0.5$, the horizontal motion decay to zero whereas the vertical motion does not, which means there is no resonance but still excitation of the vertical motion.

| (a) | (b) |
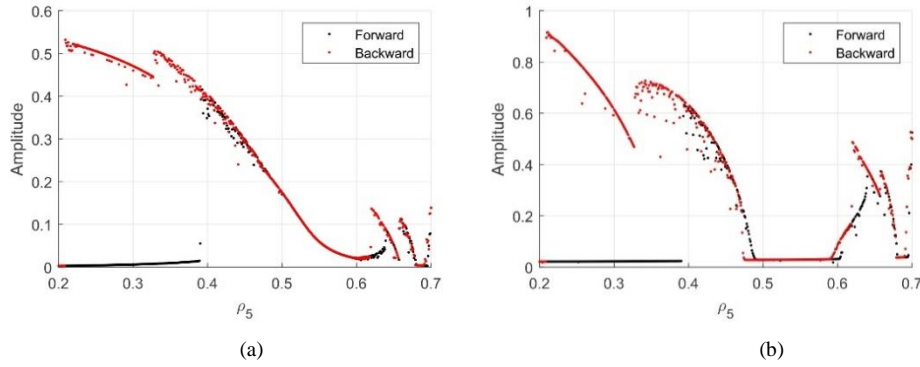
Figure 2. Frequency-response of the system, (a) Vertical motion, (b) Horizontal motion

Next, some frequencies-responses will be shown to show the influence of the piezoelectric material on the system, its energy harvesting and how worthy it is harvesting energy by considering saturation phenomenon.

3.2. Piezoelectric material coupled to the mid-span of the supported beam

When coupling the piezoelectric material to the structure, it changes a little bit the dynamics of the system due to the effect of the PZT material into the stiffness and also converting the mechanical energy from the vibrations into electrical energy.

Then, Figs. 3 show the frequencies-responses of the system with the piezoelectric material coupled to the mid-span of the supported beam. The softening behavior still comes up and it is very important because, without it, it would not be possible to obtain the peak of energy harvesting. In addition, the interval of saturation phenomenon is reduced as the PZT material is making the beam stiffer, and consequently, making it more difficult to reach in the critical amplitude to saturation occurs.

In this way, looking at Figs. 3a and 3b, the forward variation shows that a small initial condition will contribute weakly to reach at the resonance of the system so that the interval in which the system harvests high levels of energy is $0.409 \leq \rho_5 \leq 0.6$ in which the harvested power is $3.32 \leq P_{avg} \leq 0.036$. However, in the backward variation, the system goes to a different trajectory due to the high initial condition in which the power gets a peak of energy of $P_{avg} = 9.947$ (at $\rho_5 = 0.162$). It is important to highlight that when the energy is at this peak, saturation phenomenon is occurring, then, becoming

459

important the analysis of the energy harvesting from the column, as it will be presented in the next section.
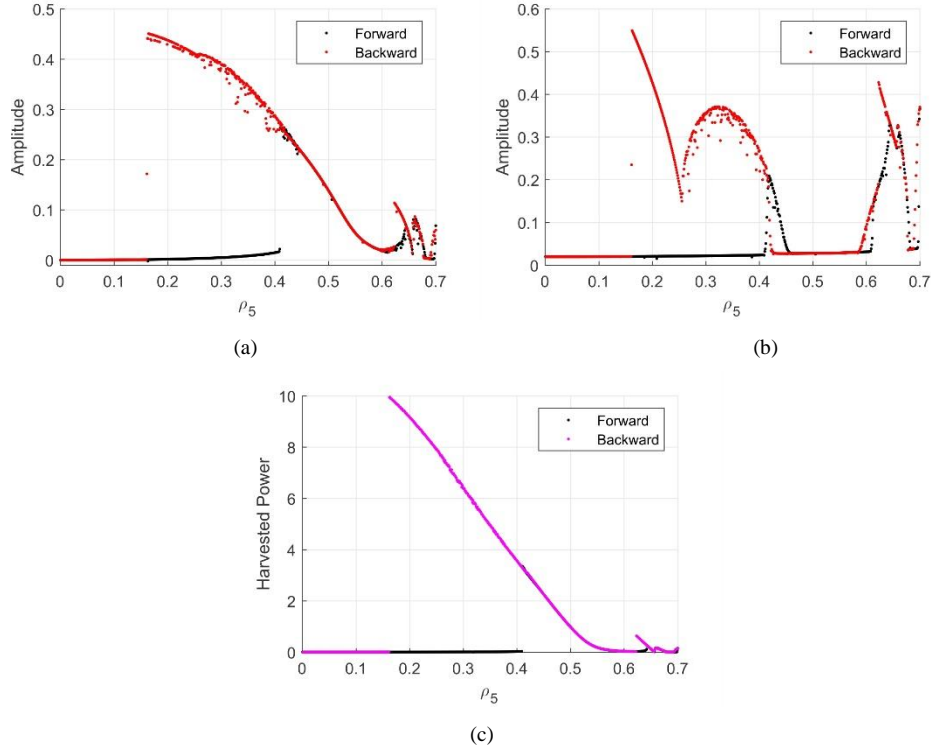
(a)

(b)

(c)

Figure 3. Frequency-response of the system with the piezoelectric material coupled to the mid-span of the supported beam, (a) Vertical motion, (b) Horizontal motion, (c) Energy harvesting

3.3. Piezoelectric material coupled a column

When the piezoelectric is coupled to one of the columns, the horizontal motion is affected, as mentioned before due to the beam becomes stiffer, which, consequently, changes the natural frequency of the sway mode.

Therefore, it is possible to see those differences through the frequencies-responses of Figs. 4 for the horizontal and vertical displacements and the energy harvesting with that. With the PZT coupled to the beam, it is noted that the softening is kept, however, shifting its interval to a smaller value of ρ_5. The saturation phenomenon then occurs in the interval of $0.158 \leq \rho_5 \leq 0.364$ in which the harvested power is $11.25 \leq P_{avg} \leq 0.104$, where $P_{max} = 11.25$ (at $\rho_5 = 0.158$) is the maximum harvested power extracted from the column.
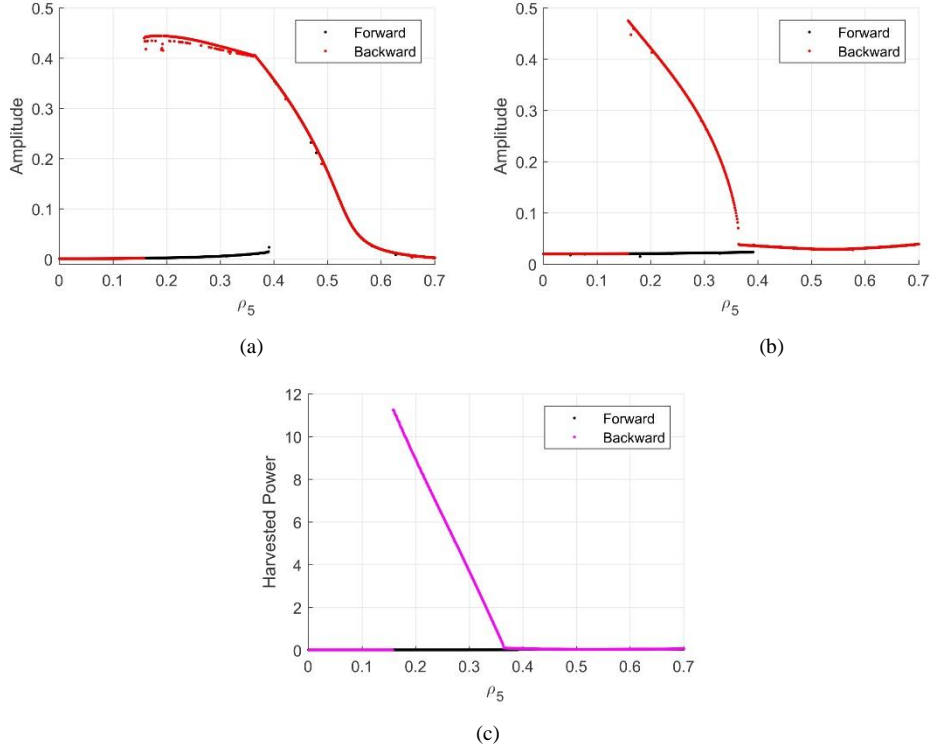
Figure 4. Frequency-response of the system with the piezoelectric material coupled to a column, (a) Vertical motion, (b) Horizontal motion, (c) Energy harvesting

3.4. Piezoelectric coupled to both column and beam

According to the previous two subsections, harvesting energy from the column or the excited supported beam is very efficient and can provide a big amount of power. Then, it is worthy to evaluate the harvested power when there are both piezoelectric coupled at the same time and see their effectiveness.

Figures 5a and 5b show the frequencies-responses for the system with piezoelectric materials coupled to the mid-span of the supported beam and a column. The interval of parameters in which saturation phenomenon occurs reduced even more with the PZT coupled to both beams. However, as the system still presents softening, the amplitudes are high enough to harvest a good amount of power.

Figure 5c shows the total harvested power from the system, i.e., the sum of the energy harvested from both supported beam and column. It is possible to see that in $0.252 \leq \rho_5 \leq 0.6$, the energy harvesting is due to only the supported beam. However, when $0.157 \leq \rho_5 \leq 0.251$, there is the contribution of the column, which is the interval where saturation phenomenon starts to appear. In this interval, the harvested power increases a lot reaching a maximum of $P_{max} = 13.89$ (at $\rho_5 = 0.157$).

(a)

(b)

(c)
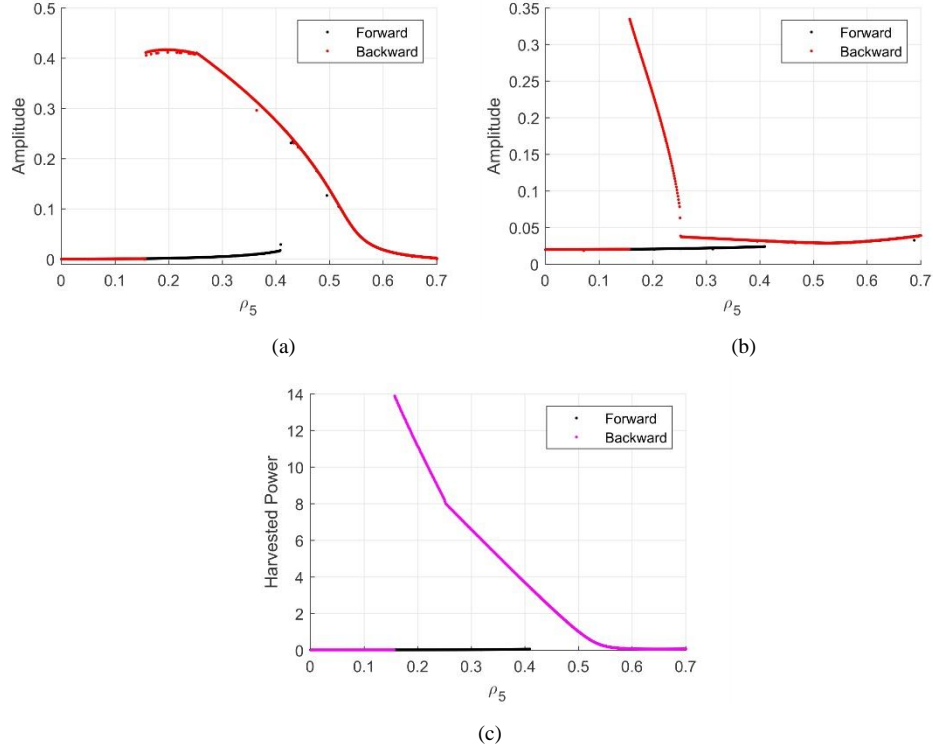
Figure 5. Frequency-response of the system with the piezoelectric material coupled to both column and beam, (a) Vertical motion, (b) Horizontal motion, (c) Energy harvesting

4. Conclusions

Basically, this work shows the effect of 3 (three) possible configurations of a piezoelectric material in a portal frame of two-degrees-of-freedom.

The configurations, in which it will be said as a case, consisted of in a case when there is only a PZT coupled to the mid-span of the supported beam, or only coupled to a column, or coupled to both beam and column.

Due to saturation phenomenon, the harvesting of energy was possible by coupling the PZT to the column, and with a high amount of power. Comparing both cases of isolated PZTs, the energy harvesting is more efficient when there is saturation phenomenon, due to the higher amplitude of vibration of the column than in the beam. However, when considering both PZT harvesting energy at the same time, there is a gain of energy when saturation comes up, so that the extraction of energy is due to beam plus column vibrations.

In addition, the DC motor has a great influence on the behavior of the system, because it is possible to see some irregular motion in the resonance region (near saturation region), even because there is softening behavior, which is not common in this system when excited by a shaker of a harmonic force [13].

Acknowledgments

References

[1] Rocha, R. T., Balthazar, J. M., Tusset, A. M., and Quinn, D. D. An analytical approximated solution and numerical simulations of a non-ideal system with saturation phenomenon. *Nonlinear Dynamics* 94,1 (2018), 429-442.

[2] Cveticanin, L., and Zukovic, M. Motion of a motor-structure non-ideal system. *European Journal of Mechanics-A/Solids,* 53 (2015), 229-240.

[3] Cveticanin, L., and Zukovic, M. Non-ideal mechanical system with an oscillator with rational nonlinearity. *Journal of Vibration and Control* 21, 11(2015), 2149-2164.

[4] Preumont, A. *Mechatronics: dynamics of electromechanical and piezoelectric systems (Vol. 136).* Springer Science & Business Media, 2006.

[5] Priya, S. and Inman, D. J. *Energy harvesting technologies (Vol. 21).* New York: Springer, 2009

[6] Stephen, N. G. (2006). On energy harvesting from ambient vibration. *Journal of sound and vibration* 293,1-2 (2016), 409-425.

[7] Syta, A., Bowen, C. R., Kim, H. A., Rysak, A., & Litak, G. (2015). Experimental analysis of the dynamical response of energy harvesting devices based on bistable laminated plates. *Meccanica*, *50*(8), 1961-1970.

[8] Jalili, N. (2009). Piezoelectric-based vibration control: from macro to micro/nano scale systems. Springer Science & Business Media.

[9] Crawley, E. F., & Anderson, E. H. (1990). Detailed models of piezoceramic actuation of beams. Journal of Intelligent Material Systems and Structures,1(1), 4-25.

[10] Triplett, A., and Quinn, D. D. The effect of non-linear piezoelectric coupling on vibration-based energy harvesting. *Journal of Intelligent Material Systems and Structures* 20, 16 (2009), 1959-1967.

[11] DuToit, N. E., & Wardle, B. L. (2007). Experimental verification of models for microfabricated piezoelectric vibration energy harvesters. AIAA journal, 45(5), 1126-1137.

[12] Iliuk, I., Balthazar, J. M., Tusset, A. M., Piqueira, J. R. C., de Pontes, B. R., Felix, J. L. P., & Bueno, Á. M. (2013). A non-ideal portal frame energy harvester controlled using a pendulum. The European physical journal. Special topics, 222(7), 1575-1586.

[13] Rocha, R. T. *On saturation phenomenon in energy harvesting based on nonlinear piezoelectric materials coupled to a portal frame foundation with ideal and non-ideal excitations.* Ph.D. thesis, São Paulo State University, 2016, José Manoel Balthazar.

[14] Daqaq, M. F., Masana, R., Erturk, A., & Quinn, D. D. (2014). On the role of nonlinearities in vibratory energy harvesting: a critical review and discussion. Applied Mechanics Reviews, 66(4), 040801.

[15] Nayfeh, A. H., and Mook, D. T. *Nonlinear oscillations*. John Wiley & Sons, 2008.

[16] Mook, D. T., Plaut, R. H., and HaQuang, N. (1985). The influence of an internal resonance on non-linear structural vibrations under subharmonic resonance conditions. Journal of Sound and Vibration, 102(4):473-492.

[17] Nayfeh, A. H. (2000). Nonlinear interactions. Wiley.

[18] Lee, Y., Frank Pai, P., and Feng, Z. (2008). Nonlinear complex response of a parametrically excited tuning fork. Mechanical Systems and Signal Processing, 22(5):1146-1156.

[19] Mankala, R. and Quinn, D. D. (2004). Resonant dynamics and saturation in a coupled system with quadratic nonlinearities.

[20] Felix, J. L. P., Balthazar, J. M., and Brasil, R. M. L. R. F. (2005). On saturation control of a non-ideal vibrating portal frame foundation type shear-building. Journal of Vibration and Control, 11(1):121-136.

[21] Golnaraghi, M. F. (1991). Vibration suppression of exible structures using internal resonance. Mechanics Research Communications, 18(2-3):135-143.

Rodrigo Tumolin Rocha, Ph.D.: Federal University of Technology – Parana at Department of Electronics, Av. Monteiro Lobato – Neighborhood: Jardim Carvalho, 84016-210 Ponta Grossa-PR, Brazil (*digao.rocha@gmail.com*).

Remei Haura Junior, M.Sc. (Ph.D. Student): Sao Paulo State University at Department of Electrical Engineering, Av. Eng. Luís Edmundo Carrijo Coube – Neighborhood: Vargem Limpa, 17033-360 Bauru-SP, Brazil (*remeihaurajunior@hotmail.com*).

Wagner Barth Lenz, M.Sc. Student: Federal University of Technology – Parana at Department of Electronics, Av. Monteiro Lobato – Neighborhood: Jardim Carvalho, 84016-210 Ponta Grossa-PR, Brazil (*mau.ap.ribeiro@gmail.com*).

Maurício Aparecido Ribeiro, Ph.D.: Federal University of Technology – Parana at Department of Electronics, Av. Monteiro Lobato – Neighborhood: Jardim Carvalho, 84016-210 Ponta Grossa-PR, Brazil (*mau.ap.ribeiro@gmail.com*).

Angelo Marcelo Tusset, Associate Professor: Federal University of Technology – Parana at Department of Electronics, Av. Monteiro Lobato – Neighborhood: Jardim Carvalho, 84016-210 Ponta Grossa-PR, Brazil (*tusset@utfpr.edu.br).

José Manoel Balthazar, Professor: Federal University of Technology – Parana at Department of Electronics, Av. Monteiro Lobato – Neighborhood: Jardim Carvalho, 84016-210 Ponta Grossa-PR, Brazil, and, Sao Paulo State University at Department of Electrical Engineering, Av. Eng. Luís Edmundo Carrijo Coube – Neighborhood: Vargem Limpa, 17033-360 Bauru-SP, Brazil (*jmbaltha@gmail.com*). The author gave a presentation of this paper during one of the conference sessions.

Elzbieta Jarzebowska, Associate Professor: Warsaw University of Technology at Department of Power and Aeronautical Engineering, Plac Politechniki 1, 00-661 Warszawa, Poland (*elajarz@meil.pw.edu.pl*).

Investigation of a tensegrity structure with multiple equilibrium configurations as jumping motion system

Philipp Schorr, Valter Böhm, Lena Zentner, Klaus Zimmermann

Abstract: Often, the operating range of mobile robots is limited by environmental circumstances like obstacles or gaps. Therefore, an adaptation of the motion principle is required to enable an operating continuation of such robots. A jumping motion is a promising approach. This motion type allows to cross gaps or to overcome obstacles where common motion principles which bases on wheels or legs fail. However, especially during landing large forces occur as a consequence of the impact with the ground. This issue encourages the use of compliant tensegrity structures which feature a great shock resistance. In this paper a tensegrity structure with multiple equilibrium configurations is considered. The two-dimensional structure is equipped with two actuators to vary the prestress of the system. The tensegrity structure is in contact to a horizontal plane due to gravity. Two actuation strategies are derived. Beside varying the prestress state of the structure, a jump can be realized by changing the equilibrium configuration. Both actuation strategies and the corresponding motion characteristics are evaluated by numeric simulations. The results emphasize the advantageous properties of tensegrity structures for a jumping motion system. In particular, the multistabilty of the structure allows a simple actuation strategy for a reliable jumping motion.

1. Introduction

Nowadays, mobile robots are applied for the investigation of unknown terrain, like the exploration of new planets or the operation in dangerous areas. However, often the environmental circumstances are unknown and the motion performances of these robots cannot be predicted anymore. Especially the occurrence of obstacles or gaps limits the operating range of most of the conventional mobile motion systems which base on wheels or legs. This issue encourages the investigation of jumping motion systems which allow to overcome obstacles or gaps. Therefore, an extension of the reachable area can be realized.

The general principle of the jumping motion bases on a great pulse on the ground which yields a take-off of the system. Therefore, the realization of a jump usually requires high dynamic actuators as presented in [3, 13]. Another possibility is the use of mechanisms which enable a sudden release of prestressed systems as shown in [4, 6, 7]. However, both approaches are vulnerable to damage because of the impact with the ground during the

take-off and the landing sequence. This issue encourages the investigation of compliant structures featuring great shock-resistance. Tensegrity structures represent a special kind of prestressed framework consisting of one-dimensional members which are loaded by tension or compression. According to the tensegrity principle all compressed members are connected to each other only by tensioned members. Thus, great loads occurring during the impact are distributed within the entire structure. Although tensegrity structures were established in the fields of architecture these structures can also be applied as motion system. In [8] a motion system based on a tensegrity structure is investigated. The motion is realized by successive tilting sequences controlled by varying the prestress of the structure. A tensegrity-based rolling system is shown in [5]. In [12] a worm-like motion is realized by a tensegrity structure. In [10] a multistable tensegrity structure is applied as vibration driven motion system. A multimodal motion system based on a multistable tensegrity is shown in [9].

In this paper a jumping motion system is developed. In section 2 the structural dynamics are derived. Two possible actuation strategies of the jumping motion system are presented in section 3. In section 4 numerical simulation for both actuation strategies are evaluated with regard to the corresponding motion characteristics. In section 5 the results are concluded and further research topics are discussed.

2. Mechanical Model of the Tensegrity Structure

2.1. Structural Topology and Modeling

The two-dimensional tensegrity structure illustrated in Fig. 1 is considered. The structure consists of 11 members ($j = 1, 2, \ldots, 11$) which are connected in 6 nodes ($i = 1, 2, \ldots, 6$). These nodes are modeled as frictionless planar revolute joints. The members of the tensegrity structure are divided into compressed members and tensioned members with regard to the occurring load. For the given structural topology, the members $j = 1, 2, 3$ are compressed members. The remaining members ($j = 4, 5, \ldots, 11$) are tensioned members.
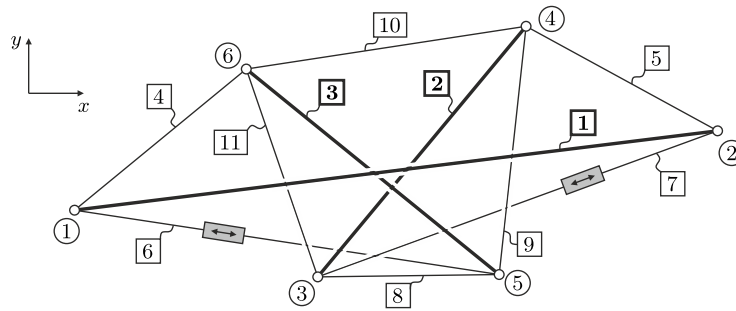
Figure 1. Investigated two-dimensional tensegrity structure.

A descriptive approach to represent the topology of the tensegrity structure is the use of the incidence matrix $\mathbf{B}$ known from the graph theory. This matrix represents the connectivity of the members and the nodes of the structure. Each member j, represented by the jth column of $\mathbf{B}$, is connected to two nodes (lower node number $\rightarrow$ -1, higher node number $\rightarrow$ $+1$). Each node i is represented by the ith row of $\mathbf{B}$.

$$\mathbf{B} = (b_{ij}) = \begin{bmatrix} -1 & 0 & 0 & -1 & 0 & -1 & 0 & 0 & 0 & 0 & 0 \\ +1 & 0 & 0 & 0 & -1 & 0 & -1 & 0 & 0 & 0 & 0 \\ 0 & -1 & 0 & 0 & 0 & 0 & +1 & -1 & 0 & 0 & -1 \\ 0 & +1 & 0 & 0 & +1 & 0 & 0 & 0 & -1 & -1 & 0 \\ 0 & 0 & -1 & 0 & 0 & +1 & 0 & +1 & +1 & 0 & 0 \\ 0 & 0 & +1 & +1 & 0 & 0 & 0 & 0 & 0 & +1 & +1 \end{bmatrix} \tag{1}$$

The compressed members ($j = 1, 2, 3$) are assumed as rigid with constant length L_j and mass M_j. The tensioned members ($j = 4, 5, \ldots, 11$) are modeled as parallel arrangement of a linear spring (stiffness k_j, free length l_j) and a visco-elastic linear damper (damping coefficient c_j). The mass of the tensioned members is neglectable comparing to the properties of the compressed members. Based on the experience of already existing tensegrity prototypes, the parameter values listed in Tab. 1 are selected. Moreover, the structure is equipped with two actuators connected to the tensioned members 6 and 7 which enable the control of the free length of the spring (actuation parameters: Δl_6, Δl_7).

Table 1. Selected parameter values of the tensegrity structure.

Compressed Members			Tensioned Members			
j	M_j [kg]	L_j [m]	j	l_j [m]	k_j [N/m]	c_j [Ns/m]
1	0.100	0.200	4, 5, 6, 7	0.040	1000	0.2
2, 3	0.040	0.080	8, 9, 10, 11	0.020	4000	0.2

2.2. Equations of Motion and Equilibrium Configurations

For the derivation of the equations of motion the EINSTEIN summation convention is supposed. The current configuration of the tensegrity structure can be defined by the position $\boldsymbol{r}_i = (x_i, y_i)^{\text{T}}$ of the nodes i respective to a fixed Cartesian coordinate system $\{x, y\}$. The vector $\boldsymbol{q} = (q_1, q_2, \ldots, q_{12})^{\text{T}} = (x_1, y_1, x_2, y_2, \ldots, x_6, y_6)^{\text{T}}$ contains all node coordinates. Using the incidence matrix from (1) the distance vector $\boldsymbol{d}_j$ and the geometric center $\boldsymbol{s}_j$ of all members j can be calculated as shown in (2).

$$\boldsymbol{d}_j = b_{ij}\boldsymbol{r}_i; \qquad \boldsymbol{s}_j = \frac{b_{ij}^2}{2}\boldsymbol{r}_i \qquad (j = 1, 2, \ldots, 11) \tag{2}$$

However, because of the non-deformable behavior of the compressed members additional holonomic constraints $\psi_b = 0$ $(b = 1, 2, 3)$ have to be taken into account. For the derivation of the equations of motion the LAGRANGE formulation with additional multipliers λ_b is applied. This approach is given in (3). Here, the parameters T and U represent the kinetic energy and potential energy of the tensegrity structure. The vector $\boldsymbol{F}_i$ describes the nodal forces considering damping forces and external forces, e.g. contact forces, friction forces, gravity, etc. (see section 4.1).

$$\frac{\mathrm{d}}{\mathrm{d}t}\frac{\partial T}{\partial \dot{q}_a} - \frac{\partial T}{\partial q_a} + \frac{\partial U}{\partial q_a} = \boldsymbol{F}_i \cdot \frac{\partial \boldsymbol{r}_i}{\partial q_a} + \lambda_b \frac{\partial \psi_b}{\partial q_a} \qquad (a = 1, 2, \ldots, 12)$$

$$\psi_b = |\boldsymbol{d}_b| - L_b = 0 \qquad (b = 1, 2, 3) \tag{3}$$

The kinetic energy T is defined in (4). The parameter φ_j describes the orientation of the compressed member j respective to the positive x-axis. The potential energy U is characterized by the deformation of the tensioned members. This approach is shown in (5).

$$T = \sum_{j=1}^{3} \left(\frac{M_j}{2}|\dot{\boldsymbol{s}}_j|^2 + \frac{M_j|\boldsymbol{d}_j|^2}{24}\dot{\varphi}_j^2 \right) \qquad \text{with } \varphi_j = \arctan\left(\frac{\boldsymbol{d}_j \cdot \boldsymbol{e}_y}{\boldsymbol{d}_j \cdot \boldsymbol{e}_x} \right) \tag{4}$$

$$U = \sum_{j=4}^{11} \frac{k_j}{2}(|\boldsymbol{d}_j| - (l_j + \Delta l_j))^2 \qquad \text{with } \Delta l_j \equiv 0 \quad \forall\, j \setminus \{6, 7\} \tag{5}$$

Furthermore, a stabilization of the numerical integration is required in order to avoid the drift-off of the holonomic constraints. Therefore, the BAUMGARTE method (see [1]) is applied. Hence, the holonomic constraints are varied to ensure the stable integration despite of numerical accuracy. Moreover, the BAUMGARTE parameters α and β are chosen respective to the step size Δt $(\alpha = \beta = \Delta t^{-1}$, see [2]). This approach is shown in (6).

$$\frac{\mathrm{d}}{\mathrm{d}t}\frac{\partial T}{\partial \dot{q}_a} - \frac{\partial T}{\partial q_a} + \frac{\partial U}{\partial q_a} = \boldsymbol{F}_i \cdot \frac{\partial \boldsymbol{r}_i}{\partial q_a} + \lambda_b \frac{\partial \psi_b}{\partial q_a} \qquad (a = 1, 2, \ldots, 12)$$

$$\ddot{\psi}_b + 2\alpha\dot{\psi}_b + \beta^2 \psi_b = 0 \qquad (b = 1, 2, 3) \tag{6}$$

For the determination of the static equilibrium configurations of the investigated tensegrity structure (6) is simplified. Beside neglecting the dynamic terms also the environmental influences $\boldsymbol{F}_i$ are ignored. This yields the nonlinear system of equations formulated in (7).

$$\frac{\partial U}{\partial q_a} = \lambda_b \frac{\partial \psi_b}{\partial q_a} \qquad (a = 1, 2, \ldots, 12)$$

$$\psi_b = 0 \qquad (b = 1, 2, 3) \tag{7}$$

For the selected parameter values 8 equilibrium configuration are detected. Moreover, the stability of these equilibria is evaluated considering the bordered Hessian of the potential energy U. This yields 4 stable (I, III, V, VII) and 4 unstable (II, IV, VI, VIII) equilibrium configurations. These configurations are displayed in Fig. 2. In order to highlight the different states despite of the similar shape node 5 is marked by a black square.
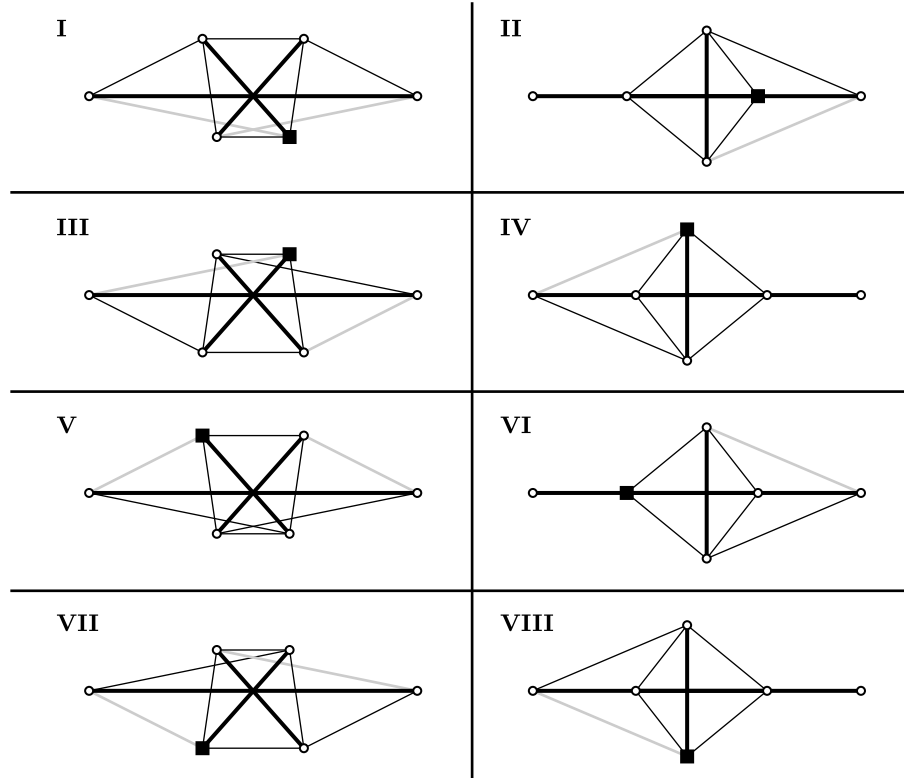
Figure 2. Detected equilibrium configurations of the investigated tensegrity structure (node 5 marked by a black square).

3. Actuation Strategy

3.1. Variation of the Prestress State

The potential energy U characterizes the prestress of the tensegrity structure and can be controlled by the actuation parameters Δl_6 and Δl_7 (see (5)). Moreover, the potential energy depends on the current equilibrium state. However, based on the results of [9] the detected equilibrium configuration exist only for a limited parameter set of Δl_6 and Δl_7. The results of the potential energy U are depicted in Fig. 3 for all stable equilibrium configurations. The

white areas represent the parameter ranges where the according equilibrium state does not exist. These results confirm the influence of the actuation on the potential energy of the structure. Therefore, a sudden change into a configuration with lower energy level can result in a jumping motion (approximation by conservation of energy: $T + U =$ const.; $U \downarrow$, $T \uparrow$). This principle requires a high dynamic actuation to realize this change in marginal time.
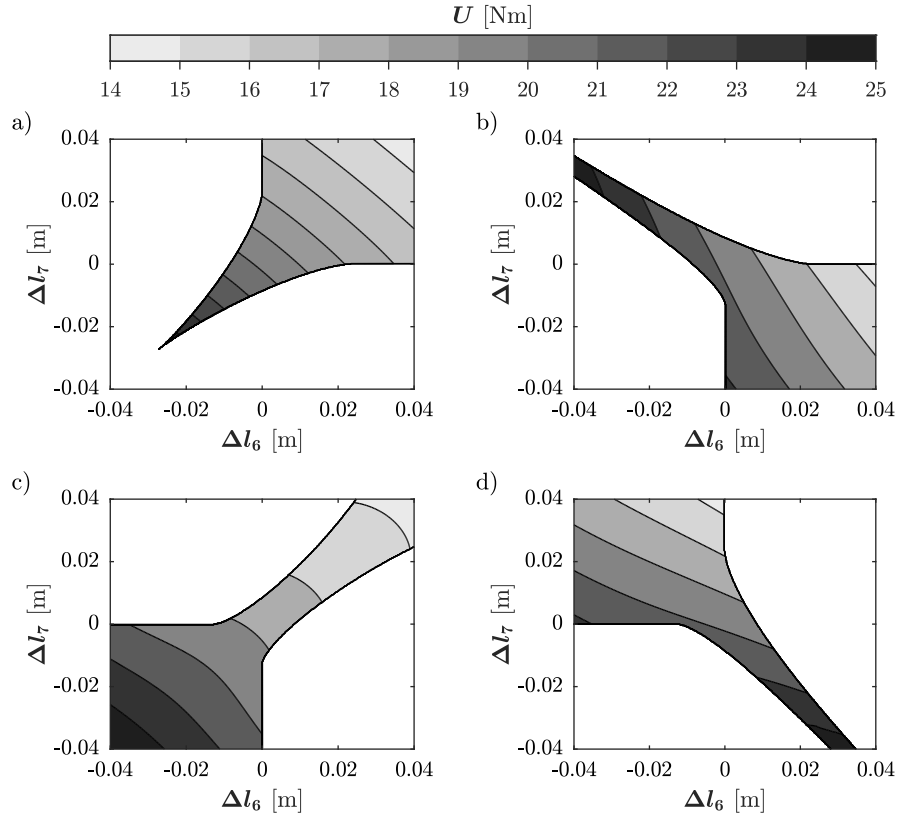
Figure 3. Potential energy of the tensegrity structure for the actuation parameters Δl_6 and Δl_7 - a) equilibrium I, b) equilibrium III, c) equilibrium V, d) equilibrium VII.

3.2. Change of the Equilibrium Configuration

Another possibility to initialize a jump is the utilization of the multistability of the structure. Therefore, by changing into a stable equilibrium configuration with lower potential energy a jumping motion can be realized. The change between the stable states is controlled by leaving the existence ranges which are depicted in Fig. 3. However, the resulting configuration cannot be predicted if multiple equilibria exist for the selected actuation. Therefore, the boundary

of the initial state has to be crossed into a parameter range where only one stable equilibrium configuration exists. This yields the curve displayed in Fig. 4. Moreover, depending on the location where this limiting curve is crossed different energy difference can be realized. The according results are illustrated in Fig. 4.
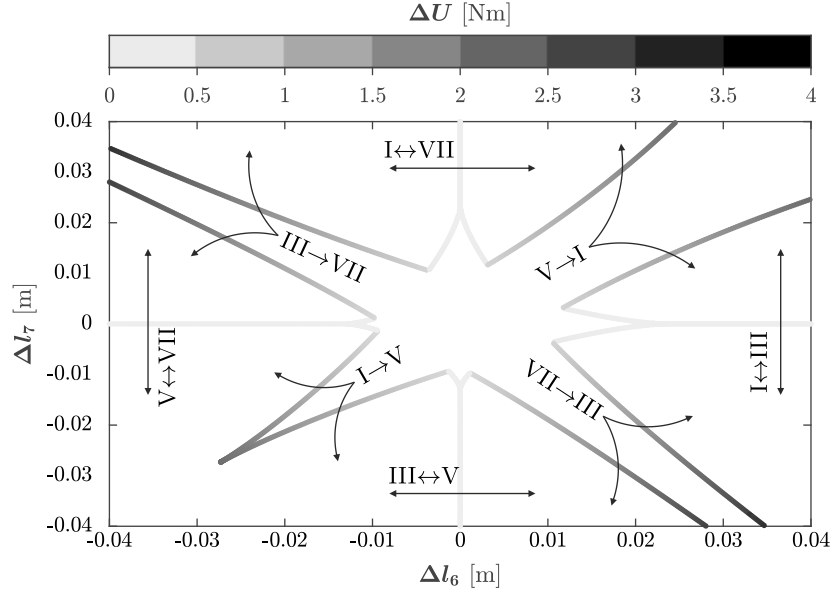
Figure 4. Potential energy of the tensegrity structure for the actuation parameters Δl_{06} and Δl_{07} - a) equilibrium I, b) equilibrium III, c) equilibrium V, d) equilibrium VII.

These results confirm the occurrence of energy differences by changing between the stable states. In particular, changing between states which are not located next to each other (I↔V, III↔VII) seems to be the most efficient opportunity to realize great energy difference. Furthermore, the great advantage of this actuation strategy is that there are no sophisticated requirements on the actuators. Crossing the existence limit of the equilibrium state in a controlled way is sufficient to realize a jump. No dynamic actuation is required.

4. Simulation of the Jumping Motion

The equations of motion formulated in (6) are solved numerically using 4th order Runge-Kutta-Method with a suitable constant step size ($\Delta t = 10^{-4}$ s). As initial state the jumping motion system is assumed to start in a stable equilibrium configuration (I, III, V or VII) and the entire system is supposed to be in rest ($\dot{q} = 0$). Furthermore, the environmental influences as well as the actuation of the structure are taken into account.

4.1. Modeling of Environment and the Actuation

The tensegrity structure is in contact with a horizontal plane due to gravity ($\boldsymbol{g} = -g\boldsymbol{e}_y$ with $|\boldsymbol{g}| = 9.81$ m/s^2). Occurring friction effects are taken into account by COULOMB's Law of Friction. Moreover, stiction is modeled using KARNOPP's method and the dynamic partitioning method (see [11]). Therefore, the nodal forces caused by the environmental conditions represent the influence of gravity, friction and the contact forces. The contact force $\boldsymbol{F}_{\text{contact,i}}$ at the node i is modeled by (8).

$$
\boldsymbol{F}_{\text{contact,i}} = \begin{cases} -k_g y_i \ \boldsymbol{e}_y & \text{if } y_i < 0 \\ (-k_g y_i - c_g \dot{y}_i) \ \boldsymbol{e}_y & \text{if } y_i < 0 \text{ and } \dot{y}_i < 0 \\ \boldsymbol{0} & \text{else} \end{cases} \tag{8}
$$

The jumping motion is simulated for two different actuation strategies which are qualitatively illustrated in Fig. 5. The actuation strategy in Fig. 5a) bases on the approach of section 3.1. The prestress is varied to realize a configuration which greater potential energy. Afterwards, a sudden return into the original state (see $t \approx 1$ s) should release this energy. As result of the approach of section 3.2 the actuation strategy displayed in Fig. 5b) is derived. Varying the prestress into a critical state which yields a change into another stable configuration is sufficient for the actuation. Therefore, this approach does not require any sophisticated high-dynamic actuators.
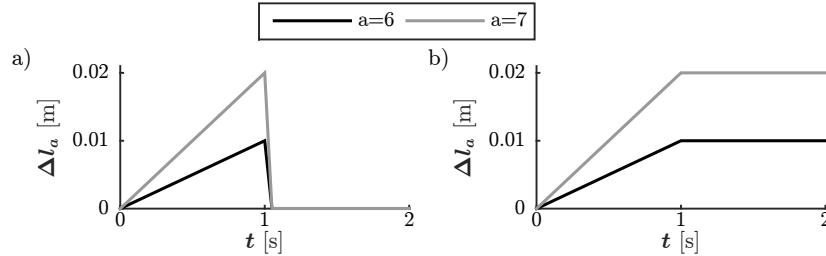
Figure 5. Investigated actuation strategies - a) sudden change into a configuration with lower energy level, b) change of the equilibrium state.

4.2. Motion Characteristics of the Jumping Motion

The motion of the structure is evaluated until the first impact with the ground after the take-off (the structure was at least for one time instant not in contact with the ground). Further jumps as consequence of the impact are not considered for the jumping performance.

4.2.1. Jumping by varying the prestress state

The actuation strategy displayed in Fig. 5a) is formulated in (9). Here, $\Delta l_{a,\max}$ ($a = 6, 7$) describes the maximum actuation parameters. For the parameters ranges illustrated in Fig. 3 the motion behavior of the system is simulated. The result of the jumping height are shown in Fig. 6. However, only for few small isolated parameter configurations a take-off occurs ($H > 5$ mm). Instead, the released potential energy is transferred into high frequent oscillations of the structure. Therefore, this actuation strategy is classified as inefficient for the chosen actuated members. Thus, the consideration of further motion characteristics like jumping distance is not evaluated.

$$\Delta l_a(t) = \begin{cases} \Delta l_{a,\max}\, t & \text{if } t \leq 1 \\ 0 & \text{else} \end{cases} \qquad (a = 6, 7) \qquad (9)$$
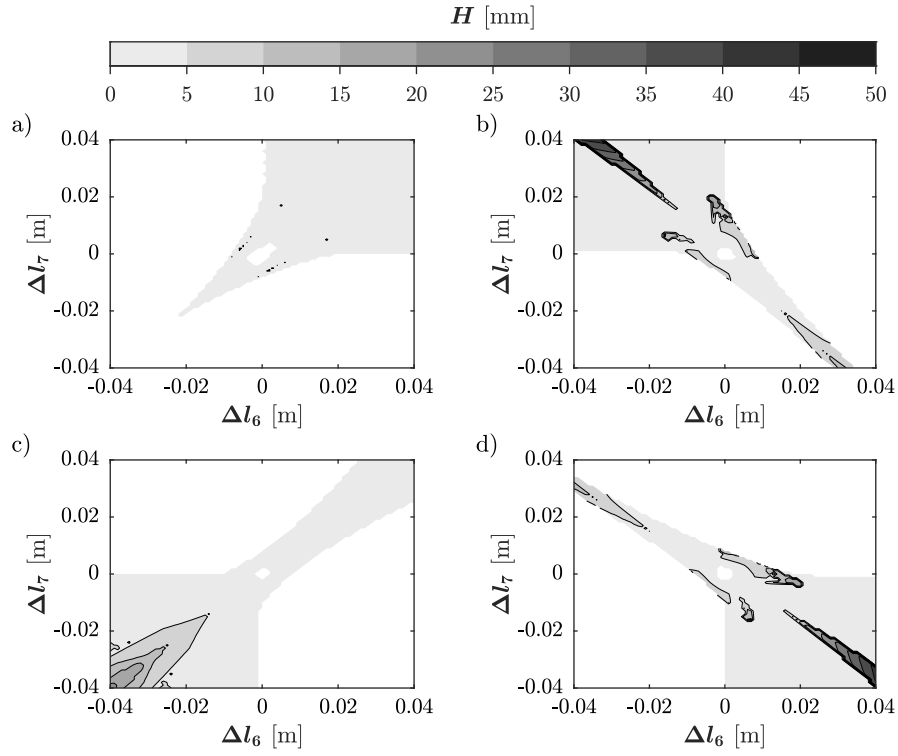
Figure 6. Jumping height of the motion system operating in - a) equilibrium I, b) equilibrium III c) equilibrium V, d) equilibrium VII.

4.2.2. Jumping by changing the equilibrium state

For the change of the equilibrium configuration the actuation strategy formulated in (10) is applied (see. Fig. 5b)). Moreover, the parameter values of $\Delta l_{a,\max}$ ($a = 6, 7$) are chosen as illustrated in (11).

$$\Delta l_a(t) = \begin{cases} \Delta l_{a,\max} \, t & \text{if } t \leq 1 \\ \Delta l_{a,\max} & \text{else} \end{cases} \qquad (a = 6, 7) \tag{10}$$

$$\Delta l_{6,\max} = \cos(\alpha) \cdot 0.04 \text{ m}, \qquad \Delta l_{7,\max} = \sin(\alpha) \cdot 0.04 \text{ m}$$

$$\text{with } \begin{cases} \boldsymbol{q}(t = 0) \mathrel{\widehat{=}} \text{I} & \text{if } \alpha \in (0, \pi/2], \quad \boldsymbol{q}(t = 0) \mathrel{\widehat{=}} \text{III} \quad \text{if } \alpha \in (\pi/2, \pi] \\ \boldsymbol{q}(t = 0) \mathrel{\widehat{=}} \text{V} & \text{if } \alpha \in (\pi, 3\pi/2], \quad \boldsymbol{q}(t = 0) \mathrel{\widehat{=}} \text{VII} \quad \text{if } \alpha \in (3\pi/2, 2\pi] \end{cases} \tag{11}$$
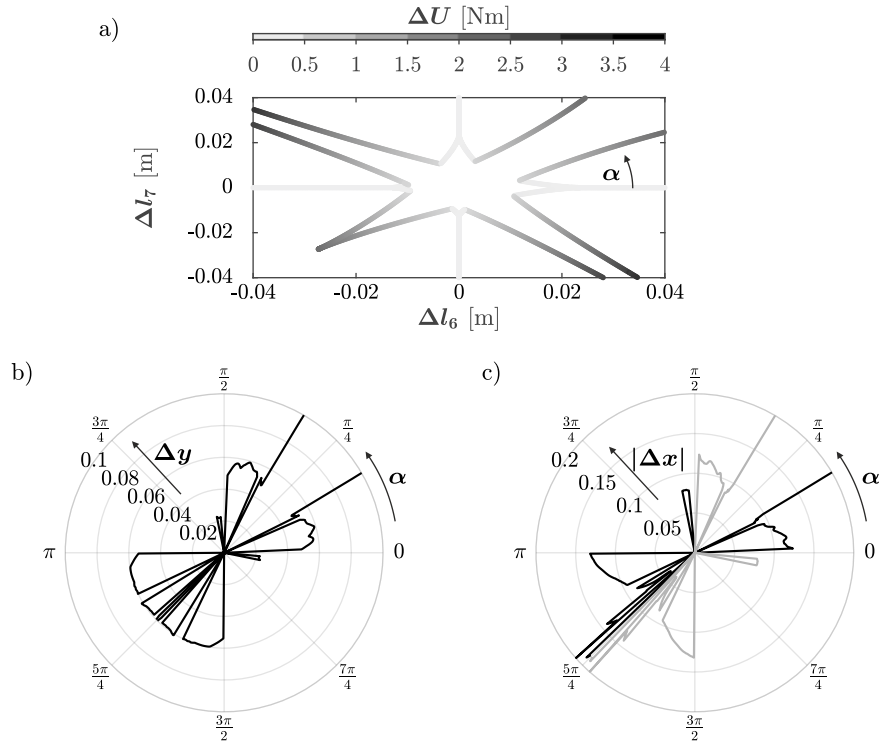
Figure 7. Motion characteristics of the jump, a) actuation parameter range, b) jumping height Δy, c) jumping distance $|\Delta x|$ (black: jump forward, grey: jump backward).

The results of the jumping motion controlled by the change of the equilibrium state are displayed in Fig. 7. These results show that indeed a jumping motion can be realized by a controllable change between the stable states I and V. The motion characteristics corresponding to the change between the states III and VII also represent a reliable jump. However, after the take-off a second impact occurs. Therefore, the resulting motion is not considered. Moreover, the jumping direction can be varied by changing the parameter value of α. Because of the symmetric topology of the system a feasible control of the direction of motion is possible. In general, this actuation strategy represents a simple opportunity to realize a reliable jumping motion.

5. Conclusion

This paper deals with the use of tensegrity structures as jumping motion system. A two-dimensional tensegrity structure featuring 4 stable equilibrium configurations is considered. Based on the potential energy of the tensegrity structure two actuation strategies in order to realize a controllable jump are derived. Beside varying the prestress state of the structure, a controllable change between the stable states is utilized to realize a jump. Numerical simulations are evaluated to validate these approaches. However, the simulation results show that varying the prestress state does not yield an efficient jumping motion. Instead of initializing a jump the released energy is transformed into high-frequent oscillations of the compliant tensegrity structure. Only utilizing the multistability of the structure enables a reliable jumping motion by changing between different stable configurations. Moreover, because of the symmetry of the structure a feasible control of the jumping direction is possible. This issue encourages the application of multistable tensegrity structures as jumping motion system.

Acknowledgments

References

[1] BAUMGARTE, J. Stabilization of constraints and integrals of motion in dynamical systems. *Computer Methods in Applied Mechanics and Engineering 1*, 1 (1972), 1–16.

[2] BURGERMEISTER, B., ARNOLD, M., AND ESTERL, B. Dae time integration for real-time applications in multi-body dynamics. *ZAMM - Journal of Applied Mathematics and Mechanics 86*, 10 (2006), 759–771.

[3] HOSODA, K., SAKAGUCHI, Y., TAKAYAMA, H., ET AL. Pneumatic-driven jumping robot with anthropomorphic muscular skeleton structure. *Autonomous Robots 28*, 3 (2010), 307–316.

[4] Jung, G., Casarez, C., Jung, S., et al. An integrated jumping-crawling robot using height-adjustable jumping module. *IEEE International Conference on Robotics and Automation (ICRA)* (2016), 4680–4685.

[5] Kaufhold, T., Schale, F., Böhm, V., et al. Indoor locomotion experiments of a spherical mobile robot based on a tensegrity structure with curved compressed members. *IEEE AIM* (2017), 523–528.

[6] Kovač, M., Schlegel, M., Sufferey, J., et al. Steerable miniature jumping robot. *Autonomous Robots 28*, 3 (2010), 295–306.

[7] Ni, F., Rojas, D., Tang, K., et al. A jumping robot using soft pneumatic actuator. *IEEE International Conference on Robotics and Automation (ICRA)* (2015), 3154–3159.

[8] Sabelhaus, A., Bruce, J., Caluwaerts, K., et al. System design and locomotion of superball,an untethered tensegrity robot. *IEEE ICRA* (2015), 2867–2873.

[9] Schorr, P., Böhm, V., Stépán, G., et al. Multi-mode motion system based on a multistable tensegrity structure. *Advances in Mechanism and Machine Science* (2019), 3007–3016.

[10] Schorr, P., Böhm, V., Zentner, L., et al. Motion characteristics of a vibration driven mobile tensegrity structure with multiple stable equilibrium states. *Journal of Sound and Vibration 437* (2018), 198–208.

[11] Synnestvedt, R. G. An effective method for modeling stiction in multibody dynamic systems. *Journal of Dynamic Systems Measurement and Control-transactions of The Asme 118* (1996).

[12] Tietz, B. R., Carnahan, R. W., Bachmann, R. J., et al. Tetraspine: Robust terrain handling on a tensegrity robot using central pattern generators. *IEEE ASME* (2013), 261–267.

[13] Zhao, J., Yan, W., Xi, N., et al. A miniature 25 grams running and jumping robot. *IEEE International Conference on Robotics and Automation (ICRA)* (2014), 5115–5120.

Philipp Schorr, M.Sc. (Ph.D. student): Technische Universität Ilmenau, Technical Mechanics Group, Max-Planck-Ring 12, D-98693 Ilmenau, Germany (*philipp.schorr@tu-ilmenau.de*). The author gave a presentation of this paper during one of the conference sessions.

Valter Böhm, Professor: Ostbayerische Technische Hochschule Regensburg, Mechanics Group, Galgenbergstr. 30, D-93053 Regensburg, Germany (*valter.boehm@oth-regensburg.de*).

Lena Zentner, Professor: Technische Universität Ilmenau, Technical Mechanics Group, Max-Planck-Ring 12, D-98693 Ilmenau, Germany (*lena.zentner@tu-ilmenau.de*).

Klaus Zimmermann, Professor: Technische Universität Ilmenau, Technical Mechanics Group, Max-Planck-Ring 12, D-98693 Ilmenau, Germany (*klaus.zimmermann@tu-ilmenau.de*).

Piezoaeroelastic system based on a double aerodynamic pendulum

Yury D. Selyutskiy, Andrei P. Holub, Ching-Huei Lin

Abstract: During last decades, possibilities of using piezoelectric generators to harvest energy from the flow using various mechanical devices that perform flow-induced oscillations are intensively studied (for instance, those that can be classified as aeroelastic systems). In this work, an electromechanical system is considered that consists of a double aerodynamic pendulum connected with a piezoelectric element. The element is connected to a load resistance. When the pendulum oscillates, the piezoelectric element is deformed, and electric voltage is generated. Aerodynamic forces acting upon the pendulum are described using the quasi-steady approach. Periodic solutions of the resulting dynamic system are studied depending on values of different parameters (such as wind speed, load resistance, etc.). It is shown, in particular, that it is possible to choose parameters of the system in such a way that the trivial equilibrium (where both links of the pendulum are oriented along the wind) is unstable when the wind speed belongs to a certain finite range of values, and asymptotically stable outside this range.

1. Introduction

Wind power generation became an important part of power industry in many countries. Wind generators are widely used both in industry and in households. There exist different types of such facilities (horizontal axis wind turbines, Darrieus wind turbines, Savonius rotor, etc.) These devices convert the flow energy into the energy of rotation of a working element (turbine, rotor) connected to electric generator.

However, in recent years, there appeared an interest to investigation of another type of devices intended to convert energy of air (or water) flow: devices where the working element performs not rotational, but oscillatory motion. Such developments and research are conducted by many groups of researchers in different countries. In systems of this type, various effects are used — wing flutter [3, 5], vortex-induced oscillations of bluff structures [2], or galloping [8]. A comprehensive review of various systems generating electric energy using oscillations induced by flow is provided in [1].

Dynamics of an elastically mounted double aerodynamic pendulum was studied in [6]. It was shown that such system can perform self-oscillations under the action of the flow and, thus, can be used to extract power from the flow.

In this paper, a scheme is proposed for the use of self-oscillations of a double aerodynamic pendulum for generating electic power using piezoelectric elements.

2. Description of the system and equations of motion

Consider a mechanical system consisting of a double aerodynamic pendulum $O_1O_2O_3$, the first link of which is connected with two identical piezoelectric elements P_1 and P_2 (see Fig. 1). We assume that the axes of rotation of the links of the pendulum are vertical. Let the pendulum be placed in a flow of a medium whose velocity at infinity is constant and equal to V. Introduce a fixed coordinate system with the origin on the axis of rotation of the first link, and the abscissa axis is directed along the flow velocity.
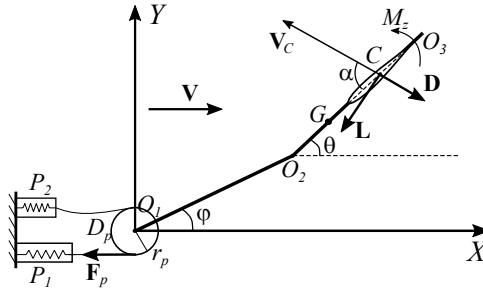
Figure 1. Sketch of the double aerodynamic pendulum connected with piezoelements.

Let φ, θ be the angles between the first and second links of the pendulum and the x-axis.

We assume that the first link of the pendulum is connected with the piezoelements with inextensible cords. These cords are fixed to the disk D_p installed on the axis of rotation of the first link and rigidly connected to this link. Thus, when the first link is rotated by the angle φ (say, counterclockwise), one of the piezoelectric elements is deformed by the value $\Delta = r_p\varphi$ (where r_p is the radius of the disk D_p). The second piezoelement remains undeformed due to the slacking of the corresponding cord. It gets deformed when the first link rotates in clockwise direction.

To describe the aerodynamic effect on the pendulum, we will use a quasistatic model, assuming that this effect is reduced to the force of the drag $\mathbf{D}$ and the lift force $\mathbf{L}$ applied in the middle of the C chord wing, as well as the moment M_z about this point.

$$\mathbf{D} = \frac{1}{2}\rho\sigma V_C C_d(\alpha)\mathbf{V}_C, \quad \mathbf{L} = \frac{1}{2}\rho\sigma V_C C_l(\alpha)\mathbf{e}_z \times \mathbf{V}_C, \quad M_z = \frac{1}{2}\rho\sigma b V_C^2 C_m(\alpha) \tag{1}$$

Here ρ is the air density; σ is the wing area; b is the length of the wing chord; C_d, C_l, C_m are dimensionless coefficients of the drag, lift force, and aerodynamic moment with respect to the point C, respectively; $\mathbf{e}_z$ is the unit vector normal to the plane of motion, $\mathbf{V}_C$ is the airspeed of the point C (i.e. the speed of this point with respect to the incoming flow); α is the instantaneous angle of attack, i.e. the angle between the vector $\mathbf{V}_C$ and the wing chord.

The angle of attack and airspeed are determined by the following kinematic relations:

$$V_C \cos \alpha = V \cos \theta + l_1 \dot{\varphi} \sin (\varphi - \theta)$$
$$V_C \sin \alpha = V \sin \theta + l_1 \dot{\varphi} \cos (\varphi - \theta) + r \dot{\theta} \tag{2}$$

Here l_1 is the length of the first link, and r is the distance between the inter-link joint O_2 and point C.

To simulate piezoelectric elements, we will use the phenomenological approach proposed in [4]. It describes the change of the voltage U generated by the piezoelement depending on the strain rate using an ODE:

$$C_p \dot{U} + \frac{U}{R} + \chi \dot{\Delta} = 0. \tag{3}$$

Here C_p is the capacitance of this element, χ is the coefficient of electromechanical interaction, R is the external resistance in the electric circuit, k_p, h_p are the coefficients of the effective stiffness and damping of each piezoelement. Paper [4] provides the following characteristic values of these parameters:

$$C_p = 120 \text{ nF}, \chi = 1.55 \text{ mNV}^{-1}, k_p = 1000 \text{ kgc}^{-2}, h_p = 27.43 \text{ kgs}^{-1}, R = 10^5 \text{Ohm}.$$

We will use these values in subsequent numerical simulations.

Given the above, equations of motion of the system have the following form:

$$\left(J_1 + ml_1^2\right) \ddot{\varphi} + ml_1 l_2 \cos (\theta - \varphi) \ddot{\theta} - ml_1 l_2 \sin (\theta - \varphi) \dot{\theta}^2$$
$$= -\frac{\rho \sigma V_C l_1}{2} C_d(\alpha) \left(V \sin \varphi + l_1 \dot{\varphi} + r \cos (\theta - \varphi) \dot{\theta}\right)$$
$$+\frac{\rho \sigma V_C l_1}{2} C_l(\alpha) \left(-V \cos \varphi + r \sin (\theta - \varphi) \dot{\theta}\right) - r_p^2 \left(k_p \varphi + h_p \dot{\varphi}\right) + r_p \chi U$$
$$\left(J_2 + ml_2^2\right) \ddot{\theta} + ml_1 l_2 \cos (\theta - \varphi) \ddot{\varphi} + ml_1 l_2 \sin (\theta - \varphi) \dot{\varphi}^2 \tag{4}$$
$$= -\frac{\rho \sigma V_C r}{2} C_d(\alpha) \left(V \sin \theta + r \dot{\theta} + l_1 \cos (\theta - \varphi) \dot{\varphi}\right)$$
$$+\frac{\rho \sigma V_C r}{2} C_l(\alpha) \left(-V \cos \theta + l_1 \sin (\theta - \varphi) \dot{\varphi}\right) + \frac{\rho \sigma V_C^2 b}{2} C_m(\alpha)$$
$$C_p \dot{U} + \frac{U}{R} + \chi r_p \dot{\varphi} = 0$$

Here J_1 is the moment of inertia of the first link relative to the axis of rotation, J_2 is the central moment of inertia of the second link, m is the mass of the second link, l_2 is the distance from the point O_2 to the center of mass G of the second link.

In order to simplify the notation and reduce the number of parameters, we introduce the dimensionless time $\tau = tV_0/b$ (here V_0 is a certain characteristic flow speed), as well as the following dimensionless variables and parameters:

$$\bar{U} = \frac{UC_p}{b\chi}, \quad \bar{J}_{1,2} = \frac{2J_{1,2}}{\rho \sigma b^3}, \quad \bar{m} = \frac{2m}{\rho \sigma b}, \quad \bar{l}_{1,2} = \frac{l_{1,2}}{b}, \quad \bar{r} = \frac{r}{b}, \quad \bar{r}_p = \frac{r_p}{b},$$

$$\bar{V} = \frac{V}{V_0}, \quad \bar{V}_C = \frac{V_C}{V_0}, \quad \bar{k}_p = \frac{2k_p b}{\rho \sigma V_0^2}, \quad \bar{h}_p = \frac{2h_p}{\rho \sigma V_0}, \quad \bar{\xi} = \frac{2\chi^2 b}{\rho \sigma V_0^2 C_p}, \quad \bar{R} = \frac{RC_p V_0}{b}$$

After this procedure, the equations of motion can be written as follows (for convenience, we use dot to designate the derivative with respect to τ, and omit bars over dimensionless values):

$$\left(J_1 + ml_1^2\right)\ddot{\varphi} + ml_1 l_2 \cos\left(\theta - \varphi\right)\ddot{\theta} - ml_1 l_2 \sin\left(\theta - \varphi\right)\dot{\theta}^2$$

$$= -V_C l_1 C_d(\alpha)\left(V\sin\varphi + l_1\dot{\varphi} + r\cos\left(\theta - \varphi\right)\dot{\theta}\right)$$

$$+V_C l_1 C_l(\alpha)\left(-V\cos\varphi + r\sin\left(\theta - \varphi\right)\dot{\theta}\right) - r_p^2\left(k_p\varphi + h_p\dot{\varphi}\right) + r_p\xi U$$

$$\left(J_2 + ml_2^2\right)\ddot{\theta} + ml_1 l_2 \cos\left(\theta - \varphi\right)\ddot{\varphi} + ml_1 l_2 \sin\left(\theta - \varphi\right)\dot{\varphi}^2 \qquad (5)$$

$$= -V_C r C_d(\alpha)\left(V\sin\theta + r\dot{\theta} + l_1\cos\left(\theta - \varphi\right)\dot{\varphi}\right)$$

$$+V_C r C_l(\alpha)\left(-V\cos\theta + l_1\sin\left(\theta - \varphi\right)\dot{\varphi}\right) + V_C^2 C_m(\alpha)$$

$$\dot{U} + \frac{U}{R} + r_p\dot{\varphi} = 0$$

We assume that the wing has a symmetrical profile. Then $C_m(0) = C_l(0) = 0$. One can readily see that in this case the system has a trivial equilibrium $\varphi = \theta = U \equiv 0$, which corresponds to the position where both links are stretched along the flow. It was shown in [6] that this equilibrium position for a two-link aerodynamic pendulum in an elastic suspension (without connection to electric circuit) is unstable, if parameters of the system belong to a certain range.

Here, we need to study the stability of this equilibrium taking into account the electric part of the system.

3. Intability and periodic solutions

First, we analyze the influence of system parameters (wing position, wind speed, moments of inertia of pendulum links) upon stability of the "along the flow" equilibrium. We take $V_0 = 5$ m/s and use the following values of our dimensionless parameters:

$$l_1 = 1, l_2 = 2, r_p = 0.1, m = 100, R = 1, \xi = 3, k_p = 150, h_p = 200.$$

We use aerodynamic coefficients for the standard NACA0012 airfoil [7] (but the drag coefficient in the range of small angles of attack is increased in order to take into account resistance of other elements of the system).

In Fig. 2, domains of instability are shown (with grey color) in the (V, r_a) plane for different values of J_1 and J_2.
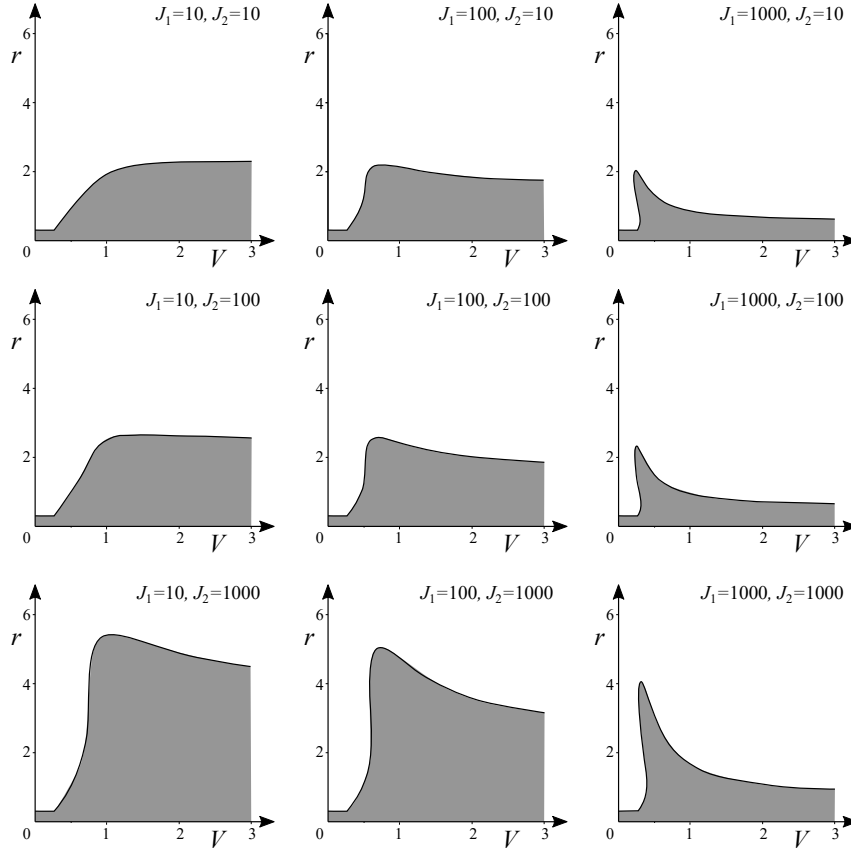
Figure 2. Areas of instability depending on moments of inertia of pendulum links.

From these figures, the following general conclusions can be drawn. Instability arises for small enough values of r, that is, when the wing is located close enough to the inter-link joint. For small r, the equilibrium is unstable for any values of other parameters. The instability area decreases when J_1 increases, and, contrarily, increase in the moment of inertia of the second link results in increase of the instability area.

It is interesting to emphasize the following phenomenon. For certain values of parameters, increase in the wind speed first leads to stability loss; but if the wind speed keeps growing, the asymptotic stability is recovered (at least, in the considered range of V). This effect is more pronounced when the moment of inertia of the first link is large enough.

Consider the behavior of our system in this case in somewhat more detail. Choose $J_1 = 100$, $r = 2$, and let J_2 take the same values as in calculations represented in Fig. 2: 10, 100, 1000.

Then the trivial equilibrium is asymptotically stable for small enough wind speeds. When V reaches a certain critical value V_1, the stability is lost, and an attracting limit cycle is born (Andronov-Hopf-type bifurcation). Naturally, V_1 depends upon other parameters of the system.

Evolution of this cycle with the increase of V is illustrated in Fig. 3, where amplitudes φ_* of the first link, amplitude θ_* of the second link, and amplitude U_* of the output voltage are represented (blue lines).
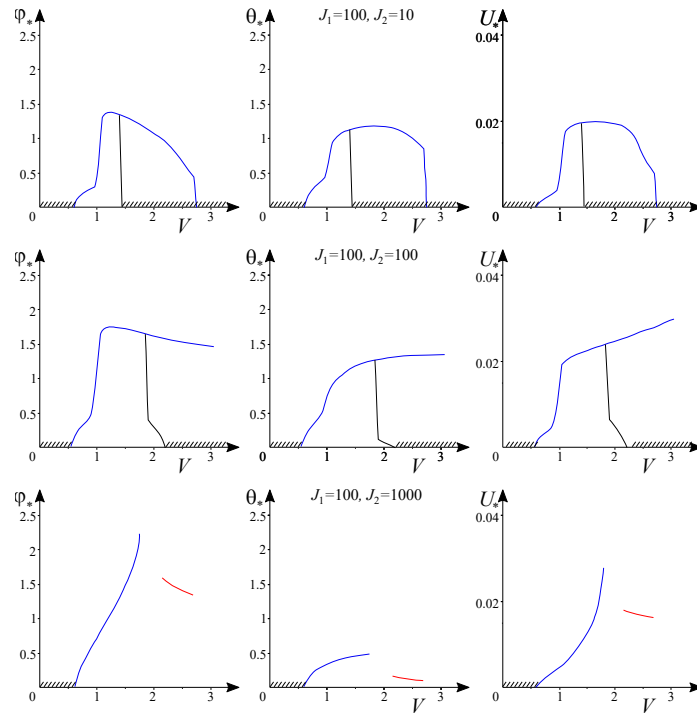
Figure 3. Amplitudes φ_* and θ_* of oscillations of pendulum links and dimensionless output voltage amplitude U_* vs wind speed.

For "moderate" values of J_2 (10 and 100), the asymptotic stability of the considered equilibrium is recovered, when V becomes large enough. Here, again, an Andronov-Hopf-type bifurcation occurs. The corresponding limit cycle (black line) is also attracting, however, it exists only in a rather narrow interval of wind speeds. Ranges of V, where the asymptotic stability takes place, are shown in Fig. 3 with hatching.

It is interesting to note that, in the case of $J_2 = 10$, the limit cycle disappears, when V gets large enough. From the practical point of view, this means that the pendulum

"automatically" stops under sufficiently strong wind.

For $J_2 = 100$, the first limit cycle exists for all $V > V_1$. Evidently, a hysteresis is observed in both discussed cases when the wind speed increases and then decreases.

In the case of "large" J_2, the equilibrium remains unstable in the studied range of wind speeds exceeding V_1. The amplitude of oscillations of the first link grows with V. Then, the limit cycle becomes multi-periodic (such cycles are not represented in Fig. 3). For still larger V, there appears another single-periodic limit cycle (shown with red lines in Fig. 3). However, when the wind speed reaches a certain value, this cycle also disappears, giving birth to a couple of limit cycles located symmetrically with respect to the origin (not shown in Fig. 3).

It seems that the described effect of stability loss and recovery when the wind speed increases could be used for practical purposes. One of important problems of wind generators is necessity to brake them when the wind speed exceeds a certain value. In our case, if parameters are selected in such a way that the trivial equilibrium is asymptotically stable for large V, it is sufficient to decelerate the system, so that it would reach the basin of attraction of the equilibrium, and then it stops itself. After that, no active control is required due to the stability. Moreover, if there are no attracting limit cycles for such wind speeds, it is not necessary even to use special control to brake the system: it stops by itself. When the wind speed gets smaller, the equilibrium becomes unstable, and the system resumes operation (though, due to the mentioned hysteresis effect, it may get to the limit cycle with smaller amplitude).

4. Conclusions

Mathematical model of the electromechanical system consisting of a double aerodynamic pendulum connected with piezoelements is considered. Numerical simulation shows that parameters of this system can be selected in such a way that there exists an attracting limit cycle. Under certain conditions, the "along the flow" equilibrium of the pendulum is asymptotically stable both for small and relatively large wind speeds, while being unstable in a certain range of "moderate" wind speeds.

This makes the system potentially suitable for use as a mini wind power generator.

References

[1] ABDELKEFI, A., GHOMMEM, M., NUHAIT, A., AND M.R., H. Nonlinear analysis and

enhancement of wing-based piezoaeroelastic energy harvesters. *J. Sound and Vibration 333* (2014), 166177.

[2] BARRERO-GIL, A., PINDADO, S., AND AVILA, S. Extracting energy from vortex-induced vibrations: a parametric study. *Appl. Math. Model. 36*, 7 (2012), 3153–3160.

[3] BRYANT, M., AND GARCIA, E. Modeling and testing of a novel aeroelastic flutter energy harvester. *ASME J. Vib. Acoust. 133*, 1 (2011), 011010–1–011010–11.

[4] ERTURK, A., VIEIRA, W., DE MARQUI, C., AND INMAN, D. Nonlinear analysis and enhancement of wing-based piezoaeroelastic energy harvesters. *Appl. Phys. Lett. 96* (2010), 184103.

[5] MCCARTHY, J., WATKINS, S., DEIVASIGAMANI, A., AND JOHN, S. Fluttering energy harvesters in the wind: A review. *J. Sound and Vibration 361* (2016), 355–377.

[6] SELYUTSKIY, Y., HOLUB, A., AND DOSAEV, M. Elastically mounted double aerodynamic pendulum. *Int. J. Struct. Stab. Dyn. 19*, 5 (2019), 1941007.

[7] SHELDAHL, R., AND KLIMAS, P. Aerodynamic characteristics of seven symmetrical airfoil sections through 180-degree angle of attack for use in aerodynamic analysis of vertical axis wind turbines. *Sandia Tech. Rep.*, SAND-80-2114 (1981).

[8] YANG, Y., ZHAO, L., AND TANG, L. Comparative study of tip cross-sections for efficient galloping energy harvesting. *Appl. Phys. Lett. 102* (2013), 064105–1–0641054–4.

Yury D. Selyutskiy, Ph.D.: Lomonosov Moscow State University, Institute of Mechanics, 119192, Michurinsky prosp., 1, Moscow, Russia (*seliutski@imec.msu.ru*). The author gave a presentation of this paper during one of the conference sessions.

Andrei P. Holub, M.Sc. (Ph.D. student): Lomonosov Moscow State University, Institute of Mechanics, 119192, Michurinsky prosp., 1, Moscow, Russia (*holub.imech@gmail.com*).

Ching-Huei Lin, Ph.D.: Chien Hsin University of Science and Technology, Electrical Engineering Department, Chien-Hsin Road 229, Jung-li city, Taoyuan, Taiwan (*chlin@mail.edu*).

Instability and vibration control
by means of piezoceramic element

Krzysztof Sokół

Abstract: The control of vibration frequency and stability of slender systems is a very important issue in engineering. The control phenomenon can be realized with the use of different methods, while prestressing is one of them. In this paper, the studies on an influence of the prestressing caused by a force generated by a piezoceramic element on stability and vibrations of a multi-member column subjected to the specific load are presented. At this load one can find divergence and divergence-pseudoflutter shapes of the characteristic curves. The boundary problem is formulated by use of Hamilton's principle on the basis of which the differential equations of motion as well as natural boundary conditions are obtained. The main goal of this study is to find such a magnitude of the presressing force at which the control of vibration frequency can be done as well as the change of instability regions at different parameters of the loading unit.

1. Introduction

The piezoceramic sensors and actuators are used as elements responsible for active/passive control of systems subjected to static or dynamic excitation. The vibration control [1] is the main direction of research is many scientific departments. Taking into account the variety of shapes of piezoelements and their mechanical limitations they can be easily integrated with the host structures and successfully complete their tasks.

In the studies done in [2, 3] it was presented that one can achieve the shape control of initially deformed structures. In such a structures the piezorods can be installed symmetrically in relation to the main elements, what allows one to obtain the axial deformation or bending. Moreover, piezoelements can also be used when active dynamic instability control is the goal [4, 5].

Faria [6] has studied a case of an increase of the buckling critical forces of single beams with piezoelements. In the considered system (with both fixed ends) the elements have generated tensile axial forces. Sokół and Uzny [7] has discussed an influence of the residual longitudinal forces on the instability of the column subjected to Euler's load.

It has been shown that the conventional method of gluing of piezoelements on the surface or between the layers of the basic structure is not the only one available. In [8] Chaudhry and Rogers have proposed the discrete eccentric connection of the piezoelement to the beam. Finally, on the basis

of the obtained results of numerical and experimental investigations it was stated that higher level of control of transversal displacement can be achieved when the new method of installation is used.

Taking into account that most of engineering structures have shape and assembly imperfection Przybylski and Sokół [9] have proposed an eccentric installation of a piezoceramic in order to control the defection of the system. It was concluded that after the voltage has been applied to the piezoceramic rod the investigated column have regained the rectilinear form of static equilibrium.

The main purposes of this paper is to investigate an influence of the residual force generated by the piezorod on the vibrations and loading capacity of a column subjected to the specific load realized with heads with circular outline. Due to used heads the columns loses stability by divergence having divergence or divergence – psedoflutter shape of the characteristic curve.

2. Boundary problem formulation

In fig. 1 the investigated system subjected to the specific load has been presented. The structure of loading heads is described in [10].
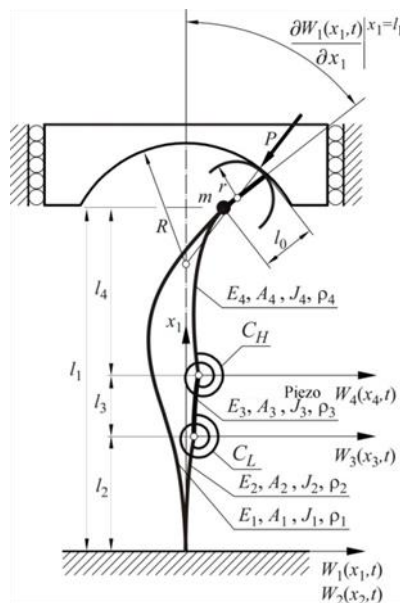
Figure 1. Bent axes of the investigated column

Rod *1* is a continuous element and is a part of external member *I*. Rods *2*, *3* and *4* are included in internal member *II*. Each of rods can be made of piezoceramic material, but having in mind cost and problematic production of long piezo it is proposed to use rod *3* as piezoceramic one. The connection to the host structure will be realized with pins and rotational springs C_L and C_H what

allows one to simulate different connection stiffness without consideration of mechanical design. The continuity of displacements, longitudinal forces, deflection angles and bending moments can be satisfied with the natural boundary conditions. Each od rods have length l_1, l_2, l_3, l_4. The total length of a column is $l = l_1 = l_2 + l_3 + l_4$. The loading heads have mass m and radiuses R (loading head) and r (load receiving head). The radius R has a center in the pole point which is located on the undeformed axis of a column. The distance between the end of the column and the contact point of both heads is l_0. The physical model of a investigated system can be a flat frame or a column composed of two coaxial tubes or rube and rod.

The boundary problem formulation is divided into two section. In first one on the basis of Hamilton's principle (Eq. 1) the differential equations of motion as well as boundary conditions are found. While in the second the calculation of residual internal force is presented. The combination of those two gives final description of the boundary problem.

$$\delta \int_{t_1}^{t_2} \left[T - (V_1 + V_2) \right] dt = 0. \tag{1}$$

The kinetic and potential energies are as follows:

$$T = \frac{1}{2} \sum_{i=1}^{4} \int_0^{l_i} \rho_i A_i \left[\frac{\partial W_i(x_i,t)}{\partial x_i} \right]^2 dx_i + \frac{1}{2} m \left[\frac{\partial W_i(x_i,t)}{\partial t} \Big|^{x_1=l_1} \right]^2, \tag{2}$$

$$V_1 = \frac{1}{2} \sum_{i=1}^{4} \int_0^{l_i} E_i J_i \left[\frac{\partial^2 W_i(x_i,t)}{\partial x_i^2} \right]^2 dx_i + \frac{1}{2} C_L \left(\frac{\partial W_3(x_3,t)}{\partial x_3} \Big|_{x_3=0} - \frac{\partial W_2(x_2,t)}{\partial x_2} \Big|^{x_2=l_2} \right)^2 +$$

$$+ \frac{1}{2} C_H \left(\frac{\partial W_4(x_4,t)}{\partial x_4} \Big|_{x_4=0} - \frac{\partial W_3(x_3,t)}{\partial x_3} \Big|^{x_3=l_3} \right)^2 + \tag{3a}$$

$$+ \frac{1}{2} \sum_{i=1}^{4} \int_0^{l_i} E_i A_i \left[\frac{\partial U_i(x_i,t)}{\partial x_i} + \frac{1}{2} \left(\frac{\partial W_i(x_i,t)}{\partial x_i} \right)^2 \right]^2,$$

$$V_2 = P U_1(l_1,t) - \frac{1}{2} P l_0 \left(\frac{\partial W_1(x_1,t)}{\partial x_1} \Big|^{x_1=l_1} \right)^2 +$$

$$+ \frac{1}{2} P r \left\{ \left[\frac{\partial W_1(x_1,t)}{\partial x_1} \Big|^{x_1=l_1} \right]^2 - \chi^2 \right\} + \frac{1}{2} P \chi W^*. \tag{3b}$$

where

$$\chi = \frac{1}{R-r} \left(W_1(l_1,t) + (l_0 - r) \frac{\partial W_1(x_1,t)}{\partial x_1} \Big|^{x_1=l_1} \right), \tag{4}$$

$$W^* = W_1(l_1,t) + \left.\frac{\partial W_1(x_1,t)}{\partial x_1}\right|^{x_1=l_1}(l_0 - r) + r\chi. \tag{5}$$

E_i – Young's modulus [GPa], J_i – moment of inertia [m^4], A_i – cross-sectional area [m^2], ρ_i – material density [kg/m^3], $C_{H,L}$ – rotational spring stiffness [Nm], P – external load [N], W_i – transversal displacement [m], U_i – longitudinal displacement [m], R – radius of the loading head [m], r – radius of the load receiving head [m], m – mass of heads [kg], l_0 – transom length [m].

After performing variation and integration operations, one obtains inter alia equations of motion:

$$E_i J_i \frac{\partial^4 W_i(x_i,t)}{\partial x_i^4} - E_i A_i \frac{\partial}{\partial x_i}\left[\left[\frac{\partial U_i(x_i,t)}{\partial x_i} + \frac{1}{2}\left(\frac{\partial W_i(x_i,t)}{\partial x_i}\right)^2\right]\frac{\partial W_i(x_i,t)}{\partial x_i}\right] + \quad i = 1 \dots 4$$
$$+ \rho_i A_i \frac{\partial^2 W_i(x_i,t)}{\partial t^2} = 0. \tag{6}$$

and a set of natural boundary conditions supplemented with geometrical ones:

$$W_1(x_1,t)\big|_{x_1=0} = 0, \left.\frac{\partial W_1(x_1,t)}{\partial x_1}\right|_{x_1=0} = 0, W_2(x_2,t)\big|_{x_2=0} = 0, \left.\frac{\partial W_2(x_2,t)}{\partial x_2}\right|_{x_2=0} = 0, \tag{7-10}$$

$$W_2(x_2,t)\big|^{x_2=l_2} = W_3(x_3,t)\big|_{x_3=0}, W_3(x_3,t)\big|^{x_3=l_3} = W_4(x_4,t)\big|_{x_4=0}, \tag{11,12}$$

$$W_1(x_1,t)\big|^{x_1=l_1} = W_4(x_4,t)\big|^{x_4=l_4}, \left.\frac{\partial W_1(x_1,t)}{\partial x_1}\right|^{x_1=l_1} = \left.\frac{\partial W_4(x_4,t)}{\partial x_4}\right|^{x_4=l_4}, \tag{13,14}$$

$$-E_3 J_3 \left.\frac{\partial^2 W_3(x_3,t)}{\partial x_3^2}\right|_{x_3=0} + C_L\left(\left.\frac{\partial W_3(x_3,t)}{\partial x_3}\right|_{x_3=0} - \left.\frac{\partial W_2(x_2,t)}{\partial x_2}\right|^{x_2=l_2}\right) = 0, \tag{15}$$

$$E_2 J_2 \left.\frac{\partial^2 W_2(x_2,t)}{\partial x_2^2}\right|^{x_2=l_2} - C_L\left(\left.\frac{\partial W_3(x_3,t)}{\partial x_3}\right|_{x_3=0} - \left.\frac{\partial W_2(x_2,t)}{\partial x_2}\right|^{x_2=l_2}\right) = 0, \tag{16}$$

$$-E_4 J_4 \left.\frac{\partial^2 W_4(x_4,t)}{\partial x_4^2}\right|_{x_4=0} + C_H\left(\left.\frac{\partial W_4(x_4,t)}{\partial x_4}\right|_{x_4=0} - \left.\frac{\partial W_3(x_3,t)}{\partial x_3}\right|^{x_3=l_3}\right) = 0, \tag{17}$$

$$E_3 J_3 \left.\frac{\partial^2 W_3(x_3,t)}{\partial x_3^2}\right|^{x_3=l_3} - C_H\left(\left.\frac{\partial W_4(x_4,t)}{\partial x_4}\right|_{x_4=0} - \left.\frac{\partial W_3(x_3,t)}{\partial x_3}\right|^{x_3=l_3}\right) = 0, \tag{18}$$

$$E_2 J_2 \frac{\partial^3 W_2(x_2,t)}{\partial x_2^3}\bigg|^{x_2=l_2} + S_2 \frac{\partial W_2(x_2,t)}{\partial x_2}\bigg|^{x_2=l_2} - E_3 J_3 \frac{\partial^3 W_3(x_3,t)}{\partial x_3^3}\bigg|_{x_3=0} - S_3 \frac{\partial W_3(x_3,t)}{\partial x_3}\bigg|_{x_3=0} = 0, \tag{19}$$

$$E_3 J_3 \frac{\partial^3 W_3(x_3,t)}{\partial x_3^3}\bigg|^{x_3=l_3} + S_3 \frac{\partial W_3(x_3,t)}{\partial x_3}\bigg|^{x_3=l_3} - E_4 J_4 \frac{\partial^3 W_4(x_4,t)}{\partial x_4^3}\bigg|_{x_4=0} - S_4 \frac{\partial W_4(x_4,t)}{\partial x_4}\bigg|_{x_4=0} = 0, \tag{20}$$

$$E_1 J_1 \frac{\partial^2 W_1(x_1,t)}{\partial x_1^2}\bigg|^{x_1=l_1} + E_4 J_4 \frac{\partial^2 W_4(x_4,t)}{\partial x_4^2}\bigg|^{x_1=l_4} + \qquad , \tag{21}$$

$$+ P \frac{r-l_0}{R-r}\left(\frac{\partial W_1(x_1,t)}{\partial x_1}\bigg|^{x_1=l_1} (R-l_0) - W_1(x_1,t)\big|^{x_1=l_1} \right) = 0,$$

$$S_1 + S_2 = P, \quad S_2 = S_3 = S_4, \tag{22-24}$$

$$E_1 J_1 \frac{\partial^3 W_1(x_1,t)}{\partial x_1^3}\bigg|^{x_1=l_1} + E_4 J_4 \frac{\partial^3 W_4(x_4,t)}{\partial x_4^3}\bigg|^{x_1=l_4} + \tag{25}$$

$$+ P \frac{1}{R-r}\left(\frac{\partial W_1(x_1,t)}{\partial x_1}\bigg|^{x_1=l_1} (R-l_0) - W_1(x_1,t)\big|^{x_1=l_1} \right) - m \frac{\partial^2 W_1(x_1,t)}{\partial t^2}\bigg|^{x_1=l_1} = 0.$$

The solution of the boundary problem has been performed with the small parameter method [11, 12].

It assumed that rod *3* is made of piezoceramic material. Additionally the considered structure keeps the rectilinear form of static equilibrium. Applying voltage to the piezoelement in direction perpendicular to the axis of the column results in compression or tension what leads to prestressing. The energetic method [13] is used in order to present this phenomenon. The potential energy is equal to:

$$E_p = \frac{1}{2}\sum_{i=1}^{4}\int_{\Omega_i} \sigma_{xi}\varepsilon_{xi}d\Omega_i - \frac{1}{2}\sum_{i=1}^{4}\int_{\Omega_i} D_z E_z d\Omega_p. \tag{26}$$

where:

$$\sigma_{xi} = E_i \varepsilon_{xi}(x_i)\, i=1,2,4 \quad, \quad \varepsilon_{xi} = \frac{dU_i(x_i)}{dx_i}\, i=1,2,4 \quad, \tag{27,28}$$

$$\sigma_{x3} = E_3 \varepsilon_{x3}(x_3) - e_{31}E_z \ , \quad D_z = e_{31}\varepsilon_{x3}(x_3) + \psi E_z. \tag{29, 30}$$

Stress-strain relationships are given with (27-29) while (30) stands for electrical displacement which is induced by electrical field E_z. Moreover: ε_{xi} − axial strain, E_i − Young's modulus, e_{31} − piezoelectric constant, ψ_{33} − piezoelectric conductivity. The electric field is defined as $E_z = V/h$ and the piezoelectric force as $F = -be_{31}V$. After performing some mathematical

operations with assumption of constant voltage applied to the piezo element finally obtains the formula for residual force F. The F force depends not only on applied voltage but also on length of the rods and compression stiffness:

$$F_{\text{Rez}} = F \frac{E_1 A_1 E_2 A_2 E_4 A_4 l_3}{E_3 A_3 Q l_2 + E_2 A_2 \left(Q l_3 + E_3 A_3 \left(E_4 A_4 l_1\right) + E_1 A_1 l_4\right)}, \tag{31}$$

$$Q = E_1 A_1 E_4 A_4. \tag{32}$$

The residual force in accordance with the piezoelectric principle causes prestressing of the column. Thus, in the absence of an external load or its low value in relation to the applied voltage, its individual members can be tensioned or compressed alternately. In a special case, the residual force may balance the components of the forces coming from the external load. At the same time, the absolute value of the residual force in all bars is the same.

The residual for must be introduced into equations of motion in the form:

$$E_i J_i \frac{\partial^4 W_i(x_i,t)}{\partial x_i^4} - \left(S_i(t) \pm F_i\right) \frac{\partial^2 W_i(x_i,t)}{\partial x_i^2} + \rho_i A_i \frac{\partial^2 W_i(x_i,t)}{\partial t^2} = 0, \tag{33}$$

$$\left|F_1\right| = \left|F_2\right| = \left|F_3\right| = \left|F_4\right| = \left|F_{\text{Rez}}\right|. \tag{34}$$

Derived dependencies will be used in the further part of the work to determine the influence of the prestressing force on the vibration and stability control.

3. Numerical simulation results

This section is devoted to the influence of the voltage applied to the piezoelement on the correction of the loading capacity curves as well as characteristic ones as a function of the r_{21} parameter describing bending stiffness relationship. The results are plotted in the non-dimensional form, where:

$$p = \frac{P l^2}{E_1 J_1 + E_2 J_2}, f = \frac{F l^2}{E_1 J_1 + E_2 J_2}, c_L = \frac{C_L l}{E_1 J_1 + E_2 J_2},$$

$$c_H = \frac{C_H l}{E_1 J_1 + E_2 J_2}, r_{21} = \frac{E_2 J_2}{E_1 J_1}, r_{32} = \frac{E_3 J_3}{E_2 J_2}, r_{43} = \frac{E_4 J_4}{E_3 J_3},$$

$$\zeta_A = \frac{R}{l}, \zeta_B = \frac{r}{R}, \zeta_C = \frac{l_0}{R}, \zeta_D = \frac{m}{\left(\rho_1 A_1 + \rho_2 A_2\right) l}, \tag{35a-n}$$

$$\omega = \sqrt{\Omega^2 \frac{\left(\rho_1 A_1 + \rho_2 A_2\right) l^4}{E_1 J_1 + E_2 J_2}}, d_2 = \frac{l_2}{l}, d_3 = \frac{l_3}{l}.$$

The instability regions are devoted to the local and global. The local region can be found then the critical load of the corresponding linear system (without internal rods, marked as *KL*) is greater than bifurcation load of the non-linear one. The global instability region is at the opposite situation.

Depending on the direction of the electric field vector applied to the piezoceramic element, it is possible to obtain reduction/increase of the local and global instability regions (fig 2 – 3). In the presented cases, it was observed that the stiffer connections of the rod 3 to the 2 and 4, the smaller the change of the area of local and global instability in relation to the unprestressed system. In addition, an increase in r_{21} causes a decrease in the loading capacity, at the same voltage level applied.
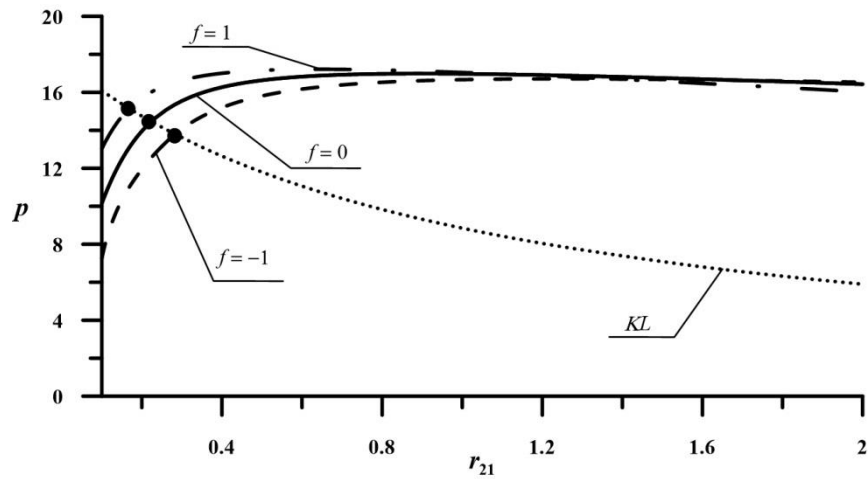
Figure 2. The effect of the change in bending stiffness r_{21} on the value of the bifurcation load of a geometrically non-linear column, at different levels of prestressing, ($\zeta_A = 0.2$, $\zeta_B = 0.2$, $\zeta_C = 0.5$, $r_{32} = r_{43} = 1$, $d_2 = 0.25$, $d_3 = 0.2$, $c_H = 5$, $c_L = 5$)
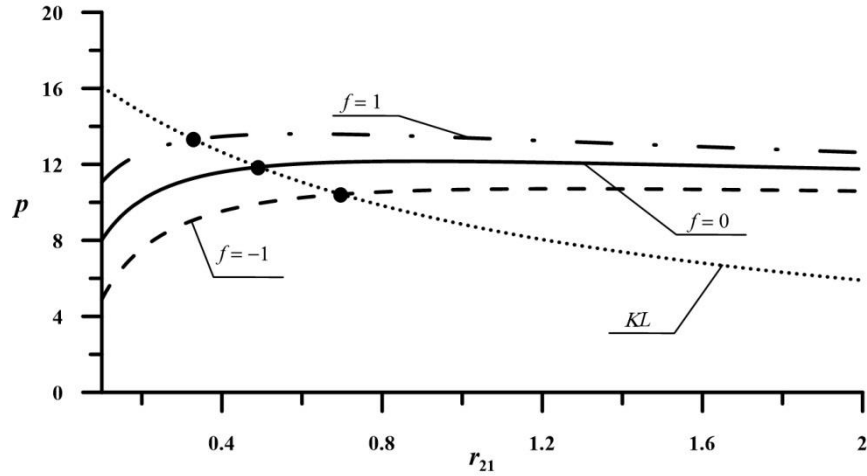
Figure 3. The effect of the change in bending stiffness r_{21} on the value of the bifurcation load of a geometrically non-linear column, at different levels of prestressing, ($\zeta_A = 0.2$, $\zeta_B = 0.2$, $\zeta_C = 0.5$, $r_{32} = r_{43} = 1$, $d_2 = 0.25$, $d_3 = 0.2$, $c_H = 0.5$, $c_L = 5$)

When springs with different stiffness are used (fig. 3) increase in r_{21} results in no curves intersection in the entire considered range for the prestressed and unprestressed systems. It was also observed that the smaller the r_{21}, the greater the influence of the same voltage level on the transfer of the external loads.

The characteristic curves (fig. 4 - 6) are plotted at $r_{21} = 0.4$, 1 and 1.6; the other parameters of the system are as follows $\zeta_A = 0.2$, $\zeta_B = 0.2$, $\zeta_C = 0.5$, $\zeta_D = 0.2$, $r_{21} = 0.4$, $r_{32} = r_{43} = 1$, $d_2 = 0.25$, $d_3 = 0.2$, $c_H = 0.5$, $c_L = 5$. To the piezoceramic rod the voltage has been applied with different direction of the electric field vector, the non-dimensional magnitude of the prestressing force was $f = \pm 2$. It was observed that with a flexible connection of rods of a multi-element member, depending on the direction of the electric field vector, a reduction or increase in the natural frequency can be obtained for each of the considered values of the parameter r_{21}. It was found that the smaller the r_{21}, the greater the effect of the applied voltage on the correction of the characteristic curves.
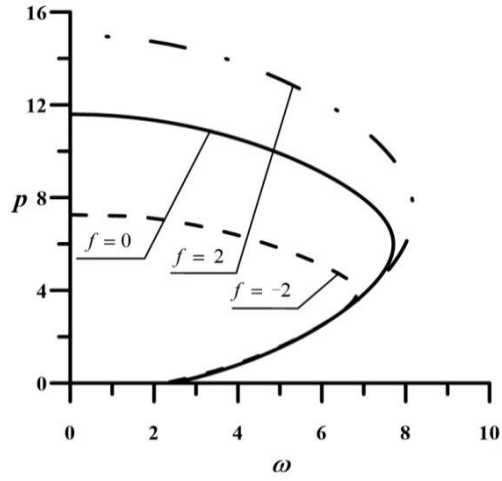
Figure 4. The effect of prestressing on the shape of characteristic curves,
($\zeta_A = 0.2$, $\zeta_B = 0.2$, $\zeta_C = 0.5$, $\zeta_D = 0.2$, $r_{21} = 0.4$, $r_{32} = r_{43} = 1$, $d_2 = 0.25$, $d_3 = 0.2$, $c_H = 0.5$, $c_L = 5$)
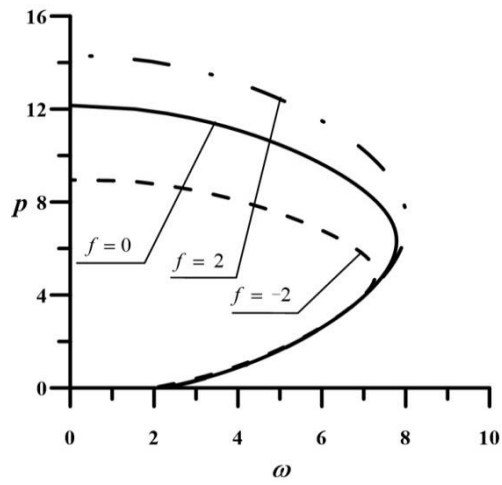
Figure 5. The effect of prestressing on the shape of characteristic curves,
($\zeta_A = 0.2$, $\zeta_B = 0.2$, $\zeta_C = 0.5$, $\zeta_D = 0.2$, $r_{21} = r_{32} = r_{43} = 1$, $d_2 = 0.25$, $d_3 = 0.2$, $c_H = 0.5$, $c_L = 5$)
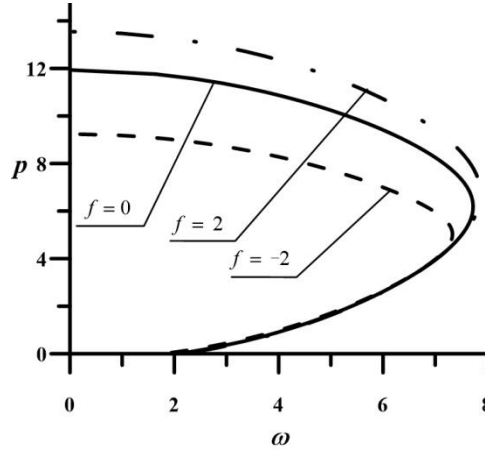
Figure 6. The effect of prestressing on the shape of characteristic curves,
($\zeta_A = 0.2$, $\zeta_B = 0.2$, $\zeta_C = 0.5$, $\zeta_D = 0.2$, $r_{21} = 1.6$, $r_{32} = r_{43} = 1$, $d_2 = 0.25$, $d_3 = 0.2$, $c_H = 0.5$, $c_L = 5$)

The generation of $+f$ forces causes smaller changes in the shape of curves p - ω than forces with identical absolute value but causing tension of rod 1 (-f). In each of the analyzed cases, the initial parts of the characteristic curves of the column run very close to each other, and the effect of the prestressing generated by the piezoelement on their shape is small. With an increase in the external load magnitude, at the same absolute value of the prestressing force a significant changes of the discussed curves can be found.

The generation of compressive/tensile forces with the use of voltage applied to the piezoceramic rod which is a part of a column subjected to a specific load realized by means of heads with circular outline allows one to achieve the control of vibration frequency as well as loading capacity. The control ranges depend not only on the parameters of the heads, but also on the rigidity of the used springs (what is not discussed in this paper) and the coefficients describing the relationships between the rods.

4. Conclusions

In this paper, the investigations into control of loading capacity and vibration frequency of a column subjected to the specific load realized by circular elements of heads were discussed. The phenomenon of control was achieved by means of the piezoceramic rod. The connection of piezorod with the host elements was modeled with pins and rotational springs.

Finally, it can be concluded that:

- the induction of compressive/tensile forces by means of the application of the voltage to the piezoceramic element allows one to obtain the control both of vibration frequency and loading capacity,
- the size of control depends not only on the magnitude of the applied voltage but also on other parameters of the system such as spring stiffness or bending rigidity relationships,
- prestressing of the column with piezorod changes the regions of local and global instability,
- the characteristic curves of the host system and the prestressed one are overlapping each other at low magnitude of the external load.

As presented the piezorods can be used to control the stability of the slender systems. In the future studies on the area of control of vibration frequency as well as loading capacity should be done taking into account other important factors of the system such as parameters of the loading heads or length ratio between elements of the internal member.

Acknowledgments

References

[1] Song, G., Sethi, V., Li H.-N. Vibration control of civil structures using piezoceramic smart materials: A review. *Engineering Structures* 28, 11 (2006), 1513-1524.

[2] Irschik, H. A review on static and dynamic shape control of structures by piezoelectric actuation. *Engineering Structures* 24, 1 (2002), 5-11.

[3] Thompson, S., Loughlan, J. The active buckling control of some composite column strips using piezoceramic actuators. *Composite Structures* 32, (1995), 59-67.

[4] Mukherjee, A., Saha Chaudhuri, A. Active control of dynamic instability of piezolaminated imperfect columns. *Smart Materials and. Structures* 11, (2002), 874–879.

[5] Mukherjee, A., Saha Chaudhuri, A. Exact solutions for instability control of piezolaminated imperfect struts. *AIAA Journal* 42, (2004), 857-859.

[6] Faria, A.R. On buckling enhancement of laminated beams with piezoelectric actuators via stress stiffening. *Composite Structures* 65, 2 (2004), 187-192.

[7] Sokół, K., Uzny S., Linear and nonlinear vibrations control of a two member column by means of piezoceramic element. *AIP Conference Proceedings* 1648, (2015), DOI: 10.1063/1.4913076.

[8] Chaudhry, Z., Rogers, C.A. Enhancing induced strain actuator authority through discrete attachment structural elements. *AIAA Journal* 31, (1993), 1287-1292.

[9] Przybylski, J., Sokół K. Shape control of an eccentrically loaded column by means of a piezoceramic rod. *Thin – Walled Structures* 49, (2011), 652-659.

[10] Tomski, L., Uzny, S. Vibrations and stability of a column subjected to the specific load realized by circular elements of heads. *Mechanics and Mechanical Engineering* 17, (2013), 197 – 206.

[11] Evensen, D.A. Nonlinear vibrations of beams with various boundary conditions, *AIAA* 6, (1968), 370 – 372.

[12] Nayfeh A.H. *Perturbation methods*, Wiley&Sons, New York, 1973.

[13] Crawley, E., De Luis, L. Use of piezoelectric actuators as elements of intelligent structures, *American Institute of Aeronautics and Astronautics Journal* 25, (1987), 1373 – 1385.

Krzysztof Sokół, Ph.D.: Politechnika Częstochowska, ul. J.H. Dąbrowskiego 69 42-201 Częstochowa, Poland, sokol@imipkm.pcz.pl. The author gave a presentation of this paper during one of the conference sessions.

Vibration Busters – an interdisciplinary approach to education of dynamical systems

Ryszard Walentyński, Damian Słota, Marcin Szczygieł

Abstract: A group of 6 pre-graduated students of Civil Engineering, Mathematics and Mechatronics studied problems of dynamics of structures within a project called *Vibration Busters* [5] implemented in a formula of Project Based Learning [1,2]. They worked under supervision of professors from the above mentioned faculties. Students, according to their competencies, implemented a procedure of numerical analysis of the problem within *Mathematica* system, built a physical model of a frame and loaded it with vibrating electrical motors and measured behavior of the structure. The aim of the project was to develop methods of passive and active controlling of vibrations of building structures. A technology of 3D printing was implemented to build a structure. Thanks to the project students had an opportunity to share their skills and knowledge and receive several new hard and soft competencies. It was also a unique experience for supervisors and great opportunity to extend fields of interdisciplinary cooperation. The aim of the presentation is to share results and achieved experience gained thanks to this extraordinary and successful educational project.

1. Introduction

Project Based Learning [1,2] formula is an innovative way of student education which introduces soft competences connected with project management and team cooperation among not only students and supervisors from different faculties but faculties themselves, too. *Vibration Busters* [5] is a generic name of the project implemented within a program [3] at the Silesian University of Technology. It was a second edition of the project "Individual Study Programs implemented in the form of Project Based Learning" , This edition was directed to the pre-graduated students (first level).

Recruited students are awarded with Individual Study Programs (IPS) where half of European Credit Transfer Points (ECTS) are gained thanks to the IPS. Consequently some subjects of the regular courses were replaced, but required effects of learning had to be fulfilled.

31 proposals of the projects have been submitted in that edition [4]. They were considered by experts and 12 of them were awarded. Our proposal has got the highest score as it was the most interdisciplinary and satisfied also other requirements of PBL formula. The students to the project were recruited according to their achievements in studies and activity in other projects. All selected students studied on 6th semester of the bachelor level (pre-graduated).

1.1. Supervisors and expert

The work of the students was supervised by 3 professors:

1. Ryszard Walentyński – the main supervisor from the Faculty of Civil Engineering
2. Damian Słota – the auxiliary supervisor from the Faculty of Applied Mathematics
3. Marcin Szczygieł – the auxiliary supervisor from the Faculty of Electrical Engineering.

To sort out specific problems an expert prof. Wojciech Burlikowski was employed to give several lectures and tutorials for students.

1.2. Students

The following students were recruited to the *Vibration Busters* project:

1. Grzegorz Fulczyk – from the Faculty of Civil Engineering
2. Monika Drzewiecka – from the Faculty of Applied Mathematics
3. Roman Kluger – from the Faculty of Applied Mathematics
4. Agata Wilk – from the Faculty of Applied Mathematics
5. Szymon Jarzombek – from the Faculty of Electrical Engineering (Mechatronics)
6. Mateusz Skorupiński – from the Faculty of Electrical Engineering (Mechatronics).

The one of the problem that had to be solved is to implement the project in the way which will fulfill learning effects required by curricula of each faculty.

2. Targets

2.1. Hard targets

The main hard targets of the project were:

1. Implement a procedure of dynamical analysis of discretized bar structures in *Mathematica* system.
2. Compare the results of the above procedure with the ones obtained from student versions of professional programs for structural designing based on Finite Element Method.
3. Design and construction of a model of 3D frame with application of 3D printing and design tools for that technology.
4. Building an electronic system of vibration generation, control and measurement.
5. Analysis of vibrations and comparison measurements with theoretical models.
6. Attempts of implementing of the passive and active methods of vibration dumping. This was the final aim of the project and therefore we called the project *Vibration Busters.*

2.2. Soft targets

The main soft targets were:

1. Work in an interdisciplinary project team and implementation of general rules of project management
2. Training in designing elements in 3D virtual space and implementation of it in 3D printers
3. Training and perfecting skills in application Mathematica system, Finite Element Method system, programs for 3D printing and signal analysis.

3. Implementation

Due to size limitation of the paper we will only show selected extracts of the final report [5]. The implementation can be divided to 3 parts: mathematical, structural and mechatronic.

3.1. Mathematical part

Students of Applied Mathematics Faculty were responsible for implementing procedures within *Mathematica* system. Here are some extracts from their work:

Procedure for finding eigenvectors:

```
wektoryWlasneT = Table[0, {i, 1, n}];
        Do[
            mac2[kk] = macK0 - (\omega0[[kk]])^2 macB;
            mr[kk] = MatrixRank[mac2[kk]];
            ww[kk] = Table[w1[kk][i], {i, 1, n}];
            wektorzerowy = Table[0, {i, 1, n}];
            rr[kk] = Solve[mac2[kk].ww[kk] == wektorzerowy, ww[kk]];
            wekW[kk] = ww[kk] /. rr[kk][[1]];
            wektoryWlasneT[[kk]] = wekW[kk],
            {kk, 1, n}];
```

The above procedure computes eigenvectors for the matrix:

$$\mathbf{M} = \mathbf{K} - \omega^2 \mathbf{B},$$

where $\mathbf{K}$ is a stiffness matrix, $\mathbf{B}$ is an inertia matrix and ω is an angular frequency.

Solution of differential equation of not dumped vibrations:

$$y''(t) + \omega^2 y(t) = \frac{P}{m}$$

```
DSolve[D[y[[i]],{t,2}]    +    \[Omega][[i]]^2    y[[i]]    ==
wspP[[i]]/wspM[[i]], y[t], t]
```

Differential equation of dumped equations:

$$y''(t) + 2c\, y'(t) + \omega^2 y(t) = \frac{P}{m}$$

```
    D[y[[i]],{t,2}]+2 wspM[[i]] c[[i]] D[y[[i]],t]
  \[Omega] [[i]]^2 y[[i]] = wspP[[i]]/wspM[[i]]
```

3.2. Structural part

Within this part 2D and 3D models were analyzed within a Finite Element Method program (Figs. 1 and 2) and results were first used to verify mathematical procedures. It was done by students of Civil Engineering and Mathematics
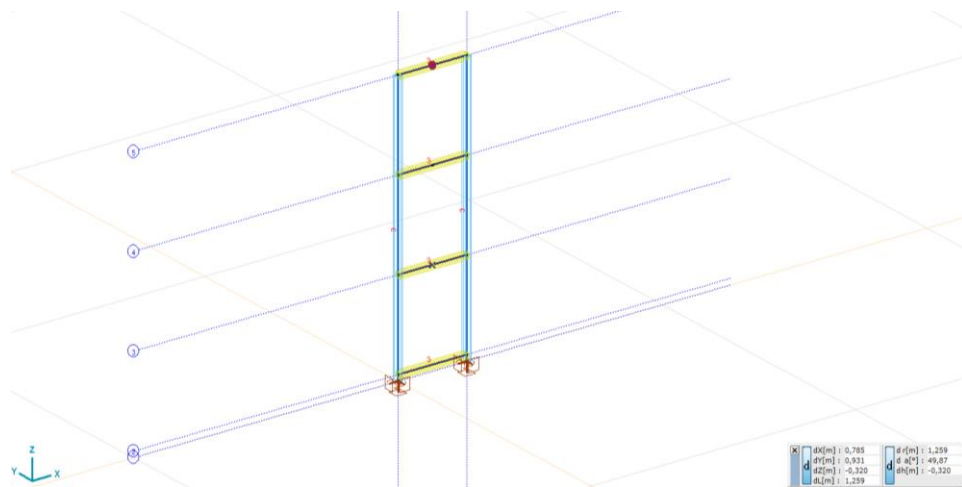
Figure 1. Structural analysis of 2D model.
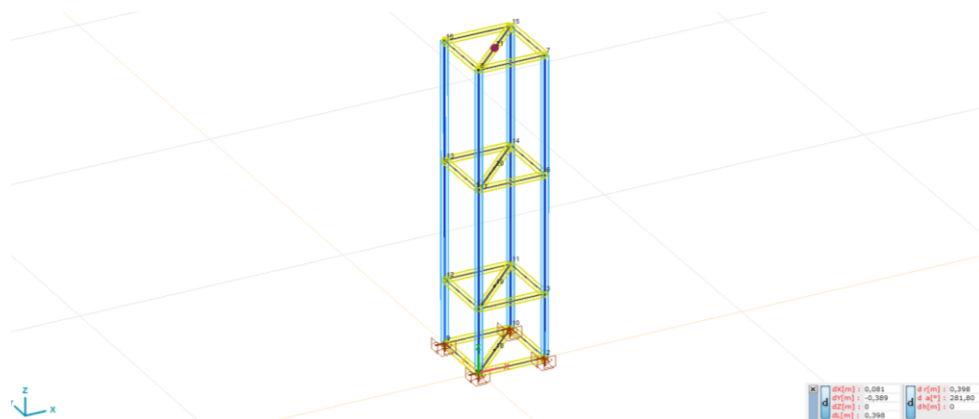
Figure 2. Structural analysis of 3D model.

The computations were used to design a frame and to plan an experimental part.

In the next stage all students learned to design elements for 3D frame. 3D printing is a modern technology of incremental production that allows you to recreate a virtual 3D model in reality. Depending on the type of printer, this technology allows you to create objects, including plastic, metal or concrete. The printer used in the project allows you to create objects from plastic using the FDM (Fused Deposition Modeling) method. This method involves applying molten material layer by layer using a head moving in three axes of the coordinate system (x, y, z). This was the most time consuming part of the project mainly because troubleshooting with 3D printing connected with high accuracy and particular shape of elements of the structure. First elements were designed in Autodesk Inventor, Fig. 3. Next the model was transferred to the 3D printing program, which controlled work of 3D printer, Fig.4. The printed out elements are showed in Fig. 5.
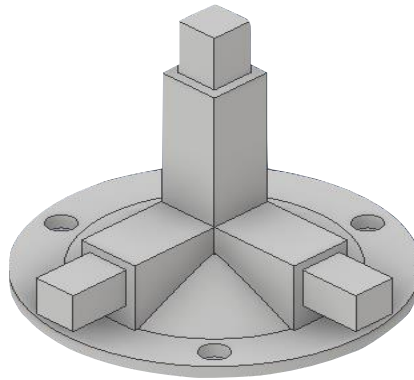
Figure 3. Model of the frame support element in Autodesk Inventor.
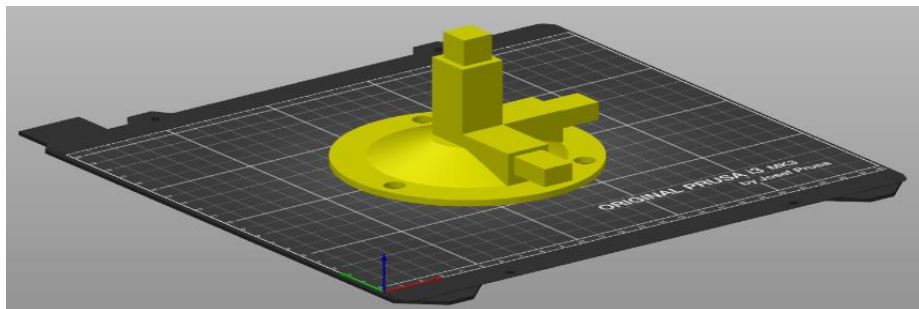
Figure 4. Model in the 3D printing program.
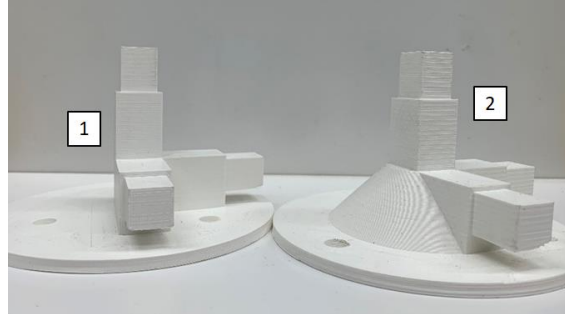
Figure 5. Printed out elements: in higher resolution of printing (1) and in lower resolution of printing.

Autodesk Inventor was used to calculate dynamic characteristic of the structure (modal frequency analysis) as a 3D model, Fig. 6. Results was compared with discrete models developed in the previous stage.
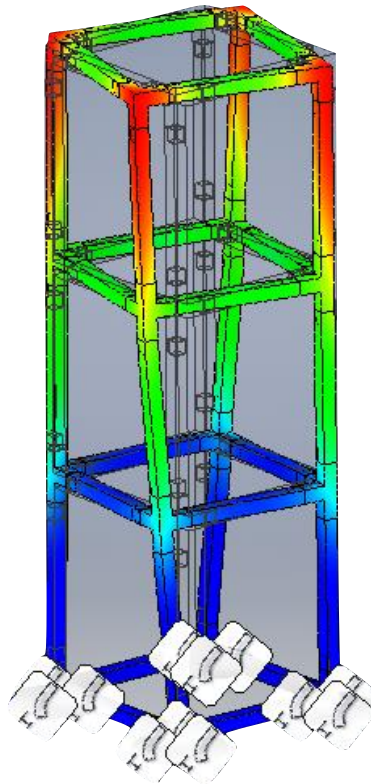
Figure 6. Modal analysis of the frame.

3.3. Mechatronic part

The research stand is presented in Fig. 7. It was mounted in the laboratory of the Department of Mechatronics at the Faculty of Electrical Engineering. The frame is loaded with 4 electrical DC motors generating vibrations with varied frequencies. In the configuration presented here 2 motors were placed on the upper level in vertical position and two a level below in horizontal position. Students did experiments in different configurations.

Figure 7. Research installation.

One of the phenomena observed during the experiment was rumble of vibrations of the structure if frequency of excitation is close to one of the natural frequencies of the structure. The characteristic course of the phenomenon is shown in Fig. 8. The displacement shown here were measured with a precise laser detectors.

Figure 8. Sample analysis of vibrations.

Figure 9 shows results of the analysis of the experiment of the active vibration control using the phenomenon of dumping with motors working with rumbling frequencies. Due to time limitation we have only checked that this phenomenon can be researched with this installation and we plan to continue it in future.
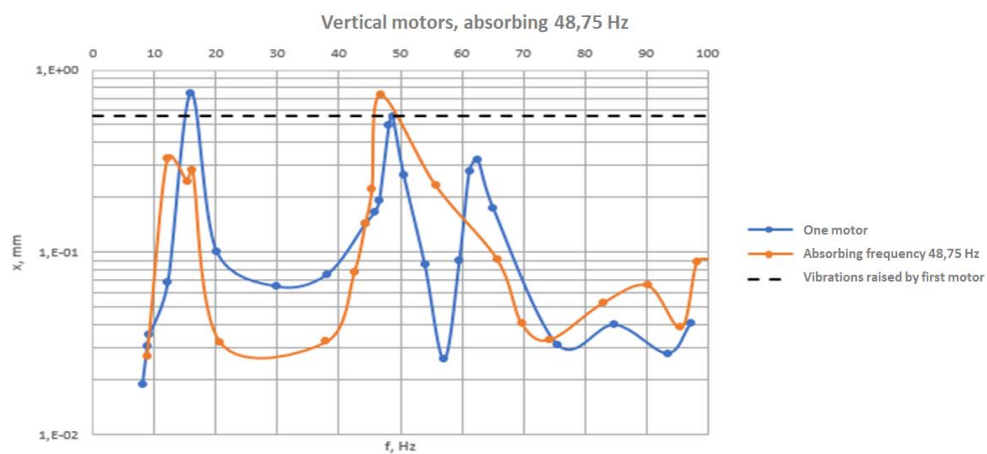
Figure 9. Sample frequency analysis of active vibration dumping.

4.   Shared experience

All of us gained new knowledge, skills and competencies. Mathematicians found, first of all, that their vast knowledge has important practical application. Civil engineers, whose education is based mostly on designing, had opportunity to work in the laboratory of mechatronics. Mechatronics had first of all possibility to extend their field to the bigger scale of space.

5.   Conclusions

Despite problems encountered within implementation of the project we can say that crucial results fulfilled expected targets. The hard results of the project, especially the newly developed installation will be used in further research and education. We plan to continue the project within Master Degree course next year. The most important are unique soft competencies achieved both by students and supervisors. The extraordinary experience will bear fruits for all of us, our University and further employers of our students. They gained ability for working in interdisciplinary teams, knowledge and skills in solving difficult problems of dynamics. It is worth to mention that all of this was done on the early stage of their studies. They were students of the bachelor course. For supervisors it was also a possibility to learn about for future cooperation among faculties within other projects.

Acknowledgments

References

[1]   Project-Based Learning, Edutopia, [2016], https://www.edutopia.org/project-based-learning

[2]   What is Project Based Learning, Defined STEM, https://www.definedstem.com/blog/what-is-project-based-learning/

[3]   Politechnika Śląska jako Centrum Nowoczesnego Kształcenia opartego o badania i innowacje, https://www.polsl.pl/Jednostki/CZP/CZP5/Strony/Politechnika%C5%9Al%C4%85skajakoCentrumNowoczesnegoKszta%C5%82ceniaopartegoobadaniaiinnowacje.aspx.

[4] University News: Student recruitment at Project Based Learning, SUT, [2018] https://www.polsl.pl/Lists/AktualnosciUczelniane/DispForm.aspx?ID=2479

[5]   *Vibration Busters*, Final report of the PBL project, Silesian University of Technology [2019].

Ryszard Walentyński, Associate Professor: Silesian University of Technology/Faculty of Civil Engineering/Chair of Mechanics and Bridges, ul. Akademicka 5, 44-100 Gliwice, Poland (*Ryszard.Walentynski@polsl.pl*).

Damian Słota, Associate Professor: Silesian University of Technology/Faculty of Applied Mathematics/Institite of Mathematics, ul. Kaszubska 23, 44-100 Gliwice, Poland (*Damian.Slota@polsl.pl*).

Marcin Szczygieł, Assistant Professor: Silesian University of Technology/Faculty of Electrical Engineering/Chair of Mechatronics, ul. Akademicka 10A, 44-100 Gliwice, Poland (*Marcin.Szczygiel@polsl.pl*).

Nonlinear forced oscillations of the coupled masses between repelling magnets

Krzysztof Witkowski, Grzegorz Kudra, Sergii Skurativskyi, Grzegorz Wasilewski, Jan Awrejcewicz

Abstract: In these studies, we consider oscillations in the physical model consisting of two carts mounted on a guide. The movement of these carts is restricted by the repelling magnets. The interaction between carts is provided by spring or impact element. The harmonic external loading is applied to one of the carts. To describe this system, the nonlinear mathematical model is developed. The results of model parameter identification are presented. Moreover, the procedure of model validation on the bases of experimental and numerical analysis of system dynamics is discussed as well.

1. Introduction

A large amount of natural and artificial systems incorporates the influences of mechanical, magnetic, and electric fields. When small deviations from the steady state are considered, the description of each field is very similar and can be carried out separately from others. Beyond the linear approach the peculiarities of forces, namely the character of nonlinearity and cooperative effects, are manifested. In particular, a wide range of fascinating phenomena are revealed in the oscillating systems consisting of mechanical elements [1, 2], like a spring, dash-pot or impact, and magnetic parts [3]. Our research is concerned with the studies of cooperative actions of mechanical and magnetic forces, when nonlinear character of both fields is essential. To do this, the magneto-mechanical experimental system performing the forced oscillations is established. Classification of modes observed experimentally, the development of proper mathematical models and their validation keep in our focus as well.

2. Experimental rig

To begin with, let us describe the main steps of experimental studies. Fig. 1 exhibits an experimental stand of two-degree-of-freedom mechanical oscillator with linear mechanical and non-linear magnetic stiffness and external harmonic forcing, modeled and analyzed in the present work.
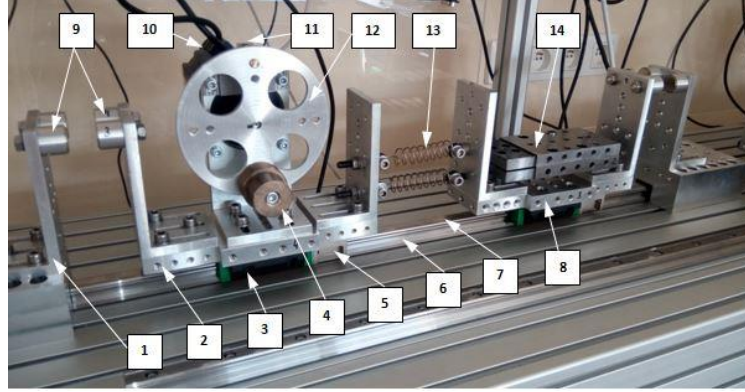
Figure 1. Experimental stand.

The experimental stand consists of two carts (2 and 8) connected with the spring (13) and moving, via linear rolling bearing blocks (3), along a common rail (6). Positions of the carts are measured by the use of Hall sensors (5) and magnetic tape (7) integrated with the bearing blocks and the rail, respectively. The cart (2) is equipped with stepper motor (10) generating harmonic forcing via the disc (12) with an unbalanced mass (4). The transoptor (11) mounted behind the disc (12) allows one to control the absolute angular position of the stepper motor. Both carts on the outer sides have pair of permanent magnets (9) interacting repulsively with the identical ones mounted on the fixed supports (1). Mass of the second cart can be modified by the use of additional mass elements (14).

The peculiarities of experiment procedure can be found in [1]. To be convinced that we correctly understand the observed phenomena, the mathematical model for the experimental stand is developed.

3. Mathematical model
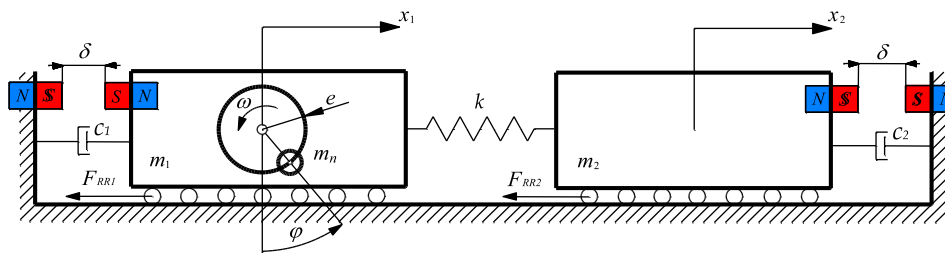
Figure 2. Physical model.

To construct the equations of motion for the experimental rig, let us consider the physical model, presented in Fig.2. The coordinates x_1 and x_2 define the displacements of two masses m_1 and m_2,

connected with the spring of stiffness k. Each mass undergoes the rolling friction force $F_{RRi} = T_i sgn(\dot{x}_i) \approx T_i \frac{\dot{x}_i}{\sqrt{\dot{x}_i^2 + \varepsilon_i^2}}$, viscous damping $c_i \dot{x}_i$ and interacts with the wall via the magnetic repulsive force F_M acting between pair of permanent magnets with the gap δ. A disc is mounted on the body of mass m_1 and rotates with the angular frequency of forcing $\dot{\varphi} = \omega$ providing the harmonic external disturbances. An additional unbalanced body of a mass m_n is placed on radius e of the disc. Utilizing the second Newton law leads us to the following equations of motion

$$m_1 \ddot{x}_1 + k(x_1 - x_2) + F_{R1}(\dot{x}_1) - F_M(x_1 + \delta) + F_M(\delta) = f_0 \dot{\varphi}^2 \sin\varphi,$$
$$m_2 \ddot{x}_2 + k(x_2 - x_1) + F_{R2}(\dot{x}_2) + F_M(\delta - x_2) - F_M(\delta) = 0, \tag{1}$$

where

$$F_{Ri}(y) = c_i y + T_i \frac{y}{\sqrt{y^2 + \varepsilon_i^2}},$$

$$F_M(y) = \frac{F_{M0}}{(d_3 y^3 + d_2 y^2 + d_1 y + 1)^n}.$$

To validate the derived model, at first, we elucidate the degree of magnetic force nonlinearity and establish the analytic expression for it assuming that magnets are the point objects and force magnitude depends only on the distance to the magnet.

4. Parameter's estimation

4.1. Magnetic springs' characteristics

Static characteristics of two (P1 and P2) of four pairs of magnets used in the experimental stand presented in Fig. 1 have been investigated using special equipment. The experimental results along with fit theoretical model in two versions A and B there are presented in Fig. 3, where z is distance between the magnets. The corresponding parameters of the model are given in Tab. 1.

Table 1. Parameters of the magnetic springs' models for pairs of magnets P1 and P2.

Model	Magnets	F_{M0} [N]	n	d_1 [m^{-1}]	d_2 [m^{-2}]	d_3 [m^{-3}]	F_O [mm^2]
A	P1	107.0	3.571	60.37	0	0	0.2401
	P2	101.2	3.771	54.96	0	0	0.1650
	P1, P2	104.4	3.624	58.66	0	0	1.2885
B	P1	109.5	1.727	143.0	186.6	$2.015 \cdot 10^5$	0.0160
	P2	103.1	1.989	115.9	189.1	$1.125 \cdot 10^5$	0.0200
	P1, P2	106.8	1.719	141.1	387.0	$1.919 \cdot 10^5$	1.0916

The objective function F_O is defined as average squared difference between magnetic forces F_M obtained experimentally and from the model.
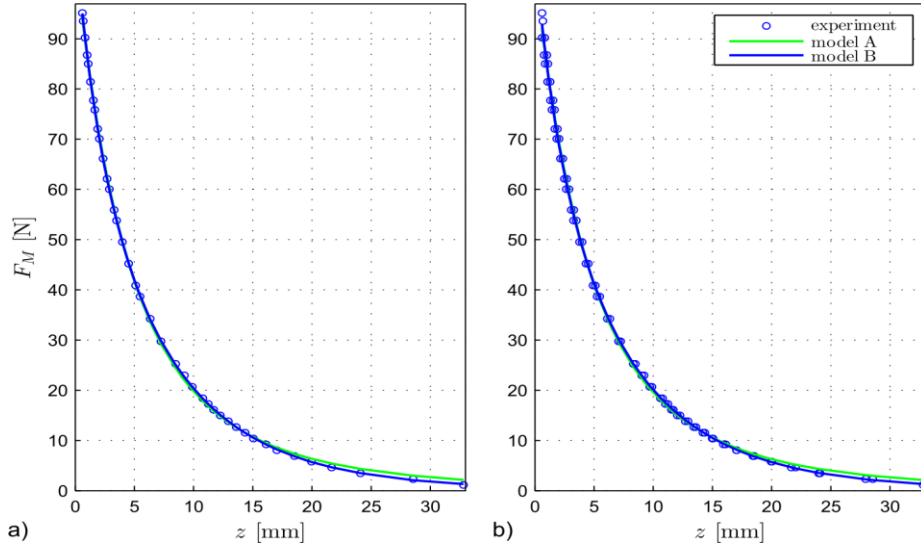
Figure 3. Magnetic springs' characteristics for the pair P1 (a) and the joined data of two pairs of magnets P1 and P2 (b)

4.2. Estimation of the dynamical model parameters

Masses of the carts were measured and assumed to be fixed during identification and all presented numerical simulations: $m_1 = 8.0985$ kg, $m_2 = 6.7838$ kg. Moreover we assume $\varepsilon_1 = \varepsilon_2 = 10^{-6}$ m/s. Additionally the following quantities were measured directly before the experiment used in the identification: $\delta_1 = 0.022984$ m and $\delta_2 = 0.022994$ m, where δ_1 and δ_2 are distances between the magnets on the left and right side of the experimental rig, respectively, when the measurement system is reset. We use ten periodic experimental orbits in the identification process, for the external forcing frequencies: $\omega = 19.37$, 19.57, 19.78, 20.995, 20.205, 20.43, 20.62, 20.84, 21.46, 21.665 rad/s.

The minimized objective function is defined in the following way

$$F_O(\boldsymbol{\mu}) = \frac{1}{2N} \sum_{j=1}^{N} \sum_{i=1}^{2} \frac{w_x \int_{t_{1j}}^{t_{2j}} \left(x_{ije}(t) - x_{ij}(t)\right)^2 dt + w_v \int_{t_{1i}}^{t_{2i}} \left(v_{ije}(t) - v_{ij}(t)\right)^2 dt}{t_{2j} - t_{1j}}, \tag{2}$$

where x_{ij} and v_{ij} are displacement and velocity of ith body in the jth solution obtained numerically from the model, while x_{ije} and v_{ije} are corresponding experimental solutions, $\boldsymbol{\mu} = (f_0, k, c_{1,2},$

$T_{1,2}, \delta, F_{M0}, d_{1,2,3}, n$) is the set of parameters for estimation. The symbols w_x and w_v stand for the corresponding weights, and they were assumed as $w_x = 0.9$ 1/mm and $w_v = 0.1$ s/mm.

The experimental displacements used in the formula (2) are obtained in the following way

$$x_{1je} = x_{1je0} + \delta_1 - \delta,$$

$$x_{2je} = x_{2je0} + \delta - \delta_2, \tag{3}$$

where x_{ije0} is displacement obtained during experiment and burdened with some shift error. Velocities v_{ije} are obtained by numerical differentiation of experimental displacement.

The parameters of magnetic force model were identified again, because of some differences between the four pairs of magnets used in the experimental rig. The estimated values of model parameters obtained after the procedure of minimizing the function $F_O(\boldsymbol{\mu})$ are presented in Table 2.

Table 2. Estimated values of the model parameters.

Model	f_0 [m]	k [N/m]	c_1 [N·s/m]	T_1 [N]	c_2 [N·s/m]	T_2 [N]	δ [m]
A	0.040612	1284.7	4.6298	2.3144	14.408	3.2669	0.022825
B	0.041544	1256.6	2.6617	3.1295	17.164	2.6265	0.022411

Model	F_{M0} [N]	n	d_1 [m^{-1}]	d_2 [m^{-2}]	d_3 [m^{-3}]	F_O
A	178.40	4.1087	46.946	0	0	2.4345
B	132.22	1.5283	93.879	201.63	$3.3943 \cdot 10^5$	1.8255

Using the parameters for model B from Table 2, the solution of system (1) was derived and compared with experimental profile (Fig.4) at different frequencies of external loading ω. We can see the good coincidence of profiles on the intervals of moderate rate of profile growth and permissible its deviation in the vicinity of extrema.

5. Bifurcation dynamics and model validation

Aforementioned results testifying the good agreement between experimental and numerical data at finite time interval and fixed values of parameter ω allow us to continue the model validation and use the Poincaré section technique for the bifurcation diagram construction when the angular frequency $\omega(t)$ increases as shown in Fig.5a. To get the experimental and simulation bifurcation diagrams (Fig.5b-d), the cart positions are sampled at instances fulfilling the condition $\varphi = 2\pi i$, ($i \in Z$). The final part of motion for decreasing forcing frequency was cut off and ignored. It is worth noting that the nonstationarity of $\omega(t)$ does not influence essentially on the bifurcation diagram due to the small rate of ω increasing. Additional comparison of simulation diagrams derived at constant

frequency $\omega(t)$ confirms this conclusion (Fig.5e,f). As shown in Fig.5b, the scenario of period doubling bifurcation is realized at ω increasing. This leads to the chaotic attractor creation.
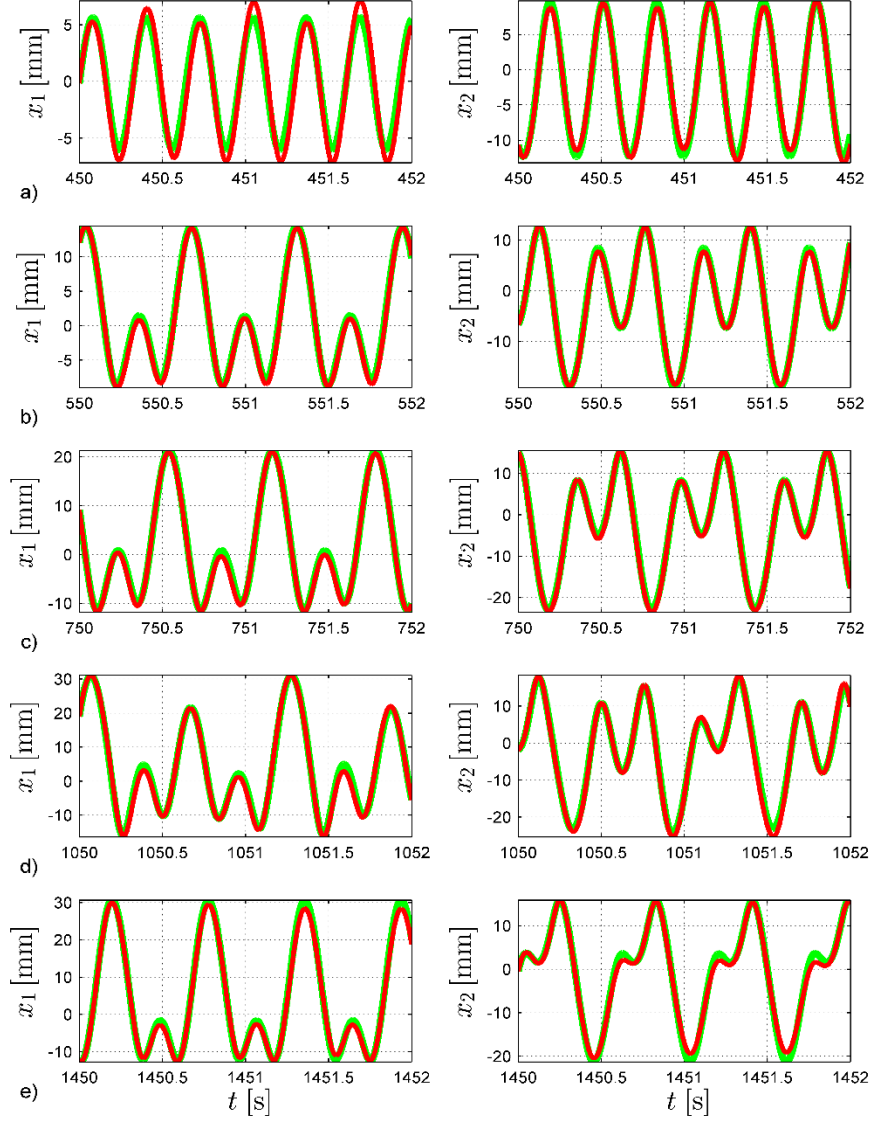
Figure 4. Final agreement between selected periodic experimental solutions (green colour) and the corresponding numerical simulations (red colour) obtained during the model B parameters' estimation, for $\omega = 19.57$ (a), 19.78 (b), 20.205 (c), 20.84 (d), 21.665 rad/s (e).
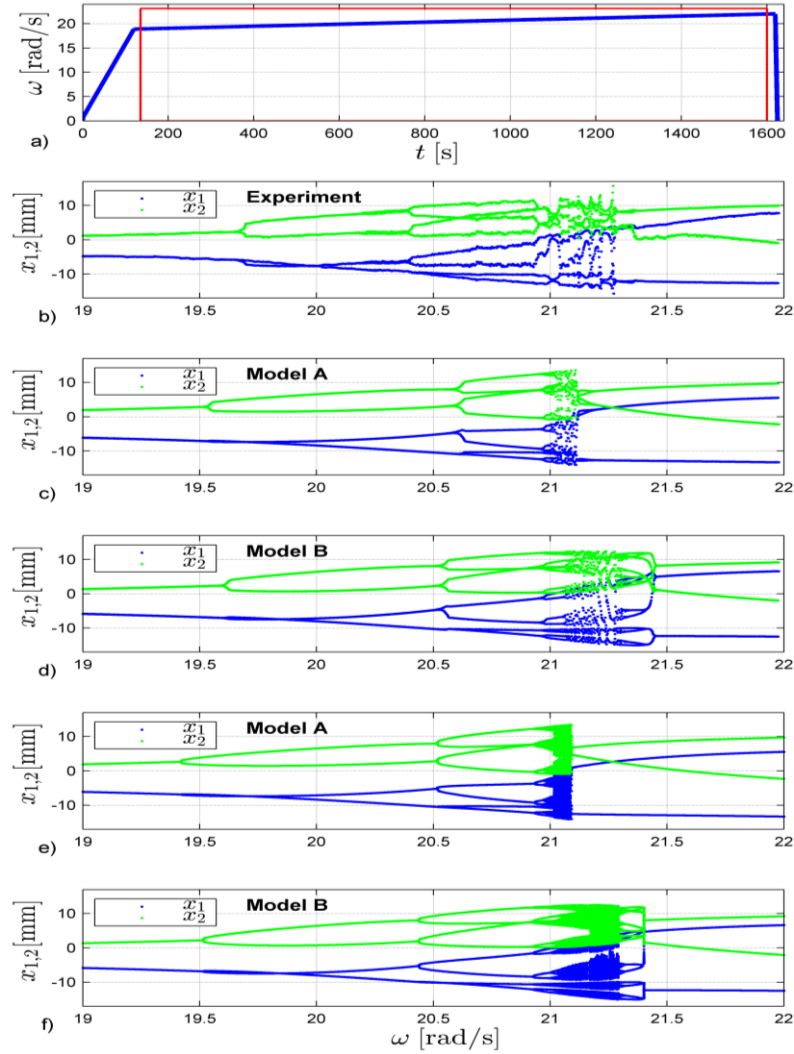
Figure 5. Angular velocity of the forcing $\omega(t)$ applied in the experiment (a) and the corresponding experimental bifurcation diagram (b), bifurcation diagrams of the models A and B obtained for the experimental forcing (c, d) and the corresponding numerical bifurcation diagrams obtained classically (e, f).

There is also the critical value of frequency when an abrupt chaotic attractor collapse is observed. Instead, the stable periodic regime exists. Qualitatively the same behavior demonstrates the model A and B (Fig.5c,d). However, the detailed analysis of bifurcation diagrams shows that the model B matches the experimental data better and, thus, is preferable for the further studies.

6. Conclusions

We thus developed the experimental rig suitable for the studies of mutual influence of mechanical and magnetic forces and validated corresponding mathematical model. We have shown that the magnetic force introduces into the system strong nonlinearity playing the essential role in the formation of complex system's behavior including chaotic. Our results provide the starting point for the detailed analytical and numerical investigations of the developed mathematical model. It should be noted also that the system in question can be easily expanded by incorporating the additional structural elements, for instance impact bond.

References

[1] Witkowski, K., Kudra, G.,Wasilewski, G., Awrejcewicz, J. Modelling and experimental validation of 1-degree-of-freedom impacting oscillator. *J. Syst. Control Eng.* (2018) 1–13.

[2] Skurativskyi, S., Kudra, G., Wasilewski, G., and Awrejcewicz, J. Properties of impact events in the model of forced impacting oscillator: Experimental and numerical investigations International *Journal of Non-Linear Mechanics* 113 (2019) 55–61.

[3] Wojna, G., Wijata, A., Wasilewski, G., and Awrejcewicz, J. Numerical and experimental study of a double physical pendulum with magnetic interaction *Journal of Sound and Vibration* 430 (2018) 214–230.

Krzysztof Witkowski, M.Sc. (Ph.D. student): Lodz University of Technology/Department of Automation, Biomechanics and Mechatronics, Stefanowskiego 1/15, 90-924, Lodz, Poland (*krzys_wit@wp.pl*). The author gave a presentation of this paper during one of the conference sessions.

Grzegorz Kudra, Associate Professor: Lodz University of Technology/Department of Automation, Biomechanics and Mechatronics, Stefanowskiego 1/15, 90-924, Lodz, Poland (*grzegorz.kudra@p.lodz.pl*).

Sergii Skurativskyi, Associate Professor: Subbotin Institute of Geophysics, Palladin av. 32, Kyiv, Ukraine (*skurserg@gmail.com*).

Grzegorz Wasilewski, PhD: Lodz University of Technology/Department of Automation, Biomechanics and Mechatronics, Stefanowskiego 1/15, 90-924, Lodz, Poland (*grzegorz.wasilewski@p.lodz.pl*).

Jan Awrejcewicz, Professor: Lodz University of Technology/Department of Automation, Biomechanics and Mechatronics, Stefanowskiego 1/15, 90-924, Lodz, Poland (*jan.awrejcewicz@p.lodz.pl*).

The pair of oscillators coupled by the electromagnetic field

Mateusz Wojna, Grzegorz Wasilewski, Jan Awrejcewicz

Abstract: The paper concerns numerical and experimental study of a system consisting of two identical oscillators coupled by the electromagnetic field. A system contains two permanent neodymium magnets hung up on the two vertical springs and vibrating in the hollows of two coils. The system with both, linear and non-linear springs has been considered and studied. The coils are connected in series, what makes the oscillators coupled. The coupling is determined by the currents which are induced by moving magnets in the nearby of coils. Based on the Faraday's law, the coupling variables are velocities of the magnets. Such a system can be easily applicable. One of the potential use in the field of energy harvesting is scavenging the energy from ocean waves. The work consists of modelling, numerical simulation and experimental study of the earlier introduced mathematical model. The results of numerical simulations are confronted with experimental data and taken under discussion.

1. Introduction

The progress of modern technologies and challenges faced by researchers indicates the need for interdisciplinary approach. At the present time the old, known and traditional methods of solving engineering problems are not enough. Research problems are increasingly rarely solved employing only one nature of the field, e.g. mechanical field. This interdisciplinarity states the synthesis of fields of various origins, which has become the subject of consideration of an increasing number of dynamical systems researchers. The paper presents a system consisting of the pair of oscillators coupled by the electromagnetic field. A system contains two permanent neodymium magnets hung up on the two vertical springs and vibrating in the hollows of two coils. The coils are connected in series, what makes the oscillators coupled enabling the transfer of energy from one oscillator to another. It should be emphasized that this paper is the authors' first approach to the problem and it should be treated as an introduction to the further considerations. Such a system covers investigations in the subjects as follows: coupled oscillators, the electromagnetic field modelling and identification, energy harvesting and real non-linear stiffness elements.

Modelling of the magnetic field in electromagnetic spherical actuators has been presented in Yan et al. [1]. The authors proposed a novel approach based on an equivalent energized coil and Biot-Savart law to formulate a complex magnetic field distribution in three-dimensional space. The energized coil model has been used to replace the poles of a cylindrical permanent magnet. Generally, this method

can be employed for both electromagnets and permanent magnets modelling. Another non-linear system with magnets has been presented in Eissa et al. [2]. The isolation of horizontal vibrations of the magnetically levitating body has been achieved by using the time delayed non-linear saturation controller. The body is exposed to both external and modulated forces. Wei et al. [3] deal with disturbance rejection in magnetic levitation system. A time-varying active disturbance rejection solution is proposed and validated in both numerical and experimental results. A synthesis of analytical calculations of magnetic parameters (field, force, torque, stiffness) in cylindrical magnets and coils is demonstrated in Ravaud et al. [4]. They show that a thin coil or a cylindrical magnet axially magnetized have the same mathematical model. The paper deals also with the analytical calculation of the force and the stiffness between thin coils or ring permanent magnets. The analytical expressions are based on elliptic integrals. A novel approach for calculating the torque between two filamentary circular coils with inclined axes whose centres are at the same plane is proposed by Babic and Akyel in [5]. The filament method is applied to the combination including a filamentary circular coil and a thin wall solenoid. The same authors in [6,7] derive new semi-analytical expressions for calculating the electromagnetic torque between inclined circular coils in air. The torque calculation has been obtained from the corresponding mutual inductance between inclined circular coils using the filament method. Robertson et al. [8] publish a variety of analytical methods for calculating the axial force between a cylindrical magnet and a solenoid that consists of many turns both radially and axially. Dolisy et al. [9] propose three-dimensional analytical method for modelling a permanent magnets axial field magnetic coupling. The magnetic field calculation allows the determination of global quantities like axial force and torque.

The considered in this paper system can be easily applicable. One of the potential use in the field of energy harvesting is scavenging the energy from ocean waves. Thank to electromagnetic coupling the oscillators can be separated by a huge distance and can operate in severe conditions. Harvesting the energy from similar system is still state-of-the-art solution. However, there are papers where their work and promising future prospects have been published. Repulsive magnetic scavenger is considered by Masoumi and Wang in [10]. The paper studies a magnetic levitation characteristic used in a vibration based energy harvester, which is capable of harvesting ocean wave energy with a unique repulsive permanent magnets stack. The authors demonstrate a procedure to find the restoring force applied to the levitating magnet stack. Additionally, the Duffing vibration equation of the harvester is solved and the frequency response function is calculated for various force amplitudes and electrical damping so as to investigate the effect of these parameters on the response of the system. Another ocean wave energy harvester is shown in [11]. The research introduces a development of a novel and efficient pitching harvester with capacity of frequency conversion and force magnification to convert the low-frequency ocean wave energy to usable electricity based on the piezoelectric effect. The advantages

of the proposed harvester over existing ocean wave energy harvesters are the characteristics of its minimized components and space, which are vital for the survivability and sustainability on harsh ocean conditions. The energy harvesting system, based on magnetic levitation, is presented in Kecik et al. [12]. The system based on the relative movement of the magnet to the electromagnetic coil is considered. The novelty of the model lies on the definition of the coupling coefficient, called inductive coefficient, which links the mechanical and electrical parts of the system together. It has been proven that the parameter has a non-linear structure and depends on the mutual configuration of the pair magnet – coil. A multi-stable electromagnetic-induction energy harvesting system by magnetic levitation oscillation is proposed in Gao et al. [13]. Thanks to its non-linear stiffness characteristic it has a wide range of its frequency response. The system exhibits such phenomena as dynamical bifurcation, escape from potential wells, high energy orbits and chaos. Commonly cited paper (Mann and Sims [14]) investigates the design and analysis of a novel energy harvesting device that uses magnetic levitation to produce an oscillator with a tunable resonance. Mann and Owens in [15] demonstrate an electromagnetic-induction energy harvester that directly powers an electrical load. It consists of one suspended magnet and few stationary outer permanent magnets.

The authors of this work have been dealing with magneto-electro-mechanical systems for some time. The result of this work are articles presented in scientific journals [16-21].

The paper is organized in the following way. Firstly the experimental rig is described. Section 3 is devoted to derivation of the governing equations of motion. Section 4 discusses some of the experimental studies and numerical predictions. Concluding remarks are presented in section 5.

2. Experimental rig

The test stand consists of two identical mass – spring oscillators mounted on a common base and separated from each other a considerable distance. The physical model is shown in Fig. 1. The moving masses m_i are two cylindrical neodymium permanent magnets with dimensions of $\Phi22$mm x 10mm. They interact with two single-layer electromagnetic coils with 20 turns each and move in their axes. The coils are made of enamelled copper wire with a diameter of $\Phi1.15$mm. The radius of particular coil is a_i and its height is L_i. Coils of both oscillators are connected in series with each other. It enables the transfer of energy in the system and makes a system electromagnetically coupled. The magnets are supported by springs with stiffness k_i. The system with both, linear and non-linear springs has been considered and studied. The movement of the magnet causes the appearance of induced currents in the closed electrical circuit of the coils and results in the occurrence of a force acting on the magnet of the second oscillator. The equilibrium position for both oscillators is b_i. As mentioned above, the distance between the oscillators is considerable (about 1.2m) in order to avoid direct interaction between the magnets.
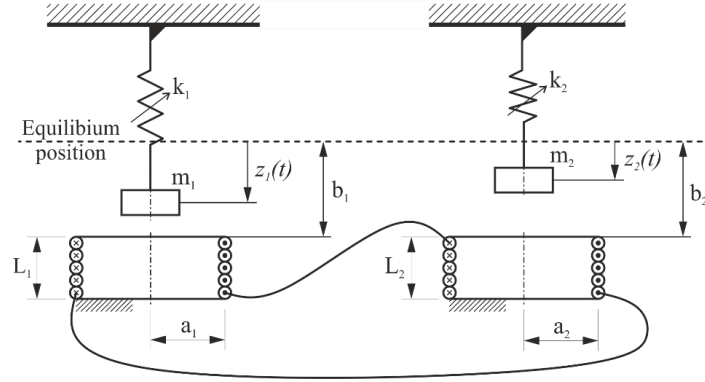
Figure 1. Physical model of a system.

The oscillators are assumed to be identical. Real pictures of the one oscillator is shown in Fig 2. The construction of each of the oscillators consists of a base 1 on which are mounted other components. The walls consist of a rear wall 2 and side walls 3' and 3''. A laser linear displacement sensor 4 is also attached directly to the base. Element 5 is a shelf with a 20-turns single-layer coil. On a shelf 6 is fixed coil setting the positional initial conditions.
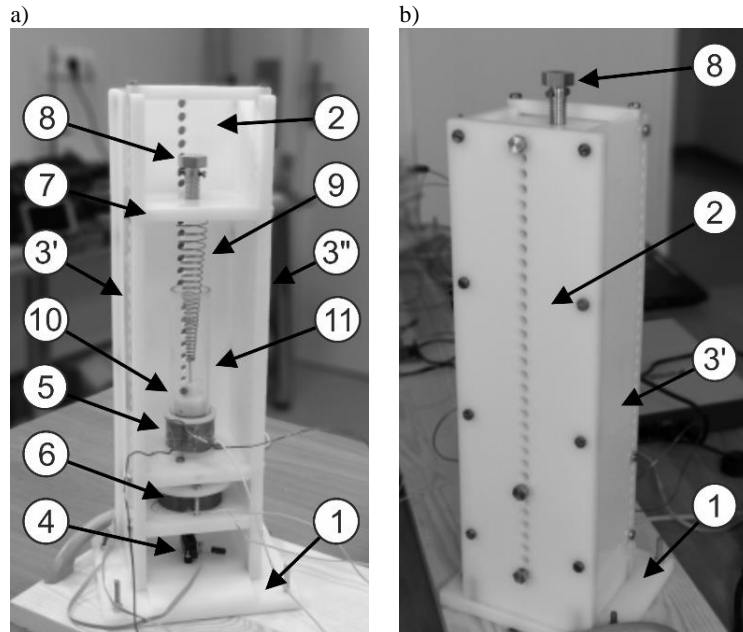
Figure 2. The construction of a single oscillator: a front (a) and a rear view (b)

(components identification is mentioned in the text).

At the beginning of motion recording, the coil forcing initial conditions is energized and pulls magnet 10 inside its hollow. Then the coil circuit is broken and the magnet falls down freely starting its movement. The magnet 10 is the oscillator's bob and is supported vertically by the spring 9. The upper end of the spring is mounted in the axial hole of the bolt 8, which is screwed into the shelf 7. Only linear displacements along the magnet axis are examined in the experiments. In order to prevent magnets from moving in other directions, in some cases it was necessary to use guides in the form of transparent tubes 11 made of plexiglass. The whole mechanical construction of the experimental rig has been made of non-magnetic materials. The main elements are made of POM-C polyacetal, which possesses good strength properties, rigidity and high temperature resistance. All threaded connections have been made with brass bolts.

3. System modelling

The physical model of the coupled oscillator system shown in Fig. 1 contains the parameters: m_i – oscillator mass (the magnet mass and its spring clamp), k_i – spring stiffness, L_i – coil height ($L_i = N_i \cdot d_i$ where N_i – number of turns, d_i – wire diameter), a_i – winding radius of the coil, b_i – distance of the coil face from the equilibrium position of the magnet, $z_i(t)$ – variable determining the elongation of the spring measured from the equilibrium position along the axis of the magnet and coil. One of the assumptions of the system is the uniformity of the oscillators, i.e. the oscillators have been constructed so that their individual components have the same properties and parameters. Then the quantities describing the features of specific elements can be entered without indexing them (e.g., $k_1 = k_2 = k$). Assume that the resistances of particular coils are R_1 and R_2 respectively, then ε_1, ε_2 define the electromotive forces generated in the circuit by moving magnets. The μ is the magnet dipole moment and B_ρ is the radial component of the magnetic field (which can be governed by magnetic dipole approximation [22, 23]).

The elementary length of the coil along the vertical axis dz meets the relationship $dN = (N/L)dz$. The formula governs the electromotive force is as follows

$$\varepsilon_i = \frac{N}{L}(2\pi a^2)\mu v \left[\frac{1}{(a^2+b^2)^{3/2}} - \frac{1}{(a^2+(b+L)^2)^{3/2}}\right]. \tag{1}$$

According to Faraday's law, the elementary force dF acting on the elementary length of the coil dz conducting the current $di = (Ni/L)dz$ stands as follows

$$dF = di(2\pi a)B_\rho = \left(\frac{Ni}{L}\right)(2\pi a)\frac{3\mu a z \, dz}{(a^2+z^2)^{5/2}}, \tag{2}$$

and finally after integration the force F is described in the following way

$$F = \left(\frac{Ni}{L}\right)(2\pi a)\mu a \left[\frac{1}{(a^2+b^2)^{3/2}} - \frac{1}{(a^2+(b+L)^2)^{3/2}}\right]. \tag{3}$$

Since the current induced in an N-turns coil is described as $i = \varepsilon_i/R$, the Eq. 3 can be rewritten as

$$F = \left(\frac{N}{L}2\pi a^2\mu\right)^2 \frac{v}{R}\left[\frac{1}{(a^2+b^2)^{3/2}} - \frac{1}{(a^2+(b+L)^2)^{3/2}}\right]^2. \tag{4}$$

Electromotive forces $\varepsilon_1(t)$, $\varepsilon_2(t)$ generated in the circuit by moving magnets with positional variables $z_1(t)$, $z_2(t)$ respectively can be govern as (e.g. for $\varepsilon_1(t)$)

$$\varepsilon_1(t) = \frac{N}{L}(2\pi a^2)\mu \dot{z}_1\left[\frac{1}{[(a^2+(b_1-z_1)^2)]^{3/2}} - \frac{1}{[(a^2+(b_1-z_1+L)^2)]^{3/2}}\right]. \tag{5}$$

The current flowing in the coil circuit can be described on the basis of Kirchhoff's law in the following way

$$i(t) = \frac{\varepsilon_1(t)-\varepsilon_2(t)}{R_1+R_2}, \tag{6}$$

assuming small displacements $z_i(t)$ and system symmetry we have

$$i = \frac{(2\pi a^2)N}{L}\mu\left[\frac{1}{(a^2+b^2)^{3/2}} - \frac{1}{(a^2+(b+L)^2)^{3/2}}\right]\left(\frac{\dot{z}_1-\dot{z}_2}{R_1+R_2}\right). \tag{7}$$

Then, based on Eq. 4, the magnetic force in considered system can be described as follows

$$F = \left(\frac{N}{L}2\pi a^2\mu\right)^2 \left[\frac{1}{(a^2+b^2)^{3/2}} - \frac{1}{(a^2+(b+L)^2)^{3/2}}\right]^2\left(\frac{\dot{z}_1-\dot{z}_2}{R_1+R_2}\right). \tag{8}$$

It is worth noting that the right side of the above equation, except for the velocities difference $\dot{z}_1 - \dot{z}_2$, contains only constant parameters. Let us write the collapsed form of the expression for the magnetic force by entering the constant C $[1/s]$

$$F = mC(\dot{z}_1 - \dot{z}_2). \tag{9}$$

Thus the equation of motion of one oscillator can be presented as follows

$$m\ddot{z}_1 = -kz_1 - mC(\dot{z}_1 - \dot{z}_2), \tag{10}$$

and using the relationship of the natural frequency $\omega_0 = \sqrt{\frac{k}{m}}$, we can write the system of equations of motion of the system with springs with linear characteristics and linear stiffness k in the following way

$$\begin{cases} \ddot{z}_1 + C\dot{z}_1 + \omega_0^2 z_1 = C\dot{z}_2 \\ \ddot{z}_2 + C\dot{z}_2 + \omega_0^2 z_2 = C\dot{z}_1 \end{cases}. \tag{11}$$

In the case of a system with non-linear spring characteristics, approximation of this characteristic employs two components: a linear stiffness component (β coefficient from the Duffing equation) and a non-linear stiffness component (α coefficient from the Duffing equation).

4.   Numerical simulations and experimental data

The experimental study carried out on the constructed stand can be divided into two groups according to the type of springs used to support the magnets. The time series of the positions of both magnets and the voltage caused by the occurrence of induced current in the electric circuit of the coils have been recorded. In all considered tests both magnets are oriented in the same way, i.e. in both magnets the north pole N is on the magnet clamping side, and the S pole outside – facing the coil.

Fig. 3 presents time series of a system consisting the linear springs in a case when one of the magnet initial position is pre-set.
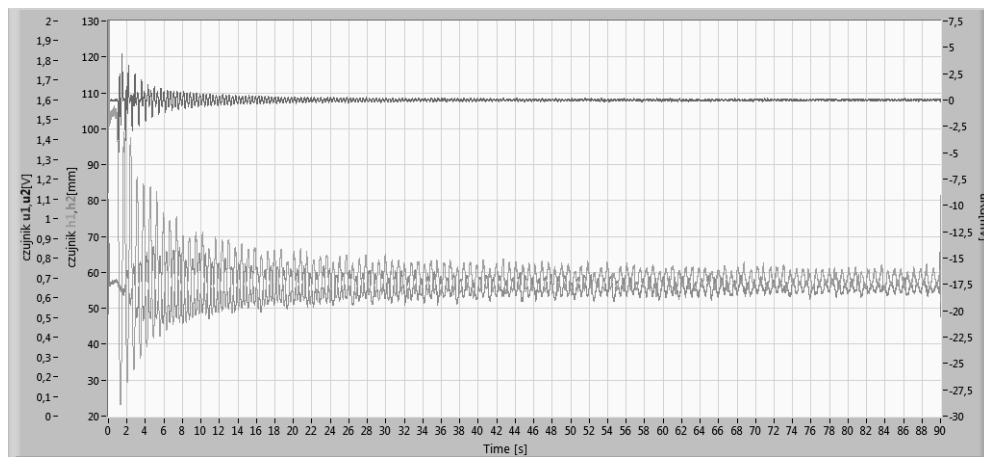
Figure 3. Time series of the magnets positions (h_1, h_2) and corresponding induced voltage signal (u_{Rd}) in a case when magnet indexed 1 is initial positioned – linear spring case

Motion recording has been taken for 90 seconds. After these 90 seconds, the oscillation amplitudes of both oscillators were still a few mm each. Fig. 4 shows fragments of the graph from Fig. 3 describing the first stage of the motion, the middle segment and the last 10 seconds of recording. In the first 10 seconds it can be seen how oscillator 1 begins to vibrate with a large amplitude associated with the predetermined initial conditions. These vibrations are damped. At the same time, oscillator 2 is excited by the flow of energy in the coil circuit. The force origins in electromotive induction is alternately dragging or retarding. The maximum vibration amplitude of the excited oscillator is around 10 mm. Oscillators vibrate in counter-phase from the very beginning. It takes about 5 minutes for the magnets to stop completely in the current configuration of the test stand components. At the beginning of the motion, the series of induced voltage has the most interesting character and reaches the highest values. According to Eq. 7, the value of induced current depends directly on the relative velocity of the magnets. Firstly, it is not a sine wave but a curve with many inflection points. In the next seconds of motion, the vibrations gradually fade out and the series of induced voltage changes almost periodically.
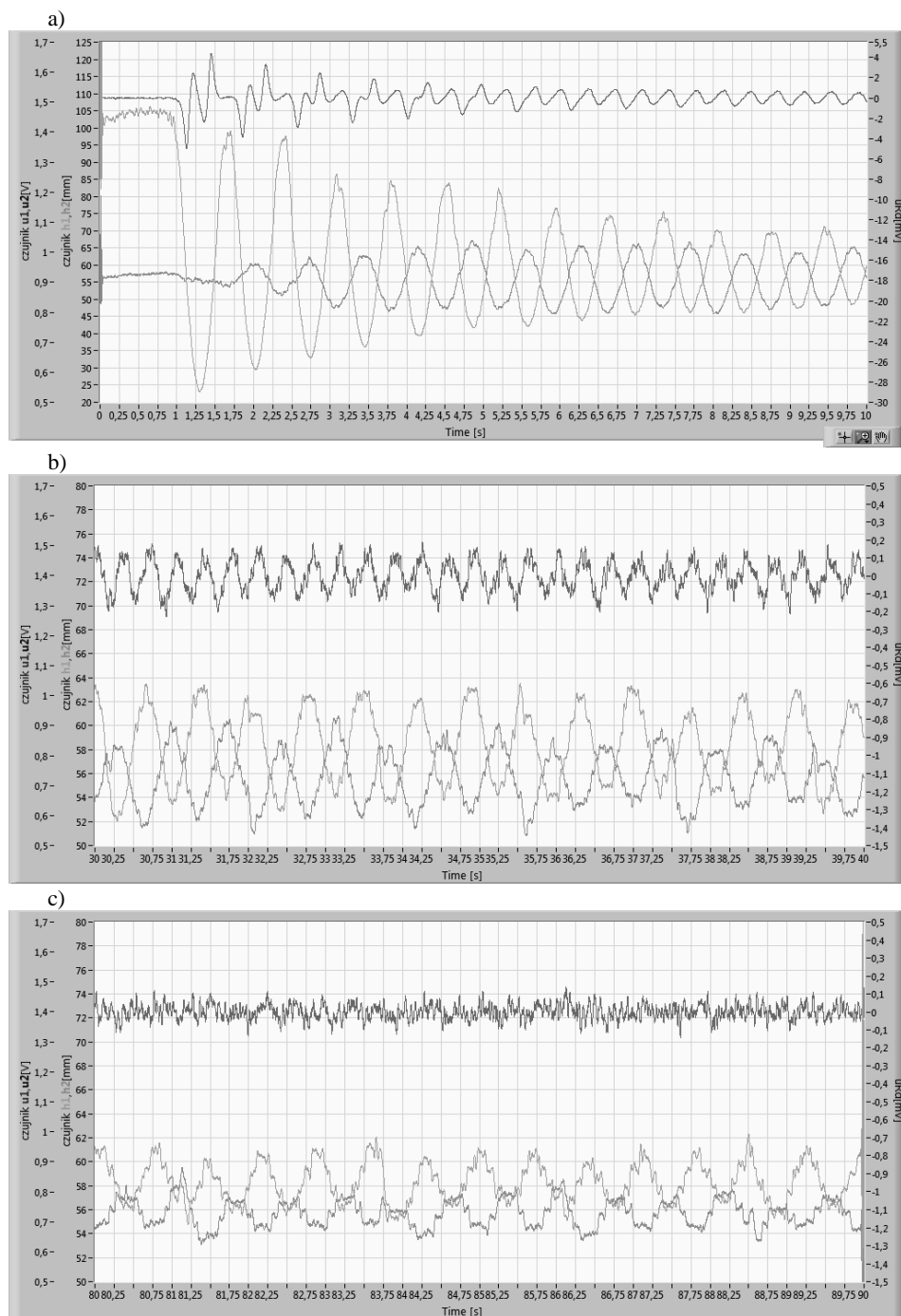
Figure 4. Fragments of the time series of magnets positions (h_1, h_2) and the induced voltage (u_{Rd})

in the coil circuit: first 10s of recording (a), range 30 – 40s (b), final 10s (c)

The non-linear springs used have non-linear characteristics only under compression. Therefore, it was decided to turn the whole stand upwards so that the magnet was constantly above the spring. To avoid moving the magnet in directions other than axial, it was necessary to use axial guidance in the form of plexiglass tubes. Fig. 5 presents the exemplary time series.
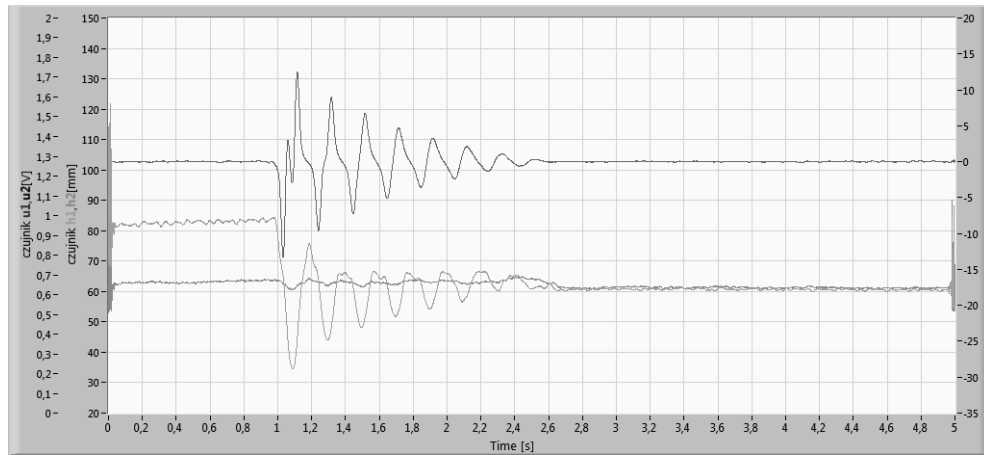
Figure 5. Time series of the magnets positions (h_1, h_2) and corresponding induced voltage signal (u_{Rd}) in a case when magnet indexed 1 is initial positioned – non-linear spring case

Due to the high stiffness and occurring resistance to motion (mainly friction) on the contact surfaces of the magnet clamping and the tube, the recorded movement is quite short. The fragment containing excitation of oscillator 2 is shown in Fig. 6. It can be seen that the current induced by the moving magnet 1 affects the second oscillator, but in a slight way.
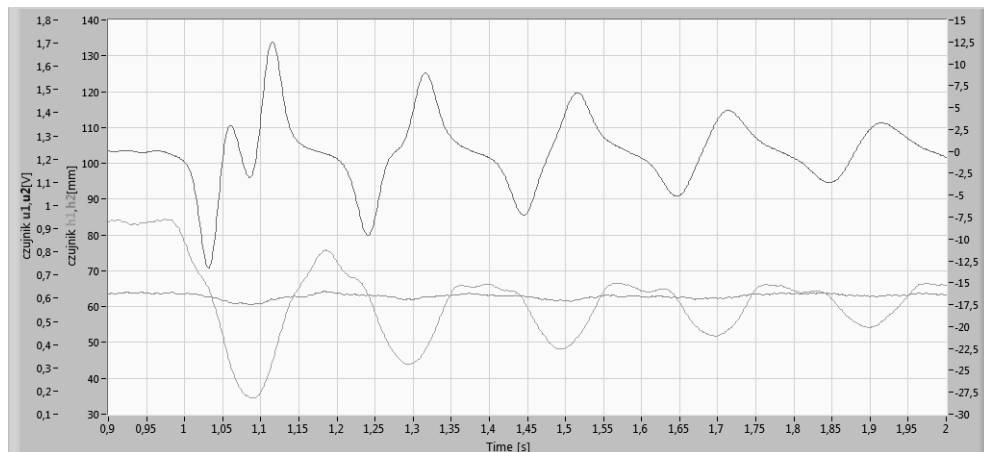
Figure 6. Fragments of the beginning of time series of magnets positions and the induced voltage

The reason for this is the high friction value on the guide elements present in the system. Work is currently underway on a modernized stand construction. The stand is to be augmented by very precise linear aerostatic bearings of the authors project. This type of solution can ensure both the elimination of undesirable friction and also guarantee perfect axial guidance of moving masses.

5.   Concluding remarks

The paper covers the first approach to the system of a pair of oscillators coupled by the electromagnetic field. The introduction of the article indicates the direction in which the authors would like to further consider this system, i.e. advanced modelling using magnetic field theory based on the dynamics of magneto-electro-mechanical systems. Another interesting and potential application of this system is the study of electromagnetic energy harvester.

The construction of the experimental rig presented in section 2 is an example of a universal research stand. Elements with both linear and non-linear characteristics have been used. It is also possible to test springs such as purely magnetic springs. The presented experimental data shows that even linear system can provide many suppositions. An thought-provoking finding seems to be the time series of the induced current in the coils system, as a curve with many inflection points.

Presented in the paper mathematical model provides a possibility to confirm the experimental studies through numerical simulations. Such an analysis will be a subject of further investigations and future authors' papers. The plans also develop the dynamics of the system with harmonic excitation of the one of the oscillators and investigate how efficiently the system works as an energy scavenger.

References

[1]   Yan L., Wu Z., Jiao Z., Chen C.-Y., Chen I.-M., *Equivalent energized coil model for magnetic field of permanent-magnet spherical actuators*, Sensors and Actuators A. 229 (2015), 68–76.

[2]   Eissa M., Kandil A., El-Ganaini W.A., Kamel M., *Vibration suppression of a nonlinear magnetic levitation system via time delayed nonlinear saturation controller*, International Journal of Non-Linear Mechanics. 72 (2015), 23–41.

[3]   Wei W., Xue W., Li D., *On disturbance rejection in magnetic levitation*, Control Engineering Practice. 82 (2019), 24–35.

[4]   Ravaud R., Lemarquand G., Babic S., Lemarquand V., Akyel C., *Cylindrical magnets and coils: Fields, forces, and inductances*, IEEE Transactions on Magnetics. 46 (2010), 3585–3590.

[5]   Babic S., Akyel C., *New formulas for calculating torque between filamentary circular coil and thin wall solenoid with inclined axis whose axes are at the same plane*, Progress In Electromagnetics Research M. 73 (2018), 141–151.

[6]   Babic S.I., Akyel C., *Magnetic Force Calculation Between Thin Coaxial Circular Coils in Air*, IEEE Transactions on Magnetics. 44 (2008), 445–452.

[7]   Babic S.I., Akyel C., *Torque calculation between circular coils with inclined axes in air*, International Journal of Numerical Modelling: Electronic Networks, Devices and Fields. 24 (2011), 230–243.

[8]   Robertson W., Cazzolato B., Zander A., *Axial Force Between a Thick Coil and a Cylindrical Permanent Magnet: Optimizing the Geometry of an Electromagnetic Actuator*, IEEE Transactions on Magnetics. 48 (2012), 2479–2487.

[9]   Dolisy B., Lubin T., Mezani S., Leveque J., *Three-Dimensional Analytical Model for an Axial-Field Magnetic Coupling*, Progress In Electromagnetics Research M. 35 (2014), 173–182.

[10] Masoumi M., Wang Y., *Repulsive magnetic levitation-based ocean wave energy harvester with variable resonance: Modeling, simulation and experiment*, Journal of Sound and Vibration. 381 (2016), 192–205.

[11] Viet N.V., Wang Q., *Ocean wave energy pitching harvester with a frequency tuning capability*, Energy. 162 (2018), 603–617.

[12] Kecik K., Mitura A., Lenci S., Warminski J., *Energy harvesting from a magnetic levitation system*, International Journal of Non-Linear Mechanics. 94 (2017), 200-206.

[13] Gao M., Wang Y., Wang Y., Wang P., *Experimental investigation of non-linear multi-stable electromagnetic-induction energy harvesting mechanism by magnetic levitation oscillation*, Applied Energy. 220 (2018), 856–875.

[14] Mann B.P., Sims N.D., *Energy harvesting from the nonlinear oscillations of magnetic levitation*, Journal of Sound and Vibration. 319 (2009), 515–530.

[15] Mann B.P., Owens B.A., *Investigations of a nonlinear energy harvester with a bistable potential well*, Journal of Sound and Vibration. 329 (2009), 1215–1226.

[16] Wojna M., Wijata A., Wasilewski G., Awrejcewicz J., *Numerical and experimental study of a double physical pendulum with magnetic interaction*, Journal of Sound and Vibration 430 (2018), 214-230.

[17] Wojna M., Wasilewski G., Awrejcewicz J., *Double Physical Pendulum with Magnetic Interaction*, Mechatronics 2017 - Ideas for Industrial Applications. Advances in Intelligent Systems and Computing, Springer, Cham, 934 (2019), 455-464.

[18] Wojna M., Wasilewski G., Awrejcewicz J., Wijata A., *Dynamics of a double physical pendulum with magnetic interaction*, Vibration, Control and Stability of Dynamical Systems, DAB&M of TUL Press, Lodz, (2017), 559–570.

[19] Polczyński K., Wijata A., Awrejcewicz J., Wasilewski G., *Numerical and experimental study of dynamics of two pendulums under a magnetic field*, Proceedings of the Institution of Mechanical Engineers. Part I: Journal of Systems and Control Engineering. 233 Issue 4 (2019), 441-453.

[20] Polczyński K., Wijata A., Wasilewski G., Kudra G., Awrejcewicz J., *Modelling and Analysis of Bifurcation Dynamics of Two Coupled Pendulums with a Magnetic Forcing*, IUTAM Symposium on Exploiting Nonlinear Dynamics for Engineering Systems, Springer, 37 (2020), 213-223.

[21] Polczyński K., Wasilewski G., Awrejcewicz J., Wijata A., *Modeling and experimental investigation of dynamics of two pendulums elastically coupled and driven by magnetic field*, Engineering Dynamics and Life Sciences, DAB&M of TUL Press, Lodz, (2017), 451–462.

[22] Jackson J.D., *Classical Electrodynamics*, Wiley-VCH, New York, 1962.

[23] Donoso G., Ladera C.L., Martín P., *Magnetically coupled magnet–spring oscillators*, Eur. J. Phys. 31 (2010), 433–452.

Mateusz Wojna, M.Sc. (Ph.D. student): Lodz University of Technology, Faculty of Mechanical Engineering, Department of Automation, Biomechanics and Mechatronics, Stefanowskiego 1/15, 90-924, Lodz, POLAND (*mateusz.wojna@edu.p.lodz.pl*). The author gave a presentation of this paper during one of the conference sessions.

Grzegorz Wasilewski, Ph.D.: Lodz University of Technology, Faculty of Mechanical Engineering, Department of Automation, Biomechanics and Mechatronics, Stefanowskiego 1/15, 90-924, Lodz, POLAND (*grzegorz.wasilewski@p.lodz.pl*).

Jan Awrejcewicz, Professor: Lodz University of Technology, Faculty of Mechanical Engineering, Department of Automation, Biomechanics and Mechatronics, Stefanowskiego 1/15, 90-924, Lodz, POLAND (*jan.awrejcewicz@p.lodz.pl*).

Effect of the rotor support elements lubricated by magnetic fluids on chaotic and regular vibration of rotors during rubbing

Jaroslav Zapoměl, Petr Ferfecki, Jan Kozánek

Abstract: The change of the damping in the rotor support elements makes it possible to achieve a compromise between the vibration attenuation and minimizing the forces transmitted between the rotor and the stationary part. To do this a new design variant of a support element has been proposed. It consists of a squeeze film bearing lubricated by magnetically sensitive oil and of a hydrodynamic bearing inserted in it. The damping is controlled by changing the magnetic field passing through the layer of magnetic fluid. This paper deals with influence of the proposed support element on character of the rotor vibration during rubbing. The system is excited by the rotor unbalance and by impact forces caused by the collisions. The pressure distribution in the oil films is governed by the modified Reynolds equations. The dry friction is considered in the contact areas. The goal of the study was to investigate the effect of a magnetic field on regularity of the rotor vibration. The results of the computational simulations show that in cases when the collisions occurr (i) character of the induced vibration depends on speed of the rotor rotation and (ii) application of the magnetic field can change irregular oscillation into regular one. The performed study contributed to learning more on the effect of magnetically controlable fluids lubricating the rotor bearings on character of the rotor vibration.

1. Introduction

The rotors are often mounted in hydrodynamic bearings. To enable their operation at high angular velocity, the bearings are inserted in squeeze film dampers. This increases damping in the rotor supports and suppresses vibration of large amplitude. A simple dynamical analysis reported in [1] shows that to achieve optimum performance of the damping devices in a wide interval of running velocities their damping must be adaptable to the rotor operating speed.

This arrived at the development of a number of semiactive controllable damping devices working on different physical principles. The design utilizing the mechanical and hydraulic phenomena to control the damping force is reported in [2], [3]. Electromagnetic damping devices of a reluctance type in combination with rolling element bearings are discussed in [4]. The further possibility is offered by smart liquid materials, sensitive to electric or magnetic fields [5], [6].

This paper deals with the proposal of a new controllable support element intended for rotors working in a wide range of running velocities. The element is composed of a hydrodynamic bearing inserted in a magnetorheological squeeze film damper. Its effect on vibration attenuation of rigid

rotors working at normal operation conditions was studied in [7]. This paper is focused on its influence on the motion of flexible rotors in the case when collisions between the disc and the stationary part occur. The results of computational simulations show that character of the rotor vibration depends on speed of the rotor rotation and that in some cases increased damping in the rotor supports makes it possible to change the oscillation from chaotic to regular.

Semiactive damping devices in the rotor supports become a source of nonlinear properties of rotating machines and may induce their irrgegular oscillation. The tools for its identification and qauntification can be found e.g. in [8].

2. The studied support element

The studied support element (Fig. 1) consists of a hydrodynamic bearing and a squeeze film damper, the main parts of which are two concentric rings, between which there is a thin layer of magnetorheological oil. In the damper housing there is embedded an electric coil, which generates magnetic flux passing through the magnetically sensitive lubricant. The hydrodynamic bearing is inserted in the inner ring, which is connected with the housing by a cage spring. Lateral vibration of the shaft squeezes the oil film, which produces the damping force. As resistance agains the flow of magnetic fluids depends on magnetic induction, the change of the applied current can be used to control the damping effect.

1 - outer ring
2 - inner ring
3 - magnetorheological oil
4 - normal oil
5 - electric coil
6 - cage spring
7 - damper housing
8 - shaft
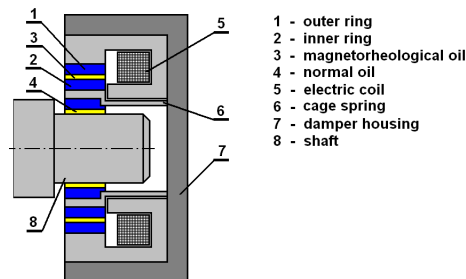
Figure 1. The studied support element.

The pressure distribution in the individual oil layer is governed by the Reynolds equations. The one related to the magnetically sensitive oil was adapteded to bilinear material. More details on derivation and solutions of the Reynolds equations can be found in [9], [10]. In cavitated regions it is assumed that pressure of the medium remains constant. Components the hydraulic forces are calculated by integration of the pressure distribution along the length and around the circumference of the individual oil layers. The pressure profile in the layer of magnetorheological oil depends of the yielding shear stress, which can be changed by means of magnetic induction. This manipulation makes it possible to control the damping force. More details can be found in [9], [11].

3. The investigated rotor system

The properties of the studied support element and its influence on the rotor vibration and its attenuation was investigated by means of computer simulations.

The drawing of the examined rotor is depicted in Fig. 2. The disc is placed in an opening of a square shape. The rotor rotates at constant angular speed, is loaded by its weight, and is excited by the disc unbalance and by the impact forces, if collisions between the disc and the stationary part occur. The cage springs of both dampers are prestressed to eliminate their deflection due to the rotor weight.
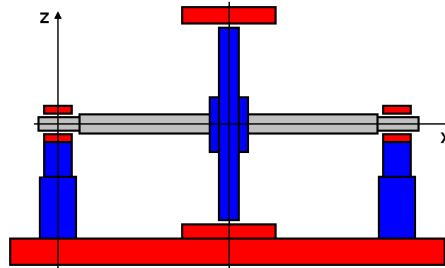
Figure 2. The investigated rotor system.

In the computational model the rotor is represented by a Jeffcott one, the support elements by springs and hydraulic forces, and the collisions by impact forces. Material damping and the damping caused by the environment are considered to be viscous. Because of the system symmetry, lateral vibration of the rotor is described by a set of six nonlinear differential equations

$$m\ddot{y}_D + (b_P + b_M)\dot{y}_D - b_M \dot{y}_J + k_S y_D - k_S y_J + \dot{\vartheta}b_M z_D - \dot{\vartheta}b_M z_J = m e_T \dot{\vartheta}^2 \cos\vartheta + F_{cony} \tag{1}$$

$$m\ddot{z}_D + (b_P + b_M)\dot{z}_D - b_M \dot{z}_J + k_S z_D - k_S z_J - \dot{\vartheta}b_M y_D + \dot{\vartheta}b_M y_J = m e_T \dot{\vartheta}^2 \sin\vartheta - mg + F_{conz} \tag{2}$$

$$-b_M \dot{y}_D + b_M \dot{y}_J - k_S y_D + k_S y_J - \dot{\vartheta}b_M z_D + \dot{\vartheta}b_M z_J = F_{hdy} \tag{3}$$

$$-b_M \dot{z}_D + b_M \dot{z}_J - k_S z_D + k_S z_J + \dot{\vartheta}b_M y_D - \dot{\vartheta}b_M y_J = F_{hdz} \tag{4}$$

$$k_R y_R = -F_{hdy} + F_{mry} + F_{psy} \tag{5}$$

$$k_R z_R = -F_{hdz} + F_{mrz} + F_{psz} \tag{6}$$

m is the disc mass, b_P is the coefficient of viscous damping caused by the environment, b_M is the coefficient of viscous damping caused by the shaft material, k_S is the shaft bending stiffness, k_R is the cage spring bending stiffness of one damper, e_T is the eccentricity of the disc center of gravity, g is the gravity acceleration, y_D, z_D, y_J, z_J, y_R, z_R are the displacements of the disc, journal, inner damper ring centers in the y and z directions, respectively, ϑ is the angle of the rotor rotation, F_{hdy}, F_{hdz} are the y and z components of the hydraulic force acting on the rotor journal, F_{mry}, F_{mrz} are the y and z

components of the magnetorheological damper force acting on the inner damper ring, F_{psy}, F_{psz} are the y and z components of the prestress force, F_{cony}, F_{conz} are the y and z components of the impact force acting on the disc, and $(\cdot)$, $(\cdot\cdot)$ denote the first and second derivatives with respect to time, respectively.

The impact forces have two components, normal and tangential. The normal component is induced by the elastic deformation and damping of material in the vicinity of the impact point

$$F_{conn} = k_{con}\Delta + b_{con}\dot{\Delta} \tag{7}$$

Δ is the penetration of the disc in the stationary part and is calculated as the difference between the displacement of the disc towards the stationary part and the width of gap, k_{con} is the contact stiffness, and b_{com} is the coefficient of damping in material in the contact area.

The normal component of the impact force can be only compressive and is always directed towards the disc. If it should be tensile, its value is considered to be zero.

The tangential component of the impact force is induced by dry friction in the contact area and is always oriented against the disc rotation

$$F_{cont} = f_{con}F_{conn} \tag{8}$$

f_{con} is the coefficient of friction between the disc and the stationary part.

The Adams-Moulton method was chosen to solve the set of governing equations (1) - (6).

4.   The investigated rotor system

The main technological parameters of the studied rotor system are: the mass of the rotor 450 kg, the bending stiffness of the staft 20 MN/m, the stiffness of one cage spring 5 MN/m, the hydrodynamic bearing diameter/length 110/60 mm, the bearing clearance 0.2 mm, the bearing oil dynamic viscosity 0.01 Pas, the damper diameter/length 150/40 mm, the damper clearance 0.8 mm, the magnetorheological oil dynamic viscosity when not effected by a magnetic field 0.3 Pas, eccentricity of the disc center of gravity 50 μm, the contact stiffness 1 GN/m, and the friction coefficient in the contact area 0.2.

Fig. 3 and 4 show the steady state trajectories of the disc center for rising the rotor angular velocity from 100 to 400 rad/s and the regime when no current is applied. The change of their character and size is evident. The steady state orbits related to speeds of 200 and 300 rad/s are periodic (or very close to periodic) while trajectories corresponding to velocities 100 and 400 rad/s have a chaotic character. This is confirmed by the band Fourier spectra depicted in Fig. 5, which is a characteristic feature for a chaotic motion. The excitation frequencies corresponding to the speed of the rotor rotation are dominant in the spectra.
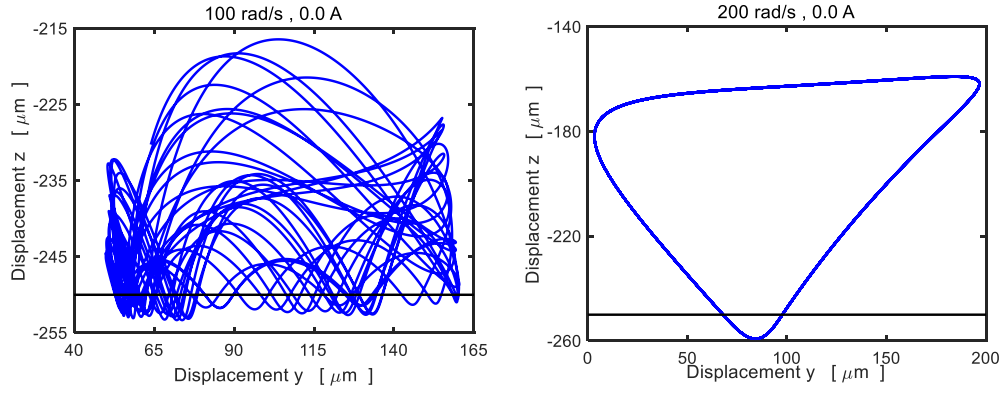
Figure 3. Trajectory of the disc center (speed 100, 200 rad/s, current 0.0 A).
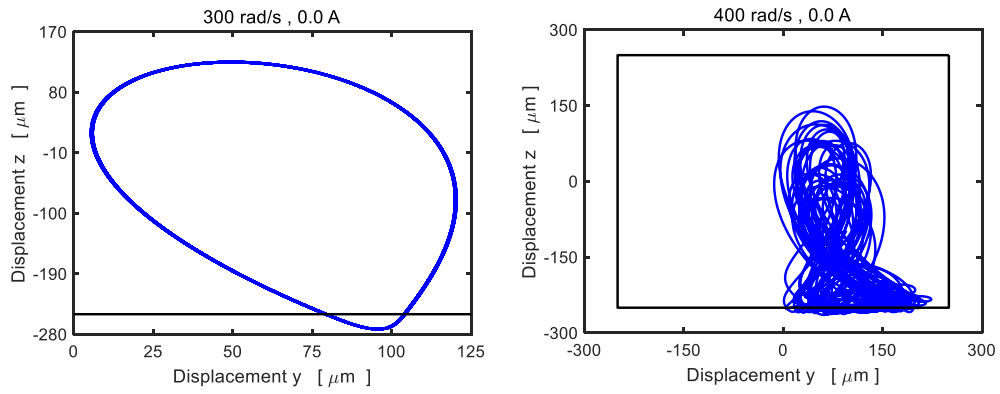
Figure 4. Trajectory of the disc center (speed 300, 400 rad/s, current 0.0 A).
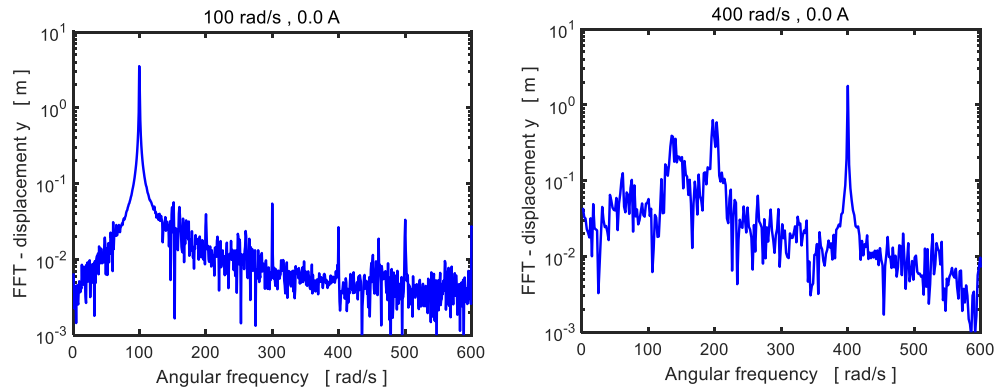
Figure 5. Fourier transform - disc center displacement y (current 0.0 A).

The bifurcation diagram is drawn in Fig. 6. It shows that the rotor exhibits irregular motion in the vicinity of angular speeds of 100 and 400 rad/s. In other speed intervals its character remains regular.
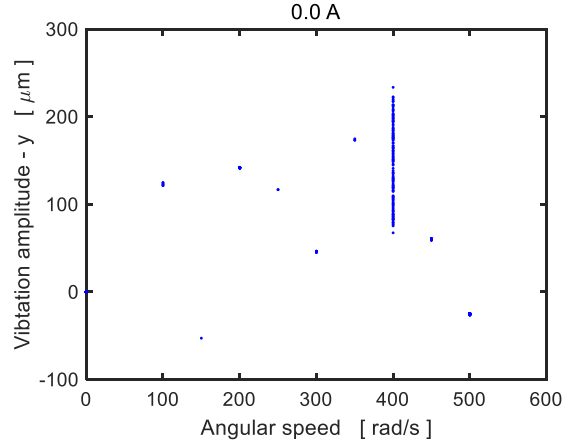
Figure 6. Bifurcation diagram (current 0.0 A).

Fig. 7 shows the change of the steady state trajectory of the rotor rotating at angular speed of 100 rad/s after application of the current. The size of the orbit goes down and for the current of 4.0 A the motion character changes from irregular to periodic.
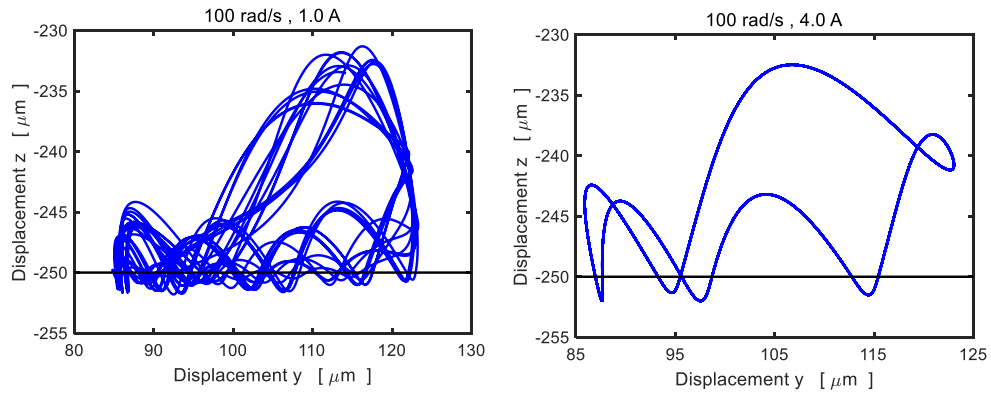
Figure 7. Trajectory of the disc center (speed 100 rad/s, current 1.0, 4.0 A).

The trajectory depicted in Fig. 8 gives evidence that increase of damping in the rotor supports by application of the current does not arrive at both reduction of the size nor to irregular character of the rotor vibration.
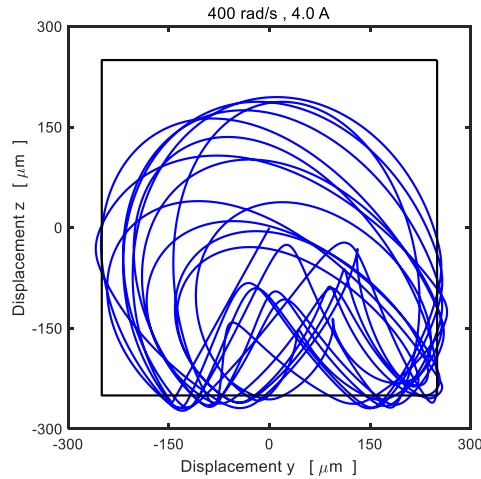
Figure 8. Trajectory of the disc center (speed 400 rad/s, current 4.0 A).

5. Conclusions

The rotors of high speed turbomachinery are often coupled with the stationary part by hydrodynamic bearings inserted in squeeze film dampers. This paper deals with properties of a new semiactive support element consisting of a magnetorheological squeeze film damper and a hydrodynamic bearing and with its effect on the rotor behavior during rubbing. The results of the computational simulations show that (i) collisions between the disc and the stationary part can induce both regular and chaotic vibrations depending on speed of the rotor rotation and amount of damping in the rotor supports, and that (ii) increase of damping can in some cases convert chaotic vibration in regular. The proposed support element makes it possible to utilize all advantages of hydrodynamic bearings. The control of the damping effect is very simple as the damper works only in the on/off regime. The performed study contributes to learning more on undesirable phenomena induced by the rotor rubbing and on the possible ways of their suppression.

Acknowledgments

References

[1] Zapoměl, J., Ferfecki, P. Kozánek, J. Determination of the transient vibrations of a rigid rotor attenuated by a semiactive magnetorheological damping device by means of computational modelling. *Applied and Computational Mechanics* 7 (2013), pp. 223-234.

[2] Mu, C., Darling, J., Burrows, C.R. An appraisal of a proposed active squeeze film damper. *ASME Journal of Tribology* 113 (1991), pp. 750-754.

[3] El-Shafei, A., El-Hakim, M. Experimental investigation of adaptive control applied to HSFD supported rotors. *ASME Journal of Engineering for Gas Turbines and Power* 122 (2000), pp. 685-692.

[4] Tonoli, A., Silvagni, M., Amati, N., Staples, B., Karpenko, E. Design of electromagnetic damper for aero-engine applications. *Proceedings of the International Conference on Vibration in Rotating Machinery*, Exeter, England, (2008), pp. 761-774.

[5] Morishita, S., Mitsui, J. Controllable squeeze film damper (An application of electro-rheological fluid). *ASME Journal of Vibration and Acoustics* 114 (1992), pp. 354-357.

[6] Aravindhan, T.S., Gupta, K. Application of magnetorheological fluid dampers to rotor vibration control. *Advances in Mechanical Engineering* 5 (2006), pp. 369-380.

[7] Zapoměl, J., Ferfecki, P., Kozánek, J., Savin, L. Controllable magnetically sensitive rotor support element for reducing oscillation and force transmission. In: Uhl, T. (ed) *Advances in Mechanism and Machine Science, Proceedings of the 15th IFToMM World Congress on Mechanism and Machine Science*, Krakow, Poland, Springer, (2019), pp. 3385–3394.

[8] Awrejcewicz, J., Dzyubak, L., Grebogi, C. A direct numerical method for quantifying regular and chaotic orbits, *Chaos, Solitons & Fractals* 19 (2004), pp. 503-507.

[9] Zapoměl, J. Computer Modelling of Lateral Vibration of Rotors Supported by Hydrodynamical Bearings and Squeeze Film Damper. VŠB-Technical University of Ostrava, Ostrava, 2007, (in Czech).

[10] Zapoměl, J., Ferfecki, P., Forte, P. A new mathematical model of a short magnetor-heological squeeze film damper for rotordynamic applications based on a bilinear oil representation - derivation of the governing equations. *Applied Mathematical Modeling* 52, (2017), pp. 558-575.

[11] Ferfecki, P., Zapoměl, J., Kozánek, J. Analysis of the vibration attenuation of rotors sup-ported by magnetorheological squeeze film dampers as a multiphysical finite element problem. *Advances in Engineering Software* 104, (2017), pp. 1-11.

Jaroslav Zapoměl, Professor: VŠB-Technical University of Ostrava, Department of Applied Mechanics, 17. listopadu 15/2172, 708 00 Ostrava-Poruba, Czech Republic (*jaroslav.zapomel@vsb.cz*).

Jaroslav Zapoměl, Professor: Institute of Thermomechanics, Department of Dynamics and Vibrations, Dolejškova 1402/5, 182 00 Prague 8, Czech Republic (*zapomel@it.cas.cz*).

Petr Ferfecki, Research engineer: VŠB-Technical University of Ostrava, Department of Applied Mechanics, 17. listopadu 15/2172, 708 00 Ostrava-Poruba, Czech Republic (*petr.ferfecki@vsb.cz*).

Petr Ferfecki, Research engineer: VŠB-Technical University of Ostrava, IT4Innovations National Supercomputing Center, 17. listopadu 15/2172, 708 33 Ostrava-Poruba, Czech Republic (*petr.ferfecki@vsb.cz*).

Jan Kozánek, Research engineer: Institute of Thermomechanics, Department of Dynamics and Vibrations, Dolejškova 1402/5, 182 00 Prague 8, Czech Republic (*kozanek@it.cas.cz*).

Structure and control strategies of exoskeletons for fatigue limitation of a healthy man

Adam Zawadzki, Tomasz Mirosław, Jakub Deda, Zbigniew Żebrowski

Abstract: During last few years an idea of exoskeletons amplifying human force and reducing body effort during activities turned to be a real solution. Because of many interdisciplinary problems – medical, mechanical and mechatronics – and individual features of human body, designs are still looking for better and better solutions. A lot of money is spent for research, especially when we take into account almost unlimited application of such an equipment. Some designers are following the leaders in this domain and don't see other efficient solutions which are well known for many years. In this paper authors present overview of solutions and applications of exoskeletons for healthy men with oriented on ergonomics and energy management aspects. For energy management aspects authors present analyses of typical movement and energy conversion in human body. The mechanic, electric and hydraulic drive solutions are presented and characterized by their possibilities to follow the human body. The new hybrid solution with energy saving and recuperation is presented. Authors of this paper aim on providing a concise comparison between most commonly used control strategies for exoskeletons for healthy persons. The paper will focus on reviewing most common strategies and analyzing them in terms of utilizing in products for the rescue services and the army. The conclusions for each solution will be backed up with authors experiences on this field coming from developing own solution of a lower limb exoskeleton for soldiers and rescue services.

1. Overview of the current exoskeleton solutions for healthy persons

During last ten years exoskeletons became popular thanks to big projects like Lockheed Martin's HULC [1] or Berkley University of Technology's BLEEX [2]. Exoskeletons appear in headlines of magazines and build excitement. The major division in exoskeletons is on target users: medical patients and elderly or healthy people. This paper considers the second group and the discussion is only about such solutions even though some parts are common for both applications.

Exoskeleton solutions for healthy people can be divided on three categories: active, semipassive, passive (see Fig. 1). It is not possible to build an inexpensive active exoskeleton (with motors and power source) that is why some of the market players focused on passive exoskeletons (static unloading by utilizing springs, brakes etc. in the construction). Each of the current solutions is based on springs and the structure that is locked in working position allowing springs to transfer load to the ground. Such an approach is elegant, simple and reliable. The biggest disadvantage is that it can use its full potential only in stationary applications. Semipassive solutions are somewhere in between i.e. they utilize powered actuators, but they are low power, only used for changing working characteristics of load bearing, passive elements like springs.
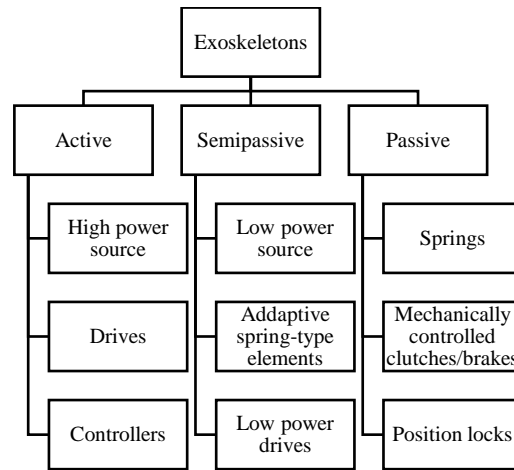
Figure 1. Exoskeletons classification.

Such wide diversity of solutions utilizes broad spectrum of energy sources. A model of energy transformation in a human body including the change cycles is given in Fig. 2a.
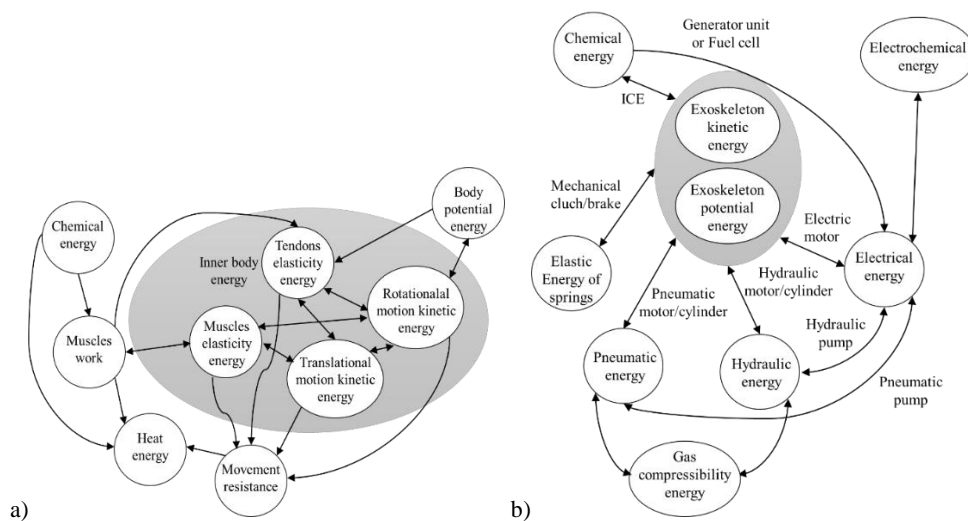
Figure 2. a) Energy transformation graphs for a human body (a), an exoskeleton (b).

The chemical energy coming from food goes to the muscles. They contact and extend moving the body. When there is a resistance, the muscle tension accumulates the elasticity energy. It is problematic to keep this tension for a longer time that is why this energy is converted into heat (this happens e.g. during walking downstairs). Unfortunately, there is no biological mechanism for converting mechanical energy into chemical energy in a human body.

When muscles overcome external resistance forces the body moves changing the position of the center of gravity. This causes change in potential and kinetic energy according to the energy conservation law. This is a repeatable process during the gait cycle. The energy loses coming from movement resistance (wind, friction etc.) are covered by muscles work.

The energy of an exoskeleton is strictly mechanical, that is why only potential and kinetic energy is considered for calculations. Logically the exoskeleton shall support itself, that is why energy must be delivered to the system in order to overcome mechanical and thermal losses (see Fig. 2b).

Depending on eigen gait cycle of an individual the control pattern changes. It can be observed in Fig. 4 where gait cycles with short and long steps are compared.
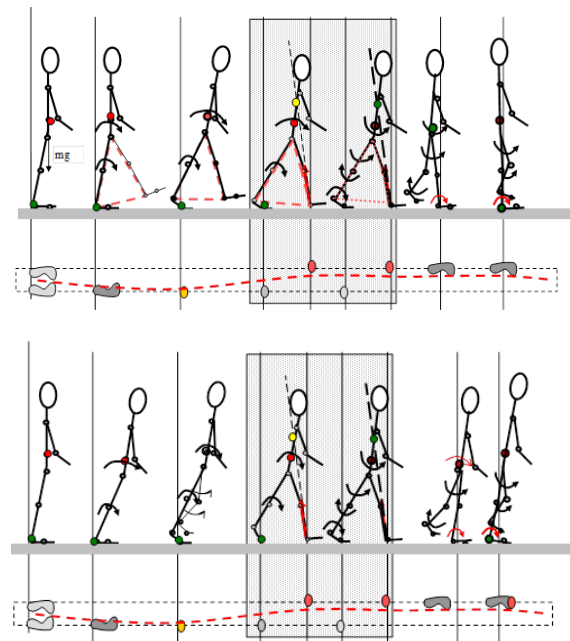
Figure 3. Gait cycle a) short steps b) long steps

It causes problems in active and semipassive exoskeleton solutions but does not influence purely mechanical control of passive exoskeletons.

There are many publications describing specific solutions of control algorithms. For active exoskeletons they were reviewed by Anam, and Al-Jumaily [3] and divided in four groups: model based control systems, hierarchy based controls Systems, physical parameters based control system, usage based Control systems.

In most cases either a fine model of the system is needed or large number of sensors. I the first case there are methods for obtaining equations of motion for such complex systems like matrix

method [4], ending with control algorithms based on inverse kinematics [5, 6]. In the second case the demanded position is estimated and predicted based on multiple sensors data [7, 8, 9].

There is no paper that would analyze generally control strategies for passive exoskeletons therefore authors give such a review in this paper.

2. Possible control strategies for passive exoskeletons

Since only strictly passive solutions are analyzed, not semi passive that can be controlled using similar algorithms and methods as active exoskeletons, authors consider possibilities of controlling the machine without external power source – using only mechanisms. Since human body requires varying supporting force/moment during gait cycle, changing characteristics of passive elements must be utilized. Typically, in passive solutions helical springs are used in order to support a user during stationary actions (heavy tool manipulations, heavy weights lifting). Elements like brakes and clutches are used to change the mode of operations and allow a user to e.g. move from one working position to another or to move with the load to another area.

In Fig. 4 force characteristics for knee and ankle joints are provided. It can be noted that depending on angle range they are either progressive, linear or degressive. At 180 degrees these forces are zero or near zero because static unloading occurs and only a small fraction of forces are transferred by actuators (depending on mounting geometry).
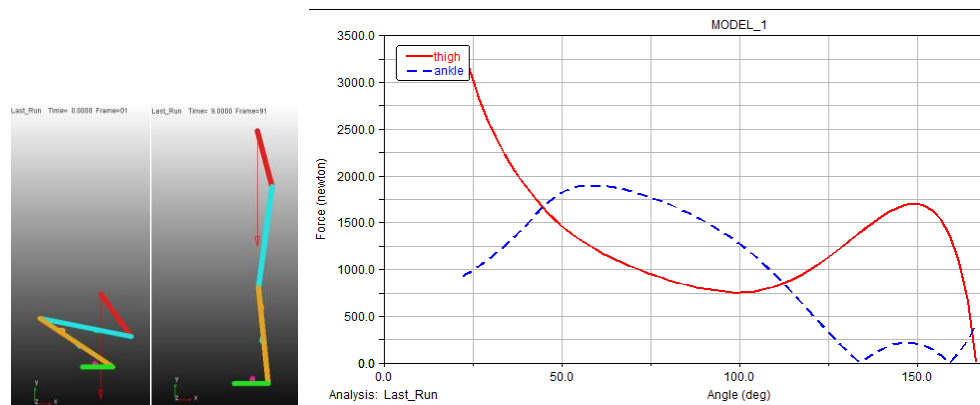
Figure 4. Forces in actuators during crouching for different joints' rotation angles.

Such behavior of the system indicates using different kinds of springs (as actuators) depending on movement range: for progressive part gas or conical springs, for linear part cylindrical springs, for degressive part Belleville springs. It is not possible to base the design only on one kind of springs for the designs where an exoskeleton shall walk, run etc. There are couple of ways to expanding the working range of a spring in this application (Fig. 5):

1. limiting usage of the exoskeleton to walking – crouching, running not possible,
2. adding a damper to get a hysteresis – for bigger damping factors progressive-degressive characteristic is possible to obtain,
3. utilizing brakes or clutches in order to engage or to disengage sets of spring depending on working mode or range,
4. changing stiffness of the spring by setting preload,
5. using oleo-pneumatic shock absorbers.

a	b	c	d	e
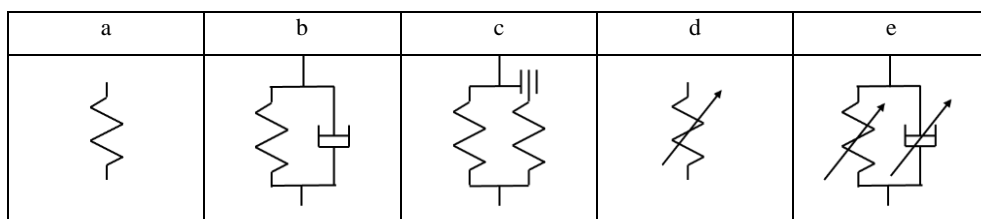
Figure 5. Control strategies for passive exoskeletons.

Each of mentioned ways is correct for specific applications. The simplest method is to restrict the movement range. Such an approach is valid for industrial exoskeletons that are used in repeatable scenarios like moving packs in a warehouse or manipulating heavy power tools. A user does not need movement freedom due to the job profile.

When more dynamic procedures are performed, and heavy loads are in use typically a damper must be used. It regulates the velocity of the expanding or contracting spring allowing higher precision of movement.

For applications where high movement range is a must, another approach is needed. One way out is to use a set of springs that can act parallelly on mounting points but are engaged or disengaged using brake or clutch in specific moments allowing for more natural loads transfer (compare Fig. 4). This solution is much more complicated because special elements must be designed in order to meet packaging requirements. What is more using more springs and brakes increases weight of the system.

Simple solutions mentioned above are not able to copy complex movement characteristics of human body. That is why they need to be joined with other mechanical elements that will assure correct forces transfer in time.

Two main strategies can be mentioned here: angular strategy and time strategy. In the first one (Fig. 6a) user's body has full control over spring element. There is a direct relationship between human joint rotation angle and spring displacement. In order to support a user uniformly an additional transmission must be used (Fig. 6b). One approach is to use a cam for controllable conversion of a force into a moment in reference to joint's rotation angle. It allows for manipulation of output characteristics during spring expansion and even constant moment can be achieved using reasonable

dimensions of a cam. To obtain even better results using a simple spring element a clutch (or a brake) can be used to disengage the system when very small support is needed or when the system actually disturbs a user (situation depicted in Fig. 6c). Such situation occurs when stiff springs are used to support crouching and standing up.
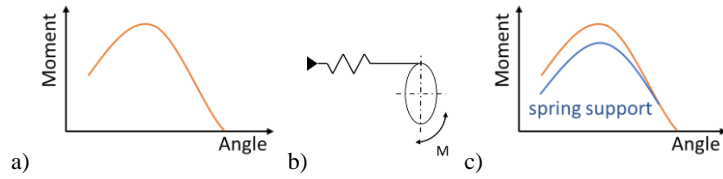
Figure 6. Angular control strategy: a) moment occurring in a knee joint, b) a cam-spring mechanism, c) moment generated by a spring.

The second strategy allows for energy accumulation. During some usage scenarios when a very dynamic movement comes into play (e.g. running) it is possible to harvest energy from exoskeleton and human body inertia. As depicted in Fig. 7a the energy is accumulated in one phase of the movement and then released in a controlled manner in time in the second phase. Such approach uses dampers in layouts like in Fig. 5b or 5e. The more complex 5e system changes the damping factor with direction of travel. It means it allows for accumulation of energy in one direction but it can release it only when triggered.
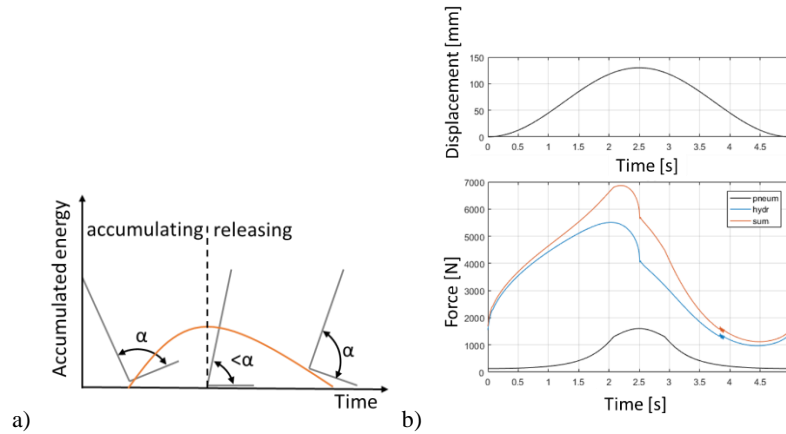
Figure 7. Time control strategy: a) energy accumulation, b) example of simulated time characteristic for an oleo-pneumatic shock absorber.

Depending on system complexity the energy releasing might not occur just after accumulating but can be shifted in time by utilizing logic switches. For a case described above (ankle joint) only

two logic switches would be needed to control releasing the energy – one in front and one on the back of the shoe sole.

Such a strategy although more complex, allows for support in the whole range of movement. What is more there are already commercially available systems that can be utilized to passive exoskeletons after minor modifications – shock absorbers. Authors conducted experiments to find working characteristics of a double chamber oleo-pneumatic shock absorber (Fig. 8). Such systems are already provided with regulation valves for control of energy accumulating and releasing. Authors of this publication have already conducted ad-hoc experiments with CO_2 cartridges for manual changing working characteristics during use. The results are promising and research in this field is continued.
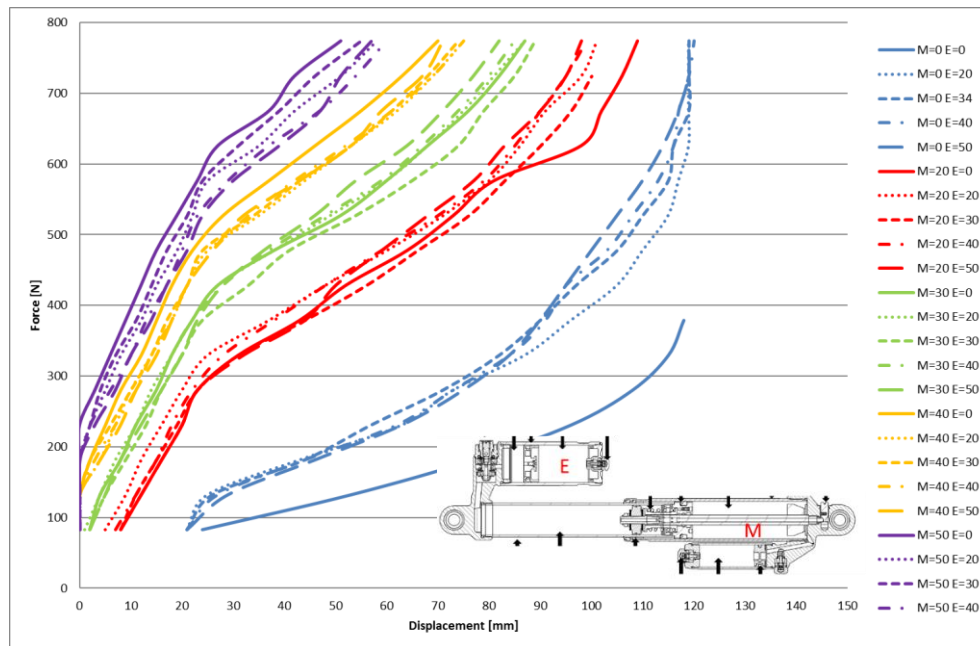
Figure 8. Force in function of a displacement dependent on air pressures (psi) in work chambers for an oleo-pneumatic shock absorber.

3. Conclusions

Authors analyzed possibilities of controlling passive exoskeletons without using any external power supply. A full review on passive elements utilization for exoskeletons propelling is provided starting from simple spring and ending on adapted oleo-pneumatic shock absorbers. Also the problem of energy accumulations was discussed with a feasibility study. Authors proposed two kinds of control

strategies: angular control and time control. Both of them have weaknesses but the second one can be used for a whole range of movement.

In addition to the time control strategy authors proposed a solution – utilizing commercially available double chamber oleo-pneumatic shock absorbers with modifications – for precise manual control of exoskeleton's supporting force characteristic.

References

[1] Protonex powers Lockheed Martin HULC exoskeleton. (2010). Fuel Cells Bulletin, 2010(2), 4-5.

[2] Ghan, J., Steger, R., & Kazerooni, H. (2006). Control and system identification for the Berkeley lower extremity exoskeleton (BLEEX). Advanced Robotics, 20(9), 989-1014.

[3] Anam, & Al-Jumaily. (2012). Active Exoskeleton Control Systems: State of the Art. Procedia Engineering, 41(C), 988-994.

[4] Borisov, & Rozenblat. (2017). Matrix method of constructing the differential equations of motion of an exoskeleton and its control. Journal of Applied Mathematics and Mechanics, 81(5), 351-359.

[5] Brahmi, Brahim, Saad, Maarouf, Brahmi, Abdelkrim, Luna, Cristobal Ochoa, & Rahman, Mohammad Habibur. (2018). Compliant control for wearable exoskeleton robot based on human inverse kinematics. International Journal of Advanced Robotic Systems, 15(6), International Journal of Advanced Robotic Systems, 22 November 2018, Vol.15(6).

[6] Wu, G., & Zhou, C. (2018). A Sliding Mode Control Algorithm of Improved Reaching Law in Lower Limb Exoskeleton System. Journal of Physics: Conference Series, 1069, 012160.

[7] Long, Y., Du, Z., Chen, C., Wang, W., He, L., Mao, X., . . . Dong, W. (2018). Hybrid Control Scheme of a Hydraulically Actuated Lower Extremity Exoskeleton for Load-Carrying. Journal of Intelligent & Robotic Systems, 91(3-4), 493-500.

[8] Weiguang Huo, S., Mohammed, Amirat, & Kyoungchul Kong. (2018). Fast Gait Mode Detection and Assistive Torque Control of an Exoskeletal Robotic Orthosis for Walking Assistance. IEEE Transactions on Robotics, 34(4), 1035-1052.

[9] Li, Z., Huang, B., Ye, Z., Deng, M., & Yang, C. (2018). Physical Human-Robot Interaction of a Robotic Exoskeleton By Admittance Control. IEEE Transactions on Industrial Electronics, 65(12), 9614-9624.

Adam Zawadzki, D.Eng.: Warsaw University of Technology, Narbutta 84, 02-524 Warsaw, Poland (adam.zawadzki@pw.edu.pl). The author gave a presentation of this paper during one of the conference sessions.

Tomasz Mirosław, D.Eng..: Warsaw University of Technology, Narbutta 84, 02-524 Warsaw, Poland (tomasz.miroslaw@pw.edu.pl).

Jakub Deda, M.Sc. (M.S., D.Eng. student): Warsaw University of Technology, Narbutta 84, 02-524 Warsaw, Poland (jakub.deda@pw.edu.pl).

Zbigniew Żebrowski, Professor: Warsaw University of Technology, Narbutta 84, 02-524 Warsaw, Poland (zbigniew.zebrowski@pw.edu.pl).

Numerical analysis of phase change during solidification

S. Zermout, F. Mokhtari, F.Haddad, A.Merah, I.Lasloudji

Abstract: In this paper, a transient model is used to investigate the evolution of the liquid-solid interface during solidification. Internal radiation in semi-transparent solid is modelled with the discrete ordinates model (DO) and the phase change with the enthalpy method. During crystallization, the maximum convexity of the m-c interface coincides with the development of an angle on the m-c interface near the free surface leading to the appearance of re-melting zone that affects the solid quality and reduces significantly its diameter.

1. Introduction

During solidification, the crucible transfers heat for melting the feedstock. This heat arises from three zones: upper, side and bottom heaters. In order to prevent heat loss from the furnace, insulation shields are surrounding the crucible walls and heaters.

In this work, we propose to use the finite volume method to perform a time-dependant analysis of the solidification interface shape and the crystal length during KY growth process. The formation mechanism of the re-melting zone at the shoulder stage and its effect on crystal quality are discussed.

2. Modelling

The melt is assumed to be laminar incompressible and Newtonian fluid satisfying the Boussinesq approximation. The governing equations can be expressed as follows:

Continuity

$$\nabla . \vec{u} = 0, \text{ (1)}$$

Momentum

$$\rho \frac{\partial \vec{u}}{\partial t} + \rho \vec{u}.\nabla \vec{u} = -\nabla p + \nabla .\left(\mu \left(\nabla \vec{u} \right) \right) + \rho \vec{g} \beta \left(T - T_m \right) \big/ C_p - S_{\vec{u}}, \text{ (2)}$$

Energy

$$\rho C_p \frac{\partial T}{\partial t} + \rho C_p \vec{u}.\nabla T = \nabla .\left(k \nabla T \right) + \nabla .q_{rad} - S_T, \text{ (3)}$$

Where $\vec{u}$, T, P and t are velocity, temperature, pressure and time. ρ, μ, β, C_p, k and $\vec{g}$ representdensity, dynamic viscosity, thermal expansion coefficient, specific heat, thermal conductivity

and gravitational acceleration vector,respectively. $S_{\vec{u}}, S_T$ and $\nabla.\vec{q}_{rad}$ are source terms which will be defined below.

The model adopted for describing the heat transfer in the phase change is based on the enthalpy formulation proposed by V.R.Voller [4-6].

In this approach, the m-c interface is considered to be a porous region having a porosity equal to the liquid fraction f_l.

The term source $S_{\vec{u}}$ is added to the momentum equations: $S_{\vec{u}} = A_{mush}\left(1-f_l\right)\vec{u}$. It serve to block the velocities in solid cells. The mushy zone constant (A_{mush}) is a characteristic constant of the growth interface quantifiying the loss of speed in the zone where the phase change occurs.

During the phase change, the enthalpy method [5,6] takes into account the latent heat of solidification corresponding to the cell temperature that is adjusted to reflect its evolution, this adjustment is included in a source term added to the energy equation. In the case of the growth of a pure material, Brent et al. [6] proposed the following formula for the source term,

$$S_T = \rho.C_p.L\frac{df_l}{dt}, \quad (5)$$

Where L is the latent heat of solidification

To simulate the internal radiation in oxide crystals, several models are used, both the Rosseland approximation [7] and differential approximation P1 [8] are valid for optically thick materials and discrete ordinates method DO [9,10] that gives a relatively high accuracy and low computational cost. In our case, the crystal has an intermediate optical thickness, so the internal radiation is solved with the DO method.

The DO model solves the radiative transfer equation for a finite number of solid angles, each associated with a fixed direction vector in the global cartesian system (x, y and z).

For the semi-transparent solid, radiative heat transfer is evaluated by the divergence of radiation flux defined by Eq. (6) along a particular direction $\vec{s}$:

$$\nabla.\left(I\left(\vec{r},\vec{s}\right)\vec{s}\right)+aI\left(\vec{r},\vec{s}\right)=an^2I_b, \quad (6)$$

Where I is the radiation intensity at position $\vec{r}$ in direction $\vec{s}$, a is the absorption coefficient, n is the refractive index and I_b is the black body intensity given by Planck function. The 4π solid angle domain is divided into10x10 discrete, nonoverlapping solid angles and the partial differential equation for the radiative intensity in the discrete direction spanning the solid angle is obtained in Eq. (7). Consequently, the radiative heat flux $\vec{q}_{rad}$ can be written as follows :

$$\vec{q}_{rad} = \sum_m \omega_m \cdot \left(\vec{\Omega}_m . \vec{n}\right) I_m \ (7)$$

where ω_m is the angular quadrature weight which sums to the surface area of the unit sphere of the unit sphere, I_m is the radiative intensity for the discrete direction $\vec{\Omega}_m$ and $\vec{n}$ is the unite normal vector. Concerning the boundary conditions for radiation intensity, all walls are considered as opaque diffuse-gray boundaries.

3. Results and discussion

During the solidification process, it is very important to follow the evolution of m-c interface because it has a direct impact on the quality of grown crystal.The advancement of the solidification front over time is shown in Fig.1.
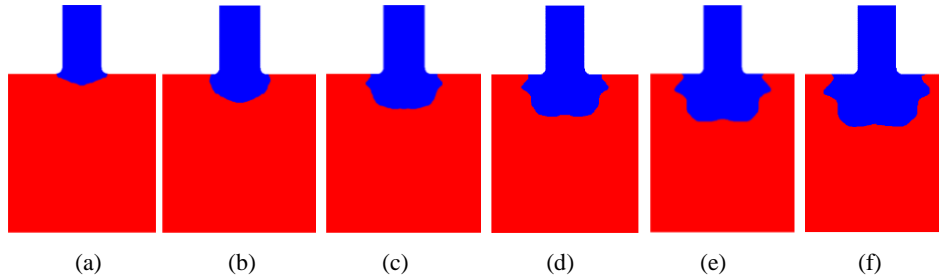
Fig. 1. Evolution of melt-crystal interface shape at different growth stages: Time interval between two successive cases is 2 hours.

The morphology of the m-c interface at the early stageis conical downwards (Fig.1a); the growth occurs in the vertical direction (z).While the crystal advances in the melt during shouldering stage, the interface shape becomes hemispherical (Fig.1b); the growth occurs in the radial direction (r) and vertical direction (z).Fig. 1(c) shows that the interface has lost its hemispherical shape where appears an obtuse angle ($\theta = 96°$) directed towards the side wall of the crucible. This stage of the growth corresponds to a reduction in melt height and thus an increase in crystal length.

Figs.1(d-f) show that θ angle on the m-c interface decreases over time (90°, 81°, 74°) and orients its tip slightly toward the crucible wall up $\theta = 63°$ (Fig.1g).As a result, the origin of the re-melting zones phenomenon and then the irregular ingot shape may be explained by the formation of this angle during the shouldering growth stage. When the remelting-zone occurs excessively, a significant portion of the

ingot has a strong possibility of having microscopic and macroscopic defects that affect the crystal quality and subsequently translate into a loss of mass and energy.

The convexity is one of the most important parameters affecting the crystal quality. Indeed, a small convexity of the m-c interface is required to obtain good quality crystals. The convexity of the m-c interface defined by $C = \max Z_h - \min Z_h$,

Where Z_h is the height of the m-c interface in the z direction.

Fig. 2 shows the evolution of the convexity of the m-c interface over time. During the growth process, one can clearly see that the convexity of m-c interface increases from C = 14 mm to C = 43.27 mm corresponding to conical and hemispherical shape respectively. Then this convexity reaches its maximum value $C_{max} = 87.12$ mm (Fig.2).At this growth stage, m-c interface has a wavy shape which can cause the formation of defects in crystal. Then the convexity decreases significantly until C = 53.63 mm, it continues to decrease until C = 8.53 mm. In this step, convexity remains almost constant then m-c interface shape becomes flat. The convexity increases to C = 25.25 mm corresponding to the presence of fluid stagnation region at the corner of the crucible. During the last growth stages, the interface convexity decreases gradually until its suppression where the liquid portion was completely transformed into crystal.
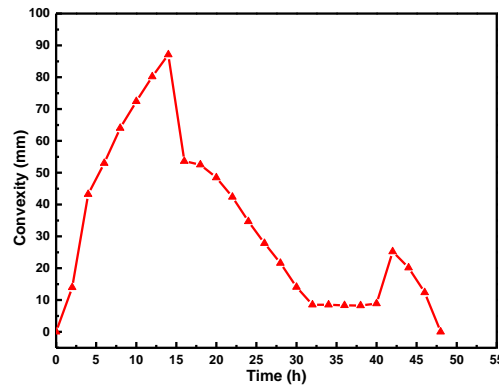
Fig. 2. The convexity of m-c interface vs time during the whole growth process.

Crystal length evolution over time

Fig. 3 presents the crystal length evolution over time. We can see that the growth process can be divided into three zones A, B and C following the different curve slopes. Zone A corresponds to the Shouldering growth stage where the crystal length increases rapidly. At the atomic scale, such growth rate could prevent the atoms to reorganize in ordered atomic lattice. This causes dislocations in the

crystal inducing then a poor crystal quality. However, a break of slope is detected to go from zone (A) to zone B so-called equal diameter stage where the crystal grows in radial and vertical directions.
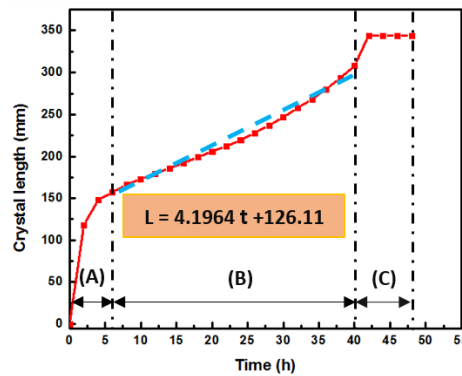
It is found that the length of the crystal increases linearly up to H = 308 mm following the formula: H = 4.1964 t + 126.11 with slight growth rate dH/dt = 4.19 mm/h allowing the atoms to arrange regularly following well-defined crystalline lattice.and therefore this stage of growth is characterized by less defects. In the last growth stage corresponding to the zone C, a linear increase in length was registered before it approaches the crucible bottom. At the ending growth, the resulting ingot is about 344 mm.

4. Conclusions

(1) Convexity of the m-c interface has a significant impact on crystal quality and seems an essential parameter in view of the interesting information it provides. This interface takes a conical and hemispherical shape at the early growth stages then an irregular shape at the shoulder stage. The gradual decrease of the convexity leads to a flat interface.

(2) Angle appearance on the m-c interface causes the development of a wavy interface shape and leads to re-melting zone.

(3) Due to the large growth rate and angle formation at the first stage of the growth process, defects in crystal are higher. The numerical simulation results show that more than 45% of crystal was grown with average rate about 4.19 mm/h.

References

[1]Demina, S.E., Bystrova, E.N., Lukanina, M.A., Mamedov, V.M., Yuferez, V.S., Eskov, E.V., Nikolenko M.V., Postolov V.S., Kalaev V.V., Opt. Mater. 30 (2007) 62-65.

[2] Fang, H. S., Wang, S., Jin Z. L., Tian, J., and Xu, J. F., Cryst. Res. Technol. 48, No. 9, (2013) 649–657.

[2] Chen, C., Chen, H.J., Yan, W.B., Min, C.H., Yu, H.Q., Wang, Y.M., Cheng, P., Liu, C.C., J. Cryst. Growth.388 (2014)29–34.

[3] Fang, H.S., Jin, Z.L., Zhang, M.J., Zhang, Z., Zhao C.J., Int. J. Heat Mass Transfer.67 (2013) 967–973.

[4] Voller, V.R., Journal of Numerical Analysis. Vol 5, 201–214 (1985).

[5] Voller, V.R., Prakash, C., Int. J. Heat Mass Transfer. Vol.30 No 8 (1987) pp1709-1719.

[6] Brent, A.D., Voller, V.R., Reid, K.J., Numerical Heat Transfer. Vol.13 (1988) pp297-318.

[7] Vizman, D., Nicoara, I., Müller, G., J. Cryst. Growth.212 (2000) 334–339.

[8] Lan, C.W., Tu, C.Y., Lee, Y.F., Int. J. Heat Mass Transfer. 46 (2003) 1629–1640.

[9] Lee, W.J., Y.C. Lee, H.H. Jo, Y.H. Park, J. Cryst. Growth.324 (2011) 248–254.

[10] Chandrasekhar, S., Radiative Transfer, Dover Publications. London, 1960.

Samir Zermout, PhD, University Mouloud Mammeri of Tizi Ouzou, Algeria

Faiza Mokhtari, PhD, University of Science and Technology Houari Boumediene. BP 32 Elalia, Bab Ezzouar, Algiers, Algeria (email: faiza_mokhtari@yahoo.fr). The author gave a presentation of this paper during one of the conference sessions.

Fadila Haddad, PhD, University of Science and Technology Houari Boumediene. BP 32 Elalia, Bab Ezzouar, Algiers, Algeria

Abdelkrim Merah, PhD, University M'hammed Bougara of Boumerdes UMBB, Boumerdes, Algeria

Idir Lasloudji, PhD, University of Science and Technology Houari Boumediene. BP 32 Elalia, Bab Ezzouar, Algiers, Algeria

Synchronicity phenomenon of circular cylindrical shell under random excitation

Antonio Zippo, Francesco Pellicano, Giovanni Iarriccio

Abstract: In the present paper is deeply described an experimental campaign focused on the random vibrations of circular cylindrical shells under thermal gradients across the shell thickness and broadband random loading. Many engineering fields are involved in this subject and in real environments, the excitations are likely non-deterministic, moreover, extreme thermal conditions can cause differences of the temperature inside and outside the shell, as in thermal ex-changers. Due to the importance of the subject the literature on shell vibration is extremely wide, it is not analyzed here for the sake of brevity; however, it is to note that the number of papers containing experimental results is not large. Under a random forcing, a system generally expects a random response, however, in some particular conditions (e.g. internal resonances, parametric resonances, ...) the presence of nonlinearity in the systems can give rise to a surprising phenomenon: the synchronization of non-linear oscillators subjected to random forcing that has been partially studied in the literature for its remarkable characteristic of conveying the spectral energy of a random forcing over specific frequencies. This work takes advantage of previous setup and experimental techniques developed by the present research team. The phenomenon of synchronicity is clearly observed for some particular thermal conditions: a strong transfer of energy from a broadband excitation signal to an almost harmonic response is experimentally observed.

1. Introduction

Thin walled structures have a central function in several engineering fields from aerospace to civil and automotive, for example storage tower, bodywork panels, fuselage or aircraft and satellite panels.

A critical circumstance in thin structures, of significant attention for many engineering fields, is the performance of these structures subjected to random forcing whose dynamics, characterized by strong non-linearity, leads to the rise of complex phenomena that cannot be predicted with current design tools, as finite element modeling. It is well known that when a chain of non-linear oscillators, used to model physical or biological structures, is subjected to intense periodic forcing, could presents a "mode-locking" phenomenon that synchronizes the forcing load with the system response.

A similar phenomenon, but much less known and studied, can occur in the case of broadband random forcing [1] if certain conditions occurs of internal resonance the random motions are found to be quasi-stationary, with steady oscillatory terms in the response moments. This suggests the possibility of entrainment of regular harmonic responses by the system.

This phenomenon, called synchronization of non-linear oscillators subjected to random forcing [2,7], has been partially studied in the literature for its remarkable characteristic of conveying the spectral energy of a random forcing over specific frequencies, determining remarkable vibration amplitudes: Jansen et alt. showed that a single, nonresonant periodic forcing is insufficient to activate the mode-locking phenomenon, but the supplement of a reasonable quantity of broadband noise allows transient mode-locking to the original periodic drive to occur.

In literature could be found some experimental studies on thin structures like circular cylindrical shells, that presents often a strong nonlinear dynamic behavior, that leads designers and engineers to deal with it conditions to be able to forecast as accurate as possible the structure response due to external loadings, in [3] Zippo et. alt studied experimentally the behavior of the response of a thin circular cylindrical shell, it was shown that in tests performed with a sinusoidal axial forcing load clarify the role of the preload in enlarging the instability regions and the coexistence of more than one stable states when the shell is pre-loaded and excited with a moderately large sinusoidal excitation: the dynamic scenario is completely different if the frequency step is reduced from 1 Hz to 0.1 Hz.

In a study published on Nonlinear Dynamics [4] is shown that the effect of temperature strongly affects the instability regions and the magnitude of the measured kinematic quantity and has been pointed out that high environmental temperature leads to a more complex shell dynamic, also in other fields novel techniques [5] are useful to identify intricate behaviors of complex systems that lead to unpredictable circumstances of systems under different conditions, one of this condition that could certainly be critical is the occurrence of thermal gradients.

The possible condition of critical temperature and thermal gradients through the thickness of shells lead to a change in the mechanical properties of the structure with a consequent complexity in predicting the behavior of the structures; from a deep analysis of the scientific literature it is possible to observe that there is a gap in the experimental studies and in the dynamic vibrational modeling of thin walled structures subject to strong thermal gradients, which presents only a few publications in this field: the effect of temperature has been deeply studied in [6] where is clarified the role of thermal gradients, in particular the damping and stiffness properties of the shell shown a complex behavior that imply that using linear modelling could underestimate the dynamic response of the structure, in contrast only theoretical studies are present about the mechanism that induce an energy transfer, under noise or random loading, to other modes of a structure.

Similar studies involve the synchronization of chaos [8] referred to a process in which several chaotic systems adapt a certain property of their dynamics to a common behavior due to a coupling or a periodic or random forcing and analytical and numerical work [9] has been presented showing the synchronization induced by noise in chaotic systems. Cicek and Ertas [10] conducted a sets of experiments on a beam tip mass and pendulum system subjected to random excitation to determine the autoparametric interaction between the two modes of the system in the neighborhood of the autoparametric region, in particular the response behaves as ultra-narrowband process in the neighborhood of exact internal resonance that converge into a periodic response. Some experimental studies on very simple systems can be found in the literature, Ibrahim [11] presented a review article on experimental investigations of random excitation of dynamic systems; A study carried out [12] by Roberts presents an analytical and experimental comparison with the broad band random excitation of a two degree of freedom vibratory system with non-linear coupling of autoparametric type which consists of a cantilever beam with at tip clamped another cantilever beam; attached to a primary vibratory system in such a way that response of the primary system imposes an axial motion on the cantilever. The system is a common structural arrangement, representing the fuselage-tail plane coupling in aircraft structures.

2. Setup

In the present work a random broadband loading has been applied at the base of a circular cylindrical shell with a top disk fixed at a electrodynamic shaker: the role of the disk is to impose a rigid body displacement at the top end of the shell and to exert an inertial axial load to the shell when a motion is imposed.

The shell under investigation has been 3d printed to avoid any geometrical imperfection and to allow the repeatability of the experimental campaign without geometrical errors: the specimen is made of Polyethylene terephthalate (P.E.T.) a thermoplastic polymer. The cylindrical sample present at the top end a rigid thick disk (the top disk) glued with special epoxy glue, resistant to high temperature, and its base is clamped to the fixture by means of a shaft collar that guarantees a uniform connection to the vibration table adapter.

In Table 1 are reported the geometrical and material parameters of the shell and the material properties of the fixture and top disk.

The system description is completed by Figure 1 where a schematic representation of the system is shown: an accelerometer is located on the fixture, such accelerometer is used by the control system of the shaker when a closed loop strategy is selected, three triaxial accelerometers are located equally spaced on the top disk, they are used to measure all the six dofs of the rigid body, this allows to detect axisymmetric modes, asymmetric modes, beam-like modes and torsional modes.

Inside the shell a cartridge heater is present and is used to modify the temperature inside the shell and to create a thermal gradient across the shell wall, see figure 2; the specimen under investigation is mounted on a Es40 Dongling shaker coupled with a climate chamber that allow to set the outer temperature of the shell and hold it constant. The temperature ranges of the climate chamber are -70°C up to +180°C; the climate chamber is provided by an inspection hole from witch a laser vibrometer beam go through and is deflect by a mirror periscope to measure the velocity of a lateral point located on the opposite side respect to the hole, yellow circle in figure 2. Two thermocouples are used to measure the temperature, inside and outside the shell. Moreover, a laser telemeter measures the displacement of a point, green circle in figure 2, of the shell out of phase of about 135° respect to the vibrometer measurement point.
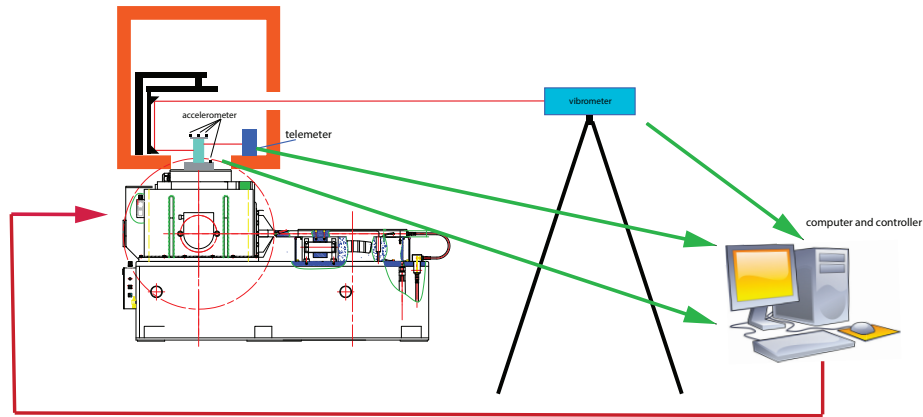
Figure 1. schematic view of experimental setup

Table 1. Geometrical and material parameters of the shell, the fixture and top disk

Fixture and Top disk		
Material	Aluminium Alloy	
General	Mass Density	2700 kg/m^3
Stress	Young's Modulus	68.9 GPa
	Poisson's Ratio	0.33
Shell		

Material	P.E.T.	
General	Mass Density	1366 kg/m^3
Stress	Young's Modulus	3.05 GPa at 30°C
	Poisson's Ratio	0.417
Dimension	Diameter	80 mm
	Thickness	0.35 mm
	Height	160 mm
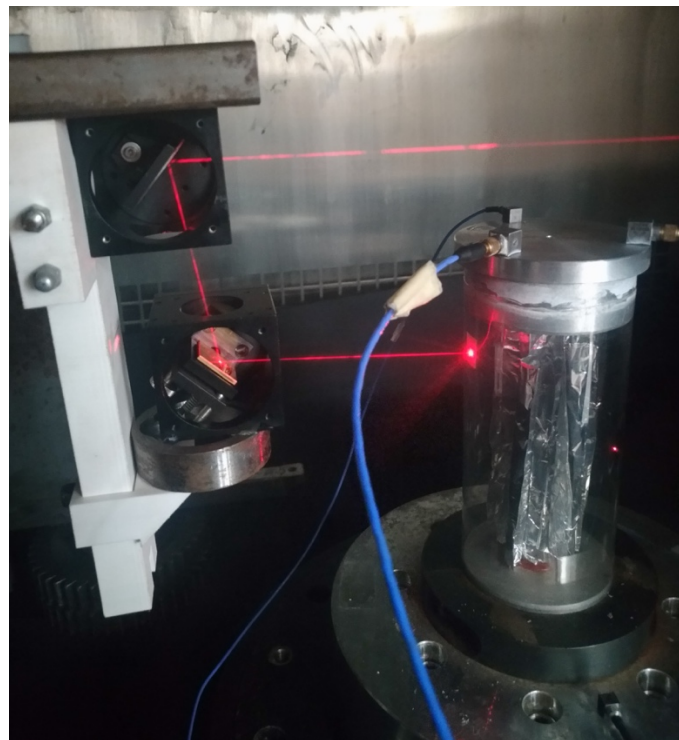
Figure 2. Picture of the specimen inside the climate chamber, highlighted the vibrometer spot light (yellow circle) and telemeter (green circle)

The experimental test campaign consists of a random forcing load applied through the electrodynamic shaker at the specimen, the Siemens LMS Scadas mobile has been used to generate a random signal that is controlled by means of the accelerometer placed at the base of the shell, for each test different increasing rms amplitude levels have been applied consecutively.

On the first, temperature is set for the climatic chamber and an adequate amount of time has been waited to stabilize the external temperature for about 1 hour, after the inner temperature is raised slowly to reach the desired gradient, the system is left for another hour to reach a thermic stability.

When the temperature is stable a forcing random load is applied together with the thermal gradient across the shell thickness; such gradient will induce a continuous variation of elastic and dissipative properties through the thickness of the shell.

The test campaigns were carried out at different level of rms amplitude and at different bandwidth, in figure 3 is shown the experimental measured controlled base acceleration of one of the test.

Afterwards, data was saved and imported into MATLAB where each level was analyzed computing spectrum, power spectral density, and spectrogram.

Several tests have been performed changing the temperature parameter, inside and outside the shell, testing homogenous temperature and gradients and different frequency broadband at different amplitudes.
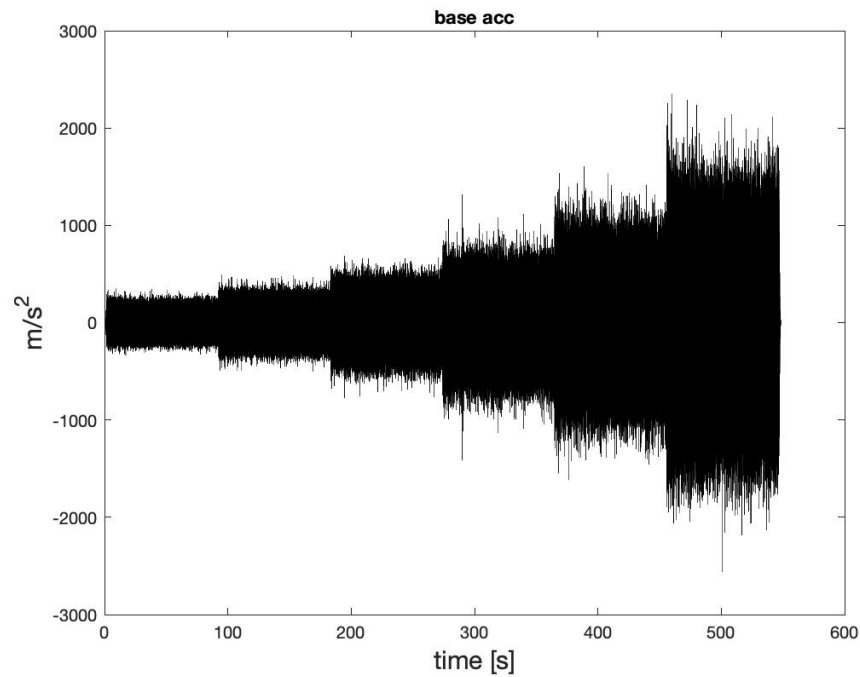
Figure 3. time history of base acceleration, test case 24°C outer temperature - 74°C inner temperature

3. RESULTS

In linear condition as homogenous temperature at 20°C and with a bandwidth of random signal between 50 hz and 2000hz what ones can normally expect is that the system response is linear and is amplified

due to the first axial-symmetric mode at about 467hz, in figure 4 is shown the random forcing load at the base of the shell with a flat PSD, and in figure 5 the linear response of the structure with his natural amplification due to the resonance at 467Hz.
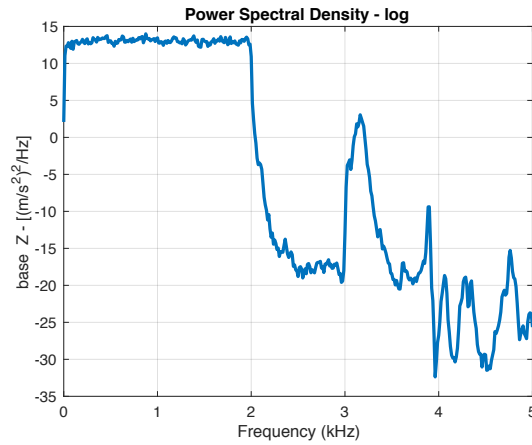
Figure 4. PSD of driven base forcing load, random broadband between 50Hz and 2000Hz
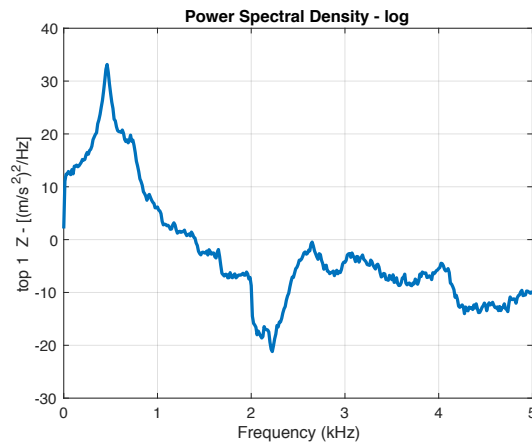
Figure 5. PSD of top acceleration response

The scenario changes considerably in particular condition of thermal gradient and frequency forcing band: to sake of brevity only one test case will be shown in the following paragraph: a broadband random signal between 900 Hz and 1500 Hz has been applied at the specimen with a 28°C thermal gradient from 48°C in the inner surface and 20°C in the outer surface. In figures from 6 to 9 is shown the Power Spectral Density of, respectively, the base acceleration, top acceleration, lateral displacement and lateral velocity; it is clearly visible that respect to the uniform frequency band of the

base, the top acceleration and the lateral vibration of the shell show an energy transfer in particular to the first axial-symmetric mode at 467Hz,
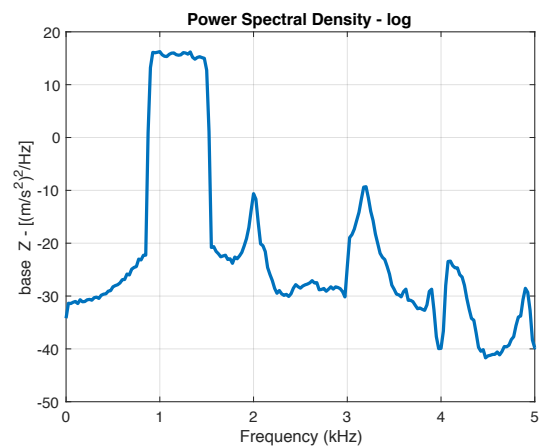
Figure 6. PSD of random forcing load
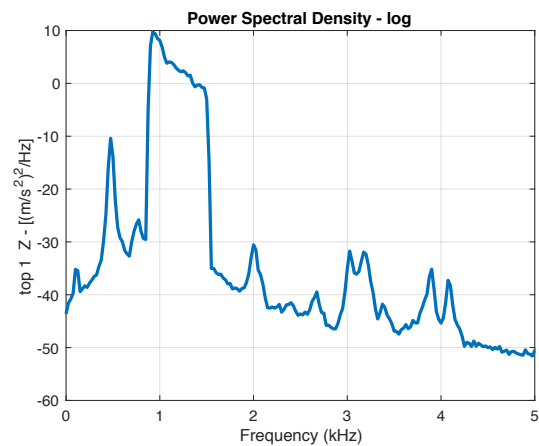
Figure 7. PSD of response of top acceleration
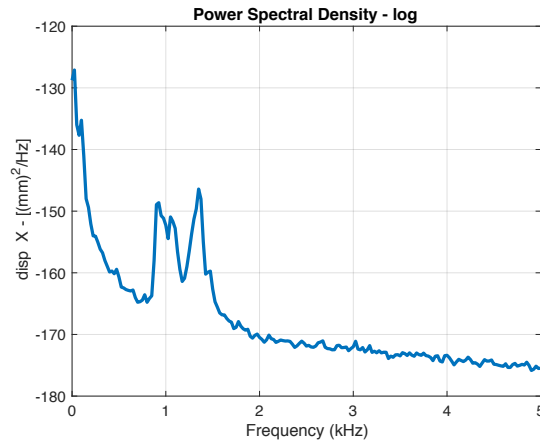
Figure 8. PSD of lateral displacement
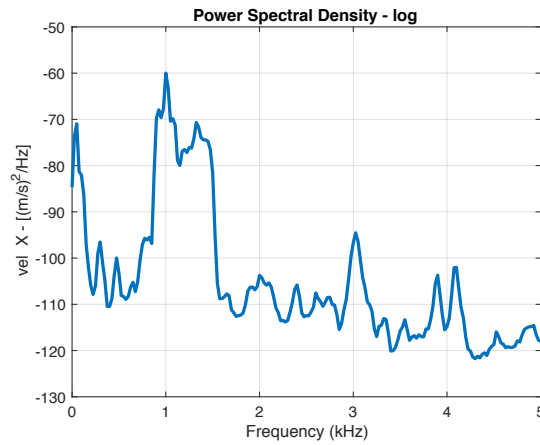
Figure 9. PSD of lateral velocity

4.   Conclusions

In the presented experimental study, a thin cylindrical shell has been driven with a random base excitation and the response has been analyzed, the excitation is random with a flat spectrum between 900 Hz and 1500Hz. In the response is present an energy transfer to the first axial symmetric mode, that is 450Hz far from the excitation band, and this phenomena is more visible in the top acceleration response, respect to the lateral vibration, that however show an articulated spectrum, more complex respect to the flat spectrum of the base acceleration.

5. References

[1] Ibrahim R. A. and Roberts J. W., Broad Band Random Excitation of a two-degree-of-freedom autoparametric coupling, J. of Sound and Vibration 44(3), 335-348 (1976). https://doi.org/10.1016/0022-460X(76)90506-X.

[2] Jensen, R.V. , Synchronization of randomly driven nonlinear oscillators (1998) Physical Review E - Statistical Physics, Plasmas, Fluids, and Related Interdisciplinary Topics, 58 (6), pp. R6907-R6910. DOI: 10.1103/PhysRevE.58.R6907

[3] Zippo, A., Barbieri, M., Pellicano, F., "Experimental analysis of pre-compressed circular cylindrical shell under axial harmonic load" (2017) International Journal of Non-Linear Mechanics, 94, pp. 417-440. DOI: 10.1016/j.ijnonlinmec.2016.11.004

[4] Zippo, A., Barbieri, M., Iarriccio, G., Pellicano F., Nonlinear vibrations of circular cylindrical shells with thermal effects: an experimental study, Nonlinear Dynamics, (in press) (2019). https://doi.org/10.1007/s11071-018-04753-1.

[5] Gelman, L., Harish Chandra, N., Kurosz, R., Pellicano, F., Barbieri, M., Zippo, A., Novel spectral kurtosis technology for adaptive vibration condition monitoring of multi-stage gearboxes, Insight: Non-Destructive Testing and Condition Monitoring, 58 (8), pp. 409-416 (2016), DOI: 10.1784/insi.2016.58.8.409.

[6] Zippo, A., Barbieri, M., Pellicano, F. Temperature gradient effect on dynamic properties of a polymeric circular cylindrical shell (2019) Composite Structures, 216, pp. 301-314. DOI: 10.1016/j.compstruct.2019.02.098

[7] Jensen, R.V. Synchronization of driven nonlinear oscillators (2002) American Journal of Physics, 70 (6), pp. 607-619. DOI: 10.1119/1.1467909

[8] Boccaletti, S., Kurths, J., Osipov, G., Valladares, D.L., Zhou, C.S. The synchronization of chaotic systems (2002) Physics Report, 366 (1-2), pp. 1-101. DOI: 10.1016/S0370-1573(02)00137-0

[9] Toral, R., Mirasso, C.R., Hernández-García, E., Piro, O. Analytical and numerical studies of noise-induced synchronization of chaotic systems (2001) Chaos, 11 (3), pp. 665-673. DOI: 10.1063/1.1386397

[10] I. Cicek, A. Ertas, Experimental investigation of beam-tip mass and pendulum system under random excitation, Mechanical Systems and Signal Processing, Volume 16, Issue 6, (2002) Pages 1059-1072, ISSN 0888-3270, https://doi.org/10.1006/mssp.2001.1475.

[11] Ibrahim RA. Nonlinear Random Vibration: Experimental Results. ASME. Appl. Mech. Rev. 1991;44(10):423-446. doi:10.1115/1.3119487.

[12] J.W. Roberts, Random excitation of a vibratory system with autoparametric interaction, Journal of Sound and Vibration, Volume 69, Issue 1, (1980), Pages 101-116, ISSN 0022-460X, https://doi.org/10.1016/0022-460X(80)90437-X.

Antonio Zippo, Ph.D.: DIEF, Università di Modena e Reggio Emilia, Dipartimento di Ingegneria "Enzo Ferrari", Via Pietro Vivarelli 10, 41125, modena, Italy (IT), (antonio.zippo@unimore.it)

Francesco Pellicano, Full Professor: DIEF, Università di Modena e Reggio Emilia, Dipartimento di Ingegneria "Enzo Ferrari", Via Pietro Vivarelli, 10 - 41125 Modena, Italy (IT), (frank@unimore.it)

Giovanni Iarriccio, M.Sc. (Ph.D. student): DIEF, Università di Modena e Reggio Emilia, Dipartimento di Ingegneria "Enzo Ferrari", Via Pietro Vivarelli 10, 41125 Modena, Italy (IT), (Giovanni.Iarriccio@unimore.it)

Non-smooth nonlinear model of suspension based on piecewise linear luz(…) and tar(…) projections

Dariusz Żardecki

Abstract: Strong nonlinear phenomena are attributes of suspension systems of vehicles operated at high dynamic loads and high speeds. The causes of these phenomena are dry friction and clearance in the mechanisms, detachment of the wheel from the roadway, impact on the bumper element, etc. Therefore detailed descriptions of vehicle "vertical dynamics" should express these non-smooth nonlinearities, even their structural physical models are discrete mechanical systems with only several masses. Modeling of strong nonlinear phenomena can be based on a piecewise linear approach. For simplification mathematical description of such phenomena special piecewise linear luz(…) and tar(…) projections have been proposed and elaborated by Żardecki. These projections have surprisingly simple mathematical apparatus which enable analytical operations (eg. reductions) for differential and algebraic equations and inclusions with non-smooth nonlinearities and simplify numerical simulations. Applications of this method due to modeling of car steering systems with inclusion freeplay and stick-slip processes have been reported in several authors' papers. This paper presents examples due to suspension systems.

1. Introduction

Non-smooth nonlinearities apply to processes characterized by abruptly changing properties. In mechanical systems this is primarily due to the occurrence of backlash, dry friction and collisions. A rapid change in the mechanical structure of the object may be the reason for its peculiar behavior - non-linear vibrations, motion instability, etc. [2], which is also observed in road vehicles [1]. In the case of modeling the "vertical dynamics" of the car, the non-smooth nonlinearities result from dry friction and clearance in the suspension mechanisms, the action of active elements according to the sky-hook principle, detachment of the wheel from the roadway, impact on the bumper element, etc. They can manifest themselves both in the case of small interactions (e.g. in stick-slip processes) and large ones (e.g. in the operation of the stopper). Meanwhile, the analysis of numerous publications on the vertical dynamics of vehicles, in particular "state-of-the-art" papers [3], [8] indicate that non-smooth nonlinearities in mathematical models of suspension systems are considered quite rarely. Such models appear only in studies on suspension systems treated as Multi Body Systems (MBS). The analysis of publications shows that in the design of modern – semi-active and active suspension systems, very simplified "quarter car" models describing vibrations in a one-wheel independent suspension system modeled as a dual-mass linear system are adopted as control objects. The quarter car suspension models

are a very important category of models used by researchers and engineers in the description of the vehicle vertical dynamics (see review paper [5]). It seems that in the era of interest in such models it is worth undertaking research on quarter models considering non-smooth nonlinearities.

Modeling and simulation of processes with non-smooth nonlinearities are generally quite difficult problems. Models of such processes are differential inclusions or equations with a variable structure with algebraic constraints, which is dramatically complicate, and thus lengthen simulation calculations. The method of solving Linear Complementary Problems (LCP) [7], or the formalism of so-called differential sequences [4] are used in simulation (but only off-line). However, the challenge remains real-time simulation (on-line), which requires simple, and therefore without complications, dynamic models. The method of modeling and simulation of systems dynamics with non-smooth nonlinearities developed by Żardecki (descriptions, among others, in [9], [10], [11]) using special piecewise linear luz(...) and tar (...) projections and their original mathematical apparatus seems to be an attractive research tool for simplification complicated models and simulation procedures. The method has already been used in several of works (e.g [6]), especially in analysis of the car lateral dynamics (taking into account the backlash in the gear box and dry friction in the king-pins of the steering system). This paper presents the method of usage piecewise linear luz(...) and tar(...) projections in modeling the dynamics of a one-wheel suspension system, and then of a MBS-type subsystem

2. Piecewise linear luz(…) and tar(…) projections

General theory of piecewise linear systems refers to modeling, static and dynamic analysis, numerical procedures, and so on. In the beginning (second half of the 20th century) this theory has been worked up together with the non-linear theory of electrical circuits, non-linear control theory, as well as non-linear multibody systems. This theory is based on piecewise linear models which are created by linear combinations of piecewise linear elementary functions, pseudofunctions as well as inclusions. Special piecewise linear projections can be built for specific applications. Piecewise linear luz(…) and tar(…) projections with their surprisingly simple mathematical apparatus have been elaborated especially for description contact mechanics in multibody systems.

The piecewise linear luz(…) and tar(…) projections are defined as following:

$$luz(x,a) = x + \frac{|x-a|-|x+a|}{2} \qquad\qquad tar(x,a) = x + a \cdot s^* \qquad\qquad (1), (2)$$

$$\text{where } s^* \in [-1,1], a \geq 0.$$

Note, that these projections are like inverse functions (see fig.1)
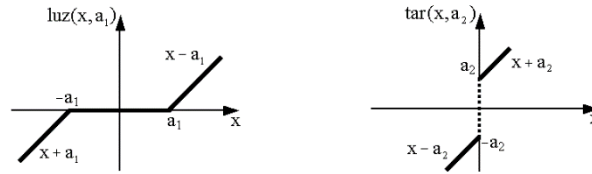
Figure 1. Topological interpretation of luz(…) and tar(…) projections

The luz(...) and tar(...) projections have surprisingly simple properties. Their formulas compose some mathematical apparatus. Here only example formulas are shown. Constants a, k,... appearing in the formulas are non-negative.

$$k \cdot luz(x, a) = luz(k \cdot x, k \cdot a) \tag{3}$$

$$k \cdot tar(x, a) = tar(k \cdot x, k \cdot a) \tag{4}$$

$$k_1 \cdot tar(x, a_1) + k_2 \cdot tar(x, a_2) = (k_1 + k_2) \cdot tar\left(x, \frac{k_1 \cdot a_1 + k_2 \cdot a_2}{k_1 + k_2}\right) \tag{5}$$

If $luz(y, b) = k \cdot luz(x - y, a)$ then $luz(y, b) = \frac{k}{k+1} \cdot luz(x, a + b)$ \tag{6}

Note: For a linear system $(a = b = 0)$ it means the well known dependence $y = \frac{k}{k+1} \cdot x$

If $\varepsilon \cdot \dot{x}(t) \in y(t) - b \cdot tar(x(t), a)$ and $\varepsilon \to 0$ then $x(t) = luz\left(\frac{y(t)}{b}, a\right)$ \tag{7}

Extensive lists of mathematical theorems (with proofs) are described in the Żardecki's papers.

The luz(…) and tar(…) projection can be used as basic projection for description different piecewise linear characteristics. More complicate dependences can be expressed also by projections' series. Examples of such typical characteristics are presented (fig.2).
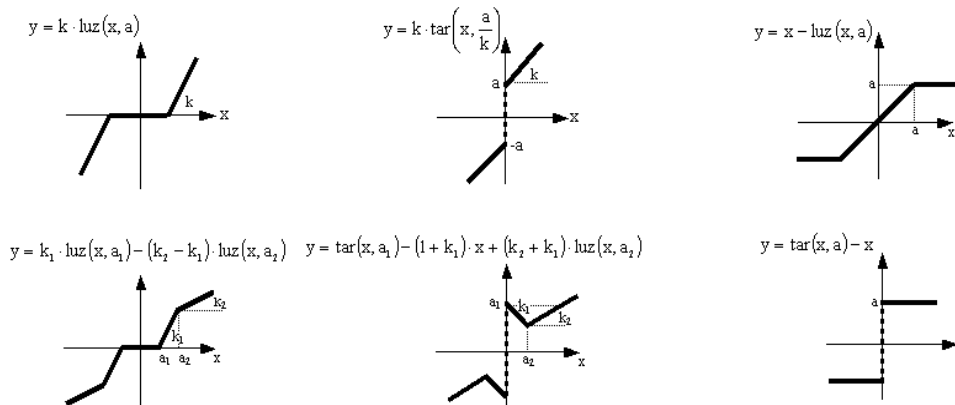
Figure 2. Examples of piecewise linear characteristics basing on luz(…) or/and tar(…)

These examples concern characteristics with symmetry in relation to the point (0,0). When the symmetry deals with the shifted point the well-known rules of description of function with deflexed arguments should be applied. When characteristics has not any symmetries it can be treated as a part of full symmetrical characteristics having large deflection parameter. Description of non-linear characteristics with using the luz(…) and tar(…) projections depends on researcher's inventions. Representative example of application luz(…) and tar(…) in description of piecewise linear characteristics is presented in p.3.

The formulas of mathematical apparatus simplify analytic operations concerning piecewise linear models expressed by differential equations and inclusions with constrains. This is important for simulation studies especially when analytic transformations give the model without implicit forms. Application of ready-to-use formulas of the luz(...) and tar(...) apparatus in a formal synthesis of such models has appeared very useful and efficient. This is presented in p.4.

3. Example 1 - Modeling of quarter-car suspension system

A simplified model presented in this paper concerns an independent suspension system of a passenger car driving with constant speed on a straight uneven road. The substitute mechanical scheme of the system (fig.3) includes the most important suspension and tire attributes related to the description of vertical movement dynamics, i.e. piecewise linear suspension elasticity (including limiter action), viscous friction (damping) and dry friction in the shock absorber, as well as piecewise linear elasticity in the tire – road interactions, taking into account wheel detachment from the road surface (more detailed description of tire motion is not analyzed).
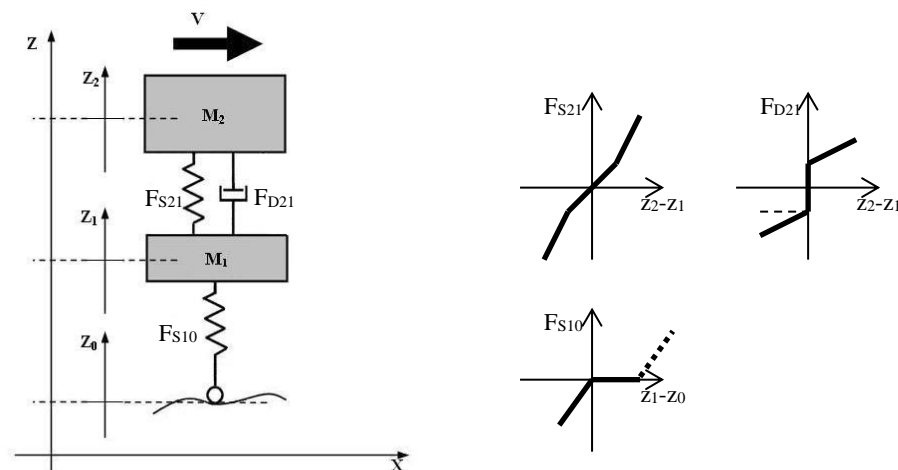
Figure 3. Substitute mechanical scheme of suspension system with piecewise liner spring and dissipative characteristics

Notation:

t - time

(0XZ) – global coordinate system

$Z_0(t)$ - road profile as a function of time

$Z_1(t)$ - vertical displacement of the wheel center

$Z_2(t)$ - vertical displacement of the sprung mass

ΔZ_{21L} - maximum deformation of the suspension system without limiter's action

K_{10} - stiffness coefficient of the tire

K_{21} - stiffness coefficient of the suspension

K_{21L} - stiffness coefficient of the suspension with limiter's action

C_{21} - damping coefficient of the shock absorber

F_{D210} - maximum dry friction (we assume the same values for static and kinetic dry friction)

M_1 - unspring mass (of the wheel)

M_2 - sprung mass (of the quarter car body)

g – gravitation acceleration

Piecewise linear characteristics of spring and dissipative elements presented in fig. 1 can be described with using luz(…) and tar(…) projections, as follow:

$$F_{S21}(z_2 - z_1) = K_{21}(z_2 - z_1) + (K_{21L} - K_{21})luz(z_2 - z_1), \Delta z_{21L}) \tag{8}$$

$$F_{S10}(z_1 - z_0) = K_{10}luz(z_1 - z_0 - a, a) \qquad a >> 0 \tag{9}$$

Note: Wheel detachment from the road surface means that in such state the force should be equal zero. This is described by specific characteristics type of kluz(x-a, a), where shift parameter a has a "big" value due to x.

$$F_{D21}(\dot{z}_1 - \dot{z}_2) = C_{21}tar\left((\dot{z}_1 - \dot{z}_2), \frac{F_{D210}}{C_{21}}\right) \tag{10}$$

Initial mathematical model describing motions in local coordinates is done by two differential inclusions (inclusions because of the dry friction action):

$$M_1\ddot{z}_1(t) + C_{21}tar\left((\dot{z}_1(t) - \dot{z}_2(t)), \frac{F_{D210}}{C_{21}}\right) + K_{21}(z_1(t) - z_2(t)) +$$
$$+ (K_{21L} - K_{21})luz(z_1(t) - z_2(t), \Delta z_{21L}) + K_{10}luz(z_1(t) - z_0(t) - a, a) + M_1g \in 0 \tag{11}$$

$$M_2\ddot{z}_2(t) + C_{21}tar\left((\dot{z}_2(t) - \dot{z}_1(t)), \frac{F_{D210}}{C_{21}}\right) + K_{21}(z_2(t) - z_1(t)) +$$
$$+ (K_{21L} - K_{21})luz(z_2(t) - z_1(t), \Delta z_{21L}) + M_2g \in 0 \tag{12}$$

Using methodology presented in [11], these differential inclusions create the model in differential equation form (here with variable structure).

$$M_1\ddot{z}_1(t) = \begin{cases} -F_{D210}\,sgn(\dot{z}_1(t) - \dot{z}_2(t)) + F_1(t) & if \quad \dot{z}_1(t) \neq \dot{z}_2(t) \\ \frac{M_1(F_1(t)+F_2(t))}{M_1+M_2} + luz\left(\frac{M_2F_1(t)-M_1F_2(t)}{M_1+M_2}, F_{D210}\right) & if \quad \dot{z}_1(t) = \dot{z}_2(t) \end{cases} \tag{13}$$

$$M_2\ddot{z}_2(t) = \begin{cases} F_{D210}\,sgn(\dot{z}_1(t) - \dot{z}_2(t)) + F_2(t) & if \quad \dot{z}_1(t) \neq \dot{z}_2(t) \\ \frac{M_2(F_1(t)+F_2(t))}{M_1+M_2} - luz\left(\frac{M_2F_1(t)-M_1F_2(t)}{M_1+M_2}, F_{D210}\right) & if \quad \dot{z}_1(t) = \dot{z}_2(t) \end{cases} \tag{14}$$

where:

$$F_1(t) = -C_{21}(\dot{z}_1(t) - \dot{z}_2(t)) - K_{21}(z_1(t) - z_2(t)) +$$
$$- (K_{21L} - K_{21})luz((z_1(t) - z_2(t)), \Delta z_{21L}) - K_{10}luz(z_1(t) - z_0(t) - a, a) - M_1 g \tag{15}$$

$$F_2(t) = -F_1(t) + K_{10}luz(z_1(t) - z_0(t) - a, a) + M_1 g - M_2 g \tag{16}$$

In the case of small road unnevennesses, the model non-linearities relate practically only to the friction description. When dry fiction effects are neglected the piecewise linear model taking into account also for big unevennesses is as follow:

$$M_1\ddot{z}_1(t) + C_{21}(\dot{z}_1(t) - \dot{z}_2(t)) + K_{21}(z_1(t) - z_2(t)) + (K_{21L} - K_{21})luz(z_1(t) - z_2(t), \Delta z_{21L}$$
$$+ K_{10}luz(z_1(t) - z_0(t) - a, a) + M_1 g = 0 \tag{17}$$

$$M_2\ddot{z}_2(t) + C_{21}(\dot{z}_2(t) - \dot{z}_1(t)) + K_{21}(z_2(t) - z_1(t)) +$$
$$+ (K_{21L} - K_{21})luz(z_2(t) - z_1(t), \Delta z_{21L}) + M_2 g = 0 \tag{18}$$

The time course of the road profile is an excitation in the model. With the given profile $z_0(x(t))$, an appropriate transformation of the variables should be performed. When the vehicle is traveling at a constant speed V, then $z_0(x(t)) = z_0(Vt)$, which means that the parameter V is a time scaling factor. For a random, polyharmonic or sinusoidal course of variable $z_0(Vt)$), one obtains a slow-changing waveform - for small speeds, and a fast-changing waveform - for large speeds. In a similar way, we can treat input signal constituting by half of sinusoid period (mapping of a single hummock). As the speed increases, the excitation takes the shape of a single pulse.

4. Example 2 - Modeling of MBS-type suspension subsystem

The luz(…) and tar(…) mathematical apparatus is very useful in formal synthesis MBS-type non-smooth systems. Representative example expressing the method of modeling corresponds with models of suspension system having clearances and limiters of the movements.

This system (fig.4) is a combination of four solid elements through elastic elements. There is a clearance between elements 2 and 3. Solid elements 2 and 3 have very low masses. The stiffness between elements 2 and 3 is very high. We will assume that dynamic excitations are small enough to justify not including plastic collisions in the physical model.
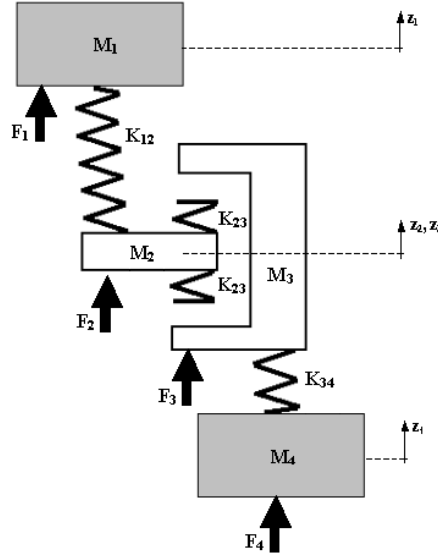
Figure 4. Substitute mechanical scheme of MBS-type suspension subsystem

Notation and assumptions:

z_1, z_2, z_3, z_4 – replacements of solid elements,

F_2, F_2, F_3, F_4 – external forces; we will assume that $F_2 = 0, F_3 = 0$,

t – time,

M_1, M_2, M_3, M_4 – masses, $M_1, M_4 \gg M_2, M_3$; we will assume that $M_2 = 0, M_3 = 0$,

k_{12}, k_{23}, k_{34} – stiffness coefficients, $k_{23} \gg k_{12}, k_{34}$; we will assume that $k_{23} \to \infty$,

$(z_3 - z_4)_0$ – clearance parameter,

Using Lagrange second type equations of motion one obtains initial form of the model:

$$M_1 \cdot \ddot{z}_1(t) + k_{12} \cdot (z_1(t) - z_2(t)) = F_1(t) \tag{19}$$

$$M_2 \cdot \ddot{z}_2(t) - k_{12} \cdot (z_1(t) - z_2(t)) + k_{23} \cdot luz\big((z_2(t) - z_3(t)), (z_2 - z_3)_0\big) = 0 \tag{20}$$

$$M_3 \cdot \ddot{z}_3(t) - k_{23} \cdot luz\big((z_2(t) - z_3(t)), (z_2 - z_3)_0\big) + k_{34} \cdot (z_3(t) - z_4(t)) = 0 \tag{21}$$

$$M_4 \cdot \hat{z}_4(t) - k_{34} \cdot (z_3(t) - z_4(t)) = F_4(t). \tag{22}$$

When $M_2 = 0, M_3 = 0$ the model is reduced to the differential - algebraic form. Algebraic non-linear constraints equations are:

$$-k_{12} \cdot (z_1(t) - z_2(t)) + k_{23} \cdot luz\big((z_2(t) - z_3(t)), (z_2 - z_3)_0\big) = 0 \tag{23}$$

$$-k_{23} \cdot luz\big((z_2(t) - z_3(t)), (z_2 - z_3)_0\big) + k_{34} \cdot (z_3(t) - z_4(t)) = 0. \tag{24}$$

Release from these equations and elimination of z_2, z_3 will be here made using basic formulas of luz(...) and tar(...) mathematical apparatus. These mathematical operations are following:

- Firstly, in order to reduce, we determine $z_3(t)$ from the first equation of constraints (23):

$$z_3(t) = z_2(t) - tar\left(\left(\frac{k_{12}}{k_{23}}(z_1(t) - z_2(t))\right), (z_2 - z_3)_0\right). \tag{25}$$

- Then, after setting to the second equation (24), we have

$$k_{34} \cdot \left(\frac{1}{p}\left(z_2(t) - tar\left(\left(\frac{k_{12}}{k_{23}}(z_1(t) - z_2(t))\right), (z_2 - z_3)_0\right)\right) - z_4(t)\right) = k_{12}(z_1(t) - z_2(t)) \tag{26}$$

- Hence we obtain successively:

$$z_2(t) - z_4(t) = \frac{k_{12}}{k_{34}}(z_1(t) - z_2(t)) + tar\left(\left(\frac{k_{12}}{k_{23}}(z_1(t) - z_2(t))\right), (z_1 - z_2)_0\right), \tag{27}$$

$$z_2(t) - z_4(t) = \frac{k_{12}}{k_{34}}(z_1(t) - z_2(t)) + \frac{k_{12}}{k_{23}}tar\left((z_1(t) - z_2(t)), \frac{(z_2 - z_3)_0}{\frac{k_{12}}{k_{23}}}\right), \tag{28}$$

$$z_2(t) - z_4(t) = \frac{k_{12}}{k_{34}}tar((z_1(t) - z_2(t)), 0) + \frac{k_{12}}{k_{23}}tar\left((z_1(t) - z_2(t)), \frac{(z_2 - z_3)_0}{\frac{k_{12}}{k_{23}}}\right). \tag{29}$$

- Using the formulas (5) we have:

$$z_2(t) - z_4(t) = \left(\frac{k_{12}}{k_{34}} + \frac{k_{12}}{k_{23}}\right) tar\left((z_1(t) - z_2(t)), \left(\frac{(z_2 - z_3)_0}{\frac{k_{12}}{k_{34}} + \frac{k_{12}}{k_{23}}}\right)\right). \tag{30}$$

And then

$$z_1(t) - z_2(t) = \frac{1}{\frac{k_{12}}{k_{34}} + \frac{k_{12}}{k_{23}}} luz\left((z_1(t) - z_4(t)), (z_2 - z_3)_0\right), \tag{31}$$

$$z_1(t) - z_2(t) = \frac{1}{\frac{k_{12}}{k_{34}} + \frac{k_{12}}{k_{23}}} luz(z_1(t) - z_2(t) - (z_1(t) - z_4(t)), (z_2 - z_3)_0), \tag{32}$$

i.e.

$$luz\left((z_1(t) - z_2(t)), 0\right) = \frac{1}{\frac{k_{12}}{k_{34}} + \frac{k_{12}}{k_{23}}} luz(z_1(t) - z_2(t) - (z_1(t) - z_4(t)), (z_2 - z_3)_0). \tag{33}$$

Using formulas (6) we obtain an uninvolved form

$$z_1(t) - z_2(t) = \frac{\frac{1}{\frac{k_{12}}{k_{34}} + \frac{k_{12}}{k_{23}}}}{\frac{1}{\frac{k_{12}}{k_{34}} + \frac{k_{12}}{k_{23}}} + 1} luz\left((z_1(t) - z_4(t)), (z_2 - z_3)_0\right). \tag{34}$$

By combination of the constraints equations (23), (24) we receive

$$z_1(t) - z_2(t) = \frac{k_{34}}{k_{12}} \cdot (z_3(t) - z_4(t)), \tag{35}$$

Then

$$z_3(t) - z_4(t) = \frac{k_{12}}{k_{34}}\frac{\frac{1}{\frac{k_{12}}{k_{34}} + \frac{k_{12}}{k_{23}}}}{\frac{1}{\frac{k_{12}}{k_{34}} + \frac{k_{12}}{k_{23}}} + 1} luz\left((z_1(t) - z_4(t)), (z_2 - z_3)_0\right). \tag{36}$$

Finally, assuming a substitute stiffness parameter

$$k_{14} = \frac{1}{\frac{1}{k_{12}} + \frac{1}{k_{23}} + \frac{1}{k_{34}}}, \tag{37}$$

we obtain the model without constraints equations, and without variables $z_2(t)$ i $z_3(t)$:

$$M_1 \cdot \ddot{z}_1(t) + k_{14} \cdot luz\big((z_1(t) - z_4(t)), (z_2 - z_3)_0\big) = F_1(t) \tag{38}$$

$$M_4 \cdot \ddot{z}_4(t) - k_{14} \cdot luz\big((z_1(t) - z_4(t)), (z_2 - z_3)_0\big) = F_4(t) \tag{39}$$

Note that $\quad k_{14} = \dfrac{1}{\frac{1}{k_{12}} + \frac{1}{k_{23}} + \frac{1}{k_{34}}} \quad \rightarrow \quad \dfrac{1}{\frac{1}{k_{12}} + \frac{1}{k_{34}}}$, when $\quad k_{23} \rightarrow \infty \tag{40}$

This model describes the dynamics of the system in the presence of play and infinitely high stiffness (i.e. limiter) in meshing.

5. Conclusion

The presented method of modeling strong non-linearities in vehicle suspension and non-linear vertical dynamics of a vehicle, the method based on piecewise linear luz(…) and tar(…) projections is very effective. It can be quite easily applied to more sophisticated models of suspension systems, also to 3D models. In this case, it is necessary to enter vector dependencies, which will result in a more complex non-linear description. This also applies to the spatial description of the tire - road interaction.

References

[1] Andrzejewski R., Awrejcewicz J., *Nonlinear dynamics of a wheeled vehicle*, Springer, 2005.

[2] Brogliatto B., *Nonsmooth mechanics: models, dynamics and control,* Springer, 1999.

[3] Dongu Cao, Xubin Song, Mahdi Ahmadian *Editors' perspectives: road vehicle suspension design", Special issue on „Advanced Suspension Systems and Dynamics for Future Road Vehicles".* Vehicle System Dynamics, Vol. 49, Issue 1-2, 2011.

[4] Grzesikiewicz W., *Dynamika układów mechanicznych z więzami*, Prace Naukowe Politechniki Warszawskiej. Mechanika. Nr 117, 1990 (in Polish).

[5] Lozia Z. *The use of a linear quarter-car model to optimize the damping in a passive automotive suspension system – a follow-on from many authors' works of the recent 40 years*, The Archives of Automotive Engineering – Archiwum Motoryzacji, Vol. 71, No. 1, 2016, pp. 39-71.

[6] Lozia Z., Żardecki D., *Vehicle Dynamics Simulation with Inclusion of Freeplay and Dry Friction in Steering System* (SAE Paper 2002-01-0619). SAE 2002 Transactions. Journal of Passenger Cars – Mechanical Systems, 2002, pp. 907-923.

[7] Pfeiffer F., Glocker C., *Multibody Dynamics with Unilateral Contacts*, Willey&Sons, N.York, 1996.

[8] Sharp R S. Crolla D A., *Road vehicle suspension system design – a review*. Vehicle System Dynamics, Vol.16, 1987, pp. 167-192.

[9] Żardecki D., *Piecewise Linear luz(...) and tar(...) Projections. Part 1 – Theoretical Background*. Journal of Theoretical and Applied Mechanics, Vol.44, No.1, 2006, pp. 163-184.

[10] Żardecki D., *Piecewise Linear luz(...) and tar(...) Projections. Part 2 – Application in Modeling of Dynamic Systems with Freeplay and Friction*. Journal of Theoretical and Applied Mechanics, Vol.44, No.1, 2006, pp. 185-202.

[11] Żardecki D., *Piecewise Linear Modeling of Friction and Stick-Slip Phenomenon in Discrete Dynamical Systems*. Journal of Theoretical and Applied Mechanics, Vol.44, No.2, 2006, pp. 255-277.

Dariusz Żardecki, Professor: Military University of Technology (WAT). Faculty of Mechanical Engineering, Warszawa, Poland (dariusz.zardecki@*wat.edu.pl*).

INDEX OF AUTHORS